**Title**

Strong correlation with symmetry, topology and anomaly

**Permalink**

https://escholarship.org/uc/item/3kn456ng

**Author**

Zeng, Meng

**Publication Date**

2024

Peer reviewed|Thesis/dissertation

UNIVERSITY OF CALIFORNIA SAN DIEGO

Strong correlation with symmetry, topology and anomaly

A dissertation submitted in partial satisfaction of the
requirements for the degree Doctor of Philosophy

in

Physics

by

Meng Zeng

Committee in charge:

> Professor Yi-Zhuang You, Chair
> Professor Daniel P. Arovas
> Professor Michael Galperin
> Professor Tarun Grover
> Professor Kenneth Arthur Intriligator
> Professor John A. McGreevy

2024

The Dissertation of Meng Zeng is approved, and it is acceptable in quality and form for publication on microfilm and electronically.

University of California San Diego

2024

## DEDICATION

To my family.

TABLE OF CONTENTS

# LIST OF FIGURES

# LIST OF TABLES

ACKNOWLEDGEMENTS

First and foremost I would like to thank my advisor Prof. Yi-Zhuang You for being such an amazing mentor. As someone as busy as him, Yi-Zhuang is always extremely generous with his time when it comes to his students, be it physics discussions, having food together, or just chit-chatting and gossiping about all kinds of random things. It is not uncommon that many of us were lining up to meet with him that he had no time for dinner and would just snack on something during the discussions. Yi-Zhuang is also an extremely brilliant physicist. His passion, versatility, and broad interests in various areas of physics make every conversation with him an invaluable and fun learning experience for us. I am not the smartest and often times it takes me long to understand things, and Yi-Zhuang would always tirelessly guide me through each step of the thinking process till I get a clear picture of the physics. We learned in physics that no physical quantity can be infinite, so I came to the conclusion that his patience with students is not a physical quantity in the sense of physics. There is so much more I could say about him that can fill up the pages, but it is his kindness, empathy, open-mindedness, diligence and passion for science that created such a vibrant and conducive research group that I felt deeply grateful and profoundly privileged to be part of, every second of the day.

I would also like to thank my first advisor at UCSD Prof. Congjun Wu before he left to take up a full-time position at Westlake university in China. Congjun is never short of interesting ideas and can often look at problems from refreshing perspectives. One thing I'll never forget is his "unwillingness" to look at my lengthy calculations during meetings with him because he would expect me to describe to him the essential physics without referring to the equations. As a then beginning physics graduate student, I was and had always been quite fond of manipulating with equations mathematically, and trying to see what came out of the math, which indeed worked fine for those well-established textbook results, but not for open-ended research problems as it turned out. After countless times of struggling to paint a clear physical picture of the problem without using equations in Congjun's office and witnessing him doing it effortlessly, I slowly started to pick up bits and pieces on how to do it myself. Now it has become a part of me

and it is my personal gold standard to determine whether I truly understand something or not.

As for the life as a graduate student, I am always grateful to have been able to be around a group of brilliant young people that are either post-docs, graduate student or undergraduate students. I have had the great privilege to work with and learn from many of them. In particular, Lei Su, Dr. Lun-Hui Hu, Dr. Hong-Ye Hu, Da-Chuan Lu, Wanda Hou and Dr. Juven Wang. I would also like to thank the so many friends I made over the years in playing table tennis, either on the UCSD team or the clubs off-campus. Table tennis is my passion outside of physics, and my table tennis friends are like my other family. When research life becomes challenging and stressful, I could always get my mind off the problem for a while by hitting some ping pong balls with them, followed by some nice food together. I could not imagine my graduate life here without them.

Last but not least, I would of course like to thank my parents, who came from a modest background without the privilege of receiving the education that I did but nevertheless did a fantastic job in raising me and being supportive of whatever decision I made for myself along the way even if they have no idea what was going on most of the time. At the same time, I am also blessed with a large family that is loving and caring, my cousins that I grew up with, my uncles and aunts and my grandparents. I wish my grandpa is still here with us, I knew he would be the proudest grandpa in the world if he sees me walking on that podium. My family is part of me and shaped what I am today. Nothing is possible without them.

Chapter 1, in full, is a reprint of the material as it appears in Meng Zeng, Zheng Zhu, Juven Wang, and Yi-Zhuang You, Physical Review Letters 128 (18), 185301 (2022).

Chapter 2, in full, is a reprint of the material as it appears in Da-Chuan Lu, Meng Zeng, Juven Wang, and Yi-Zhuang You, Physical Review B 107 (19), 195133 (2023).

Chapter 3, in full, is a reprint of the material as it appears in Da-Chuan Lu, Meng Zeng, and Yi-Zhuang You, Physical Review B 108 (20), 205117 (2023).

Chapter 4, in part, Meng Zeng, Fu Xu, Da-Chuan Lu, and Yi-Zhuang You, is currently being prepared for submission for publication of the material.

Chapter 5, in full, Lei Su and Meng Zeng, is recently accepted in Physical Review B.

Chapter 6, in full, is a reprint of the material as it appears in Meng Zeng, Lun-Hui Hu, Hong-Ye Hu, Yi-Zhuang You, and Congjun Wu, Science China Physics, Mechanics & Astronomy 67 (3), 237411 (2024)

Chapter 7, in full, is a reprint of the material as it appears in Meng Zeng, Dong-Hui Xu, Zi-Ming Wang, Lun-Hui Hu, and Fu-Chun Zhang, Communications Physics 7 (1), 10 (2024)

Chapter 8, in full, is a reprint of the material as it appears in Meng Zeng, Dong-Hui Xu, Zi-Ming Wang, and Lun-Hui Hu, Physical Review B 107 (9), 094507 (2023)

Chapter 9, in part, Zi-Ming Wang, Meng Zeng, Chen Lu, Da-Shuai Ma, Rui-Xing Zhang, Lun-Hui Hu, and Dong-Hui Xu, is currently being prepared for submisson for publication of the material.

# VITA

2014   Bachelor of Science, Nanyang Technological University, Singapore

2014–2015 Teaching Assistant, Nanyang Technological University, Singapore

2016–2017 Research Assistant, Nanyang Technological University, Singapore

2024   Doctor of Philosophy, University of California San Diego

ABSTRACT OF THE DISSERTATION

Strong correlation with symmetry, topology and anomaly

by

Meng Zeng

Doctor of Philosophy in Physics

University of California San Diego, 2024

Professor Yi-Zhuang You, Chair

In this thesis, I will present mainly three directions of research: symmetric mass genera-
tion (SMG), anomaly-constrained gapless quantum phases, and unconventional superconductivity.

SMG is a new mass generation mechanism through strong interactions that preserve the symmetries, different from the conventional Yukawa-Higgs mechanism. I will discuss its applications in chiral lattice gauge theory, symmetric gapping of Fermi liquids, Green's function properties and the corresponding optical responses of SMG insulators. Then I will discuss about emergent anomalies in many-body systems, and its implications for low-energy phases. In particular, we will see how gapless symmetry protected topological phases and symmetry-enriched topological ordered phases can arise through through effective partial gauging. Last but not least, for the unconventional superconductivity part, I will focus on the exotic time-reversal symmetry breaking normal state of multi-gap superconductors, and the stabilization and topology of superconductors with pairings involving multiple orbitals.

# Introduction

One of the most fascinating and fundamental questions in physics is the origin of mass. In the Standard Model of elementary particles, that question has been convincingly answered by the Higgs mechanism, which involves symmetry breaking. For the past 15 years or so, it has been realized there is another mass generation mechanism through symmetry-preserving strong interactions, named symmetric mass generation (SMG). SMG has numerous applications in both high-energy physics and condensed matter physics, and it will be the topic of the first four chapters of the thesis. The first application of SMG we will be looking at is the lattice regularization of chiral fermions, which is a long-standing problem in high-energy physics due to the fermion doubling problem. In Chapter 1 of the thesis we provided a valid lattice regularization scheme in 1d chiral gauge theory by studying the anomaly-free 3-4-5-0 chiral fermion model based on the mirror fermion approach, first proposed almost 40 years ago. We realized the 1d chiral fermion theory on the edges of a 2d Chern insulator, with one edge called the chiral light sector and the opposite edge called the mirror sector. Using the density matrix renormalization group numerical method, we successfully demonstrated that the mirror sector can be gapped through the SMG mechanism by introducing strong symmetry-preserving interactions, while the chiral light sector remains gapless. Our work represents an important step towards the full resolution of the long-standing chiral fermion problem in the Standard Model. Furthermore, the important role played by Chern insulators in the process is another nice example showcasing the synergistic relation between condensed matter physics and high-energy physics, which contributes even more to my fascination in this area.

As a followup work detailed in Chapter 2, we found the exact 1d lattice regularization of

the 3-4-5-0 chiral fermion model, where there are two bands of lattice fermions with the four Fermi points representing the four fermion flavors at low energy. This way, SMG is generalized to systems at finite density, i.e. with Fermi surfaces. The Fermi surfaces can be symmetrically gapped as long as the Fermi surface anomaly vanishes. We also studied a concrete lattice model in 2d, where there are two species of fermions whose fillings have to satisfy certain relations in order to cancel the anomaly, similar to the Lieb-Shultz-Mattis anomaly. The existence of a symmetrically gapped phase is also numerically verified.

In another followup work, we investigate in Chapter 3 the Green's function zeros of the SMG phase, after the anomaly-free Fermi surface is symmetrically gapped out. We found that after the Fermi surface, which is a surface of Green's function poles, is gapped, a surface of Green's function zeros, called the Luttinger surface, appears. We verified both analytically and numerically that the volume enclosed by the Luttinger surface is the same with that enclosed by the Fermi surface. Therefore, in the gapped SMG phase, the Luttinger theorem still holds, where the Luttinger volume is now determined by the Luttinger surface instead of the Fermi surface. This is in stark contrast with gapping the Fermi surface by symmetry breaking orders, which do not have a Luttinger surface in the gapped phase. We also discussed the possible experimental detection of Green's function zeros using spectroscopy.

In Chapter 4, inspired by a recent work claiming non-trivial electromagnetic response using an effective field theory constructed from SMG Green's function in relativistic setting, we investigate further this counter-intuitive result using concrete but general lattice models. Our results, in contrast, show that in the well-regularized lattice models, the SMG insulator does not have low-energy electromagnetic responses. We claim the discrepancy comes from their incorrect definition of current operator in the constructed effective theory. In particular, in the presence of Green's function zeros, their current operator turns out to be unbounded.

Chapter 5 switches gear to my other current interest involves the role of quantum anomaly and topology in many-body physics. These non-perturbative measures are extremely powerful and elegant, and can often provide important insight on the possible phases and the transitions

between them. In a recent work, we look at a system in d-dimensions with a continuous global symmetry $G$, where one of its finite normal subgroup $N$ is gauged by coupling to discrete gauge degrees of freedom. After the gauging, there will be a dual $(d-1)$-form symmetry , giving rise to the new global symmetry $G/N \times \hat{N}$. Under certain conditions $G/N$ and $\hat{N}$ can have a mixed anomaly, which implies the ground state cannot be trivially gapped. In the specific example of $Z_2$-gauged boson-Hubbard model in two spatial dimensions, the symmetry is $U(1)$ and a 1-form $\hat{Z}_2$, with a mixed anomaly between them. The ground state is either a $U(1)$-enriched topological order (with 1-form $\hat{Z}_2$ broken) or a superfluid ($U(1)$ broken) with the 1-form $\hat{Z}_2$ preserved. We also showed that the superfluid phase is also a gapless symmetry-protected topological phase with symmetry protected edge modes when there is an open boundary. The transition between the two exotic phases is a generalized deconfined critical point.

Another important part of my research is concerned with the intriguing world of un-conventional SC, whose pairings are different from the ordinary BCS type. After decades of development, unconventional SC still remains one of the most active and exciting areas of research. Many unconventional SCs feature intriguing interplay between multiple gap functions. In Chapter 6 we explore a generic subclass of systems with two gaps that belong to different sym-metry representations and therefore the lowest order of coupling is of the second order Josephson type. The second order coupling could lead to Ising symmetry breaking, resulting in a time-reversal symmetry breaking phase or nematic phase. By doing loop-level renormalization group analysis, we discovered that Ising symmetry breaking can occur at a temperature higher than the superconducting transition, indicating that the normal state can exhibit symmetry-breaking phases due to Josephson coupling before transitioning to the superconducting state. Surprisingly, we also observed the emergence of the elusive charge-4e state as another possible intermediate phase, where not Cooper pair but pairs of Cooper pairs, four electrons each in total, condense. As of now, both of the two exotic phases have been observed in recent experiments.

Another large class of unconventional superconductors happens in materials involving multiple orbitals. However, orbital-dependent pairings have been under explored due to the

conventional belief that such pairings are energetically unfavorable because the degeneracy of the two orbitals is lifted by orbital hybridization or crystal field splitting. In Chapter 7, by solving the weak-coupling linearized gap equation, we showed that orbital-dependent pairing can actually be stabilized as long as the pairing satisfies certain condition determined by the effective orbital hybridization in the system. This opened up a plethora of new possibilities for systems consisting of multiple orbitals, for example valley or sublattice degrees of freedom. With this general result established, we further considered the mixing of even parity spin-singlet orbital triplet pairing with spin-singlet orbital independent pairing. The mixing is allowed since they belong to the same symmetry representation. We showed that such mixing can give rise to either nodal or fully gapped SCs, which can be used to explain the gap features in certain Fe-based SCs.

Building on the results in Chapter 7, we explore in Chapter 8 various interesting properties of orbital-dependent pairings. One fascinating phenomenon is Pauli limit violation, i.e. the large in-plane upper critical field, due to the existence of atomic SOC, which has different mechanism from that of a type II Ising SC. Another interesting result is the onset of time-reversal invariant/breaking topological SCs with helical/chiral Majorana edge states, in the absence of external applied magnetic field or Zeeman field. Furthermore, when the orbital-dependent pairing spontaneously breaks time-reversal symmetry, the resultant orbital polarization will induce spin polarization due to the SOC even though the pairing is spin-singlet. The spin-resolved density of states has asymmetrical gap, in contrast to that of a spin-triplet SC.

As another followup, in Chapter 9 we look at the possibility of higher-order topology in multi-orbital systems. In contrast to the usual 1st-order topology with gapless surface states, higher-order topological phases have gapped surface and only have zero modes at the kinks (corners, hinges, etc) of the surface. In particular we considered the time-reversal breaking $d + id$-wave SC in 2d, where one of the d-wave gaps is orbital-independent and the other is orbital-dependent. We demonstrated that this fully gapped SC can have Majorana zero modes at the corners but not on the edges, due to the non-trivial 2nd-order topology protected by rotation, in stark contrast with the conventional chiral d-wave SC with chiral edge states.

# Chapter 1

# Symmetric mass generation in the 1 + 1 dimensional chiral fermion 3-4-5-0 Model

# Symmetric Mass Generation in the 1 + 1 Dimensional Chiral Fermion 3-4-5-0 Model

Meng Zeng[1], Zheng Zhu[2,3] Juven Wang[4] and Yi-Zhuang You[1]

[1]*Department of Physics, University of California San Diego, La Jolla, California 92093, USA*
[2]*Kavli Institute for Theoretical Sciences, University of Chinese Academy of Sciences, Beijing 100190, China*
[3]*CAS Center for Excellence in Topological Quantum Computation, University of Chinese Academy of Sciences, Beijing 100190, China*
[4]*Center of Mathematical Sciences and Applications, Harvard University, Cambridge, Massachusetts 02138, USA*

Lattice regularization of chiral fermions has been a long-standing problem in physics. In this Letter, we present the density matrix renormalization group simulation of the 3-4-5-0 model of $(1 + 1)D$ chiral fermions with an anomaly-free chiral U(1) symmetry, which contains two left-moving and two right-moving fermions carrying U(1) charges 3,4 and 5,0, respectively. Following the Wang-Wen chiral fermion model, we realize the chiral fermions and their mirror partners on the opposite boundaries of a thin strip of $(2 + 1)D$ lattice model of multilayer Chern insulator, whose finite width implies the quantum system is effectively $(1 + 1)D$. By introducing two sets of carefully designed six-fermion local interactions to the mirror sector only, we demonstrate that the mirror fermions can be gapped out by the interaction beyond a critical strength without breaking the chiral U(1) symmetry, via the symmetric mass generation mechanism. We show that the interaction-driven gapping transition is in the Berezinskii-Kosterlitz-Thouless universality class. We determine the evolution of Luttinger parameters before the transition, which confirms that the transition happens exactly at the point when the interaction term becomes marginal. As the mirror sector is gapped after the transition, we check that the fermions in the light chiral fermion sector remain gapless, which provides the desired lattice regularization of chiral fermions.

*Introduction.*—It has been a long-standing issue to regularize chiral gauge theories (e.g., the weak interaction in the standard model) on the lattice due to the Nielsen-Ninomiya no-go theorem [1], which asserts that any free fermion lattice model in even-dimensional spacetime with locally realized chiral symmetry will necessarily give rise to equal numbers of left-handed and right-handed fermion fields at low energy, hence rendering the theory vectorlike. Over the past few decades, much effort [2–7] has been devoted to circumventing the fermion doubling problem by lifting different assumptions of the no-go theorem.

In particular, the no-go theorem assumes the fermion theory to be infrared free, i.e., fermion interactions, if there are any, must be perturbatively irrelevant under the renormalization group (RG) flow. Lifting this assumption by introducing nonperturbative (strong enough) fermion interactions could potentially circumvent the problem. Efforts along this line are generally referred to as the mirror fermion approach, which dates back to Eichten and Preskill [8]. The basic idea is to start with a vectorlike theory containing both chiral fermions and their mirror fermion partners, which can be put on a lattice without any issue. Then one attempts to generate a mass gap in the mirror sector by introducing interactions among mirror fermions, such that the remaining light (chiral fermion) sector survives in the low-energy spectrum, providing the basis for lattice realizations of chiral gauge theories.

However, early numerical tests [9–18] appeared to invalidate the mirror fermion approach, as strong fermion interactions typically result in the condensation of fermion bilinear mass at low energy, which spontaneously breaks the chiral symmetry and gaps out the light sector together with the mirror sector.

In recent years, a series of developments [19–34] in the many-body quantum matter community have significantly deepened our understanding. It is realized that in order to gap out the mirror sector by interactions without breaking the chiral symmetry, two conditions must be satisfied: (i) the mirror fermions must be *anomaly free* under the full spacetime-internal symmetry, (ii) the interaction must be appropriately designed to satisfy certain *consistent gapping* conditions [26,33]. Along this line, recent numerical studies [35–51] have successfully demonstrated examples of interaction-driven fermion mass generation without spontaneous symmetry breaking in various spacetime dimensions. The phenomenon is known as the symmetric mass generation (SMG) [52–56]. Therefore, solving the chiral fermion problem boils down to achieving the SMG for mirror fermions in even spacetime dimensions.

Nevertheless, most numerical works realizing SMG in even spacetime dimensions have been focused on vectorlike lattice models [39–41,44,45,48,49,51], which still have some distance from the goal of regularizing chiral fermions. Recently, Catterall [50] studied the SMG of a chiral

fermion lattice model with a chiral discrete $\mathbb{Z}_4$ symmetry. In this work, we demonstrate the SMG in the 3-4-5-0 model of $(1 + 1)D$ chiral fermions that cancels the $\mathbb{Z}$-class *perturbative* local anomaly of the chiral continuous U(1) symmetry, which is closer to the situation of perturbative chiral anomaly cancellation in the $3 + 1D$ standard model [such as the chiral $U(1)_Y$ electroweak hypercharge]. We propose a lattice model of interacting fermions, and investigate the model using the density matrix renormalization group (DMRG) numerical method [57,58]. Our numerical results provide clear evidence for the SMG in the mirror sector, successfully achieving our goal of regularizing chiral fermions in the 3-4-5-0 model on a lattice.

*The 3-4-5-0 model.*—The 3-4-5-0 model describes four gapless complex fermions in $(1 + 1)D$,

$$S = \int dt\, dx \sum_{I=1}^{4} \psi_I^\dagger (i\partial_t + iv_I\partial_x)\psi_I, \qquad (1)$$

with two left-moving modes $\psi_1$, $\psi_2$ (of $v_1 = v_2 = +1$) and two right-moving modes $\psi_3$, $\psi_4$ (of $v_3 = v_4 = -1$). The fermions are charged under a chiral U(1) symmetry: $\psi_I \to e^{iq_I\theta}\psi_I$, with the charge assignment $(q_1, q_2, q_3, q_4) = (3, 4, 5, 0)$ (hence the name "3-4-5-0"). This seemingly peculiar charge assignment is designed to cancel the U(1) symmetry's 't Hooft anomaly, which is a $\mathbb{Z}$-class perturbative local anomaly. The anomaly index is given by $\sum_I v_I q_I^2 = 3^2 + 4^2 - 5^2 - 0^2 = 0$, which vanishes for the charge assignment of the 3-4-5-0 model. The model is also free of the gravitational anomaly. As the field theory is anomaly-free, it should admit a lattice regularization in $(1 + 1)D$ spacetime.

Following Wang-Wen's chiral fermion model [26,33], the $(1 + 1)D$ chiral fermions and their mirror partners can be viewed as the chiral edge modes on the opposite boundaries of a $(2 + 1)D$ multilayer Chern insulator [59], each layer with a Chern number $\pm 1$. To construct the chiral fermions on a lattice, we start with four layers of Chern insulators on a two-leg ladder as shown in Fig. 1(a). On each lattice site $i$, we introduce four complex fermions, described by the annihilation operators $\psi_{i,I}$ (with $I = 1, 2, 3, 4$ being the layer or flavor index). The fermion hopping is governed by the lattice Hamiltonian

$$H_{\text{free}} = \sum_{I=1}^{4} \sum_{i,j} (t_{I,ij}\psi_{I,i}^\dagger \psi_{I,j} + \text{H.c.}), \qquad (2)$$

where the hopping parameters $t_{I,ij}$ are nonzero only on the nearest and next-nearest-neighbor links. For the first two layers $I = 1, 2$, the nearest neighbor hoppings are purely imaginary with $t_{I,ij} = e^{i\pi/4}t_1$ if $j \to i$ follows the link direction, and the next-nearest neighbor hoppings are real with $t_{I,ij} = t_2$ (or $-t_2$) on the solid (or dashed) links, as shown in Fig. 1(a). We fix $t_1 = 1$ and $t_2 = 0.5$. This
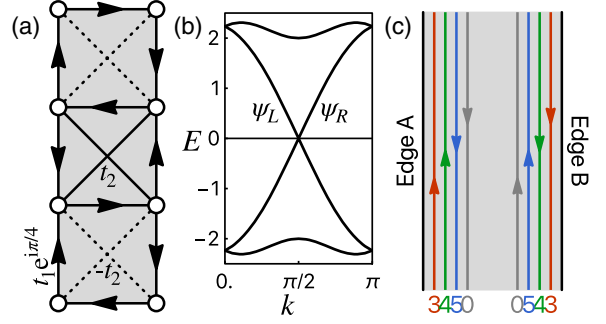


FIG. 1. (a) The fermion hopping pattern on the two-leg ladder lattice for the first layer. Arrow link: $t_1 e^{i\pi/4}$ (along the arrow direction); solid link: $t_2$; dashed link: $-t_2$. This $(2 + 1)D$ thin strip is effectively the same as $(1 + 1)D$ by regarding the finite-width dimension as internal degrees of freedom of the $(1 + 1)D$ system. (b) Energy dispersion for $t_1 = 1$, $t_2 = 0.5$. Gapless edge modes are strictly localized on the two boundaries of the ladder. (c) Schematic diagram showing the configuration of the four flavors of chiral fermions on the edges.

hopping pattern ensures a $\pi$ Berry flux through each square plaquette, realizing a minimal model of Chern insulator in each layer. For the last two layers $I = 3, 4$, the hopping parameters are complex conjugated, such that the band Chern numbers in the last two layers are opposite to those of the first two layers.

The lattice model has a four-site unit cell that repeats along the ladder direction, hence the lattice momentum $k$ along the ladder direction is a good quantum number, and the system is effectively $(1 + 1)D$. In each layer, the single-particle energy dispersion (band structure) is shown in Fig. 1(b), which includes two gapped bulk bands together and two gapless edge modes of opposite velocities (localized separately on the two boundaries). Stacking all layers together, the lattice model realizes four chiral fermions (as two pairs of counterpropagating modes) on each edge, as illustrated in Fig. 1(c). Since the four layers of fermions are decoupled at the free fermion level, we are free to assign them with the 3,4,5,0 chiral U(1) charges, respectively, such that the low-energy edge modes realize the 3-4-5-0 chiral fermions and their mirror partners. We treat the edge $A$ as the light (chiral fermion) sector, and the edge $B$ as the mirror sector (to be gapped out). If we can generate a mass gap for the edge $B$ fermions only without breaking the chiral U(1) symmetry, we will succeed in achieving a lattice regularization of the 3-4-5-0 field theory Eq. (1) in this $(1 + 1)D$ system in terms of the gapless edge $A$ fermions.

The fact that the U(1) 't Hooft anomaly vanishes for the 3-4-5-0 model indicates that it should be possible to gap out the edge $B$ fermions trivially without breaking the chiral U(1) symmetry. However, the chiral U(1) symmetry is restrictive enough to prevent the gapping to happen on the free-fermion level, because any fermion bilinear term that produces a gap must take the form of $\psi_I^\dagger \psi_J$ (Dirac mass) or $\psi_I \psi_J$ (Majorana mass), with $I \in \{1, 2\}$ and $J \in \{3, 4\}$, that

mixes the left- and right-moving fermions. Since the four layers of fermions all carry distinct chiral U(1) charges that do not add or subtract to zero, any layer-mixing fermion bilinear term necessarily breaks the chiral U(1) symmetry explicitly. The symmetry breaking mass on the $B$ edge will also induce similar bilinear mass for the edge $A$ fermion by the proximity effect, thereby gapping out all fermions together.

Therefore, we resort to the idea of gapping out the mirror fermions by interactions, which has been previously explored by Chen, Giedt, and Poppitz (CGP) [18] in the 3-4-5-0 lattice model, where all U(1) symmetry allowed interactions are included. Unfortunately, the CGP result shows a singular nonlocal behavior for the gauge field polarization tensor in the mirror sector, which indicates the mirror sector still has surviving gapless modes charged under the gauge field. The reason could be that the CGP approach introduces too many interaction terms, and some of them are harmful. In order to achieve the SMG, the fermion interaction must be carefully selected to satisfy the gapping condition (i.e., the interaction operators must be self-bosonic and mutual-bosonic in terms of the operator braiding statistics [60–63]), as elaborated in recent works [26,33]. It turns out that the lowest order interactions that satisfy the gapping condition are the following six-fermion local interactions [26],

$$H_{int} = \sum_{i \in B} g_1 (\psi_{1,i}\psi_{2,i}^\dagger\psi_{2,i+1}^\dagger\psi_{3,i}\psi_{4,i}\psi_{4,i+1} + H.c.)$$
$$+ g_2 (\psi_{1,i}\psi_{1,i+1}\psi_{2,i}\psi_{3,i}^\dagger\psi_{3,i+1}^\dagger\psi_{4,i} + H.c.). \quad (3)$$

These are seemingly irrelevant dimension-five operators in the perturbative RG around the gapless free fermion fixed point. The interaction respects the chiral U(1) symmetry, and is only applied to sites on the $B$ edge (denoted as $i \in B$), with $i + 1$ being the next site of $i$ along the $B$ edge. The interaction looks highly irrelevant in the free-fermion limit. However, strong enough interaction (strong in the sense that the interaction energy scale $E_{int}$ is large but still in the same order of magnitude as the kinetic energy $E_{free}$, thus $E_{int}/E_{free} \simeq \mathcal{O}(1)$ is nonperturbative) may still generate nonperturbative effect that gaps out the edge $B$ fermions. Our central goal is to numerically verify that the proposed interaction Eq. (3) indeed drives the SMG in and only in the mirror sector.

*DMRG results.*—We study the lattice model $H = H_{free} + H_{int}$ by the DMRG method [57] using the ITensor software library [64]. For simplicity, we set $g_1 = g_2 = g$ as the only interaction parameter. The simulation is performed on a two-leg ladder of 20 unit cells, where three different matrix product state bond dimensions $\mathcal{D} = 6000$, 7000, and 8000 are used [65]. Computed physical quantities are then extrapolated to the $\mathcal{D} \to \infty$ limit assuming a $1/\mathcal{D}$ scaling. Figure 2 shows the ground state energy $E_{GS}$ (of the full Hamiltonian $H$) per unit cell as a function of the interaction strength $g$, where the inset shows its first-order
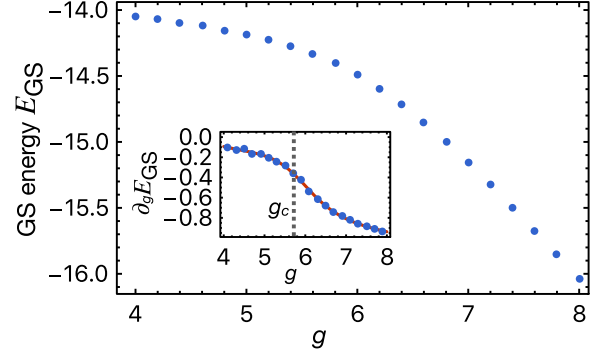


FIG. 2. Ground state (GS) energy per unit cell as a function of interaction strength $g$. The inset shows the first-order derivative of the GS energy with respect to $g$. The features around $g \approx 5.7$ (indicated by the gray dashed line) signal a quantum phase transition.

derivative $\partial_g E_{GS}$. The onset of a nonzero $\partial_g E_{GS} = g^{-1}\langle H_{int}\rangle$ around $g_c \approx 5.7$ signifies the development of the $\langle H_{int}\rangle \neq 0$ condensation across the SMG transition. The smooth kink of $\partial_g E_{GS}$ indicates a (high-order) continuous transition.

To further confirm the existence of the critical point $g_c$, we calculate the fermion correlation functions $C_\psi(r) \equiv \langle\psi_{I,i+r}^\dagger\psi_{I,i}\rangle$ on both edge $A$ and edge $B$ across the transition. It turns out that the behavior of $C_\psi$ is the same for all $I = 1, 2, 3, 4$, such that it is sufficient to show one of the four flavors. Figures 3(a), 3(c) and Figs. 3(b), 3(d) show
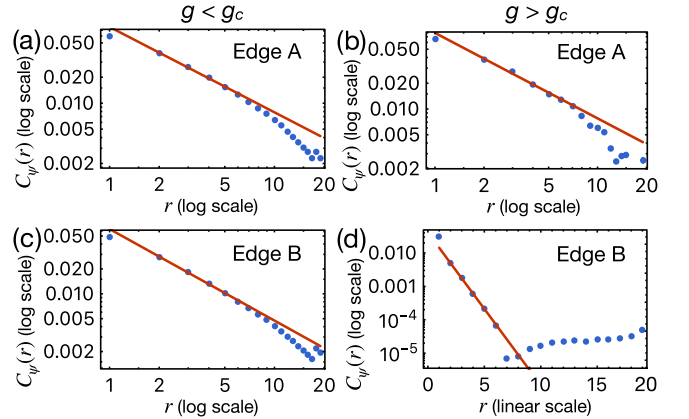


FIG. 3. Correlations on both edges before and after transition. Linear fit (red line) is performed for intermediate distances from $r = 2$ to $r = 6$ in each case, in order to faithfully extract the low energy physics while avoiding the artifacts due to the gap caused by finite bond dimension in the matrix product state representation. (a) $g = 5.0 < g_c$ for edge $A$. The log-log plot shows a power-law decay for intermediate distances. (b) $g = 7.0 > g_c$ for edge $A$. The log-log plot again shows a power-law decay. (c) $g = 5.0 < g_c$ for edge $B$. The log-log plot shows a power-law decay. (d) $g = 7.0 > g_c$ for edge $B$. The semilog plot indicates an exponential decay, i.e., edge $B$ becomes gapped.
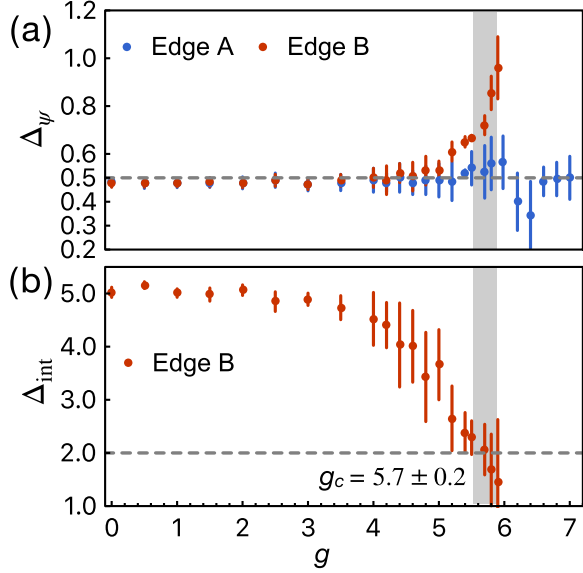
FIG. 4. (a) The evolution of fermion scaling dimension $\Delta_\psi$ on both edges as the interaction strength $g$ approaches the critical point. The scaling dimension is obtained from the power-law fitting as in Fig. 3. The horizontal dashed line indicates the free fermion limit. The gray stripe shows the estimated critical interaction strength $g_c$ with some uncertainty. (b) The solved scaling dimension for the interaction terms on edge $B$ based on the scaling dimensions of multiple operators (refer to SM, Sec. III [66] for details). The horizontal dashed line indicates the marginal value 2 of $\Delta_{\text{int}}$, across which the phase transition is expected to happen.

the correlation functions for each edge before and after the transition, respectively. We observe that edge $A$ is always gapless with power-law correlations. In contrast, edge $B$ is gapless when $g < g_c$ but becomes gapped with an exponential-decay correlation when $g > g_c$. The two qualitatively different behaviors must be separated by a quantum phase transition.

By fitting the power-law correlation function $C_\psi(r) \sim 1/r^{2\Delta_\psi}$ before the transition, we can extract the fermion scaling dimension $\Delta_\psi$ on both edges. The result is shown in Fig. 4(a). In the free-fermion limit ($g = 0$), the fermion scaling dimension is $\Delta_\psi = \frac{1}{2}$ on both edges. The finite-size effect tends to reduce the scaling dimension slightly. A finite-size scaling of the scaling dimension in the free fermion limit is performed in Supplemental Material (SM), Sec. I [66], confirming that our result converges to the long-distance limit correctly. As $g$ increases toward $g_c$, the fermion scaling dimension on the edge $B$ increases continuously from $\frac{1}{2}$ to about 0.67 (near $g_c$), indicating that fermion operators get renormalized by the interaction significantly. For $g > g_c$, the correlation on the edge $B$ becomes short-ranged, such that the fermion scaling dimension is no longer defined (although the power-law fitting on the finite-size data will continue give some estimated exponent that extrapolates beyond the critical

point before the correlation length shrinks below the system size). However, on the edge $A$, the fermion scaling dimension, while experiencing some fluctuations near the critical point, generally stays close to the free fermion limit regardless of the interaction strength. The scaling dimension remains stable even after $g$ goes across the transition point $g_c$ by a significant amount. This implies that the edge $A$ remains gapless and almost free, as the edge $B$ interaction can only induce a perturbative interaction on the edge $A$ through the proximity effect.

To verify that the chiral U(1) symmetry is not broken spontaneously by the condensation of fermion bilinear masses, we measure correlation functions of Dirac and Majorana mass operators on the $B$ edge, i.e., $C_{\psi_I^\dagger \psi_J}(r) \equiv \langle \psi_{J,i+r}^\dagger \psi_{I,i+r} \psi_{I,i}^\dagger \psi_{J,i} \rangle$ and $C_{\psi_I \psi_J}(r) \equiv \langle \psi_{J,i+r}^\dagger \psi_{I,i+r} \psi_{I,i} \psi_{J,i} \rangle$. Figure 2 in SM, Sec. II [66] shows the correlations for all the eight mass terms are short-ranged (exponential decay) along the $B$ edge in the strong coupling gapped phase ($g > g_c$), which confirms that the mirror fermions on the $B$ edge are gapped by the SMG mechanism without long-range ordering of bilinear masses. Therefore, the remaining gapless fermions on the $A$ edge successfully realize the lattice regularization of chiral fermions in the 3-4-5-0 model preserving the chiral U(1) symmetry.

*Luttinger liquid RG analysis.*—To better understand the nature of the SMG transition at $g_c$, we perform the Luttinger liquid RG analysis for the edge $B$ fermions. We first bosonize the mirror fermions by $\psi_I \sim e^{i\phi_I}$. Then the $(1 + 1)D$ interacting mirror fermions can be described by the Luttinger liquid effective field theory in terms of the $\phi = (\phi_1, \phi_2, \phi_3, \phi_4)^\intercal$ fields

$$\mathcal{L} = \frac{1}{4\pi}(\partial_t \phi^\intercal K \partial_x \phi + \partial_x \phi^\intercal V \partial_x \phi) + \sum_{\alpha=1,2} g_\alpha \cos(l_\alpha^\intercal \phi), \quad (4)$$

where $K = \sigma^{30}$ and $V = \sigma^{00}$ (in the uv limit) are $4 \times 4$ matrixes (where $\sigma^{\mu\nu} = \sigma^\mu \otimes \sigma^\nu$ denotes the tensor product of Pauli matrices). The two interaction terms $g_1$, $g_2$ in Eq. (3) correspond to the cosine terms in Eq. (4) specified by the vectors $l_1 = (1, -2, 1, 2)^\intercal$ and $l_2 = (2, 1, -2, 1)^\intercal$, respectively. The RG flow with respect to the log-energy-scale $\ell = -\ln \Lambda$ is given by [67]

$$\frac{dg_\alpha}{d\ell} = (2 - \Delta_{l_\alpha})g_\alpha - \frac{1}{2}\sum_{l_\beta \pm l_\gamma = l_\alpha} g_\beta g_\gamma,$$

$$\frac{dV^{-1}}{d\ell} = \frac{1}{2}\sum_\alpha g_\alpha^2(K^{-1}l_\alpha l_\alpha^\intercal K^{-1} - V^{-1}l_\alpha l_\alpha^\intercal V^{-1}), \quad (5)$$

where $\Delta_l = \frac{1}{2}l^\intercal V^{-1}l$ denotes the scaling dimension of the vertex operator $e^{il^\intercal \phi}$. Under the RG flow, the $V$ matrix gets renormalized to the general form

$$V = \sqrt{1 + y_1^2 + y_2^2}\sigma^{00} - y_1\sigma^{10} - y_2\sigma^{22}, \quad (6)$$

TABLE I. Operator scaling dimensions and Luttinger parameters at the free-fermion limit ($g = 0$) and at the critical point ($g = g_c$).

| | $l^{\mathsf{T}}$ | $\Delta_l$ | Free | Critical |
|---|---|---|---|---|
| $\psi_1$ | $(1,0,0,0)$ | $\frac{1}{2}\sqrt{1 + y_1^2 + y_2^2}$ | $\frac{1}{2}$ | $0.67 \pm 0.07$ |
| $\psi_1^\dagger \psi_3$ | $(-1, 0, 1, 0)$ | $\sqrt{1 + y_1^2 + y_2^2} - y_1$ | $1$ | $0.76 \pm 0.05$ |
| $\psi_1 \psi_4$ | $(1,0,0,1)$ | $\sqrt{1 + y_1^2 + y_2^2} - y_2$ | $1$ | $0.73 \pm 0.01$ |
| | | $y_1$ | $0$ | $0.72 \pm 0.18$ |
| | | $y_2$ | $0$ | $0.70 \pm 0.15$ |

where $y_1$, $y_2$ are Luttinger parameters that depend on the RG scale $\ell$. Table I concludes the scaling dimensions of the fermion, Dirac mass, and Majorana mass operators. We numerically determine the scaling dimensions of these operators before the transition ($g < g_c$), by fitting the power-law exponents of their correlation functions (see SM Sec. III [66] for details).

From the scaling dimensions, we infer the Luttinger parameters $y_1$, $y_2$, and calculate the scaling dimension of the interaction operator $\Delta_{\text{int}} := \Delta_{l_1} = \Delta_{l_2} = \sqrt{1 + y_1^2 + y_2^2} - 3y_1 - 4y_2$. The evolution of $\Delta_{\text{int}}$ is shown in Fig. 4(b), which drops continuously from $\Delta_{\text{int}} = 5$ at the free-fermion limit ($g = 0$) to $2.17 \pm 0.27$ at the SMG transition ($g = g_c$). Although the interaction is perturbatively irrelevant at the free-fermion fixed point, finite strength of the interaction can renormalize the Luttinger parameter, which reduces its own scaling dimension. Our numerical result indicates that the SMG transition is triggered exactly when the interaction scaling dimension is reduced to marginal $\Delta_{\text{int}} = 2$, which matches the mechanism of the Berezinskii-Kosterlitz-Thouless (BKT) transition. This scenario was also proposed by Tong in a recent theoretical study [55]. Our numerical study provides more detailed RG analysis and more solid evidence in support of the BKT transition scenario.

*Conclusion and discussions.*—We numerically demonstrate the lattice regularization of $(1 + 1)D$ chiral fermions in the 3-4-5-0 model. This is achieved by gapping out the anomaly-free mirror sector using properly designed interactions via the SMG mechanism, leaving the light sector gapless. By simulating the lattice model with the DMRG method, we identify the SMG transition point $g_c$. In the strong coupling phase ($g > g_c$), we show that the mirror fermions are gapped without breaking the chiral symmetry, and the light fermions remain gapless. We numerically determine the scaling dimension of the interaction operator before the transition, which evolves continuously from irrelevant to marginal. This behavior clearly indicates the BKT nature of the SMG transition in our model. Once the anomaly-free U(1) symmetry is dynamically gauged, we expect to obtain a $(1 + 1)D$ lattice chiral gauge theory coupled to chiral fermions, which could potentially be simulated by the quantum Monte Carlo method [68], as our

proposed six-fermion interaction in Eq. (3) admits the following Yukawa decomposition (with site indices omitted for brevity)

$$
\begin{aligned}
H_{\text{Yuk}} = &(\phi_1^2 \psi_1 \psi_3 + \phi_1^\dagger \psi_2^\dagger \psi_4 + \text{H.c.}) + \frac{1}{\tilde{g}_1} \phi_1^\dagger \phi_1 \\
&+ (\phi_2^2 \psi_2 \psi_4 + \phi_2^\dagger \psi_1 \psi_3^\dagger + \text{H.c.}) + \frac{1}{\tilde{g}_2} \phi_2^\dagger \phi_2, \quad (7)
\end{aligned}
$$

such that integrating out the Yukawa bosons $\phi_\alpha$ reproduces our interaction at the leading order of $g_\alpha \sim \tilde{g}_\alpha^2$. Based on the equivalence between the U(1) anomaly-free and gapping conditions in $(1 + 1)D$ [26,33], hopefully our work can prompt future simulations on other $(1 + 1)D$ lattice chiral fermion–gauge theory models.

---

[1] H. B. Nielsen and M. Ninomiya, Phys. Lett. **105B**, 219 (1981).

[2] P. H. Ginsparg and K. G. Wilson, Phys. Rev. D **25**, 2649 (1982).

[3] P. Swift, Phys. Lett. **145B**, 256 (1984).

[4] J. Smit, Acta Phys. Pol. B **17**, 531 (1986), https://www.actaphys.uj.edu.pl/R/17/6/531.

[5] T. Banks and A. Dabholkar, Phys. Rev. D **46**, 4016 (1992).

[6] D. B. Kaplan, Phys. Lett. B **288**, 342 (1992).

[7] Y. Shamir, Nucl. Phys. **B406**, 90 (1993).

[8] E. Eichten and J. Preskill, Nucl. Phys. **B268**, 179 (1986).

[9] W. Bock and A. K. De, Phys. Lett. B **245**, 207 (1990).

[10] W. Bock, A. K. De, and J. Smit, Nucl. Phys. **B388**, 243 (1992).

[11] W. Bock, A. K. De, E. Focht, and J. Smit, Nucl. Phys. **B401**, 481 (1993).

[12] W. Bock, J. Smit, and J. C. Vink, Nucl. Phys. **B414**, 73 (1994).

[13] A. Hasenfratz, W. Liu, and T. Neuhaus, Phys. Lett. B **236**, 339 (1990).

[14] A. Hasenfratz, P. Hasenfratz, K. Jansen, J. Kuti, and Y. Shen, Nucl. Phys. **B365**, 79 (1991).

[15] I.-H. Lee, J. Shigemitsu, and R. E. Shrock, Nucl. Phys. **B334**, 265 (1990).

[16] I. Montvay, Nucl. Phys. B, Proc. Suppl. **29**, 159 (1992).

[17] M. F. L. Golterman, D. N. Petcher, and E. Rivas, Nucl. Phys. **B395**, 596 (1993).

[18] C. Chen, J. Giedt, and E. Poppitz, J. High Energy Phys. 04 (2013) 001.

[19] L. Fidkowski and A. Kitaev, Phys. Rev. B **81**, 134509 (2010).

[20] L. Fidkowski and A. Kitaev, Phys. Rev. B **83**, 075103 (2011).

[21] A. M. Turner, F. Pollmann, and E. Berg, Phys. Rev. B **83,** 075102 (2011).
[22] S. Ryu and S.-C. Zhang, Phys. Rev. B **85,** 245132 (2012).
[23] X.-L. Qi, New J. Phys. **15,** 065002 (2013).
[24] H. Yao and S. Ryu, Phys. Rev. B **88,** 064507 (2013).
[25] X.-G. Wen, Chin. Phys. Lett. **30,** 111101 (2013).
[26] J. Wang and X.-G. Wen, arXiv:1307.7480.
[27] C. Wang and T. Senthil, Phys. Rev. B **89,** 195124 (2014).
[28] Z.-C. Gu and M. Levin, Phys. Rev. B **89,** 201113(R) (2014).
[29] M. A. Metlitski, L. Fidkowski, X. Chen, and A. Vishwanath, arXiv:1406.3032.
[30] Y.-Z. You and C. Xu, Phys. Rev. B **90,** 245120 (2014).
[31] E. Witten, Phys. Rev. B **94,** 195150 (2016).
[32] Y. Kikukawa, Prog. Theor. Exp. Phys. **2019,** 073B02 (2019).
[33] J. Wang and X.-G. Wen, Phys. Rev. D **99,** 111501(R) (2019).
[34] J. Wang and X.-G. Wen, Phys. Rev. Research **2,** 023356 (2020).
[35] V. Ayyar and S. Chandrasekharan, Phys. Rev. D **91,** 065035 (2015).
[36] K. Slagle, Y.-Z. You, and C. Xu, Phys. Rev. B **91,** 115121 (2015).
[37] S. Catterall, J. High Energy Phys. 01 (2016) 121.
[38] V. Ayyar and S. Chandrasekharan, Phys. Rev. D **93,** 081701 (R) (2016).
[39] S. Catterall and D. Schaich, Phys. Rev. D **96,** 034506 (2017).
[40] V. Ayyar and S. Chandrasekharan, J. High Energy Phys. 10 (2016) 058.
[41] V. Ayyar, arXiv:1611.00280.
[42] Y.-Y. He, H.-Q. Wu, Y.-Z. You, C. Xu, Z. Y. Meng, and Z.-Y. Lu, Phys. Rev. B **94,** 241111(R) (2016).
[43] M. DeMarco and X.-G. Wen, arXiv:1706.04648.
[44] V. Ayyar and S. Chandrasekharan, Phys. Rev. D **96,** 114506 (2017).
[45] D. Schaich and S. Catterall, EPJ Web Conf. **175,** 03004 (2018).
[46] S. Catterall and N. Butt, Phys. Rev. D **97,** 094502 (2018).
[47] N. Butt and S. Catterall, in *Proceedings of the 36th Annual International Symposium on Lattice Field Theory, 2018* (Michigan State University, East Lansing, Michigan, USA, 2018), p. 294.
[48] N. Butt, S. Catterall, and D. Schaich, Phys. Rev. D **98,** 114514 (2018).
[49] S. Catterall, N. Butt, and D. Schaich, arXiv:2002.00034.
[50] S. Catterall, Phys. Rev. D **104,** 014503 (2021).
[51] N. Butt, S. Catterall, and G. C. Toga, arXiv:2111.01001.
[52] Y.-Z. You, Y.-C. He, C. Xu, and A. Vishwanath, Phys. Rev. X **8,** 011026 (2018).
[53] Y.-Z. You, Y.-C. He, A. Vishwanath, and C. Xu, Phys. Rev. B **97,** 125112 (2018).
[54] S. S. Razamat and D. Tong, Phys. Rev. X **11,** 011063 (2021).
[55] D. Tong, arXiv:2104.03997.
[56] N. Butt, S. Catterall, A. Pradhan, and G. C. Toga, Phys. Rev. D **104,** 094504 (2021).
[57] S. R. White, Phys. Rev. Lett. **69,** 2863 (1992).
[58] U. Schollwöck, Rev. Mod. Phys. **77,** 259 (2005).
[59] F. D. M. Haldane, Phys. Rev. Lett. **61,** 2015 (1988).
[60] F. D. M. Haldane, Phys. Rev. Lett. **74,** 2090 (1995).
[61] A. Kapustin and N. Saulina, Nucl. Phys. **B845,** 393 (2011).
[62] J. C. Wang and X.-G. Wen, Phys. Rev. B **91,** 125124 (2015).
[63] M. Levin, Phys. Rev. X **3,** 021009 (2013).
[64] M. Fishman, S. R. White, and E. M. Stoudenmire, arXiv:2007.14822.
[65] https://github.com/meng-zeng/julia-code-for-chiral-fermion-dmrg.
[66] See Supplemental Material at http://link.aps.org/supplemental/10.1103/PhysRevLett.128.185301 for free fermion correlation benchmark, scaling dimensions of fermion bilinear mass terms before SMG, correlations of fermion bilinear mass terms after SMG, and solving for the scaling dimension of the interaction terms.
[67] B. A. Katzir, A. Stern, E. Berg, and N. H. Lindner, arXiv:2011.13950.
[68] C. Chen, J. Giedt, and E. Poppitz, J. High Energy Phys. 04 (2013) 131.

# Supplementary Material for "Symmetric Mass Generation in the 1+1 Dimensional Chiral Fermion 3-4-5-0 Model"

Meng Zeng,[1] Zheng Zhu,[2,3] Juven Wang,[4] and Yi-Zhuang You[1]

[1] *Department of Physics, University of California San Diego, La Jolla, California 92093, USA*
[2] *Kavli Institute for Theoretical Sciences, University of Chinese Academy of Sciences, Beijing 100190, China*
[3] *CAS Center for Excellence in Topological Quantum Computation,*
*University of Chinese Academy of Sciences, Beijing 100190, China*
[4] *Center of Mathematical Sciences and Applications, Harvard University, MA 02138, USA*

## I. SCALING DIMENSIONS IN FREE FERMION LIMIT

In the free fermion limit, correlation functions and consequently scaling dimensions can be calculated analytically. Here we work out the free fermion case on the lattice as a benchmark to the DMRG calculation at $g = 0$.

### A. Fermion scaling dimension

For the free fermion-fermion correlation, we can just pick the fermion flavor $f_3$ without loss of generality. The two-point correlation is given by (with the flavor index ignored)

$$C_\psi(r) = \langle \psi_{i+r}^\dagger \psi_i \rangle \sim r^{-\nu}. \tag{1}$$

On a finite lattice with real space Hamiltonian $\mathcal{H}$, we can do a change basis from the fermionic operators in real space fermionic operators in energy eigenspace, so that the correlation at half-filling can be more conveniently calculated. Assuming $\mathcal{H}$ has eigenstates $|\epsilon_n\rangle$ with corresponding eigenenergies $\epsilon_n$, then the change of basis is given by $\psi^\dagger(i) = \sum_n \langle \epsilon_n | i \rangle \psi_n^\dagger$. Eventually the correlation becomes

$$C_\psi(r) = \sum_{n,m} \langle \epsilon_n | i \rangle \langle j | \epsilon_m \rangle \langle \psi_n^\dagger \psi_m \rangle. \tag{2}$$

Since the ground state is half-filled, the above summation in $n$ or $m$ is only over the lower half of the energy spectrum. The system we have in the main text consists of 20 unit cells. Exact diagonalization can be done in the free fermion limit and the correlation can then be calculated using Eq. (2). With open boundary condition (same as the DMRG setup), the correlation with log-log scale is plotted in Fig. 1(a) together with a linear fit. The power law exponent obtained is less than 1, which explains the deviation of the scaling dimension $\Delta_\psi$ from 0.5 for $g = 0$ in Fig. 4(a) in the main text. This deviation is mainly a finite-size effect, demonstrated in Fig. 1(b). In the large-system-size limit, the free fermion scaling dimension of 0.5 is recovered.
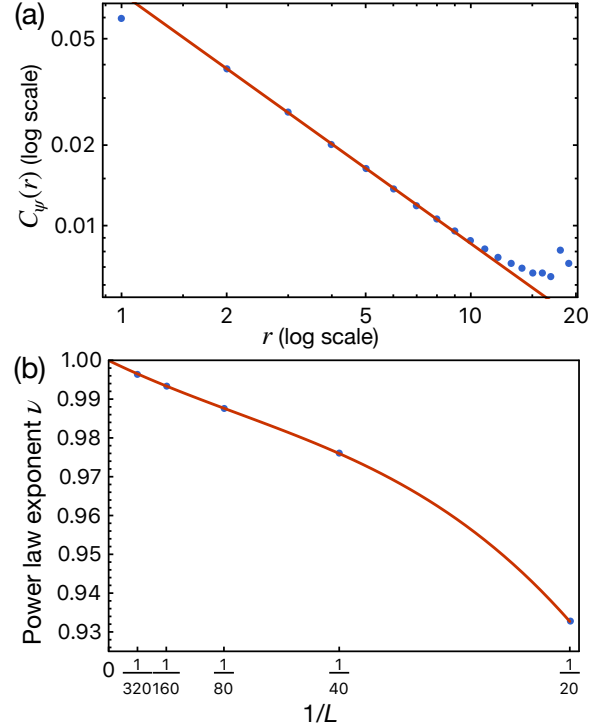


FIG. 1. (a) Linear fit for the correlation function on a log-log scale when the system has 20 unit cells. The power law exponent obtained is around 0.936, which is smaller than 1. (b) Finite-size scaling for the exponent using a polynomial function for system sizes $L = 20, 40, 80, 160, 320$. The extrapolation to $L = \infty$ recovers the ideal $\nu = 1$ limit.

### B. Mass term scaling dimensions

Other than the fermion-fermion correlation, correlations of various mass terms on a finite lattice can also be calculated analytically in the free fermion limit. In this case, the expected scaling dimension for a bilinear in the large-system-size limit is 1. Taking the fermion bilinear $\psi_1 \psi_3^\dagger$ as an example, the correlation on the lattice is given by (using Wick's theorem)

$$\begin{aligned} C_{\psi_1^\dagger \psi_3}(r) &= \langle \psi_{1,i+r}^\dagger \psi_{3,i+r} \psi_{3,i}^\dagger \psi_{1,i} \rangle \\ &= \langle \psi_{1,i+r}^\dagger \psi_{1,i} \rangle \langle \psi_{3,i+r} \psi_{3,i}^\dagger \rangle \\ &\sim r^{-2\nu}, \end{aligned} \tag{3}$$
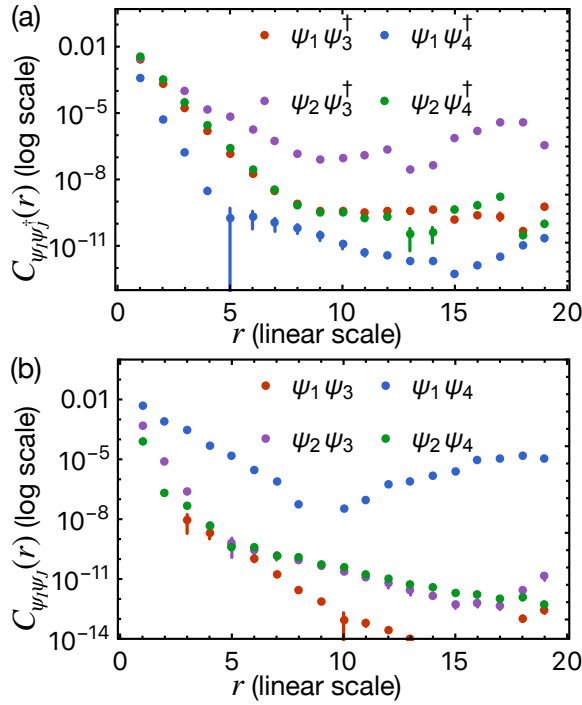
FIG. 2. Semi-log correlations for the various mass terms in the gapped phase. (a) Dirac masses $\psi_I \psi_J^\dagger$. The interaction strengths chosen for the four mass terms $\psi_1\psi_3^\dagger$, $\psi_1\psi_4^\dagger$, $\psi_2\psi_3^\dagger$ and $\psi_2\psi_4^\dagger$ in the gapped phase are 6.5, 6.5, 6.6 and 6.4 respectively. (b) Majorana masses $\psi_I \psi_J$. The interaction strengths chosen for the four mass terms $\psi_1\psi_3$, $\psi_1\psi_4$, $\psi_2\psi_3$ and $\psi_2\psi_4$ in the gapped phase are 6.4, 6.3, 6.3 and 7.2 respectively.

i.e., the fermion bilinear exponent is simply double of that for the single fermion, as expected. Therefore, the finite-size behavior should also be the same.

## II. MASS TERM CORRELATIONS IN THE GAPPED PHASE FOR EDGE B

In this section, we present the correlations for the mass terms on edge B after the gapping transition to demonstrate that the U(1) chiral symmetry is preserved in the gapped phase. The correlations for the Dirac masses are shown in Fig. 2(a) and the correlations for the Majorana masses are shown in Fig. 2(b). We see clear evidence for exponential decays for all the eight different mass terms at relatively shorter length scales $r \lesssim 5$, where the correlation is expected to be dominated by the SMG gap. The non-monotonic behavior of the correlation function for larger distance $r \gtrsim 5$ is an artifact arising from the finite MPS bond dimension, and should not be trusted. Different interaction strengths are chosen for the different mass terms in order to better demonstrate the exponential decay features. Thus, we conclude that the chiral U(1) symmetry is preserved in the gapped phase on edge B.
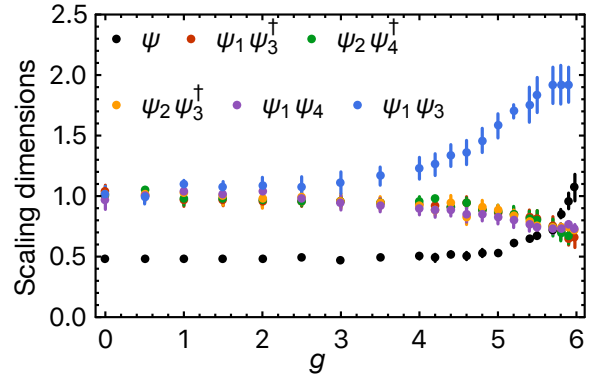


FIG. 3. Evolution of scaling dimensions for some of the mass terms under RG on edge B. The fermion scaling dimension $\Delta_\psi$ is also shown for comparison.

## III. SCALING DIMENSIONS UNDER RG

The scaling dimensions of some of the interesting operators are summarized in Table I.

| Operators | $l$ | $\Delta_l$ |
|---|---|---|
| $\psi_1$ | $(1,0,0,0)$ | $\frac{1}{2}\sqrt{1+y_1^2+y_2^2}$ |
| $\psi_1\psi_3^\dagger$ | $(1,0,-1,0)$ | $-y_1 + \sqrt{1+y_1^2+y_2^2}$ |
| $\psi_1\psi_4^\dagger$ | $(1,0,0,-1)$ | $y_2 + \sqrt{1+y_1^2+y_2^2}$ |
| $\psi_2\psi_3^\dagger$ | $(0,1,-1,0)$ | $-y_2 + \sqrt{1+y_1^2+y_2^2}$ |
| $\psi_2\psi_4^\dagger$ | $(0,1,0,-1)$ | $-y_1 + \sqrt{1+y_1^2+y_2^2}$ |
| $\psi_1\psi_3$ | $(1,0,1,0)$ | $y_1 + \sqrt{1+y_1^2+y_2^2}$ |
| $\psi_1\psi_4$ | $(1,0,0,1)$ | $-y_2 + \sqrt{1+y_1^2+y_2^2}$ |
| $\psi_2\psi_3$ | $(0,1,1,0)$ | $y_2 + \sqrt{1+y_1^2+y_2^2}$ |
| $\psi_2\psi_4$ | $(0,1,0,1)$ | $y_1 + \sqrt{1+y_1^2+y_2^2}$ |
| $\psi_1\psi_3\psi_2^\dagger\partial_x\psi_2^\dagger\psi_4\partial_x\psi_4$ | $(1,-2,1,2)$ | $-3y_1-4y_2+5\sqrt{1+y_1^2+y_2^2}$ |
| $\psi_1\partial_x\psi_1\psi_3^\dagger\partial_x\psi_3^\dagger\psi_2\psi_4$ | $(2,1,-2,1)$ | $-3y_1-4y_2+5\sqrt{1+y_1^2+y_2^2}$ |

TABLE I. Scaling dimensions of the various operators, some of which are used to solve the two parameters $y_1$ and $y_2$.

These scaling dimensions can in principle be measured by calculating the power-law correlation using DMRG. Here we are interested in the scaling dimensions of the gapping terms under RG before the Luttinger liquid becomes gapped. However, for large scaling dimensions, the power-law decay is too fast to be measured accurately. Therefore, in order to solve for the parameters $y_1$ and $y_2$, we only use the correlations for operators with relatively smaller scaling dimensions, which, based on Table I, include $\psi_1, \psi_1\psi_3^\dagger, \psi_2\psi_3^\dagger, \psi_2\psi_4^\dagger$ and $\psi_1\psi_4$. Fig. 3 shows the evolution of the scaling dimensions for some of the mass terms under RG flow.

Instead of using two of the different scaling dimensions to solve for the two parameters, we try to make use of all the five aforementioned operators to have a faithful representation of the available DMRG data. For a particular interaction strength $g$, denote the five scaling
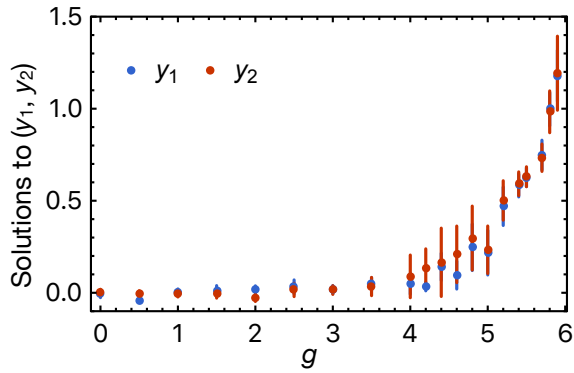
FIG. 4. Solutions to the Luttinger parameters $(y_1, y_2)$ based on RG equation and some of the measured scaling dimensions using DMRG.

dimensions from RG calculation by $\Delta_i^{(\mathrm{RG})}(y_1(g), y_2(g))$ and the DMRG counterparts by $\Delta_i^{(\mathrm{DMRG})}(g)$ with errors $\delta\Delta_i^{(\mathrm{DMRG})}(g)$. Then $y_1$ and $y_2$ are solved by minimizing the following error function at each $g$:

$$f_{\mathrm{error}}(g) \equiv \sum_i \frac{\left(\Delta_i^{(\mathrm{RG})}(y_1(g), y_2(g)) - \Delta_i^{(\mathrm{DMRG})}(g)\right)^2}{\delta\Delta_i^{(\mathrm{DMRG})}(g)^2}, \tag{4}$$

where $\frac{1}{\delta\Delta_i^{(\mathrm{DMRG})}(g)^2}$ can be considered as the weight of each contribution to the total error function. The solutions $(y_1, y_2)$ with error bars are obtained in the following way. At each $g$, a numerical value for the DMRG scaling dimension is randomly drawn from the interval $[\Delta_i^{(\mathrm{DMRG})} - \delta\Delta_i^{(\mathrm{DMRG})}, \Delta_i^{(\mathrm{DMRG})} + \delta\Delta_i^{(\mathrm{DMRG})}]$, then the error function $f_{\mathrm{error}}$ is minimized to find $(y_1, y_2)$, with the weight of this particular solution given by $\frac{1}{f_{\mathrm{error}}^2}$. This process is repeated 100 times for each $g$, after which weighted average is taken to obtain the mean of $(y_1, y_2)$ with the errors given by the weighted uncertainty. The evolution of the two parameters with RG flow is shown in Fig. 4. The solved $y_1$ and $y_2$ can then be used to calculate the scaling dimension of the gapping terms $\Delta_{\mathrm{int}}$ plotted in Fig. 4(b) in the main text.

## Acknowledgements

# Chapter 2

# Fermi surface symmetric mass generation

# Fermi surface symmetric mass generation

Da-Chuan Lu [1] Meng Zeng [1] Juven Wang,[2] and Yi-Zhuang You [1,*]

[1]*Department of Physics, University of California, San Diego, California 92093, USA*
[2]*Center of Mathematical Sciences and Applications, Harvard University, Cambridge, Massachusetts 02138, USA*

Symmetric mass generation (SMG) is a mechanism to give gapless fermions a mass gap by nonperturbative interactions without generating any fermion bilinear condensation. The previous studies of SMG have been limited to Dirac/Weyl/Majorana fermions with zero Fermi volume in the free fermion limit. In this paper, we generalize the concept of SMG to Fermi liquid (FL) with a finite Fermi volume and discuss how to gap out the Fermi surfaces (FSs) by interactions without breaking the U(1) loop group symmetry or developing topological orders. We provide examples of FS SMG in both (1+1)-dimensional [(1+1)D] and (2+1)-dimensional FL systems when several FSs together cancel the FS anomaly. However, the U(1) loop group symmetry in these cases is still restrictive enough to rule out all possible fermion bilinear gapping terms, such that a nonperturbative interaction mechanism is the only way to gap out the FSs. This symmetric FS reconstruction is in contrast to the conventional symmetry-breaking gapping mechanism in the FL. As a side product, our model provides a pristine one-dimensional lattice regularization for the (1+1)D U(1) symmetric chiral fermion model (e.g., the 3-4-5-0 model) by utilizing a lattice translation symmetry as an emergent U(1) symmetry at low energy. This opens up the opportunity for efficient numerical simulations of chiral fermions in their own dimensions without introducing mirror fermions under the domain wall fermion construction.

## I. INTRODUCTION

Fermi liquids (FLs) are gapless quantum many-body systems of fermions that possess Fermi surfaces (FSs) and well-defined quasiparticle excitations at low energy. They are the models for the most commonly seen metallic materials in nature. They are probably also some of the most studied quantum phases of matter in condensed matter physics since Landau [1,2]. However, there are still many aspects of FLs that might not have been well recognized. In this paper, we explore one such aspect: the phenomenon of *symmetric mass generation* (SMG, see a recent overview [3] and references therein) in FLs.

One intriguing property of the FL is the surprising stability of the FS under generic local interactions of fermions. Although the system is gapless with vastly degenerated ground states, local interactions often do not immediately lift the ground state degeneracy and destabilize the FL toward gapped phases. Early understanding of this property came from the perturbative renormalization group (RG) analysis, as the FL theory can emerge as a stable RG fixed point of interacting fermion systems [4–10].

Recently, a modern understanding arose under the name of a *FS anomaly* [11–13], which states that the stability of the FS can be viewed as protected by the quantum anomaly of an emergent LU(1) loop group symmetry at low energy, extending and unifying many related discussions [14–29] about Luttinger's theorem [30] and the Lieb-Schultz-Mattis

(LSM) theorem [31] in fermionic systems. Loosely speaking, the LU(1) symmetry corresponds to the fermion number $n_{\mathbf{k}}$ conservation at each momentum point $\mathbf{k}$ on the FS, which is preserved by the Landau FL Hamiltonian $H_{\mathrm{FL}} = \sum_{\mathbf{k}\in\mathrm{FS}} \epsilon_{\mathbf{k}} n_{\mathbf{k}} + \sum_{\mathbf{k},\mathbf{k}'\in\mathrm{FS}} f_{\mathbf{k}\mathbf{k}'} n_{\mathbf{k}} n_{\mathbf{k}'} + \cdots$. In the presence of the FS anomaly, the FL can only be gapped by either (i) spontaneously breaking the LU(1) symmetry or (ii) spontaneously developing anomalous topological orders (or other non-FL exotic states) that saturate the FS anomaly. The anomaly matching is a kinematic constraint, which is nonperturbative and more robust than the perturbative RG analysis of the FL low-energy dynamics.

Over the past decade, the quantum anomaly [32–35] has been realized as an important theoretical tool in analyzing the protected gapless boundary states of interacting topological insulators/superconductors, which belong to symmetry-protected topological (SPT) phases in a grand scope (see overviews [36–38] and references therein). An interesting phenomenon, known as SMG [39–51], was discovered in the study of interacting fermionic SPT states. It was realized that certain SPT states might look nontrivial at the free-fermion (noninteracting) level but can be smoothly deformed into a trivial gapped phase with a unique ground state by fermion interactions. This implies some integer $\mathbb{Z}$ classification of noninteracting SPT states can be reduced to a finite Abelian elementary order-$n$ group $\mathbb{Z}_n$ classification for some interacting SPT states, emphasized by Fidkowski and Kitaev [39,40]. Correspondingly, their gapless boundary states can be gapped out by (and only by) interaction without breaking the symmetry or developing the topological order (breaking emergent higher-form symmetry). This provides a

*yzyou@physics.ucsd.edu

mechanism to generate a mass for zero-density relativistic gapless fermions (e.g., Dirac/Weyl/Majorana fermions occupying only Fermi points with zero Fermi volumes at the Fermi level, colloquially known as Dirac/Weyl/Majorana cones) without symmetry breaking, which has been proposed to provide lattice regularization for the standard model and grand unified theories [45,52–56]. This mechanism is called SMG, or a mass-without-mass term [57,58], which is distinct from the conventional Higgs mechanism that relies on symmetry breaking for fermion mass generation.

However, the SMG mechanism has not yet been extended to fermion systems at a finite filling (with a finite density). The FL is the most notable examples of such, which possesses a FS enclosing a finite Fermi volume. It is natural to ask: Can SMG happen on the FS as well, gapping out the FS by interaction without breaking the loop group symmetry of interest? As we will demonstrate in this paper, the answer is yes.

Given the spacetime-internal symmetry $G$ of a fermion system, the conditions [3] for SMG to happen are (i) the system must be free from $G$ anomaly such that symmetric gapping (without topological order) becomes possible, and (ii) the symmetry $G$ must be restricted enough to rule out any symmetric fermion bilinear gapping term such that the gapping can only be achieved by interaction. These defining conditions of SMG can be applied to the FL system by considering $G$ as the emergent loop group symmetry on the FS. Based on this understanding, we will investigate the FS SMG in the presence of the LU(1) symmetry. The general feature is that, even though a single FS is anomalous, it is possible to cancel the FS anomaly among multiple FSs (or FSs with multiple fermion flavors), such that interactions can drive the transition from the FL phase to a symmetric gapped phase. We shall name this phenomenon as the FS SMG.

The FS SMG provides us a different possibility to create a gap to all excitations on the FS without condensing any fermion bilinear order parameter, which makes it distinct from the superconducting gap (i.e., condensing Cooper pairs) or the density wave gap (i.e., condensing excitons) that are more familiar in condensed matter physics. Nevertheless, it does involve condensing some multifermion bound states that transform trivially under the symmetry transformation. The simplest example is the charge-$4e$ superconductor [59–66], which condenses fermion quartets (four-fermion bound states) that preserve at least the $\mathbb{Z}_4$ subgroup of the charge U(1) symmetry. In this paper, we provide more carefully designed examples preserving the full U(1) symmetry (and other lattice symmetries), but the essential idea of condensing symmetric multifermion operators to generate a many-body excitation gap is the same. Therefore, the FS SMG is intrinsically a strong nonperturbative interaction effect of fermions. The interaction may look irrelevant at the free-fermion (or the FL) fixed point. However, strong enough interaction can still drive the gap-opening transition through nonperturbative effects.

This paper is organized as follows. In Sec. II, we present a lattice model of FS SMG in (1+1) dimensions [(1+1)D], as the pristine lattice regularization of the 3-4-5-0 chiral fermion model, whose phase diagram can be reliably analyzed by the RG approach. In Sec. III, we extend the discussion of FS SMG to (2+1) dimensions [(2+1)D] in a concrete lattice model, which can be exactly solved in both the weak and strong
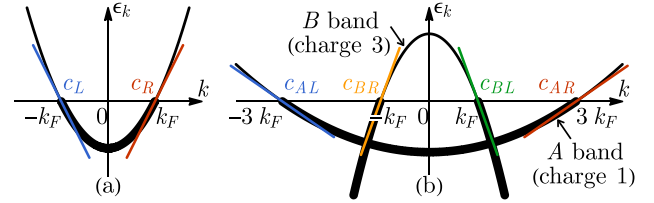


FIG. 1. (a) A typical single-band Fermi liquid (FL) with Fermi surface (FS) anomaly. (b) Two-band model of a FL with the FS anomaly canceled. Chiral fermions with linearized dispersions around different Fermi points emerge at low energy.

interaction limits. Through these examples, we establish the FS SMG as a general mechanism to gap out anomaly-free FSs in different dimensions. We summarize our result and discuss its connection to future directions in Sec. IV.

## II. FS SMG IN (1+1)D

### A. (1+1)D Fermi liquid and Fermi surface anomaly

In the free-fermion limit, the (1+1)D FL can be realized as a system of fermions occupying a segment of single-particle momentum eigenstates in the one-dimensional (1D) momentum space (or Brillouin zone), which can be described by a Hamiltonian $H = \sum_k c_k^\dagger \epsilon_k c_k$, where $c_k$ (or $c_k^\dagger$) is the fermion annihilation (or creation) operator of the single-particle mode at momentum $k$. For now, we only consider spinless fermions, such that the $c_k$ operator does not carry spin (or any other internal degrees of freedom). As an example, suppose the band structure is described by $\epsilon_k = (k^2 - k_F^2)/(2m)$ for nonrelativistic fermions with a finite chemical potential $\mu = k_F^2/(2m)$. The ground state of the Hamiltonian $H$ will have fermions occupying the momentum segment $k \in [-k_F, k_F]$ bounded by the Fermi momentum $k_F$, as illustrated in Fig. 1(a).

The low-energy degrees of freedom in the (1+1)D FLs can be modeled by the chiral fermions near the zero-dimensional (0D) FSs (namely, Fermi points) at $\pm k_F$, which are described by the following Lagrangian density:

$$\mathcal{L} = c_L^\dagger(i\partial_t - v_F i\partial_x)c_L + c_R^\dagger(i\partial_t + v_F i\partial_x)c_R, \quad (1)$$

where $v_F = k_F/m$ is the Fermi velocity. The operator $c_L$ (or $c_R$) annihilates the left (or right)-moving fermion modes, defined as

$$c_{R/L}(x) = \int_{-\Lambda}^{\Lambda} d\kappa \, c_{\pm k_F + \kappa} \exp[i(\pm k_F + \kappa)x] \quad (2)$$

around the Fermi points within a small momentum cutoff $\Lambda \ll k_F$. The low-energy effective theory $\mathcal{L}$ in Eq. (1) has an emergent U(1)$_L$ × U(1)$_R$ symmetry (more precisely as an emanant symmetry [67] since the translation and charge conservation symmetry are not the subgroup of U(1)$_L$ × U(1)$_R$ symmetry), corresponding to the separate charge conservation of the left- and right-moving chiral fermions. Under the symmetry transformation with the periodic $\phi_L$ and $\phi_R$ in $[0, 2\pi)$:

$$\text{U(1)}_L : c_L \to \exp(i\phi_L)c_L, \quad c_R \to c_R;$$
$$\text{U(1)}_R : c_L \to c_L, \quad c_R \to \exp(i\phi_R)c_R. \quad (3)$$

They can be as well understood as a recombination of the vector $U(1)_V$ and axial $U(1)_A$ symmetries by rewriting $\phi_L = \phi - k_F \, \delta x$ and $\phi_R = \phi + k_F \, \delta x$:

$$U(1)_V : c_k \rightarrow e^{i\phi}c_k \Rightarrow \begin{cases} c_L \rightarrow e^{i\phi}c_L, \\ c_R \rightarrow e^{i\phi}c_R; \end{cases}$$

$$U(1)_A : c_k \rightarrow e^{ik\,\delta x}c_k \Rightarrow \begin{cases} c_L \rightarrow \exp(-ik_F\,\delta x)c_L, \\ c_R \rightarrow \exp(+ik_F\,\delta x)c_R. \end{cases} \quad (4)$$

More precisely, the combined symmetry group should be denoted as $U(1)_V \times_{\mathbb{Z}_2^F} U(1)_A \equiv \frac{U(1)_V \times U(1)_A}{\mathbb{Z}_2^F}$ because the $U(1)_V$ and $U(1)_A$ symmetries share the fermion parity $\mathbb{Z}_2^F$ subgroup (under which $c_{L,R} \rightarrow -c_{L,R}$). The physical meaning of the vector $U(1)_V$ symmetry is the total $U(1)$ charge conservation of the fermions, and the axial $U(1)_A$ symmetry can be considered an effective representation of the translation symmetry in the infrared (IR) limit (that translates all fermions by displacement $\delta x$ along the 1D system). Although translation symmetry is described by a noncompact symmetry group $\mathbb{Z}$ at the lattice scale, its action on the low-energy chiral fermion fields $c_L$, $c_R$ behaves as a compact $U(1)_A$ emergent symmetry [26,68].

The stability of the FL is protected by the FS anomaly, which can be viewed as the mixed anomaly between the $U(1)_V$ and $U(1)_A$ symmetries. The anomaly index is given by [24,30,31]

$$1 \times k_F - 1 \times (-k_F) = 2k_F = 2\pi\nu, \quad (5)$$

which can be related to the fermion filling fraction $\nu$. The system is anomalous if the filling $\nu$ is not an integer. Without breaking the charge $U(1)$ and translation symmetries, it is impossible to drive the FL to a trivial gap phase due to the nonvanishing FS anomaly. This can be viewed as a consequence of the LSM theorem [31]. The situation is also like the chiral fermion edge states on the (1+1)D boundary of a (2+1)D quantum Hall insulator.

### B. Two-band model and anomaly cancellation

To generate a gap for these low-energy fermions in (1+1)D FLs, the FS anomaly must be canceled. Here, we present a two-band toy model that achieves anomaly cancellation and enables gapping out the FS without breaking the charge $U(1)$ and translation symmetries and without generating any Fermi bilinear condensation. It will provide a concrete example of SMG in (1+1)D FLs.

Consider a 1D lattice (a chain of sites) with two types of fermions $c_{iA}$ and $c_{iB}$ per site. The $A$-type fermion $c_{iA}$ carries charge $q_A$ under a global $U(1)$ symmetry, and the $B$-type fermion $c_{iB}$ carries charge $q_B$ under the same $U(1)$ symmetry. The Hamiltonian takes the general form of

$$H = -\sum_{ij}\left(t_{ij}^A c_{iA}^\dagger c_{jA} + t_{ij}^B c_{iB}^\dagger c_{jB} + \text{H.c.}\right)$$
$$- \sum_i (\mu_A c_{iA}^\dagger c_{iA} + \mu_B c_{iB}^\dagger c_{iB}) + H_{\text{int}}, \quad (6)$$

with $H_{\text{int}}$ being some fermion interactions to be specified later in Eq. (16). The specific details of the hopping coefficients $t_{ij}^A$ and $t_{ij}^B$ are not important to our discussion if they produce a band structure that looks like Fig. 1(b) in the Brillouin zone.

The $A$-type fermion forms an electronlike band, and the $B$-type fermion forms a holelike band. The two bands overlap in the energy spectrum. This will realize a two-band FL in general. The Hamiltonian $H$ in Eq. (6) has a $U(1) \times (\mathbb{Z} \rtimes \mathbb{Z}_2)$ symmetry (parameterized by a periodic angle $\phi \in [0, 2\pi)$ and an integer $n \in \mathbb{Z}$ as follows):

$$U(1) : c_{iA} \rightarrow \exp(iq_A\phi)c_{iA}, \quad c_{iB} \rightarrow \exp(iq_B\phi)c_{iB};$$
$$\mathbb{Z} : c_{iA} \rightarrow c_{(i+n)A}, \quad c_{iB} \rightarrow c_{(i+n)B};$$
$$\mathbb{Z}_2 : c_{iA} \rightarrow c_{(-i)A}, \quad c_{iB} \rightarrow c_{(-i)B}. \quad (7)$$

They correspond to the total charge conservation symmetry $U(1)$, the lattice translation symmetry $\mathbb{Z}$, and the lattice reflection symmetry $\mathbb{Z}_2$. The question is whether we can gap the FL without breaking all these symmetries in (1+1)D.

One significant obstruction toward gapping is the FS anomaly, which can also be interpreted as a mixed anomaly between the charge $U(1)$ and (the IR correspondence of) the translation symmetry. To cancel the FS anomaly, we need to fine-tune the chemical potentials $\mu_A$ and $\mu_B$ such that the anomaly index vanishes:

$$q_A\nu_A + q_B\nu_B = 0 \mod 1, \quad (8)$$

where $\nu_A$ and $\nu_B$ are the filling fractions of the $A$ and $B$ bands (for the holelike $B$ band, we may assign $\nu_B < 0$ such that $|\nu_B|$ corresponds to the hole-filling). This is also known as the *charge compensation* condition in semiconductor physics.

If the $A$- and $B$-type fermions carry the same charge as $q_A = q_B = 1$, the anomaly cancellation condition in Eq. (8) simply requires $\nu_A = -\nu_B$. In this case, the electronlike FS of the $A$-type fermion and the holelike FS of the $B$-type fermion are perfectly nested (with zero nesting momentum). A gap can be opened simply by tuning on a fermion bilinear term $\sum_i(c_{iA}^\dagger c_{iB} + \text{H.c.})$ in the Hamiltonian, which preserves the full $U(1) \times (\mathbb{Z} \rtimes \mathbb{Z}_2)$ symmetry. This is the familiar band hybridization mechanism to open a band gap in a charge-compensated FL, which drives a metal to a band insulator without breaking symmetry.

However, we are more interested in the nontrivial case when the fermions carry different charges $q_A \neq q_B$. For example, let us consider the case of $q_A = 1$ and $q_B = 3$. Then the anomaly cancellation condition in Eq. (8) requires $\nu_A = -3\nu_B$, i.e., the electronlike Fermi volume in the $A$ band must be three times as large as the holelike Fermi volume in the $B$ band to cancel the FS anomaly. Defining the fermion operators $c_{kA}$, $c_{kB}$ in the momentum space by the Fourier transformation:

$$c_{kA} = \sum_i c_{iA}e^{-iki}, \quad c_{kB} = \sum_i c_{iB}e^{-iki}, \quad (9)$$

the desired band structure can be effectively described by the following band Hamiltonian (suppressing the interaction for now):

$$H = \sum_k (c_{kA}^\dagger \epsilon_{kA} c_{kA} + c_{kB}^\dagger \epsilon_{kB} c_{kB}), \quad (10)$$

with the band dispersions [see Fig. 1(b)]:

$$\epsilon_{kA} = \frac{k^2 - (3k_F)^2}{2m_A}, \quad \epsilon_{kB} = -\frac{k^2 - k_F^2}{2m_B}. \quad (11)$$

TABLE I. Charge assignments of low-energy fermions. See also the model in Ref. [69] on the same charge assignments.

| Fermion $c_a$ | Chirality sgn $v_a$ | U(1)$_V$ $q_a^V$ | U(1)$_A$ $q_a^A$ | U(1)$_{\frac{3V+A}{2}}$ $\frac{1}{2}(3q_a^V + q_a^A)$ | U(1)$_{\frac{3V-A}{2}}$ $\frac{1}{2}(3q_a^V - q_a^A)$ |
|---|---|---|---|---|---|
| $c_{AR}$ | −1 (left) | 1 | 3 | 3 | 0 |
| $c_{BR}$ | −1 (left) | 3 | −1 | 4 | 5 |
| $c_{BL}$ | +1 (right) | 3 | 1 | 5 | 4 |
| $c_{AL}$ | +1 (right) | 1 | −3 | 0 | 3 |

Here, we assume $m_A, m_B > 0$. The Fermi momentum $k_F = |v_B|\pi$ is set by the filling $|v_B|$ which is typically an irrational number (without fine-tuning). The key feature is that the Fermi momenta of the $A$ and $B$ energy bands must have a $3:1$ ratio that matches the inverse charge ratio $(q_A/q_B)^{-1}$ precisely. In this case, the energy band hybridization is forbidden by the charge U(1) symmetry as the two bands now carry different charges. Even if the band hybridization is spontaneously generated at the price of breaking the U(1) symmetry, it does not gap the FL because the FSs of the two bands are no longer nested at the Fermi level, such that the band hybridization will only create some avoided energy band crossing below the Fermi level. Then the system remains metallic because the (upper) hybridized band still crosses the Fermi level.

One can show that it is impossible to symmetrically gap the FL by any fermion bilinear terms in this charge-compensated two-band system with $q_A = 1$ and $q_B = 3$, even if the FS anomaly has already been canceled by the charge-compensated filling $v_A = -3v_B$. Although the anomaly vanishes (i.e., there is no obstruction toward gapping in principle), the symmetry is still restrictive enough to forbid any fermion bilinear gapping term, such that the only possible gapping mechanism rests on nonperturbative fermion interaction effects.

To see this, we can single out the low-energy chiral fermions near the four Fermi points:

$$c_{AR} = c_{(3k_F)A}, \quad c_{BR} = c_{(-k_F)B},$$
$$c_{BL} = c_{(k_F)B}, \quad c_{AL} = c_{(-3k_F)A}, \quad (12)$$

where $A$, $B$ label the bands that they originated from and $L$, $R$ label their chiralities (i.e., left- or right-moving), according to Fig. 1(b). Like Eq. (1), the low-energy effective Lagrangian density reads

$$\mathcal{L} = \sum_a c_a^\dagger (i\partial_t + v_a i\partial_x) c_a, \quad (13)$$

where the index $a$ sums over the four Fermi point labels $AR$, $BR$, $BL$, and $AL$. Here, $v_a$ denotes the Fermi velocity near the Fermi point $a$.

The original U(1) × $\mathbb{Z}$ symmetry at the lattice fermion level reduces to the emergent U(1)$_V \times_{\mathbb{Z}_2^F}$ U(1)$_A$ symmetry for the low-energy chiral fermions $c_a$ (see Appendix A for more explanations):

$$\text{U}(1) \Rightarrow \text{U}(1)_V : c_a \to \exp\left(iq_a^V \phi_V\right) c_a,$$
$$\mathbb{Z} \Rightarrow \text{U}(1)_A : c_a \to \exp\left(iq_a^A \phi_A\right) c_a. \quad (14)$$

Table I summarizes their charge assignment under U(1)$_V$ and U(1)$_A$, where the vector U(1)$_V$ symmetry is just the charge U(1) symmetry, and the axial U(1)$_A$ symmetry is an emergent symmetry corresponding to the lattice translation symmetry $\mathbb{Z}$. Alternatively, they can be recombined into the U(1)$_{\frac{3V+A}{2}} \times$ U(1)$_{\frac{3V-A}{2}}$ symmetry, such that it becomes obvious that all fermion bilinear back-scattering terms (either the Dirac mass $c_a^\dagger c_b$ or the Majorana mass $c_a c_b$ for $a \neq b$ and $a, b \in \{AR, BR, BL, AL\}$) are forbidden by the symmetry because they are all charged nontrivially under the U(1)$_{\frac{3V+A}{2}} \times$ U(1)$_{\frac{3V-A}{2}}$ symmetry due to the distinct charge assignment to every chiral fermion. Given this situation, the only hope to gap the FL is to evoke the SMG mechanism that generates the mass for all chiral fermions by nonperturbative multifermion interactions.

### C. SMG interaction and RG analysis

It is worth mentioning that the charge-compensated two-band model with $q_A = 1$ and $q_B = 3$ essentially regularizes the 3-4-5-0 chiral fermion model [70,71] on a pristine 1D lattice (without introducing any compact extra dimensions). The emergent U(1)$_{\frac{3V\pm A}{2}}$ symmetries act as the lattice translations decorated by appropriate internal U(1) rotations, described by the following $\mathbb{Z}$ symmetry groups (parameterized by integer $n \in \mathbb{Z}$) at the lattice level (see Appendix A for derivation):

$$\mathbb{Z}\left(for\ \frac{3V \pm A}{2}\right) : \begin{cases} c_{iA} \to \exp(\pm i 3 k_F n) c_{(i+n)A}, \\ c_{iB} \to \exp(\pm i 9 k_F n) c_{(i+n)B}. \end{cases} \quad (15)$$

The 3-4-5-0 model is a toy model for studying the long-standing problem: the lattice regularization of the chiral fermion theory in high-energy physics [55,72–79]. Many variants of the model are studied in the lattice community (see references therein [80,81]). This model is anomaly-free—perturbative local gauge anomaly free within any linear combination of the U(1)$_V \times_{\mathbb{Z}_2^F}$ U(1)$_A$ checked by the Adler-Bell-Jackiw method [82,83], perturbative local gravitational anomaly free because of the zero chiral central charge $c_L - c_R = 0$, also nonperturbative global anomaly free from any gauge or gravitational fields checked by the cobordism [84]. However, it was known much later that symmetric gapping can only be achieved by minimally six-fermion interactions among the four flavors of 3-4-5-0 fermions. The SMG interaction was proposed by Wang and Wen [46,51], which was later discussed by Tong [85] and only recently verified by the density matrix RG (DMRG) [86,87] numerical simulation in Ref. [88].

Given the existing knowledge about the SMG interaction in the 3-4-5-0 chiral fermion model, we can map the Wang-Wen interaction [46,51] back to our lattice model following the correspondence listed in Table I, which gives us the following SMG interaction (see Appendix B for more details):

$$H_{\text{int}} = g \sum_i c_{(i-1)B}^\dagger c_{(i-1)A} c_{iB} c_{iA} c_{(i+1)B}^\dagger c_{(i+1)A} + \text{H.c.} \quad (16)$$

This is a six-fermion interaction across three adjacent sites on the 1D lattice. It describes the process that first annihilates both $A$- and $B$-type fermions on the center site (which annihilates four units of charges on the site $i$) and then separately
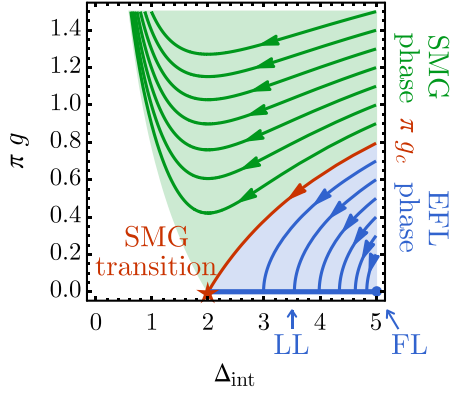
FIG. 2. The renormalization group (RG) flow of the coupling $g$ and the scaling dimension $\Delta_{\text{int}}$ of the SMG interaction. The abbreviations stand for the following terminology: SMG for symmetric mass generation, FL for Fermi liquid, EFL for ersatz FL, LL for Luttinger liquid.

converts $A$-type fermions to $B$-type fermions on the two adjacent sites (which creates two units of charges on each of the site $i − 1$ and $i + 1$), such that the U(1)$_V$ charge is conserved. The interaction is also manifestly translation and reflection symmetric, so the full U(1)$_V \times (\mathbb{Z} \rtimes \mathbb{Z}_2)$ symmetry is preserved by the interaction as expected. With this interaction, we claim that the lattice model in Eq. (6) will exhibit an (ersatz) FL to SMG insulator transition when the interaction strength $g$ exceeds a finite critical value $g_c$.

To show that the proposed interaction in Eq. (16) indeed drives the FL to a gapped interacting insulator, we bosonize [89,90] the fermion operator $c_a \sim \,: \exp(i\varphi_a) :$ (with $a \in \{AR, BR, BL, AL\}$) and cast the lattice model to an effective Luttinger liquid (LL) theory, described by the following Lagrangian density:

$$\mathcal{L} = \frac{1}{4\pi}(\partial_t \varphi^{\mathsf{T}} K \partial_x \varphi - \partial_x \varphi^{\mathsf{T}} V \partial_x \varphi) + \sum_{\alpha=1,2} g_\alpha \cos\left(l_\alpha^{\mathsf{T}} \varphi\right),$$

(17)

where $\varphi = (\varphi_{AR}, \varphi_{BR}, \varphi_{BL}, \varphi_{AL})^{\mathsf{T}}$ are compact scalar bosons. The $K$ matrix and the $l_\alpha$ vectors are given by

$$K = \begin{bmatrix} 1 & 0 & 0 & 0 \\ 0 & 1 & 0 & 0 \\ 0 & 0 & -1 & 0 \\ 0 & 0 & 0 & -1 \end{bmatrix}, \quad l_1 = \begin{bmatrix} 1 \\ -2 \\ 1 \\ 2 \end{bmatrix}, \quad l_2 = \begin{bmatrix} 2 \\ 1 \\ -2 \\ 1 \end{bmatrix}.$$

(18)

As shown in Appendix B, the six-fermion interaction $H_{\text{int}}$ in Eq. (16) translates to the cosine terms $g_1$ and $g_2$ in the LL theory in Eq. (17), with $g_1 = g_2 = g$ enforced by the $\mathbb{Z}_2$ reflection symmetry (as the $\mathbb{Z}_2$ transformation exchanges the $g_1$ and $g_2$ terms). The RG flow in the log energy scale $\ell = −\ln\Lambda$ is given by [91,92]

$$\frac{dg}{d\ell} = (2 - \Delta_{\text{int}})g, \qquad \frac{d\Delta_{\text{int}}^{-1}}{d\ell} = \pi^2 g^2,$$

(19)

where $\Delta_{\text{int}}$ is the scaling dimension of the SMG interaction. The RG flow diagram is shown in Fig. 2.

At the FL fixed point, we have $\Delta_{\text{int}} = \frac{1}{2}l_\alpha^{\mathsf{T}} l_\alpha = 5 > 2$, meaning that the SMG interaction is perturbatively irrelevant. If the bare coupling $g$ (the interaction strength at the lattice scale) is weak ($g < g_c$), it will just flow to zero and disappear in the IR theory. However, the scaling dimensions of all operators will be renormalized as the coupling $g$ flows toward zero. Therefore, the FL fixed point will be deformed into the LL fixed-line, along which the fermion quasiparticle is no longer well defined, but the system remains gapless. Despite the different dynamical properties, the LL still preserves all the kinematic properties (e.g., emergent symmetries and anomalies) as the FL, which can be unified under the concept of *ersatz FL* (EFL) [11].

If the bare coupling $g$ is strong enough ($g > g_c$), the scaling dimension $\Delta_{\text{int}}$ can be reduced to $\Delta_{\text{int}} < 2$ such that the SMG interaction becomes relevant and flows strong. As the cosine term in Eq. (17) gets strong, the corresponding vertex operators $\exp(il_\alpha^{\mathsf{T}} \varphi)$ ($\alpha = 1, 2$) condense. Any other operators that braid nontrivially with the condensed operators will be gapped, which includes all the fermion operators. Therefore, the system enters the SMG insulating phase with all fermion excitations gapped without breaking the U(1) $\times$ ($\mathbb{Z} \rtimes \mathbb{Z}_2$) symmetry. This has been confirmed by the DMRG simulation in Ref. [88] for a related model using the domain wall fermion construction, where it has been verified that the fermion two-point function indeed decays exponentially in the SMG phase—a direct piece of evidence for the gap generation. On the lattice level, this corresponds to condensing the six-fermion bound state by developing the ground state expectation value of $\langle c_{(i-1)B}^\dagger c_{(i-1)A} c_{iB} c_{iA} c_{(i+1)B}^\dagger c_{(i+1)A} \rangle \neq 0$. So the gapping is achieved by the multifermion condensation (involving more than two fermions), which is distinct from the fermion bilinear condensation in the conventional gapping mechanisms of FLs (such as the band hybridization or Cooper pairing mechanisms).

The RG analysis also indicates that the EFL-to-SMG insulator transition (at $g = g_c$) is of the Berezinskii-Kosterlitz-Thouless (BKT) [93–95] transition universality in (1+1)D.

The above analysis established the FS SMG phenomenon in the lattice model in Eq. (6) [equipped with the gapping interaction in Eq. (16)]. The significance of this lattice model is that it provides a pristine 1D lattice regularization of the 3-4-5-0 chiral fermion model by using lattice translation to realize the axial U(1)$_A$ symmetry at low energy. In contrast to the domain wall fermion constructions [51,55,88], our construction does not require the introduction of a (2+1)D bulk to realize the chiral fermions as boundary modes. Such a pristine 1D lattice regularization is advantageous for the numerical simulation of chiral fermions, as the model contains no redundant bulk (or mirror) fermions, such that the computational resources can be used more efficiently. We will leave the numerical exploration of this model to future research.

## III. FS SMG IN (2+1)D

### A. (2+1)D Fermi liquid and Fermi surface anomaly

Given the example of FS SMG in (1+1)D, we would like to further explore similar physics in higher dimensions. The most important low-energy features of a (2+1)D FL are the

gapless fermions on its 1D FS. Suppose we parametrize the 1D FS $\mathbf{k}_F(\theta) \in \partial \mathcal{V}_F$ by a continuous and periodic parameter $\theta$, such that $\mathbf{k}_F(\theta + 2\pi) = \mathbf{k}_F(\theta)$ (where we do not require $\theta$ to literally represent the geometrical angle, as the FS may not be a perfect circle in general). The fermions $c_\theta$ on the FS have an emergent symmetry described by the loop group of U(1) [11,12], denoted as LU(1), under which

$$\text{LU(1)} : c_\theta \to \exp[i\phi(\theta)]c_\theta, \tag{20}$$

where the U(1) phase factor $\exp[i\phi(\theta)]$ is a smooth function of $\theta$ with the periodicity $\exp[i\phi(\theta + 2\pi)] = \exp[i\phi(\theta)]$. Both the (global) charge U(1) and the translation symmetries $\mathbb{R}^2$ are subgroups of LU(1):

$$\text{U(1)} : c_\theta \to e^{iq\phi}c_\theta, \quad \mathbb{R}^2 : c_\theta \to \exp[i\,\delta\mathbf{x} \cdot \mathbf{k}_F(\theta)]c_\theta, \tag{21}$$

assuming the fermions $c_\theta$ carry charge $q$ under the global U(1) symmetry and are translated by the vector $\delta\mathbf{x} \in \mathbb{R}^2$.

The presence of the FS causes a mixed anomaly between the U(1) and translation symmetries [96], which is characterized by the anomaly index:

$$\frac{q}{2(2\pi)^2} \oint d\theta (\mathbf{k}_F \times \partial_\theta \mathbf{k}_F)_3 = \frac{q\mathcal{V}_F}{(2\pi)^2} = q\nu, \tag{22}$$

where $\mathcal{V}_F$ stands for the Fermi volume in the momentum space, and $\nu$ is the filling factor. If the FS anomaly is nonvanishing, it is impossible to trivially gap out the FL without breaking any symmetry or developing any topological order. The FS SMG is only possible if the FL system contains multiple FSs of opposite anomaly indices, such that their anomalies cancel as a whole.

### B. Kagome-triangular lattice model

We present a concrete lattice model to demonstrate the FS SMG in (2+1)D. Consider two types of spinless fermions labeled by $A$ and $B$ that are charged under a global U(1) symmetry with charges $q_A = 1$ and $q_B = 3$, respectively. The $A$-type (or $B$-type) fermion is defined on a kagome (or triangular) lattice. As depicted in Fig. 3(a), the kagome and the triangular lattices lie on top of each other, with the site $I$ of the triangular lattice aligned with the upper triangle $\triangle_I$ on the kagome lattice. We will use the lowercase letters $i$, $j$ (or the uppercase letters $I$, $J$) to label the kagome (or the triangular) lattice sites.

The lattice model is described by the following Hamiltonian:

$$H = H_A + H_B + H_{\text{int,CF}},$$

$$H_A = -t_A \sum_{\langle ij \rangle} (c_i^\dagger c_j + \text{H.c.}) - \mu_A \sum_i c_i^\dagger c_i,$$

$$H_B = -t_B \sum_{\langle IJ \rangle} (c_I^\dagger c_J + \text{H.c.}) - \mu_B \sum_I c_I^\dagger c_I,$$

$$H_{\text{int,CF}} = -g \sum_I \sum_{ijk \in \triangle_I} (c_I^\dagger c_i c_j c_k + \text{H.c.}), \tag{23}$$

where $\langle ij \rangle$ (or $\langle IJ \rangle$) denotes the nearest-neighboring link on the $A$ (or $B$) lattices, and $ijk \in \triangle_I$ stands for the three $A$-sites $i, j, k$ at the vertices of the upper triangle surrounding the
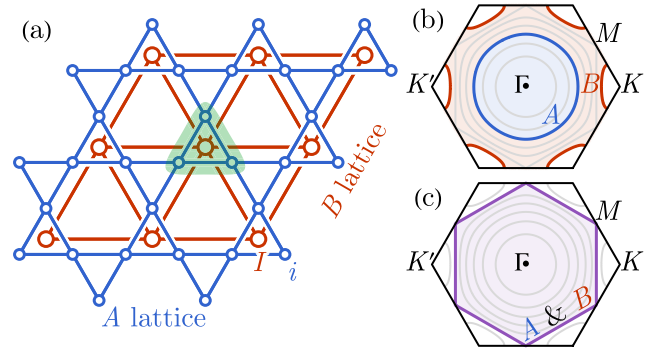


FIG. 3. (a) In the real space, we design the overlapping kagome ($A$) and triangular ($B$) lattices. The green triangle marks out the unit cell. In the momentum $k$ space, we draw many contours to represent various equal energy curves of the energy band, at different filling levels (equally spaced by $\frac{1}{8}$ filling fraction). We illustrate the $A$-type (in blue) and $B$-type (in red) Fermi surfaces (FSs) (b) at a general filling such as $\nu_A = \frac{3}{8}$ and $\nu_B = \frac{7}{8}(= -\frac{1}{8})$, or (c) at a special filling $\nu_A = \nu_B = \frac{3}{4}(= -\frac{1}{4})$ where the FSs coincide.

$B$-site labeled by $I$. The model has a U(1) symmetry that acts as

$$\text{U(1)} : c_i \to e^{i\phi}c_i, \quad c_I \to e^{i3\phi}c_I. \tag{24}$$

The Hamiltonian in Eq. (23) preserves the internal U(1) symmetry and all symmetries of the kagome-triangular lattice (most importantly, the lattice translation symmetry).

The model in Eq. (23) describes the two types of fermions hopping separately on their corresponding lattices. Because every unit cell contains four sites (three from the kagome lattice and one from the triangle lattice), the hopping model will give rise to four energy bands (three bands for $A$-type fermions and one band for $B$-type fermions). The chemical potentials $\mu_A$ and $\mu_B$ are adjusted to ensure the desired filling of these fermions. We will focus on a simple case when only the lowest $A$-type (kagome lattice) bands and the single $B$-type (triangular lattice) bands are filled by filling fractions $\nu_A$ and $\nu_B$, respectively, such that the FS only involves two of the four bands.

The $A$- and $B$-type fermions are coupled together only through a four-fermion interaction $H_{\text{int,CF}}$ in Eq. (23) that fuses three $A$-type (charge-1) fermions to one $B$-type (charge-3) fermions (and vice versa) within each unit cell. We will call it a *charge fusion* (CF) interaction. The CF interaction breaks the separate U(1) charge conservation laws for $A$- and $B$-type fermions in the hopping model to a joint U(1) charge conservation, associated with the symmetry action in Eq. (24). Similar interactions also appear in a recent study [97] of quantum breakdown.

Without interaction ($g = 0$), the system is in a FL phase. According to Eq. (22), the FS anomaly cancellation condition requires

$$q_A \nu_A + q_B \nu_B = 0 \mod 1. \tag{25}$$

Given the charge assignment of $q_A = 1$ and $q_B = 3$, it requires $\nu_A = -3\nu_B$. There is no further requirement on the choice of $\nu_A$ itself. With a generic choice of filling (assuming $\nu_A < 3/4$) as in Fig. 3(b), the $A$-type fermions (on the kagome lattice)

will form an electronlike FS, whose Fermi volume is three times as large as that of the holelike FSs formed by the *B*-type fermions (on the triangular lattice). Although the FL has a vanishing FS anomaly, the charge U(1) and the lattice translation symmetries are still restrictive enough to forbid any gap opening on the free-fermion level. For example, any pairing (charge-2*e* superconducting) gap will break the U(1) symmetry. The only possibility to gap the FL relies on the multifermion interaction.

We claim that the CF interaction $H_{\text{int,CF}}$ in Eq. (23) is a valid SMG interaction that drives the FL into a trivially gaped insulator without breaking symmetry (or developing any topological order). To see this, we go to the strong coupling limit by taking $g \to \infty$. Of course, the chemical potentials $\mu_A, \mu_B$ must increase correspondingly to keep the fermion fillings fixed. The model Hamiltonian decouples to each unit cell in the strong coupling limit:

$$H = \sum_{I|ijk\in\triangle_I} -\mu_A(n_i + n_j + n_k) - \mu_B n_I - g(c_I^\dagger c_i c_j c_k + \text{H.c.}),$$

(26)

where $n_i = c_i^\dagger c_i$ (and $n_I = c_I^\dagger c_I$) denotes the fermion number operator. Within each unit cell, there are only two relevant states $|1110\rangle$ and $|0001\rangle$ (in the Fock state basis $|n_i n_j n_k n_I\rangle$) acted upon by the Hamiltonian. Their hybridization will produce the ground state in each unit cell. The full-system ground state will be the following direct product state:

$$|\text{SMG}\rangle = \bigotimes_I (\sqrt{p}|1110\rangle + \sqrt{1-p}|0001\rangle)_I,$$

(27)

where $p = \frac{1}{2}[1 + \frac{-3\mu_A + \mu_B}{\sqrt{(-3\mu_A + \mu_B)^2 + 4g^2}}]$ is the probability to observe the $|1110\rangle$ state in the unit cell, which is tunable by adjusting $\mu_A, \mu_B$ relative to $g$. The fermion fillings (per unit cell) in the ground state $|\text{SMG}\rangle$ will be

$$\nu_A = 3p, \quad \nu_B = 1 - p = -p \mod 1,$$

(28)

which automatically satisfies the anomaly cancellation condition $\nu_A = -3\nu_B$ (as it should be). The ground state $|\text{SMG}\rangle$ is nondegenerated and gapped from all excited states (with a gap of the order $g$). It also preserves the charge U(1) and all the lattice symmetries and does not have topological order. Therefore, we have explicitly shown that the system ends up in the SMG insulator phase as $g \to \infty$. As a gapped phase, we expect it to be stable against perturbations (such as the hopping terms $t_A$, $t_B$) over a finite region in the parameter space. The SMG phase is a strongly interacting insulating phase, which has no correspondence in the free-fermion picture.

Having established the FL (metallic) phase at $g = 0$ and the SMG insulator phase at $g \to \infty$, there must be an SMG transition (an interaction-driven metal-insulator transition) at some intermediate coupling strength $g_c$. However, the nature of the transition is still an open question, which we will leave for future numerical study. In the following, we will only analyze the SMG transition at a special filling: $\nu_A = \nu_B = \frac{3}{4}$, where the FSs coincide precisely and take the perfect hexagon shapes, as shown in Fig. 3(c). This allows us to gain some analytic control of the problem.

## C. RG analysis of the SMG transition

In this subsection, we analyze the interaction effect in Eq. (23) when the filling is $\nu_A = \nu_B = \frac{3}{4}$. In this case, the FS of the system contains three Van Hove singularities (VHSs), also known as hot spots, located at three distinct *M* points, as shown in Fig. 3(c). This allows us to study the interaction effects using the hot-spot RG method at the one-loop level [98–105]. The hot-spot RG approach assumes that the low-energy physics emerges from the correlated effects of fermions near the VHSs, where the density of states diverges. This divergence leads to the a high instability toward gap opening.

Under RG, the CF interaction $H_{\text{int,CF}}$ will generate two types of density-density interactions at the one-loop level, namely, $H_{\text{int,AA}} = \sum_{i,j} n_i n_j$ and $H_{\text{int,AB}} = \sum_{i,I} n_i n_I$, as well as other (less important) exchange interactions. These density-density interactions are more important in the sense that they will in turn contribute to the correction of $H_{\text{int,CF}}$. Therefore, we should include $H_{\text{int,CF}}, H_{\text{int,AA}}, H_{\text{int,AB}}$ altogether in the RG analysis and study the RG flow jointly.

To proceed, we transform the interactions into the momentum space. The fermion operators are labeled by the flavor index $S = A, B$ and the hot-spot index $\alpha, \beta \in \{1, 2, 3\}$ (referring to the three different VHSs). We note that $H_{\text{int,CF}}$ would vanish if it is naively restricted to the hot spots because the momentum conservation requires multiple *A*-type fermion operators to appear on the same hot spot, which violates the Pauli exclusion principle of fermions. Thus, we need to introduce point splitting in the momentum space around each hot spot. Our strategy is to further split the *A*-type fermion into three modes $A_s$ labeled by $s = 1, 2, 3$, and define the interaction:

$$H_{\text{int,CF}} = g_{\text{rs}} \sum_\alpha \epsilon^{ijk} c_{B\alpha}^\dagger c_{A_i\alpha} c_{A_j\alpha} c_{A_k\alpha}$$

$$+ g_{\text{rt}} \sum_{\alpha\neq\beta} \epsilon^{ijk} c_{B\alpha}^\dagger c_{A_i\alpha} c_{A_j\beta} c_{A_k\beta} + \text{H.c.},$$

(29)

where $g_{\text{rs}}$ and $g_{\text{rt}}$ are the CF interaction decomposed into different momentum transfer channels: the intra-hot-spot scattering $g_{\text{rs}}$ and the inter-hot-spot scattering $g_{\text{rt}}$.

These CF interactions receive corrections from the following density-density interactions at the one-loop level:

$$H_{\text{int,AA}} + H_{\text{int,AB}} = g_{\text{as}} \sum_{\alpha,st} n_{A_s\alpha} n_{A_t\alpha} + (A_s \leftrightarrow A_t)$$

$$+ g_{\text{bt}} \sum_{\alpha\neq\beta,s} n_{B\alpha} n_{A_s\beta} + (A_s \leftrightarrow B)$$

$$+ \text{H.c.} + \dots,$$

(30)

where $\dots$ refers to the other interactions that are decoupled from $g_{\text{rs}}, g_{\text{rt}}, g_{\text{as}}, g_{\text{bt}}$ in the RG equations. The scattering processes of these four important interactions are illustrated in Fig. 4. The complete set of all possible interactions is presented in Appendix C.

We derive the RG equations based on the systematic approach developed in Ref. [106]. Since we are interested in the
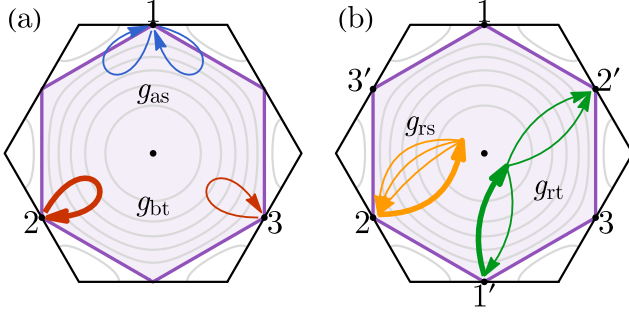
FIG. 4. Scattering of fermions between Van Hove singularities (VHSs) by (a) density-density interactions $g_{bt}$ (red), $g_{as}$ (blue) and (b) nonvanishing processes $g_{rs}$ (yellow), $g_{rt}$ (green) of $H_{int,CF}$. Thin (or thick) arrows correspond to $A$-type (or $B$-type) fermions.

flow of $H_{int,CF}$, the relevant part of the RG equations reads

$$\frac{dg_{bt}}{d\ell} = 2d_0 d_{AB} g_{bt}^2, \quad \frac{dg_{as}}{d\ell} = -2g_{as}^2,$$

$$\frac{dg_{rs}}{d\ell} = -6g_{as}g_{rs}, \quad \frac{dg_{rt}}{d\ell} = 4d_0 d_{AB} g_{bt} g_{rt} - 2g_{as}g_{rt}. \quad (31)$$

where the RG parameter is defined by the Cooper-pairing susceptibility of $A$-type fermions $\ell = \chi_{pp,AA}(\mathbf{k} = 0, E) \sim \nu_0 \ln^2(\Lambda/E)$, in which $\nu_0 \ln(\Lambda/E)$ is the diverging density of states at the VHS, $E$ is the running energy scale, and $\Lambda$ is the high-energy cutoff. Here, $d_0 = d\chi_{ph,AA}(\mathbf{Q})/d\ell \leqslant 1$ is the nesting parameter of $A$-type fermions, which saturates to one in the perfectly nested limit ($d_0 \to 1$). In our case, different VHSs are half-nested (only one of the two crossing FSs is perfectly nested between every pair of different VHSs), so $d_0 = \frac{1}{2}$ is a suitable estimation. Similarly, we define $d_{AB} = d\chi_{pp,AB}(\tilde{\mathbf{0}})/d\ell$, which depends on the energies of $A$- and $B$-type fermions near the VHS. The full RG equations and details are listed in Appendix C.

According to the one-loop RG equations, if the density-density interactions $g_{bt}, g_{as}$ are initially zero, then the CF interactions $g_{rs}, g_{rt}$ remain marginal along the RG flow. However, if we turn on small density-density interactions $g_{bt}, g_{as}$ with correct signs ($g_{bt} > 0$ or $g_{as} < 0$), the CF interactions $g_{rs}, g_{rt}$ will be marginally relevant. The solutions of the RG equations in Eq. (31) are

$$g_{bt}(\ell) = \frac{g_{bt}(0)}{1 - 2d_0 d_{AB} g_{bt}(0)\ell}, \quad g_{as}(\ell) = \frac{g_{as}(0)}{1 + 2g_{as}(0)\ell},$$

$$g_{rs}(\ell) = \frac{g_{rs}(0)}{[1 + 2g_{as}(0)\ell]^3},$$

$$g_{rt}(\ell) = \frac{g_{rt}(0)}{[1 + 2g_{as}(0)\ell][1 - 2d_0 d_{AB} g_{bt}(0)\ell]^2}. \quad (32)$$

As the RG parameter $\ell$ increases under the RG flow, the coupling strengths can diverge at some critical scale $\ell_c$, when any of the denominators in Eq. (32) vanish. The critical scale is set by the bare density-density interaction strengths $g_{bt}(0)$ and $g_{as}(0)$, but the CF interaction strengths $g_{rs}, g_{rt}$ diverge faster than the density-density interactions as the critical scale is approached. Therefore, the RG fixed points are characterized by the behavior of $g_{rs}, g_{rt}$.
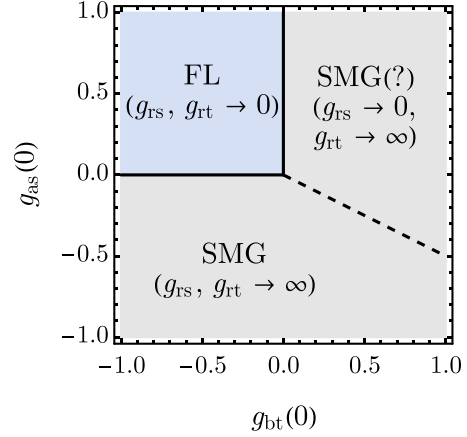


FIG. 5. The renormalization group (RG) phase diagram with respect to the density-density interactions $g_{as}, g_{bt}$. In the Fermi liquid (FL) phase, the gapping interaction flows to zero. In the symmetric mass generation (SMG) phase, the gapping interaction flows to infinity.

Depending on the bare density-density interaction strengths $g_{as}(0)$ and $g_{bt}(0)$, the system can flow toward different RG fixed points, as shown Fig. 5. When $g_{as}(0) > 0$ and $g_{bt}(0) < 0$, all interactions flow to zero, which corresponds to the FL fixed point. When $g_{as}(0) < \min[0, -d_0 d_{AB} g_{bt}(0)]$, both CF interactions $g_{rs}, g_{rt}$ flow to infinity, which should correspond to the SMG phase according to the previous lattice model analysis. However, we also find a region in the phase diagram, described by $g_{bt} > \max(0, -g_{as}/d_0 d_{AB})$, where $g_{rs} \to 0$ and $g_{rt} \to \infty$, i.e., flowing toward different limits. We are not sure how to interpret the physical meaning of this RG fixed point. It might still be in the SMG phase as one interaction still flows strong, but it could as well end up in a spontaneous symmetry breaking (SSB) phase that breaks the LU(1) symmetry since the $A$- and $B$-type FSs have pretty strong nesting instability. This might also be an artifact of the hot-spot RG method, as it does not fully capture all low-energy fermionic degrees of freedom of the FS.

Admittedly, it is not possible to determine whether the full FS is gapped using the hot-spot RG analysis alone. This is because the hot-spot RG approach only considers the fermions near the VHSs and not the FS freedom away from the VHSs. To determine whether the strong coupling fixed point is a fully gapped state, we have to rely on lattice model analysis in the strong coupling limit. The exact ground-state solution in Eq. (27) provides evidence to support the argument that the strong coupling fixed point is indeed a fully gapped state.

To improve, functional RG [107–110] might provide a better resolution of the FS and remove the uncertainty in the phase diagram in Fig. 5. A recent study [111] has demonstrated the functional RG method in a triangle lattice model with spinless fermions. The same technique might apply to our model as well. However, we will leave such a study for future research.

By tuning $g_{as}(0)$ across zero on the $g_{bt}(0) < 0$ side, one can drive a FL-to-SMG transition. The gapping interaction is marginally relevant at the transition point. According to
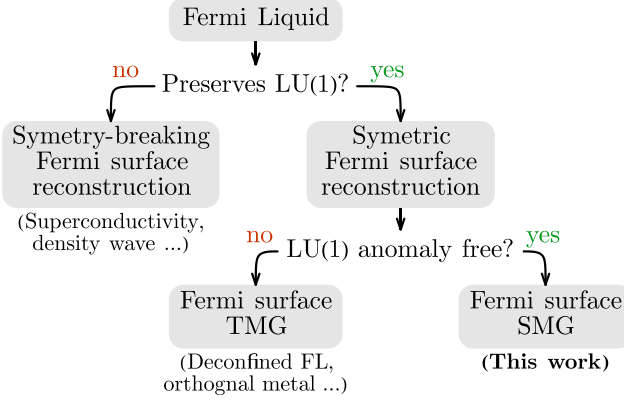
FIG. 6. Classification of Fermi surface (FS) reconstruction mechanisms, based on the LU(1) loop group symmetry. Symmetric FS reconstruction (SFSR) contains two broad classes: (1) FS symmetric mass generation (SMG) if the total FS anomaly is canceled and (2) FS topological mass generation (TMG) if the total FS anomaly is matched by topological order with low energy topological field theory.

the solution of the RG equations in Eq. (32), the coupling diverges at the critical scale $\ell_c \sim \nu_0 \ln^2(\Lambda/\Delta_{\text{SMG}})$ when the denominator $[1 + 2g_{\text{as}}(0)l_c]$ vanishes. This implies that the SMG gap $\Delta_{\text{SMG}}$ (the energy gap between the ground state and the first excited state) opens up as [112,113]

$$\Delta_{\text{SMG}} \sim \Lambda \exp\left[-\frac{c}{\sqrt{g_{\text{as}}(0)\nu_0}}\right], \qquad (33)$$

where $\Lambda$ is the ultraviolet (UV) cutoff energy scale, $\nu_0$ is the coefficient in front of the diverging density of state at the VHS, and $c$ is some nonuniversal constant.

## IV. SUMMARY AND DISCUSSION

In this paper, we propose the concept of FS SMG: a mechanism to gap out FSs by nonperturbative interaction effects without breaking the LU(1) symmetry. This phenomenon can only happen when the FS anomaly is canceled out in the fermion system. We present (1+1)D and (2+1)D examples of FS SMG. We expect that the mechanism can generally occur in all dimensions.

FS SMG belongs to a broader class of phenomena, called the symmetric FS reconstruction (SFSR), as summarized in Fig. 6. The SFSR is in contrast to the more conventional symmetry-breaking FS reconstruction, where the FS is reconstructed (or gapped) by developing SSB orders. Depending on the cancellation of the FS anomaly, the SFSR further splits into two classes: the FS SMG if the anomaly vanishes or the FS topological mass generation (TMG) if the anomaly does not vanish. The former class, the FS SMG, is the focus of this paper. The latter class, the FS TMG, is also discussed in the literature, where the nonvanishing FS anomaly is absorbed by an anomalous topological quantum field theory, such that the SFSR is achieved by developing the corresponding topological order. This gives rise to deconfined/fractionalized FL (FL*) [114–116] or orthogonal metal [117–119].

Symmetry extension [120] has provided a unified framework to understand TMG and SMG for bosons or fermions of zero Fermi volume [121–126], where the symmetric gapping can be achieved by extending the symmetry group to lift any gapping obstruction that was otherwise imposed by the symmetry. Similar constructions can be applied to understand SFSR more generally.

FS SMG deforms an anomaly-free (charge-compensated) FL state to a fully gapped product state. Although the resulting SMG gapped state does not have nontrivial features like topological order, the SMG transition from the FL phase to the SMG phase can still be quite exotic. The SMG transition of relativistic fermions has been proposed as a deconfined quantum critical point [127,128], where the physical fermion fractionalizes to bosonic and fermionic partons with emergent gauge fluctuations at and only at the critical point. It is conceivable that similar scenarios might apply to the FS SMG transition as well, where deconfined FL (orthogonal metal) could emerge at the critical point. The lattice models presented in this paper lay the ground for future theoretical and numerical studies of the exotic SMG transition in these models.

It is also known that the fermion single-particle Green's function has symmetry-protected zeros at zero frequency in the SMG phase [129–132]. It will be interesting to investigate further the Green's function structure in the FS SMG phase. Whether the SMG interaction will replace the original FS (a loop of poles) with a loop of zeros in the Green's function is still an open question to explore.

Another potential experimental connection is to apply the FS SMG to understand the nature of pseudogap phases, which is an exotic state of electrons where the FS is partially gapped without obvious symmetry breaking. It has been observed in many correlated materials. The recent proposal of the ancilla qubit approach [133,134] for pseudogap physics draws a connection between the pseudogap metal-to-FL transition with the FS SMG transition in the ancilla layers, as both transitions are described by field theories of fermionic deconfined quantum critical points [127,128,135–137]. The FS anomaly constrains the dynamical behavior of such field theories and can potentially shed light on the open problem of pseudogap transition in correlated materials.

## APPENDIX A: EMERGENT U(1) SYMMETRIES IN THE (1+1)D TWO-BAND MODEL

Start from the definition of charge U(1) (parameterized by a periodic angle $\phi \in [0, 2\pi)$) and lattice translation $\mathbb{Z}$ (parameterized by an integer $n \in \mathbb{Z}$) symmetries as defined in Eq. (7):

$$\text{U(1)} : c_{iA} \to \exp(iq_A\phi)c_{iA}, \quad c_{iB} \to \exp(iq_B\phi)c_{iB};$$
$$\mathbb{Z} : c_{iA} \to c_{(i+n)A}, \quad c_{iB} \to c_{(i+n)B}. \tag{A1}$$

Follow the definition in Eq. (9) of the fermion operators in the momentum space:

$$c_{kA} = \sum_i c_{iA} e^{-iki}, \quad c_{kB} = \sum_i c_{iB} e^{-iki}, \tag{A2}$$

where the wave number $k \in [-\pi, \pi)$ is a dimensionless periodic variable defined in the first Brillouin zone. (Note: the dimensionful momentum $p$ should be related to the dimensionless wave number $k$ by $p = \hbar k/a$, with $a$ being the lattice constant, and the site coordinate $x \in \mathbb{R}$ is related to the site index $i \in \mathbb{Z}$ by $x = ai$, such that the Fourier factor $e^{-ipx/\hbar} = e^{-iki}$ is consistent with the quantum mechanics convention.) It is straightforward to show that the U(1) $\times \mathbb{Z}$ symmetry acts in the momentum space as

$$\text{U(1)} : c_{kA} \to \exp(iq_A\phi)c_{kA}, \quad c_{kB} \to \exp(iq_B\phi)c_{kB};$$
$$\mathbb{Z} : c_{kA} \to e^{ikn}c_{kA}, \quad c_{kB} \to e^{ikn}c_{kB}. \tag{A3}$$

Apply these transformations to the low-energy fermion near the four Fermi points. According to Eq. (12):

$$c_{AR} = c_{(3k_F)A}, \quad c_{BR} = c_{(-k_F)B},$$
$$c_{BL} = c_{(k_F)B}, \quad c_{AL} = c_{(-3k_F)A}, \tag{A4}$$

Eq. (A3) becomes

$$\text{U(1)} : \begin{cases} c_{AR} \to \exp(iq_A\phi)c_{AR}, \\ c_{BR} \to \exp(iq_B\phi)c_{BR}, \\ c_{BL} \to \exp(iq_B\phi)c_{BL}, \\ c_{AL} \to \exp(iq_A\phi)c_{AL}; \end{cases}$$
$$\mathbb{Z} : \begin{cases} c_{AR} \to \exp(3ik_F n)c_{AR}, \\ c_{BR} \to \exp(-ik_F n)c_{BR}, \\ c_{BL} \to \exp(ik_F n)c_{BL}, \\ c_{AL} \to \exp(-3ik_F n)c_{AL}. \end{cases} \tag{A5}$$

Because $k_F = |v_B|\pi$ is almost always (i.e., with probability 1) an irrational multiple of $\pi$ (because $|v_B|$ is almost always an irrational number without fine tuning), $k_F n \mod 2\pi$ can approach any angle in $[0, 2\pi)$ (with $2\pi$ periodicity) as close as we want (given $n \in \mathbb{Z}$). This allows us to define two angular variables $\phi_V$ and $\phi_A$, both are periodic in $[0, 2\pi)$:

$$\phi_V = \phi, \quad \phi_A = k_F n \mod 2\pi, \tag{A6}$$

then Eq. (A5) can be compactly written as

UV symmetry $\Rightarrow$ IR symmetry

$$\text{U(1)} \Rightarrow \text{U(1)}_V : c_a \to \exp\left(iq_a^V \phi_V\right)c_a,$$
$$\mathbb{Z} \Rightarrow \text{U(1)}_A : c_a \to \exp\left(iq_a^A \phi_A\right)c_a, \tag{A7}$$

for $a = AR, BR, BL, AL$, enumerating over the four Fermi point labels, together with the charge vectors (given that $q_A = 1$ and $q_B = 3$):

$$\mathbf{q}^V = \begin{bmatrix} q_A \\ q_B \\ q_B \\ q_A \end{bmatrix} = \begin{bmatrix} 1 \\ 3 \\ 3 \\ 1 \end{bmatrix}, \quad \mathbf{q}^A = \begin{bmatrix} 3 \\ -1 \\ 1 \\ -3 \end{bmatrix}. \tag{A8}$$

Therefore, the global charge U(1) symmetry is simply reinterpreted as the U(1)$_V$ vector symmetry, and the translation symmetry (described by a noncompact $\mathbb{Z}$ group) in the UV becomes an emergent U(1)$_A$ axial symmetry (described by a compact U(1) group) in the IR. The symmetry transformation in Eq. (A7) precisely matches Eq. (14) with the correct charge assignment as listed in Table I.

Recombining the charge vectors of U(1)$_V$ and U(1)$_A$, we can define two alternative emergent U(1) symmetries, denoted as U(1)$_{\frac{3V \pm A}{2}}$ with the charge vectors:

$$\mathbf{q}^{\frac{3V \pm A}{2}} = \tfrac{1}{2}(3\mathbf{q}^V \pm \mathbf{q}^A), \tag{A9}$$

as their names implied. More explicitly, the charge vectors match the chiral charge assignments for the 3-4-5-0 fermions:

$$\mathbf{q}^{\frac{3V+A}{2}} = \begin{bmatrix} 3 \\ 4 \\ 5 \\ 0 \end{bmatrix}, \quad \mathbf{q}^{\frac{3V-A}{2}} = \begin{bmatrix} 0 \\ 5 \\ 4 \\ 3 \end{bmatrix}. \tag{A10}$$

The fermions are expected to transform under U(1)$_{\frac{3V \pm A}{2}}$ as (parameterized by the periodic angles $\phi_\pm \in [0, 2\pi)$)

$$\text{U(1)}_{\frac{3V \pm A}{2}} : c_a \to \exp\left[i\tfrac{1}{2}\left(3q_a^V \pm q_a^A\right)\phi_\pm\right]c_a. \tag{A11}$$

This can be viewed as the combined transformation of U(1)$_V$ and U(1)$_A$ with the vector rotation angle $\phi_V$ and the axial rotation angle $\phi_A$ given by

$$\phi_V = \tfrac{3}{2}\phi_\pm, \quad \phi_A = \pm\tfrac{1}{2}\phi_\pm, \tag{A12}$$

as can be verified by comparing Eq. (A11) with Eq. (A7). Now we can connect these rotation angles back to the original U(1) $\times \mathbb{Z}$ symmetry of the lattice fermions using the relation in Eq. (A6):

$$\phi = \tfrac{3}{2}\phi_\pm, \quad \pm\tfrac{1}{2}\phi_\pm = k_F n \mod 2\pi. \tag{A13}$$

Eliminate $\phi_\pm$ from the equations, and we obtain the relation:

$$\phi = \pm 3k_F n \mod 2\pi, \tag{A14}$$

for the U(1)$_{\frac{3V \pm A}{2}}$ symmetries. Therefore, to reproduce the IR emergent U(1)$_{\frac{3V \pm A}{2}}$ symmetries, the corresponding UV symmetries (at the lattice level) must be implemented such that every $n$-step translation should be followed by a charge U(1) rotation with the rotation angle $\phi = \pm 3k_F n$. Thus, we establish the following correspondence between the IR and UV

symmetries:

$$\text{IR symmetry} \Rightarrow \text{UV symmetry}$$

$$\mathrm{U}(1)_{\frac{3V \pm A}{2}} \Rightarrow \mathbb{Z}\left(\frac{3V \pm A}{2}\right): \begin{cases} c_{iA} \to \exp(\pm 3iq_A k_F n)c_{(i+n)A}, \\ c_{iB} \to \exp(\pm 3iq_B k_F n)c_{(i+n)B}. \end{cases}$$

$$(A15)$$

Here, the compact U(1) symmetries in the IR get mapped to the noncompact symmetries $\mathbb{Z}$ in the UV because the UV symmetries are parameterized by the integer variable $n \in \mathbb{Z}$. Given that $q_A = 1$ and $q_B = 3$, Eq. (A15) becomes Eq. (15), as claimed in the main text. Therefore, the 3-4-5-0 chiral fermion model is indeed realized by the (1+1)D two-band lattice model at low energy.

## APPENDIX B: WANG-WEN INTERACTION

In the bonsonization language, the Wang-Wen interaction is described by

$$\mathcal{L}_{\text{int}} = \sum_{\alpha=1,2} g_\alpha \cos\left(l_\alpha^\mathsf{T} \varphi\right), \tag{B1}$$

with $\varphi = (\varphi_{AR}, \varphi_{BR}, \varphi_{BL}, \varphi_{AL})^\mathsf{T}$ and the interaction vectors given by

$$l_1 = \begin{bmatrix} 1 \\ -2 \\ 1 \\ 2 \end{bmatrix}, \quad l_2 = \begin{bmatrix} 2 \\ 1 \\ -2 \\ 1 \end{bmatrix}. \tag{B2}$$

Mapping back to the chiral fermions by the correspondence $c_a \sim\,: \exp(i\varphi_a):$, the interaction reads

$$H_{\text{int}} = \frac{g_1}{2}(c_{AR}c_{BL})(c_{BR}^\dagger c_{AL})^2 + \text{H.c.}$$
$$+ \frac{g_2}{2}(c_{BR}c_{AL})(c_{AR}c_{BL}^\dagger)^2 + \text{H.c.} \tag{B3}$$

According to Eq. (12) and using the inverse Fourier transformation:

$$c_{AR} = c_{(3k_F)A} = \sum_i c_{iA} \exp(3ik_F i),$$

$$c_{BR} = c_{(-k_F)B} = \sum_i c_{iB} \exp(-ik_F i),$$

$$c_{BL} = c_{(k_F)B} = \sum_i c_{iB} \exp(ik_F i),$$

$$c_{AL} = c_{(-3k_F)A} = \sum_i c_{iA} \exp(-3ik_F i). \tag{B4}$$

Plugging Eq. (B4) into Eq. (B3), the interaction becomes

$$H_{\text{int}} = \sum_{i_1,\cdots,i_6} g_{i_1\cdots i_6}\left(c_{i_1B}^\dagger c_{i_2A}\right)\left(c_{i_3B} c_{i_4A}\right)\left(c_{i_5B}^\dagger c_{i_6A}\right) + \text{H.c.},$$

$$(B5)$$

with

$$g_{i_1\cdots i_6} = \frac{g_1}{2} \exp[ik_F(i_1 - 3i_2 + i_3 + 3i_4 + i_5 - 3i_6)]$$
$$+ \frac{g_2}{2} \exp[ik_F(-i_1 + 3i_2 - i_3 - 3i_4 - i_5 + 3i_6)].$$

$$(B6)$$

Notice that, under lattice reflection symmetry $\mathbb{Z}_2 : c_{iA} \to c_{(-i)A}, c_{iB} \to c_{(-i)B}$, $g_1$ and $g_2$ map to each other. To simplify, we can impose the reflection symmetry which requires $g_1 = g_2 = g$. Then the coupling coefficient is

$$g_{i_1\cdots i_6} = g \cos[k_F(i_1 - 3i_2 + i_3 + 3i_4 + i_5 - 3i_6)]. \tag{B7}$$

The dominant $s$-wave interaction is given by

$$i_1 - 3i_2 + i_3 + 3i_4 + i_5 - 3i_6 = 0, \tag{B8}$$

such that $g_{i_1\cdots i_6} = g$ is uniform. We seek a local interaction that has minimal span on the lattice. The optimal solution of Eq. (B8) is given by

$$i_1 = i_2 = i - 1, \quad i_3 = i_4 = i, \quad i_5 = i_6 = i + 1, \tag{B9}$$

for any choice of $i$. With this solution in Eq. (B9), Eq. (B5) reduces to

$$H_{\text{int}} = g \sum_i c_{(i-1)B}^\dagger c_{(i-1)A} c_{iB} c_{iA} c_{(i+1)B}^\dagger c_{(i+1)A} + \text{H.c.}, \tag{B10}$$

which is the SMG interaction in Eq. (16) proposed in the main text.

## APPENDIX C: FULL RG EQUATIONS

We start with the interaction $H_{\text{int,CF}}$:

$$H_{\text{int,CF}} = g_{\text{rs}} \sum_\alpha \epsilon^{ijk} c_{B\alpha}^\dagger c_{A_i\alpha} c_{A_j\alpha} c_{A_k\alpha}$$
$$+ g_{\text{rt}} \sum_{\alpha\neq\beta} \epsilon^{ijk} c_{B\alpha}^\dagger c_{A_i\alpha} c_{A_j\beta} c_{A_k\beta} + \text{H.c.} \tag{C1}$$

Under RG, the following density-density and exchange interactions will be generated:

$$H_{\text{int,AA}} = g_{\text{as}} \sum_{\alpha,st} n_{A_s\alpha} n_{A_t\alpha} + g_{\text{at}} \sum_{\alpha\neq\beta,st} n_{A_s\alpha} n_{A_t\beta}$$
$$+ g_{\text{ae}} \sum_{\alpha\neq\beta,st} c_{A_s\alpha}^\dagger c_{A_s\beta} c_{A_t\beta}^\dagger c_{A_t\alpha}$$
$$+ (A_s \leftrightarrow A_t) + \text{H.c.}, \tag{C2}$$

and

$$H_{\text{int,AB}} = g_{\text{bs}} \sum_{\alpha,s} n_{B\alpha} n_{A_s\alpha} + g_{\text{bt}} \sum_{\alpha\neq\beta,s} n_{B\alpha} n_{A_s\beta}$$
$$+ g_{\text{be}} \sum_{\alpha\neq\beta,s} c_{B\alpha}^\dagger c_{B\beta} c_{A_s\beta}^\dagger c_{A_s\alpha} + (A_s \leftrightarrow B) + \text{H.c.} \tag{C3}$$

There is an additional density-density interaction that will correct $H_{\text{int,AA}}, H_{\text{int,AB}}$:

$$H_{\text{int,BB}} = g_{\text{bb}} \sum_{\alpha\beta} n_{B\alpha} n_{B\beta} - c_{B\alpha}^\dagger c_{B\beta} c_{B\beta}^\dagger c_{B\alpha}. \quad \text{(C4)}$$

Putting all interactions together, the complete RG equations are

$$\frac{dg_{\text{bb}}}{d\ell} = 4d_0 d_{\text{BB}} g_{\text{bb}}^2 + 3d_0 g_{\text{be}}^2,$$

$$\frac{dg_{\text{bs}}}{d\ell} = -2d_{\text{AB}} g_{\text{bs}}^2 + \frac{9g_{\text{rs}}^2}{2} + g_{\text{rt}}^2,$$

$$\frac{dg_{\text{bt}}}{d\ell} = 2d_0 d_{\text{AB}} g_{\text{bt}}^2,$$

$$\frac{dg_{\text{be}}}{d\ell} = -6d_0 g_{\text{ae}} g_{\text{be}} + 2d_0 g_{\text{at}} g_{\text{be}} + 4d_0 d_{\text{BB}} g_{\text{bb}} g_{\text{be}}$$
$$+ 3g_{\text{rs}} g_{\text{rt}} + \frac{g_{\text{rt}}^2}{2},$$

$$\frac{dg_{\text{as}}}{d\ell} = -2g_{\text{as}}^2,$$

$$\frac{dg_{\text{at}}}{d\ell} = 2d_0 g_{\text{at}}^2 - d_0 d_{\text{AB}} g_{\text{rt}}^2,$$

$$\frac{dg_{\text{ae}}}{d\ell} = -d_0 d_{\text{AB}} g_{\text{rt}}^2 + 4d_0 g_{\text{ae}} g_{\text{at}} - 6d_0 g_{\text{ae}}^2 - 2d_0 d_{\text{BB}} g_{\text{be}}^2,$$

$$\frac{dg_{\text{rs}}}{d\ell} = -6g_{\text{as}} g_{\text{rs}},$$

$$\frac{dg_{\text{rt}}}{d\ell} = 4d_0 d_{\text{AB}} g_{\text{bt}} g_{\text{rt}} - 2g_{\text{as}} g_{\text{rt}},$$

where $d_{\text{AB}} = d\chi_{pp,\text{AB}}(\mathbf{0})/d\ell$, $d_{\text{BB}} = d\chi_{pp,\text{BB}}(\mathbf{0})/d\ell$. These ratios depend on the energies of $A$- and $B$-type fermions near the VHSs. The two types of fermions have similar band structures, which can be approximated as $E_{\mathbf{k}}^{A,B} = \epsilon^{A,B} f(\mathbf{k})$. The ratios are then given by $d_{\text{AB}} = \frac{2|\epsilon^A|}{|\epsilon^A|+|\epsilon^B|}$ and $d_{\text{BB}} = \frac{|\epsilon^A|}{|\epsilon^B|}$. If $A$- and $B$-type fermions have the same band structure, then $d_{\text{AB}} = d_{\text{BB}} = 1$.

[1] L. Landau and E. Lifshitz, in *Statistical Physics. Part 1*, 3rd Ed. Course of Theoretical Physics, Vol. 5 (Elsevier Butterworth-Heinemann, Oxford, 1980).

[2] E. M. Lifshitz and L. P. Pitaevskii, in *Statistical Physics. Part 2: Theory of the Condensed State*, Course of Theoretical Physics, Vol. 9 (Butterworth-Heinemann Ltd, Oxford, 1980).

[3] J. Wang and Y.-Z. You, Symmetric mass generation, Symmetry **14**, 1475 (2022).

[4] R. Shankar, Renormalization group for interacting fermions in $d > 1$, Physica A **177**, 530 (1991).

[5] R. Shankar, Renormalization-group approach to interacting fermions, Rev. Mod. Phys. **66**, 129 (1994).

[6] A. C. Hewson, Renormalization group and Fermi liquid theory, Adv. Phys. **43**, 543 (1994).

[7] G. Y. Chitov and D. Sénéchal, Renormalization-group study of interacting electrons, Phys. Rev. B **52**, 13487 (1995).

[8] N. Dupuis and G. Y. Chitov, Renormalization-group approach to Fermi-liquid theory, Phys. Rev. B **54**, 3040 (1996).

[9] G. Y. Chitov and D. Sénéchal, Fermi liquid as a renormalization-group fixed point: The role of interference in the Landau channel, Phys. Rev. B **57**, 1444 (1998).

[10] L. Rademaker and M. Ortuño, Explicit Local Integrals of Motion for the Many-Body Localized State, Phys. Rev. Lett. **116**, 010404 (2016).

[11] D. V. Else, R. Thorngren, and T. Senthil, Non-Fermi Liquids as Ersatz Fermi Liquids: General Constraints on Compressible Metals, Phys. Rev. X **11**, 021005 (2021).

[12] D. V. Else and T. Senthil, Strange Metals as Ersatz Fermi Liquids, Phys. Rev. Lett. **127**, 086601 (2021).

[13] D.-C. Lu, J. Wang, and Y.-Z. You, Definition and classification of Fermi surface anomalies, arXiv:2302.12731.

[14] M. Oshikawa, M. Yamanaka, and I. Affleck, Magnetization Plateaus in Spin Chains: "Haldane Gap" for Half-Integer Spins, Phys. Rev. Lett. **78**, 1984 (1997).

[15] M. Oshikawa, Commensurability, Excitation Gap, and Topology in Quantum Many-Particle Systems on a Periodic Lattice, Phys. Rev. Lett. **84**, 1535 (2000).

[16] M. Oshikawa, Topological Approach to Luttinger's Theorem and the Fermi Surface of a Kondo Lattice, Phys. Rev. Lett. **84**, 3370 (2000).

[17] G. Misguich, C. Lhuillier, M. Mambrini, and P. Sindzingre, Degeneracy of the ground-state of antiferromagnetic spin-$\frac{1}{2}$ Hamiltonians, Eur. Phys. J. B **26**, 167 (2002).

[18] A. Paramekanti and A. Vishwanath, Extending Luttinger's theorem to $\mathbb{Z}_2$ fractionalized phases of matter, Phys. Rev. B **70**, 245118 (2004).

[19] F. D. M. Haldane, Luttinger's theorem and bosonization of the Fermi surface, arXiv:cond-mat/0505529.

[20] M. B. Hastings, Sufficient conditions for topological order in insulators, Europhys. Lett. **70**, 824 (2005).

[21] H. Watanabe, H. C. Po, A. Vishwanath, and M. Zaletel, Filling constraints for spin-orbit coupled insulators in symmorphic and nonsymmorphic crystals, Proc. Natl. Acad. Sci. USA **112**, 14551 (2015).

[22] M. Cheng, M. Zaletel, M. Barkeshli, A. Vishwanath, and P. Bonderson, Translational Symmetry and Microscopic Constraints on Symmetry-Enriched Topological Phases: A View from the Surface, Phys. Rev. X **6**, 041068 (2016).

[23] Y.-M. Lu, Y. Ran, and M. Oshikawa, Filling-enforced constraint on the quantized Hall conductivity on a periodic lattice, Ann. Phys. **413**, 168060 (2017).

[24] G. Y. Cho, C.-T. Hsieh, and S. Ryu, Anomaly manifestation of Lieb-Schultz-Mattis theorem and topological phases, Phys. Rev. B **96**, 195105 (2017).

[25] C.-M. Jian, Z. Bi, and C. Xu, Lieb-Schultz-Mattis theorem and its generalizations from the perspective of the symmetry-protected topological phase, Phys. Rev. B **97**, 054412 (2018).

[26] M. A. Metlitski and R. Thorngren, Intrinsic and emergent anomalies at deconfined critical points, Phys. Rev. B **98**, 085140 (2018).

[27] N. Bultinck and M. Cheng, Filling constraints on fermionic topological order in zero magnetic field, Phys. Rev. B **98**, 161119(R) (2018).

[28] X.-Y. Song, Y.-C. He, A. Vishwanath, and C. Wang, Electric polarization as a nonquantized topological response and boundary Luttinger theorem, Phys. Rev. Res. **3**, 023011 (2019).

[29] Y. Yao and M. Oshikawa, Generalized Boundary Condition Applied to Lieb-Schultz-Mattis-Type Ingappabilities and Many-Body Chern Numbers, Phys. Rev. X **10**, 031008 (2020).

[30] J. M. Luttinger, Fermi surface and some simple equilibrium properties of a system of interacting fermions, Phys. Rev. **119**, 1153 (1960).

[31] E. Lieb, T. Schultz, and D. Mattis, Two soluble models of an antiferromagnetic chain, Ann. Phys. **16**, 407 (1961).

[32] S. Ryu, J. E. Moore, and A. W. W. Ludwig, Electromagnetic and gravitational responses and anomalies in topological insulators and superconductors, Phys. Rev. B **85**, 045104 (2012).

[33] X.-G. Wen, Classifying gauge anomalies through symmetry-protected trivial orders and classifying gravitational anomalies through topological orders, Phys. Rev. D **88**, 045013 (2013).

[34] A. Kapustin and R. Thorngren, Anomalies of discrete symmetries in various dimensions and group cohomology, arXiv:1404.3230.

[35] J. C. Wang, Z.-C. Gu, and X.-G. Wen, Field-Theory Representation of Gauge-Gravity Symmetry-Protected Topological Invariants, Group Cohomology, and Beyond, Phys. Rev. Lett. **114**, 031601 (2015).

[36] T. Senthil, Symmetry protected topological phases of quantum matter, Annu. Rev. Condens. Matter Phys. **6**, 299 (2015).

[37] E. Witten, Fermion path integrals and topological phases, Rev. Mod. Phys. **88**, 035001 (2016).

[38] X.-G. Wen, Zoo of quantum-topological phases of matter, Rev. Mod. Phys. **89**, 041004 (2017).

[39] L. Fidkowski and A. Kitaev, Effects of interactions on the topological classification of free fermion systems, Phys. Rev. B **81**, 134509 (2010).

[40] L. Fidkowski and A. Kitaev, Topological phases of fermions in one dimension, Phys. Rev. B **83**, 075103 (2011).

[41] S. Ryu and S.-C. Zhang, Interacting topological phases and modular invariance, Phys. Rev. B **85**, 245132 (2012).

[42] X.-L. Qi, A new class of $(2 + 1)$-dimensional topological superconductors with $\mathbb{Z}_8$ topological classification, New J. Phys. **15**, 065002 (2013).

[43] H. Yao and S. Ryu, Interaction effect on topological classification of superconductors in two dimensions, Phys. Rev. B **88**, 064507 (2013).

[44] Z.-C. Gu and M. Levin, Effect of interactions on two-dimensional fermionic symmetry-protected topological phases with $Z_2$ symmetry, Phys. Rev. B **89**, 201113(R) (2014).

[45] X.-G. Wen, A lattice non-perturbative definition of an SO(10) chiral gauge theory and its induced standard model, Chin. Phys. Lett. **30**, 111101 (2013).

[46] J. Wang and X.-G. Wen, Nonperturbative regularization of $(1+1)$-dimensional anomaly-free chiral fermions and bosons: On the equivalence of anomaly matching conditions and boundary gapping rules, Phs. Rev. B **107**, 014311 (2013).

[47] K. Slagle, Y.-Z. You, and C. Xu, Exotic quantum phase transitions of strongly interacting topological insulators, Phys. Rev. B **91**, 115121 (2015).

[48] V. Ayyar and S. Chandrasekharan, Massive fermions without fermion bilinear condensates, Phys. Rev. D **91**, 065035 (2015).

[49] S. Catterall, Fermion mass without symmetry breaking, J. High Energy Phys. 01 (2016) 121.

[50] V. Ayyar and S. Chandrasekharan, Origin of fermion masses without spontaneous symmetry breaking, Phys. Rev. D **93**, 081701(R) (2016).

[51] J. Wang and X.-G. Wen, Solution to the $1 + 1$ dimensional gauged chiral Fermion problem, Phys. Rev. D **99**, 111501(R) (2019).

[52] Y.-Z. You, Y. BenTov, and C. Xu, Interacting topological superconductors and possible origin of 16$n$ chiral fermions in the standard model, arXiv:1402.4151.

[53] Y.-Z. You and C. Xu, Interacting topological insulator and emergent grand unified theory, Phys. Rev. B **91**, 125147 (2015).

[54] Y. Kikukawa, On the gauge invariant path-integral measure for the overlap Weyl fermions in 16 of SO(10), PTEP **2019**, 113B03 (2019).

[55] J. Wang and X.-G. Wen, Nonperturbative definition of the standard models, Phys. Rev. Res. **2**, 023356 (2020).

[56] S. S. Razamat and D. Tong, Gapped Chiral Fermions, Phys. Rev. X **11**, 011063 (2021).

[57] Y. BenTov, Fermion masses without symmetry breaking in two spacetime dimensions, J. High Energy Phys. 07 (2015) 034.

[58] Y. BenTov and A. Zee, Origin of families and SO(18) grand unification, Phys. Rev. D **93**, 065036 (2016).

[59] S. A. Kivelson, V. J. Emery, and H. Q. Lin, Doped antiferromagnets in the weak-hopping limit, Phys. Rev. B **42**, 6523 (1990).

[60] H. Kamei and K. Miyake, On quartet superfluidity of fermionic atomic gas, J. Phys. Soc. Jpn. **74**, 1911 (2005).

[61] E. Berg, E. Fradkin, and S. A. Kivelson, Theory of the striped superconductor, Phys. Rev. B **79**, 064515 (2009).

[62] L. Radzihovsky and A. Vishwanath, Quantum Liquid Crystals in an Imbalanced Fermi Gas: Fluctuations and Fractional Vortices in Larkin-Ovchinnikov States, Phys. Rev. Lett. **103**, 010404 (2009).

[63] E. Berg, E. Fradkin, and S. A. Kivelson, Charge-4$e$ superconductivity from pair-density-wave order in certain high-temperature superconductors, Nat. Phys. **5**, 830 (2009).

[64] E. V. Herland, E. Babaev, and A. Sudbo, Phase transitions in a three dimensional $U(1) \times U(1)$ lattice London superconductor, Phys. Rev. B **82**, 134511 (2010).

[65] E.-G. Moon, Skyrmions with quadratic band touching fermions: A way to achieve charge 4$e$ superconductivity, Phys. Rev. B **85**, 245123 (2012).

[66] Y.-F. Jiang, Z.-X. Li, S. A. Kivelson, and H. Yao, Charge-4$e$ superconductors: A Majorana quantum Monte Carlo study, Phys. Rev. B **95**, 241103 (2017).

[67] M. Cheng and N. Seiberg, Lieb-Schultz-Mattis, Luttinger, and 't Hooft—Anomaly matching in lattice systems, arXiv:2211.12543.

[68] Z. Darius Shi, H. Goldman, D. V. Else, and T. Senthil, Gifts from anomalies: Exact results for Landau phase transitions in metals, SciPost Phys. **13**, 102 (2022).

[69] J. Wang, $CT$ or $P$ problem and symmetric gapped fermion solution, Phys. Rev. D **106**, 125007 (2022).

[70] T. Bhattacharya, M. R. Martin, and E. Poppitz, Chiral lattice gauge theories from warped domain walls and Ginsparg-Wilson fermions, Phys. Rev. D **74**, 085028 (2006).

[71] J. Giedt and E. Poppitz, Chiral lattice gauge theories and the strong coupling dynamics of a Yukawa-Higgs model with Ginsparg-Wilson fermions, J. High Energy Phys. 10 (2007) 076.

[72] H. B. Nielsen and M. Ninomiya, Absence of neutrinos on a lattice: (I). Proof by homotopy theory, Nucl. Phys. B **185**, 20 (1981).

[73] H. B. Nielsen and M. Ninomiya, Absence of neutrinos on a lattice: (II). Intuitive topological proof, Nucl. Phys. B **193**, 173 (1981).

[74] H. B. Nielsen and M. Ninomiya, A no-go theorem for regularizing chiral fermions, Phys. Lett. B **105**, 219 (1981).

[75] P. Swift, The electroweak theory on the lattice, Phys. Lett. B **145**, 256 (1984).

[76] E. Eichten and J. Preskill, Chiral gauge theories on the lattice, Nucl. Phys. B **268**, 179 (1986).

[77] D. B. Kaplan, A method for simulating chiral fermions on the lattice, Phys. Lett. B **288**, 342 (1992).

[78] T. Banks and A. Dabholkar, Decoupling a fermion whose mass comes from a Yukawa coupling: Nonperturbative considerations, Phys. Rev. D **46**, 4016 (1992).

[79] I. Montvay, Mirror fermions in chiral gauge theories, Nucl. Phys. B, Proc. Suppl. **29**, 159 (1992).

[80] E. Poppitz and Y. Shang, Chiral lattice gauge theories via mirror-fermion decoupling: A mission (im)possible? Int. J. Mod. Phys. A **25**, 2761 (2010).

[81] C. Chen, J. Giedt, and E. Poppitz, On the decoupling of mirror fermions, J. High Energy Phys. 04 (2013) 131.

[82] S. L. Adler, Axial-vector vertex in spinor electrodynamics, Phys. Rev. **177**, 2426 (1969).

[83] J. S. Bell and R. Jackiw, A PCAC puzzle: $\pi^0 \to \gamma\gamma$ in the $\sigma$-model, Il Nuovo Cimento A (1965-1970) **60**, 47 (1969).

[84] Z. Wan and J. Wang, Higher anomalies, higher symmetries, and cobordisms I: Classification of higher-symmetry-protected topological states and their boundary fermionic/bosonic anomalies via a generalized cobordism theory, Ann. Math. Sci. Appl. **4**, 107 (2019).

[85] D. Tong, Comments on symmetric mass generation in 2$d$ and 4$d$, J. High Energ. Phys. 07 (2022) 001.

[86] S. R. White, Density Matrix Formulation for Quantum Renormalization Groups, Phys. Rev. Lett. **69**, 2863 (1992).

[87] U. Schollwöck, The density-matrix renormalization group, Rev. Mod. Phys. **77**, 259 (2005).

[88] M. Zeng, Z. Zhu, J. Wang, and Y.-Z. You, Symmetric Mass Generation in the 1 + 1 Dimensional Chiral Fermion 3-4-5-0 Model, Phys. Rev. Lett. **128**, 185301 (2022).

[89] J. Luttinger, An exactly soluble model of a many-fermion system, J. Math. Phys. **4**, 1154 (1963).

[90] M. P. A. Fisher and L. I. Glazman, Transport in a one-dimensional Luttinger liquid, arXiv:cond-mat/9610037.

[91] J. M. Kosterlitz, The critical properties of the two-dimensional $xy$ model, J. Phys. C **7**, 1046 (1974).

[92] J. V. José, L. P. Kadanoff, S. Kirkpatrick, and D. R. Nelson, Renormalization, vortices, and symmetry-breaking perturbations in the two-dimensional planar model, Phys. Rev. B **16**, 1217 (1977).

[93] V. L. Berezinsky, Destruction of long-range order in one-dimensional and two-dimensional systems having a continuous symmetry group. I. Classical Systems, Zh. Eksp. Teor. Fiz. **59**, 907 (1970) [Sov. Phys. JETP **32**, 493 (1971)].

[94] V. L. Berezinskiĭ, Destruction of long-range order in one-dimensional and two-dimensional systems possessing a continuous symmetry group. II. Quantum systems, Zh. Eksp. Teor. Fiz. **61**, 1144 (1971) [Sov. Phys. JETP **34**, 610 (1972)].

[95] J. M. Kosterlitz and D. J. Thouless, Ordering, metastability and phase transitions in two-dimensional systems, J. Phys. C **6**, 1181 (1973).

[96] X.-G. Wen, Low-energy effective field theories of fermion liquids and the mixed $U(1) \times \mathbb{R}^d$ anomaly, Phys. Rev. B **103**, 165126 (2021).

[97] B. Lian, A quantum breakdown model: From many-body localization to chaos with scars, Phys. Rev. B **107**, 115171 (2023).

[98] N. Furukawa, T. M. Rice, and M. Salmhofer, Truncation of a Two-Dimensional Fermi Surface due to Quasiparticle Gap Formation at the Saddle Points, Phys. Rev. Lett. **81**, 3195 (1998).

[99] S. Raghu and S. A. Kivelson, Superconductivity from repulsive interactions in the two-dimensional electron gas, Phys. Rev. B **83**, 094518 (2011).

[100] R. Nandkishore, L. S. Levitov, and A. V. Chubukov, Chiral superconductivity from repulsive interactions in doped graphene, Nat. Phys. **8**, 158 (2012).

[101] H. Isobe, N. F. Q. Yuan, and L. Fu, Unconventional Superconductivity and Density Waves in Twisted Bilayer Graphene, Phys. Rev. X **8**, 041041 (2018).

[102] Y.-P. Lin and R. M. Nandkishore, Chiral twist on the high-$T_c$ phase diagram in moiré heterostructures, Phys. Rev. B **100**, 085136 (2019).

[103] Y.-P. Lin and R. M. Nandkishore, Parquet renormalization group analysis of weak-coupling instabilities with multiple high-order Van Hove points inside the Brillouin zone, Phys. Rev. B **102**, 245122 (2020).

[104] T. Park, M. Ye, and L. Balents, Electronic instabilities of kagome metals: Saddle points and Landau theory, Phys. Rev. B **104**, 035142 (2021).

[105] Y.-Z. You and A. Vishwanath, Kohn-Luttinger superconductivity and inter-valley coherence in rhombohedral trilayer graphene, arXiv:2109.04669.

[106] D.-C. Lu, T. Wang, S. Chatterjee, and Y.-Z. You, Correlated metals and unconventional superconductivity in rhombohedral trilayer graphene: A renormalization group analysis, Phys. Rev. B **106**, 155115 (2022).

[107] C. Wetterich, Exact evolution equation for the effective potential, Phys. Lett. B **301**, 90 (1993).

[108] M. Salmhofer and C. Honerkamp, Fermionic renormalization group flows—technique and theory, Prog. Theor. Phys. **105**, 1 (2001).

[109] N. Dupuis, L. Canet, A. Eichhorn, W. Metzner, J. M. Pawlowski, M. Tissier, and N. Wschebor, The nonperturbative functional renormalization group and its applications, Phys. Rep. **910**, 1 (2021).

[110] W.-S. Wang, Y.-Y. Xiang, Q.-H. Wang, F. Wang, F. Yang, and D.-H. Lee, Functional renormalization group and variational monte carlo studies of the electronic instabilities in graphene near $\frac{1}{4}$ doping, Phys. Rev. B **85**, 035414 (2012).

[111] N. Gneist, D. Kiese, R. Henkel, R. Thomale, L. Classen, and M. M. Scherer, Functional renormalization of spinless triangular-lattice fermions: N-patch vs. truncated-unity scheme, Eur. Phys. J. B **95**, 157 (2022).

[112] D. T. Son, Superconductivity by long-range color magnetic interaction in high-density quark matter, Phys. Rev. D **59**, 094019 (1999).

[113] E.-G. Moon and A. Chubukov, Quantum-critical Pairing with Varying Exponents, J. Low Temp. Phys. **161**, 263 (2010).

[114] T. Senthil, S. Sachdev, and M. Vojta, Fractionalized Fermi Liquids, Phys. Rev. Lett. **90**, 216403 (2003).

[115] T. Senthil, M. Vojta, and S. Sachdev, Weak magnetism and non-Fermi liquids near heavy-fermion critical points, Phys. Rev. B **69**, 035111 (2004).

[116] S. Gazit, F. F. Assaad, and S. Sachdev, Fermi Surface Reconstruction without Symmetry Breaking, Phys. Rev. X **10**, 041057 (2020).

[117] R. Nandkishore, M. A. Metlitski, and T. Senthil, Orthogonal metals: The simplest non-Fermi liquids, Phys. Rev. B **86**, 045128 (2012).

[118] M. Hohenadler and F. F. Assaad, Fractionalized Metal in a Falicov-Kimball Model, Phys. Rev. Lett. **121**, 086601 (2018).

[119] C. Chen, X. Y. Xu, Y. Qi, and Z. Y. Meng, Metal to Orthogonal Metal Transition, Chin. Phys. Lett. **37**, 047103 (2020).

[120] J. Wang, X.-G. Wen, and E. Witten, Symmetric Gapped Interfaces of SPT and SET States: Systematic Constructions, Phys. Rev. X **8**, 031048 (2018).

[121] Y. Tachikawa, On gauging finite subgroups, SciPost Phys. **8**, 015 (2020).

[122] J. Wang, K. Ohmori, P. Putrov, Y. Zheng, Z. Wan, M. Guo, H. Lin, P. Gao, and S.-T. Yau, Tunneling topological vacua via extended operators: (Spin-)TQFT spectra and boundary deconfinement in various dimensions, Prog. Theor. Exp. Phys. **2018**, 053A01 (2018).

[123] M. Guo, K. Ohmori, P. Putrov, Z. Wan, and J. Wang, Fermionic finite-group gauge theories and interacting symmetric/crystalline orders via cobordisms, Commun. Math. Phys. **376**, 1073 (2020).

[124] R. Kobayashi, K. Ohmori, and Y. Tachikawa, On gapped boundaries for SPT phases beyond group cohomology, J. High Energy Phys. 11 (2019) 131.

[125] A. Prakash, J. Wang, and T.-C. Wei, Unwinding short-range entanglement, Phys. Rev. B **98**, 125108 (2018).

[126] A. Prakash and J. Wang, Unwinding fermionic SPT phases: Supersymmetry extension, Phys. Rev. B **103**, 085130 (2021).

[127] Y.-Z. You, Y.-C. He, C. Xu, and A. Vishwanath, Symmetric Fermion Mass Generation as Deconfined Quantum Criticality, Phys. Rev. X **8**, 011026 (2018).

[128] Y.-Z. You, Y.-C. He, A. Vishwanath, and C. Xu, From bosonic topological transition to symmetric fermion mass generation, Phys. Rev. B **97**, 125112 (2018).

[129] Y.-Z. You, Z. Wang, J. Oon, and C. Xu, Topological number and fermion Green's function for strongly interacting topological superconductors, Phys. Rev. B **90**, 060502(R) (2014).

[130] S. Catterall and D. Schaich, Novel phases in strongly coupled four-fermion theories, Phys. Rev. D **96**, 034506 (2016).

[131] S. Catterall and N. Butt, Topology and strong four fermion interactions in four dimensions, Phys. Rev. D **97**, 094502 (2018).

[132] Y. Xu and C. Xu, Green's function zero and symmetric mass generation, arXiv:2103.15865.

[133] Y.-H. Zhang and S. Sachdev, From the pseudogap metal to the Fermi liquid using ancilla qubits, Phys. Rev. Res. **2**, 023172 (2020).

[134] Y.-H. Zhang and S. Sachdev, Deconfined criticality and ghost Fermi surfaces at the onset of antiferromagnetism in a metal, Phys. Rev. B **102**, 155124 (2020).

[135] L. Zou and D. Chowdhury, Deconfined metallic quantum criticality: A $U(2)$ gauge-theoretic approach, Phys. Rev. Res. **2**, 023344 (2020).

[136] L. Zou and D. Chowdhury, Deconfined metal-insulator transitions in quantum Hall bilayers, Phys. Rev. Res. **2**, 032071 (2020).

[137] W. Hou and Y.-Z. You, Variational Monte Carlo study of symmetric mass generation in a bilayer honeycomb lattice model, arXiv:2212.13364.

**Acknowledgements**

# Chapter 3

# Green's function zeros in Fermi surface symmetric mass generation

# Green's function zeros in Fermi surface symmetric mass generation

Da-Chuan Lu, Meng Zeng ⓞ, and Yi-Zhuang You ⓞ

*Department of Physics, University of California, San Diego, California 92093, USA*

The Fermi surface symmetric mass generation (SMG) is an intrinsically interaction-driven mechanism that opens an excitation gap on the Fermi surface without invoking symmetry-breaking or topological order. We explore this phenomenon within a bilayer square lattice model of spin-1/2 fermions, where the system can be tuned from a metallic Fermi liquid phase to a strongly interacting SMG insulator phase by an interlayer spin-spin interaction. The SMG insulator preserves all symmetries and has no mean-field interpretation at the single-particle level. It is characterized by zeros in the fermion Green's function, which encapsulate the same Fermi volume in momentum space as the original Fermi surface, a feature mandated by the Luttinger theorem. Utilizing both numerical and field-theoretical methods, we provide compelling evidence for these Green's function zeros across both strong and weak coupling regimes of the SMG phase. Our findings highlight the robustness of the zero Fermi surface, which offers promising avenues for experimental identification of SMG insulators through spectroscopy experiments despite potential spectral broadening from noise or dissipation.

## I. INTRODUCTION

Symmetric mass generation (SMG) [1–8] is an interaction-driven mechanism that creates many-body excitation gaps in anomaly-free fermion systems *without* condensing any fermion bilinear operator or developing topological orders. It has emerged as a alternative symmetry-preserving approach for mass generation in relativistic fermion systems, which is distinct from the traditional symmetry-breaking Higgs mechanism [9–14]. The prospect of SMG offering a potential solution to the long-standing fermion doubling problem [15–21] has sparked significant interest in the lattice gauge theory community [22–46]. In condensed matter physics, SMG was initially explored within the framework of the interaction-reduced classification of fermionic symmetry protected topological (SPT) states [1,2,47–68], and has been recently extended to systems with Fermi surfaces [69–74], given the growing understanding that Fermi liquids can be perceived as fermionic SPT states within the phase space [75,76].

One important feature of the SMG gapped state lies in the zeros of fermion Green's function [77–82] at low energy. Investigations reveal that the poles of the fermion Green's function in the pristine gapless fermion state will be replaced by zeros in the gapped SMG state as the fermion system goes across the SMG transition upon increasing the interaction strength. This pole-to-zero transition was postulated [78] as a direct indicator of the SMG transition [80,83] that can be probed by spectroscopy experiments. However, the presence of similar zeros in the Green's function within Fermi surface SMG states has not been investigated yet, and it is the focus of our present research.

Fermi surface SMG [74] refers to the occurrence of SMG phenomena on Fermi surfaces with nonzero Fermi volumes. It describes scenarios where the fermion interaction transforms a gapless Fermi liquid state (metal) into a nondegenerate, gapped, direct product state (trivial insulator), without

breaking any symmetry (for example, without invoking Cooper pairing or density wave orders). Such a metal-insulator transition is viable when Fermi surfaces collaboratively cancel the Fermi surface anomaly [74,84,85]. This anomaly can be perceived as a mixed anomaly between the translation symmetry and the charge conservation U(1) symmetry on the lattice [84–90], or as an anomaly of an emergent loop LU(1) symmetry [91–93] in the infrared theory.

In this work, we present evidence of robust Green's function zeros in Fermi surface SMG states. Let $t$ be the energy scale of band dispersion and $J$ be the energy scale of SMG gapping interaction, we investigate the problem from two parameter regimes.

(1) Deep in the SMG phase ($J/t \gg 1$), we start with an exact-solvable SMG product state in a lattice model and calculate the fermion Green's function by treating the fermion hopping as perturbation [94]. We find that the Green's function $G_{\text{SMG}}(\omega, \boldsymbol{k})$ deep in the SMG phase takes the following form

$$G_{\text{SMG}}(\omega, \boldsymbol{k}) = \frac{\omega + \alpha \epsilon_{\boldsymbol{k}}/J^2}{(\omega - \epsilon_{\boldsymbol{k}}/2)^2 - J^2}, \tag{1}$$

where $(\omega, \boldsymbol{k})$ labels the frequency-momentum of the fermion. $\epsilon_{\boldsymbol{k}}$ is the energy dispersion of the original band structure in the free-fermion limit, and $\alpha$ is an order-one number depending on other details of the system. One salient feature of $G_{\text{SMG}}$ is that it has a series of zeros at $\omega = -\alpha \epsilon_{\boldsymbol{k}}/J^2$ in the frequency-momentum space. At $\omega = 0$, the Green's function zeros form a zero Fermi surface that replaces the original Fermi surface.

(2) If the SMG phase is adjacent to a spontaneous symmetry breaking (SSB) phase, we use perturbative field theory to argue that the Green's function in the SMG phase near the symmetry-breaking transition ($J/t \gtrsim 1$) should take the form of

$$G'_{\text{SMG}}(\omega, \boldsymbol{k}) = \frac{\omega + \epsilon_{\boldsymbol{k}}}{\omega^2 - \epsilon_{\boldsymbol{k}}^2 - \Delta_0^2} \tag{2}$$

where we assume that the SSB order parameter retains a finite amplitude $\Delta_0$ in the SMG phase, but its phase is randomly fluctuating [95]. Again, $G'_{SMG}$ features a series of zeros at $\omega = -\epsilon_k$, with the same zero Fermi surface.

Many previous works [96–99] suggest that the Luttinger theorem [100] will not be violated in the presence of the interaction that preserves the translation and charge conservation symmetry. However, quasiparticles (poles of Green's function) may not exist in the strongly correlated systems, the Fermi surface is instead defined by the surface of Green's function zeros at zero frequency, i.e., $G(0, \boldsymbol{k}) = 0$, and the Green's function changes sign on the two sides of the *zero Fermi surface*, or the so-called Luttinger surface [91,98,101–103]. This can be regarded as the remnant of the conventional Fermi surface in the strongly interacting gapped phase. Our analysis shows that the volume enclosed by the zeros of the Green's function in the SMG phase is the same as the Fermi volume in the Fermi liquid phase, which agrees with the Luttinger theorem.

The paper will be structured as follows. We start by introducing a concrete lattice model for Fermi surface SMG in Sec. II A and briefly discussing its phase diagram. We give theoretical arguments for Green's function zeros in the SMG phase from the Luttinger theorem in Sec. II B (general), and the particle-hole symmetry in Sec. II C (specific). We provide numerical and field theoretical evidence of Green's function zeros from both the strong coupling Sec. III A and the weak coupling Sec. III B perspectives. We comment on the robustness of probing the zero structure in spectroscopy experiments in Sec. IV. We conclude in Sec. V with a discussion of the relevance of our model to the nickelate superconductor $La_3Ni_2O_7$.

## II. ARGUMENT FOR GREEN'S FUNCTION ZEROS

### A. Lattice model and phase diagram

As a specific example of Fermi surface SMG, we consider a bilayer square lattice [104–106] model of spin-1/2 fermions, as illustrated in Fig. 1(a). Let $c_{il\sigma}$ be the fermion annihilation operator on site-$i$ layer $l$ ($l = 1, 2$) and spin $\sigma$ ($\sigma = \uparrow, \downarrow$). The model is described by the following Hamiltonian:

$$H = -t \sum_{\langle ij \rangle, l, \sigma} (c^\dagger_{il\sigma} c_{jl\sigma} + \text{H.c.}) + J \sum_i \boldsymbol{S}_{i1} \cdot \boldsymbol{S}_{i2}, \quad (3)$$

where $\boldsymbol{S}_{il} := \frac{1}{2} c^\dagger_{il\sigma} \boldsymbol{\sigma}_{\sigma\sigma'} c_{il\sigma'}$ denotes the spin operator with $\boldsymbol{\sigma} := (\sigma^1, \sigma^2, \sigma^3)$ being the Pauli matrices. The Hamiltonian $H$ contains a nearest-neighbor hopping $t$ of the fermions within each layer and an interlayer Heisenberg spin-spin interaction with antiferromagnetic coupling $J > 0$. The Heisenberg interaction should be understood as a four-fermion interaction, that there is no explicitly formed local moment degrees of freedom. Unlike the standard $t$-$J$ model [107], we do *not* impose any on-site single-occupancy constraint [108] here. We assume that the fermions are half-filled in each layer.

In the noninteracting limit ($J/t \to 0$), the ground state of the tight-binding Hamiltonian in Eq. (3) is a Fermi liquid with a fourfold degenerated (two layers and two spins) square-shaped Fermi surface in the Brillouin zone, as shown
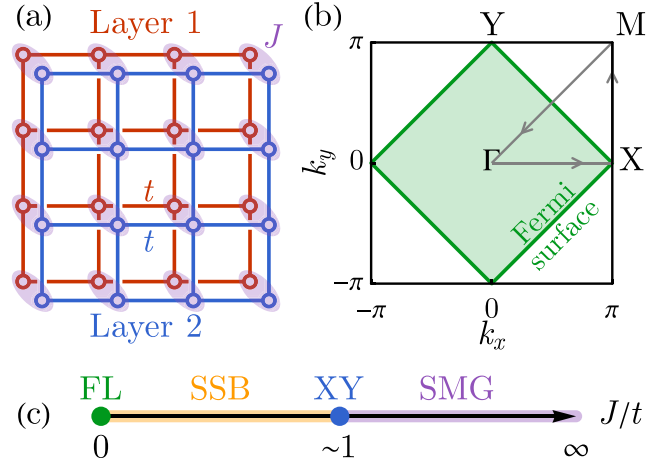


FIG. 1. (a) Bilayer square lattice model with intralayer hopping and interlayer spin interaction. (b) Fermi sea and Fermi surface at $J = 0$ in the Brillouin zone. A high-symmetry path is traced out in gray. (c) A conjectured phase diagram consist of a Fermi liquid (FL) fixed point, a spontaneous symmetry breaking (SSB) phase, a XY transition, and a SMG insulating phase.

in Fig. 1(b). The fermion system is gapless in this limit. However, given that the fermion carries one unit charge under the U(1) symmetry, the Fermi surface anomaly vanishes due to [76,87]

$$\sum_{a=1}^4 q_a \nu_a = 4 \times 1 \times \frac{1}{2} = 0 \mod 1, \quad (4)$$

where $a$ indexes the fourfold degenerated Fermi surface with $q_a = 1$ being the U(1) charge carried by the fermion and $\nu_a = 1/2$ being the filling fraction. This implies there must be a way to gap out the Fermi surface into a trivial insulator while preserving both the translation and the U(1) charge conservation symmetries. Nevertheless, these symmetry requirements are restrictive enough to rule out all possible fermion bilinear gapping mechanisms, leaving Fermi surface SMG the only available option.

One possible SMG gapping interaction is the interlayer Heisenberg spin-spin interaction $J$ in Eq. (3). In the strong interaction limit ($J/t \to \infty$), the system has a unique ground state, given by

$$|0\rangle = \bigotimes_i (c^\dagger_{i1\uparrow} c^\dagger_{i2\downarrow} - c^\dagger_{i1\downarrow} c^\dagger_{i2\uparrow})|\text{vac}\rangle, \quad (5)$$

which is a direct product of the interlayer spin-singlet state on every site. $|\text{vac}\rangle$ stands for the vacuum state of fermions (i.e., $c_{il\sigma}|\text{vac}\rangle = 0$). The SMG ground state $|0\rangle$ does not break any symmetry and does not have topological order. All excitations are gapped by an energy of the order $J$ from the ground state. Any local perturbation far below the energy scale $J$ can not close this excitation gap, so the SMG phase is expected to be stable in a large parameter regime as long as $J \gg t$.

Given the distinct ground states in the two limits of $J/t$, we anticipate at least one quantum phase transition separating the Fermi liquid and the SMG insulator. However, due to the perfect nesting of the Fermi surface, the Fermi liquid state is

unstable towards spontaneous symmetry breaking (SSB) upon infinitesimal interaction, so a more plausible phase diagram should look like Fig. 1(c), where an intermediate SSB phase sets in. A mean-field analysis based on the Fermi liquid fixed point shows that there are two degenerated leading instabilities: (i) the interlayer exciton condensation (EC) and (ii) the interlayer superconductivity (SC). They are respectively described by the following order parameters

$$\phi_{\mathrm{EC}} = \sum_{i,\sigma} (-)^i c_{i1\sigma}^\dagger c_{i2\sigma}, \quad \phi_{\mathrm{SC}} = \sum_{i,\sigma} (-)^\sigma c_{i1\sigma}^\dagger c_{i2\bar\sigma}^\dagger. \quad (6)$$

Here, $(-)^i$ denotes the stagger sign on the square lattice of lattice momentum $(\pi, \pi)$. $(-)^\sigma = +1$ for $\sigma = \uparrow$ and $-1$ for $\sigma = \downarrow$. $\bar\sigma$ stands for the opposite spin of $\sigma$.

The energetic degeneracy of these two SSB orders can be explained by the fact that their order parameters $\phi_{\mathrm{EC}}$ and $\phi_{\mathrm{SC}}$ are related by a particle-hole transformation $c_{i2\sigma} \to (-)^i(-)^\sigma c_{i2\bar\sigma}^\dagger$ in the second layer only, which is a symmetry of the model Hamiltonian in Eq. (3). The EC $\langle\phi_{\mathrm{EC}}\rangle \neq 0$ spontaneously breaks the translation and interlayer U(1) symmetry, and the SC $\langle\phi_{\mathrm{SC}}\rangle \neq 0$ spontaneously breaks the total U(1) symmetry. Both of them gap out the Fermi surfaces fully, leading to an SSB insulator (or superconductor). The SSB and SMG phases are likely separated by an XY transition, at which the symmetry gets restored. We will leave the numerical verification of the proposed phase diagram Fig. 1(c) for future study, as the main focus of this research is to investigate the structure of fermion Green's function in the SMG insulating phase.

We note that the model Eq. (3) was also introduced as the "coupled ancilla qubit" model to describe the pseudo-gap physics in the recent literature [70,72,73]. Its honeycomb lattice version has been investigated in recent numerical simulations [109], where a direct quantum phase transition between semimetal and insulator phases was observed.

### B. Luttinger theorem and Green's function zeros

The Luttinger theorem [100,110] asserts that in a fermion many-body system with lattice translation and charge U(1) symmetries, the ground state charge density $\langle N\rangle/V$ [i.e., the U(1) charge per unit cell] is tied to the momentum space volume in which the real part of the zero-frequency fermion Green's function is positive $\mathrm{Re}\, G(0, \boldsymbol{k}) > 0$. This can be formally expressed as

$$\frac{\langle N\rangle}{V} = N_f \int_{\mathrm{Re}\, G(0,\boldsymbol{k})>0} \frac{d^2\boldsymbol{k}}{(2\pi)^2}. \quad (7)$$

Here, the U(1) symmetry generator $N = \sum_{i,l,\sigma} c_{il\sigma}^\dagger c_{il\sigma}$ measures the total charge, and the volume $V = \sum_i 1$ is defined as the number of unit cells in the lattice system. $N_f = 4$ counts the fermion flavor number (or the Fermi surface degeneracy), including two layers and two spins. The Green's function $G(\omega, \boldsymbol{k})$ in Eq. (7) is defined by the fermion two-point correlation as

$$\langle c_{l\sigma}(\omega, \boldsymbol{k}) c_{l'\sigma'}(\omega, \boldsymbol{k})^\dagger \rangle = G(\omega, \boldsymbol{k}) \delta_{ll'} \delta_{\sigma\sigma'}. \quad (8)$$

The correlation function is proportional to an identity matrix in the flavor (layer-spin) space because of the layer

U(1) : $c_{l\sigma} \to e^{(-)^l i\theta} c_{l\sigma}$, the layer interchange $\mathbb{Z}_2$ : $c_{1\sigma} \leftrightarrow c_{2\sigma}$, and the spin SU(2) : $c_{l\sigma} \to (e^{i\boldsymbol{\theta}\cdot\boldsymbol{\sigma}/2})_{\sigma\sigma'} c_{l\sigma'}$ symmetries.

The Luttinger theorem applies to the Fermi liquid and SMG states in the bilayer square lattice model Eq. (3), as both states preserve the translation and charge U(1) symmetries. Given that the fermions are half-filled ($\nu = 1/2$) in the system, the Fermi volume should be

$$\int_{\mathrm{Re}\, G(0,\boldsymbol{k})>0} \frac{d^2\boldsymbol{k}}{(2\pi)^2} = \frac{\langle N\rangle}{V N_f} = \nu = \frac{1}{2}. \quad (9)$$

The Fermi volume is enclosed by the Fermi surface, across which $\mathrm{Re}\, G(0, \boldsymbol{k})$ changes sign. The sign change can be achieved either by poles or zeros in the Green's function.

In the Fermi liquid state, the required Fermi volume is satisfied via Green's function poles along the Fermi surface, as pictured in Fig. 1(b). However, the SMG insulator is a fully gapped state of fermions that has no low-energy quasiparticles (below the energy scale $J$). Consequently, the Green's function $G(\omega, \boldsymbol{k})$ cannot develop poles at $\omega = 0$, meaning the required Fermi volume can only be satisfied by Green's function zeros. Therefore the Lutinger theorem implies that there must be robust Green's function zeros at low energy in the SMG phase, and the zero Fermi surface must enclose half of the Brillouin zone volume in place of the original pole Fermi surface.

It is known that the Luttinger theorem can be violated in the presence of topological order [86,88,102,111–117]. However, this concern does not affect our discussion in the SMG phase, because the SMG insulator is a trivial insulator without topological order.

### C. Particle-hole symmetry and zero Fermi surface

The Luttinger theorem only constrains the Fermi volume but does not impose requirements on the shape of the Fermi surface. However, in this particular example of the bilayer square lattice model Eq. (3), the system has sufficient symmetries to determine even the shape of the Fermi surface.

The key symmetry here is a particle-hole symmetry $\mathbb{Z}_2^C$, which acts as

$$c_{il\sigma} \to (-)^i(-)^\sigma c_{il\bar\sigma}^\dagger. \quad (10)$$

The Hamiltonian $H$ in Eq. (3) is invariant under this transformation. Since the Green's function is an identity matrix in the flavor space Eq. (8) which is invariant under any flavor basis transformation, we can omit the flavor indices and focus on the frequency-momentum dependence of the Green's function, written as

$$G(\omega, \boldsymbol{k}) = \sum_{t,\boldsymbol{x},t',\boldsymbol{x}'} \langle c(t, \boldsymbol{x}) c(t', \boldsymbol{x}')^\dagger \rangle e^{i(\omega(t-t')-\boldsymbol{k}\cdot(\boldsymbol{x}-\boldsymbol{x}'))}. \quad (11)$$

Given Eq. (10), the fermion field $c(t, \boldsymbol{x})$ transforms under the $\mathbb{Z}_2^C$ symmetry as

$$c(t, \boldsymbol{x}) \to c(t, \boldsymbol{x})^\dagger e^{i\boldsymbol{Q}\cdot\boldsymbol{x}}, \quad c(t, \boldsymbol{x})^\dagger \to c(t, \boldsymbol{x}) e^{-i\boldsymbol{Q}\cdot\boldsymbol{x}}, \quad (12)$$

where $\boldsymbol{Q} = (\pi, \pi)$ is the momentum associated with the stagger sign factor $(-)^i$ on the square lattice. As a consequence, the Green's function transforms as

$$G(\omega, \boldsymbol{k}) \to -G(-\omega, \boldsymbol{Q} - \boldsymbol{k}). \quad (13)$$

Furthermore, there are also two diagonal reflection symmetries on the square lattice, which maps $\boldsymbol{k} = (k_x, k_y)$ to $(k_y, k_x)$ or $(-k_y, -k_x)$ in the momentum space.

Both the Fermi liquid and the SMG states preserve the particle-hole symmetry $\mathbb{Z}_2^C$ and the lattice reflection symmetry, which requires the Green's function to be invariant under the combined symmetry transformations. So the zero-frequency Green's function must satisfy

$$G(0, k_x, k_y) = -G(0, \pi \pm k_y, \pi \pm k_x), \tag{14}$$

meaning that the sign change of $G(0, \boldsymbol{k})$ should happen along $k_x \pm k_y = \pi \mod 2\pi$, which precisely describes the shape of the Fermi surface. The Fermi surface is polelike in the Fermi liquid state and becomes zerolike in the SMG state, but its shape and volume remain the same.

However, it should be noted that the precise overlap of the zero Fermi surface in the SMG insulator and the pole Fermi surface in the Fermi liquid is a fine-tuned feature of the bilayer square lattice model Eq. (3). In more general cases, such as including further neighbor hopping in the model, the particle-hole symmetry would cease to exist, thus the invariance in the shape of the Fermi surface is no longer guaranteed. Nevertheless, the Luttinger theorem can still ensure the invariance in the Fermi volume, thereby providing the SMG insulator with robust Green's function zeros.

To verify this proposition, we will analyze the behavior of the Green's function in the SMG phase from both strong and weak coupling perspectives in Sec. III. Our calculations suggest that, for this specific model, the SMG state indeed possesses a Fermi surface (of Green's function zeros) that is identical in shape to that in the Fermi liquid state.

## III. EVIDENCE OF GREEN'S FUNCTION ZEROS

### A. Strong coupling analysis

We will first focus on the strong interaction limit ($J/t \to \infty$), where the system is deep in the SMG phase and the exact ground state is known [see Eq. (5)]. We start from this limit and turn on the hopping term as a perturbation. We employ exact diagonalization and cluster perturbation theory (CPT) [94,118] to compute the Green's function in the SMG phase. The details of our method are described in Appendix. It is valid to use a small cluster to reconstruct the Green's function in the SMG phase since the ground state is close to a product state that does not have long-range correlation or long-range quantum entanglement. This is quite different from the Hubbard model, where the Fermi surface anomaly is nonvanishing, and the infrared phase must be either SSB order or topological order [86,111,114,115]. In either case, the ground state wave functions cannot be reconstructed from the small clusters due to the long-range correlation/entanglement. This argument has been noted in the original paper on the CPT method [94].

To be specific, we first partition the square lattice (including both layers) into $2 \times 2$ square clusters as shown in Fig. 2. Let us first ignore the intercluster hopping. Within each cluster, we represent the Hamiltonian in the many-body Hilbert space and use the Lanczos method to obtain the lowest $\sim 2000$ eigenvalues and eigenvectors. The Green's function in the cluster can then be obtained by the Källén-Lehmann
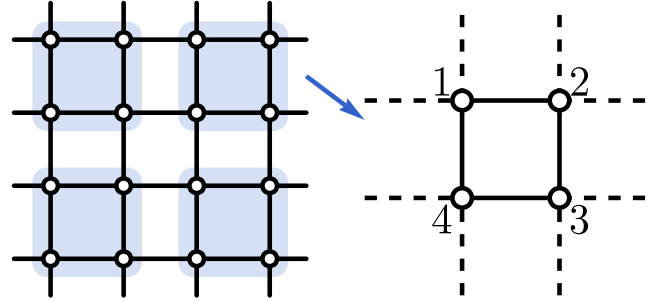


FIG. 2. Partition the square lattice into $2 \times 2$ clusters. The many-body Hamiltonian is exactly diagonalized within each cluster. The effect of intercluster hopping is included in an RPA-like approach.

representation

$$G_0(\omega)_{ij} = \sum_{m>0} \frac{\langle 0|c_i|m\rangle\langle m|c_j^\dagger|0\rangle}{\omega - (E_m - E_0)} + \frac{\langle m|c_i|0\rangle\langle 0|c_j^\dagger|m\rangle}{\omega + (E_m - E_0)}, \tag{15}$$

where $|m\rangle$ is the $m$th excited state with energy $E_m$, and $|0\rangle$ is the ground state with energy $E_0$, whose wave function was previously given in Eq. (5). Since the four fermion flavors (two spins and two layers) are identical under the internal flavor symmetry, we can drop the flavor index in the Green's function and only focus on one particular flavor with the site indices $i$, $j$, where $i, j = 1, 2, 3$, and 4 as indicated in Fig. 2. The convergence of the Green's function can be verified by including more eigenstates from the Lanczos method. We checked that increasing the number of eigenpairs to $\sim 8000$ will not change the result significantly, indicating that the result with $\sim 2000$ eigenpairs has already converged.

Now we restore the intercluster hoping to extend the Green's function from small clusters to the infinite lattice. The Green's function of superlattice momentum $\boldsymbol{k}$ can be obtained from the random phase approximation (RPA) approach [94],

$$G(\omega, \boldsymbol{k})_{ij} = \left(\frac{G_0(\omega)}{1 - T(\boldsymbol{k})G_0(\omega)}\right)_{ij}, \tag{16}$$

where the $T(\boldsymbol{k})$ matrix

$$T(\boldsymbol{k}) = -t \begin{pmatrix} 0 & e^{-i2k_x} & 0 & e^{i2k_y} \\ e^{i2k_x} & 0 & e^{i2k_y} & 0 \\ 0 & e^{-i2k_y} & 0 & e^{i2k_x} \\ e^{-i2k_y} & 0 & e^{-i2k_x} & 0 \end{pmatrix} \tag{17}$$

describes the intercluster fermion hopping. The resulting Green's function $G(\omega, \boldsymbol{k})_{ij}$ is defined in the folded Brillouin zone $\boldsymbol{k} \in (-\pi/2, \pi/2)^{\times 2}$ with sublattice indices $i$, $j$. To unfold the Green's function to the original Brillouin zone $\boldsymbol{k} \in (-\pi, \pi]^{\times 2}$, we perform the following (partial) Fourier transform

$$G(\omega, \boldsymbol{k}) = \frac{1}{L} \sum_{i,j} e^{-i\boldsymbol{k}\cdot(\boldsymbol{r}_i - \boldsymbol{r}_j)} G(\omega, \boldsymbol{k})_{ij}. \tag{18}$$

We numerically calculated the unfolded Green's function $G(\omega, \boldsymbol{k})$ using the above-mentioned cluster perturbation method. We take a large interaction strength $J/t = 8$ deep in the SMG phase and present the resulting Green's function
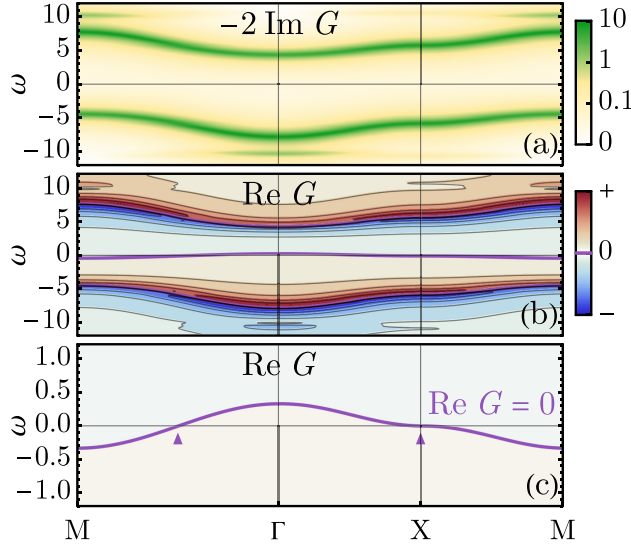
FIG. 3. Fermion Green's function Eq. (18) deep in the SMG insulator phase, at $J = 8t$. (a) The imaginary part (spectral function) $-2 \operatorname{Im} G(\omega + i0_+, \boldsymbol{k})$ shows the pole (spectral peak) structure. (b) The real part $\operatorname{Re} G(\omega, \boldsymbol{k})$ shows the pole (divergence) and zero (purple contour) structures. (c) Same as (b) but zoomed in near $\omega = 0$ to show the dispersion of Green's function zeros.

in Fig. 3. From Fig. 3(a), the poles of the Green's function form two dispersing bands around $\omega = \pm J$, which resembles the upper and lower Hubbard bands in the Hubbard model. This indicates the quasiparticles are fully gapped in the SMG phase. Meanwhile, from Figs. 3(b) and 3(c), the zeros of the Green's function appear around $\omega = -\alpha \epsilon_{\boldsymbol{k}}/J^2$ with some nonuniversal but positive coefficient $\alpha > 0$. We find that the "dispersion" of zeros is reversed compared to the original band dispersion $\epsilon_{\boldsymbol{k}}$. In Fig. 4, we also numerically confirmed that the "bandwidth" $w_{\text{zero}}$ of zeros is suppressed by the interaction $J$ as $w_{\text{zero}} \sim J^{-2}$ as $J \to \infty$.

Building upon the above observation of the poles and zeros of the Green's function, we put forth the following empirical formula:

$$G_{\text{SMG}}(\omega, \boldsymbol{k}) = \frac{\omega + \alpha \epsilon_{\boldsymbol{k}}/J^2}{(\omega - \epsilon_{\boldsymbol{k}}/2)^2 - J^2}, \qquad (19)$$
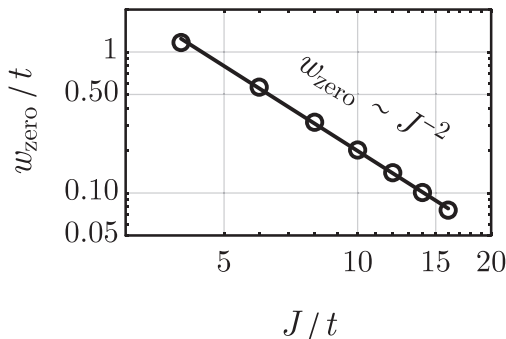


FIG. 4. Scaling of the Green's function zero "bandwidth" $w_{\text{zero}}$ with the interaction strength $J$. Circles represent the numerically calculated $w_{\text{text}}$ at different $J$, and the line is a fit to the data.

as an approximate description of our numerical result Eq. (18). An important aspect of this formula is the positioning of the Green's function zeros precisely around the initial Fermi surface (where $\epsilon_{\boldsymbol{k}} = 0$) at $\omega = 0$. This is indicated by the small arrows in Fig. 3(c).

Assuming $\operatorname{Re} G_{\text{SMG}}(0, \boldsymbol{k}) = 0$ as the definition of the zero Fermi surface in the SMG phase, it would encompass the same Fermi volume as the pole Fermi surface in the Fermi liquid phase. As both translation and charge conservation symmetries remain unbroken in the SMG phase, the Luttinger theorem mandates the preservation of the Fermi volume. Given that the SMG state is a fully gapped trivial insulator, there is no pole (no quasiparticle) at low energy, thus the Green's function can only rely on zeros to fulfill the Fermi volume required by the Luttinger theorem, which is explicitly demonstrated by Eq. (19).

### B. Weak coupling analysis

Nevertheless, SMG is not the sole mechanism for gapping out the Fermi surface. SSB might also open a full gap on the Fermi surface, which corresponds to the Higgs mechanism for fermion mass generation. Specifically, in the bilayer square lattice model Eq. (3), due to the perfect nesting of the Fermi surface, the Fermi liquid exhibits strong instability toward SSB orders. Without loss of generality, we will focus on the interlayer exciton condensation in the weak coupling limit. The corresponding order parameter $\phi_{\text{EC}}$ was introduced in Eq. (6), which carries momentum $\boldsymbol{Q} = (\pi, \pi)$. The exciton condensation leads to an SSB insulating phase, as noted in the phase diagram Fig. 1(c). However, there are significant differences between the SMG insulator and the SSB insulator, especially in terms of the structure of Green's function zeros.

In the SSB insulator phase, the Brillouin zone folds by the nesting vector $\boldsymbol{Q} = (\pi, \pi)$. The fermion Green's function can be written in the $(c_{\boldsymbol{k}}, c_{\boldsymbol{k}+\boldsymbol{Q}})^\intercal$ basis (omitting layers and spins freedom) as

$$G_{\text{SSB}}(\omega, \boldsymbol{k}) = \frac{\omega \sigma^0 + \epsilon_{\boldsymbol{k}} \sigma^3 + \operatorname{Re} \Delta \sigma^1 + \operatorname{Im} \Delta \sigma^2}{\omega^2 - \epsilon_{\boldsymbol{k}}^2 - |\Delta|^2}, \qquad (20)$$

where $\Delta = J \langle \phi_{\text{EC}} \rangle$ denotes the exciton gap induced by the exciton condensation $\langle \phi_{\text{EC}} \rangle \neq 0$. The properties of $G_{\text{SSB}}$ are illustrated in Fig. 5. The spectral function in Fig. 5(a) depicts the quasiparticle peak along the band dispersion, reflecting a gapped (insulating) band structure.

Since $G_{\text{SSB}}$ is a matrix, its zero structure should be defined by its determinant being zero, i.e., $\det G_{\text{SSB}}(\omega, \boldsymbol{k}) = 0$, which is the only way to define the zero structure in a basis independent manner. Figure 5(b) indicates the determinant of $G_{\text{SSB}}$ remains the same sign within the band gap induced by the exciton condensation. Since $G_{\text{SSB}}$ does not preserve the translation symmetry (as $\Delta \to -\Delta$ is translation-odd), and $\Delta$ is nonzero, $\det G_{\text{SSB}}$ does not have zeros crossing $\omega = 0$ at the original Fermi surface. These two observations are linked: the absence of translation symmetry makes the Luttinger theorem ineffective, hence there is no expectation for the zero Fermi surface in the SSB insulator.

As the interaction $J$ intensifies, the SSB insulator ultimately transitions into the SMG insulator, as depicted in the phase diagram Fig. 1(c). During this transition, the
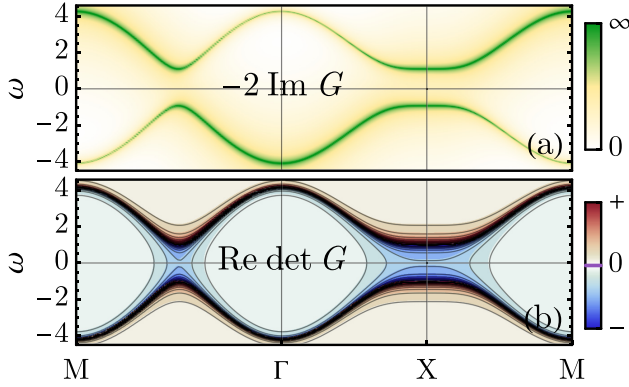
FIG. 5. Fermion Green's function Eq. (20) $G_{\mathrm{SSB}}$ in the SSB insulator phase, assuming a gap size of $|\Delta| = t$. (a) The imaginary part $-2\,\mathrm{Im}\,G(\omega + \mathrm{i}0_+, \boldsymbol{k})_{11}$ in the $\langle c_{\boldsymbol{k}}^{\dagger} c_{\boldsymbol{k}} \rangle$ channel, showing the pole (quasiparticle peak) along gapped bands. (b) The real part of the determinant $\mathrm{Re}\,\det G(\omega, \boldsymbol{k})$. No zero within the gap. In both plots, the frequency is shifted by a small imaginary part $\omega \to \omega + 0.01\mathrm{i}t$ for better visualization of spectral features.

broken symmetry is restored, yet the fermion excitation gap remains intact, similar to the pseudo-gap phenomenon seen in correlated materials [119,120]. In the context of modeling fermion spectral functions, the pseudogap phenomenon can be interpreted as a consequence of the phase (or orientation) fluctuations of fermion bilinear order parameters [121–128]. In this picture, the order parameter $\Delta = \Delta_0 e^{i\theta}$ maintains a finite amplitude $\Delta_0$ as we enter the SMG phase from the adjacent SSB phase, but its phase $\theta$ is disordered by long-wavelength random fluctuations. Consequently, on the large scale, $\Delta$ cannot condense to form long-range order; but on a smaller scale, $\Delta_0$ still provides a local excitation gap everywhere for fermions.

Based on this picture of the SMG state, the simplest treatment is to focus on the long wavelength fluctuation of $\Delta$ and estimate its self-energy correction for the fermion by

$$\Sigma(\omega, \boldsymbol{k}) = \begin{matrix}\cdot\cdot\cdot\cdot\end{matrix} = \mathbb{E}_{\Delta} \hat{\Delta}^{\dagger} G_0(\omega, \boldsymbol{k}) \hat{\Delta} = \frac{\Delta_0^2}{\omega\sigma^0 + \epsilon_{\boldsymbol{k}}\sigma^3}, \quad (21)$$

where the vertex operator is $\hat{\Delta} := \mathrm{Re}\,\Delta\sigma^1 + \mathrm{Im}\,\Delta\sigma^2$ and the bare Green's function is $G_0(\omega, \boldsymbol{k}) = (\omega\sigma^0 - \epsilon_{\boldsymbol{k}}\sigma^3)^{-1}$. Here we have assumed that the correlation length $\xi$ of the bosonic field $\Delta$ is long enough that its momentum is negligible for fermions. This assumption is valid near the transition to the SSB phase, as the correlation length diverges ($\xi \to \infty$) at the transition.

Using this self-energy to correct the bare Green's function, we obtain

$$\begin{aligned} G(\omega, \boldsymbol{k}) &= (G_0(\omega, \boldsymbol{k})^{-1} - \Sigma(\omega, \boldsymbol{k}))^{-1} \\ &= \frac{\omega\sigma^0 + \epsilon_{\boldsymbol{k}}\sigma^3}{\omega^2 - \epsilon_{\boldsymbol{k}}^2 - \Delta_0^2}. \end{aligned} \quad (22)$$

Since the translation symmetry has been restored in the SMG phase, we can unfold the Green's function back to the original Brillouin zone [by taking the $G(\omega, \boldsymbol{k})_{11}$ component], which leads to a weak coupling description of the Green's function
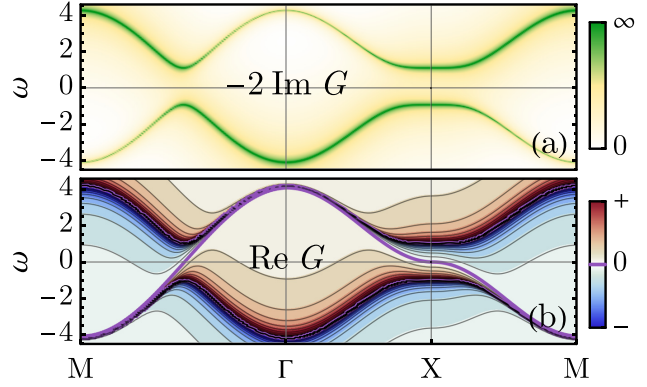
FIG. 6. Fermion Green's function Eq. (23) $G'_{\mathrm{SMG}}$ in the SMG insulator phase near the phase transition to an adjacent SSB phase, assuming a local gap size of $\Delta_0 = t$. (a) The imaginary part (spectral function) $-2\,\mathrm{Im}\,G(\omega + \mathrm{i}0_+, \boldsymbol{k})$ shows the pole (quasiparticle peak) along gapped bands. (b) The real part $\mathrm{Re}\,G(\omega, \boldsymbol{k})$ exhibits the zero (purple contour) crossing $\omega = 0$ at the original Fermi surface. In both plots, the frequency is shifted by a small imaginary part $\omega \to \omega + 0.01\mathrm{i}t$ for better visualization of spectral features.

in the shallow SMG phase near the transition to the SSB phase

$$G'_{\mathrm{SMG}}(\omega, \boldsymbol{k}) = \frac{\omega + \epsilon_{\boldsymbol{k}}}{\omega^2 - \epsilon_{\boldsymbol{k}}^2 - \Delta_0^2}. \quad (23)$$

A more rigorous treatment of a similar problem can be found in Ref. [95], which includes finite momentum fluctuations of $\Delta$. The major effect of these fluctuations is to introduce a spectral broadening for the fermion Green's function as if replacing $\omega \to \omega + \mathrm{i}\delta$ in Eq. (23). It was also found that the broadening $\delta \sim \xi^{-1}$ scales inversely with the correlation length $\xi$ of the order parameter, which justifies our simple treatment in the large-$\xi$ regime. Similar Green's functions as Eq. (23) was previously constructed to describe non-Fermi liquid [98] statisfying the Luttinger theorem. However, its physical meaning is now clarified as Green's function in the SMG phase.

The features of $G'_{\mathrm{SMG}}$ in Eq. (23) are presented in Fig. 6. When comparing Figs. 6(a) and 5(a), we can observe that the pole structure of $G'_{\mathrm{SMG}}$ is identical to that of $G_{\mathrm{SSB}}$ (in the diagonal component), both showcasing a gapped spectrum. However, they significantly differ in their zero structures, as seen by comparing Figs. 6(b) and 5(b). Due to the restoration of symmetry, the low-energy zeros reemerge in the Green's function in the SMG phase. Additionally, its zero Fermi surface perfectly aligns with the original pole Fermi surface, fulfilling the Luttinger theorem's requirement for the Fermi volume.

Comparing the Green's function in the SMG phase derived from the strong coupling analysis Eq. (19) and the weak coupling analysis Eq. (23) (see also Figs. 3 and 6), we find that despite the apparent difference in high-energy spectral features, the zero Fermi surface defined by $G(0, \boldsymbol{k}) = 0$ remains a resilient low-energy feature. The persistent zero Fermi surface in the SMG phase is a consequence of the Luttinger theorem.

Nonetheless, besides the low-energy zero structure, it is also intriguing to understand how the high-energy spectral feature deforms from the weak coupling case to the strong
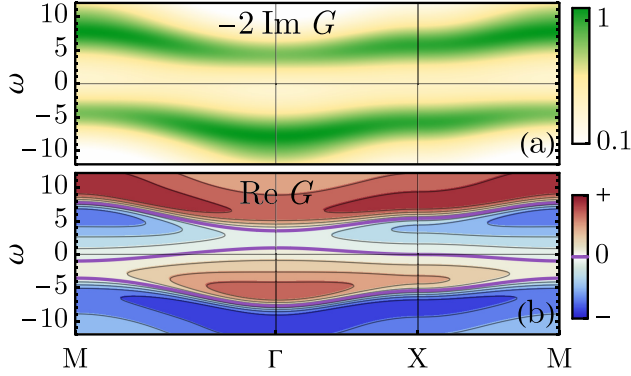
FIG. 7. (a) Broadened spectral function from the one in Fig. 3. (b) Reconstructed Green's function real part by the KK relation, showing robust Green's function zeros (purple contour) crossing $\omega = 0$.

coupling case. However, this problem requires nonperturbative numerical simulations. Fortunately, the bilayer square lattice model Eq. (3) admits a sign-problem-free [129] quantum Monte Carlo [130–134] simulation. We will leave this interesting direction for future research.

## IV. PROBING GREEN'S FUNCTION ZEROS

While Green's function zeros are an important feature of the SMG insulator, they are not directly observable in experiments. Spectroscopy experiments, such as angle-resolved photoemission spectroscopy (ARPES), can directly probe the fermion's spectral function $A(\omega, \boldsymbol{k}) = -2 \operatorname{Im} G(\omega + i0_+, \boldsymbol{k})$, which is the imaginary part of Green's function. By employing the Kramers-Kronig (KK) relation to recover the real part of Green's function from the spectral function,

$$\operatorname{Re} G(\omega, \boldsymbol{k}) = \frac{1}{2\pi} \mathcal{P} \int d\omega' \frac{A(\omega', \boldsymbol{k})}{\omega' - \omega}, \qquad (24)$$

we can indirectly study the zero structure of the Green's function.

However, the spectral function might be broadened in experimental data due to noise or dissipation. We are interested in studying how sensitive the reconstructed Green's function zero is to these disturbances, in order to understand the stability of the method. Following Sec. III A, we start from the strong coupling limit and use the CPT approach to calculate Green's function. To account for the spectral broadening effect, we replace $\omega$ with $\omega + i\delta$, where $\delta$ is relatively large, say, about the order of the hopping $t$. Based on the broadened spectral function in Fig. 7(a), we use the KK relation to reconstruct the real part, as shown in Fig. 7(b). We find that the zero Fermi surface maintains the same shape, but the zero "dispersion" bandwidth gets larger.

The increase in bandwidth can be understood by taking the SMG Green's function $G_{\text{SMG}}(\omega, \boldsymbol{k})$ in Eq. (19), and solving for its zeros $\operatorname{Re} G(\omega + i\delta, \boldsymbol{k}) = 0$. To the leading order of $1/J$ and $\delta$, the solution is given by

$$\omega(\boldsymbol{k}) = -\left(1 + \frac{\delta^2}{\alpha}\right) \frac{\alpha \epsilon_{\boldsymbol{k}}}{J^2} + \cdots, \qquad (25)$$

meaning that the bandwidth of Green's function zero dispersion will increase by $\delta^2/\alpha$, but the corresponding Luttinger surface remains unchanged. Therefore the Green's function zero in the SMG phase is a robust feature that can be potentially identified from spectroscopy measurements, even in the presence of noises or dissipations.

## V. SUMMARY AND DISCUSSIONS

In this paper, we investigated the Fermi surface SMG in a bilayer square lattice model. A crucial finding of this study lies in the robust Green's function zero in the SMG phase. Traditionally, a Fermi liquid state is characterized by poles in the Green's function along the Fermi surface. However, as the fermion system is driven into the SMG state by interaction effects, these poles are replaced by zeros. This is a robust phenomenon underlined by the constraints of the Luttinger theorem.

Our exploration is not limited to theoretical assertions. We also offer a tangible demonstration of this occurrence in the bilayer square lattice model. By applying both strong and weak coupling analyses, we provide a comprehensive portrayal of the fermion Green's function across different interaction regimes. We highlight that the emergence of the zero Fermi surface is not an ephemeral or fine-tuned phenomenon, but rather a robust and enduring feature of the SMG phase. We show that even when the system is subjected to spectral broadening, the zero Fermi surface persists, retaining the Fermi volume.

The results of this study confirm the robustness of the zero Fermi surface and underscore the possibility of observing it in experimental setups, such as through ARPES. Despite not being directly observable, the zero structure of the Green's function could be inferred indirectly via the KK relation.

The bilayer square lattice model may be relevant to the nickelate superconductor recently discovered in pressurized $La_3Ni_2O_7$ [135,136], which is a layered two-dimensional material where each layer consists of nickel atoms arranged in a bilayer square lattice. The Fermi surface is dominated by $d_{z^2}$ and $d_{x^2-y^2}$ electrons of Ni. The $d_{z^2}$ electron has a relatively small intralayer hopping $t$ due to the rather localized $d_{z^2}$ orbital wave function in the $xy$ plane but enjoys a large interlayer antiferromagnetic Heisenberg interaction $J$ due to the super-exchange mechanism mediated by the apical oxygen. This likely puts the $d_{z^2}$ electrons in an SMG insulator phase in the bilayer square lattice model and opens up opportunities to investigate the proposed Green's function zeros in real materials. The potential implication of SMG physics on the nickelate high-$T_c$ superconductor still requires further theoretical research in the future.

## APPENDIX: CLUSTER PERTURBATION THEORY

Here we review the details of cluster perturbation theory (CPT) originally developed in [94]. Denote the superlattice lattice points by $\boldsymbol{R}$, then the position of any original lattice point would be given by $\boldsymbol{R} + \boldsymbol{r}$, where $\boldsymbol{r}$ is the relative position of the lattice point to the location $\boldsymbol{R}$ of the cluster containing that particular lattice point. For clusters of size $L$, the generic Green's function in real space can be denoted by $G_{i,j}^{\boldsymbol{R},\boldsymbol{R}'}$, with $i, j = 1, \ldots, L$, where the time dependence is implicitly assumed and same goes for the frequency dependence in Fourier space. Due to the translation invariance of the clusters on the *superlattice*, the real space Green's function can be firstly partially Fourier-transformed to give

$$G_{i,j}^{\boldsymbol{R},\boldsymbol{R}'} = \frac{1}{N} \sum_{\boldsymbol{q}} G(\boldsymbol{q})_{ij} e^{i\boldsymbol{q}\cdot(\boldsymbol{R}-\boldsymbol{R}')}, \qquad \text{(A1)}$$

where the $\boldsymbol{q}$ summation is over the Brillouin zone (BZ) of the superlattice and $N$ is the number of clusters on the superlattice, which goes to infinity in the thermodynamic limit. In contrast to the translation invariance of the $(\boldsymbol{R}, \boldsymbol{R}')$ part of $G_{i,j}^{\boldsymbol{R},\boldsymbol{R}'}$, or equivalently it only depends on the difference $\boldsymbol{R} - \boldsymbol{R}'$ as can be seen in Eq. (A1), the $(i, j)$ part of the Green's function loses translation invariance due to the introduction of clusters. This is so because correlation between two points within the same cluster is not manifestly the same with the correlation between another pair of equally separated points *across* clusters. Therefore it takes two lattice momenta to fully characterize $G_{i,j}^{\boldsymbol{R},\boldsymbol{R}'}$ in Fourier space. More precisely, we have,

$$G(\boldsymbol{k}, \boldsymbol{k}') = \frac{1}{NL} \sum_{\boldsymbol{R},\boldsymbol{R}'} \sum_{i,j} G_{i,j}^{\boldsymbol{R},\boldsymbol{R}'} e^{i\boldsymbol{k}\cdot(\boldsymbol{R}+\boldsymbol{r}_i)-i\boldsymbol{k}'\cdot(\boldsymbol{R}'+\boldsymbol{r}_j)}. \qquad \text{(A2)}$$

Then we can plug Eq. (A1) into Eq. (A2) and integrate out the superlattice lattice vectors $\boldsymbol{R}, \boldsymbol{R}'$ to obtain the following:

$$G(\boldsymbol{k}, \boldsymbol{k}') = \frac{1}{L} \sum_{i,j} \sum_{\boldsymbol{q}} G(\boldsymbol{q})_{ij} \tilde{\delta}_{\boldsymbol{k},\boldsymbol{q}} \tilde{\delta}_{\boldsymbol{k}',\boldsymbol{q}} e^{i(\boldsymbol{k}\cdot\boldsymbol{r}_i - \boldsymbol{k}'\cdot\boldsymbol{r}_j)}, \qquad \text{(A3)}$$

where the $\tilde{\delta}$ function denotes the fact that the two wave vectors are equivalent only up to a superlattice reciprocal lattice vector $\boldsymbol{Q}$ because $\boldsymbol{Q} \cdot \boldsymbol{R} = 2\pi\mathbb{Z}$ in the phase factor. More precisely, we have

$$\tilde{\delta}_{\boldsymbol{k},\boldsymbol{q}} = \sum_{s=1}^{L} \delta_{\boldsymbol{k},\boldsymbol{q}+\boldsymbol{Q}_s}, \qquad \text{(A4)}$$

where $\boldsymbol{Q}_s$ with $s = 1, \ldots, L$ are the $L$ inequivalent wave vectors in the reciprocal lattice of the original lattice (see the 1d case shown in Fig. 8). Then we can perform the $\boldsymbol{q}$ summation in Eq. (A3) to have

$$G(\boldsymbol{k}, \boldsymbol{k}') = \frac{1}{L} \sum_{i,j} \sum_{s,s'} G(\boldsymbol{k} - \boldsymbol{Q}_s)_{ij} \delta_{\boldsymbol{k}'-\boldsymbol{k},\boldsymbol{Q}_s-\boldsymbol{Q}_{s'}} e^{i(\boldsymbol{k}\cdot\boldsymbol{r}_i - \boldsymbol{k}'\cdot\boldsymbol{r}_j)}$$

$$= \sum_{i,j} \sum_{\Delta\boldsymbol{Q}} G(\boldsymbol{k})_{ij} \delta_{\boldsymbol{k}'-\boldsymbol{k},\Delta\boldsymbol{Q}} e^{i(\boldsymbol{k}\cdot\boldsymbol{r}_i - \boldsymbol{k}'\cdot\boldsymbol{r}_j)}, \qquad \text{(A5)}$$

where we have used the fact that $G(\boldsymbol{q})_{ij}$ is invariant under the shift by a superlattice reciprocal lattice vector $\boldsymbol{Q}_s$.

The translation invariant approximation for the Green's function on the original lattice is obtained when $\Delta\boldsymbol{Q} = 0$, i.e.,



FIG. 8. Reciprocal lattice in 1d for a four-site cluster. $K$ labels the reciprocal lattice vector for the original lattice and $Q$ labels the reciprocal lattice vector for the superlattice. More precisely, $K_s = \frac{2\pi}{a}s$ and $Q_s = \frac{2\pi}{La}s$, where $a$ is the lattice constant of the original lattice, $L = 4$ here and $s \in \mathbb{Z}$.

$\boldsymbol{k} = \boldsymbol{k}'$. Therefore the Green's function becomes

$$G(\boldsymbol{k}) = \sum_{i,j} G(\boldsymbol{k})_{ij} e^{i\boldsymbol{k}\cdot(\boldsymbol{r}_i - \boldsymbol{r}_j)}. \qquad \text{(A6)}$$

Now we just need to calculate $G_{i,j}(\boldsymbol{k})$ using cluster perturbation. The idea is to treat hopping between clusters as perturbation when consider strong on-site interactions. In particular,

$$\hat{H} = \hat{H}_0 + \hat{V}, \qquad \text{(A7)}$$

where $\hat{H}_0$ contains intracluster terms and $\hat{V}$ contains intercluster hopping. Considering nearest-neighbor hopping between the square clusters used in the main text. The cluster construction is reproduced in Fig. 9 with the four sites in each cluster labeled by 1–4. The hopping matrix is given by (setting lattice constant $a = 1$)

$$V_{i,j}^{\boldsymbol{R},\boldsymbol{R}'} = -t\delta_{\boldsymbol{R},\boldsymbol{R}'-2\hat{x}}(\delta_{i,2}\delta_{j,1} + \delta_{i,3}\delta_{j,4})$$

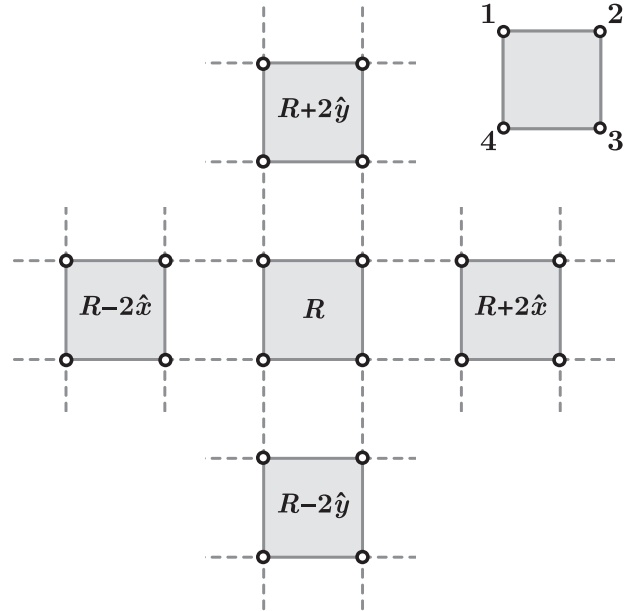$$-t\delta_{\boldsymbol{R},\boldsymbol{R}'+2\hat{x}}(\delta_{i,1}\delta_{j,2} + \delta_{i,4}\delta_{j,3})$$



FIG. 9. Cluster diagram showing the hopping between neighboring clusters (dashed line). The four sites inside each cluster are numbered as shown.

$$- t\delta_{\boldsymbol{R},\boldsymbol{R'}-2\hat{y}}(\delta_{i,1}\delta_{j,4} + \delta_{i,2}\delta_{j,3})$$
$$- t\delta_{\boldsymbol{R},\boldsymbol{R'}+2\hat{y}}(\delta_{i,3}\delta_{j,2} + \delta_{i,4}\delta_{j,1}). \quad \text{(A8)}$$

Fourier transforming $V_{i,j}^{\boldsymbol{R},\boldsymbol{R'}}$ into the superlattice reciprocal space, we have

$$V_{i,j}(\boldsymbol{q}) = -te^{i2q_x}(\delta_{i,2}\delta_{j,1} + \delta_{i,3}\delta_{j,4})$$
$$- te^{-i2q_x}(\delta_{i,1}\delta_{j,2} + \delta_{i,4}\delta_{j,3})$$
$$- te^{i2q_y}(\delta_{i,1}\delta_{j,4} + \delta_{i,2}\delta_{j,3})$$
$$- te^{-i2q_y}(\delta_{i,3}\delta_{j,2} + \delta_{i,4}\delta_{j,1})$$

$$= -t\begin{pmatrix} 0 & e^{-i2\boldsymbol{q}_x} & 0 & e^{i2\boldsymbol{q}_y} \\ e^{i2\boldsymbol{q}_x} & 0 & e^{i2\boldsymbol{q}_y} & 0 \\ 0 & e^{-i2\boldsymbol{q}_y} & 0 & e^{i2\boldsymbol{q}_x} \\ e^{-i2\boldsymbol{q}_y} & 0 & e^{-i2\boldsymbol{q}_x} & 0 \end{pmatrix}_{i,j}, \quad \text{(A9)}$$

which is the form presented in Eq. (17) in the main text. Then the interacting Green's function is given by

$$\hat{G}(\boldsymbol{q}) = \frac{1}{\omega - \hat{H}} = \frac{1}{\omega - \hat{H}_0 - \hat{V}(\boldsymbol{q})} = \frac{\hat{G}_0}{1 - \hat{V}(\boldsymbol{q})\hat{G}_0}, \quad \text{(A10)}$$

where $\hat{G}_0 \equiv (\omega - \hat{H}_0)^{-1}$ is the intracluster Green's function that can be easily obtained by exact diagonalization as long as the cluster size is not too big. The obtained $G(\boldsymbol{q})_{ij}$ can now be plugged into Eq. (A6) to calculate the CPT Green's function for the interacting system.

[1] L. Fidkowski and A. Kitaev, Effects of interactions on the topological classification of free fermion systems, Phys. Rev. B **81**, 134509 (2010).

[2] L. Fidkowski and A. Kitaev, Topological phases of fermions in one dimension, Phys. Rev. B **83**, 075103 (2011).

[3] J. Wang and X.-G. Wen, Non-perturbative regularization of $1 + 1d$ anomaly-free chiral fermions and bosons: On the equivalence of anomaly matching conditions and boundary gapping rules, Phys. Rev. B **107**, 014311 (2023).

[4] K. Slagle, Y.-Z. You, and C. Xu, Exotic quantum phase transitions of strongly interacting topological insulators, Phys. Rev. B **91**, 115121 (2015).

[5] V. Ayyar and S. Chandrasekharan, Massive fermions without fermion bilinear condensates, Phys. Rev. D **91**, 065035 (2015).

[6] S. Catterall, Fermion mass without symmetry breaking, J. High Energy Phys. 01 (2016) 121.

[7] D. Tong, Comments on symmetric mass generation in 2d and 4d, J. High Energy Phys. 07 (2022) 001.

[8] J. Wang and Y.-Z. You, Symmetric mass generation, Symmetry **14**, 1475 (2022).

[9] Y. Nambu, Quasi-particles and gauge invariance in the theory of superconductivity, Phys. Rev. **117**, 648 (1960).

[10] Y. Nambu and G. Jona-Lasinio, Dynamical model of elementary particles based on an analogy with superconductivity. I, Phys. Rev. **122**, 345 (1961).

[11] J. Goldstone, A. Salam, and S. Weinberg, Broken symmetries, Phys. Rev. **127**, 965 (1962).

[12] P. W. Anderson, Plasmons, gauge invariance, and mass, Phys. Rev. **130**, 439 (1963).

[13] F. Englert and R. Brout, Broken symmetry and the mass of gauge vector mesons, Phys. Rev. Lett. **13**, 321 (1964).

[14] P. W. Higgs, Broken symmetries and the masses of gauge bosons, Phys. Rev. Lett. **13**, 508 (1964).

[15] H. B. Nielsen and M. Ninomiya, Absence of neutrinos on a lattice: (II). Intuitive topological proof, Nucl. Phys. B **193**, 173 (1981).

[16] H. B. Nielsen and M. Ninomiya, Absence of neutrinos on a lattice (I). Proof by homotopy theory, Nucl. Phys. B **185**, 20 (1981).

[17] H. B. Nielsen and M. Ninomiya, A no-go theorem for regularizing chiral fermions, Phys. Lett. B **105**, 219 (1981).

[18] P. Swift, The electroweak theory on the lattice, Phys. Lett. B **145**, 256 (1984).

[19] E. Eichten and J. Preskill, Chiral gauge theories on the lattice, Nucl. Phys. B **268**, 179 (1986).

[20] J. Smit, Fermions on a lattice, Acta Phys. Pol. B **17**, 531 (1986).

[21] D. B. Kaplan, A method for simulating chiral fermions on the lattice, Phys. Lett. B **288**, 342 (1992).

[22] X.-G. Wen, A lattice non-perturbative definition of an SO(10) chiral gauge theory and its induced standard model, Chin. Phys. Lett. **30**, 111101 (2013).

[23] Y.-Z. You, Y. BenTov, and C. Xu, Interacting topological superconductors and possible origin of $16n$ chiral fermions in the standard model, arXiv:1402.4151.

[24] Y.-Z. You and C. Xu, Interacting topological insulator and emergent grand unified theory, Phys. Rev. B **91**, 125147 (2015).

[25] Y. BenTov, Fermion masses without symmetry breaking in two spacetime dimensions, J. High Energy Phys. 07 (2015) 034.

[26] V. Ayyar and S. Chandrasekharan, Origin of fermion masses without spontaneous symmetry breaking, Phys. Rev. D **93**, 081701(R) (2016).

[27] V. Ayyar and S. Chandrasekharan, Fermion masses through four-fermion condensates, J. High Energy Phys. 10 (2016) 058.

[28] V. Ayyar, Search for a continuum limit of the PMS phase, arXiv:1611.00280.

[29] M. DeMarco and X.-G. Wen, A novel non-perturbative lattice regularization of an anomaly-free $1 + 1d$ chiral $SU(2)$ gauge theory, arXiv:1706.04648.

[30] V. Ayyar and S. Chandrasekharan, Generating a non-perturbative mass gap using Feynman diagrams in an asymptotically free theory, Phys. Rev. D **96**, 114506 (2017).

[31] D. Schaich and S. Catterall, Phases of a strongly coupled four-fermion theory, EPJ Web Conf. **175**, 03004 (2018).

[32] N. Butt and S. Catterall, Four fermion condensates in SU(2) Yang-Mills-Higgs theory on a lattice, arXiv:1811.01015.

[33] N. Butt, S. Catterall, and D. Schaich, SO(4) invariant Higgs-Yukawa model with reduced staggered fermions, Phys. Rev. D **98**, 114514 (2018).

[34] Y. Kikukawa, On the gauge-invariant path-integral measure for the overlap Weyl fermions in 16 of SO(10), Prog. Theor. Exp. Phys. **2019**, 113B03 (2019).

[35] Y. Kikukawa, Why is the mission impossible? Decoupling the mirror Ginsparg-Wilson fermions in the lattice models for two-dimensional Abelian chiral gauge theories, Prog. Theor. Exp. Phys. **2019**, 073B02 (2019).

[36] J. Wang and X.-G. Wen, Solution to the $1+1$ dimensional gauged chiral Fermion problem, Phys. Rev. D **99**, 111501(R) (2019).

[37] J. Wang and X.-G. Wen, Nonperturbative definition of the standard models, Phys. Rev. Res. **2**, 023356 (2020).

[38] S. Catterall, N. Butt, and D. Schaich, Exotic phases of a Higgs-Yukawa model with reduced staggered fermions, Pos **363** (2020), doi:10.22323/1.363.0044.

[39] S. S. Razamat and D. Tong, Gapped chiral fermions, Phys. Rev. X **11**, 011063 (2021).

[40] S. Catterall, Chiral lattice fermions from staggered fields, Phys. Rev. D **104**, 014503 (2021).

[41] N. Butt, S. Catterall, A. Pradhan, and G. C. Toga, Anomalies and symmetric mass generation for Kähler-Dirac fermions, Phys. Rev. D **104**, 094504 (2021).

[42] N. Butt, S. Catterall, and G. C. Toga, Symmetric mass generation in lattice gauge theory, Symmetry **13**, 2276 (2021).

[43] M. Zeng, Z. Zhu, J. Wang, and Y.-Z. You, Symmetric mass generation in the $1+1$ dimensional chiral fermion 3-4-5-0 model, Phys. Rev. Lett. **128**, 185301 (2022).

[44] S. Catterall and A. Pradhan, Induced topological gravity and anomaly inflow from Kähler-Dirac fermions in odd dimensions, Phys. Rev. D **106**, 014509 (2022).

[45] S. Catterall, 't Hooft anomalies for staggered fermions, Phys. Rev. D **107**, 014501 (2023).

[46] Y. Guo and Y.-Z. You, Symmetric mass generation of Kähler-Dirac fermions from the perspective of symmetry-protected topological phases, arXiv:2306.17420.

[47] A. M. Turner, F. Pollmann, and E. Berg, Topological phases of one-dimensional fermions: An entanglement point of view, Phys. Rev. B **83**, 075102 (2011).

[48] S. Ryu and S.-C. Zhang, Interacting topological phases and modular invariance, Phys. Rev. B **85**, 245132 (2012).

[49] X.-L. Qi, A new class of $(2+1)$-dimensional topological superconductors with $\mathbb{Z}_8$ topological classification, New J. Phys. **15**, 065002 (2013).

[50] H. Yao and S. Ryu, Interaction effect on topological classification of superconductors in two dimensions, Phys. Rev. B **88**, 064507 (2013).

[51] Z.-C. Gu and M. Levin, Effect of interactions on two-dimensional fermionic symmetry-protected topological phases with $Z_2$ symmetry, Phys. Rev. B **89**, 201113(R) (2014).

[52] C. Wang and T. Senthil, Interacting fermionic topological insulators/superconductors in three dimensions, Phys. Rev. B **89**, 195124 (2014).

[53] M. A. Metlitski, L. Fidkowski, X. Chen, and A. Vishwanath, Interaction effects on 3D topological superconductors: Surface topological order from vortex condensation, the 16 fold way and fermionic Kramers doublets, arXiv:1406.3032.

[54] A. Kapustin, R. Thorngren, A. Turzillo, and Z. Wang, Fermionic symmetry protected topological phases and cobordisms, J. High Energy Phys. 12 (2015) 052.

[55] Y.-Z. You and C. Xu, Symmetry-protected topological states of interacting fermions and bosons, Phys. Rev. B **90**, 245120 (2014).

[56] M. Cheng, Z. Bi, Y.-Z. You, and Z.-C. Gu, Classification of symmetry-protected phases for interacting fermions in two dimensions, Phys. Rev. B **97**, 205109 (2018).

[57] T. Yoshida and A. Furusaki, Correlation effects on topological crystalline insulators, Phys. Rev. B **92**, 085114 (2015).

[58] Y. Gu and X.-L. Qi, Axion field theory approach and the classification of interacting topological superconductors, arXiv:1512.04919.

[59] X.-Y. Song and A. P. Schnyder, Interaction effects on the classification of crystalline topological insulators and superconductors, Phys. Rev. B **95**, 195108 (2017).

[60] R. Queiroz, E. Khalaf, and A. Stern, Dimensional hierarchy of fermionic interacting topological phases, Phys. Rev. Lett. **117**, 206405 (2016).

[61] E. Witten, The "parity" anomaly on an unorientable manifold, Phys. Rev. B **94**, 195150 (2016).

[62] Q.-R. Wang and Z.-C. Gu, Towards a complete classification of symmetry-protected topological phases for interacting fermions in three dimensions and a general group supercohomology theory, Phys. Rev. X **8**, 011055 (2018).

[63] A. Kapustin and R. Thorngren, Fermionic SPT phases in higher dimensions and bosonization, J. High Energy Phys. 10 (2017) 080.

[64] J. Wang, K. Ohmori, P. Putrov, Y. Zheng, Z. Wan, M. Guo, H. Lin, P. Gao, and S.-T. Yau, Tunneling topological vacua via extended operators: (Spin-)TQFT spectra and boundary deconfinement in various dimensions, Prog. Theor. Exp. Phys. **2018**, 053A01 (2018).

[65] Q.-R. Wang and Z.-C. Gu, Construction and classification of symmetry-protected topological phases in interacting fermion systems, Phys. Rev. X **10**, 031055 (2020).

[66] M. Guo, K. Ohmori, P. Putrov, Z. Wan, and J. Wang, Fermionic finite-group gauge theories and interacting symmetric/crystalline orders via cobordisms, Commun. Math. Phys. **376**, 1073 (2020).

[67] D. Aasen, P. Bonderson, and C. Knapp, Characterization and classification of fermionic symmetry enriched topological phases, arXiv:2109.10911.

[68] M. Barkeshli, Y.-A. Chen, P.-S. Hsin, and N. Manjunath, Classification of $(2+1)$D invertible fermionic topological phases with symmetry, Phys. Rev. B **105**, 235143 (2022).

[69] L. Zou and D. Chowdhury, Deconfined metal-insulator transitions in quantum hall bilayers, Phys. Rev. Res. **2**, 032071 (2020).

[70] Y.-H. Zhang and S. Sachdev, From the pseudogap metal to the Fermi liquid using ancilla qubits, Phys. Rev. Res. **2**, 023172 (2020).

[71] L. Zou and D. Chowdhury, Deconfined metallic quantum criticality: A U(2) gauge-theoretic approach, Phys. Rev. Res. **2**, 023344 (2020).

[72] Y.-H. Zhang and S. Sachdev, Deconfined criticality and ghost Fermi surfaces at the onset of antiferromagnetism in a metal, Phys. Rev. B **102**, 155124 (2020).

[73] A. Nikolaenko, M. Tikhanovskaya, S. Sachdev, and Y.-H. Zhang, Small to large Fermi surface transition in a single-band model using randomly coupled ancillas, Phys. Rev. B **103**, 235138 (2021).

[74] D.-C. Lu, M. Zeng, J. Wang, and Y.-Z. You, Fermi surface symmetric mass generation, Phys. Rev. B **107**, 195133 (2023).

[75] D. Bulmash, P. Hosur, S.-C. Zhang, and X.-L. Qi, Unified topological response theory for gapped and gapless free fermions, Phys. Rev. X **5**, 021018 (2015).

[76] D.-C. Lu, J. Wang, and Y.-Z. You, Definition and classification of Fermi surface anomalies, arXiv:2302.12731v2.

[77] V. Gurarie, Single-particle Green's functions and interacting topological insulators, Phys. Rev. B **83**, 085426 (2011).

[78] Y.-Z. You, Z. Wang, J. Oon, and C. Xu, Topological number and fermion Green's function for strongly interacting topological superconductors, Phys. Rev. B **90**, 060502(R) (2014).

[79] S. Catterall and D. Schaich, Novel phases in strongly coupled four-fermion theories, Phys. Rev. D **96**, 034506 (2017).

[80] Y.-Z. You, Y.-C. He, C. Xu, and A. Vishwanath, Symmetric fermion mass generation as deconfined quantum criticality, Phys. Rev. X **8**, 011026 (2018).

[81] S. Catterall and N. Butt, Topology and strong four fermion interactions in four dimensions, Phys. Rev. D **97**, 094502 (2018).

[82] Y. Xu and C. Xu, Green's function zero and symmetric mass generation, arXiv:2103.15865.

[83] Y.-Z. You, Y.-C. He, A. Vishwanath, and C. Xu, From bosonic topological transition to symmetric fermion mass generation, Phys. Rev. B **97**, 125112 (2018).

[84] C. Wang, A. Hickey, X. Ying, and A. A. Burkov, Emergent anomalies and generalized Luttinger theorems in metals and semimetals, Phys. Rev. B **104**, 235113 (2021).

[85] X.-G. Wen, Low-energy effective field theories of fermion liquids and the mixed $U(1) \times R^d$ anomaly, Phys. Rev. B **103**, 165126 (2021).

[86] M. Cheng, M. Zaletel, M. Barkeshli, A. Vishwanath, and P. Bonderson, Translational symmetry and microscopic constraints on symmetry-enriched topological phases: A view from the surface, Phys. Rev. X **6**, 041068 (2016).

[87] G. Y. Cho, C.-T. Hsieh, and S. Ryu, Anomaly manifestation of Lieb-Schultz-Mattis theorem and topological phases, Phys. Rev. B **96**, 195105 (2017).

[88] N. Bultinck and M. Cheng, Filling constraints on fermionic topological order in zero magnetic field, Phys. Rev. B **98**, 161119(R) (2018).

[89] R. Thorngren and D. V. Else, Gauging spatial symmetries and the classification of topological crystalline phases, Phys. Rev. X **8**, 011040 (2018).

[90] M. Cheng and N. Seiberg, Lieb-Schultz-Mattis, Luttinger, and 't Hooft – anomaly matching in lattice systems, SciPost Phys. **15**, 051 (2023).

[91] D. V. Else, R. Thorngren, and T. Senthil, Non-fermi liquids as ersatz fermi liquids: general constraints on compressible metals, Phys. Rev. X **11**, 021005 (2021).

[92] D. V. Else and T. Senthil, Strange metals as ersatz fermi liquids, Phys. Rev. Lett. **127**, 086601 (2021).

[93] Z. Darius Shi, H. Goldman, D. V. Else, and T. Senthil, Gifts from anomalies: Exact results for Landau phase transitions in metals, SciPost Phys. **13**, 102 (2022).

[94] D. Sénéchal, D. Perez, and M. Pioro-Ladrière, Spectral weight of the hubbard model through cluster perturbation theory, Phys. Rev. Lett. **84**, 522 (2000).

[95] X.-C. Wang and Y. Qi, Phase fluctuations in two-dimensional superconductors and pseudogap phenomenon, Phys. Rev. B **107**, 224502 (2023).

[96] B. L. Altshuler, A. V. Chubukov, A. Dashevskii, A. M. Finkel'stein, and D. K. Morr, Luttinger theorem for a spin-density-wave state, Europhys. Lett. **41**, 401 (1998).

[97] M. Oshikawa, Topological approach to Luttinger's theorem and the Fermi surface of a Kondo lattice, Phys. Rev. Lett. **84**, 3370 (2000).

[98] I. Dzyaloshinskii, Some consequences of the Luttinger theorem: The Luttinger surfaces in non-Fermi liquids and Mott insulators, Phys. Rev. B **68**, 085113 (2003).

[99] N. V. Gnezdilov and Y. Wang, Solvable model for a charge-4$e$ superconductor, Phys. Rev. B **106**, 094508 (2022).

[100] J. M. Luttinger, Fermi surface and some simple equilibrium properties of a system of interacting fermions, Phys. Rev. **119**, 1153 (1960).

[101] T. D. Stanescu, P. Phillips, and T.-P. Choy, Theory of the Luttinger surface in doped Mott insulators, Phys. Rev. B **75**, 104503 (2007).

[102] M. S. Scheurer, S. Chatterjee, W. Wu, M. Ferrero, A. Georges, and S. Sachdev, Topological order in the pseudogap metal, Proc. Natl. Acad. Sci. USA **115**, E3665 (2018).

[103] T. Xiang and C. Wu, *D-wave Superconductivity* (Cambridge University Press, 2022), Chap. 4.

[104] H. Zhai, F. Wang, and D.-H. Lee, Antiferromagnetically driven electronic correlations in iron pnictides and cuprates, Phys. Rev. B **80**, 064517 (2009).

[105] R. Rüger, L. F. Tocchio, R. Valentí, and C. Gros, The phase diagram of the square lattice bilayer Hubbard model: a variational Monte Carlo study, New J. Phys. **16**, 033010 (2014).

[106] J.-W. Rhim and B.-J. Yang, Classification of flat bands according to the band-crossing singularity of Bloch wave functions, Phys. Rev. B **99**, 045107 (2019).

[107] K. A. Chao, J. Spałek, and A. M. Oleś, Canonical perturbation expansion of the hubbard model, Phys. Rev. B **18**, 3453 (1978).

[108] M. C. Gutzwiller, Effect of correlation on the ferromagnetism of transition metals, Phys. Rev. **134**, A923 (1964).

[109] W. Hou and Y.-Z. You, Variational Monte Carlo study of symmetric mass generation in a bilayer honeycomb lattice model, arXiv:2212.13364.

[110] J. M. Luttinger and J. C. Ward, Ground-state energy of a many-fermion system. II, Phys. Rev. **118**, 1417 (1960).

[111] T. Senthil, S. Sachdev, and M. Vojta, Fractionalized fermi liquids, Phys. Rev. Lett. **90**, 216403 (2003).

[112] T. Senthil, M. Vojta, and S. Sachdev, Weak magnetism and non-Fermi liquids near heavy-fermion critical points, Phys. Rev. B **69**, 035111 (2004).

[113] A. Paramekanti and A. Vishwanath, Extending Luttinger's theorem to $\mathbb{Z}_2$ fractionalized phases of matter, Phys. Rev. B **70**, 245118 (2004).

[114] M. Oshikawa and T. Senthil, Fractionalization, topological order, and quasiparticle statistics, Phys. Rev. Lett. **96**, 060601 (2006).

[115] R. Nandkishore, M. A. Metlitski, and T. Senthil, Orthogonal metals: The simplest non-Fermi liquids, Phys. Rev. B **86**, 045128 (2012).

[116] S. Sachdev, Topological order, emergent gauge fields, and Fermi surface reconstruction, Rep. Prog. Phys. **82**, 014001 (2019).

[117] J. Skolimowski and M. Fabrizio, Luttinger's theorem in the presence of Luttinger surfaces, Phys. Rev. B **106**, 045109 (2022).

[118] D. Sénéchal, D. Perez, and D. Plouffe, Cluster perturbation theory for Hubbard models, Phys. Rev. B **66**, 075129 (2002).

[119] P. A. Lee, N. Nagaosa, and X.-G. Wen, Doping a Mott insulator: Physics of high temperature superconductivity, Rev. Mod. Phys. **78**, 17 (2006).

[120] B. Keimer, S. A. Kivelson, M. R. Norman, S. Uchida, and J. Zaanen, From quantum matter to high-temperature superconductivity in copper oxides, Nature (London) **518**, 179 (2015).

[121] M. Franz and A. J. Millis, Phase fluctuations and spectral properties of underdoped cuprates, Phys. Rev. B **58**, 14572 (1998).

[122] H.-J. Kwon and A. T. Dorsey, Effect of phase fluctuations on the single-particle properties of underdoped cuprates, Phys. Rev. B **59**, 6438 (1999).

[123] H.-J. Kwon, A. T. Dorsey, and P. J. Hirschfeld, Observability of quantum phase fluctuations in cuprate superconductors, Phys. Rev. Lett. **86**, 3875 (2001).

[124] M. Franz and Z. Tešanović, Algebraic fermi liquid from phase fluctuations: "Topological" fermions, vortex "berryons," and $QED_3$ theory of cuprate superconductors, Phys. Rev. Lett. **87**, 257003 (2001).

[125] P. Curty and H. Beck, Thermodynamics and phase diagram of high temperature superconductors, Phys. Rev. Lett. **91**, 257002 (2003).

[126] T. Li and D.-W. Yao, Pairing origin of the pseudogap as observed in ARPES measurement in the underdoped cuprates, arXiv:1805.05530.

[127] T. Li and D.-W. Yao, Why is the antinodal quasiparticle in the electron-doped cuprate $Pr_{1.3-x}La_{0.7}Ce_xCuO_4$ immune to the antiferromagnetic band-folding effect? Europhys. Lett. **124**, 47001 (2018).

[128] M. Ye and A. V. Chubukov, Hubbard model on a triangular lattice: Pseudogap due to spin density wave fluctuations, Phys. Rev. B **100**, 035135 (2019).

[129] M. Troyer and U.-J. Wiese, Computational complexity and fundamental limitations to fermionic quantum Monte Carlo simulations, Phys. Rev. Lett. **94**, 170201 (2005).

[130] F. Fucito, E. Marinari, G. Parisi, and C. Rebbi, A proposal for monte carlo simulations of fermionic systems, Nucl. Phys. B **180**, 369 (1981).

[131] D. J. Scalapino and R. L. Sugar, Method for performing monte carlo calculations for systems with fermions, Phys. Rev. Lett. **46**, 519 (1981).

[132] R. Blankenbecler, D. J. Scalapino, and R. L. Sugar, Monte Carlo calculations of coupled Boson-fermion systems. I, Phys. Rev. D **24**, 2278 (1981).

[133] J. E. Hirsch, D. J. Scalapino, R. L. Sugar, and R. Blankenbecler, Efficient Monte Carlo procedure for systems with fermions, Phys. Rev. Lett. **47**, 1628 (1981).

[134] J. E. Hirsch, Two-dimensional Hubbard model: Numerical simulation study, Phys. Rev. B **31**, 4403 (1985).

[135] H. Sun, M. Huo, X. Hu, J. Li, Z. Liu, Y. Han, L. Tang, Z. Mao, P. Yang, B. Wang, J. Cheng, D.-X. Yao, G.-M. Zhang, and M. Wang, Signatures of superconductivity near 80 K in a nickelate under high pressure, Nature (London) **621**, 493 (2023).

[136] J. Hou, P. T. Yang, Z. Y. Liu, J. Y. Li, P. F. Shan, L. Ma, G. Wang, N. N. Wang, H. Z. Guo, J. P. Sun, Y. Uwatoko, M. Wang, G. M. Zhang, B. S. Wang, and J. G. Cheng, Emergence of high-temperature superconducting phase in the pressurized $La_3Ni_2O_7$, arXiv:2307.09865.

**Acknowledgements**

# Chapter 4

# Optical conductivity of symmetric mass generation insulator

# Optical Conductivity in Symmetric Mass Generation Insulators

Meng Zeng,[1] Fu Xu,[2] Da-Chuan Lu,[1] and Yi-Zhuang You[1, *]

[1]*Department of Physics, University of California at San Diego, La Jolla, CA 92093, USA*
[2]*Department of Physics, Nanjing University, Nanjing, Jiangsu 210093, China*
(Dated: May 10, 2024)

Symmetric mass generation (SMG) insulators are interaction-driven, featureless Mott insulating states in quantum many-body fermionic systems. Recent advancements suggest that zeros in the fermion Green's function could lead to non-vanishing negative optical conductivity in SMG insulators, even below the charge excitation gap. This study explores the origin of this unusual behavior through the lens of pole-zero duality, highlighting a critical issue where the current operator becomes unbounded, rendering the response function unphysical. By employing a lattice model, we derive a well-behaved lattice regularization of the current operator, enabling a detailed study of optical conductivity in SMG insulators. Utilizing both analytical and numerical methods, including strong-coupling expansions, we confirm that SMG insulators exhibit no optical conductivity at low energies below the charge gap, effectively resolving the paradox. This work not only deepens our understanding of quantum many-body phenomena but also lays a robust theoretical groundwork for future experimental explorations of SMG materials.

*Introduction.* — Symmetric mass generation (SMG) insulators [1–30] represent a novel class of interaction-driven *featureless* Mott insulating states in quantum many-body systems of fermions. These systems feature the cancellation of all quantum anomalies [31–33], such that a symmetric gapped state without spontaneous symmetry breaking (SSB) or topological order is allowed, which we refer to as "featureless". SMG insulators are characterized by a full energy gap to all fermionic and bosonic excitations, including collective charge and current excitations. The excitation gap arises from non-perturbative interaction effects and eludes mean-field theoretical explanations.

Central to the theoretical understanding of SMG insulators is the behavior of the fermion Green's function, defined as: $G(k) := -\langle \psi_k \psi_k^\dagger \rangle$, where $\psi_k$ is the fermion operator at the energy-momentum $k = (\omega, \boldsymbol{k})$. A key aspect of the SMG insulator is that its fermion Green's function determinant approaches zero as energy-momentum tends to zero [34–49], i.e.

$$\det G(k) = 0 \text{ as } k_\mu k^\mu \to 0. \quad (1)$$

This property, the zero of the Green's function, raises an intriguing question regarding its experimental implications [29, 45–48, 50]. Recently, Golterman and Shamir [49] proposed that these zeros might significantly influence the electromagnetic response of the SMG insulator when the fermions are coupled to a background U(1) gauge field, particularly suggesting a scenario where the SMG insulator exhibits non-vanishing charge conductivity at low energy, even below the energy gap of all excitations.

This apparent puzzle of how an *insulator* might exhibit *conductive* behavior without charge excitations below the insulating gap presents a fascinating paradox. This research aims to postulate a potential resolution of this paradox, offering new insights into the behavior of the optical conductivity in SMG insulators and expanding our understanding of quantum many-body phenomena.

*Pole-Zero Duality.* — Let us first revisit the Golterman-Shamir construction [49], and reproduce their results through the broader lens of pole-zero duality in the fermion Green's function.

The analysis starts with the fermion two-point correlation function $G(k) = -\langle \psi_k \psi_k^\dagger \rangle$ in the energy-momentum space. At this point, Golterman and Shamir introduced a pivotal *assumption* that the fermion system can be approximated by a *free* effective action,

$$S[\psi] = -\sum_k \psi_k^\dagger G(k)^{-1} \psi_k = -\int d^d x \, \psi^\dagger G(i\partial)^{-1} \psi, \quad (2)$$

such that the Green's function will be consistently reproduced by the fermion path integral:

$$G(k) = \frac{1}{Z} \int \mathcal{D}[\psi] \, (-\psi_k \psi_k^\dagger) e^{-S[\psi]}, \quad (3)$$

with $Z = \int \mathcal{D}[\psi] e^{-S[\psi]}$ being the partition function. It is crucial to acknowledge that this approach to reconstructing the effective action from the two-point correlation is only valid under the premise that the fermions behave as free or generalized free fields [51–55]. In such cases, higher-point correlations decompose into two-point correlations via Wick's theorem. Should the fermions deviate from generalized free field behavior, it becomes necessary to incorporate higher-order terms in the effective action to model higher-point correlation functions.

If we accept the effective action $S[\psi]$ in Eq. (2), we can proceed to gauge the U(1) symmetry of the fermion field $\psi$, under which $\psi \to e^{i\theta}\psi$. By introducing the U(1) gauge field $A$ through minimal coupling, the effective action becomes:

$$S[\psi, A] = -\int d^d x \, \psi^\dagger G(i\partial - A)^{-1} \psi. \quad (4)$$

Integrating out the fermion field $\psi$, the fermion path integral $e^{-S[A]} = \int \mathcal{D}[\psi] e^{-S[\psi, A]}$ defines an effective action $S[A]$ for the gauge field $A$:

$$S[A] = \mathrm{Tr} \log G(\mathrm{i}\partial - A)$$
$$= \sum_{n=0}^{\infty} \frac{1}{n!} \Pi_n^{\mu_1 \mu_2 \cdots \mu_n} A_{\mu_1} A_{\mu_2} \cdots A_{\mu_n}, \quad (5)$$

where $\Pi_n^{\mu_1 \mu_2 \cdots \mu_n} := \delta_{A_{\mu_1}} \delta_{A_{\mu_2}} \cdots \delta_{A_{\mu_n}} S[A]$ corresponds to the $n$th order current correlation, or loosely denoted as $\Pi_n = \delta_A^n S[A]$. These correlations $\Pi_n$ encode the responses of the fermion system to the external electromagnetic field at different orders. The goal is to understand their behaviors across the SMG transition.

The SMG transition refers to the fermion gap-opening transition driven by the fermion interaction [33]. On the weakly interacting side, the fermion system is metallic, characterized by gapless single-particle excitations at low energy, manifested as poles in the fermion Green's function. In contrast, on the strongly interacting side, the system transitions into the SMG insulating phase, where the original poles in the Green's function are replaced by zeros. For instance, in the case of the relativistic fermions discussed in Ref. 49, the propagator poles and zeros are respectively modeled by $G_{\mathrm{Dirac}}$ and $G_{\mathrm{SMG}}$ as

$$G_{\mathrm{Dirac}}(k) = \frac{1}{\gamma^0 \gamma^\mu k_\mu}, \quad G_{\mathrm{SMG}}(k) = -\frac{\gamma^0 \gamma^\mu k_\mu}{m^2}. \quad (6)$$

The concept of pole-zero duality [35, 42, 43, 46] offers a compelling framework for relating the low-energy behaviors of Green's functions across the SMG transition. This duality is articulated through a transformation of the fermion Green's function,

$$G(k) \to \tilde{G}(k) \propto G(-k)^{-1}, \quad (7)$$

under which poles and zeros replace each other. For example, $G_{\mathrm{Dirac}}$ and $G_{\mathrm{SMG}}$ in Eq. (6) are related by the pole-zero duality.

Under the pole-zero duality defined in Eq. (7), the effective gauge action $S[A] = \mathrm{Tr} \log G(\mathrm{i}\partial - A)$ in Eq. (5) transforms as

$$S[A] \to \mathrm{Tr} \log G(-\mathrm{i}\partial + A)^{-1} = -S[-A], \quad (8)$$

then the $n$th order current correlation $\Pi_n = \delta_A^n S[A]$ transforms as

$$\Pi_n \to -\delta_A^n S[-A] = -(-1)^n \Pi_n. \quad (9)$$

This implies that if the fermion Green's functions across the SMG transition are related by pole-zero duality, as exemplified by $G_{\mathrm{Dirac}}$ and $G_{\mathrm{SMG}}$ in Eq. (6), then their corresponding electromagnetic response functions will also be related by (for $n = 2, 3$)

$$\Pi_{2,\mathrm{SMG}} = -\Pi_{2,\mathrm{Dirac}}, \quad \Pi_{3,\mathrm{SMG}} = \Pi_{3,\mathrm{Dirac}}, \quad (10)$$

which reproduce the main conclusions in Ref. 49 that, compared to free Dirac fermions, the vacuum polarization $\Pi_2$ changes sign in the SMG insulator while the triangle diagram $\Pi_3$ remains the same.

These results are remarkably general and do not depend on the specific form of the Green's function $G(k)$. Provided we accept the effective action $S[\psi, A]$ in Eq. (4) as our starting point, the conclusions outlined above are inevitable under the principle of pole-zero duality.

The implications of these results are significant. Since vacuum polarization is connected to optical conductivity by $\mathrm{Re}\,\sigma(\omega, \boldsymbol{k}) = -\frac{1}{\omega} \mathrm{Im}\,\Pi_2(\omega, \boldsymbol{k})$ [56], the relationship $\Pi_{2,\mathrm{SMG}} = -\Pi_{2,\mathrm{Dirac}}$ would imply that $\sigma_{\mathrm{SMG}} = -\sigma_{\mathrm{Dirac}}$, indicating that the gapped SMG insulator would exhibit a conductivity that is finite and opposite to that of the gapless Dirac semimetal. However, we should not anticipate finite conductivity in an insulator below the charge excitation gap. Additionally, the notion of negative conductivity raises concerns about the potential violation of the fluctuation-dissipation theorem and the loss of unitarity in the theory.

*Unbounded Current Operator* — Given the perplexing behavior of conductivity, we are motivated to examine the foundational assumptions of the Golterman-Shamir construction. Specifically, it is presumed that the effective action $S[\psi, A]$ described in Eq. (4) models the physics of the SMG insulator in a background electromagnetic field. Starting from this premise, the current operator in the system should be given by

$$J^\mu = -\delta_{A_\mu} S[\psi, A \to 0] = \sum_k \psi_k^\dagger \partial_{k_\mu} G(k)^{-1} \psi_k. \quad (11)$$

For Dirac fermions described by $G_{\mathrm{Dirac}}(k)$ in Eq. (6), Eq. (11) gives the current operator in the conventional form $J^\mu = \sum_k \bar{\psi}_k \gamma^\mu \psi_k$ (where $\bar{\psi} := \psi^\dagger \gamma^0$), which has a bounded spectrum. However, for the SMG insulator, if we naively substitute the Green's function $G_{\mathrm{SMG}}(k)$ from Eq. (6) into Eq. (11),

$$J^\mu = \sum_k \frac{m^2}{k^4} (2k_\mu k_\nu - k^2 \delta_{\mu\nu}) \bar{\psi}_k \gamma^\nu \psi_k, \quad (12)$$

we find that the resulting current operator $J^\mu$ would diverge as $k^2 := k_\mu k^\mu \to 0$. This divergence is a direct consequence of the Green's function zeros along the light cone $(k^2 = 0)$ below the SMG insulating gap. Such a current operator has an unbounded spectrum, which is unphysical because this would imply the existence of quantum states in which the velocity of charge movement could potentially exceed the speed of light.

Starting from such an unbounded current operator to define the current-current correlation $\Pi_2^{\mu\nu} = -\langle J^\mu J^\nu \rangle$ could potentially lead to unphysical results. This perspective makes the unusual behavior of $\Pi_2$ less surprising. It implies that $S[\psi, A]$ in Eq. (4) might not be a complete theory for describing the SMG insulator. Given

that the SMG insulator is intrinsically a strongly inter-acting system, it is reasonable to suspect that the action should include various higher-order terms to cancle the divergence of the current operator, thereby ensuring a well-defined bounded current operator.

*Lattice Modeling* — Having recognized the critical issue with the unbounded current operator, our goal is to move beyond the effective action $S[\psi, A]$ and explore the electromagnetic response of the SMG insulator from a more fundamental perspective.

To address this challenge, we turn to a concrete lattice model for the SMG insulator. Consider a system comprising four flavors of fermions $c_{ia}$ (where $a = 1, 2, 3, 4$) on each lattice site $i$, governed by the following Hamiltonian

$$H = -\sum_{ij} t_{ij} e^{iA_{ij}} c_{ia}^\dagger c_{ja} - g \sum_i c_{i1}^\dagger c_{i2}^\dagger c_{i3} c_{i4} + \text{h.c.}, \quad (13)$$

where the repeated flavor index $a$ in $c_{ia}^\dagger c_{ja}$ will be implicitly summed over, and "h.c." represents the Hermitian conjugate terms. In this model, a background U(1) gauge connection $A_{ij}$ is introduced between every pair of sites to gauge the global U(1) symmetry of the fermions (acting as $c_{ia} \to e^{i\theta} c_{ia}$).

We further specify that the fermions in the system are *half-filled*, a crucial condition for cancelling the Fermi-surface anomaly [57–73] and enabling an SMG insulating state [26, 27]. To enforce the half-filling condition without fine-tuning the chemical potential, a simple approach is to first assume a bipartite lattice structure (e.g., a square or honeycomb lattice that can be partitioned into $A$ and $B$ sublattices), and then impose an anti-unitary sublattice particle-hole symmetry $\mathbb{Z}_2^S$ (also known as the chiral symmetry [74, 75]), under which $c_{ia} \to \mathcal{K}(-)^i c_{ia}^\dagger$, with an alternating sign $(-)^i = \pm 1$ for the site $i$ in $A$ and $B$ sublattices respectively. Here $\mathcal{K}$ represents the complex conjugation operator that $\mathcal{K}^2 = 1$ and $\mathcal{K}i\mathcal{K} = -i$.

Let us first turn off the background gauge field by setting $A_{ij} = 0$. In the free fermion limit ($g = 0$), the Hamiltonian $H$ describes a fermion hopping model on a bipartite lattice with a chiral symmetry $\mathbb{Z}_2^S$. In the momentum space, the $\mathbb{Z}_2^S$ symmetry transforms the fermions as $c_{\boldsymbol{k}a} \to \mathcal{K}\sigma^3 c_{\boldsymbol{k}a}^\dagger$, enforcing the Hamiltonian to take the form $H = \sum_{\boldsymbol{k}} c_{\boldsymbol{k}a}^\dagger \xi_{\boldsymbol{k}} \sigma^1 c_{\boldsymbol{k}a}$, where $\sigma^\alpha$ ($\alpha = 0, 1, 2, 3$) denote the Pauli matrices acting within the sublattice Hilbert space. The specific details of the band dispersion $\xi_{\boldsymbol{k}}$ are not crucial to our discussion. Without fine-tuning the band structure, $\xi_{\boldsymbol{k}}$ typically exhibits a Fermi surface, rendering the fermion system as a gapless Fermi liquid in general.

Conversely, in the strong interaction limit ($g \to \infty$), the hopping term $t_{ij}$ can be omitted relative to $g$, and the model is decoupled to individual sites, permitting an independent solution for each site. In this limit, the exact many-body ground state of $H$ is a product state:

$$|\Psi_{\text{SMG}}\rangle = \prod_i \frac{1}{\sqrt{2}} (c_{i1}^\dagger c_{i2}^\dagger - c_{i3}^\dagger c_{i4}^\dagger)|0\rangle, \quad (14)$$

where $|0\rangle$ represents the vacuum state of the fermions. This solution arises because the four-fermion interaction $g$ directly hybridizes the two-fermion states $c_{i1}^\dagger c_{i2}^\dagger |0\rangle$ and $c_{i3}^\dagger c_{i4}^\dagger |0\rangle$ on each site, thereby lowering the energy of the particular superposition state of them in Eq. (14). The resulting product state $|\Psi_{\text{SMG}}\rangle$ maintains the full symmetry of the Hamiltonian $H$ and exhibits a gap of order $g$ to all excitations, therefore realizing an SMG insulator (in its ideal limit). It is noteworthy that the fermions are automatically half-filled on every site, which is precisely why we emphasize the half-filling condition from the outset. Otherwise, we would have to violate the fermion number conservation when driving the system into the SMG insulating state as we increase the interaction strength $g$.

*Ideal SMG Limit.* — As long as at half-filling, regardless of the band structure of $\xi_{\boldsymbol{k}}$, strong enough interaction $g$ in this model will always drive the fermion system into the SMG insulating phase. Understanding how the SMG transition happens, as a metal-insulator transition, is a fascinating yet challenging problem. However, this inquiry is beyond the scope of our current analysis. Instead, our focus will be on the strongly interacting regime where $g \gg t_{ij}$, and we aim to study the current correlation in the SMG insulating phase.

First, to properly define the current operator in the lattice model Eq. (13), we start by introducing the background gauge field $A_{ij}$, differentiating $H$ with respect to $A_{ij}$ and subsequently taking the limit of $A_{ij} \to 0$,

$$J_{ij} = \frac{\delta H}{\delta A_{ij}} = -(it_{ij} c_{ia}^\dagger c_{ja} + \text{h.c.}). \quad (15)$$

This current operator $J_{ij}$, well-defined on the lattice, has a bounded spectrum and does not suffer from the previous problem of unbounded current in the effective action approach. We can observe that the on-site interaction $g$ has no influence on the definition of the current operator in Eq. (15), as the interaction term was not modified by the U(1) background field $A_{ij}$ in the Hamiltonian Eq. (13) to begin with. The lattice current operator $J_{ij}$ is entirely determined by the hopping term. Therefore, in momentum space, the current operator $\boldsymbol{J} = \sum_{\boldsymbol{k}} c_{\boldsymbol{k}a}^\dagger \partial_{\boldsymbol{k}} \xi_{\boldsymbol{k}} \sigma^1 c_{\boldsymbol{k}a}$ can also be expressed as solely dependent on the band dispersion $\xi_{\boldsymbol{k}}$, the same as in the free fermion limit.

Then, we can compute the current-current correlation on the lattice as $\Pi(t) = -i\langle [J_{ij}(t), J_{kl}(0)]\rangle \Theta(t)$, where $J_{ij}(t) = e^{-iHt} J_{ij} e^{iHt}$. Evaluating the operator expectation values on the ideal ground state $|\Psi_{\text{SMG}}\rangle$ in Eq. (14) of SMG insulator in the $g \gg t_{ij}$ limit, we find $\Pi(t) = 4|t_{ij}|^2 \sin(2gt)\Theta(t)\delta_{il}\delta_{jk}$. Fourier transform to

the frequency domain and averaging over all sites, the optical conductivity $\operatorname{Re}\sigma(\omega) = -\frac{1}{\omega}\operatorname{Im}\Pi(\omega)$ reads

$$\operatorname{Re}\sigma(\omega) = \frac{2\pi|t|^2}{2g}\big(\delta(\omega - 2g) + \delta(\omega + 2g)\big), \qquad (16)$$

where $|t|^2 := \sum_j |t_{ij}|^2$ characterizes the overall hopping strength. This result illustrates the expected reasonable behavior of the conductivity in an ideal SMG insulator: $\operatorname{Re}\sigma(\omega)$ should vanish at low frequencies $|\omega| < 2g$ within the charge gap $2g$. The presence of sharp peaks at $\omega = \pm 2g$ is attributed to the fact that all excitations exhibit flat dispersion in the ideal SMG state, as the system decouples among independent sites. Deviating from this ideal limit, for a finite $t_{ij}/g$, we should anticipate the peaks to broaden into continua above the charge gap.

*Beyond Ideal Limit.* — To elucidate the general behavior of optical conductivity in the SMG insulator beyond the strong interaction limit, we engage a perturbative expansion in $t_{ij}/g$ around the ideal state $|\Psi_{\mathrm{SMG}}\rangle$ and calculate the correlation functions in the perturbed state. The perturbation theory has been thoroughly analyzed in Ref. 46. The results indicate that the fermion Green's function in the SMG insulator of a $\mathbb{Z}_2^{\mathcal{S}}$-symmetric two-band system can be approximated by:

$$G_{\mathrm{SMG}}(k) = \frac{\omega\sigma^0 + \xi_{\boldsymbol{k}}\sigma^1}{\omega^2 - \xi_{\boldsymbol{k}}^2 - \Delta^2}, \qquad (17)$$

where $\Delta \sim g$ represents the single-particle gap (i.e., the fermion mass) renormalized from its bare value $g$ set by the interaction strength. It is worth emphasizing that the gap $\Delta$ here is not a symmetry-breaking order parameter and has no mean-field interpretation. Notably, $G_{\mathrm{SMG}}(k)$ exhibits zeros along $\omega = \pm\xi_{\boldsymbol{k}}$, a distinguishing feature of SMG insulators. By contrast, in systems where the gap opens due to spontaneous symmetry breaking (SSB), the fermion Green's function would take the following form:

$$G_{\mathrm{SSB}}(k) = \frac{\omega\sigma^0 + \xi_{\boldsymbol{k}}\sigma^1 + \Delta\sigma^3}{\omega^2 - \xi_{\boldsymbol{k}}^2 - \Delta^2}, \qquad (18)$$

where the extra term $\Delta\sigma^3$ on the numerator breaks the $\mathbb{Z}_2^{\mathcal{S}}$ symmetry, which is particularly absent in $G_{\mathrm{SMG}}$.

In any scenario, the charge $\Pi^{00}$ and current $\Pi^{ij}$ correlation functions can be characterized by the following equations:

$$\begin{aligned}\Pi^{00}(q) &= \operatorname{Tr}(G(k+q)G(k)),\\ \Pi^{ij}(q) &= \operatorname{Tr}(v_i G(k+q)v_j G(k)).\end{aligned} \qquad (19)$$

In these expressions, the charge vertex operator is always $\sigma^0$, and the current vertex operator is $\boldsymbol{v} = \partial_{\boldsymbol{k}}\xi_{\boldsymbol{k}}\sigma^1$. These vertex operators align with the lattice current operators derived in Eq. (15), ensuring a bounded operator spectrum.

For example, consider a square lattice fermion model characterized by the dispersion relation $\xi_{\boldsymbol{k}} =$
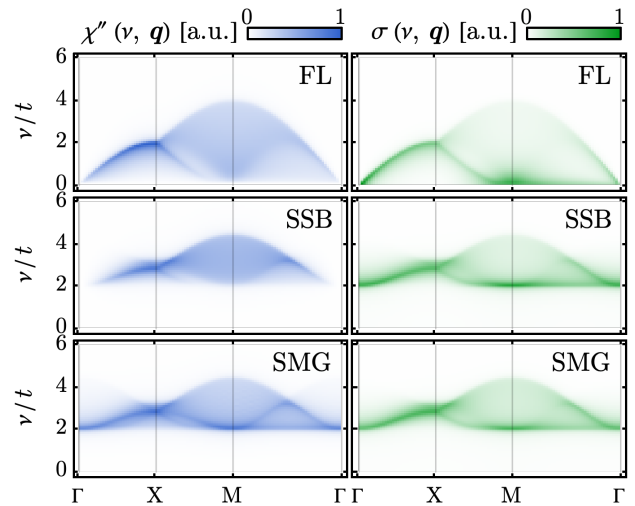


FIG. 1. The dynamic charge susceptibility $\chi''(\nu, \boldsymbol{q})$ (imaginary part) and optical conductivity $\sigma(\nu, \boldsymbol{q})$ as a function of frequency $\nu$ along a cut through $\Gamma(0,0)$, $\mathrm{X}(\pi,0)$, $\mathrm{M}(\pi,\pi)$ points in the momentum space, for 2D square lattice fermions in the Fermi liquid (FL), spontaneous symmetry breaking (SSB), and symmetric mass generation (SMG) phases respectively.

$-2t(\cos k_x + \cos k_y)$ given the hopping parameter $t$ (set as the energy unit). We can numerically evaluate the spectral weight of the dynamic charge susceptibility $\chi''(\nu, \boldsymbol{q}) = -2\operatorname{Im}\Pi^{00}(\nu + \mathrm{i}0_+, \boldsymbol{q})$ and the optical conductivity $\sigma(\nu, \boldsymbol{q}) = -\frac{1}{\nu}\operatorname{Im}\Pi^{ii}(\nu + \mathrm{i}0_+, \boldsymbol{q})$ as outlined in Eq. (19). Plugging in the fermion Green's function in different phases: $G_{\mathrm{FL}}(k) = (\omega\sigma^0 - \xi_{\boldsymbol{k}}\sigma^1)^{-1}$, $G_{\mathrm{SSB}}(k)$ in Eq. (18), and $G_{\mathrm{SMG}}(k)$ in Eq. (17) (assuming $\Delta = t$ in the SSB and SMG cases), their resulting electromagnetic response functions are compared in Fig. 1. Much like that in the SSB insulator, the SMG insulator's electromagnetic response is gapped, displaying only subtle differences in detail. Contrarily, it does not resemble the gapless response typical of a Fermi liquid.

This analysis can be extended to SMG in non-chiral Dirac/Weyl fermions, where on-site local gapping interactions generally exist, ensuring that the current operator remains unaffected by interactions. This is a crucial element for our argument concerning the lattice regularization of the current operator. However, for chiral fermions, such as in the 3-4-5-0 model [19, 24, 76, 77], where the SMG interaction is not on-site, regularizing the current operator is an open problem for future research. Thus, while the paradox regarding how the SMG insulator can exhibit finite optical conductivity despite its gap is effectively resolved for non-chiral fermions, further work is needed for chiral systems. This resolution hinges on a nuanced understanding of the current operator in the SMG phase using lattice regularization. These insights reinforce the SMG state's insulating nature while clarifying its distinctive low-energy electromagnetic prop-

erties, laying a theoretical foundation for future experimental exploration of featureless Mott insulators.

* yzyou@physics.ucsd.edu

[1] J. Wang and X.-G. Wen, arXiv e-prints , arXiv:1307.7480 (2013), arXiv:1307.7480 [hep-lat].

[2] V. Ayyar and S. Chandrasekharan, Phys. Rev. D 91, 065035 (2015), arXiv:1410.6474 [hep-lat].

[3] K. Slagle, Y.-Z. You, and C. Xu, Phys. Rev. B 91, 115121 (2015), arXiv:1409.7401 [cond-mat.str-el].

[4] Y. BenTov, Journal of High Energy Physics 7, 34 (2015), arXiv:1412.0154 [cond-mat.str-el].

[5] S. Catterall, Journal of High Energy Physics 1, 121 (2016), arXiv:1510.04153 [hep-lat].

[6] V. Ayyar and S. Chandrasekharan, Phys. Rev. D 93, 081701 (2016), arXiv:1511.09071 [hep-lat].

[7] V. Ayyar and S. Chandrasekharan, Journal of High Energy Physics 10, 58 (2016), arXiv:1606.06312 [hep-lat].

[8] E. Witten, Phys. Rev. B 94, 195150 (2016), arXiv:1605.02391 [hep-th].

[9] V. Ayyar, ArXiv e-prints (2016), arXiv:1611.00280 [hep-lat].

[10] Y.-Y. He, H.-Q. Wu, Y.-Z. You, C. Xu, Z. Y. Meng, and Z.-Y. Lu, Phys. Rev. B 94, 241111 (2016), arXiv:1603.08376 [cond-mat.str-el].

[11] M. DeMarco and X.-G. Wen, arXiv e-prints , arXiv:1706.04648 (2017), arXiv:1706.04648 [hep-lat].

[12] V. Ayyar and S. Chandrasekharan, Phys. Rev. D 96, 114506 (2017), arXiv:1709.06048 [hep-lat].

[13] Y.-Z. You, Y.-C. He, A. Vishwanath, and C. Xu, Phys. Rev. B 97, 125112 (2018), arXiv:1711.00863 [cond-mat.str-el].

[14] D. Schaich and S. Catterall, in European Physical Journal Web of Conferences, European Physical Journal Web of Conferences, Vol. 175 (2018) p. 03004, arXiv:1710.08137 [hep-lat].

[15] Y. Kikukawa, PTEP 2019, 113B03 (2019), arXiv:1710.11618 [hep-lat].

[16] Y. Kikukawa, Progress of Theoretical and Experimental Physics 2019, 073B02 (2019), arXiv:1710.11101 [hep-lat].

[17] N. Butt and S. Catterall, in The 36th Annual International Symposium on Lattice Field Theory. 22-28 July (2018) p. 294, arXiv:1811.01015 [hep-lat].

[18] N. Butt, S. Catterall, and D. Schaich, Phys. Rev. D 98,

114514 (2018), arXiv:1810.06117 [hep-lat].

[19] J. Wang and X.-G. Wen, Physical Review Research 2, arXiv:1809.11171 (2020), arXiv:1809.11171 [hep-th].

[20] S. Catterall, N. Butt, and D. Schaich, arXiv e-prints , arXiv:2002.00034 (2020), arXiv:2002.00034 [hep-lat].

[21] S. S. Razamat and D. Tong, Physical Review X 11, 011063 (2021), arXiv:2009.05037 [hep-th].

[22] S. Catterall, Phys. Rev. D 104, 014503 (2021), arXiv:2010.02290 [hep-lat].

[23] N. Butt, S. Catterall, and G. C. Toga, arXiv e-prints , arXiv:2111.01001 (2021), arXiv:2111.01001 [hep-lat].

[24] M. Zeng, Z. Zhu, J. Wang, and Y.-Z. You, Phys. Rev. Lett. 128, 185301 (2022), arXiv:2202.12355 [cond-mat.str-el].

[25] W. Hou and Y.-Z. You, arXiv e-prints , arXiv:2212.13364 (2022), arXiv:2212.13364 [cond-mat.str-el].

[26] D.-C. Lu, M. Zeng, J. Wang, and Y.-Z. You, arXiv e-prints , arXiv:2210.16304 (2022), arXiv:2210.16304 [cond-mat.str-el].

[27] D.-C. Lu, J. Wang, and Y.-Z. You, arXiv e-prints , arXiv:2302.12731 (2023), arXiv:2302.12731 [cond-mat.str-el].

[28] Y. Guo and Y.-Z. You, Phys. Rev. B 108, 115139 (2023), arXiv:2306.17420 [cond-mat.str-el].

[29] D.-C. Lu, M. Li, Z.-Y. Zeng, W. Hou, J. Wang, F. Yang, and Y.-Z. You, arXiv e-prints , arXiv:2308.11195 (2023), arXiv:2308.11195 [cond-mat.str-el].

[30] Z. H. Liu, Y. Da Liao, G. Pan, M. Song, J. Zhao, W. Jiang, C.-M. Jian, Y.-Z. You, F. F. Assaad, Z. Y. Meng, and C. Xu, Phys. Rev. Lett. 132, 156503 (2024), arXiv:2308.07380 [cond-mat.str-el].

[31] D. Tong, arXiv e-prints , arXiv:2104.03997 (2021), arXiv:2104.03997 [hep-th].

[32] N. Butt, S. Catterall, A. Pradhan, and G. C. Toga, Phys. Rev. D 104, 094504 (2021), arXiv:2101.01026 [hep-th].

[33] J. Wang and Y.-Z. You, Symmetry 14, 1475 (2022), arXiv:2204.14271 [cond-mat.str-el].

[34] V. Gurarie, Phys. Rev. B 83, 085426 (2011), arXiv:1011.2273 [cond-mat.mes-hall].

[35] Y.-Z. You, Z. Wang, J. Oon, and C. Xu, Phys. Rev. B 90, 060502 (2014), arXiv:1403.4938 [cond-mat.str-el].

[36] S. Catterall and D. Schaich, ArXiv e-prints (2016), arXiv:1609.08541 [hep-lat].

[37] Y.-Z. You, Y.-C. He, C. Xu, and A. Vishwanath, Physical Review X 8, 011026 (2018), arXiv:1705.09313 [cond-mat.str-el].

[38] S. Catterall and N. Butt, Phys. Rev. D 97, 094502 (2018), arXiv:1708.06715 [hep-lat].

[39] Y. Xu and C. Xu, arXiv e-prints , arXiv:2103.15865 (2021), arXiv:2103.15865 [cond-mat.str-el].

[40] D. Lessnich, S. M. Winter, M. Iraola, M. G. Vergniory, and R. Valentí, Phys. Rev. B 104, 085116 (2021), arXiv:2103.02624 [cond-mat.str-el].

[41] H. Hu, L. Chen, C. Setty, M. Garcia-Diez, S. E. Grefe, A. Prokofiev, S. Kirchner, M. G. Vergniory, S. Paschen, J. Cano, and Q. Si, arXiv e-prints , arXiv:2110.06182 (2021), arXiv:2110.06182 [cond-mat.str-el].

[42] D. B. Kaplan and S. Sen, arXiv e-prints , arXiv:2112.06954 (2021), arXiv:2112.06954 [cond-mat.mes-hall].

[43] D. B. Kaplan and S. Sen, arXiv e-prints , arXiv:2205.05707 (2022), arXiv:2205.05707 [cond-mat.str-el].

[44] C. Setty, S. Sur, L. Chen, F. Xie, H. Hu, S. Paschen,

J. Cano, and Q. Si, arXiv e-prints , arXiv:2301.13870 (2023), arXiv:2301.13870 [cond-mat.str-el].

[45] W.-X. Chang, S. Guo, Y.-Z. You, and Z.-X. Li, arXiv e-prints , arXiv:2311.09970 (2023), arXiv:2311.09970 [cond-mat.str-el].

[46] D.-C. Lu, M. Zeng, and Y.-Z. You, Phys. Rev. B 108, 205117 (2023), arXiv:2307.12223 [cond-mat.str-el].

[47] C. Setty, F. Xie, S. Sur, L. Chen, S. Paschen, M. G. Vergniory, J. Cano, and Q. Si, arXiv e-prints , arXiv:2311.12031 (2023), arXiv:2311.12031 [cond-mat.str-el].

[48] L. Chen, H. Hu, M. G. Vergniory, J. Cano, and Q. Si, arXiv e-prints , arXiv:2401.12156 (2024), arXiv:2401.12156 [cond-mat.str-el].

[49] M. Golterman and Y. Shamir, Phys. Rev. Lett. 132, 081903 (2024), arXiv:2311.12790 [hep-lat].

[50] J.-X. Zhang, H.-K. Zhang, Y.-Z. You, and Z.-Y. Weng, arXiv e-prints , arXiv:2309.05726 (2023), arXiv:2309.05726 [cond-mat.str-el].

[51] O. Greenberg, Annals of Physics 16, 158 (1961).

[52] M. Dütsch and K.-H. Rehren, Annales Henri Poincar&eacute; 4, 613 (2003), arXiv:math-ph/0209035 [math-ph].

[53] J. Liu, E. Perlmutter, V. Rosenhaus, and D. Simmons-Duffin, arXiv e-prints , arXiv:1808.00612 (2018), arXiv:1808.00612 [hep-th].

[54] T. M. Nebabu and X. Qi, arXiv e-prints , arXiv:2306.16687 (2023), arXiv:2306.16687 [hep-th].

[55] X. Zeng and L.-Y. Hung, Entropy 25, 1543 (2023), arXiv:2309.03178 [hep-th].

[56] G. D. Mahan, *Many-particle physics* (Springer Science & Business Media, 2013).

[57] J. M. Luttinger, Phys. Rev. 119, 1153 (1960).

[58] A. Paramekanti and A. Vishwanath, Phys. Rev. B 70, 245118 (2004), arXiv:cond-mat/0406619 [cond-mat.str-el].

[59] F. D. M. Haldane, arXiv e-prints , cond-mat/0505529 (2005), arXiv:cond-mat/0505529 [cond-mat.str-el].

[60] G. Başar, D. E. Kharzeev, and I. Zahed, Phys. Rev. Lett. 111, 161601 (2013), arXiv:1307.2234 [hep-th].

[61] H. Watanabe, H. C. Po, A. Vishwanath, and M. Zaletel, Proceedings of the National Academy of Science 112, 14551 (2015), arXiv:1505.04193 [cond-mat.str-el].

[62] M. Cheng, M. Zaletel, M. Barkeshli, A. Vishwanath, and P. Bonderson, Physical Review X 6, 041068 (2016), arXiv:1511.02263 [cond-mat.str-el].

[63] Y.-M. Lu, Y. Ran, and M. Oshikawa, arXiv e-prints , arXiv:1705.09298 (2017), arXiv:1705.09298 [cond-mat.str-el].

[64] G. Y. Cho, C.-T. Hsieh, and S. Ryu, Phys. Rev. B 96, 195105 (2017), arXiv:1705.03892 [cond-mat.str-el].

[65] N. Bultinck and M. Cheng, Phys. Rev. B 98, 161119 (2018), arXiv:1808.00324 [cond-mat.str-el].

[66] X.-Y. Song, Y.-C. He, A. Vishwanath, and C. Wang, arXiv e-prints , arXiv:1909.08637 (2019), arXiv:1909.08637 [cond-mat.mes-hall].

[67] D. V. Else, R. Thorngren, and T. Senthil, Physical Review X 11, 021005 (2021), arXiv:2007.07896 [cond-mat.str-el].

[68] X.-G. Wen, Phys. Rev. B 103, 165126 (2021), arXiv:2101.08772 [cond-mat.str-el].

[69] D. V. Else and T. Senthil, Phys. Rev. Lett. 127, 086601 (2021), arXiv:2010.10523 [cond-mat.str-el].

[70] R. Ma and C. Wang, arXiv e-prints , arXiv:2110.09492 (2021), arXiv:2110.09492 [cond-mat.str-el].

[71] C. Wang, A. Hickey, X. Ying, and A. A. Burkov, Phys. Rev. B 104, 235113 (2021), arXiv:2110.10692 [cond-mat.str-el].

[72] Z. Darius Shi, H. Goldman, D. V. Else, and T. Senthil, arXiv e-prints , arXiv:2204.07585 (2022), arXiv:2204.07585 [cond-mat.str-el].

[73] M. Cheng and N. Seiberg, arXiv e-prints , arXiv:2211.12543 (2022), arXiv:2211.12543 [cond-mat.str-el].

[74] S. Ryu, A. P. Schnyder, A. Furusaki, and A. W. W. Ludwig, New Journal of Physics 12, 065010 (2010), arXiv:0912.2157 [cond-mat.mes-hall].

[75] C.-K. Chiu, J. C. Y. Teo, A. P. Schnyder, and S. Ryu, Reviews of Modern Physics 88, 035005 (2016), arXiv:1505.03535 [cond-mat.mes-hall].

[76] J. Wang and X.-G. Wen, Phys. Rev. D 99, 111501 (2019), arXiv:1807.05998 [hep-lat].

[77] M. van Beest, P. Boyle Smith, D. Delmastro, Z. Komargodski, and D. Tong, arXiv e-prints , arXiv:2306.07318 (2023), arXiv:2306.07318 [hep-th].

[78] L. Su and M. Ivar (2024), to appear.

**Acknowledgements**

Chapter 4, in part, Meng Zeng, Fu Xu, Da-Chuan Lu, and Yi-Zhuang You, is currently being

prepared for submission for publication of the material.

# Chapter 5

# Gapless symmetry protected topological phases and generalized deconfined critical points from gauging a finite subgroup

# Gapless symmetry protected topological phases and generalized deconfined critical points from gauging a finite subgroup

Lei Su[1] and Meng Zeng[2]

[1]*Department of Physics, University of Chicago, Chicago, Illinois 60637, USA*
[2]*Department of Physics, University of California, San Diego, California 92093, USA*

Gauging a finite subgroup of a global symmetry can map conventional phases and phase transitions to unconventional ones. In this work, we study, as a concrete example, an emergent $\mathbb{Z}_2$-gauged system with global symmetry $U(1)$, namely, the $\mathbb{Z}_2$-gauged Bose-Hubbard model both in 1-D and in 2-D. In certain limits, there is an emergent mixed 't Hooft anomaly between the quotient $\tilde{U}(1)$ symmetry and the dual $\hat{\mathbb{Z}}_2$ symmetry. In 1-D, the superfluid phase is mapped to an intrinsically gapless symmetry-protected topological (SPT) phase, as supported by density-matrix renormalization group (DMRG) calculations. In 2-D, the original superfluid-insulator transition becomes a generalized deconfined quantum critical point (DQCP) between a gapless SPT phase, where a SPT order coexists with Goldstone modes, and a $\tilde{U}(1)$-symmetry-enriched topological (SET) phase. We also discuss the stability of these phases and the critical points to small perturbations and their potential experimental realizations. Our work demonstrates that partial gauging is a simple and yet powerful approach in constructing novel phases and quantum criticalities.

## I. INTRODUCTION

The popular Landau paradigm has been tremendously successful in describing different phases and phase transitions among them. However, more novel phases and phase transitions beyond the traditional paradigm have been found over the past few decades. For example, the deconfined quantum critical point (DQCP) [1] between two phases that break different *ordinary* (0-form) symmetries cannot be explained simply by spontaneous symmetry breaking (SSB) from Landau order parameters. Topologically ordered phases [2], as another example, cannot be captured by SSB of ordinary symmetries.

It was realized recently that some DQCPs can be explained using mixed 't Hooft anomalies, which can be emergent at low energy between the two associated symmetries [3, 4]. The concept of 't Hooft anomalies, widely studied in high energy physics, has also found deep and broad applications in condensed matter physics since the discovery of topological insulators or, more generally, symmetry protected topological (SPT) phases [5–12]. These anomalies characterize global symmetries that cannot be gauged consistently. Related to this work, more recently emergent anomalies have been used to construct gapless SPT phases [13–17] which are "intrinsic" in the sense that not only are the topological edge modes robust against the gapless bulk of the system, but also the SPT nature relies crucially on the gaplessness [18–21]. 't Hooft anomalies thus play an important role in extending the Landau paradigm.

Another perspective in extending the Landau paradigm comes from recent development in expanding the definition of "symmetries" to generalized symmetries [22–24] (non-invertible symmetries included [25, 26]) after it was realized that symmetry generators are essentially topological defects. In particular, ordinary (0-form) symmetries, whose charged objects are 0-dimensional, have been generalized to $p$-form symmetries, whose charged objects are $p$-dimensional. Topologically ordered phases can be interpreted as SSB of some higher-form symmetries. Moreover, it was realized that the Higgs phase can be viewed as a SPT phase protected by higher-form symmetries and is stable to weak explicit breaking of these higher-form symmetries [27, 28].

One more perspective comes from gauging, i.e. coupling systems to dynamical gauge fields. Gauging a theory of matter fields can yield a rich phase diagram. A prominent example is the Fradkin and Shenker model whose phase diagram can contain a confined phase, a Higgs phase, and a deconfined phase [29]. The gauging technique can also be used to extract information in the original system. For example, gauging different SPT phases can lead to distinct topologically ordered phases where quasiparticles have different braiding statistics [30].

Anomalies, higher-form symmetries, and gauging form a powerful toolkit and have led to many interesting new discoveries. It is known that coupling a system to a flat gauge field produces a dual higher-form symmetry and that *partially* gauging a discrete symmetry can produce a mixed anomaly between the quotient symmetry and the new dual symmetry [31, 32]. It was emphasized in Ref. [33] that gauging a finite subgroup is a general approach to construct exotic critical points from ordinary continuous ones. In 1-D, the critical point where the global symmetry is spontaneously broken is mapped to a DQCP between two SSB phases associated with the quotient symmetry and the dual symmetry [34]. In higher dimensions, it is a generalized DQCP between an ordinary SSB phase and a symmetry enriched topological (SET) phase. We will analyze the generalized DQCP after partial gauging using the new perspectives from higher-form symmetries and mixed anomalies.

In this work, we study the emergent $\mathbb{Z}_2$-gauging of a system with global $U(1)$ symmetry. In next section, we

describe the general ideas. Starting from Sec. III, we will focus on a concrete model, i.e. the Bose-Hubbard model both in 1-D and in 2-D, coupled to Ising spins on the bonds, where the bosonic parity is effectively gauged. We adapt the argument in the recently proposed "Higgs = SPT" paradigm [27, 28] to argue that the gauged 1-D superfluid phase is actually an intrinsically gapless SPT phase by considering both the periodic boundary condition (PBC) and the open boundary condition (OBC). The critical low energy theory is a $\mathbb{Z}_2$-gauged compact boson conformal field theory (CFT). These statements are corroborated by density-matrix renormalization group (DMRG) computations. In Sec. IV, we will argue that in 2-D, the superfluid is also a type of gapless SPT where the gaplessness comes from the Goldstone modes and thus the generalized DQCP is between a gapless SPT phase and a SET phase. We also discuss the effect of some perturbations that explicitly break the dual symmetry, and comment on potential realizations in experiments. We conclude our discussion in Sec. V with some future directions. Some details are presented in the appendices.

## II. GENERAL IDEAS

Gauging a finite Abelian ordinary (0-form) symmetry in $d$-D space induces a dual $(d-1)$-form symmetry generated by the Wilson operators [22]. The charged objects of the dual $(d-1)$-form symmetry are $(d-1)$-dimensional. One can gauge a finite Abelian normal subgroup $\Gamma$ of the global symmetry $G$ (discrete or continuous), then the global symmetry becomes $G/\Gamma \times \hat{\Gamma}^{(d-1)}$ where $\hat{\Gamma}^{(d-1)} = \mathrm{hom}(\Gamma, U(1))$, the Pontryagin dual of $\Gamma$, is the dual $(d-1)$-form symmetry. If $G$ is a nontrivial extension of $G/\Gamma$ by $\Gamma$, then there is a mixed anomaly between the $G/\Gamma$ and $\hat{\Gamma}^{(d-1)}$[31]. As a corollary, there is no trivially gapped (i.e. nondegenerate, gapped, and symmetric under both symmetries) ground state.

Starting with a general ordinary second order phase transition of Landau type in $d$-D where the global symmetry $G$ is completely spontaneously broken, we can obtain a generalized DQCP by gauging a finite normal subgroup $\Gamma$ of $G$ [33]. The two phases separated by the generalized DQCP are associated with the SSB of $G/\Gamma$ and $\hat{\Gamma}^{(d-1)}$, respectively. In particular, the SSB of a higher-form symmetry $\hat{\Gamma}^{(d-1)}$ ($d \geq 2$) leads to a topologically ordered phase [22, 23]. For example, we can gauge the $\Gamma = \mathbb{Z}_2$ subgroup of a $\mathbb{Z}_4$ clock model in 2-D where there is an ordinary second order phase transition across which the unbroken $G = \mathbb{Z}_4$ is completely broken. The transition point now becomes a generalized DQCP between a SSB phase where the quotient $\tilde{\mathbb{Z}}_2$ is broken and a SET phase enriched by the quotient $\tilde{\mathbb{Z}}_2$ (see Ref. [33] and also Appendix A). Using the argument in Refs. [27, 28], we claim that the the quotient $\tilde{\mathbb{Z}}_2$ SSB phase in fact has boundary modes as long as the dual 1-form $\hat{\mathbb{Z}}_2$ (as well as the

original $\mathbb{Z}_4$ symmetry) is preserved. If $G$ is continuous, the SSB of $G/\Gamma$ leads to Goldstone modes, the winding number of which is the charge under the dual $\hat{\mathbb{Z}}_2$ symmetry. Thus, in the corresponding phase, the boundary modes coexist with the gapless bulk.

It is even more interesting if there is an intermediate phase sandwiched between phases where the global symmetry is preserved or completely broken, such that, after gauging, the dual symmetry and the quotient symmetry are both preserved. For instance, the intermediate critical phase for the 1-D $q$-state clock model with $q \geq 5$ has an emergent $U(1)$ (see Appendix A). This is similar to the superfluid phase in the 1-D $XY$ model with global symmetry $U(1)$. We argue that the critical phase is an intrinsically gapless SPT phase in the $\mathbb{Z}_2$-gauged model, described by a symmetry-enriched CFT [16]. The response action that dictates the symmetry protected edge modes is similar to that in the gauged Ising model in the Ref. [27]. However, as a result of partial gauging, there is a subtle 't Hooft anomaly matching that governs the gaplessness of the SPT phase. This idea is not limited to bosonic systems and can be similarly applicable to fermionic systems. In our following discussions, we will focus on the bosonic case with $G = U(1)$.

## III. 1-D $\mathbb{Z}_2$-GAUGED BOSE-HUBBARD MODEL

### A. Model

Consider a 1-D Bose-Hubbard model (on the sites, see Fig. 1(a)) coupled to Ising spins (on the bonds) as follows:

$$H = -t\sum_i b_i^\dagger \sigma_{i+1/2}^z b_{i+1} + U\sum_i n_i(n_i - 1)$$
$$- K\sum_i \sigma_{i-1/2}^x (-1)^{n_i} \sigma_{i+1/2}^x, \qquad (1)$$

where $t$ is the hopping, $U > 0$ is the on-site Hubbard repulsion, and $n_i = b_i^\dagger b_i$ is the local boson number. In the last term, the Ising spins are coupled to the local boson parity operator $(-1)^{n_i}$. If $K$ is taken to be much larger than the rest of the parameters, then it becomes an emergent parity-gauged Bose-Hubbard model

$$H = -t\sum_i b_i^\dagger \sigma_{i+1/2}^z b_{i+1} + U\sum_i n_i(n_i - 1) \qquad (2)$$

with the gauge constraints

$$G_i = \sigma_{i-1/2}^x (-1)^{n_i} \sigma_{i+1/2}^x = 1. \qquad (3)$$

Note that in the Hamiltonian, for simplicity, we consider the canonical ensemble where the total boson number $N = \sum_i n_i$ is conserved. In our following discussion, we consider even system size $L$, regardless of boundary conditions, with one boson per site. This makes the presentation more neat while retaining the essential physics [35].

57
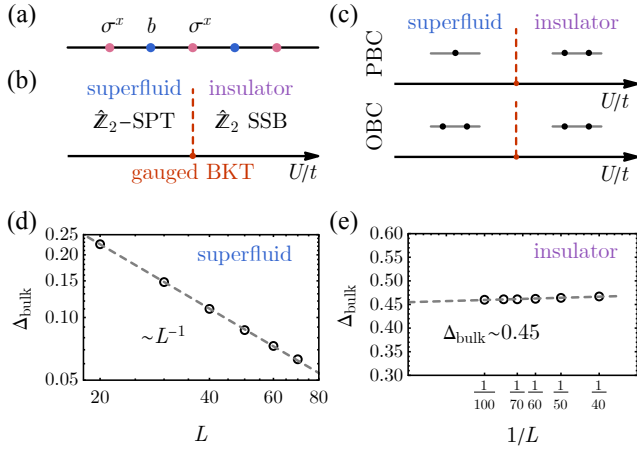
FIG. 1: (a) Schematic diagram for the 1-D Bose-Hubbard model (blue sites) coupled to Ising spins (violet bonds). (b) Schematic phase diagram. The original BKT transition between the superfluid and the insulator phase is enriched to a gauged BKT transition between a gapless SPT superfluid phase, protected by $\tilde{U}(1)$ and the dual $\hat{\mathbb{Z}}_2$ symmetry $W$, and the insulator phase with $W$ spontaneously broken. (c) Degeneracies in the superfluid and the insulator phase with PBC and OBC, respectively. (d, e) Finite size scaling of the gap $\Delta_{\text{bulk}}$ in both the superfluid ($t = 1.0, U = 1.0$) and the insulator phase ($t = 0.1, U = 1.0$). $\Delta_{\text{bulk}}$ is defined to be the gap in spectrum above the (possibly) degenerate ground states. OBC is used in both cases.

The microscopic model has two symmetries: spin flip symmetry generated by

$$W = \prod_i \sigma^z_{i+1/2}, \qquad (4)$$

and boson particle number conservation $U(1)$ symmetry acting as:

$$X(\theta) = \prod_i e^{i\theta n_i} \qquad (5)$$

with $X(\theta) = X(\theta + 2\pi)$. The boson parity

$$P = \prod_i (-1)^{n_i} \qquad (6)$$

is a subgroup of $U(1)$.

In the low energy theory, we can interpret the Ising spins as Ising gauge fields. Effectively, bosons on sites are minimally coupled to the Ising gauge field on the bonds. The boson parity, viewed as a $\mathbb{Z}_2$ subgroup of the $U(1)$ symmetry, is gauged, while $W$ can be viewed the dual $\hat{\mathbb{Z}}_2$ symmetry generated by Wilson loops. Using PBC, it is easy to see that the UV *physical* symmetry $P$ acts trivially in the IR theory since $P = \prod_i(-1)^{n_i} = \prod_i(\sigma^x_{i+1/2})^2 = 1$. This is equivalent to (trivially) projecting out the parity odd sector of the Hilbert space and at

the same time adding the twisted sector. Thus, in the IR theory, the original $U(1)$ symmetry effectively reduces to the quotient $\tilde{U}(1) \equiv U(1)/\mathbb{Z}_2$ symmetry whose action is now

$$\tilde{X}(\theta) = \prod_i \tilde{X}_i(\theta) \equiv \prod_i e^{i\theta n_i/2}. \qquad (7)$$

Due to the gauge constraints, $\tilde{X}(\theta + 2\pi) = \tilde{X}(\theta)$ is satisfied when PBC is used. In our following discussion, we will sometimes refer to $\mathbb{Z}_2$ groups using their generator for simplicity.

We must distinguish the UV symmetry $W \times U(1)$, where $P$ is a subgroup and hence physical, and the IR symmetry $W \times \tilde{U}(1)$, where the $\mathbb{Z}_2$ parity is a gauged symmetry. They will play an important role in our later discussion when it comes to the question whether a 't Hooft anomaly is emergent and whether it should be canceled. Also, even though $P = 1$ is trivial in the UV because we are considering the case with even $N = L$, it still plays a nontrivial role in the IR. The discussion about the grand canonical ensemble with a finite chemical potential $\mu$ adds more features and is discussed in Appendix C.

Before coupling to Ising spins, the Bose-Hubbard model can have two phases: a superfluid or a Mott insulator. The superfluid-insulator transition is a Berezinskii–Kosterlitz–Thouless (BKT) transition point where the transition is due to fluctuations of vortices in the phase [36, 37]. The transition occurs around $t/U \approx 0.3$ [38–40]. Note that in the supefluid phase, the $U(1)$ symmetry is not broken due to the celebrated Mermin-Wagner theorem [41], but there is a quasi-long range order, where $\langle b^\dagger_i b_j \rangle \sim r^{-\eta_b}$ decays algebraically for large $r = |j - i|$ with $\eta_b = \tilde{K}/2$, $\tilde{K}$ being the Luttinger parameter. Similarly, the disorder parameter $|\langle X_R(\theta)\rangle| = |\langle \prod_{i \in R} e^{i\theta n_i}\rangle|$, where $R$ is a line segment with $r = |R|$, decays algebraically.

Typical phase transitions are insensitive to boundary conditions in the thermodynamical limit. Gauging the $\mathbb{Z}_2$ subgroup is equivalent to averaging over untwisted and twisted sectors. Thus, gauging the $\mathbb{Z}_2$ subgroup does not change the position of critical point in the phase diagram. A continuous phase transition in the gauged model is directly inherited from the ungauged one but with many new features due to the interplay between the quotient $\tilde{U}(1)$ and the dual $\hat{\mathbb{Z}}_2$ symmetry $W$. The original BKT transition is now gauged (see Fig. 1(b)).

The intuitions are justified by DMRG computations. After gauging, $\langle b^\dagger_i b^\dagger_i b_j b_j \rangle$ remains gauge-invariant. The scaling law remains the same as in the ungauged system. $\langle b^\dagger_i b_j \rangle$, however, has to be dressed with gauge fields $\sigma^z_i$ to remain gauge-invariant: $\langle b^\dagger_i \sigma^z_{i+1/2} ... \sigma^z_{j-1/2} b_j \rangle$. The latter has the same scaling law as $\langle b^\dagger_i b_j \rangle$ in the ungauged system. An example of both order parameters in the superfluid phase is shown in Fig. 2(a-b) where a power-law decay as a function of large $r = |j - i|$ in both parameters can be seen. In the insulator phase, they both decay
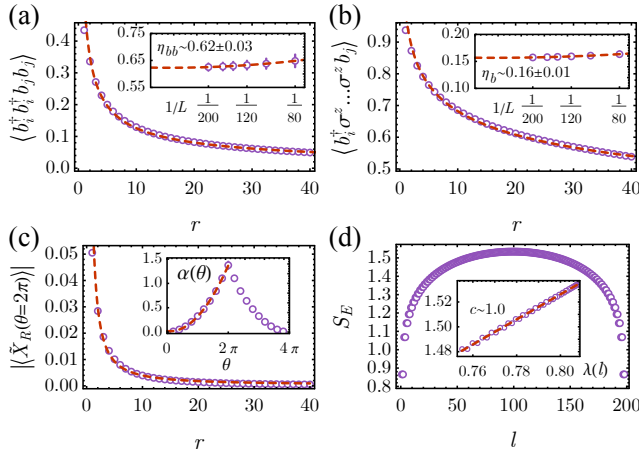
FIG. 2: (a) Boson pair correlation function, which is shown to follow a power law $\langle b_i^\dagger b_i^\dagger b_j b_j \rangle \sim r^{-\eta_{bb}}$ in the superfluid phase. The inset shows the extrapolation of the exponent $\eta_{bb}$ to the thermodynamic limit using finite-size scaling. Error bars are obtained from the upper and the lower bound of the extrapolation. (b) Gauge-invariant boson correlation, which also follows power law $\langle b_i^\dagger \sigma^z ... \sigma^z b_j \rangle \sim r^{-\eta_b}$. The inset shows the extrapolation of $\eta_b$. (c) The $\tilde{U}(1)$ disorder operator $|\langle \tilde{X}_R(\theta)\rangle|$ decays as power law $r^{-\alpha(\theta)}$ in $r$. The main plot shows the $\theta = 2\pi$ case. The inset shows the $\theta$-dependence of the exponent $\alpha$, which is $4\pi$-periodic. $\alpha$ is symmetric about $2\pi$, and a quadratic fit (dashed line) is performed for the segment from 0 to $2\pi$. (d) Subsystem von Neumann entanglement entropy $S_E$ as a function of subsystem size $l$. The inset shows the linear dependence of $S_E$ on $\lambda(l) \equiv \frac{1}{6} \log \left( \frac{2L}{\pi} \sin \left( \frac{\pi l}{L} \right) \right)$. The central charge $c$, which is given by the slope, is shown to be almost exactly 1. All the main plots are for $L = 100$, $t = 0.5$ and $U = 1.0$.

exponentially to zero. The disorder parameter $|\langle \tilde{X}_R(\theta)\rangle|$ also remains intact. It saturates to a constant in the insulator phase. Its behavior in the superfluid phase is shown in Fig. 2(c) where the angle dependence of $\alpha(\theta)$ is also displayed. $\alpha(\theta)$ has a quadratic dependence on $\theta$. As we will discuss below, this is compatible with the charge fractionalization in the superfluid phase. Note that even though OBC is used when these quantities are calculated, the bulk behavior is the same as in the PBC case.

On the other hand, the new Ising degrees of freedom also behave differently in the superfluid and the insulator phase. As a result of the emergent gauge constraints, the relation $\langle \sigma_i^x \sigma_j^x \rangle = \langle \prod_{i \in R} (-1)^{n_i} \rangle = \langle \tilde{X}_R(2\pi) \rangle$ holds in either phase. It relates an "order parameter" associated with $W$ to a disorder parameter associated with $\tilde{U}(1)$. As we will discuss soon, this is a manifestation of the emergent mixed anomaly between $\tilde{U}(1)$ and the dual $\hat{\mathbb{Z}}_2$ symmetry $W$. In the insulator case, the magnetization $|\langle \sigma_i^x \rangle|$ in the thermodynamical limit is nonzero, $W$ is spontaneously broken, and the spin-spin correlation $|\langle \sigma_i^x \sigma_j^x \rangle|$ saturates to a constant. In the superfluid phase,
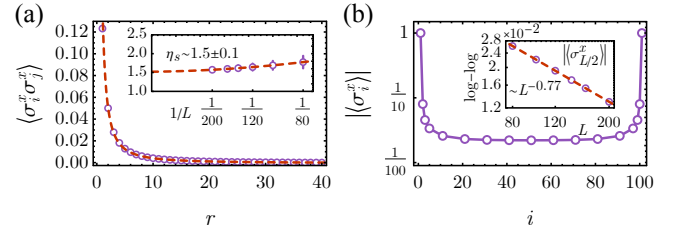


FIG. 3: (a) The bulk spin-spin correlation in the superfluid phase with a power-law fit (dash line) $|\langle \sigma_i^x \sigma_j^x \rangle| \sim r^{-\eta_s}$. The inset shows the extrapolation of the critical exponent $\eta_s$ to the thermodynamic limit using finite-size scaling. (b) The magnetization $|\langle \sigma_i^x \rangle|$ in the superfluid phase across the system with OBC. The spins on the edges are perfectly polarized and the magnetization decays to a small value to the bulk. The inset shows the center spin magnetization $|\langle \sigma_{L/2}^x \rangle|$ follows a power law decay as system size increases, compatible with the fact that magnetization vanishes when PBC is used. $L = 100$, $t = 0.5$ and $U = 1.0$ for both plots.

the bulk magnetization vanishes and the bulk spin-spin correlation $|\langle \sigma_i^x \sigma_j^x \rangle| \sim r^{-\eta_s}$ decays algebraically regardless of whether PBC or OBC is used. See Fig. 3(a) for the bulk correlation with OBC [42].

In our DMRG calculations, the local bosonic Hilbert space dimension is truncated to 5 (beyond which the critical exponents almost saturate). Bond dimensions less than 400 are sufficient for the results to converge. To obtain the power law exponents, the correlation functions are fitted with a power law decay with $i$ and $j$ far away from both edges. Finite-size scaling is performed with system sizes (number of boson sites) up to $L = 200$. For each system size, the mean and the error bar are obtained by fitting different segments/bins of data points. The extrapolated mean value is obtained by a quadratic fit against $1/L$. The extrapolated error bar comes from the difference between the extrapolated upper bound and lower bound of the exponent across different system sizes. The DMRG calculations are done using the ITensor package [43].

**B. Emergent mixed anomaly**

In the low energy theory, there is an emergent mixed anomaly between the quotient $\tilde{U}(1)$ and the dual $\hat{\mathbb{Z}}_2$ symmetry $W$ (considering PBC for simplicty). One manifestation of the mixed anomaly is that $\tilde{U}(1)$ and $W$ cannot be simultaneously realized on-site. Here $\tilde{U}(1)$ and $W$ seem to be realized on-site. However, $\tilde{U}(1)$ is only exact when the gauge condition in Eq. (18) is enforced, i.e., $K \to \infty$, and the Hilbert space then is not a tensor product. We can follow Ref. [33] to eliminate the gauge constraints and find that either $\tilde{U}(1)$ or $W$ is realized non-on-site (see Appendix B).

59

If we turn on the background gauge field $A^{\tilde{U}(1)}$ and $A^W$ associated with $\tilde{U}(1)$ and $W$ respectively, the mixed anomaly is characterized by a response action in (2+1)-D: $\omega = A^W \cup dA^{\tilde{U}(1)}/4\pi$ where $\cup$ is a cup product, a discrete analogue of the wedge product of differential forms [44]. Thus, $\tilde{U}(1)$ and $W$ cannot be gauged consistently in the $(1+1)$-D system we are studying which may be viewed as the boundary of the $(2+1)$-D bulk (Appendix D). The system, viewed as the boundary of the bulk, usually cannot have boundaries because the boundary of a boundary is an empty set. This is not a contradiction because in our work the mixed anomaly is emergent in the low energy sector. After some suitable modifications of boundary terms, we can put this model on a lattice with open boundary conditions while preserving both symmetries in the Hamiltonian, which plays a crucial role in the "Higgs = SPT" argument in Refs. [27, 28] and our argument in the following for the gapless SPT phase.

As a result of the emergent mixed anomaly, the ground state cannot be trivially gapped, meaning that in a gapped phase $W$ must be spontaneously broken since $\tilde{U}(1)$ cannot be spontaneously broken due the Mermin-Wagner theorem. Indeed, $W$ is spontaneously broken in the insulating phase, while in the superfluid phase both $\tilde{U}(1)$ and $W$ are preserved. As we have discussed above, in the superfluid phase, both $\langle b_i^\dagger b_i^\dagger b_j b_j \rangle$ and $|\langle \sigma_i^x \sigma_j^x \rangle|$ are shown to have a power law decay (Fig. 2(a) and 3(a)). These correlated ordering/disordering behaviors are already encoded in the relation $\langle \sigma_i^x \sigma_j^x \rangle = \langle \prod_{i \in R}(-1)^{n_i} \rangle = \langle \tilde{X}_R(2\pi) \rangle$ we mentioned earlier. This relation implies that $\tilde{U}(1)$ is preserved if $W$ is spontaneously broken and that $\tilde{U}(1)$ is spontaneously broken if $W$ is preserved.

Another manifestation of the mixed anomaly is symmetry fractionalization. We take $W$ to act on a segment of sites $R$ instead of the entire chain. This is a disordered operator for the Ising spins. The emergent gauge constraints imply that the string operator has to be dressed with $b$ or $b^\dagger$ to act nontrivially on the low-energy sector. In other words, $\langle b_i^\dagger \sigma_{i+1/2}^z ... \sigma_{j-1/2}^z b_j \rangle$ is effectively gauge invariant. Note that both $b$ or $b^\dagger$ are fractionally charged under $\tilde{X}(\theta)$ in Eq. (7). Similarly, the disorder operator for $\tilde{X}_R(\theta)$ is fractionally charged under $W$. This can be seen from that $\tilde{X}_i(2\pi) = (-1)^{n_i}$ and $\langle \sigma_{i-1/2}^x (-1)^{n_i}...(-1)^{n_j} \sigma_{j+1/2}^x \rangle = 1$. Since the edge spins are charged under $W$, linearity implies that the end points of the disorder operator $\tilde{X}_R(\theta)$ are fractionalized.

### C. Gapless SPT phase

In this subsection, we show that the superfluid phase is a gapless SPT phase.

We first adapted the "Higgs = SPT" argument in Ref. [27] to argue for the existence of edge modes if $W$ and $P$ both commute with the Hamiltonian and an open boundary is chosen such that the emergent gauge con-

straints in Eq. (3) are preserved. Note that we treat $P$ as the physical symmetry in the UV. The emergent gauge constraints force $P = \sigma_{1/2}^x \sigma_{L+1/2}^x$ in the IR. There are different ways to impose boundary conditions on the edges to guarantee the (dynamical) gauge-invariance. If the edge degrees of freedom are not fixed, Ref. [27] argues that $P$ is a physical symmetry, similar to the observation made about asymptotic symmetries in Ref. [45]. In our discussion, we find it more transparent to simply treat $P$ as a UV symmetry. Since the Hamiltonian is local, it must commute with the two $\sigma^x$ individually. The anti-commutativity between $\sigma^x$ with $W$ implies that there are necessarily edges modes if $W$ or $P$ is preserved. To be more explicit, let $|\psi\rangle$ be a ground state of the Hamiltonian that satisfies $W|\psi\rangle = \eta|\psi\rangle$ with $\eta = \pm 1$, then the state $|\tilde{\psi}\rangle \equiv \sigma^x|\psi\rangle$ is another degenerate state because $W|\tilde{\psi}\rangle = -\eta|\tilde{\psi}\rangle$. If the bulk is non-degenerate, the degeneracy necessarily comes from the edges. In fact, either $W$ or $P$ is spontaneously broken by the edges while the bulk remains gapless. These observations can be justified by the DMRG computations.

First, we compare the degeneracy for PBC and OBC in both the insulator and the superfluid phase. From Fig. 1(c), we can see that the ground state in the insulator phase is doubly degenerate, be it with PBC or OBC. This is expected due to the SSB of the dual $\hat{\mathbb{Z}}_2$ symmetry. There are no edge modes in this phase. On the other hand, if PBC is used, the ground state of the superfluid phase is unique, while if OBC is used, there is a double degeneracy. This is a result of the SSB of $W$ on the edges we mentioned above. Indeed, we present the magnetization $|\langle \sigma_i^x \rangle|$ in Fig. 3(b). Even though the bulk magnetization decays to zero in the thermodynamical limit as in the PBC case, the edge spins are clearly polarized. In fact, due to the constraint from $P = \sigma_{1/2}^x \sigma_{L+1/2}^x = 1$, two edge spins are perfectly correlated. Note that the degeneracy in this phase is exact even in finite-size systems. This means that the edge modes are strictly localized on the edges, and the edge localization length $\xi_e$, defined as $e^{-L/\xi_e} \sim \Delta_{\text{bdry}}$, is exactly 0. The wave function can be interpreted as a fixed point SPT state.

Next, we discuss the finite size scaling in the bulk gap $\Delta_{\text{bulk}}$ to show the bulk is indeed gapless in the thermodynamic limit. As we can see from Fig. 1(d), the bulk gap, the first excited state from the doubly degenerate ground state, is inversely proportional to the system size $L$. In the thermodynamic limit, the bulk correlation length $\xi_b$ diverges and the bulk becomes gapless [46]. This is compatible with the fact that there is a mixed anomaly between $\tilde{U}(1)$ and the dual $\hat{\mathbb{Z}}_2$ symmetry $W$. As we have already mentioned, both $\tilde{U}(1)$ and $W$ are preserved, which is supported by algebraically decaying $\langle b_i^\dagger b_i^\dagger b_j b_j \rangle$ (Fig. 2(a)) and $|\langle \sigma_i^x \sigma_j^x \rangle|$ (Fig. 3(a)). The gap $\Delta_{\text{bulk}}$ in the insulator phase, on the other hand, remains finite in the thermodynamical limit, as extrapolated by finite-size scaling (Fig. 1(e)). Thus, we have showed that the superfluid phase is a gapless SPT phase.

We can discuss the effective action of this gapless SPT phase. Let us recall that the microscopic on-site symmetry of the Hamiltonian in Eq. (1) is $U(1) \times W$. The emergent symmetry acting nontrivially in the IR is $\tilde{U}(1) \times W$. To capture the edge degeneracy, we may write down a response action as [27]

$$\alpha = \frac{1}{2} A^W \cup A^P, \qquad (8)$$

where $A^W$ and $A^P$ is the background field of $W$ and $P$ in the spacetime $M$, respectively. If $A^P$ and $A^W$ are flat, $dA^P = 0$ and $A^W = 0$. Then if $M$ is closed, $\alpha$ is gauge invariant and describes a SPT phase protected by $W$ and $P$. Indeed, if $M$ has a nontrivial boundary, there can be an open Wilson line terminating on the $\partial M$ where $dA^W \neq 0$. Then the action $S_M = 2\pi \int_M \alpha$ changes by is $\lambda A^W/2$ under the gauge transformation $A^P \rightarrow A^P + d\lambda^P$. To compensate this change, there must be edge modes.

On the other hand, $P$ is a subgroup of $U(1)$. If we turn on a flat background field $A^{U(1)}$, the closedness of $A^{U(1)}$ requires $dA^P = dA^{\tilde{U}(1)}/2\pi$ mod 2 (see Appendix D), i.e., $A^P$ may no longer be closed. The action $S_M = 2\pi \int_M \alpha$ now is no longer invariant under $A^W \rightarrow A^W + d\lambda^W$ even if $M$ is closed. This is a 't Hooft anomaly between $W$ and $P$! Since both $W$ and $P$ are UV onsite symmetries, this 't Hooft anomaly must be canceled by some other terms. Luckily, we find that the emergent mixed anomaly can play the role.

Indeed, we have already seen that there is an emergent mixed anomaly between $\tilde{U}(1)$ and $W$. If we denote the $(2+1)$-D bulk as $Y$ such that its boundary is the $(1+1)$-D spacetime $M$ that we are studying, i.e. $\partial Y = M$, then the corresponding anomaly action can be written as $\omega = A^W \cup dA^{\tilde{U}(1)}/4\pi$ where $A^{\tilde{U}(1)}$ and $A^W$ are extended into $Y$. Note that $\alpha$ and $\omega$ satisfy the anomaly vanishing equation [18]

$$\omega = d\alpha, \qquad (9)$$

so the partition function

$$Z = e^{2\pi i \int_Y \omega} e^{-2\pi i \int_M \alpha} \qquad (10)$$

is anomaly free. In other words, the emergent mixed anomaly compensates the 't Hooft anomaly in $\alpha$. If $M$ has a nontrivial boundary, the gauge invariance argument again justifies the existence of edge modes. Thus, the gapless SPT phase can be captured by $\alpha$ and $\omega$ together. For more details, see Appendix D.

It is not surprising that Eq. (8) is also the effective action of the 1-D SPT phase in Ref. [27] where an Ising model is gauged. However, the total symmetry we are considering is $U(1) \times W$ instead of $W \times P$ in that work. Instead of the Higgs phase, our focus here is more on the critical phase. In Ref. [27], they suggested that the critical point is a "symmetry-enriched quantum critical point" studied in Ref. [16] . Here, our critical phase is more closely related to the "intrinsically gapless SPT phase" proposed in Ref. [18]. In that work,

the (fermionic) parity is gapped by interactions, while in our discussion, the parity is simply gapped by emergent gauging. The SPT string order parameter in our case is simply $\langle \sigma_{i-1/2}^x (-1)^{n_i}...(-1)^{n_j} \sigma_{j+1/2}^x \rangle = 1$ while Higgs order parameter $\langle b_i^\dagger \sigma_{i+1/2}^z ... \sigma_{j-1/2}^z b_j \rangle$ vanishes in the thermodynamical limit. Since $H^2(U(1) \times \mathbb{Z}_2, U(1)) = 0$, there is no nontrivial *gapped* SPT phase protected by $U(1) \times W$, based on the complete classification of conventional bosonic SPT phases in 1-D [5]. In other words, if OBC is used for our gapless SPT phase, we cannot gap out the bulk without destroying the edge degeneracy or breaking the total symmetry.

Conceptually, constructing intrinsically gapless SPT phases using partial gauging as we discussed in this work is easier than the approach used in Ref. [18]. The mixed anomaly between the quotient symmetry and the dual symmetry is a direct consequence of the nontrivial group extension and does not depend on the details of the Hamiltonian. In Ref. [18], the authors considered a fermionic system, but the analysis above is obviously generalizable to fermionic systems even though the fermionic parity cannot be spontaneously broken and spin structures may need to be taken into account. As long as there is no other SSB order, the gauged Luttinger liquid of spinless fermions with $W = \prod_i \sigma_{i+1/2}^z$ preserved is a gapless SPT phase.

Even though we have focused on a canonical ensemble with even parity, the analysis carries over to a grand canonical ensemble. Then both even and odd parity sectors should be taken into account, especially when OBC is used. The essential physics stays almost unchanged. For example, the ground state degeneracy for both PBC and OBC is the same as in Fig. 1(b). The anomaly analysis is similar. For more details, see Appendix C.

### D. Conformal field theory

Since the BKT transition can be described by a compact boson CFT [47], we expect that the gauged BKT transition and the superfluid phase is also captured by gauging the $\mathbb{Z}_2$ symmetry of the compact boson CFT which is also a compact boson CFT. Indeed, the compact boson CFT contains two global $U(1)$'s, one associated with momentum and the other with winding. They are dual to each other and there is a mixed anomaly between them. Gauging a $\mathbb{Z}_2$ subgroup of a compact boson CFT not only changes the radius of the compactification, but also maps order operators to disorder operators and vice versa [24, 33]. The $\mathbb{Z}_2$-charged sectors and the $\mathbb{Z}_2$-twisted sectors are exchanged under this operation. The states in the $\mathbb{Z}_2$-twisted sectors are charged under the dual $\hat{\mathbb{Z}}_2$ symmetry. This dual $\hat{\mathbb{Z}}_2$ symmetry can be viewed as a subgroup of the $U(1)$ symmetry associated with winding.

This expectation again can be verified by the DMRG results. We first check the central charge $c$ in the superfluid phase in the gauged system. Indeed, as shown

in Fig. 2(d), the subsystem entanglement entropy $S_E = -\text{tr}(\rho_R \ln \rho_R)$, associated with the reduced density matrix $\rho_R$ of a subsystem $R$, scales linearly with the factor $\lambda(l) \equiv \frac{1}{6} \log\left(\frac{2L}{\pi} \sin\left(\frac{\pi l}{L}\right)\right)$ [48]. Here $L$ is the total system size of the open chain and $l$ is the size of the subsystem $R$ on one side of the entanglement cut. The slope gives us the central charge $c \sim 1$, the nominal central charge of a compact boson CFT.

Next, we identify the microscopic operators with the primary vertex operators. Before gauging, the (Euclidean) action is given by

$$S = \frac{1}{4\pi} \int dz d\bar{z} \partial_z \phi \partial_{\bar{z}} \phi, \qquad (11)$$

where $z = \exp(\tau + ix)$, and the free boson field $\phi$ is compactified on a circle of radius $R$, i.e. $\phi(z, \bar{z}) \sim \phi(z, \bar{z}) + 2\pi R$. Split $\phi(z, \bar{z})$ into the left-moving and the right-moving components: $\phi(z, \bar{z}) = X_L(z) + X_R(\bar{z})$. Then the local primary operators are:

$$V_{n,w}(z, \bar{z}) \qquad (12)$$
$$= \exp\left[i\left(\frac{n}{R} + wR\right) X_L(z) + i\left(\frac{n}{R} - wR\right) X_R(\bar{z})\right],$$

where $n \in \mathbb{Z}$ and $w \in \mathbb{Z}$ are the momentum number and the winding number, respectively. After gauging, $R \to R/2$, which is equivalent to redefining $n$ and $w$: $n \in \frac{1}{2}\mathbb{Z}$ and $w \in 2\mathbb{Z}$ and $\phi(z, \bar{z}) \sim \phi(z, \bar{z}) + 4\pi R$ while fixing $R$ [33, 49]. The conformal weights of $V_{n,w}$ are

$$h_{n,w} = \frac{1}{4}\left(\frac{n}{R} + wR\right)^2, \quad \bar{h}_{n,w} = \frac{1}{4}\left(\frac{n}{R} - wR\right)^2, \quad (13)$$

and conformal dimensions

$$\Delta_{n,w} = h_{n,w} + \bar{h}_{n,w} = \frac{1}{2}\left(\frac{n^2}{R^2} + w^2 R^2\right). \qquad (14)$$

At a generic radius, the CFT has global symmetry $U(1)_n \times U(1)_w$ which act on $X_{L/R}$ as:

$$U(1)_n : X_{L/R}(z) \to X_{L/R}(z) + R\theta_n,$$
$$U(1)_w : X_{L/R}(z) \to X_{L/R}(z) \pm \frac{1}{4R}\theta_w, \qquad (15)$$

where $\theta_{n/w} \sim \theta_{n/w} + 2\pi$. On the gauged vertex operators $V_{n,w}$, they act as

$$U(1)_n : V_{n,w} \to e^{i2n\theta_n} V_{n,w},$$
$$U(1)_w : V_{n,w} \to e^{iw\theta_w/2} V_{n,w}. \qquad (16)$$

In our case, we can identify $\tilde{U}(1)$ with $U(1)_n$ and identify $\hat{\mathbb{Z}}_2$ with the $\mathbb{Z}_2$ subgroup of $U(1)_w$. It is straightforward to see that $b^\dagger b^\dagger$ (or $bb$) can be identified with $V_{2,0}$ and $\sigma^x$ with $V_{0,1/2}$. The corresponding conformal dimensions are thus $2/R^2$ and $R^2/2$ respectively. Meanwhile, the nonlocal operator $b^\dagger$ (or $b$) corresponds to the nontrivial local operator with the lowest scaling dimension $V_{1,0}$ before gauging. Its scaling dimension should be $1/2R^2$. This is indeed supported by DMRG.

In the DMRG calculations, we choose a sample point in the superfluid phase: $t = 0.5, U = 1.0$. As shown in Fig. 2 and Fig. 3, the scaling dimension of $b^\dagger b^\dagger$ is $\eta_{bb} \sim 0.62$ and the scaling dimension of the scaling dimension of $\sigma^x$ is $\eta_s \sim 1.5$. The nonlocal correlation $\langle b_i^\dagger \sigma^z ... \sigma^z b_j \rangle \sim r^{-\eta_b}$ yields a scaling dimension $\eta_b \sim 0.16$. They are all compatible with $R^2 \sim 3.1$. Note also that the conformal dimensions of the order/disorder operators scale quadratically with the charges $n$ and $w$. Previously we have seen that the end points of the disorder operator $\tilde{X}_R(\theta)$ are fractionalized charged under the dual $\hat{\mathbb{Z}}_2$. Assuming linearity in charge fusion, we may *formally* assign a charge proportional to $\theta$ to the end points when $0 \le \theta \le 2\pi$. Thus we may expect that the conformal dimension of $\tilde{X}_R(\theta)$ should be proportional to $\theta^2$ in the interval. This is compatible with the quadratic fit in the inset of Fig. 2(c).

### E. Perturbations

In the discussions above, we have argued that the superfluid is a gapless SPT is protected by $U(1)$ and $W$. As long as the Hamiltonian (and the boundary conditions) preserve $U(1)$ and the dual $\hat{\mathbb{Z}}_2$ symmetry $W$, the edge degeneracy is protected. For instance, as verified by DMRG, adding a term $\sum \sigma_{i-1/2}^z \sigma_{i+1/2}^z$ does not lift the degeneracy. Adding a small perturbation $\lambda \sum \sigma_{i+1/2}^x$ however breaks this symmetry. The edges open up a small gap and are no longer degenerate. The situation is different in higher dimensions when the protecting symmetries include higher-form symmetries. Breaking higher-form symmetries explicitly may not lift the edge degeneracy.

## IV. 2-D $\mathbb{Z}_2$-GAUGED BOSE-HUBBARD MODEL

Having considered the 1-D case, we can generalize the analysis to higher dimensions. In this section, we consider the emergent $\mathbb{Z}_2$-gauged Bose-Hubbard model on a 2-D square lattice (Fig 4(a)):

$$H = -t \sum_{i,j \in \partial e_{ij}} b_i^\dagger \sigma_{e_{ij}}^z b_j + U \sum_i n_i(n_i - 1) - \mu \sum_i n_i,$$
$$- \frac{1}{g} \sum_p \prod_{e \in \partial p} \sigma_e^z - g \sum_e \sigma_e^x, \qquad (17)$$

with the gauge constraints

$$G_i = \prod_{i \in \partial e} \sigma_e^x (-1)^{n_i} = 1. \qquad (18)$$

Here $e_{ij}$ represents the bond connecting site $i$ and site $j$, and $p$ represents any plaquette of the lattice. Note that in order to capture the Higgs phase, we turn on the chemical potential $\mu$ and consider the grand canonical ensemble.
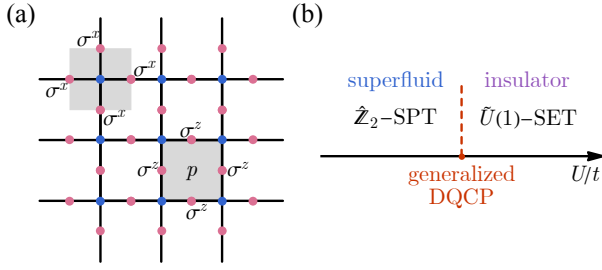
FIG. 4: (a) Schematic diagram for the 2-D Bose-Hubbard model (blue sites) coupled to Ising spins (violet bonds). A star operator related to the gauge constraints in Eq. (18) and a plaquette operator are highlighted. (b) Schematic phase diagram. The gapless SPT in the superfluid phase where $\tilde{U}(1)$ is spontaneously broken and the SET enriched by $\tilde{U}(1)$ in the insulator phase are separated by a generalized DQCP.

The 1-D case is briefly discussed in Appendix C. Similar to the 1-D version, we view the gauge constraints to be energetically enforced.

We first let $g \to 0$ so that the zero-flux (flatness) condition $\prod_{e \in \partial p} \sigma_e^z = 1$ is enforced and the transverse field term is dropped, giving rise to an emergent 1-form symmetry

$$W = \prod_{e \in \gamma} \sigma_e^z, \tag{19}$$

where $\gamma$ is a loop running along the bonds of the lattice. Nonzero $g$ perturbations will be discussed later. There is also a $\tilde{U}(1)$ with $\tilde{X}(\theta) = \prod_i e^{i\theta n_i/2}$ satisfying $\tilde{X}(\theta + 2\pi) = \tilde{X}(\theta)$. This model has been studied before in, e.g., Ref. [50] from a different perspective. In their studies, the boson field $b$ is not fundamental but emergent as a result of fractionalization. In our following discussion, we will emphasize more on higher-form symmetries and anomalies. As it is hard to study large systems using DMRG, we will focus on the theoretical analysis, although some results have been checked already in small systems using DMRG.

It is well-known that there is a second order superfluid-insulator transition in the pure Bose-Hubbard model (before coupling the Ising model) by tuning the ratio $U/t$. Unlike the 1-D version, the global $U(1)$ symmetry is spontaneously broken in the superfluid phase. For simplicity, we may also assume that the chemical potential $\mu$ has been tuned such that the boson filling is an integer. In the gauged model, the zero-flux condition ensures the flatness of the gauge field, killing all local dynamics but the topological degrees of freedom in $\sigma^z$. Thus a continuous phase transition in the gauged model is directly inherited from the ungauged one but with many new features due to the interplay between the quotient $\tilde{U}(1)$ and the dual $\hat{\mathbb{Z}}_2$ 1-form symmetry $W$.

## A. Emergent mixed anomaly

Since $U(1)$ is a nontrivial extension of $\tilde{U}(1)$ by $\mathbb{Z}_2$, there is a mixed anomaly between $\tilde{U}(1)$ and the $\hat{\mathbb{Z}}_2$ 1-form symmetry $W$(see Appendix D). Let us denote the 2-D system as $M$ (without boundaries) and view it as a boundary of a 3-D bulk $Y$. The mixed anomaly is captured by a (3+1)-D SPT bulk protected by the generalized symmetry $\tilde{U}(1) \times W$. If we turn on the 1-form background gauge field $A^{\tilde{U}(1)}$ of $\tilde{U}(1)$ and the 2-form background gauge field $A^W$ of $W$ and extend them into $Y$, then the anomaly action is given by

$$S_Y = \frac{i}{2} \int_Y A^W \cup dA^{\tilde{U}(1)}. \tag{20}$$

Here, $A^{\tilde{U}(1)}$ is compact and periodic in $2\pi$, and $A^W$ takes value in $\mathbb{Z}_2$. This action is not gauge invariant under the gauge transformations of $A^W$ in the presence of boundary $M$, a manifestation of the mixed anomaly between $\tilde{U}(1)$ and $W$ in the boundary theory which implies that it is impossible to gauge both symmetries consistently. In fact, the mixed anomaly reduces to that in the case of gauging the $\mathbb{Z}_2$ subgroup of $\mathbb{Z}_4$ [33, 51]. Analogous to the 1-D case, the end points of the disordered operators of one symmetry are fractionally charged under the other, which can be seen directly from $\langle b_i^\dagger \sigma_{i+1/2}^z ... \sigma_{j-1/2}^z b_j \rangle$ and $|\langle \tilde{X}_R(\theta) \rangle|$.

Similar to the 1-D case, the ground state of the system cannot be trivially gapped (i.e. nondegenerate, gapped, and symmetric under both symmetries). This consequence strongly constrains the phase diagram. As we will argue in this work, the critical point inherited from the ordinary superfluid-insulator transition now becomes a generalized DQCP between a gapless SPT phase where $\tilde{U}(1)$ is spontaneously broken and a SET phase where the dual $\hat{\mathbb{Z}}_2$ symmetry is spontaneously broken (Fig. 4(b)).

## B. Gapless SPT phase

We now combine the emergent mixed anomaly with the "Higgs = SPT" argument in Ref. [27] to argue in two steps that the superfluid phase after gauging becomes a gapless SPT phase.

As the first step, we show that if the 1-form symmetry $W$ is not spontaneously broken, then the ground state is a gapless SPT phase. The gaplessness is a direct consequence of the mixed anomaly: if $\tilde{U}(1)$ is also preserved, then the system is critical; on the other hand, if $\tilde{U}(1)$ is spontaneously broken, there will be Goldstone bosons. When the system has no boundary, the gauge condition Eq. (18) implies that the boson parity symmetry $P$ is trivial in the low energy effectively gauged system, $P = \prod_i (-1)^{n_i} = \prod_e (\sigma_e^x)^2 = 1$. However, when there is an open boundary (which preserves necessary symmetries), $P$ becomes non-trivial because the spin operators

on the boundary are not canceled, $P = \prod_{e \in \text{bdry}} \sigma_e^x$. Using some rough terms, we may state that in this case $P$ is not "completely" gauged even in the low-energy sector. It is manifested in the existence of "half" string operators $\sigma_{1/2}^z...\sigma_{j-1/2}^z b_j$ with one end terminating on the boundary which acts nontrivially in the low energy sector. Nevertheless, boson creation/annihilation operators still have to be attached by a string of gauge field $\sigma^z$. In particular, if the string operator does not end on the boundaries, it has to end on a creation or an annihilation operator to ensure a nontrivial action in the low energy sector. This means that the emergent mixed anomaly is still playing its due role and the ground state still cannot be trivially gapped.

To show that the state is SPT, we place it on lattice with open boundaries that preserve the dual $\hat{\mathbb{Z}}_2$ symmetry $W$. We consider a half-plane geometry with an infinitely long boundary (Fig. 5(a)), where the "rough" boundary has dangling bonds sticking out so that properly modified local gauge constraints Eq. (18) are still well-defined [52]. Then similar to the 1-D case, we can argue that if $W$ is preserved, there will necessarily be a boundary degeneracy as follows. We choose the symmetry generator of $W = \prod_{e \in \gamma} \sigma_e^z$ to be a Wilson line with one end terminating on the boundary and the other end either extending to infinity or terminating on a boson creation/annihilation operator. With $P$ and $W$ preserved in the bulk, the anti-commutativity of $P$ and $W$ implies a ground state degeneracy, which in this case necessarily comes from the boundary. This defines a SPT phase. In fact, the Higgs condensate $\langle b_i^\dagger \sigma_{i+1/2}^z ... \sigma_{j-1/2}^z b_j \rangle$ can be viewed as a SPT string order parameter here.

As the second step, we show that $W$ is preserved in the superfluid phase. To this end, we show that a 't Hooft loop operator, charged under $W$, satisfies the non-perimeter law. We take the 't Hooft loop (defined on the dual lattice) to be $\prod_{e \in \partial R} \sigma_e^x$ where $R$ is an arbitrary large connected area with perimeter $l = |\partial R|$, shown in Fig. 5(b) (we ignore the contributions from corners for simplicity). Then the gauge condition Eq. (18) implies that $|\langle \prod_{e \in \partial R} \sigma_e^x \rangle| = |\langle \prod_{i \in R} (-1)^{n_i} \rangle| = |\langle \prod_{i \in R} e^{i\pi n_i} \rangle| = |\langle \tilde{X}_R(2\pi) \rangle|$. Since $\tilde{X}_R(2\pi)$ is a disorder operator for $\tilde{U}(1)$, we can see that the order parameter of the dual $\hat{\mathbb{Z}}_2$ and the disorder parameter of the $\tilde{U}(1)$ are directly related. We interpret this relation as a direct manifestation of the mixed anomaly: if one symmetry is spontaneously broken, then the other is preserved. There is one subtlety here. In the insulating phase, $|\langle \tilde{X}_R(\theta) \rangle|$ and $|\langle \prod_{e \in \partial R} \sigma_e^x \rangle|$ both satisfy the perimeter law $e^{-\beta(\theta)l}$, where $\beta(\theta)$ is independent of $l$. Thus, $\tilde{U}(1)$ is preserved while the dual $\hat{\mathbb{Z}}_2$ is spontaneously broken in this phase. It is possible to absorb the dependence on $\partial R$ in the perimeter law by adding a local counterterm such that both quantities approach a constant for large smooth $\partial R$ [53]. This is the SET phase in Fig. 4(b) which we will discuss more later. On the other hand, in the superfluid phase, $|\langle \tilde{X}_R(\theta) \rangle|$ satisfies the scaling $\sim e^{-\alpha(\theta)l\ln l}$ where $\alpha(\theta)$ is independent
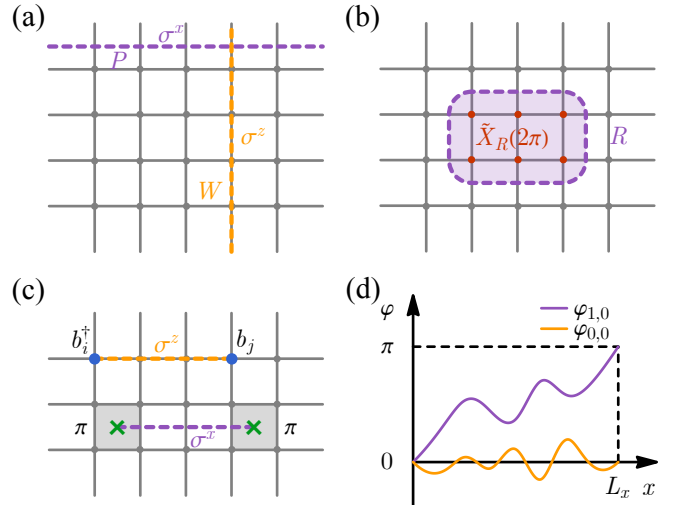


FIG. 5: (a) Action of boson parity $P$, effectively a 't Hooft line (purple), and a Wilson line $W$ (orange) terminating on the boundary (top) of a semi-infinite system. The other end of $W$ terminates either in the bulk or at infinity. The anti-commutativity of $P$ and $W$ forces a SSB on the boundary. (b) Disorder operator $\tilde{X}_R(\theta = 2\pi)$ supported on sites (highlighted in red) inside a region $R$, which is the same with with the 't Hooft loop operator, $\prod_{e \in \partial R} \sigma_e^x$, supported on the (dual lattice) boundary of $R$. (c) Gauge invariant Wilson line $W$ attached to boson operators (Higgs order operator), and a 't Hooft line connecting two $\pi$-vortices (which is suppressed by the zero-flux condition). (d) Example of two topologically distinct phase modes with winding number 1, $\varphi_{1,0}$ (red), and winding number 0, $\varphi_{0,0}$ (blue) along the $x$-direction. 0 and $L_x$ are identified.

of $l$ [54, 55], weaker than the area law. Consequently, the scaling of $|\langle \prod_{e \in \partial R} \sigma_e^x \rangle|$ is also weaker than the area law. Since it is strictly stronger than the perimeter law, it is impossible to renormalize the scaling law to a constant for large smooth $\partial R$. Thus, we claim that $W$ is unbroken.

Combining the two steps, we conclude that the superfluid is mapped to a gapless SPT phase protected by $W$ and $P$ where $\tilde{U}(1)$ is spontaneously broken. The gaplessness comes from the Goldstone bosons.

Similar to the 1-D case, we may write down the term in the effective action that dictates the existence of edge modes

$$\alpha = \frac{1}{2} A^W \cup A^P, \qquad (21)$$

where $A^W$ is the 2-form background gauge field of $W$ and $A^P$ is the 1-form background gauge field of $P$. The anomaly in $\alpha$ when $A^{\tilde{U}(1)}$ is turned on is again canceled by the anomaly action in Eq. (20). In some rough sense, $\alpha$ dictates the existence of edge modes when $dA^{\tilde{U}(1)}/2\pi = 0$ mod 2, while the mixed anomaly governs the SSB of $\tilde{U}(1)$ in the superfluid phase.

## C. Excitations in the superfluid phase

We have argued that the superfluid phase is a gapless SPT phase. Here we discuss the excitations in the phase: vortices, Goldstone bosons, and domain walls. Since the $\mathbb{Z}_2$-gauging process amounts to projecting out the $\mathbb{Z}_2$-charged sector and adding the twisted sector to the theory and the process relates some order parameters to disorder parameters [33, 51], many physical properties of this new gapless SPT phase can be inferred directly from its superfluid parent state. As we have already seen above, the disorder parameter $|\langle \hat{X}_R(\theta) \rangle|$ for $\tilde{U}(1)$ is a (fractional) order parameter for the dual $\hat{\mathbb{Z}}_2$. Similarly, $|\langle b_i^\dagger (\prod_{e \in \gamma_{ij}} \sigma_e^z) b_j \rangle|$ where $\gamma_{ij}$ connects sites $i$ and $j$ (Fig. 5(c)), viewed as a disorder parameter for the dual $\hat{\mathbb{Z}}_2$, serves as a (fractional) order parameter for $\tilde{U}(1)$.

To guarantee the exactness of the 1-form symmetry, we imposed the zero-flux condition $\prod_{e \in \partial p} \sigma_e^z = 1$, which suppresses all (dynamical) $\pi$-vortices excitations. Equivalently, an open 't Hooft line which would end on a pair of $\pi$-vortices (Fig. 5(c)) are also suppressed. In the Higgs phase, the condensate phase $\varphi$ is locked to the vortcies. The dual 1-form symmetry measures the $\mathbb{Z}_2$ winding of condensate phase $\varphi$, which takes values in $n\pi$ for integer $n$ modulo 2, along noncontractible cycles, which is equivalent to insertions of $\pi$-fluxes across noncontractible cycles (see Fig. 5(d)). We should compare the scenario with that in the "parent" superfluid phase before gauging where there is an emergent 1-form $U(1)$ symmetry in the low energy sector [22, 56, 57]. Charged objects of the emergent $U(1)$ are the winding of $\varphi$, taking values in $2n\pi$ for integer $n$. $2\pi$-vortices explicitly breaks this emergent dual $U(1)$ 1-form symmetry. However, since they are neutral under the dual $\hat{\mathbb{Z}}_2$ 1-form symmetry $W$ after the effective gauging, they do not destroy the exactness of the dual $\hat{\mathbb{Z}}_2$ 1-form symmetry.

Being put on a torus, the gapless Goldstone modes can be effectively decomposed into two parts: $\varphi = \varphi_{n,m} + \delta\varphi$, where the first term denotes winding of $n\pi$ and $m\pi$ along the two noncontractible cycles separately and the second term is the small fluctuation with respect to this configuration. Thus the topology of the Goldstone modes can be captured by the 1-form charges. It is very tempting to compare it with the topology of Goldstone modes after a continuous symmetry $G$ is spontaneously broken to a subgroup group $H$ [58]. There, the symmetry protection/enrichment of the Goldstone modes is discussed with respect to the residual symmetry $H$ (which in our case corresponds to the quotient symmetry $\tilde{U}(1)$) while the topology in the SPT phase we are studying is associated with the dual 1-form symmetry.

In the decomposition of $\varphi$ above, $n$ and $m$ label the twisted sector, and $\delta\varphi$ is neutral under the 1-form symmetry generated by $W$. Nevertheless, we may locally deform $\delta\varphi$ to some separate $\tilde{\theta}$-domain walls where locally its value jumps by $\tilde{\theta}$. Similar to the 1-D case and the discrete case, by assuming fusion linearity, we may *for-*

*mally* assign a charge $\tilde{\theta}/\pi$ for $0 \leq \tilde{\theta} \leq \pi$ under the dual 1-form symmetry to a domain wall where $\delta\varphi$ changes by $\tilde{\theta}$. This is a manifestation of the mixed anomaly and the symmetry fractionalization. In the superfluid/Higgs phase, $\delta\varphi$ is small such that the winding numbers of $\varphi$ is conserved. Proliferation of the winding, and equivalently the inserted fluxes, breaks the $\hat{\mathbb{Z}}_2$ 1-form symmetry and recovers the $\tilde{U}(1)$ simultaneously, leading to a SET phase.

## D. SET phase

Having discussed the SPT phase, we now briefly touch upon the emergent $\tilde{U}(1)$-SET phase (Fig. 4(b)).

The SSB of a discrete higher-form symmetry leads to a topologically ordered phase [22, 23], a phase with long-range entanglement and ground state degeneracy depending on the topology of the base space. The SSB of the dual $\hat{\mathbb{Z}}_2$ 1-form symmetry leads to a $\mathbb{Z}_2$-topological ordered phase whose excitations are the same as Kitaev's toric code or (untwisted) quantum double model [59]. When OBC is used, the boundaries can be gapped [52, 60]. This phase is also enriched by the $\tilde{U}(1)$ because the quotient $\tilde{U}(1)$ symmetry is preserved.

The topological charges are gauge charges $e$, $\pi$-fluxes $m$, and their bound state $em$. The last two types are not dynamical due to the exactness of the 1-form symmetry, or equivalently the zero-flux condition. Since $\tilde{U}(1)$ does not commute anyon types, there is no obstruction to the symmetry fractionalization [61]. Hence, it is classified by $[w] \in H^2(\tilde{U}(1), \mathcal{A})$ where $\mathcal{A}$ is the finite group whose elements are the Abelian topological charges of the unitary modular tensor category $\mathcal{C}$ with group multiplications given by their corresponding fusion rules [61]. In this case, $\mathcal{A} = \mathbb{Z}_2 \times \mathbb{Z}_2$, so $H^2(\tilde{U}(1), \mathcal{A}) = \mathbb{Z}_2 \times \mathbb{Z}_2$. Explicitly, a representative cocycle is given by $w(\theta, \theta') = m^{\lfloor \frac{\theta+\theta'}{2\pi} \rfloor}$, where $\theta, \theta' \in [0, 2\pi)$ parametrizes $\tilde{U}(1)$ and $\lfloor \cdot \rfloor$ is the floor function. The nontriviality of $w$, as a manifestation of the mixed anomaly we discussed above, dictates the fractionalization of charges under $\tilde{U}(1)$. Alternatively, the system can be viewed as living on the surface of a SPT phase in 3-D protected by $\tilde{U}(1)$ and $\hat{\mathbb{Z}}_2$. To trivially gap out the system, $\tilde{U}(1)$ has to be broken.

## E. Generalized DQCP

As we have discussed above, even though $\pi$-vortices are suppressed once the zero-flux condition is enforced, the proliferation of topological phase winding excitations drives the SPT phase to the SET phase. Since the original superfluid-insulator transition is continuous and only a finite subgroup is gauged, we expect this inherited transition to be continuous as well [33]. Thus, we obtain a generalized DQCP from the gapless SPT phase with preserved $\hat{\mathbb{Z}}_2$ 1-form symmetry and broken $\tilde{U}(1)$ to a SET phase with $\tilde{U}(1)$ (see Fig. 4(b)).

As a result of partial gauging of a finite group, much of the information encoded in the order/disorder parameters can be directly read from the original superfluid-insulator transition. The critical point can be determined by the change in the scaling laws of different order/disorder parameters. The symmetry breaking of higher-form symmetries at critical points has been investigated in the recent literature [62–64]. If all symmetries involved including the higher-form symmetry are preserved at the critical point in some systems, we may get a 2-D analogue of the intrinsically gapless SPT in 1-D by invoking similar anomaly arguments.

This generalized DQCP is essentially the same as the so-called $XY^*$ transition obtained from the conventional 3-D $XY$ critical point [50, 65]. The difference is that it is $\psi \sim bb$ rather than $b$ that is treated as the fundamental degree of freedom [65]. At the $XY^*$ transition, $b$ undergoes an ordinary $XY$ transition. Since $\psi$ is a composite operator of two $b$'s, the power law scaling exponent of $\langle \psi_i^\dagger \psi_j \rangle$ gets significantly modified $\eta_{bb} \sim 1.49$ from $\eta_b \sim 0.03$ for $b$. The divergence of the correlation length $\nu \sim 0.67$ and the isotropy of the space and time dimensions $z \sim 1$ were verified to be the same as in the conventional 3-D $XY$ universality class. These statements were verified numerically [65].

In terms of entanglement entropy $S_R$ of a smooth simply connected region $R$ without corners, it is known that, other than the leading perimeter law term $S_A \propto l \equiv |\partial R|$, there is a logarithmic subleading correction in a SSB phase of a continuous symmetry [66] and a topological subleading correction in a topologically ordered phase [67, 68]. At the critical point, $S_A$ takes the form of $S_A = \alpha l - \beta$ with $\beta = \beta_{XY} + \beta_{\mathbb{Z}_2}$. Here $\beta_{XY}$ comes from the ordinary $XY$ transition, i.e. SSB of $U(1)$, and $\beta_{\mathbb{Z}_2} = \ln 2$ is the topological entanglement entropy of the $\mathbb{Z}_2$ topologically ordered phase [50].

If we consider OBC, there is also a generalized boundary phase transition between the gapless SPT/Higgs phase and the $\tilde{U}(1)$-enriched topological phase. It would be interesting to investigate this boundary phase transition.

### F. Perturbations

In the above discussion, we have imposed the zero-flux condition by taking $g \to 0$ in order to preserve the exactness of the dual 1-form. The existence of the $\sum \sigma_i^x$ term in Eq. (17) explicitly breaks this symmetry. However, we expect the perturbation changes neither the topological order in the SET phase nor the gapless boundary modes in the SPT phase in 2-D due to the robustness of higer-form symmetries [23]. In particular, in the original Fradkin-Shenker phase diagram for 2-D Ising gauge theory coupled to matter with PBC, both the deconfined phase, the Higgs phase and the transition in between are robust with the introduction of the small polarizing field. To study the edge physics, the authors in Ref. [27]

numerically demonstrated the robustness of the topological edge modes in the SPT/Higgs phase. On the other hand, the robustness of $\mathbb{Z}_2$ topological order with open boundaries under perturbation is also numerically investigated in Ref. [69]. Based on their results, the robustness depends both on the boundary type (rough or smooth) and the perturbation type ($\sigma^x$ or $\sigma^z$). For rough boundaries (see Fig. 5(a)) and perturbations of the form $\sigma^x$, the topological order is robust. It is natural to expect resilience in the edge physics.

Based on the robustness of both phases, it is also natural to expect the SPT/Higgs-SET transition to remain continuous and robust, even with small perturbations that explicitly break the 1-form symmetry. In this case, we can regard the 1-form symmetry to be emergent [70], and the properties of the generalized DQCP should remain intact. In this sense, generalized DQCPs can be a generic type of quantum criticalities and deserve to be investigated in more details in future work.

### G. Experimental realizations

The Bose-Hubbard model in 1-D and higher dimensions has been realized in such systems as cold atoms on optical lattices [71–76], and the continuous superfluid-insulator transition has been observed. Lattice gauge theories have also been simulated in such systems [77–79]. Recently, the $\mathbb{Z}_2$ topological order has been realized and measured in Rydberg atoms on a 2-D Ruby lattice [80, 81]. It is more complicated to simulate gauged matter theories, but there are also some recent experimental progress in this direction. For example, a similar $\mathbb{Z}_2$-gauge Bose-Hubbard model in 2-D was studied in Ref. [82] with the idea of realizing the gauge constraints by using simplified local pseudogenerators [83]. We believe quantum simulation with cold atoms is a promising platform to realize the unconventional phases and quantum criticalities proposed in this work.

Realizations of the gapless SPT phases and the generalized DQCPs discussed in our work may be also possible in other solid state systems. For example, since the generalized DQCP is essentially the $XY^*$ transition studied before [65, 84], we may start with an ordinary Bose-Hubbard system with fractionalized excitations. As long as the low energy effective theory is described by an emergent $\mathbb{Z}_2$-gauged Bose-Hubbard model, we may test the analysis in our work.

A recent trend in the past few years has been realizing the gauging process by using finite-depth unitaries, measurement, and feedforward so topological ordered states can be obtained efficiently [85–88]. Other phases such as Higgs phases [89] and continuous symmetry breaking states [90], and phase transitions [91, 92] have been proposed. Some SET phases can also be obtained by partial gauging [93]. Realizing a SET phase by partially gauging a $U(1)$ symmetry is also very natural. To simulate and study a gapless SPT phase and the generalized DQCP

discussed in this work in these adaptive circuits is a fascinating direction.

## V. CONCLUSIONS

In this work, we investigated the emergent $\mathbb{Z}_2$-gauged matter theory of the 1-D and 2-D Bose-Hubbard model coupled to Ising degrees of freedom. We analyzed the inherited phase diagram from that of the ungauged superfluid-insulator version. In 1-D, we identified the superfluid phase to be an intrinsically gapless SPT phase protected by $W \times U(1)$, $W$ being the Ising spin reflection symmetry. In the low energy theory, $W$ can be viewed as the dual $\hat{\mathbb{Z}}_2$ symmetry. We discussed the effective action which includes a mixed anomaly term between $W$ and the quotient $\tilde{U}(1)$ symmetry $\omega$, and a topological term $\alpha$ dictating the edge degrees of freedom if there is an open boundary. The 't Hooft anomaly in $\alpha$ is matched by that in $\omega$. We argued that the gapless SPT phase is described by a $\mathbb{Z}_2$-gauged compact boson CFT, which is also supported by DMRG computations. In 2-D, we focused on the zero-flux limit and concluded, by adapting the "Higgs = SPT" argument, that the superfluid phase is also a gapless SPT protected by higher form symmetries whose gaplessness comes from the Goldstone modes due to the SSB of the quotient $\tilde{U}(1)$. We studied the excitations, especially the Goldstone modes whose winding number is related to the charge of the $\tilde{U}(1)$ domain wall under the dual $\hat{\mathbb{Z}}_2$ 1-form symmetry $W$, which is a direct manifestation of the mixed anomaly between the two symmetries. The other phase is the insulating phase corresponding to the SSB of the $W$ with $\tilde{U}(1)$ preserved, i.e. $\tilde{U}(1)$-enriched $\mathbb{Z}_2$ topological order. Then we analyzed the transition between the gapless SPT/Higgs phase and the $\tilde{U}(1)$-SET phase, which is a generalized DQCP. The robustness of the gapless SPT/Higgs phase, the SET phase, and the generalized DQCP between them toward perturbations that explicitly break the $\hat{\mathbb{Z}}_2$ 1-form symmetry is discussed. Possible experimental realizations using quantum simulations with cold atoms are also proposed.

The idea of partially gauging a finite subgroup discussed in this work is straightforward and general. In principle, we can start with any system that has a SSB of a generic continuous symmetry, including generalized symmetries, and then perform the partial gauging to arrive at novel phases and phase transitions in between. The system can even be topological at the outset. Extension to higher dimensions is straightforward. The colluding roles of the topological term $\alpha$ and the emergent anomaly $\omega$ in constructing general (intrinsically) gapless SPT phase deserve further elaboration. It would also be interesting to study deformations of the gapless SPT phases away from their fixed-point so that the edge localization length $\xi_e$ is not strictly zero.

As we have mentioned earlier on, our analysis generalizes easily to fermionic systems. In particular, the 1-D intrinsically gapless SPT phase works for a free fermion gas or a Luttinger liquid and is generalizable to generic critical point or a Fermi liquid in higher dimensions. Generically, introduction of a weakly fluctuating gauge field may destabilize the system and drive the system to other phases, such as superconductors. It would be interesting to construct such a stable intrinsically gapless fermionic SPT phase. A good starting point may be exactly solvable models of free lattice fermions coupled to Ising spins on the link. When it is not analytically solvable, numerical simulations using, e.g., the determinant quantum Monte Carlo method similar to Refs. [94, 95] can give us more valuable insights. We hope our work can stimulate more endeavors along these directions.

## Appendix A: Emergent $\mathbb{Z}_2$-gauged $q$-state clock model

In the main text, we focused on the case where the $\mathbb{Z}_2$ subgroup of the continuous $U(1)$ is effectively gauged. Some of the properties we discussed there can already be found when the total symmetry group is discrete. In this appendix, we present similar analysis of the $q$-state clock model with discrete on-site $\mathbb{Z}_q$ symmetry. We focus on even $q$ cases, so that there exists a $\mathbb{Z}_2$ subgroup that can be subsequently gauged. Both 1-D and 2-D cases are discussed.

### 1. 1-D

For the Ising model, i.e. when $q = 2$, gauging the $\mathbb{Z}_2$ is equivalent to a Kramers-Wannier transformation from the original Ising model to the dual Ising model with a dual 0-form $\hat{\mathbb{Z}}_2$ symmetry. The minimal non-trivial case corresponds to $q = 4$, which is also discussed in Refs. [33, 34]. The $\mathbb{Z}_2$-gauged 4-state clock model has global symmetry $\tilde{\mathbb{Z}}_2 \times \hat{\mathbb{Z}}_2$ with a mixed anomaly between the two symmetries characterized by the non-trivial extension class in $H^2(\tilde{\mathbb{Z}}_2, \hat{\mathbb{Z}}_2) = \mathbb{Z}_2$. A concrete lattice model

can be written down as follows,

$$H = - J \sum_j \left( C_j^\dagger \tau_{j+1/2}^z C_{j+1} + h.c. \right) - h \sum_j \left( S_j + S_j^\dagger \right)$$
$$- K \sum_j \tau_{j-1/2}^x S_j^2 \tau_{j+1/2}^x, \tag{A1}$$

where $C_j^4 = S_j^4 = 1$ and $C_j S_j = e^{i\frac{2\pi}{4}} S_j C_j$. We fix $J = 1$. Similar to the case in the main text, we have a minimal coupling between clock degrees of freedom on sites and Ising spins on bonds, where the large $K$ limit effectively implements the gauging with the gauge constraint given by $G_j = \tau_{j-1/2}^x S_j^2 \tau_{j+1/2}^x = 1$. The global symmetry is $V \times W$, with

$$V = \prod_j S_j, \quad W = \prod_j \tau_{j+1/2}^z, \tag{A2}$$

where at low energy $W$ becomes the dual $\hat{\mathbb{Z}}_2$ symmetry and $V$ is the quotient symmetry. There is a subtlety for the $V$ symmetry when there is an open boundary. For periodic boundary condition (PBC), we have $V^2 = \prod_j S_j^2 = \prod_j \tau_{j-1/2}^x \tau_{j+1/2}^x = 1$, by using the low energy gauge constraint, making $V$ explicitly $\mathbb{Z}_2$. However, for open boundary condition (OBC), we have instead the nontrivial identity $V^2 = \tau_{1/2}^x \tau_{L+1/2}^x$. Here $L$ is the number of sites in the open chain.

In the case of $h \gg 1$, $S_j$ will be polarized, which implies that $\langle \tau_{m-1/2}^x \tau_{n+1/2}^x \rangle = \prod_{m \le j \le n} S_j^2 \ne 0$, i.e. there is long range order in $\tau^x$, leading to SSB of $W$ while $V$ is preserved. On the other hand, when $h \ll 1$, there will be SSB in $V$ but with $W$ preserved. The SSB in $V$ directly inherits from the SSB of the ungauged clock model, since the $\mathbb{Z}_2$ gauging corresponds to summing over twisted boundary conditions, which does not change the long-range correlation of the order parameter [33, 34]. Due to the SSB of $V$, which is simply $\tilde{\mathbb{Z}}_2$ in the bulk, the ground state is 2-fold degenerate $|\psi_1\rangle$ and $|\psi_2\rangle$ with $V|\psi_1\rangle = |\psi_2\rangle$.

Furthermore, in the $V$ SSB phase, for either of the degenerate ground state $|\psi_\alpha\rangle$, there is non-trivial string order parameter given by $\langle C_m^\dagger \tau_{m+1/2}^z ... \tau_{n-1/2}^z C_n \rangle \ne 0$, signifying that the $V$ SSB phase is in fact the Higgs/SPT phase [27]. To see the non-trivial edge states, we consider a semi-infinite chain with one open boundary at site $L$. Then we have $V^2 = \tau_{L+1/2}^x$, so that $V^2 W = -W V^2$. For a ground state $|\psi_\alpha\rangle$, both $V^2$ and $W$ are symmetries. Due to the anti-commutation of the two symmetry operators, we can similarly argue that $V^2|\psi_\alpha\rangle$ and $|\psi_\alpha\rangle$ are degenerate and the degeneracy comes from the edge since $V^2$ is localized at the edge. This way, we explicitly see the edge degeneracy for each of the bulk degenerate ground states.

The analogue of the intrinsically gapless SPT of the $U(1)$ case shows up when $q \ge 5$. It is known that the 1-D quantum clock model without gauging has two critical points, both are of BKT type and dual to each other,
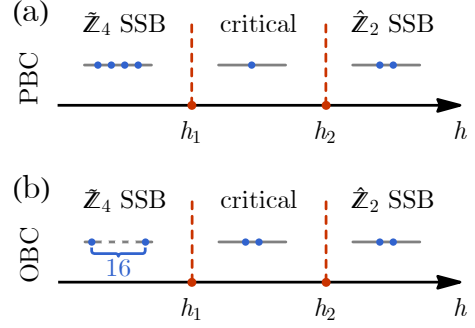


FIG. 6: Ground state degeneracy in different phases of the 1-D $\mathbb{Z}_8$-clock model with its $\mathbb{Z}_2$ subgroup gauged, under PBC (a) and under OBC (b).

and there is a critical phase with emergent $U(1)$ symmetry in between the two critical points [96]. The minimal non-trivial case with mixed anomaly after gauging is the 8-state clock model. After gauging, the emergent symmetry is $\tilde{\mathbb{Z}}_4 \times \hat{\mathbb{Z}}_2$, where there is a mixed anomaly characterized by the non-trivial extension class in $H^2(\tilde{\mathbb{Z}}_4, \hat{\mathbb{Z}}_2) = \mathbb{Z}_2$.

Fig. 6 shows the schematic phase diagram with the corresponding ground state degeneracies under both PBC and OBC. In the large $h$ limit, the dual $\hat{\mathbb{Z}}_2$ symmetry is spontaneously broken, which is labeled as the $\hat{\mathbb{Z}}_2$ SSB phase. In the small $h$ limit, we have the $\tilde{\mathbb{Z}}_4$ SSB phase. In the intermediate coupling regime ($h_1 < h < h_2$), the system is in a critical phase, where both of the two symmetries are preserved. There is an emergent symmetry $U(1) \times U(1) \supset \tilde{\mathbb{Z}}_4 \times \hat{\mathbb{Z}}_2$ and the critical phase is described by the ($\mathbb{Z}_2$-gauged) compact boson CFT. Indeed, this phase is an analogue of the intrinsically gapless SPT phase we discussed in the main text.

### 2. 2-D

For 2-D $q$-state clock model, the Hamiltonian takes similar form with that of the $\mathbb{Z}_2$-gauged Bose-Hubbard model described in the main text,

$$H = - J \sum_{i,j \in \partial e} \left( C_i^\dagger \tau_e^z C_j + h.c. \right) - h \sum_j \left( S_j + S_j^\dagger \right)$$
$$- \frac{1}{g} \sum_p \prod_{e \in \partial p} \tau_e^z - g \sum_e \tau_e^x$$
$$- K \sum_j S_j^{q/2} \prod_{e,j \in \partial e} \tau_e^x, \tag{A3}$$

where $C_j^q = S_j^q = 1$ and $C_j S_j = e^{i\frac{2\pi}{q}} S_j C_j$. We fix $J = 1$. In the zero flux limit $g \to 0$ and large $K$ limit, the global symmetries are the quotient 0-form $\tilde{\mathbb{Z}}_{q/2}$ and the 1-form

$\hat{\mathbb{Z}}_2$, given by,

$$V = \prod_j S_j, \quad W = \prod_{e \in \gamma} \tau_e^z, \quad \text{(A4)}$$

where $\gamma$ is a loop running along the bonds of the lattice. Notice that in order for there to be an emergent mixed anomaly between $V$ and $W$, the group extension of $V$ by $W$, classified by $H^2(\tilde{\mathbb{Z}}_{q/2}, \hat{\mathbb{Z}}_2) = \mathbb{Z}_{\gcd(q/2,2)}$ has to be non-trivial, meaning that $q/2$ has to be even, i.e. $q$ is an integer multiple of 4. Similar to the 1-D case, due to the mixed anomaly between $V$ and $W$, $W$ is SSB while $V$ is preserved when $h \gg 1$. This is the $\mathbb{Z}_2$ topological order enriched by $\tilde{\mathbb{Z}}_{q/2}$, classified by $H^2(\tilde{\mathbb{Z}}_{q/2}, \mathbb{Z}_2 \times \mathbb{Z}_2) = \mathbb{Z}_{\gcd(q/2,2)} \times \mathbb{Z}_{\gcd(q/2,2)}$.

When $h \ll 1$, we have SSB for $V$ with $W$ preserved. Therefore, the bulk is $q/2$-fold degenerate, and each degenerate ground state has additional degenerate edge states when there is an open boundary. The argument is the same by considering the two anti-commuting symmetries $V^{q/2}$ and $W$ of the ground states. Therefore, this is again the Higgs/SPT phase. The $\tilde{\mathbb{Z}}_{q/2}$-enriched topological order and the $\hat{\mathbb{Z}}_2$ 1-form protected SPT with $q/2$-fold bulk degeneracy are separated by a generalized DQCP.

## Appendix B: Elimination of gauge constraints

In the main text, based on the mixed anomaly between the quotient $\tilde{U}(1)$ symmetry and the dual 1-form $\hat{\mathbb{Z}}_2$ symmetry in the emergent gauge theory, we claimed that these two symmetries cannot both be on-site. This can be demonstrated easily by eliminating the gauge constraints. The elimination may be achieved by performing a unitary transformation consisting of controlled gates and Hadamard transformations [97]. Here we follow Ref. [33] to gain more intuition.

After gauging, i.e. implementing the gauge condition $\prod_{e, i \in \partial e} \sigma_e^x = (-1)^{n_i}$, the onsite boson states are divided into the boson parity even sector and the parity odd sector, depending on the sign of the star operator $\prod_{e, i \in \partial e} \sigma_e^x$. Therefore, the new onsite boson basis can be denoted as $|1, \tilde{n}\rangle$ and $|-1, \tilde{n}\rangle$, where the first number labels the onsite boson parity, determined by $\prod_{e, i \in \partial e} \sigma_e^x$, and the second number labels the new local boson states with $\tilde{n} = 0, 1, 2, ...$ in the corresponding sector. Notice that we have a one-to-one correspondence between the new basis and the original ungauged basis, given by $|1, \tilde{n}\rangle \leftrightarrow |2\tilde{n}\rangle$ and $|-1, \tilde{n}\rangle \leftrightarrow |2\tilde{n}+1\rangle$. Therefore, no degrees of freedom are lost, as it should be. Expressed in the new basis, the boson number operator becomes

$$\hat{n}_i \to \frac{1 + \prod_{e, i \in \partial e} \sigma_e^x}{2} 2\hat{\tilde{n}}_i + \frac{1 - \prod_{e, i \in \partial e} \sigma_e^x}{2}\left(2\hat{\tilde{n}}_i + 1\right)$$
$$= 2\hat{\tilde{n}}_i + \frac{1 - \prod_{e, i \in \partial e} \sigma_e^x}{2}. \quad \text{(B1)}$$

The action of the boson creation/annihilation operator should be accompanied with a flip in $\prod_{e, i \in \partial e} \sigma_e^x$ since $(-1)^{n_i}$ changes sign. Consider the gauge invariant minimal coupling term $b_i^\dagger \sigma_{e_{ij}}^z b_j$. In the new basis,

$$b_i^\dagger \sigma_{e_{ij}}^z b_j \to A_i \sigma_{e_{ij}}^z B_j. \quad \text{(B2)}$$

where

$$A_i \equiv \frac{1 + \prod_{e, i \in \partial e} \sigma_e^x}{2} + \frac{1 - \prod_{e, i \in \partial e} \sigma_e^x}{2}\tilde{b}_i^\dagger,$$
$$B_i \equiv \frac{1 + \prod_{e, i \in \partial e} \sigma_e^x}{2}\tilde{b}_i + \frac{1 - \prod_{e, i \in \partial e} \sigma_e^x}{2}. \quad \text{(B3)}$$

In the new basis, the action of the dual 1-form $\hat{\mathbb{Z}}_2$ symmetry remains unchanged as $W = \prod_{e \in \gamma} \sigma_e^z$ for closed loop $\gamma$, but the $\tilde{U}(1)$ symmetry is now implemented by

$$\tilde{X}(\theta) = \prod_i \exp\left[i\left(2\hat{\tilde{n}}_i + \frac{1 - \prod_{e, i \in \partial e} \sigma_e^x}{2}\right)\frac{\theta}{2}\right], \quad \text{(B4)}$$

which is explicitly non-onsite. It is easy to see that $\tilde{X}(\theta) = \tilde{X}(\theta + 2\pi)$ for PBC. Combining Eq. (B1) and (B2), we can obtain the Hamiltonian of the Bose-Hubbard model (with the zero-flux condition) expressed in the new basis where the gauge constraints have already been encoded.

Note that the quantity $\hat{\tilde{N}} = \sum_i \hat{\tilde{n}}_i$ itself is not conserved. Instead, the term $(1 - \prod_{e, i \in \partial e} \sigma_e^x)/2$ contributes a fractional charge $1/2$ to $\hat{\tilde{N}}$. By invoking the "electromagnetic duality" for the $\mathbb{Z}_2$ gauge field: $\sigma^x \leftrightarrow \sigma^z$, we can regard the zero-flux condition $\prod_{e \in \partial p} \sigma_e^z = 1$ as the new "Gauss law" for the "gauge field" $\sigma^x$ while $\prod_{e, i \in \partial e} \sigma_e^x$ as the new "magnetic" flux operator. Thus, the new magnetic flux carries a fractional charge under $\hat{\tilde{N}}$, a manifestation of the mixed anomaly. Since the anomalous system may be viewed as a boundary of a SPT phase in the (3+1)-D bulk, as mentioned in Ref. [33], it is natural to envision a discrete realization of the bulk by decorating the magnetic monopoles of the $\hat{\mathbb{Z}}_2$ gauge field with unit charges under $\tilde{U}(1)$, which is an analogue of the continuum construction in Ref. [98].

## Appendix C: Grand canonical ensemble in 1-D

In Sec. III, we used canonical enemble (CE) in 1-D for simplicity since the particle number conservation cannot be violated due to the Mermin-Wagner theorem. In this appendix, we support this statement by presenting some DMRG results for the $\mathbb{Z}_2$-gauged Bose-Hubbard model in the context of grand canonical ensemble (GCE) where the total particle number can vary. GCE is more general and it allows energy levels consisting of both even and odd parity states (see Fig. 7(a)). The existence of states with different parities is a consequence of the boundaries when using OBC, where the parity operator $P = \sigma_{1/2}\sigma_{L+1/2}$

can still take values $\pm 1$. However, GCE is computationally more challenging in DMRG since particle number is not fixed. On the other hand, we observed numerically that as long as the chemical potential $\mu$ is carefully tuned to ensure unit filling for the GCE ground state, both the ground state and the next excited state have no fluctuations in total boson number, i.e. they have fixed boson number. A nice consequence of this observation is that the GCE low energy states can now be related to those of the CE, which renders the numerical calculation easier and more tractable for larger system sizes. We can still show that the superfluid phase is a gapless SPT phase with double degeneracy.

The GCE Hamiltonian $H_{\text{GCE}}(\mu, \hat{N})$ is related to the CE Hamiltonian $H_{\text{CE}}(\hat{N})$ as the following,

$$H_{\text{GCE}}(\mu, \hat{N}) = H_{\text{CE}}(\hat{N}) - \mu \hat{N}, \qquad \text{(C1)}$$

where $\hat{N}$ is the total boson number operator. As mentioned previously, the chemical potential $\mu$ can be tuned to achieve a ground state with unit filling and fixed boson number, i.e. $\langle \hat{N} \rangle = L$ in the ground state. Here $L$ is the number of boson sites which for simplicity is taken to be even. Notice, however, that the proper $\mu$ has a strong size dependence. To carry out a finite size scaling of the gap, we extract the thermodynamical information by bounding the gap as follows.

For a typical set of parameters both the gap in the parity even sector $\Delta_{\text{GCE}}^{P=+1}$ and the gap in the parity odd sector $\Delta_{\text{GCE}}^{P=-1}$ are much larger than the true gap $\Delta_{\text{GCE}}$ which is between a parity even state and a parity odd state (Fig. 7(a)). Note that the ground state is exactly doubly degenerate as in the CE. The GCE ground state energy is given by,

$$E_{\text{GCE}}(\mu, L) = E_{\text{CE}}(L) - \mu L, \qquad \text{(C2)}$$

and satisfies the following conditions,

$$E_{\text{GCE}}(\mu, L) \leq E_{\text{GCE}}(\mu, L \pm 1), \qquad \text{(C3)}$$

which implies

$$\begin{aligned} \mu_L &\equiv E_{\text{CE}}(L) - E_{\text{CE}}(L-1) \\ &\leq \mu \leq E_{\text{CE}}(L+1) - E_{\text{CE}}(L) \equiv \mu_U. \end{aligned} \qquad \text{(C4)}$$

Fig. 7(b) shows the system size dependence of the lower and upper bounds of the chemical potential based on Eq. (C4). The two bounds converge to $\mu_\infty \approx -0.254$ in the thermodynamic limit, which is also reflected in the inset showing the difference between the bounds approaching 0.

Both $\Delta_{\text{GCE}}^{P=\pm 1}$ decay to zero following a power law $1/L$. Furthermore, the true gap is given by

$$\begin{aligned} \Delta_{\text{GCE}} &= \min\{E_{\text{GCE}}(\mu, L+1) - E_{\text{GCE}}(\mu, L), \\ &\qquad E_{\text{GCE}}(\mu, L-1) - E_{\text{GCE}}(\mu, L)\} \\ &= \min\{\mu_U - \mu, \mu - \mu_L\} \\ &\leq \mu_U - \mu_L. \end{aligned} \qquad \text{(C5)}$$
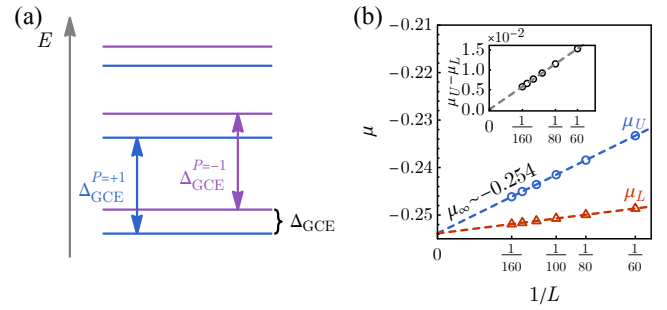


FIG. 7: (a) Schematic diagram for the energy levels in the grand canonical ensemble, where parity even and parity odd states coexist. $\Delta_{\text{GCE}}^{P=\pm 1}$ is the gap in the parity even/odd sector and $\Delta_{\text{GCE}}$ is the true gap above the doubly degenerate ground state. (b) The upper bound $\mu_U$ and the lower bound $\mu_L$ for the chemical potential in order to have unit filling at different system sizes. The inset shows the difference between the two bounds. The parameters used are $t = 0.5, U = 1.0$.

Since $\mu_U - \mu_L$ is shown to decay to 0 in the thermodynamic limit as $1/L$ (see inset of Fig. 7(b)), the bulk gap $\Delta_{\text{GCE}}$ also decays to 0 at least as fast as $1/L$.

## Appendix D: Anomaly action

In this appendix, we provide more details regarding the 't Hooft anomalies that show up in the main text. We will emphasize the comparison between the mixed anomaly from gauging a finite subgroup [31] and the emergent anomaly through separation of gapped and gapless degrees of freedom [18].

Consider the following central extension

$$1 \to \mathbb{Z}_2 \xrightarrow{i} U(1) \xrightarrow{\pi} \tilde{U}(1) \to 1. \qquad \text{(D1)}$$

Here $i$ is inclusion and $\pi$ is projection. The extension corresponds to the nontrivial element $e$ in $H^2(\tilde{U}(1), \mathbb{Z}_2) = \mathbb{Z}_2$. To Let $G = U(1)$ be the total global symmetry free from anomalies. Then we can turn on a flat background gauge field $A^{U(1)}$ on a closed (1+1)-D spacetime $M$. Then

$$A^{U(1)} = i(A^{\mathbb{Z}_2}) + r(A^{\tilde{U}(1)}), \qquad \text{(D2)}$$

where $r$ lifts $A^{\tilde{U}(1)}$ into $A^{U(1)}$ and satisfies $\pi(r) = \text{Id}$. The flatness of $A^{U(1)}$ implies that the $A^{\mathbb{Z}_2}$ sees the flux of $A^{\tilde{U}(1)}$:

$$dA^{\mathbb{Z}_2} = e(A^{\tilde{U}(1)}) = \frac{dA^{\tilde{U}(1)}}{2\pi} \mod 2, \qquad \text{(D3)}$$

where we have omitted $r$ for simplicity. We can gauge the $\mathbb{Z}_2$ subgroup of $U(1)$ by making $A^{\mathbb{Z}_2}$ dynamical which we will denote as $a^{\mathbb{Z}_2}$. Then

$$da^{\mathbb{Z}_2} = e(A^{\tilde{U}(1)}) = \frac{dA^{\tilde{U}(1)}}{2\pi} \mod 2. \qquad \text{(D4)}$$

70

After gauging $\mathbb{Z}_2$, there is a dual quantum symmetry $\hat{\mathbb{Z}}_2$ showing up [99]. It can again be coupled to its background field $A^{\hat{\mathbb{Z}}_2}$ as follows

$$S = \pi i \int_M A^{\hat{\mathbb{Z}}_2} \cup a^{\mathbb{Z}_2}. \qquad (D5)$$

Since $a^{\mathbb{Z}_2}$ is not closed when $A^{\tilde{U}(1)}$ is nontrivial, as a result of Eq. (D4), there is an mixed anomaly between the dual symmetry $\hat{\mathbb{Z}}_2$ and quotient $\tilde{U}(1)$ which is characterized by an anomaly action in a (2+1)-D dimensional bulk $Y$

$$\omega = \frac{1}{2} A^{\hat{\mathbb{Z}}_2} \cup da^{\mathbb{Z}_2} = \frac{1}{2} A^{\hat{\mathbb{Z}}_2} \cup \frac{dA^{\tilde{U}(1)}}{2\pi}, \qquad (D6)$$

where $A^{\hat{\mathbb{Z}}_2}$ and $A^{\tilde{U}(1)}$ are extended to the bulk $Y$. When $M = \partial Y$, the anomaly is canceled. In the main text, the gauge theory is emergent, so the mixed anomaly is also emergent in the low energy theory.

In Ref. [18], the $\mathbb{Z}_2$ group is not gauged but gapped out by interactions in the sense that $\mathbb{Z}_2$ only acts nontrivially on the gapped degrees of freedom while $\tilde{U}(1)$ is the symmetry that acts nontrivially on the low energy degrees of freedom. Turning on the background fields, we arrive at Eq. (D3) as well. If the symmetry $\tilde{U}(1)$ acting on the gapless degrees of freedom has an emergent anomaly, it is possible to construct a gapless SPT phase.

In particular, if $U(1)$ is broken to $\mathbb{Z}_4$, then since $H^2(\mathbb{Z}_4, U(1)) = 0$, there is no gapped SPT phase in 1-D. However, an intrinsically gapless SPT phase can exist when there is an emergent anomaly, which is captured by

$$\omega = \frac{1}{2} A^{\mathbb{Z}_2} \cup dA^{\mathbb{Z}_2} \qquad (D7)$$

in the higher-dimensional bulk $Y$. Indeed, since the total symmetry group $G = \mathbb{Z}_4$ is anomaly-free, the low energy anomaly $\omega(A^{\mathbb{Z}_2})$ must be compensated by a counterterm $\alpha(A^{\mathbb{Z}_2}, A^{\tilde{\mathbb{Z}}_2})$ satisfying the anomaly vanishing equation [18]

$$\omega(A^{\mathbb{Z}_2}) = d\alpha(A^{\mathbb{Z}_2}, A^{\tilde{\mathbb{Z}}_2}). \qquad (D8)$$

Here $A^{\tilde{\mathbb{Z}}_2}$ is the background field of the quotient symmetry $\tilde{\mathbb{Z}}_2 \equiv \mathbb{Z}_4/\mathbb{Z}_2$ acting on the gapped degrees of freedom. The partition function then may be written as

$$Z = e^{2\pi i \int_Y \omega(A^{\mathbb{Z}_2})} e^{-2\pi i \int_M \alpha(A^{\mathbb{Z}_2}, A^{\tilde{\mathbb{Z}}_2})}. \qquad (D9)$$

One solution to the anomaly vanishing equation is given by $\alpha(A^{\mathbb{Z}_2}, A^{\tilde{\mathbb{Z}}_2}) = A^{\mathbb{Z}_2} \cup A^{\tilde{\mathbb{Z}}_2}/2$. The gauge invariance of the partition function under $A^{\mathbb{Z}_2} \to A^{\mathbb{Z}_2} + d\lambda^{\mathbb{Z}_2}$ then necessarily implies the existence of an edge mode of the 1-D system.

If the total symmetry is $G = \mathbb{Z}_2' \times U(1)$, the $\mathbb{Z}_2$ subgroup of $U(1)$ can be gapped so that the symmetry acting

on the gapless degrees of freedom is $\mathbb{Z}_2' \times \tilde{U}(1)$. If the low energy theory has a mixed anomaly

$$\omega = \frac{1}{2} A^{\mathbb{Z}_2'} \cup \frac{dA^{\tilde{U}(1)}}{2\pi}, \qquad (D10)$$

then the anomaly vanishing equation yields

$$\alpha = \frac{1}{2} A^{\mathbb{Z}_2'} \cup A^{\mathbb{Z}_2}. \qquad (D11)$$

Consequently, the gauge invariance of the partition function requires the existence of an edge mode. The form of $\omega$ and $\alpha$ is very similar to those we discussed in the main text. We also note that the similarity between Eq.(D6) and Eq.(D10).

In the main text, the $\mathbb{Z}_2$ subgroup of $U(1)$ is the parity $P = \prod_i (-1)^{n_i}$. Unlike the gapping mechanism in Ref. [18], in Sec. III A, $P$ is gapped out (when PBC is used) due to the emergent gauge constraints arising from the terms $-K \sum \sigma_{i-1/2}^x (-1)^{n_i} \sigma_{i+1/2}^x$ in the Hamiltonian when $K$ is large. $W = \prod_i \sigma_{i+1/2}^z$, a UV symmetry, effectively becomes the dual symmetry of $P$. Consequently, there is an emergent mixed anomaly $\omega$ between $W$ and $\tilde{U}(1)$ as in Eq.(D6). On the other hand, we argued in the main text that there is a term $\alpha = A^W \cup A^P/2$ that dictates the SPT edge modes. $P$ and $W$ being UV symmetries, the anomaly in $\alpha$ when $A^{\tilde{U}(1)}$ is not flat requires it to be canceled by other terms. Indeed, the emergent anomaly $\omega$ serves the purpose if $dA^P = da^{\mathbb{Z}_2} = \frac{dA^{\tilde{U}(1)}}{2\pi}$ mod 2 where $a^{\mathbb{Z}_2}$ is the emergent $\mathbb{Z}_2$ gauge field. Not surprisingly, the anomaly is identical to that in Eq.(D10) after we identify $W$ with $\mathbb{Z}_2'$. This explains the resemblance between Eq.(D6) and Eq.(D10).

There is a subtlety if $M$ has boundaries. Boundary conditions need to be chosen properly to guarantee the emergent (dynamical) gauge-invariance. In principle, the true symmetry acting on the gapless modes are $W$ and $\tilde{U}(1)$, regardless of whether OBC or PBC is used. In the main text, $P$ is interpreted as a UV symmetry, and thus physical. When PBC is used, it is fully gapped. When OBC is used, it also acts nontrivially on the low energy modes. The gauge-invarinace of $\alpha = A^W \cup A^P/2$ under $A^P \to A^P + d\lambda^P$ already implies the existence of edge modes when OBC is used, irrespective of the existence of the mixed anomaly. This is because $W$ can terminate on the edges such that $dA^W \neq 0$ mod 2. It is the delicate cooperation of both $\alpha$ and $\omega$ through 't Hooft anomalies that determines the nature of the intrinsically gapless SPT phase protected by $W$ and $U(1)$ as discussed in Sec. III.

The discussion above about the mixed anomaly between the quotient symmetry and the dual symmetry after gauging a finite subgorup can be generalized to arbitrary dimensions [31]. In $d$-D, the dual $\hat{\mathbb{Z}}_2$ symmetry is $(d-1)$-form, and the anomaly action is given by $\omega = \frac{i}{2} \int_Y A^{\hat{\mathbb{Z}}_2} \cup dA^{\tilde{U}(1)}$. Here, $A^{\hat{\mathbb{Z}}_2}$ is a $d$-form background field. If the symmetry $\hat{\mathbb{Z}}_2$ again coincides with a

UV symmetry $W$ and the gauge theory is emergent as we have discussed in the main text, we then again have a SPT phase with $\alpha = A^{\hat{\mathbb{Z}}_2} \cup A^{\mathbb{Z}_2}/2$, which is again canceled by $\omega$. If both $U(1)$ and $\hat{\mathbb{Z}}_2$ are preserved, then we may have a higher dimensional intrinsically gapless SPT phase. On the other hand, if $\tilde{U}(1)$ is spontaneously broken as in the Higgs phase, the SPT phase coexists with gapless Goldstone modes.

[1] T. Senthil, Deconfined quantum critical points: a review, arXiv:2306.12638 (2023), 2306.12638.

[2] X.-G. Wen, *Quantum field theory of many-body systems: from the origin of sound to an origin of light and electrons* (Oxford University Press, New York, 2004).

[3] M. Levin and T. Senthil, Deconfined quantum criticality and Néel order via dimer disorder, Phys. Rev. B **70**, 220403 (2004).

[4] M. A. Metlitski and R. Thorngren, Intrinsic and emergent anomalies at deconfined critical points, Phys. Rev. B **98**, 085140 (2018).

[5] X. Chen, Z.-C. Gu, Z.-X. Liu, and X.-G. Wen, Symmetry protected topological orders and the group cohomology of their symmetry group, Phys. Rev. B **87**, 155114 (2013).

[6] X.-G. Wen, Classifying gauge anomalies through symmetry-protected trivial orders and classifying gravitational anomalies through topological orders, Phys. Rev. D **88**, 045013 (2013).

[7] A. Vishwanath and T. Senthil, Physics of three-dimensional bosonic topological insulators: Surface-deconfined criticality and quantized magnetoelectric effect, Phys. Rev. X **3**, 011016 (2013).

[8] A. Kapustin and R. Thorngren, Anomalous discrete symmetries in three dimensions and group cohomology, Phys. Rev. Lett. **112**, 231602 (2014).

[9] A. Kapustin, Symmetry protected topological phases, anomalies, and cobordisms: beyond group cohomology, arXiv:1403.1467 (2014), 1403.1467.

[10] A. Kapustin and R. Thorngren, Anomalies of discrete symmetries in various dimensions and group cohomology, arXiv:1404.3230 (2014), 1404.3230.

[11] T. Senthil, Symmetry-protected topological phases of quantum matter, Annu. Rev. Condens. Matter Phys. **6**, 299 (2015).

[12] E. Witten, Fermion path integrals and topological phases, Rev. Mod. Phys. **88**, 035001 (2016).

[13] A. Keselman and E. Berg, Gapless symmetry-protected topological phase of fermions in one dimension, Phys. Rev. B **91**, 235309 (2015).

[14] T. Scaffidi, D. E. Parker, and R. Vasseur, Gapless symmetry-protected topological order, Phys. Rev. X **7**, 041048 (2017).

[15] R. Verresen, N. G. Jones, and F. Pollmann, Topology and edge modes in quantum critical chains, Phys. Rev. Lett. **120**, 057001 (2018).

[16] R. Verresen, R. Thorngren, N. G. Jones, and F. Pollmann, Gapless topological phases and symmetry-enriched quantum criticality, Phys. Rev. X **11**, 041059 (2021).

[17] R. Verresen, J. Bibo, and F. Pollmann, Quotient symmetry protected topological phenomena, arXiv:2102.08967 (2021), 2102.08967.

[18] R. Thorngren, A. Vishwanath, and R. Verresen, Intrinsically gapless topological phases, Phys. Rev. B **104**, 075132 (2021).

[19] L. Li, M. Oshikawa, and Y. Zheng, Decorated defect construction of gapless-SPT states, arXiv:2204.03131 (2022), 2204.03131.

[20] R. Wen and A. C. Potter, Bulk-boundary correspondence for intrinsically gapless symmetry-protected topological phases from group cohomology, Phys. Rev. B **107**, 245127 (2023).

[21] L. Li, M. Oshikawa, and Y. Zheng, Intrinsically/purely gapless-SPT from non-invertible duality transformations, arXiv:2307.04788 (2023), 2307.04788.

[22] D. Gaiotto, A. Kapustin, N. Seiberg, and B. Willett, Generalized global symmetries, J. High Energ. Phys. **2015** (2), 1.

[23] J. McGreevy, Generalized symmetries in condensed matter, Annu. Rev. Condens. Matter Phys **14**, 57 (2023).

[24] L. Bhardwaj, L. E. Bottini, L. Fraser-Taliente, L. Gladden, D. S. Gould, A. Platschorre, and H. Tillim, Lectures on generalized symmetries, arXiv:2307.07547 (2023), 2307.07547.

[25] S. Schafer-Nameki, ICTP lectures on (non-) invertible generalized symmetries, arXiv:2305.18296 (2023), 2305.18296.

[26] S.-H. Shao, What's done cannot be undone: TASI lectures on non-invertible symmetry, arXiv:2308.00747 (2023), 2308.00747.

[27] R. Verresen, U. Borla, A. Vishwanath, S. Moroz, and R. Thorngren, Higgs condensates are symmetry-protected topological phases: I. discrete symmetries, arXiv:2211.01376 (2022), 2211.01376.

[28] R. Thorngren, T. Rakovszky, R. Verresen, and A. Vishwanath, Higgs condensates are symmetry-protected topological phases: II. $U(1)$ gauge theory and superconductors, arXiv:2303.08136 (2023), 2303.08136.

[29] E. Fradkin and S. H. Shenker, Phase diagrams of lattice gauge theories with Higgs fields, Phys. Rev. D **19**, 3682 (1979).

[30] M. Levin and Z.-C. Gu, Braiding statistics approach to symmetry-protected topological phases, Phys. Rev. B **86**, 115109 (2012).

[31] Y. Tachikawa, On gauging finite subgroups, SciPost Phys. **8**, 015 (2020).

[32] J. Wang, X.-G. Wen, and E. Witten, Symmetric gapped interfaces of SPT and SET states: Systematic constructions, Phys. Rev. X **8**, 031048 (2018).

[33] L. Su, Boundary criticality via gauging finite subgroups: a case study on the clock model, arXiv:2306.02976 (2023), 2306.02976.

[34] C. Zhang and M. Levin, Exactly solvable model for a deconfined quantum critical point in 1d, Phys. Rev. Lett. **130**, 026801 (2023).

[35] Gauging the system with an odd parity is tantamount to gauging with a discrete torsion [99]. Since $H^2(\mathbb{Z}_2, U(1)) = 0$, all gauging processes are equivalent.

[36] V. Berezinskii, Destruction of long-range order in one-dimensional and two-dimensional systems having a continuous symmetry group I. classical systems, Sov. Phys. JETP **32**, 493 (1971).

[37] J. M. Kosterlitz and D. J. Thouless, Ordering, metastability and phase transitions in two-dimensional systems, J. Phys. C: Solid State Phys. **6**, 1181 (1973).

[38] V. A. Kashurnikov and B. V. Svistunov, Exact diagonalization plus renormalization-group theory: Accurate method for a one-dimensional superfluid-insulator-transition study, Phys. Rev. B **53**, 11776 (1996).

[39] T. D. Kühner and H. Monien, Phases of the one-dimensional Bose-Hubbard model, Phys. Rev. B **58**, R14741 (1998).

[40] T. D. Kühner, S. R. White, and H. Monien, One-dimensional Bose-Hubbard model with nearest-neighbor interaction, Phys. Rev. B **61**, 12474 (2000).

[41] N. D. Mermin and H. Wagner, Absence of ferromagnetism or antiferromagnetism in one- or two-dimensional isotropic Heisenberg models, Phys. Rev. Lett. **17**, 1133 (1966).

[42] Note that, due to the edge SSB that we will discuss later, the bulk magnetization remains finite, albeit small, for finite systems. In this plot, we have subtracted the expectation $\langle \sigma_i^x \rangle \langle \sigma_j^x \rangle$ and limited $r$ to be far away from the edges.

[43] M. Fishman, S. R. White, and E. M. Stoudenmire, The ITensor Software Library for Tensor Network Calculations, SciPost Phys. Codebases , 4 (2022).

[44] The reader may treat it simply as a wedge product.

[45] D. Harlow and H. Ooguri, Symmetries in quantum field theory and quantum gravity, Commun. Math. Phys. **383**, 1669 (2021).

[46] Generically, if $\Delta_{\mathrm{bdry}}$ also has a dependence on the system size, the edge degeneracy refers to an exponential decay or at least a decay faster than the bulk gap $\Delta_{\mathrm{bulk}}$ [13–15, 18].

[47] P. Ginsparg, Applied conformal field theory, arXiv hep-th/9108028 (1988), 9108028.

[48] P. Calabrese and J. Cardy, Entanglement entropy and conformal field theory, J. Phys. A: Math. Theor. **42**, 504005 (2009).

[49] W. Ji, S.-H. Shao, and X.-G. Wen, Topological transition on the conformal manifold, Phys. Rev. Res. **2**, 033317 (2020).

[50] B. Swingle and T. Senthil, Structure of entanglement at deconfined quantum critical points, Phys. Rev. B **86**, 155131 (2012).

[51] H. Moradi, Ö. M. Aksoy, J. H. Bardarson, and A. Tiwari, Symmetry fractionalization, mixed-anomalies and dualities in quantum spin models with generalized symmetries, arXiv:2307.01266 (2023), 2307.01266.

[52] S. B. Bravyi and A. Y. Kitaev, Quantum codes on a lattice with boundary, arXiv quant-ph/9811052 (1998), 9811052.

[53] M. B. Hastings and X.-G. Wen, Quasiadiabatic continuation of quantum states: The stability of topological ground-state degeneracy and emergent gauge invariance, Phys. Rev. B **72**, 045141 (2005).

[54] E. Lake, Higher-form symmetries and spontaneous symmetry breaking, arXiv:1802.07747 (2018), 1802.07747.

[55] Y.-C. Wang, M. Cheng, and Z. Y. Meng, Scaling of the disorder operator at $(2+1)d$ $U(1)$ quantum criticality, Phys. Rev. B **104**, L081109 (2021).

[56] L. V. Delacrétaz, D. M. Hofman, and G. Mathys, Superfluids as higher-form anomalies, SciPost Phys. **8**, 047 (2020).

[57] S. D. Pace, Emergent generalized symmetries in ordered phases, arXiv:2308.05730 (2023), 2308.05730.

[58] D. V. Else, Topological goldstone phases of matter, Phys. Rev. B **104**, 115129 (2021).

[59] A. Kitaev, Fault-tolerant quantum computation by anyons, Ann. Phys. **303**, 2 (2003).

[60] A. Kitaev and L. Kong, Models for gapped boundaries and domain walls, Commun. Math. Phys. **313**, 351 (2012).

[61] M. Barkeshli, P. Bonderson, M. Cheng, and Z. Wang, Symmetry fractionalization, defects, and gauging of topological phases, Phys. Rev. B **100**, 115147 (2019).

[62] X.-C. Wu, W. Ji, and C. Xu, Categorical symmetries at criticality, J. Stat. Mech. **2021**, 073101 (2021).

[63] X.-C. Wu, C.-M. Jian, and C. Xu, Universal features of higher-form symmetries at phase transitions, SciPost Phys. **11**, 033 (2021).

[64] Y.-C. Wang, N. Ma, M. Cheng, and Z. Y. Meng, Scaling of the disorder operator at deconfined quantum criticality, SciPost Phys. **13**, 123 (2022).

[65] S. V. Isakov, R. G. Melko, and M. B. Hastings, Universal signatures of fractionalized quantum critical points, Science **335**, 193 (2012).

[66] M. A. Metlitski and T. Grover, Entanglement entropy of systems with spontaneously broken continuous symmetry, arXiv:1112.5166 (2011), 1112.5166.

[67] A. Kitaev and J. Preskill, Topological entanglement entropy, Phys. Rev. Lett. **96**, 110404 (2006).

[68] M. Levin and X.-G. Wen, Detecting topological order in a ground state wave function, Phys. Rev. Lett. **96**, 110405 (2006).

[69] A. Jamadagni, H. Weimer, and A. Bhattacharyya, Robustness of topological order in the toric code with open boundaries, Phys. Rev. B **98**, 235147 (2018).

[70] S. D. Pace and X.-G. Wen, Exact emergent higher-form symmetries in bosonic lattice models, Phys. Rev. B **108**, 195147 (2023).

[71] D. Jaksch, C. Bruder, J. I. Cirac, C. W. Gardiner, and P. Zoller, Cold bosonic atoms in optical lattices, Phys. Rev. Lett. **81**, 3108 (1998).

[72] M. Greiner, O. Mandel, T. Esslinger, T. W. Hänsch, and I. Bloch, Quantum phase transition from a superfluid to a Mott insulator in a gas of ultracold atoms, Nature **415**, 39 (2002).

[73] T. Stöferle, H. Moritz, C. Schori, M. Köhl, and T. Esslinger, Transition from a strongly interacting 1D superfluid to a Mott insulator, Phys. Rev. Lett. **92**, 130403 (2004).

[74] I. B. Spielman, W. D. Phillips, and J. V. Porto, Mott-insulator transition in a two-dimensional atomic bose gas, Phys. Rev. Lett. **98**, 080404 (2007).

[75] I. Bloch, J. Dalibard, and W. Zwerger, Many-body physics with ultracold gases, Rev. Mod. Phys. **80**, 885 (2008).

[76] A. Browaeys and T. Lahaye, Many-body physics with individually controlled Rydberg atoms, Nat. Phys. **16**, 132 (2020).

[77] M. C. Banuls, R. Blatt, J. Catani, A. Celi, J. I. Cirac, M. Dalmonte, L. Fallani, K. Jansen, M. Lewenstein, S. Montangero, *et al.*, Simulating lattice gauge theo-

ries within quantum technologies, Eur. Phys. J. D **74**, 1 (2020).

[78] U.-J. Wiese, Ultracold quantum gases and lattice systems: quantum simulation of lattice gauge theories, Ann. Phys. **525**, 777 (2013).

[79] L. Tagliacozzo, A. Celi, P. Orland, M. Mitchell, and M. Lewenstein, Simulation of non-abelian gauge theories with optical lattices, Nat. Commun. **4**, 2615 (2013).

[80] R. Verresen, M. D. Lukin, and A. Vishwanath, Prediction of toric code topological order from Rydberg blockade, Phys. Rev. X **11**, 031005 (2021).

[81] G. Semeghini, H. Levine, A. Keesling, S. Ebadi, T. T. Wang, D. Bluvstein, R. Verresen, H. Pichler, M. Kalinowski, R. Samajdar, *et al.*, Probing topological spin liquids on a programmable quantum simulator, Science **374**, 1242 (2021).

[82] L. Homeier, A. Bohrdt, S. Linsel, E. Demler, J. C. Halimeh, and F. Grusdt, Realistic scheme for quantum simulation of $Z_2$ lattice gauge theories with dynamical matter in (2+ 1)D, Commun. Phys. **6**, 127 (2023).

[83] J. C. Halimeh, L. Homeier, C. Schweizer, M. Aidelsburger, P. Hauke, and F. Grusdt, Stabilizing lattice gauge theories through simplified local pseudogenerators, Phys. Rev. Res. **4**, 033120 (2022).

[84] S. V. Isakov, M. B. Hastings, and R. G. Melko, Topological entanglement entropy of a Bose–Hubbard spin liquid, Nat. Phys. **7**, 772 (2011).

[85] N. Tantivasadakarn, R. Thorngren, A. Vishwanath, and R. Verresen, Long-range entanglement from measuring symmetry-protected topological phases, arXiv:2112.01519 (2021), 2112.01519.

[86] N. Tantivasadakarn, A. Vishwanath, and R. Verresen, Hierarchy of topological order from finite-depth unitaries, measurement, and feedforward, PRX Quantum **4**, 020339 (2023).

[87] M. Iqbal, N. Tantivasadakarn, T. M. Gatterman, J. A. Gerber, K. Gilmore, D. Gresh, A. Hankin, N. Hewitt, C. V. Horst, M. Matheny, *et al.*, Topological order from measurements and feed-forward on a trapped ion quantum computer, arXiv:2302.01917 (2023), 2302.01917.

[88] M. Foss-Feig, A. Tikku, T.-C. Lu, K. Mayer, M. Iqbal, T. M. Gatterman, J. A. Gerber, K. Gilmore, D. Gresh, A. Hankin, *et al.*, Experimental demonstration of the advantage of adaptive quantum circuits, arXiv:2302.03029 (2023), 2302.03029.

[89] Y. Kuno and I. Ichinose, Production of lattice gauge Higgs topological states in a measurement-only quantum circuit, Phys. Rev. B **107**, 224305 (2023).

[90] J. Hauser, Y. Li, S. Vijay, and M. Fisher, Continuous symmetry breaking in adaptive quantum dynamics, arXiv:2304.13198 (2023), 2304.13198.

[91] A.-R. Negari, S. Sahu, and T. H. Hsieh, Measurement-induced phase transitions in the toric code, arXiv:2307.02292 (2023), 2307.02292.

[92] Y. Kuno, T. Orito, and I. Ichinose, Bulk-measurement-induced boundary phase transition in toric code and gauge-Higgs model, arXiv:2311.16651 (2023), 2311.16651.

[93] Y. Li, H. Sukeno, A. P. Mana, H. P. Nautrup, and T.-C. Wei, Symmetry-enriched topological order from partially gauging symmetry-protected topologically ordered states assisted by measurements, Phys. Rev. B **108**, 115144 (2023).

[94] S. Gazit, M. Randeria, and A. Vishwanath, Emergent Dirac fermions and broken symmetries in confined and deconfined phases of $Z_2$ gauge theories, Nat. Phys. **13**, 484 (2017).

[95] S. Gazit, F. F. Assaad, S. Sachdev, A. Vishwanath, and C. Wang, Confinement transition of $Z_2$ gauge theories coupled to massless fermions: Emergent quantum chromodynamics and $SO(5)$ symmetry, PNAS **115**, E6987 (2018).

[96] G. Ortiz, E. Cobanera, and Z. Nussinov, Dualities and the phase diagram of the $p$-clock model, Nucl. Phys. B. **854**, 780 (2012).

[97] B. Yoshida, Topological phases with generalized global symmetries, Phys. Rev. B **93**, 155131 (2016).

[98] C.-M. Jian, X.-C. Wu, Y. Xu, and C. Xu, Physics of symmetry protected topological phases involving higher symmetries and its applications, Phys. Rev. B **103**, 064426 (2021).

[99] C. Vafa, Modular invariance and discrete torsion on orbifolds, Nucl. Phys. B **273**, 592 (1986).

**Acknowledgements**

# Chapter 6

# High-order time-reversal symmetry breaking normal state

# High-order time-reversal symmetry breaking normal state

Meng Zeng[1], Lun-Hui Hu[2], Hong-Ye Hu[1], Yi-Zhuang You[1], and Congjun Wu[3,4,5,6*]

[1]*Department of Physics, University of California, San Diego, California 92093, USA;*
[2]*Department of Physics, Zhejiang University, Hangzhou 310058, China;*
[3]*New Cornerstone Science Laboratory, Department of Physics, School of Science, Westlake University, Hangzhou 310024, China;*
[4]*Institute for Theoretical Sciences, Westlake University, Hangzhou 310024, China;*
[5]*Key Laboratory for Quantum Materials of Zhejiang Province, School of Science, Westlake University, Hangzhou 310024, China;*
[6]*Institute of Natural Sciences, Westlake Institute for Advanced Study, Hangzhou 310024, China*

Spontaneous time-reversal symmetry breaking plays an important role in studying strongly correlated unconventional superconductors. When two superconducting gap functions with different symmetries compete, the relative phase channel ($\theta_- \equiv \theta_1 - \theta_2$) exhibits an Ising-type $Z_2$ symmetry due to the second order Josephson coupling, where $\theta_{1,2}$ are the phases of two gap functions. In contrast, the $U(1)$ symmetry in the channel of $\theta_+ \equiv \frac{\theta_1+\theta_2}{2}$ is intact. The phase locking, i.e., ordering of $\theta_-$, can take place in the phase fluctuation regime before the onset of superconductivity, i.e., when $\theta_+$ is disordered. If $\theta_-$ is pinned at $\pm\frac{\pi}{2}$, then time-reversal symmetry is broken in the normal state, otherwise, if $\theta_- = 0$, or, $\pi$, rotational symmetry is broken, leading to a nematic normal state. In both cases, the order parameters possess a 4-fermion structure beyond the scope of mean-field theory, which can be viewed as a high order symmetry breaking. We employ an effective two-component $XY$-model assisted by a renormalization group analysis to address this problem. As a natural by-product, we also find the other interesting intermediate phase corresponds to ordering of $\theta_+$ but with $\theta_-$ disordered. This is the quartetting, or, charge-4$e$, superconductivity, which occurs above the low temperature $Z_2$-breaking charge-2$e$ superconducting phase. Our results provide useful guidance for studying novel symmetry breaking phases in strongly correlated superconductors.

**superconductivity, strong correlation, time-reversal breaking, charge-**4$e$

**PACS number(s):**   71.27.+a, 74.20.-z, 74.20.De, 74.25.Dw

## 1  Introduction

Unconventional superconductors (for instance, high-$T_c$ cuprates [1], heavy-fermion systems [2], and iron-based superconductors [3]) have aroused a great deal of attentions for novel symmetries in addition to the $U(1)$ symmetry breaking. Time-reversal symmetry (TRS) as well as parity and charge conjugation are fundamental discrete symmetries, hence,

spontaneous TRS-breaking superconductivity is of particular importance [4-14]. Various TRS-breaking pairing structures are theoretically proposed, including $d \pm \mathrm{i}d$ [15, 16], $p \pm \mathrm{i}p$ [11,17], $s\pm\mathrm{i}d$ [4,18], $p\pm\mathrm{i}s$ [19], and $s+\mathrm{i}s$ [14,20], and experimental evidence has been reported in various systems, such as $Re_6Zr$ [21, 22], $UPt_3$ [23, 24], $PrOs_4Sb_{12}$ [25], $URu_2Si_2$ [26, 27], $SrPtAs$ [28], $LaNiC_2$ [29], $LaNiGa_2$ [30, 31], Bi/Ni bilayers [32], and $CaPtAs$ [33] (For details refer to a recent review [34]). They are often probed by the zero-field $\mu$-spin relaxation, or, rotation [35-37], and the polar Kerr effect

phys.scichina.com   link.springer.com

[38, 39]. TRS breaking signatures have also been reported in iron-based superconductors [40, 41].

If TRS breaking arises from a complex pairing structure, it is often presumed that it develops after the onset of superconductivity. However, these two transitions are of different nature: Superconductivity is of the $U(1)$ symmetry breaking and TRS is of $Z_2$, hence, they could take place at different temperatures. It is interesting to further check whether TRS breaking can occur before the superconducting transition as the temperature is lowered. In fact, phase fluctuations are prominent in strongly correlated superconductors above but close to $T_c$, such as high $T_c$ cuprates [42] and iron-based superconductors [43].

In a two-gap superconductor, the TRS breaking can be solely determined by the relative phase between two gap functions. The phases of two channels may fluctuate in a coordinated way such that the relative phase is locked, leading to TRS breaking, while the total phase $\theta_+$ is disordered, hence, the system remains normal. In the context of 2D bosons in the $p$-band, a TRS breaking Mott-insulating ground state was studied via the Ginzburg-Landau free energy analysis and the quantum Monte Carlo simulations [44, 45]. The TRS breaking normal state has been studied in the context of three-gap superconductors as a consequence from frustrations [46].

In this article, we show that there exists an Ising symmetry breaking normal phase in a generic 2D two-gap superconductors when the gap functions belong to different symmetries and are near degeneracy. The key ingredient here, as mentioned above, is the superconduct phase fluctuations. Hence, it is a phase-fluctuation induced TRS-breaking, or, a nematic normal state. By the symmetry principle, the two gap functions couple via a second order Josephson term. Therefore, we dub the resultant symmetry-breaking normal state as the "high-order" symmetry-breaking state. In the phase fluctuation regime, the low energy physics is described by a coupled two-component $XY$-model, which is mapped to a coupled sine-Gordon model and analyzed by the renormalization group (RG) method. Unlike the small difference in the superconducting transition temperature and the TRS-breaking temperature obtained in ref. [46] from the frustration effects in the three-band model, the phase-locking, or, the $Z_2$ symmetry breaking temperature can be considerably larger than the superconducting $T_c$. Another competing order, the quartetting [47], or, charge-4$e$ phase [48], can also appear above $T_c$, which corresponds to ordered total phase $\theta_+$ but with the relative phase $\theta_-$ disordered, i.e., the $U(1)$ symmetry in the $\theta_+$ channel is broken whereas the $Z_2$ symmetry in the $\theta_-$ channel is preserved. All these phases exhibit the 4-fermion-type order parameters, and thus are difficult to analyze in mean-field theories. Quite remarkably, the $Z_2$-breaking TRS-breaking normal state has recently been experimentally observed in hole-doped $Ba_{1-x}K_xFe_2As_2$ [49, 50], where the TRS-breaking transition is identified with the onset of specific-heat anomaly and spontaneous Nernst signal is also detected in the TRS-breaking normal state. The $Z_2$-breaking nematic normal state has been observed in $Sr_2RuO_4$ [51] using optical anisotropy measurement. Even though the normal state nematicity most likely has a different origin from our theory because it can happen at much higher temperature scale, the same experimental techniques can be used to detect nematicity in the phase fluctuation regime proposed in our work. The competing charge-4$e$ state has also been observed recently in kagome superconductor $CsV_3Sb_5$ [52], where the quantization of magnetic flux in units of $hc/4e$ is observed.

The paper is structured as the following: In sect. 2 we introduce the Ginzberg-Landau theory for superconductors with two gap functions of different symmetries. They couple due to the second order Josephson effect. In sect. 3, we focus on the phase degree of freedom by mapping the theory to a coupled $XY$-model, which can be further mapped to a coupled sine-Gordon model, setting the stage for the RG study. In sect. 4, we perform detailed RG analysis of the sine-Gordon model by considering the effects of various symmetry-allowed couplings between different channels, which lead to the emergence of different phase diagram topologies. In sect. 5, we briefly discuss the application of our theory to Fe-based superconductors. Then we conclude in sect. 6.

## 2 Ginzberg-Landau theory with two gap functions

We start with the Ginzberg-Landau (GL) free-energy of superconductivity with two gap functions. Each one by itself is time-reversal invariant. These two gap functions belong to two different representations of the symmetry group, say, the $s$-wave and $d$-wave symmetries of a tetragonal system, or, different components of a two-dimensional representation, say, the $p_x$ and $p_y$-wave symmetries. They cannot couple at the quadratic level since no invariants can mix them at this level. Bearing this in mind, the GL free-energy is constructed as $\mathcal{F} = \mathcal{F}_1 + \mathcal{F}_2$ with

$$\mathcal{F}_1 = \gamma_1 |\vec{\nabla}\Delta_1|^2 + \gamma_2 |\vec{\nabla}\Delta_2|^2 + \alpha_1(T)|\Delta_1|^2 + \alpha_2(T)|\Delta_2|^2 + \beta_1 |\Delta_1|^4 + \beta_2 |\Delta_2|^4 + \kappa |\Delta_1|^2 |\Delta_2|^2, \tag{1}$$

$$\mathcal{F}_2 = \lambda \left( \Delta_1^2 \Delta_2^{*2} + \Delta_1^{*2} \Delta_2^2 \right), \tag{2}$$

where $\alpha_{1,2}(T)$ are functions of temperatures, and their zeros determine their superconducting transition temperatures

when the two gap functions decouple. $\gamma_{1,2}$, $\beta_{1,2}$ are all positive and $\kappa^2 < 4\beta_1\beta_2$ to maintain the thermodynamic stability. If the gap functions form a two-dimensional representation of the symmetry group, then $\alpha_1 = \alpha_2$, $\beta_1 = \beta_2$, and $\gamma_1 = \gamma_2$, otherwise, they are generally independent. Nevertheless, we consider the case that they are nearly degenerate, i.e., $\alpha_1 \approx \alpha_2$, when they belong to two different representations, such that they can coexist.

The $\mathcal{F}_1$-term only depends on the magnitude of $\Delta_{1,2}$, hence, is phase insensitive. We assume that the two gap functions can form a quartic invariant as the $\mathcal{F}_2$-term, as in the cases of $s$ and $d$-waves, and $p_x$ and $p_y$-wave symmetries. The $\mathcal{F}_2$-term does depend on the relative phase between $\Delta_{1,2}$, which can be viewed as a 2nd order Josephson coupling. To minimize the free energy, the relative phase between two gap functions $\theta_- = \theta_1 - \theta_2 = \pm\frac{\pi}{2}$ at $\lambda > 0$, i.e., they form $\Delta_1 \pm i\Delta_2$, breaking TRS spontaneously. On the other hand, when $\lambda < 0$, $\theta_- = 0$, or, $\pi$. They form the nematic superconductivity $\Delta_1 \pm \Delta_2$, breaking the rotational symmetry. The magnitude of the mixed gap function remains isotropic in momentum space in the former case, while that in the latter case is anisotropic. The value of $\lambda$ depends on the energetic details of a concrete system. At the mean-field level, the free energy is a convex functional of the gap function distribution in the absence of spin-orbit coupling [5,19,53]. This favors a relatively uniform distribution of gap function in momentum space, corresponding to the complex mixing $\Delta_1 \pm i\Delta_2$ , i.e., $\lambda > 0$. Nevertheless, the possibility of $\lambda < 0$ cannot be ruled out, which could take place in the presence of spin-orbit coupling [11], or as a result beyond the mean-field BCS theory. This leads to the gap function $\Delta_1 \pm \Delta_2$, which breaks the rotational symmetry leading to nematic superconductivity.

## 3  New phases due to the phase fluctuations

The above GL analysis only works in the superconducting phases in which both $\Delta_{1,2}$ develop non-zero expectation values. However, it does not apply to the phase fluctuation regime above $T_c$. Let us parameterize the gap functions as $\Delta_{1,2} = |\Delta_{1,2}|e^{i\theta_{1,2}}$. In the phase fluctuation regime, the order magnitudes $|\Delta_{1,2}|$ are already significant, and their fluctuations can be neglected. On the contrary, the soft phase fluctuations dominate the low energy physics, and the system remains in the normal state before the onset of the long-range phase coherence.

New states can arise in the phase fluctuation regime in which neither of $\Delta_{1,2}$ is ordered. A possibility is that the system remains in the normal state but $\theta_-$ is pinned: If $\theta_- = \pm\frac{\pi}{2}$, then $\text{Im}\Delta_1^*\Delta_2$ is ordered, which breaks TRS; if $\theta_- = 0, \pi$, then $\text{Re}\Delta_1^*\Delta_2$ is ordered, which breaks rotation symmetry. Similar

physics occurs in the $p$-orbital band Bose-Hubbard model, where the boson operators in the $p_{x,y}$-bands play the role of $\Delta_{1,2}$, respectively. The transitions of superfluidity and TRS breaking divide the phase diagram into four phases of superfluidity states with and without TRS breaking, and the Mott insulating state with and without TRS breaking, where TRS here corresponds to the development of the onsite orbital angular momentum by occupying the complex orbitals $p_x \pm ip_y$ [54, 55]. The TRS-breaking normal states were also studied in the context of competing orders in superconductors [56,57]. Another possibility is that the total phase $\theta_+ = \theta_1 + \theta_2$ is pinned, i.e., $\Delta_1\Delta_2$ is ordered. This corresponds to the quartetting instability, i.e., a four-fermion clustering instability analogous to the $\alpha$-particle in nuclear physics. The competition between the pairing and quartetting instabilities in one dimension has been investigated by one of the authors [47]. Later it was also studied in the context of high-$T_c$ cuprates as the charge-$4e$ superconductivity [48].

However, all the above states involve order parameters consisting of 4-fermion operators. Hence, they are beyond the ordinary mean-field theory based on fermion bilinear order parameters. To address these novel states, we map the above GL free-energy to the $XY$-model on a bilayer lattice, and perform the renormalization group (RG) analysis to study the possible phases. Since there should be no true long-range order of the $U(1)$ symmetry at finite temperatures, we mean the quasi-long-ranged ordering of the Kosterlitz-Thouless (KT) transition. The model is expressed as:

$$H = -J_1 \sum_{\langle i,j \rangle} \cos(\theta_{1i} - \theta_{1j}) - J_2 \sum_{\langle i,j \rangle} \cos(\theta_{2i} - \theta_{2j})$$
$$+ \lambda' \sum_i \cos 2(\theta_{1i} - \theta_{2i}), \tag{3}$$

where $\theta_{1,2}$ are compact $U(1)$ phases with the modulus $2\pi$. $J_{1,2}$ are the intra-layer couplings estimated as $J_{1,2} \approx \gamma_{1,2}|\Delta_{1,2}|^2$, and $\lambda'$ is the inter-layer coupling estimated as $\lambda' \approx 2\lambda|\Delta_1|^2|\Delta_2|^2$.

Following the dual representation of the 2D classic $XY$-model as detailed in the Appendix A1, the above model eq. (3) can be mapped to the following multi-component sine-Gordon model, which is often employed for studying coupled Luttinger liquids [58, 59]. Its Euclidean Lagrangian in the continuum is defined as $L = \int d^2x \mathcal{L}(x)$ [60], where

$$\mathcal{L}(x) = \frac{1}{2K_1}\left(\partial_\mu\phi_1\right)^2 + \frac{1}{2K_2}(\partial_\mu\phi_2)^2 + g_{\theta_-}\cos 2(\theta_1 - \theta_2)$$
$$- g_{\phi_1}\cos 2\pi\phi_1 - g_{\phi_2}\cos 2\pi\phi_2, \tag{4}$$

where $\phi_{1,2}$ are the dual fields to the superconducting phase fields of $\theta_{1,2}$ with commutation relations $[\theta_{1,2}(t,x), \partial_y\phi_{1,2}(t,y)] = 2\pi i\delta(x-y)$, and the Luttinger parameters $K_{1,2} = J_{1,2}/T$ (Please note that $K_{1,2}$ appear in the

denominators in eq. (4) since we are using the dual representation). The compact radius of $\theta_{1,2}$ is $2\pi$, and that of the vortex fields $\phi_{1,2}$ is 1. $g_{\theta_-}$ is proportional to $\lambda'$ in eq. (3); $g_{\phi_1,\phi_2}$ are proportional to the vortex fugacities of the phase fields $\theta_{1,2}$, respectively. For simplicity, all of these $g$-eology coupling constants have absorbed the short-distance cutoff of the lattice.

## 4  Renormalization group analysis for phase diagrams

In this section, we explore the possible phase diagrams using RG analysis for the case where the two channels are degenerate, i.e., $J_1 = J_2 \equiv J$, $g_{\phi_1} = g_{\phi_2} \equiv \frac{1}{2}g_{\phi_\pm}$, and $K_1 = K_2 = J/T \equiv K$.

Due to the permutation symmetry between these two channels, the coupled theory is rewritten in terms of the collective basis $\theta_\pm$, $\phi_\pm$ channels conveniently defined as:

$$\theta_+ \equiv (\theta_1 + \theta_2)/2, \ \theta_- \equiv \theta_1 - \theta_2,$$
$$\phi_+ \equiv \phi_1 + \phi_2, \qquad \phi_- \equiv (\phi_1 - \phi_2)/2. \tag{5}$$

The compact radius of $\theta_\pm$ can be chosen as $2\pi$, and that of the vortex fields $\phi_\pm$ remains 1. This new basis is also convenient in the sense that it makes the symmetries of the coupled system explicit and at the same time it preserves the commutation relations between the fields and the dual fields, i.e., $[\theta_\pm(t,x), \partial_y \phi_\pm(t,y)] = 2\pi i \delta(x-y)$. The Lagrangian has a $U(1)$ symmetry in $\theta_+$ channel, $\theta_+ \to \theta_+ + \alpha$ with $\alpha \in [0, 2\pi)$, and the $Z_2$ symmetry in the $\theta_-$ channel, $\theta_- \to \theta_- + \pi$, due to the $\cos 2\theta_-$ term.

Based on symmetry alone, there can exit four different phases: (i) Both $U(1)$ and $Z_2$ are unbroken, i.e., the normal phase; (ii) only $Z_2$ is broken, i.e., TRS-breaking (or nematic) normal phase; (iii) only $U(1)$ is broken, i.e., the charge-$4e$ phase; (iv) both $U(1)$ and $Z_2$ are broken, i.e., the TRS-breaking (or nematic) superconducting phase. We can start with the free theory containing only the kinetic terms, and then add on the most relevant symmetry-preserving interaction terms to obtain phase diagrams containing all of the four possible phases discussed above, but with different phase diagram topologies.

With the basis transformation defined above, the free part of the Lagrangian in eq. (4) can be equivalently written in the $\theta_\pm, \phi_\pm$ basis as:

$$\mathcal{L}_0(x) = \frac{1}{4K_+}(\partial_\mu \phi_+)^2 + \frac{1}{K_-}(\partial_\mu \phi_-)^2, \tag{6}$$

where the initial values of both $K_\pm$ are both $J/T$.

Once various interaction terms are added, the phase diagram lives in a high dimensional parameter space. As a re-

sult, it is difficult to present a complete phase diagram involving all the parameters. However, based on the symmetry analysis provided above, there are only four phases in total. Therefore, it is possible to show two dimensional (2D) slices of the phase diagram that contains the four phases. Interestingly enough, topologically distinct configurations of phase boundaries can be obtained, depending on which interaction terms dominate at low energy. In the following two subsections, we will present two generic cases showing three types of phase diagram topologies.

### 4.1  $\phi_\pm$ channels decoupled

We consider possible local vortex terms in the collective basis, which are discussed in Appendix A3. The most relevant one is $g_{\phi_{\text{int}}} \cos \pi\phi_+ \cos 2\pi\phi_-$, which couples the even and odd channels together. It originates from the vortex fugacity terms in the individual basis $\cos 2\pi\phi_1 + \cos 2\pi\phi_2$. The sign change of $\cos \pi\phi_+ \cos 2\pi\phi_-$ from shifting $\phi_+$ by 1 can be compensated by a shift of $\phi_-$ by 1/2, and *vice versa*. The next leading vortex terms are $g_{\phi_+} \cos 2\pi\phi_+$ and $g_{\phi_-} \cos 4\pi\phi_-$ in the even and odd channels, respectively, which originate from the inter-layer vortex-vortex coupling in the original basis $\cos 2\pi\phi_1 \cos 2\pi\phi_2 \pm \sin 2\pi\phi_1 \sin 2\pi\phi_2$.

We begin with the limit that the initial value of the inter-layer phase coupling $g_{\theta_-}$ is large. In this case, vortices in two layers tend to be aligned together. Hence, the independent single vortex excitation in each layer is not favored and its fugacity is suppressed, i.e., $|g_{\phi_\pm}| \gg |g_{\phi_{\text{int}}}|$. In this limit, the $g_{\phi_{\text{int}}}$-term is neglected, then the system is decoupled in the collective basis with Lagrangian given by

$$\mathcal{L}_1(x) = \frac{1}{4K_+}(\partial_\mu \phi_+)^2 + \frac{1}{K_-}(\partial_\mu \phi_-)^2$$
$$- g_{\phi_+} \cos 2\pi\phi_+ - g_{\phi_-} \cos 4\pi\phi_- + g_{\theta_-} \cos 2\theta_-. \tag{7}$$

In this decoupled case, we expect the $U(1)$-breaking transition in the $\theta_+$ channel to be completely independent from the $Z_2$-breaking transition in the $\theta_-$ channel. The phase diagram can be obtained by numerically solving the following set of RG equations (see Appendix A2 for details),

$$\frac{dg_{\phi_+}}{d\ln l} = (2 - 2\pi K_+)\,g_{\phi_+},$$
$$\frac{dg_{\phi_-}}{d\ln l} = (2 - 2\pi K_-)\,g_{\phi_-},$$
$$\frac{dg_{\theta_-}}{d\ln l} = \left(2 - \frac{2}{\pi K_-}\right)g_{\theta_-}, \tag{8}$$
$$\frac{dK_+}{d\ln l} = -2\pi^3 g_{\phi_+}^2 K_+^2,$$
$$\frac{dK_-}{d\ln l} = -4\pi^3 g_{\phi_-}^2 K_-^2 + 4\pi g_{\theta_-}^2,$$

where both of the initial values of $K_\pm$ are $J/T$.

Below we analyze the nature of the fixed points of RG for four different phases: (I) the $Z_2$ breaking SC phase; (II) $Z_2$ breaking normal phase; (III) quartetting phase; (IV) normal phase. The values of couplings at these fixed points are summarized in Table 1.

Phase I and Phase II are the $Z_2$ breaking superconducting (SC) and normal phases, respectively. In the former case, the relative phase $\theta_-$ is locked, while the $\theta_+$ is quasi-long-range ordered. Hence, $g_{\theta_-} \to \infty$ and correspondingly $K_- \to \infty$. As for the vortex term $\cos 2\pi\phi_+$ in the $\phi_+$ channel, such a vortex term should be irrelevant in Phase I, which requires that $K_+$ takes a constant value with $K_+ > 1/\pi$, and $(g_{\phi_-}, g_{\phi_+}) \to (0,0)$. In the $Z_2$-breaking normal phase, the relative phase $\theta_-$ remains locked, while the vortex $\phi_+$ proliferates such that superfluidity is lost. Notice that the $Z_2$-breaking normal state appears in the intermediate temperature, i.e., the phase fluctuations of the underlying SC state lead to the symmetry-breaking normal state above the SC critical temperature. This intermediate phase can be the TRS breaking state, or, the nematic state depending on the $\theta_-$ is pinned at $\pm\frac{\pi}{2}$, or, 0 or $\pi$, respectively. In such a phase, $g_{\theta_-} \to \infty$ and $K_- \to +\infty$, which are the same as in Phase I. On the other hand, in order to proliferate vortices in the $\phi_+$ channel, $g_{\phi_+} \to \infty$, which means $K_+ \to 0$. Then $(g_{\phi_-}, g_{\phi_+}) \to (0, \infty)$.

Phase III and Phase IV, i.e., the quartetting ($4e$) state and the normal state, are both the $Z_2$-symmetric phases. For the quartetting ($4e$) state, the vortex field in the relative channel $\phi_-$ condenses, while the $\theta_+$ channel is quasi-long-range ordered. The condensation of $\phi_-$ means that $g_{\theta_-} \to 0$ and $K_- \to 0$, and $g_{\phi_-} \to \infty$. The quasi-long-range ordering of $\theta_+$ requires $g_{\phi_+} \to 0$, which means that the renormalized value of $K_+$ reaches a constant with $K_+ > \frac{1}{\pi}$, which becomes a line of stable fixed points. As for the normal state, it means that the vortex fields in both channels condense. This simply gives rise to $g_{\phi_+} \to \infty$, $g_{\phi_-} \to \infty$, and $g_{\theta_-} \to 0$, which corresponds to $K_+ \to 0$ and $K_- \to 0$.

By numerically integrating the RG eq. (8), the above four phases are obtained. The phase diagram as a function of temperature and fugacity ratio between two channels $g_{\phi_-}/g_{\phi_+}$ is shown in Figure 1. The fixed point values of the couplings deep in the four phases as well as on the phase boundaries are listed in Table 1. As expected, when the two channels are decoupled, the $U(1)$-breaking phase boundary and the $Z_2$-breaking phase boundary are independent from each other and cross at a single point, diving the phase diagram into four regions characterized by different symmetry breaking patterns.

Along the phase boundary $P_1P_3$ (excluding the multi-critical point $O$), it represents a $Z_2$-breaking transition inside the normal state with $K_- = \frac{1}{\pi}$. Then the fixed point condition for $K_-$ can be solved to give the relation $|g_{\phi_-}| = |g_{\theta_-}|$.

The segment of $P_1O$ lies in the normal state with $g_{\phi_+} = \infty$ with $K_+ \to 0$ separating the $Z_2$-breaking normal state and the complete normal state. In contrast, the $P_3O$ lies in the region with quasi-long-range ordered $U(1)$ phase $\theta_+$ separating the $Z_2$-breaking SC state with $\theta_-$ locked and the quartetting charge-$4e$ phase. The boundary of $P_2P_4$ separates the superfluid phase and the normal phase, below which the $U(1)$ phase $\theta_+$ becomes quasi-long-range ordered. The line of $P_2O$ marks the boundary between the $Z_2$-breaking normal and SC phases. Similarly, the line of $P_4O$ marks the boundary between the quartetting phase and the normal phase.

Here we comment on the exact duality on the critical line $P_1P_3$. More precisely, it is the duality between the field $\theta_-$ and its dual $\phi_-$. To make the duality manifest, we can do a field rescaling

$$\tilde{\phi}_- \equiv \sqrt{2\pi}\phi_-, \quad \tilde{\theta}_- \equiv \theta_-/\sqrt{2\pi}, \tag{9}$$

such that the two mass terms become $\cos\sqrt{8\pi}\tilde{\phi}_-$ and $\cos\sqrt{8\pi}\tilde{\theta}_-$ respectively. At the same time, the Luttinger

**Table 1**   Values of couplings at fixed points in the four phases and on phase boundaries under RG eq. (8)

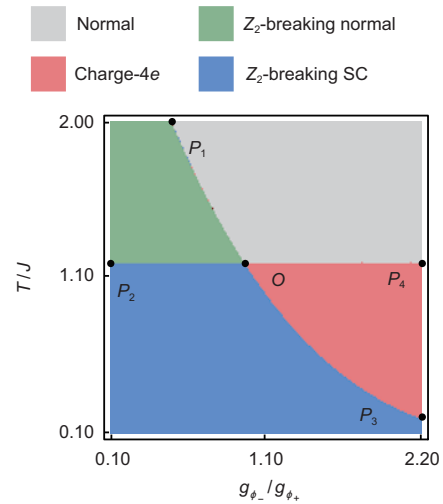| Phases and phase boundaries | $g_{\theta_-}$ | $g_{\phi_-}$ | $g_{\phi_+}$ | $K_-$ | $K_+$ |
|---|---|---|---|---|---|
| (I) $Z_2$-breaking SC | $\infty$ | 0 | 0 | $+\infty$ | $> \frac{1}{\pi}$ |
| (II) $Z_2$-breaking normal | $\infty$ | 0 | $\infty$ | $+\infty$ | 0 |
| (III) quartetting ($4e$) | 0 | $\infty$ | 0 | 0 | $> \frac{1}{\pi}$ |
| (IV) normal | 0 | $\infty$ | $\infty$ | 0 | 0 |
| $P_1O$ | $\frac{g_{\phi_-}}{g_{\theta_-}} = \pm 1$ | | $\infty$ | $\frac{1}{\pi}$ | 0 |
| $P_2O$ | $\infty$ | 0 | 0 | $+\infty$ | $\frac{1}{\pi}$ |
| $P_3O$ | $\frac{g_{\phi_-}}{g_{\theta_-}} = \pm 1$ | | 0 | $\frac{1}{\pi}$ | $\frac{1}{\pi}$ |
| $P_4O$ | 0 | $\infty$ | 0 | 0 | $\frac{1}{\pi}$ |



**Figure 1**   (Color online) Phase diagram vs. temperature and $g_{\phi_-}/g_{\phi_+}$ by numerically integrating the RG eq. (8). The initial values of coupling constants are $g_{\phi_+} = 0.2$ and $g_{\theta_-} = 0.01$. All of the four phases appear and meet at the multi-cirtical point $O$.

parameter also has to be rescaled $\tilde{K}_- \equiv \pi K_-$, which becomes 1 at the critical point. It is again straightforward to show that $|g_{\phi_-}| = |g_{\theta_-}|$ at criticality. Then the duality of exchanging $\tilde{\theta}_-$ and $\tilde{\phi}_-$ on the Lagrangian level is made explicit. Such a theory has also been studied as the field theory description of one dimensional deconfined quantum critical point with $Z_2 \times Z_2$ symmetry [61]. In our case, the first $Z_2$ acts on the field $\theta_-$, and the second $Z_2$ acts on its dual $\phi_-$. The mixed anomaly between the two $Z_2$ symmetries dictates that when one is preserved the other has to be spontaneously broken. It has also been shown that such exotic critical point can be mapped to the usual Landau symmetry-breaking transition of a 1D $Z_4$ clock model, whose critical point is just two decoupled copies of Ising CFT [61,62]. It is interesting to note that such exotic critical point can arise naturally in the two-gap superconductors that we study.

### 4.2  $\phi_\pm$ coupled through $\cos \pi \phi_+ \cos 2\pi \phi_-$

Now we add the vortex term of $\cos \pi \phi_+ \cos 2\pi \phi_-$ which couples the $\phi_\pm$ fields together. The following Lagrangian is obtained:

$$\mathcal{L}_2(x) = \frac{1}{K_-}(\partial_\mu \phi_-)^2 + \frac{1}{4K_+}(\partial_\mu \phi_+)^2$$
$$+ g_{\theta_-} \cos 2\theta_- - g_{\phi_{int}} \cos \pi \phi_+ \cos 2\pi \phi_-$$
$$- g_{\phi_-} \cos 4\pi \phi_- - g_{\phi_+} \cos 2\pi \phi_+. \tag{10}$$

The RG equations can be written down as the following (see Appendix A2):

$$\frac{dg_{\theta_-}}{d \ln l} = \left(2 - \frac{2}{\pi K_-}\right) g_{\theta_-},$$
$$\frac{dg_{\phi_{int}}}{d \ln l} = \left[2 - \frac{\pi}{2}(K_+ + K_-)\right] g_{\phi_{int}},$$
$$\frac{dK_-}{d \ln l} = -4\pi^3 K_-^2 \left(g_{\phi_-}^2 + g_{\phi_{int}}^2/8\right) + 4\pi g_{\theta_-}^2$$
$$\frac{dK_+}{d \ln l} = -4\pi^3 K_+^2 \left(g_{\phi_+}^2 + g_{\phi_{int}}^2/8\right), \tag{11}$$
$$\frac{dg_{\phi_-}}{d \ln l} = (2 - 2\pi K_-) g_{\phi_-} + \frac{\pi}{4} g_{\phi_{int}}^2,$$
$$\frac{dg_{\phi_+}}{d \ln l} = (2 - 2\pi K_+) g_{\phi_+} + \frac{\pi}{4} g_{\phi_{int}}^2.$$

By analyzing eq. (11), again we have the four stable phases as discussed in the decoupled case in the previous section before. The values of couplings at the fixed points corresponding to these phases and at the phase boundaries are summarized in Table 2. Compared with the decoupled case, the $Z_2$-breaking SC phase, the $Z_2$-breaking normal phase, and the quartetting phase further require that $g_{\phi_{int}} \to 0$. Furthermore, the quartetting phase requires $K_+ > \frac{4}{\pi}$ to ensure the

irrelevancy of the $g_{\phi_{int}}$-term. As for the normal phase, certainly $g_{\phi_{int}} \to \infty$.

A key feature of the new phase diagram after introducing the $g_{\phi_{int}}$ term is that the previous tetra-critical point $O$ splits into a pair of tri-critical points $O_1$ and $O_2$, such that there appears a direct transition across $O_1 O_2$ from the $Z_2$-breaking SC phase to the normal state [63].

A small $g_{\phi_{int}}$-term does not change the boundaries much when deep inside the $Z_2$-ordered or the superconducting regions as long as they are relatively far away from $O_1 O_2$. In this case, the RG processes in the two channels can be decomposed into fast and slow steps. For example, along the boundary $P_2 O_1$ deep inside the $Z_2$-breaking phase, $\theta_-$ is pinned, which renders the $g_{\phi_{int}}$-term highly irrelevant by disordering the $\phi_-$ field. Similarly, along the boundary $P_3 O_2$ deep inside the superfluid phase, $g_{\phi_+}$ is quickly suppressed to 0. The RG process in the $\phi_+$ channel stops quickly, such that $g_{\phi_{int}}$ does not grow much and remains small still. Furthermore, $\phi_+$ remains power-law fluctuating, which suppresses the effect of the $g_{\phi_{int}}$-term.

On the other hand, the $g_{\phi_{int}}$-term affects the boundaries surrounding the normal phase. As for the part along $P_4 O_1$ deep inside the $Z_2$-disordered region, $\phi_-$ is pinned. The $g_{\phi_{int}}$-term becomes $g' \cos \pi \phi_+$, which is a half-quantum vortex with a renormalized coupling constant $g' = g_{\phi_{int}} \langle \cos 2\pi \phi_- \rangle$. Such a term is more relevant than the one-vortex term of $g_{\phi_+}$ although its coupling is weaker. Nevertheless, it extends the region of the normal state significantly as shown in Figure 2. As for $P_1 O_1$ deep inside the normal phase, $g_{\phi_+}$-term reaches the order of 1 quickly, and $\phi_+$ is pinned. Then the $g_{\phi_{int}}$-term becomes $g'' \cos 2\pi \phi_-$ with $g'' = g_{\phi_{int}} \langle \cos \pi \phi_+ \rangle$, which is more relevant than the existing $g_{\phi_-} \cos 4\pi \phi_-$ term. It changes the competition between the condensation of $\theta_-$ and $\phi_-$, which corresponds to the $Z_2$-ordered and disordered state, respectively. The critical theory on $P_1 O_1$ is also modified as a consequence of the $g_{\phi_{int}}$-term. Based on the numerical solution near this critical line, the

**Table 2**   The values of couplings at the fixed points corresponding to four stable phases and on the phase boundaries by solving eq. (11)

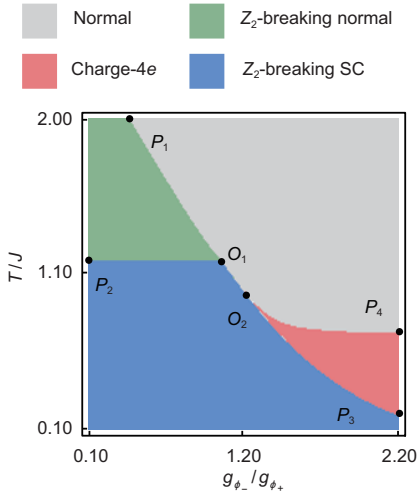| Phases | $g_{\theta_-}$ | $g_{\phi_-}$ | $g_{\phi_+}$ | $g_{\phi_{int}}$ | $K_+$ | $K_-$ |
|---|---|---|---|---|---|---|
| (I) $Z_2$-breaking SC | $\infty$ | 0 | 0 | 0 | $> \frac{1}{\pi}$ | $+\infty$ |
| (II) $Z_2$-breaking normal | $\infty$ | 0 | $\infty$ | 0 | 0 | $+\infty$ |
| (III) Quartetting ($4e$) | 0 | $\infty$ | 0 | 0 | $> \frac{4}{\pi}$ | 0 |
| (IV) Normal | 0 | $\infty$ | $\infty$ | $\infty$ | 0 | 0 |
| $P_1 O_1$ | $\infty$ | $\infty$ | $\infty$ | $\infty$ | 0 | $\frac{1}{\pi}$ |
| $P_2 O_1$ | $\infty$ | 0 | 0 | 0 | $\frac{1}{\pi}$ | 0 |
| $P_3 O_2$ | $\frac{g_{\phi_-}}{g_{\theta_-}} = \pm 1$ | 0 | 0 | 0 | $> \frac{4}{\pi}$ | $\frac{1}{\pi}$ |
| $P_4 O_2$ | 0 | $\infty$ | 0 | 0 | $\frac{1}{\pi}$ | 0 |
| $O_1 O_2$ | $\frac{g_{\phi_-}}{g_{\theta_-}} = \pm 1$ | 0 | 0 | 0 | $\frac{1}{\pi}$ | $\frac{1}{\pi}$ |

**Figure 2** (Color online) Phase diagram vs. temperature and $g_{\phi_-}/g_{\phi_+}$ by numerically integrating the RG eq. (11). The initial values of coupling constants are $g_{\phi_+} = 0.2, g_{\theta_-} = 0.01$ and $g_{\phi_{\text{int}}} = 0.001$. Different from Figure 1, this phase diagram features a direct transition boundary $O_1O_2$ between the normal state and the $Z_2$-breaking SC phase due to the coupling between the $\phi_\pm$ channels.

scaling dimensions of the two competing interaction terms, the $g_{\phi_{\text{int}}}$-term and the $g_{\theta_-}$-term both stabilize at 1, indicating the criticality belongs to the Ising universality class. In contrast, the critical behavior on $P_3O_1$ for the $\theta_-$-channel inherits from the critical line $P_3O$ in Figure 1 since $g_{\phi_{\text{int}}}$ flows to 0 and this coupling term is non-consequential.

When close to $O_1O_2$, the energy scales in the even and odd channels are close, hence, the RG processes cannot be decomposed into fast and slow steps any more. Since the $g_{\phi_{\text{int}}}$-term is the most relevant, it grows quickly and overwhelms other terms under sufficiently long RG processes. Once $g_{\phi_{\text{int}}}$ is renormalized to the strong coupling region, both $\phi_+$ and $\phi_-$ are pinned, thus the system enters into normal state. Once it is renormalized to zero, the system is in the SC state and the residual $g_{\theta_-}$-term will drive the $Z_2$ symmetry breaking. The transitions on the critical lines across the tri-critical points $O_1$ and $O_2$ are also quite interesting, but we leave the details for future study.

## 5  Discussion

We briefly discuss the application of our theory to the FeTe$_{1-x}$Se$_x$ superconductor, in which evidence to spontaneously time-reversal-symmetry breaking states has been observed by using the high-resolution laser-based photoemission method both in the superconducting and the normal states [41].

Following ref. [64], we consider two superconducting gap functions $\Delta_1$ and $\Delta_2$, which possess different pairing symmetries and each of them maintains time-reversal symmetry. It

has been argued that the pairing symmetries are constrained to be among $A_{1g(u)} \pm iA_{2g(u)}$, $B_{1g(u)} \pm iB_{2g(u)}$, or $E_{g(u)} \pm iE_{g(u)}$, based on the effects of TRS-breaking pairing on the surface Dirac cone. Here $A, B, E$ denote discrete angular momenta analogous to the $s, d, p$-wave in the continuous case. $g$ and $u$ denote even and odd parities respectively. $A_{1,2}$ means even or odd under vertical plane reflection. The Ginzburg-Landau free energy is given by

$$\mathcal{F} = \alpha_1|\Delta_1|^2 + \beta_1|\Delta_1|^4 + \alpha_2|\Delta_2|^2 + \beta_2|\Delta_2|^4 \\ + \kappa|\Delta_1|^2|\Delta_2|^2 + \lambda\left((\Delta_1^*\Delta_2)^2 + c.c.\right), \tag{12}$$

where $\alpha_1 \approx \alpha_2$ is assumed so that the two pairing channels are nearly degenerate as discussed before. And we focus on the case of $\lambda > 0$, where the relative phase between $\Delta_1$ and $\Delta_2$ as $\theta_- = \pm\frac{\pi}{2}$. Hence, the complex gap function $\Delta_1 \pm i\Delta_2$ spontaneously breaks time-reversal symmetry.

Since the FeSe$_{1-x}$Te$_x$ superconductor has strong atomic spin-orbit coupling, as allowed by symmetry, the complex gap function can directly couple to the spin magnetization $m_z$ via a cubic coupling term as:

$$\mathcal{F}_M = \alpha_m|m_z|^2 + i\gamma m_z(\Delta_1\Delta_2^* - \Delta_1^*\Delta_2), \tag{13}$$

where $\alpha_m > 0$ and $\gamma$ is proportional to the spin-orbit coupling strength [64]. This term satisfies both the $U(1)$ symmetry and time-reversal symmetry. Because of $\alpha_m > 0$, the spin magnetization can only be induced by the complex gap function via $m_z = \frac{\gamma}{\alpha_m}|\Delta_1^*\Delta_2|\sin\theta_-$ when $\theta_- = \pm\frac{\pi}{2}$. The development of $m_z$ will gap out the surface Dirac cone as observed in the experiment [41]. As detailed in ref. [64], this spontaneous breaking of TR symmetry can impose a strong constraint on the gap function symmetry in the FeSe$_{1-x}$Te$_x$ system.

Furthermore, recent experiment [41] also shows that the spin-magnetization develops nonzero values even at $T > T_c$, indicating that TRS breaking already occurs above $T_c$. It can be understood from the analysis in the main text, where we propose the $Z_2$-breaking normal state. There are no long-range superconducting orderings, i.e., the $\langle\Delta_1\rangle = \langle\Delta_2\rangle = 0$. However, the expectation value of the 4-fermion order parameter is nonzero $\langle\Delta_1^*\Delta_2\rangle \neq 0$ due to the pinning of $\theta_- = \pm\frac{\pi}{2}$.

## 6  Conclusions

To summarize, we have analyzed the possible symmetry-breaking phases in the phase fluctuation regime in a two-gap superconductors in 2D. The system has an overall $Z_2 \times U(1)$ symmetry, where the $Z_2$ in the $\theta_-$ channel is due to the second order Josephson coupling between the two gaps and the $\theta_+$ channel still has $U(1)$ symmetry. If only the $Z_2$ is broken, then we have the $Z_2$-breaking normal state, which can

be either the phase fluctuation induced TRS breaking normal state or the nematic state, depending on whether the relative phase $\theta_-$ is locked at $\pm\frac{\pi}{2}$, or, at 0 or $\pi$. On the other hand, if only the $U(1)$ symmetry is broken, then it corresponds to the ordering of the total phase $\theta_+$, even though the two gaps are not individually ordered. This is the quartetting phase, or the so-called 4$e$ phase.

Extensive RG analysis is done by including the more relevant symmetry allowed couplings. Not only have we obtained all the four possible phases, including the two interesting intermediate phases in the phase fluctuation regime, we also find a direct transition from the $Z_2$-breaking SC state to the normal state. This is because the coupling between half-vortices in the even and odd channels favors the simultaneous ordering/disordering of the two channels.

On the experimental side, the TRS-breaking normal phase has been experimentally observed recently in hole-doped $Ba_{1-x}K_xFe_2As_2$ [49, 50]. Furthermore, experimental evidence of the elusive charge-4$e$ state has also been found recently in kagome superconductor $CsV_3Sb_5$ [52]. The theory presented in this work is based on general symmetry principles. We believe the fluctuation effects and the physical consequences discussed here are quite generic and likely play a role in a wide range of multi-gap superconductors with dominant second-order Josephson couplings.

*Note added:* Upon the completion of the first version of this manuscript, we became aware of two manuscripts on related topics refs. [65, 66]. Very recently, similar physics have also been discussed in ref. [67].

**Conflict of interest**    The authors declare that they have no conflict of interest.

1   J. G. Bednorz, and K. A. Müller, Z. Phys. B-Condensed Matter **64**, 189 (1986).

2   G. R. Stewart, Rev. Mod. Phys. **56**, 755 (1984).

3   H. Takahashi, K. Igawa, K. Arii, Y. Kamihara, M. Hirano, and H. Hosono, Nature **453**, 376 (2008).

4   W. C. Lee, S. C. Zhang, and C. Wu, Phys. Rev. Lett. **102**, 217002 (2009), arXiv: 0810.0887.

5   C. Wu, and J. E. Hirsch, Phys. Rev. B **81**, 020508 (2010).

6   V. Stanev, and Z. Tešanović, Phys. Rev. B **81**, 134522 (2010), arXiv: 0912.5214.

7   M. Khodas, and A. V. Chubukov, Phys. Rev. Lett. **108**, 247003 (2012), arXiv: 1202.5563.

8   J. Garaud, and E. Babaev, Phys. Rev. Lett. **112**, 017003 (2014), arXiv: 1308.3220.

9   S. Maiti, M. Sigrist, and A. Chubukov, Phys. Rev. B **91**, 161102 (2015), arXiv: 1412.7439.

10   S. Z. Lin, S. Maiti, and A. Chubukov, Phys. Rev. B **94**, 064519 (2016), arXiv: 1607.00109.

11   Y. Wang, and L. Fu, Phys. Rev. Lett. **119**, 187003 (2017), arXiv: 1703.06880.

12   J. Kang, A. V. Chubukov, and R. M. Fernandes, Phys. Rev. B **98**, 064508 (2018), arXiv: 1805.06882.

13   Z. Wang, G. M. Zhang, Y. Yang, and F. C. Zhang, Phys. Rev. B **102**, 220501 (2020), arXiv: 2006.15928.

14   L. H. Hu, P. D. Johnson, and C. Wu, Phys. Rev. Res. **2**, 022021 (2020), arXiv: 1906.01754.

15   R. B. Laughlin, Phys. Rev. Lett. **80**, 5188 (1998), arXiv: cond-mat/9709004.

16   S. Tewari, C. Zhang, V. M. Yakovenko, and S. Das Sarma, Phys. Rev. Lett. **100**, 217004 (2008), arXiv: 0711.2329.

17   Y. Wang, M. Lin, and T. L. Hughes, Phys. Rev. B **98**, 165144 (2018), arXiv: 1804.01531.

18   C. Platt, R. Thomale, C. Honerkamp, S. C. Zhang, and W. Hanke, Phys. Rev. B **85**, 180502 (2012), arXiv: 1106.5964.

19   W. Yang, C. Xu, and C. Wu, Phys. Rev. Res. **2**, 042047 (2020).

20   M. Silaev, J. Garaud, and E. Babaev, Phys. Rev. B **95**, 024517 (2017), arXiv: 1610.05846.

21   R. P. Singh, A. D. Hillier, B. Mazidian, J. Quintanilla, J. F. Annett, D. M. K. Paul, G. Balakrishnan, and M. R. Lees, Phys. Rev. Lett. **112**, 107002 (2014), arXiv: 1401.2108.

22   G. M. Pang, Z. Y. Nie, A. Wang, D. Singh, W. Xie, W. B. Jiang, Y. Chen, R. P. Singh, M. Smidman, and H. Q. Yuan, Phys. Rev. B **97**, 224506 (2018), arXiv: 1806.03768.

23   J. A. Sauls, Adv. Phys. **43**, 113 (1994), arXiv: 1812.09984.

24   E. R. Schemm, W. J. Gannon, C. M. Wishne, W. P. Halperin, and A. Kapitulnik, Science **345**, 190 (2014), arXiv: 1410.1482.

25   Y. Aoki, A. Tsuchiya, T. Kanayama, S. R. Saha, H. Sugawara, H. Sato, W. Higemoto, A. Koda, K. Ohishi, K. Nishiyama, and R. Kadono, Phys. Rev. Lett. **91**, 067003 (2003), arXiv: cond-mat/0308196.

26   A. P. MacKenzie, and Y. Maeno, Rev. Mod. Phys. **75**, 657 (2003).

27   E. R. Schemm, R. E. Baumbach, P. H. Tobash, F. Ronning, E. D. Bauer, and A. Kapitulnik, Phys. Rev. B **91**, 140506 (2015), arXiv: 1410.1479.

28   P. K. Biswas, H. Luetkens, T. Neupert, T. Stürzer, C. Baines, G. Pascua, A. P. Schnyder, M. H. Fischer, J. Goryo, M. R. Lees, H. Maeter, F. Brückner, H. H. Klauss, M. Nicklas, P. J. Baker, A. D. Hillier, M. Sigrist, A. Amato, and D. Johrendt, Phys. Rev. B **87**, 180503 (2013).

29   A. D. Hillier, J. Quintanilla, and R. Cywinski, Phys. Rev. Lett. **102**, 117007 (2009), arXiv: 0901.3153.

30   A. D. Hillier, J. Quintanilla, B. Mazidian, J. F. Annett, and R. Cywinski, Phys. Rev. Lett. **109**, 097001 (2012), arXiv: 1206.5905.

31   Z. F. Weng, J. L. Zhang, M. Smidman, T. Shang, J. Quintanilla, J. F. Annett, M. Nicklas, G. M. Pang, L. Jiao, W. B. Jiang, Y. Chen, F. Steglich, and H. Q. Yuan, Phys. Rev. Lett. **117**, 027001 (2016), arXiv: 1605.08356.

32   X. Gong, M. Kargarian, A. Stern, D. Yue, H. Zhou, X. Jin, V. M. Galitski, V. M. Yakovenko, and J. Xia, Sci. Adv. **3**, e1602579 (2017), arXiv: 1609.08538.

33   T. Shang, M. Smidman, A. Wang, L. J. Chang, C. Baines, M. K. Lee, Z. Y. Nie, G. M. Pang, W. Xie, W. B. Jiang, M. Shi, M. Medarde, T. Shiroka, and H. Q. Yuan, Phys. Rev. Lett. **124**, 207001 (2020), arXiv: 2004.10425.

34   S. K. Ghosh, M. Smidman, T. Shang, J. F. Annett, A. D. Hillier, J. Quintanilla, and H. Yuan, J. Phys.-Condens. Matter **33**, 033001 (2021), arXiv: 2003.04357.

35   A. Schenck, *Muon Spin Rotation Spectroscopy: Principles and Applications in Solid State Physics* (Taylor and Francis, London, 1985).

36   S. L. Lee, R. Cywinski, and S. Kilcoyne, *Muon Science: Muons in Physics, Chemistry and Materials*, volume 51 (CRC Press, Boca Raton, 1999).

37   A. Yaouanc, and P. D. De Reotier, *Muon Spin Rotation, Relaxation, and Resonance: Applications to Condensed Matter*, volume 147 (Oxford University Press, Oxford, 2011).

38   S. Spielman, K. Fesler, C. B. Eom, T. H. Geballe, M. M. Fejer, and A.

Kapitulnik, Phys. Rev. Lett. **65**, 123 (1990).

39 A. Kapitulnik, J. Xia, E. Schemm, and A. Palevski, New J. Phys. **11**, 055060 (2009), arXiv: 0906.2845.

40 V. Grinenko, R. Sarkar, K. Kihou, C. H. Lee, I. Morozov, S. Aswartham, B. Büchner, P. Chekhonin, W. Skrotzki, K. Nenkov, R. Hühne, K. Nielsch, S. L. Drechsler, V. L. Vadimov, M. A. Silaev, P. A. Volkov, I. Eremin, H. Luetkens, and H. H. Klauss, Nat. Phys. **16**, 789 (2020).

41 N. Zaki, G. Gu, A. Tsvelik, C. Wu, and P. D. Johnson, Proc. Natl. Acad. Sci. U.S.A. **118**, e2007241118 (2021).

42 V. J. Emery, and S. A. Kivelson, Nature **374**, 434 (1995).

43 S. Kasahara, T. Yamashita, A. Shi, R. Kobayashi, Y. Shimoyama, T. Watashige, K. Ishida, T. Terashima, T. Wolf, F. Hardy, C. Meingast, H. Löhneysen, A. Levchenko, T. Shibauchi, and Y. Matsuda, Nat. Commun. **7**, 12843 (2016), arXiv: 1608.01829.

44 Z. Cai, and C. Wu, Phys. Rev. A **84**, 033635 (2011), arXiv: 1106.1121.

45 F. Hébert, Z. Cai, V. G. Rousseau, C. Wu, R. T. Scalettar, and G. G. Batrouni, Phys. Rev. B **87**, 224505 (2013), arXiv: 1304.0554.

46 T. A. Bojesen, E. Babaev, and A. Sudbø, Phys. Rev. B **88**, 220511 (2013), arXiv: 1306.2313.

47 C. Wu, Phys. Rev. Lett. **95**, 266404 (2005), arXiv: cond-mat/0409247.

48 E. Berg, E. Fradkin, and S. A. Kivelson, Nat. Phys. **5**, 830 (2009), arXiv: 0904.1230.

49 V. Grinenko, D. Weston, F. Caglieris, C. Wuttke, C. Hess, T. Gottschall, I. Maccari, D. Gorbunov, S. Zherlitsyn, J. Wosnitza, A. Rydh, K. Kihou, C. H. Lee, R. Sarkar, S. Dengre, J. Garaud, A. Charnukha, R. Hühne, K. Nielsch, B. Büchner, H. H. Klauss, and E. Babaev, Nat. Phys. **17**, 1254 (2021).

50 I. Shipulin, N. Stegani, I. Maccari, K. Kihou, C.-H. Lee, Y. Li, R. Hhne, H.-H. Klauss, M. Putti, F. Caglieris, E. Babaev, and V. Grinenko, arXiv: 2212.13515.

51 R. Russell, H. P. Nair, K. M. Shen, D. G. Schlom, and J. W. Harter, arXiv: 2304.02586.

52 J. Ge, P. Wang, Y. Xing, Q. Yin, H. Lei, Z. Wang, and J. Wang, arXiv: 2201.10352.

53 M. Cheng, K. Sun, V. Galitski, and S. Das Sarma, Phys. Rev. B **81**, 024504 (2010), arXiv: 0908.2805.

54 C. Wu, Mod. Phys. Lett. B **23**, 1 (2009), arXiv: 0901.1415.

55 F. Hébert, Z. Cai, V. G. Rousseau, C. Wu, R. T. Scalettar, and G. G. Batrouni, Phys. Rev. B **87**, 224505 (2013), arXiv: 1304.0554.

56 R. M. Fernandes, P. P. Orth, and J. Schmalian, Annu. Rev. Condens. Matter Phys. **10**, 133 (2019), arXiv: 1804.00818.

57 M. H. Fischer, and E. Berg, Phys. Rev. B **93**, 054501 (2016), arXiv: 1511.05177.

58 C. Wu, W. V. Liu, and E. Fradkin, Phys. Rev. B **68**, 115104 (2003), arXiv: cond-mat/0206248.

59 L. H. Hu, R. X. Zhang, F. C. Zhang, and C. Wu, Phys. Rev. B **102**, 235115 (2020), arXiv: 1912.09066.

60 E. Fradkin, *Field Theories of Condensed Matter Physics* (Cambridge University Press, Cambridge, 2013).

61 C. Zhang, and M. Levin, Phys. Rev. Lett. **130**, 026801 (2023), arXiv: 2206.01222.

62 L. Su, arXiv: 2306.02976.

63 F. F. Song, and G. M. Zhang, Phys. Rev. Lett. **128**, 195301 (2022), arXiv: 2105.05411.

64 L. H. Hu, P. D. Johnson, and C. Wu, Phys. Rev. Res. **2**, 022021 (2020), arXiv: 1906.01754.

65 R. M. Fernandes, and L. Fu, arXiv: 2101.07943.

66 S.-K. Jian, Y. Huang, and H. Yao, arXiv: 2102.02820.

67 Y.-B. Liu, J. Zhou, C. Wu, and F. Yang, arXiv: 2301.06357.

68 I. Herbut, *A Modern Approach to Critical Phenomena* (Cambridge University Press, Cambridge, 2007).

69 R. Shankar, *Quantum Field Theory and Condensed Matter: An Introduction* (Cambridge University Press, Cambridge, 2017).

70 A. M. Tsvelik, *Quantum Field Theory in Condensed Matter Physics* (Cambridge University Press, Cambridge, 2007).

# Appendix

## A1 The 2D classical *XY*-model and its dual to the sine-Gordon model

In this section, we review the duality transformation from the *XY*-model to the sine-Gordon model. We follow ref. [68] to review the duality between the *XY*-model and the sine-Gordon model. The Hamiltonian of a single-component *XY*-model with the coupling constant *J* is given by

$$H_{XY} = -J \sum_{\langle i,j \rangle} \cos(\theta_i - \theta_j). \tag{a1}$$

To map the *XY*-model to the sine-Gordon model, we start with the Villain approximation,

$$e^{-K(1-\cos\theta)} \approx \sum_{n=-\infty}^{\infty} e^{-\frac{K}{2}(\theta-2n\pi)^2}, \tag{a2}$$

which is valid when *K* is large. In this case, the dominant contribution comes from the regime that $\cos\theta \approx 1$, i.e., $\theta \approx 2n\pi$. Performing Taylor expansion around each of these values, we have $e^{-K(1-\cos\theta)} \approx \sum_n e^{-\frac{K}{2}(\theta-2n\pi)^2}$.

Using the Villain approximation, the Partition function of the *XY*-model in eq. (a1) is given by

$$Z_{XY} = \int_0^{2\pi} \prod_i \frac{\mathrm{d}\theta_i}{2\pi} e^{-\beta H_{XY}} = \int_0^{2\pi} \prod_i \frac{\mathrm{d}\theta_i}{2\pi} e^{\beta J \sum_{\langle i,j \rangle} \cos(\theta_i - \theta_j)}$$

$$= \int_0^{2\pi} \prod_i \frac{\mathrm{d}\theta_i}{2\pi} \prod_{\langle i,j \rangle} \sum_{m_{ij}} e^{-K/2(\theta_i-\theta_j-2m_{ij}\pi)^2}, \tag{a3}$$

where $K = \beta J = J/T$ and the Boltzmann constant is set to be 1 for simplicity; $m_{ij}$ are integers defined on each link of the 2D lattice. Now we perform the Hubbard-Stratonovich transformation by introducing the continuous variables $x_{ij}$ defined on each link of the lattice. The Partition function becomes

$$Z_{XY} = \int_0^{2\pi} \prod_i \frac{\mathrm{d}\theta_i}{2\pi} \int_{-\infty}^{\infty} \prod_{\langle ij \rangle} \sqrt{\frac{2K}{\pi}} \mathrm{d}x_{ij}$$

$$\times \prod_{\langle i,j \rangle} \sum_{m_{ij}} e^{-\frac{1}{2K} x_{ij}^2 - \mathrm{i}x_{ij}(\theta_i-\theta_j-2m_{ij}\pi)}. \tag{a4}$$

With the help of the Poisson resummation formula,

$$\sum_n \delta(x - nT) = \sum_m \frac{1}{T} e^{\mathrm{i}\frac{2m\pi}{T}x}, \tag{a5}$$

where *n* is an integer, the partition function $Z_{XY}$ becomes

$$Z_{XY} = \int_0^{2\pi} \prod_i \frac{\mathrm{d}\theta_i}{2\pi} \int_{-\infty}^{\infty} \prod_{\langle ij \rangle} \sqrt{\frac{2K}{\pi}} \mathrm{d}x_{ij}$$

$$\times \prod_{\langle i,j \rangle} e^{-\frac{1}{2K} x_{ij}^2 - \mathrm{i}x_{ij}(\theta_i-\theta_j)} \sum_n \delta(x_{ij} - n)$$

$$\sim \int_0^{2\pi} \prod_i \frac{d\theta_i}{2\pi} \sum_{\{m_{ij}\}} \prod_{\langle i,j\rangle} e^{-\frac{1}{2K}m_{ij}^2 - im_{ij}(\theta_i-\theta_j)}. \tag{a6}$$

To perform the above integrals, each $\theta_i$ is extracted from its neighbors,

$$Z_{XY} \sim \int_0^{2\pi} \prod_i \frac{d\theta_i}{2\pi} \sum_{\{m_{ij}\}} e^{-\frac{1}{2K}\sum_{i,\hat{\mu}} m_{i,\hat{\mu}}^2 - i\sum_{i,\hat{\mu}}(m_{i,\hat{\mu}}-m_{i,-\hat{\mu}})\theta_i}, \tag{a7}$$

where $\hat{\mu} = \hat{x}, \hat{y}$ denotes the lattice unit vectors along the bond directions. Now the angles $\theta_i$ can be integrated out,

$$Z_{XY} \sim \sum_{\{m_{ij}\}} e^{-\frac{1}{2K}\sum_{i,\hat{\mu}} m_{i,\hat{\mu}}^2} \prod_i \delta\left(\sum_{\hat{\mu}}(m_{i,\hat{\mu}} - m_{i,-\hat{\mu}})\right), \tag{a8}$$

where the $\delta$-function here is the Kronecker $\delta$.

Each integer $m_{ij}$ defined on the link can be treated as a current flown into and out of the connected lattice sites, and the $\delta$-function here basically says the current through each site is conserved. This conservation constraint is naturally satisfied if we define another set of integers $\{n_i\}$ at the sites of the dual lattice, i.e., the centers of the plaquettes of the original lattice,

$$\begin{aligned} m_{i,\hat{x}} &= n_{i+\hat{x}+\hat{y}} - n_{i+\hat{x}}, \\ m_{i,\hat{y}} &= n_{i+\hat{y}} - n_{i+\hat{x}+\hat{y}}, \\ m_{i-\hat{x},\hat{x}} &= n_{i+\hat{y}} - n_i, \\ m_{i-\hat{y},\hat{y}} &= n_i - n_{i+\hat{x}}. \end{aligned} \tag{a9}$$

With the new set of integers, the partition function now becomes,

$$Z_{XY} \sim \sum_{\{n_i\}} e^{-\frac{1}{2K}\sum_{i,\hat{\mu}}(n_{i+\hat{\mu}}-n_i)^2}. \tag{a10}$$

Comparing with the original partition function, we notice that the temperature has been inverted because $K \to 1/K$, and continuous variables has been replaced by integer variables. However, we can use Poisson summation to go back to continuous variables. Therefore,

$$\begin{aligned} Z_{XY} &\sim \int \prod_i d\phi_i \sum_{\{n_i\}} e^{-\frac{1}{2K}\sum_{i,\hat{\mu}}(\phi_{i,\hat{\mu}}-\phi_i)^2} \prod_i \delta(\phi_i - n_i) \\ &= \int \prod_i d\phi_i \sum_{\{n_i\}} e^{-\frac{1}{2K}\sum_{i,\hat{\mu}}(\phi_{i,\hat{\mu}}-\phi_i)^2 - i2\pi\sum_i n_i\phi_i}. \end{aligned} \tag{a11}$$

After adding the chemical potential term, the Partition function becomes

$$Z_{XY} \sim \int \prod_i d\phi_i \sum_{\{n_i\}} e^{-\frac{1}{2K}\sum_{i,\hat{\mu}}(\phi_{i,\hat{\mu}}-\phi_i)^2 - i2\pi\sum_i n_i\phi_i + \ln y\sum_i n_i^2}. \tag{a12}$$

Next we perform the summation over $\{n_i\}$ by using the following identity,

$$\sum_{\{n_i\}} e^{-i2\pi\sum_i n_i\phi_i + \ln y\sum_i n_i^2} = \prod_i \sum_{n_i=0,\pm1,\dots} y^{n_i^2} e^{-i2\pi n_i\phi_i}$$

$$= \prod_i (1 + 2y\cos 2\pi\phi_i + O(y^2))$$

$$= e^{2y\sum_i \cos 2\pi\phi_i}. \tag{a13}$$

The partition function eventually becomes the form of the sine-Gordon model,

$$Z_{XY} \sim \int \prod_i d\phi_i e^{-\frac{1}{2K}\sum_{i,\hat{\mu}}(\phi_{i,\hat{\mu}}-\phi_i)^2 + 2y\sum_i \cos 2\pi\phi_i}. \tag{a14}$$

## A2  RG equations from operator product expansions

### A2.1  Scaling dimensions

In this part we use the operator product expansion (OPE) to calculate the scaling dimensions of the coupling terms consisting of vertex operators of the form $\cos\beta\phi$ in the free bosonic field $\phi$ and the vertex operators $\cos\beta\theta$ in the dual field $\theta$, based on the free Lagrangian $\mathcal{L}_0 = \frac{1}{2K}(\partial_\mu\phi)^2$. Notice that the Luttinger parameter $K$ in the results presented below have to be accordingly scaled in order to be used for the theory in eq. (6).

We start with the correlation functions of the following vertex operators. Following the notation in ref. [69], the correlation function is given by

$$G_\beta(x-y) \equiv \langle e^{i\beta\phi(x)}e^{-i\beta\phi(y)}\rangle. \tag{a15}$$

By using the operator identity: $e^A e^B :=: e^{A+B} : e^{\langle AB + \frac{A^2+B^2}{2}\rangle}$, where $:\hat{O}:$ means normal ordering, we have

$$G_\beta(x-y) = \langle : e^{i\beta(\phi(x)-\phi(y))} : \rangle e^{-\frac{\beta^2}{2}\langle(\phi(x)-\phi(y))^2\rangle}$$

$$= e^{\beta\langle\phi(x)\phi(y)-\phi^2(x)\rangle} = \lim_{l\to 0}\left(\frac{l^2}{l^2+(x-y)^2}\right)^{\frac{\beta^2 K}{4\pi}}, \tag{a16}$$

where $l$ is the short distance cutoff. The following fact is used to derive the above equation,

$$\langle\phi(x)\phi(y) - \phi^2(x)\rangle = -\frac{K}{2\pi}\ln\frac{l^2}{l^2+(x-y)^2}. \tag{a17}$$

Similarly, we have for the dual field $\theta$:

$$\langle\theta(x)\theta(y) - \theta^2(x)\rangle = -\frac{1}{2\pi K}\ln\frac{l^2}{l^2+(x-y)^2}. \tag{a18}$$

Therefore, we are able to obtain the following correlation functions for two different types of vertex operators:

$$\begin{aligned} \langle e^{i\beta\phi(x)}e^{-i\beta\phi(y)}\rangle &\sim |x-y|^{-\frac{\beta^2 K}{2\pi}}, \\ \langle e^{i\beta\theta(x)}e^{-i\beta\theta(y)}\rangle &\sim |x-y|^{-\frac{\beta^2}{2\pi K}}, \end{aligned} \tag{a19}$$

based on which the scaling dimensions of the vertex operators can be calculated.

By taking $\cos\beta\phi = \frac{1}{2}(e^{i\beta\phi} + e^{-i\beta\phi})$, then

$$
\begin{aligned}
\langle\cos\beta\phi(x)\cos\beta\phi(y)\rangle = \frac{1}{4}\Big(&\langle e^{i\beta\phi(x)}e^{i\beta\phi(y)}\rangle + \langle e^{i\beta\phi(x)}e^{-i\beta\phi(y)}\rangle \\
&+ \langle e^{-i\beta\phi(x)}e^{i\beta\phi(y)}\rangle + \langle e^{-i\beta\phi(x)}e^{-i\beta\phi(y)}\rangle\Big) \\
\sim&\ |x-y|^{-\frac{\beta^2 K}{2\pi}},
\end{aligned}
$$

where we have used the fact that $\langle e^{i\beta_1\phi(x_1)}...e^{i\beta_N\phi(x_N)}\rangle = 0$ in the thermodynamic limit when $\sum_{n=1}^{N}\beta_n \neq 0$ [70]. From this we conclude that the scaling dimension of the $\cos\beta\phi$ term is $\frac{\beta^2 K}{4\pi}$. Similarly the $\cos\beta\theta$ term has scaling dimension $\frac{\beta^2}{4\pi K}$. Using these results, the composite operators consisting of this two types of basic vertex operators, like the ones in the main text, can be readily calculated.

### A2.2  The one-loop correction

For the one-loop corrections for the RG equations, we consider first the simple case where the free bosonic Lagrangian $\mathcal{L}_0 = \frac{1}{2K}(\partial_\mu\phi)^2$ is perturbed by a generic vortex term $\mathcal{L}' = \frac{g_\phi}{l^{D-\Delta_\phi}}\cos\beta\phi + \frac{g_\theta}{l^{D-\Delta_\theta}}\cos\alpha\theta$, where the short-distance cutoff $l$ is restored to make the couplings dimensionless or scale invariant [60]. The partition function can then be expanded as the following:

$$
\begin{aligned}
Z = &\int D[\phi]e^{-S} \\
= &Z^*\Bigg(1 + \int dx\frac{g_\phi}{l^{D-\Delta_\phi}}\langle\cos\beta\phi\rangle + \int dx\frac{g_\theta}{l^{D-\Delta_\theta}}\langle\cos\alpha\theta\rangle \\
&+ \frac{1}{2}\int dxdy\frac{g_\phi g_\theta}{l^{2D-\Delta_\phi-\Delta_\theta}}\langle\cos\beta\phi(x)\cos\alpha\theta(y)\rangle \\
&+ \frac{1}{2}\int dxdy\frac{g_\phi^2}{l^{2D-2\Delta_\phi}}\langle\cos\beta\phi(x)\cos\beta\phi(y)\rangle \\
&+ \frac{1}{2}\int dxdy\frac{g_\theta^2}{l^{2D-2\Delta_\theta}}\langle\cos\alpha\theta(x)\cos\alpha\theta(y)\rangle + O(g^3)\Bigg),\quad\text{(a20)}
\end{aligned}
$$

where $Z^*$ represents the free theory partition function. As we know, the conformal invariance of the free theory requires that the cross term corresponding to $g_\phi g_\theta$ vanishes at the one-loop level because the $g_\phi$ and the $g_\theta$ terms in general have different scaling dimensions. So we only need to consider the $g_\phi^2$ and $g_\theta^2$ terms.

Firstly, consider the $g_\phi^2$ term. The OPE in terms of $e^{i\beta\phi}$ is given by ref. [60],

$$
: e^{i\beta\phi(x)} :: e^{-i\beta\phi(y)} := \frac{1}{|x-y|^{2\Delta_\phi}} - \frac{1}{|x-y|^{2\Delta_\phi-2}}\frac{\beta^2}{2} : (\partial_\mu\phi)^2 :,
$$
$$\text{(a21)}$$

$$
: e^{\pm i\beta\phi(x)} :: e^{\pm i\beta\phi(y)} := \frac{1}{|x-y|^{-2\Delta_\phi}} : e^{\pm i2\beta\phi(x)} :,\quad\text{(a22)}
$$

$$
: e^{i\alpha\theta(x)} :: e^{-i\alpha\theta(y)} := \frac{1}{|x-y|^{2\Delta_\theta}} - \frac{1}{|x-y|^{2\Delta_\theta-2}}\frac{\alpha^2}{2} : (\partial_\mu\theta)^2 :,
$$
$$\text{(a23)}$$

$$
: e^{\pm i\alpha\theta(x)} :: e^{\pm i\alpha\theta(y)} := \frac{1}{|x-y|^{2\Delta_\theta}} : e^{\pm i2\alpha\theta(x)} :,\quad\text{(a24)}
$$

where it is understood that $|x-y| \to 0$. Therefore,

$$
\begin{aligned}
&: \cos\beta\phi(x) :: \cos\beta\phi(y) : \\
&= \frac{1}{4} : \Big(e^{i\beta\phi(x)} + e^{-i\beta\phi(x)}\Big) :: \Big(e^{i\beta\phi(y)} + e^{-i\beta\phi(y)}\Big) : \\
&= \frac{1/2}{|x-y|^{2\Delta_\phi}} - \frac{1/2}{|x-y|^{2\Delta_\phi-2}}\frac{\beta^2}{2} : (\partial_\mu\phi)^2 : \\
&\quad + \frac{1/2}{|x-y|^{-2\Delta_\phi}} : \cos 2\beta\phi(x) :,\quad\text{(a25)}
\end{aligned}
$$

and similarly,

$$
\begin{aligned}
&: \cos\alpha\theta(x) :: \cos\alpha\theta(y) : \\
&= \frac{1/2}{|x-y|^{2\Delta_\theta}} - \frac{1/2}{|x-y|^{2\Delta_\theta-2}}\frac{\alpha^2}{2} : (\partial_\mu\theta)^2 : \\
&\quad + \frac{1/2}{|x-y|^{-2\Delta_\theta}} : \cos 2\alpha\theta(x) : .\quad\text{(a26)}
\end{aligned}
$$

For the $g_\phi^2$ term in eq. (a20), $\frac{1}{2}\int dxdy\frac{g_\phi^2}{l^{2D-2\Delta_\phi}}\langle\cos\beta\phi(x)\cos\beta\phi(y)\rangle$, which gives rise to the one-loop correction to the $: (\partial_\mu\phi)^2 :$ term, becomes

$$
\begin{aligned}
&-\frac{\beta^2}{8}\int dxdy\frac{g_\phi^2}{l^{2D-2\Delta_\phi}}|x-y|^{-2\Delta_\phi+2}\langle : (\partial_\mu\phi)^2 :\rangle \\
&= -\frac{\beta^2}{8}\int dx\frac{g_\phi^2}{l^{2D-2\Delta_\phi}}\langle : (\partial_\mu\phi)^2 :\rangle\int dy|x-y|^{-2\Delta_\phi+2}.\quad\text{(a27)}
\end{aligned}
$$

Now we do a change of scale by changing the cutoff $l \to l + \delta l = (1 + \delta\ln l)l$. This means the domain of the above integration is changed from $|x-y| > l$ to $|x-y| > (1 + \delta\ln l)l$. Therefore, the corresponding change in the above integration becomes

$$
\frac{\beta^2}{8}\int dx\frac{g_\phi^2}{l^{2D-2\Delta_\phi}}\langle : (\partial_\mu\phi)^2 :\rangle\int_{l<|x-y|<(1+\delta\ln l)l} dy|x-y|^{-2\Delta_\phi+2},
$$
$$\text{(a28)}$$

which in the case of $D = 2$ is

$$
\frac{\beta^2\pi}{4}g_\phi^2\delta\ln l\int dx\langle : (\partial_\mu\phi)^2 :\rangle.\quad\text{(a29)}
$$

Comparing with the kinetic term $\frac{1}{2K}\int dx(\partial_\mu\phi)^2$, we obtain the correction of $K$ due to the $g_\phi$ term,

$$
\frac{d(1/K)}{d\ln l} = \frac{\pi\beta^2}{2}g_\phi^2 \Rightarrow \frac{dK}{d\ln l} = -\frac{\pi\beta^2 K^2}{2}g_\phi^2.\quad\text{(a30)}
$$

The contribution from the $g_\theta\cos\alpha\theta$ term can be similarly obtained as:

$$
\frac{dK}{d\ln l} = \frac{\pi\alpha^2}{2}g_\theta^2.\quad\text{(a31)}
$$

*A2.3 Derivation of the RG equations*

Using the basic ingredients above, we can proceed to work out the full RG equations presented in the main text. For the free theory given by

$$\mathcal{L}_0 = \frac{1}{4K_+}(\partial_\mu \phi_+)^2 + \frac{1}{K_-}(\partial_\mu \phi_-)^2 \equiv \frac{1}{2\tilde{K}_+}(\partial_\mu \phi_+)^2 + \frac{1}{2\tilde{K}_-}(\partial_\mu \phi_-)^2,$$

(a32)

where we have redefined the Luttinger parameters $\tilde{K}_+ \equiv 2K_+, \tilde{K}_- \equiv K_-/2$, so that the Lagrangian takes the standard normalization convention and the results derived from the previous section can be directly carried over. We have the following scaling dimensions for the different interaction terms:

- For $\cos \beta \phi_+$: $\Delta_{\phi_+} = \frac{\beta^2 \tilde{K}_+}{4\pi}$;
- For $\cos \beta \phi_-$: $\Delta_{\phi_-} = \frac{\beta^2 \tilde{K}_-}{4\pi}$;
- For $\cos \alpha \theta_-$: $\Delta_{\theta_-} = \frac{\alpha^2}{4\pi \tilde{K}_-}$;
- For $\cos \beta \phi_+ \cos \alpha \phi_-$: $\Delta_{\phi_+ \phi_-} = \frac{1}{4\pi}\left(\beta^2 \tilde{K}_+ + \alpha^2 \tilde{K}_-\right)$.

The scaling dimensions above give us the tree-level flow equations. For the loop-level correction of the Luttinger parameters, we again make use of the OPEs. The OPE

$$: \cos \beta \phi_+(x) :: \cos \beta \phi_+(y) :$$
$$= \frac{1/2}{|x-y|^{2\Delta_{\phi_+}}} - \frac{1/2}{|x-y|^{2\Delta_{\phi_+}-2}} \frac{\beta^2}{2} : (\partial_\mu \phi_+)^2 :,$$

(a33)

gives the following correction after repeating the real-space renormalization,

$$\delta\left(\frac{1}{2\tilde{K}_+}\right) = \frac{1}{2} \cdot \frac{\beta^2}{4} g_{\phi_+}^2 \cdot 2\pi \delta(\ln l) \Rightarrow \delta \tilde{K}_+ = -\frac{\pi}{2}\beta^2 \tilde{K}_+^2 g_{\phi_+}^2 \delta(\ln l).$$

(a34)

The OPE

$$: \cos \beta \phi_-(x) :: \cos \beta \phi_-(y) :$$
$$= \frac{1/2}{|x-y|^{2\Delta_{\phi_-}}} - \frac{1/2}{|x-y|^{2\Delta_{\phi_-}-2}} \frac{\beta^2}{2} : (\partial_\mu \phi_-)^2 :,$$

(a35)

gives the following correction to $\tilde{K}_-$,

$$\delta\left(\frac{1}{2\tilde{K}_-}\right) = \frac{1}{2} \cdot \frac{\beta^2}{4} g_{\phi_-}^2 \cdot 2\pi \delta(\ln l) \Rightarrow \delta \tilde{K}_- = -\frac{\pi}{2}\beta^2 \tilde{K}_-^2 g_{\phi_-}^2 \delta(\ln l).$$

(a36)

The OPE

$$: \cos \alpha \theta_-(x) :: \cos \alpha \theta_-(y) :$$
$$= \frac{1/2}{|x-y|^{2\Delta_{\theta_-}}} - \frac{1/2}{|x-y|^{2\Delta_{\theta_-}-2}} \frac{\alpha^2}{2} : (\partial_\mu \theta_-)^2 :,$$

(a37)

gives the following correction to $K_-$,

$$\delta\left(\frac{\tilde{K}_-}{2}\right) = \frac{1}{2} \cdot \frac{\alpha^2}{4} g_{\theta_-}^2 \cdot 2\pi \delta(\ln l) \Rightarrow \delta \tilde{K}_- = \frac{\pi \alpha^2}{2} g_{\theta_-}^2 \delta(\ln l).$$

(a38)

The OPE

$$: \cos \beta \phi_+(x) \cos \alpha \phi_-(x) :: \cos \beta \phi_+(y) \cos \alpha \phi_-(y) :$$
$$= \frac{1}{16} \sum_{\eta_{1,2,3,4}=\pm 1} : e^{i(\eta_1 \beta \phi_+(x)+\eta_2 \alpha \phi_-(x))} :: e^{i(\eta_3 \beta \phi_+(y)+\eta_4 \alpha \phi_-(y))} :$$
$$\Longrightarrow -\frac{1/8}{|x-y|^{2\Delta_{\phi_+}+2\Delta_{\phi_-}-2}} \left(\beta^2 : (\partial_\mu \phi_+)^2 : +\alpha^2 : (\partial_\mu \phi_-)^2 :\right)$$
$$+ \frac{1/4}{|x-y|^{-2\Delta_{\phi_+}+2\Delta_{\phi_-}}} : \cos 2\beta \phi_+ :$$
$$+ \frac{1/4}{|x-y|^{2\Delta_{\phi_+}-2\Delta_{\phi_-}}} : \cos 2\alpha \phi_- :,$$

(a39)

which generates the following renormalizations:

$$\delta\left(\frac{1}{2\tilde{K}_+}\right) = \frac{1}{2} \cdot \frac{\beta^2}{8} g_{\phi_{\text{int}}}^2 \cdot 2\pi \delta(\ln l) \Rightarrow \delta \tilde{K}_+$$
$$= -\frac{\pi \beta^2 \tilde{K}_+^2}{4} g_{\phi_{\text{int}}}^2 \delta(\ln l),$$
$$\delta\left(\frac{1}{2\tilde{K}_-}\right) = \frac{1}{2} \cdot \frac{\alpha^2}{8} g_{\phi_{\text{int}}}^2 \cdot 2\pi \delta(\ln l) \Rightarrow \delta \tilde{K}_-$$
$$= -\frac{\pi \alpha^2 \tilde{K}_-^2}{4} g_{\phi_{\text{int}}}^2 \delta(\ln l),$$
$$\delta g_{\phi_\pm} = \frac{1}{2} \cdot \frac{1}{4} g_{\phi_{\text{int}}}^2 \cdot 2\pi \delta(\ln l) = \frac{\pi}{4} g_{\phi_{\text{int}}}^2 \delta(\ln l).$$

(a40)

Combining the contributions from the different interaction terms, we eventually arrive at the RG equations presented in the main text.

## A3 K-matrix formulation of Luttinger liquid

In this section, we review the K-matrix formulation of the Luttinger liquid. In this framework, a Luttinger liquid is treated as the boundary of a higher-dimensional bulk and the K-matrix contains topological information about the bulk. In particular, using the K-matrix it is straightforward to calculate the braiding statistics between the various vertex operators that represent the charges, vortices or their combinations. This is a useful way to rule out non-local operators when writing down the Lagrangian based on symmetry considerations.

*A3.1 One pair of boson and dual boson*

To warm up for the case of two coupled Luttinger liquids in our paper, we look at the simpler case of one Luttinger liquid

consisting of the boson field $\theta$ and its dual $\phi$. By defining $\Phi \equiv (\theta, \phi)^{\mathrm{T}}$, the free Lagrangian density is given by

$$\mathcal{L}_0 = \frac{1}{4\pi} \left( \partial_t \Phi^{\mathrm{T}} \mathrm{K} \partial_x \Phi + \partial_x \Phi^{\mathrm{T}} \mathrm{V} \partial_x \Phi \right), \tag{a41}$$

where K is not to be confused with the Luttinger parameter $K$ that appears in the rest part of the paper. The K-matrix is given by $\mathrm{K} = \sigma^1$ and the V-matrix is given by $\mathrm{V} = \sigma^0$, where the $\sigma^\mu$ with $\mu = 0, 1, 2, 3$ are the Pauli matrices. In canonical quantization, the conjugate momentum of the $\theta$ field is given by

$$\Pi = \frac{\delta \mathcal{L}_0}{\delta \partial_t \theta} = \frac{1}{2\pi} \partial_x \phi, \tag{a42}$$

with the canonical commutation given by $[\theta(t, x), \Pi(t, y)] = \mathrm{i}\delta(x - y)$, or equivalently, $[\theta(t, x), \partial_y \phi(t, y)] = 2\pi \mathrm{i}\delta(x - y)$.

We have two basic types of vertex operators $\mathrm{e}^{\mathrm{i}\theta}$ and $\mathrm{e}^{\mathrm{i}\phi}$, whose charge vectors are given by $l_\theta = (1, 0)^{\mathrm{T}}$ and $l_\phi = (0, 1)^{\mathrm{T}}$ respectively. Then the braiding statistics between the two vertex operators is given by

$$2\pi l_\theta^{\mathrm{T}} \mathrm{K}^{-1} l_\phi = 2\pi, \tag{a43}$$

which simply states the fact that if we move a charge around its vortex, then it picks up a phase of $2\pi$. Here we take $\mathrm{e}^{\mathrm{i}\theta}$ to be the charge operator and the $\mathrm{e}^{\mathrm{i}\phi}$ to be the vortex operator to be consistent with the notation of the main text. Notice however, that in the normalization convention of the main text, the vortex is given by $\mathrm{e}^{\mathrm{i}2\pi\phi}$ instead, so there is a factor of $2\pi$ in the field rescaling for $\phi$. In the convention used here, $\theta$ and $\phi$ are put on equal footing, both without the $\pi$ factors. The normalization convention does not change the essential physics we discuss.

### A3.2 Two coupled Luttinger liquids

Now we move on to two coupled Luttinger liquids, which would correspond to two coupled *XY*-models. Choosing the basis $\Phi = (\theta_1, \phi_1, \theta_2, \phi_2)^{\mathrm{T}}$, the Lagrangian density takes the same form as in eq. (a41), but the new K-matrix and V-matrix are given by

$$\mathrm{K} = \begin{pmatrix} \sigma^x & 0 \\ 0 & \sigma^x \end{pmatrix}, \quad \mathrm{V} = \begin{pmatrix} \sigma^0 & 0 \\ 0 & \sigma^0 \end{pmatrix}. \tag{a44}$$

Then we have the following charge vectors:

$$l_{\theta_1} = (1, 0, 0, 0)^{\mathrm{T}}, \quad l_{\phi_1} = (0, 1, 0, 0)^{\mathrm{T}},$$
$$l_{\theta_2} = (0, 0, 1, 0)^{\mathrm{T}}, \quad l_{\phi_2} = (0, 0, 0, 1)^{\mathrm{T}}. \tag{a45}$$

Under the basis transformation used in the main text,

$$\theta_+ \equiv (\theta_1 + \theta_2)/2, \quad \theta_- \equiv \theta_1 - \theta_2,$$
$$\phi_+ \equiv \phi_1 + \phi_2, \quad \phi_- \equiv (\phi_1 - \phi_2)/2, \tag{a46}$$

the charge vectors for the new fields are given by

$$l_{\theta_+} = \left( \frac{1}{2}, 0, \frac{1}{2}, 0 \right)^{\mathrm{T}}, \quad l_{\phi_+} = (0, 1, 0, 1)^{\mathrm{T}},$$
$$l_{\theta_-} = (1, 0, -1, 0)^{\mathrm{T}}, \quad l_{\phi_-} = \left( 0, \frac{1}{2}, 0, -\frac{1}{2} \right)^{\mathrm{T}}. \tag{a47}$$

In a similar fashion, the braidings between the fields and the dual fields are given by

$$2\pi l_{\theta_+}^{\mathrm{T}} \mathrm{K}^{-1} l_{\phi_+} = 2\pi, \quad 2\pi l_{\theta_-}^{\mathrm{T}} \mathrm{K}^{-1} l_{\phi_-} = 2\pi,$$
$$2\pi l_{\theta_+}^{\mathrm{T}} \mathrm{K}^{-1} l_{\phi_-} = 0, \quad 2\pi l_{\theta_-}^{\mathrm{T}} \mathrm{K}^{-1} l_{\phi_+} = 0, \tag{a48}$$

i.e., the braidings between fields from different channels vanish, as it should be.

Now we are ready to check the locality of the various terms appearing in the Lagrangian, i.e., whether their braiding with the original local physical fields $\theta_{1,2}$ are integer multiples of $2\pi$.

• $\cos \phi_+$ (note again that this term is the $\cos 2\pi\phi_+$ in the main text): The charge vector is $(0, 1, 0, 1)^{\mathrm{T}}$, and its braiding with $\theta_{1,2}$ are both $2\pi$. Higher order terms are therefore also allowed.

• $\cos 2\theta_-$: The charge vector is $(1, 0, 1, 0)^{\mathrm{T}}$, and its braiding with $\theta_{1,2}$ are both 0.

• $\cos \phi_-$ (equivalent to $\cos 2\pi\phi_-$ in the main text): The charge vector is $(0, \frac{1}{2}, 0, -\frac{1}{2})^{\mathrm{T}}$, and its braiding with $\theta_{1,2}$ are $\pm\pi$ respectively, i.e., not integer multiple of $2\pi$, hence not allowed.

• $\cos 2\phi_-$ (equivalent to $\cos 4\pi\phi_-$ in the main text): The charge vector is $(0, 1, 0, -1)^{\mathrm{T}}$, and its braiding with $\theta_{1,2}$ are $\pm 2\pi$.

• $\cos \frac{1}{2}\phi_+ \cos \phi_-$ (equivalent to $\cos \pi\phi_+ \cos 2\pi\phi_-$ in the main text): The charge vector is given by $(0, 1, 0, 0)^{\mathrm{T}}$, whose braiding with $\theta_{1,2}$ are $2\pi$ and 0 respectively, hence it is local and allowed, even though neither $\cos \frac{1}{2}\phi_+$ nor $\cos \phi_-$ is allowed separately. This is consistent with the fact that this term comes from the sum of the original two local vortex terms $\cos \phi_1$ and $\cos \phi_2$.

**Acknowledgements**

# Chapter 7

# Pseudospin-triplet pairing in iron-chalcogenide superconductors

## ARTICLE

Check for updates

# Pseudospin-triplet pairing in iron-chalcogenide superconductors

Meng Zeng [1], Dong-Hui Xu[2,3], Zi-Ming Wang[2,3], Lun-Hui Hu [4,5✉] & Fu-Chun Zhang[6,7]

Understanding the pairing symmetry is a crucial theoretical aspect in the study of unconventional superconductivity for interpreting experimental results. Here we study superconductivity of electron systems with both spin and pseudospin-1/2 degrees of freedom. By solving linearized gap equations, we derive a weak coupling criterion for the even-parity spin-singlet pseudospin-triplet pairing. It can generally mix with the on-site $s$-wave pairing since both of them belong to the same symmetry representation ($A_{1g}$) and their mixture could naturally give rise to anisotropic intra-band pairing gap functions with or without nodes. This may directly explain why some of the iron-chalcogenide superconductors are fully gapped (e.g. FeSe thin film) and some have nodes (e.g. LaFePO and LiFeP). We also find that the anisotropy of gap functions can be enhanced when the principal rotation symmetry is spontaneously broken in the normal state such as nematicity, and the energetic stabilization of pseudospin-triplet pairings indicates the coexistence of nematicity and superconductivity. This could be potentially applied to bulk FeSe, where gap anisotropy has been experimentally observed.

[1] Department of Physics, University of California, San Diego, CA 92093, USA. [2] Department of Physics and Chongqing Key Laboratory for Strongly Coupled Physics, Chongqing University, Chongqing 400044, People's Republic of China. [3] Center of Quantum Materials and Devices, Chongqing University, Chongqing 400044, People's Republic of China. [4] Department of Physics, The Pennsylvania State University, University Park, PA 16802, USA. [5] Department of Physics and Astronomy, University of Tennessee, Knoxville, TN 37996, USA. [6] Kavli Institute for Theoretical Sciences, University of Chinese Academy of Sciences, 100190 Beijing, China. [7] CAS Center for Excellence in Topological Quantum Computation, University of Chinese Academy of Sciences, 100190 Beijing, China. ✉email: hu.lunhui.zju@gmail.com

The symmetry principle is one of the most powerful tools to diagnose low-energy electronic band structures, lattice vibrations, and linear responses[1], and is also valuable to explore various symmetry-breaking ordered phases such as magnetism, charge/spin density-wave, nematicity and superconductivity[2]. The crystal symmetry of a solid-state system dictates the normal band structures it hosts near the Fermi level, which could in turn determine the most favorable super-conducting pairing symmetry[3,4]. This symmetry principle for superconductors (SC) is recently extended to investigate multi-band unconventional superconductivity[5–7]. Interestingly, the orbital-independent and orbital-dependent pairings that belong to the same symmetry representation may coexist with each other[8]. Such orbital-dependent pairings have been studied in a wide variety of systems with multi-band character, including $Sr_2RuO_4$[9], iron-chalcogenide SCs[10–13], Cu-doped $Bi_2Se_3$[14] and half-Heusler compounds[15–18], from which the guiding principle by symmetry is crucial to understanding the nature of unconventional superconductivity.

A few specific systems can be effectively characterized by a general normal-state model Hamiltonian that contains both spin ($\{\uparrow, \downarrow\}$) and pseudospin ($\{1, 2\}$) degrees of freedom, where pseudospin could originate from two atomic orbitals, two sublattices, two layers, or two valleys[6]. We start from a spin-singlet centrosymmetric SC to explore the existence of even-parity pseudospin-triplet pairings, for example, $c_{1,\uparrow}(\mathbf{k})c_{2,\downarrow}(-\mathbf{k}) + c_{2,\uparrow}(\mathbf{k})c_{1,\downarrow}(-\mathbf{k}) - c_{1,\downarrow}(-\mathbf{k})c_{2,\uparrow}(-\mathbf{k}) - c_{2,\downarrow}(\mathbf{k})c_{1,\uparrow}(-\mathbf{k})$, and further investigate their valuable roles in tailoring anisotropic pairing gap functions with or without nodes[19]. Different from spin-triplet pairings, spin-singlet pseudospin-triplet pairings have not been much explored in real materials since such pairings are usually considered to be energetically unfavorable. This is partly due to the common belief that the double degeneracy of the two orbitals is lifted by orbital hybridization so that the orbital-dependent pairing would be severely suppressed under crystal field splitting or electron-electron repulsive interaction. One aim of this work is concerned with the possible condition for the existence of even-parity spin-singlet orbital-dependent pairings, and possible applications to real materials.

On the other hand, the effects of symmetry breaking in unconventional SCs is an important topic that has attracted tremendous interest. The symmetry could be broken explicitly by external fields or strain, or be broken spontaneously from many-body interactions. Two typical examples are rotational symmetry breaking[20,21] and time-reversal-symmetry (TRS) breaking[22–26]. Besides, the interplay between nematicity and superconductivity is yet to be fully understood in some real materials, such as FeSe[12,27], where gap functions can be highly anisotropic. These systems are all multi-band SCs, while symmetry-reducing signatures are experimentally observed above the superconducting transition temperature, which is mainly caused by both crystal field splittings and interaction-induced order parameters (e.g. nematicity). Thus, discovering the coexistence of nematicity and superconductivity in these multi-band systems can shed new light on understanding the underlying favorable pairing symmetries.

The main finding of this work is that the anisotropic gap functions with or without nodes could be attributed to the mixing of isotropic $s$-wave pairing and even-parity spin-singlet pseudospin-triplet pairing, even though both of them belong to the $A_{1g}$ symmetry representation. For technical conveniences, we adopt an orbital $\mathbf{d}_o(\mathbf{k})$-vector notations[11] to describe the pairing matrix and similarly a $\mathbf{g}_o(\mathbf{k})$-vector for orbital hybridization in the two-orbital subspace ($\{1, 2\}$). Solving linearized gap equations, we show that the presence of $\mathbf{g}_o$-vector generally suppresses the superconductivity with orbital $\mathbf{d}_o$-vector except for $\mathbf{d}_o(\mathbf{k}) \parallel \mathbf{g}_o(\mathbf{k})$, which is consistent with the concept of superconducting fitness[6].

This sets up weak-coupling criteria for $A_{1g}$-type orbital-dependent pairings that could naturally give rise to anisotropic gap functions in real superconducting materials. Moreover, we reveal a deep connection between two-orbital nematic SC and pseudospin-triplet pairings. Within the mean-field theory for electron-electron repulsive interactions, the nematic order develops in the orbital subspace at $T < T_{\text{nem}}$, which also contributes to the total orbital hybridization, $\mathbf{g}_{\text{tot}} = \mathbf{g}_o + \mathbf{g}_{\text{nem}}$. This leads to the stabilization of a nematic orbital $\mathbf{d}_o$-vector for $\mathbf{d}_o(\mathbf{k}) \parallel \mathbf{g}_{\text{tot}}(\mathbf{k})$, indicating the coexistence of nematicity and superconductivity. The direct applications to FeSe[12,27] are also discussed. We also generalize it to a two-valley system with $C_6$ breaking terms (e.g., Kekulé distortion). In the end, we also predict an orbital-polarized superconducting state.

## Results

**Classification of Spin-singlet Orbital-triplet pairings.** To explore the weak-coupling criterion for the energetically favorable even-parity spin-singlet pseudospin-triplet pairing, we consider the mean-field pairing Hamiltonian,

$$\mathcal{H}_\Delta = \sum_{\mathbf{k}} \sum_{s_1 a, s_2 b} \Delta^{a,b}_{s_1,s_2}(\mathbf{k}) F^\dagger_{s_1 a, s_2 b}(\mathbf{k}) + \text{h.c.}, \quad (1)$$

where $F^\dagger_{s_1 a, s_2 b}(\mathbf{k}) = c^\dagger_{s_1 a}(\mathbf{k}) c^\dagger_{s_2 b}(-\mathbf{k})$ is the creation operator of Cooper pairs, $s_1, s_2$ are indices for spins and $a, b$ are for pseudospins (e.g., two orbitals $\{1, 2\}$). A general pairing potential of a two-band model is a four-by-four matrix[6]. In particular, the spin-singlet pairing function $\Delta^{a,b}_{s_1,s_2}(\mathbf{k}) = f(\mathbf{k}) M_{a,b}(\mathbf{k})(i\sigma_2)_{s_1,s_2}$ consists of the angular form factor $f(\mathbf{k})$ and $M_{a,b}(\mathbf{k})$ in the orbital channel. The spin-singlet pairings are not mixed with spin-triplet pairings in the absence of spin-orbit coupling (SOC). In analogy to spin-triplet SCs, for the technical convenience, we then use an orbital $\mathbf{d}_o(\mathbf{k})$-vector for the spin-singlet orbital-dependent pairing potential[11],

$$\hat{\Delta}_{tot}(\mathbf{k}) = [\Delta_s \Psi_s(\mathbf{k}) \tau_0 + \Delta_o (\mathbf{d}_o(\mathbf{k}) \cdot \boldsymbol{\tau})](i\sigma_2), \quad (2)$$

where $\Delta_s$ and $\Delta_o$ are pairing strengths in orbital-independent and orbital-dependent channels, respectively. Here $\boldsymbol{\tau}$ and $\boldsymbol{\sigma}$ are Pauli matrices acting on the orbital and spin subspace, respectively, and $\tau_0$ is a 2-by-2 identity matrix. When both $\Delta_s$ and $\Delta_o$ are real, a real orbital $\mathbf{d}_o(\mathbf{k})$-vector preserves TRS while a complex one spontaneously breaks TRS ($\mathcal{T} = i\tau_0 \sigma_2 \mathcal{K}$ with $\mathcal{K}$ being complex conjugate). The Fermi statistics requires $\Psi_s(\mathbf{k}) = \Psi_s(-\mathbf{k})$, $d^{1,3}_o(\mathbf{k}) = d^{1,3}_o(-\mathbf{k})$ and $d^2_o(\mathbf{k}) = -d^2_o(-\mathbf{k})$. In other words, $d^2_o(\mathbf{k})$ describes odd-parity spin-singlet orbital-singlet pairings and the other two are for even-parity spin-singlet orbital-triplet pairings. Moreover, we provide an alternative definition of orbital $\mathbf{d}_o$-vectors in Supplementary Note 1. Even though the orbital-independent part $\Psi_s(\mathbf{k})$ is also "orbital-triplet" by statistics, it is completely trivial. Hereafter, we only refer to $d^1_o(\mathbf{k})$ and $d^3_o(\mathbf{k})$ as orbital-triplet pairings[28].

In addition, the basis functions for both $\Psi_s(\mathbf{k})$ and orbital $\mathbf{d}_o(\mathbf{k})$-vectors in Eq. (2) could be classified by crystalline symmetry.

Under the action of an $n$-fold rotation operator $C_n$ about the $z$-axis, the pairing potential $\hat{\Delta}(\mathbf{k})$ transforms as

$$\mathcal{D}[C_n] \hat{\Delta}_J(\mathbf{k}) (\mathcal{D}[C_n])^T = e^{i\frac{2\pi}{n}J} \hat{\Delta}_J(C_n^{-1}\mathbf{k}), \quad (3)$$

where $\mathcal{D}[C_n]$ is the corresponding matrix representation, $J$ is the orbital angular momentum quantum number, and also labels the irreducible representations of the $C_n$ point group. For example, $J = 0$ is for $A$ representation and $J = 2$ is for $B$ representation. Firstly, the TRS requires the coexistence of $\hat{\Delta}_J$ and $\hat{\Delta}_{-J}$ with equal weight. If the rotation symmetry $C_n$ is further imposed, then $J$

**Table 1 Classification of spin-singlet pairing potentials for Eq. (2).**

| $C_n$ | $J = -J \pmod n$ | $\Psi_s(\mathbf{k}) = \Psi_s(-\mathbf{k})$ | $\mathbf{d}_o^1(\mathbf{k}) = \mathbf{d}_o^1(-\mathbf{k})$ | $\mathbf{d}_o^2(\mathbf{k}) = -\mathbf{d}_o^2(-\mathbf{k})$ | $\mathbf{d}_o^3(\mathbf{k}) = \mathbf{d}_o^3(-\mathbf{k})$ |
|---|---|---|---|---|---|
| $n = 2$ | $J = 0$ | $1, k_x^2, k_y^2, k_z^2, k_x k_y$ | $1, k_x^2, k_y^2, k_z^2, k_x k_y$ | $k_z, k_z k_x^2, k_z k_y^2, k_z^3, k_z k_x k_y$ | $1, k_x^2, k_y^2, k_z^2, k_x k_y$ |
| | $J = 1$ | $k_x k_z, k_y k_z$ | $k_x k_z, k_y k_z$ | $k_x, k_y$ | $k_x k_z, k_y k_z$ |
| $n = 3$ | $J = 0$ | $1, k_x^2 + k_y^2, k_z^2$ | $E_g$ representation | $k_z$ | $E_g$ representation |
| $n = 4$ | $J = 0$ | $1, k_x^2 + k_y^2, k_z^2$ | $k_x^2 - k_y^2, k_x k_y$ | $k_z, k_z(k_x^2 + k_y^2), k_z^3$ | $k_x^2 - k_y^2, k_x k_y$ |
| | $J = 2$ | $k_x^2 - k_y^2, k_x k_y$ | $1, k_x^2 + k_y^2, k_z^2$ | $k_z(k_x^2 - k_y^2), k_z k_x k_y$ | $1, k_x^2 + k_y^2, k_z^2$ |
| $n = 6$ | $J = 0$ | $1, k_x^2 + k_y^2, k_z^2$ | $E_g$ representation | $k_z$ | $E_g$ representation |
| | $J = 3$ | $(k_x + i k_y)^3, (k_x - i k_y)^3$ | $E_g$ representation | $k_x^3 - 3 k_x k_y^2, 3 k_x^2 k_y - k_y^3$ | $E_g$ representation |

Here we consider a spin-singlet two-orbital superconductors with $\{d_{xz}, d_{yz}\}$-orbitals. Based on the $n$-fold rotation symmetry $C_n$ about $z$-axisd and time-reversal symmetry (TRS), we have $J = -J$ mod $n$, which leads to all the pairing channels with orbital-independent $\Psi_s(\mathbf{k})$ and orbital-dependent $\mathbf{d}_o(\mathbf{k})$-vector in Eq. (2). Here, for $J = 0$ pairing subspace of $C_3$, the $(\mathbf{d}_o^1(\mathbf{k}), \mathbf{d}_o^3(\mathbf{k}))$ forms a two-dimensional $E_g$ representation, where the basis functions are $(k_x^2 - k_y^2, k_x k_y)$ and $(k_y k_z, k_x k_z)$. For $J = 0$ pairing subspace of $C_6$, the $(\mathbf{d}_o^1(\mathbf{k}), \mathbf{d}_o^3(\mathbf{k}))$ forms a two-dimensional $E_g$ representation, where the basis functions are $(k_y k_z, k_x k_z)$; for the $J = 3$ pairing subspace of $C_6$, the $(\mathbf{d}_o^1(\mathbf{k}), \mathbf{d}_o^3(\mathbf{k}))$ forms a two-dimensional $E_g$ representation, where the basis functions are $(k_x^2 - k_y^2, k_x k_y)$.

and $-J$ have to be equivalent modulo $n$, i.e. $J \equiv -J \bmod n$. The results for the basis functions of $\Psi_s(\mathbf{k})$ and $\mathbf{d}_o(\mathbf{k})$ are summarized in Table 1 for a two-band SC with the $\{d_{xz}, d_{yz}\}$-orbitals. In this case, $\mathcal{D}[C_n] = [\cos(\frac{2\pi}{n})\tau_0 - i \sin(\frac{2\pi}{n})\tau_2] \otimes \sigma_0$. For instance, $\mathcal{D}[C_4] = -i\tau_2 \otimes \sigma_0$ explains that both $\Delta_o \tau_1$ and $\Delta_o \tau_3$ are d-wave-like pairing states[29].

At the mean-field level, the Bogoliubov de-Gennes (BdG) Hamiltonian is given by

$$\mathcal{H}_{\mathrm{BdG}} = \begin{pmatrix} \mathcal{H}_0(\mathbf{k}) & \hat{\Delta}_{tot}(\mathbf{k}) \\ \hat{\Delta}_{tot}^\dagger(\mathbf{k}) & -\mathcal{H}_0^*(-\mathbf{k}) \end{pmatrix}, \tag{4}$$

where $\mathcal{H}_0(\mathbf{k})$ represents a two-band normal-state Hamiltonian with both spin and pseudospin degrees of freedom.

In general, the BdG Hamiltonian is also invariant under the $C_n$ rotation symmetry, i.e., $\mathcal{D}_{\mathrm{BdG}}[C_n] \mathcal{H}_{\mathrm{BdG}}(\mathbf{k}) (\mathcal{D}_{\mathrm{BdG}}[C_n])^\dagger = \mathcal{H}_{\mathrm{BdG}}(C_n^{-1}\mathbf{k})$ when we define $\mathcal{D}_{\mathrm{BdG}}[C_n] = \begin{pmatrix} \mathcal{D}[C_n] & 0 \\ 0 & e^{i\frac{2\pi}{n}J}(\mathcal{D}[C_n])^* \end{pmatrix}$ based on Eq. (3).

Here we assume both inversion and time-reversal symmetries are preserved. To be specific, we consider a SOC-free Hamiltonian,

$$\mathcal{H}_0(\mathbf{k}) = \epsilon(\mathbf{k})\tau_0 \sigma_0 + \lambda_o(\mathbf{g}_o(\mathbf{k}) \cdot \boldsymbol{\tau})\sigma_0, \tag{5}$$

where the basis is $\psi_\mathbf{k}^\dagger = (c_{1,\uparrow}^\dagger(\mathbf{k}), c_{1,\downarrow}^\dagger(\mathbf{k}), c_{2,\uparrow}^\dagger(\mathbf{k}), c_{2,\downarrow}^\dagger(\mathbf{k}))$, $\epsilon(\mathbf{k}) = (k_x^2 + k_y^2)/2m - \mu$ is the band energy measured relative to the chemical potential $\mu$, $m$ is the effective mass, $\lambda_o$ represents the orbital hybridization and $\mathbf{g}_o(\mathbf{k}) = (g_1(\mathbf{k}), g_2(\mathbf{k}), g_3(\mathbf{k}))$. And the $g_3$-component leads to the different effective masses of different orbitals. As mentioned earlier, this vector notation is just for the technical convenience. Besides, the $g_1$ and $g_2$ components are determined by symmetries. For example, TRS requires $g_{1,3}(\mathbf{k}) = g_{1,3}(-\mathbf{k})$ and $g_2(\mathbf{k}) = -g_2(-\mathbf{k})$. If inversion symmetry (IS) is present, $g_2(\mathbf{k})$ (or $g_1(\mathbf{k})$) must vanish for $\mathcal{I} = \tau_0\sigma_0$ (or $\mathcal{I} = \tau_3\sigma_0$), which is the same as the constraint for the orbital $\mathbf{d}_o$-vector. The more explicit form of $\mathbf{g}_o(\mathbf{k})$ is determined by other crystal symmetries.

In general, the pseudospin-triplet (i.e. orbital-triplet) pairing state shares some similarities with the spin-triplet pairing state[30]. To show that, we first discuss the superconducting quasi-particle spectrum of orbital-triplet SCs in the absence of band-splitting caused by orbital hybridizations, i.e., $\mathbf{g}_o(\mathbf{k}) = 0$ for Eq. (5). In this case, the superconducting gaps on the Fermi surface are

$$E(\mathbf{k}) = \pm|\Delta_o|\sqrt{|\mathbf{d}_o(\mathbf{k})|^2 \pm |\mathbf{d}_o^*(\mathbf{k}) \times \mathbf{d}_o(\mathbf{k})|}, \tag{6}$$

for the $\Delta_s = 0$ limit. This indicates that there are two distinct gaps

if TRS is spontaneously broken. In the following, we mainly focus on the time-reversal-invariant superconducting states, i.e., real $\mathbf{d}_o$-vectors, for which the classification of pairing potentials is shown in Table 1 based on Eq. (3). We will show the interplay between $\Delta_s$ and $\Delta_o$ can lead to anisotropic superconducting gaps on different Fermi surfaces. Moreover, its stability against orbital-hybridization, electron-electron interactions, and applications to real materials will be discussed in detail as follows. We will also briefly comment on the effects of TRS-breaking in the end.

**Stability for spin-singlet orbital-triplet pairings.** We apply the weak-coupling scheme[6] for spin-singlet orbital-triplet pairings against crystal field splittings, which cause orbital hybridizations [i.e. the $\mathbf{g}_o(\mathbf{k})$ term in Eq. (5)]. We analytically calculate the superconductivity instability for the orbital $\mathbf{d}_o$-vector by BCS decoupling scheme. The superconducting transition temperature $T_c$ of orbital-dependent pairing channels is calculated by solving the linearized gap equation,

$$\Delta_{s_1,s_2}^{a,b}(\mathbf{k}) = -\frac{1}{\beta}\sum_{\omega_n}\sum_{s_1'a',s_2'b'} V_{s_1'a',s_2'b'}^{s_1 a, s_2 b}(\mathbf{k}, \mathbf{k}') \\ \times \left[G_e(\mathbf{k}', i\omega_n)\hat{\Delta}(\mathbf{k}')G_h(-\mathbf{k}', i\omega_n)\right]_{s_1'a',s_2'b'}, \tag{7}$$

where $\beta = 1/k_B T$, $G_e(\mathbf{k}, i\omega_n) = [i\omega_n - \mathcal{H}_0(\mathbf{k})]^{-1}$ is the Matsubara Green's function for electrons with $\omega_n = (2n + 1)\pi/\beta$ and $G_h(\mathbf{k}, i\omega_n) = -G_e^*(\mathbf{k}, i\omega_n)$. We expand the attractive interactions as $V_{s_1'a',s_2'b'}^{s_1 a, s_2 b}(\mathbf{k}, \mathbf{k}') = -\sum_{\Gamma,l}[v^\Gamma \mathbf{d}_o^{\Gamma,l}(\mathbf{k}) \cdot \boldsymbol{\tau} i\sigma_2]_{s_1 a, s_2 b}[\mathbf{d}_o^{\Gamma,l}(\mathbf{k}') \cdot \boldsymbol{\tau} i\sigma_2]_{s_1'a',s_2'b'}$ with $v^\Gamma > 0$. Here $\Gamma$ labels the irreducible representation with $l = 1, 2, ..., \mathrm{Dim}\,\Gamma$. In this work we focus on 1d representations, i.e. Dim $\Gamma = 1$, which already include many interesting cases and are sufficient for the applications discussed in later sections. Due to the possible existence of multiple pairing channels belonging to different representations, each channel has its own critical temperature $T_c^\Gamma$, the largest of which becomes the actual critical temperature of the system. In the weak-coupling theory, $T_c^\Gamma$ follows the standard BCS form and is solely determined by the corresponding pairing interaction $v^\Gamma$ in that particular channel. To the leading order of $\lambda_o k_F^2/\mu$ ($k_F = \sqrt{2m\mu}$), the equation for $T_c$ for the channel $\Gamma$ reads (see details in the Methods section),

$$\ln\left(\frac{T_c^\Gamma}{T_{c0}}\right) = \int_S d\Omega\, \mathcal{C}_0(T_c)\left(|\mathbf{d}_o^\Gamma|^2 - |\mathbf{d}_o^\Gamma \cdot \hat{\mathbf{g}}_o|^2\right), \tag{8}$$

where $T_{c0}$ is the critical temperature for $\lambda_o = 0$, $\Omega$ is the solid angle of $\mathbf{k}$, $\hat{\mathbf{g}}_o = \mathbf{g}_o(\mathbf{k})/|\mathbf{g}_o(\mathbf{k})|$ are normalized vectors. Here we take $\int_S d\Omega\, |\mathbf{d}_o^\Gamma|^2 = 1$. And $\mathcal{C}_0(T_c) = \mathrm{Re}\,[\psi^{(0)}(\frac{1}{2}) - \psi^{(0)}(\frac{1}{2} + i\frac{\lambda_o|\mathbf{g}(\mathbf{k})|}{2\pi k_B T_c})]$, where $\psi^{(0)}(z)$ is the digamma function.

We now discuss its implications. In general, the $\lambda_o$-term describes a pair-breaking term, since $\mathcal{C}_0(T_c) \leq 0$ and it monotonically decreases as $\lambda_o$ increases, hence the right-hand side of Eq. (8) suppresses $T_c$ in general. However, if we focus on one-dimensional representations, i.e. Dim $\Gamma = 1$, it is straightforward to see that $\mathbf{d}_o^\Gamma \parallel \mathbf{g}_o$ can lead to $T_c = T_{c0}$ for any value of $\lambda_o$, which indicates that the orbital $\mathbf{d}_o$-vector that is parallel with $\mathbf{g}_o$ is unaffected by the orbital hybridizations. It is worth mentioning that due to the possible suppression of $T_c$, depending on the relation between $\mathbf{d}_o^\Gamma$ and $\mathbf{g}_o$ the leading instability channel at $\lambda_o = 0$ could be suppressed more than some of the other coexisting channels and may eventually become sub-leading. This interesting behavior is discussed further in Supplementary Note 3. For notional simplicity, we will drop the representation index $\Gamma$ when there is no danger of confusion. Choosing $\mathbf{g}_o(\mathbf{k}) = (2k_x k_y, 0, k_x^2 - k_y^2)$, the numerical results are shown in Fig. 1. The black line confirms that $T_c$ is unaffected as $\lambda_o k_F^2/k_B T_{c0}$ increases for $\mathbf{d}_o(\mathbf{k}) = k_F^{-2}(2k_x k_y, 0, k_x^2 - k_y^2)$, which is the unconventional $A_{1g}$ pairing. However, $T_c$ for other $\mathbf{d}_o$-vectors are severely suppressed. The light-blue line is for $\mathbf{d}_o(\mathbf{k}) = \frac{1}{\sqrt{2}}(1, 0, 1)$, and the light-orange line for $\mathbf{d}_o(\mathbf{k}) = k_F^{-2}(k_x^2 - k_y^2, 0, -2k_x k_y)$. Therefore, we conclude that the orbital $\mathbf{d}_o$-vector could exist in SCs with two active orbitals that are not fully degenerate. This is similar to spin-triplet SCs, where the $A_{1g}$-type spin $\mathbf{d}_s$-vector could exist in noncentrosymmetric SCs because $\mathbf{d}_s \parallel \mathbf{g}_s$ is optimally satisfied[4,6].

It is worth mentioning that the results presented above is using a continuum form of the Hamiltonian based on $\mathbf{k} \cdot \mathbf{p}$ theory. For real materials, given the interaction on the lattice, the components of the interaction in terms of the basis functions of the representations might not be exactly the same with the form of the vector $\mathbf{g}_o$. As a result, the parallel condition presented above may not be exactly satisfied. However, the theory developed in this work is generally applicable and the extend to which the parallel condition holds can still be a useful criterion for the most favorable pairing.

Next, we include $\Delta_s$, and investigate the coupling between $\Psi_s$ and $\mathbf{d}_o$. Solving the coupled linearized gap equations up to

$(\lambda_o k_F^2/\mu)^2$ order (see details in Supplementary Note 3), we find that the results from Eq. (8) are still correct. Besides, the magnitude of orbital $\mathbf{d}_o$-vectors might be determined as $\mathbf{d}_o(\mathbf{k}) = \Psi_s(\mathbf{k}) \hat{\mathbf{g}}_o(\mathbf{k})$. It implies that $\Psi_s$ and $\mathbf{d}_o$ belong to the same representation of crystalline groups. Therefore, the stability of orbital $\mathbf{d}_o$-vector by Eq. (8) indicates the symmetry principle for spin-singlet orbital-triplet pairings.

We now explain Eq. (8) from the band picture. Within the band basis, the pairing potential in the orbital subspace becomes $\hat{\Delta}_{band}(\mathbf{k}) = U^\dagger(\mathbf{k})[\Delta_s \Psi_s(\mathbf{k})\tau_0 + \Delta_o(\mathbf{d}_o(\mathbf{k}) \cdot \boldsymbol{\tau})] U(\mathbf{k})$, where $U(\mathbf{k})$ is the unitary matrix in the orbital subspace, $U^\dagger(\mathbf{k})[\epsilon(\mathbf{k})\tau_0 + \lambda_o(\mathbf{g}_o(\mathbf{k}) \cdot \boldsymbol{\tau})] U(\mathbf{k}) = \text{Diag}[E_+(\mathbf{k}), E_-(\mathbf{k})]$, with the normal band dispersion

$$E_\pm(\mathbf{k}) = \epsilon(\mathbf{k}) \pm \lambda_o |\mathbf{g}_o(\mathbf{k})|. \tag{9}$$

The intra-orbital pairing naturally gives rise to the intra-band pairing. However, it is different for orbital-dependent pairings. To show that, we decompose the orbital $\mathbf{d}_o$-vector, $\mathbf{d}_o(\mathbf{k}) = d_\parallel(\mathbf{k})\hat{\mathbf{g}}_o(\mathbf{k}) + \mathbf{d}_\perp(\mathbf{k})$, where $d_\parallel(\mathbf{k}) = \mathbf{d}_o(\mathbf{k}) \cdot \hat{\mathbf{g}}_o(\mathbf{k})$ and $\mathbf{d}_\perp(\mathbf{k}) \cdot \hat{\mathbf{g}}_o(\mathbf{k}) = 0$. We find that the $d_\parallel$-part gives rise to the intra-band pairing, while the $\mathbf{d}_\perp$-part leads to the inter-band pairing (see Supplementary Note 4). If the band splitting is much larger than the pairing gap ($\lambda_o k_F^2 \gg \Delta_o$), the inter-band pairing is not energetically favorable in the weak-coupling pairing limit. It means that the inter-band pairing will be severely suppressed if we increase the orbital hybridization $\lambda_o$, consistent with Eq. (8) and results in Fig. 1. Now if we again include the orbital-independent pairing part $\Delta_s \Psi_s(\mathbf{k}\tau_0 i\sigma_2)$, the relation between $\mathbf{d}_o$ and $\Psi_s(\mathbf{k})$ obtained previously from solving the coupled linearized gap equation (see Supplementary Note 3) can also be reproduced in the band picture by considering the maximization of the condensation energy. The total condensation energy per volume and per spin of the two intra-band pairings is given by

$$\delta E = N_+ \sum_{\mathbf{k} \in \text{FS}_+} \left(\Delta_s \Psi_s(\mathbf{k}) + \Delta_o d_\parallel(\mathbf{k})\right)^2 \\ + N_- \sum_{\mathbf{k} \in \text{FS}_-} \left(\Delta_s \Psi_s(\mathbf{k}) - \Delta_o d_\parallel(\mathbf{k})\right)^2, \tag{10}$$

where $N_\pm$ are the density of states on the two Fermi surfaces ($E_\pm$). And $\Delta_s \Psi_s(\mathbf{k}) \pm \Delta_o d_\parallel(\mathbf{k})$ are the pairing gaps on these two Fermi surfaces. In order to maximize $\delta E$, we have $d_\parallel(\mathbf{k}) = \text{sign}[(N_+ - N_-)\Delta_s \Delta_o]\Psi_s(\mathbf{k})$ (See Supplementary Note 4 for details). Even though the intra-orbital pairing and the orbital-triplet pairing belong to the same symmetry representation, the different $\mathbf{k}$-dependencies of $\Psi_s(\mathbf{k})$ and $d_\parallel(\mathbf{k})$ can naturally lead to the anisotropic superconducting gap on the Fermi surface observed in experiments.

**Applications to superconductors with/without nodes.** As a consequence of the mixing of the orbital-independent pairing ($\Delta_s$) and orbital-dependent pairing ($\Delta_o$) discussed in the previous section, there could be a nodal SC. In this section, we apply the results of the previous section to study superconductors with two orbitals, where $\Delta_s$ and $\Delta_o$ coexist. It is shown that the anisotropic gap functions with/without nodes depend on the ratio of $\Delta_s$ and $\Delta_o$ superconducting order parameters. Our weak-coupling theory might have potential applications to some of the nodal/nodeless SCs in the iron-chalcogenides family. For example, the angle-resolved photoemission spectroscopy (ARPES) measurements indicate a nontrivial superconducting gap anisotropy for the monolayer FeSe thin film[31]. The penetration depth measurements on both LaFePO[32] and LiFeP[33] show a linear dependence on $T$, suggesting the presence of superconducting gap nodes.
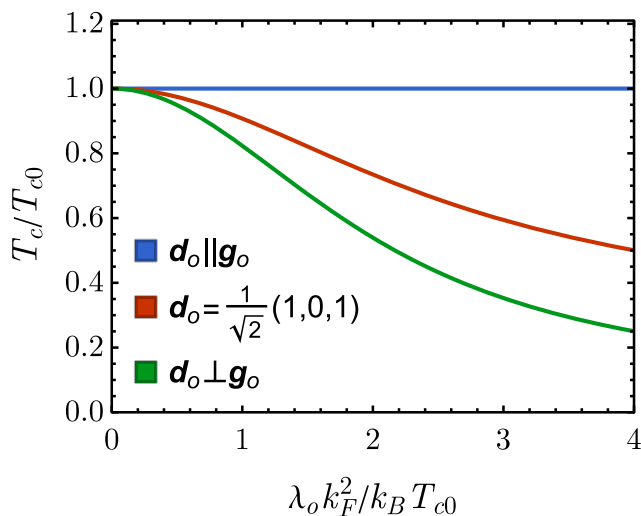


**Fig. 1 Stability of orbital $\mathbf{d}_o$-vectors vs orbital hybridization $\lambda_o$ in Eq. (5).** It shows the transition temperature $T_c/T_{c0}$ as a function of $\lambda_o k_F^2/k_B T_{c0}$ for $\mathbf{g}_o(\mathbf{k}) = (2k_x k_y, 0, k_x^2 - k_y^2)$. $T_{c0}$ is $T_c$ at $\lambda_o = 0$. The curves from top to bottom correspond to $\mathbf{d}_o(\mathbf{k}) = k_F^{-2}(2k_x k_y, 0, k_x^2 - k_y^2)$, $\mathbf{d}_o(\mathbf{k}) = \frac{1}{\sqrt{2}}(1, 0, 1)$, and $\mathbf{d}_o(\mathbf{k}) = k_F^{-2}(k_x^2 - k_y^2, 0, -2k_x k_y)$, respectively.

As an example, we consider the pairing potential in Eq. (2) for monolayer FeSe, where there is no hole pocket around the $\Gamma$-point, and a two-spin two-orbital model has been shown to be a good approximation around the electron pockets near the $M$ point of the Brillouin zone (two Fe unit cell). The density functional theory calculations show that there are four bands around the $M$ point, giving rise to only two electron pockets. In the one Fe unit cell, there is one pocket near the $X$ and $Y$ points, respectively. After folding with respect to the unit cell with two Fe, we obtain two pockets around the $M$ point. Considering spin degrees of freedom, it naturally resembles a $C_{4z}$-invariant two-orbital model[34],

$$\mathcal{H}_M(\mathbf{k}) = \left[\epsilon(\mathbf{k})\tau_0 + Ak_xk_y\tau_z\right]\sigma_0 + v_{so}\tau_x\left[k_x\sigma_y + k_y\sigma_x\right], \quad (11)$$

where $\epsilon(\mathbf{k}) = (k_x^2 + k_y^2)/(2m) - \mu$ with $m > 0$ the effective mass, $A$ leads to the anisotropic effective mass (i.e., orbital hybridization), and $v_{so}$ represents SOC that still preserves inversion symmetry. These four states are degenerate at the $M$ point since they form the four-dimensional representation of the space group No. 129 ($P4/nmm$)[35]. We take the parameters for the FeSe thin film as $\mu = 55$ meV, $1/(2m) = 1375$ meV $\cdot$ Å$^2$, $A = 600$ meV $\cdot$ Å$^2$ and $v_{so} \leq 15$ meV $\cdot$ Å[34]. The SOC is very weak to open a tiny gap along the $k_x = 0$ and $k_y = 0$ lines, shown in Fig. 2a. As what we expect, it shows two $C_{4z}$ rotational-invariant Fermi surfaces, and the maximal gap, which is induced by the $z$-component of the $\mathbf{g}_o$ vector, is around 12 meV along the (11) and (1$\bar{1}$) directions. This is larger than the typical superconducting gaps in iron-chalcogenide SCs (~4 meV), implying that the effect of the orbital hybridization on the pairing symmetries should not be neglected.

We now use the criteria derived above (Eq. (8)) to examine the superconducting states. Specifically, the weak-coupling criterion indicates that the most favorable pairing to characterize the anisotropic superconducting gap is the $A_{1g}$-type $s$-wave pairing symmetry,

$$\hat{\Delta}(\mathbf{k}) = \left[\Delta_s\tau_0 + \Delta_ok_xk_y\tau_z\right](i\sigma_2). \quad (12)$$

The ratio between $\Delta_s$ and $\Delta_o$ determines the superconducting nodal structure. To simplify the analysis, we turn off the weak SOC. In the band basis, the dispersion of $\mathcal{H}_M(\mathbf{k})$ is $\epsilon_\pm(\mathbf{k}) = (k_x^2 + k_y^2)/(2m) \pm A|k_xk_y| - \mu$. Here $\pm$ label the band index. Projecting $\hat{\Delta}(\mathbf{k})$ onto the bands leads to $\Delta_\pm = \Delta_s \pm \Delta_o|k_xk_y|$. Given that $\Delta_s, \Delta_o > 0$, nodal points can only appear for $\Delta_-$ on the "−" band. The nodal condition would be $|k_xk_y| = \Delta_s/\Delta_o$ has solution on the FS given by $\epsilon_-(\mathbf{k}) = 0$. By using the mathematical inequality $k_x^2 + k_y^2 \leq 2|k_xk_y|$, it can be shown that the nodal

condition is given by,

$$\frac{\Delta_s}{\Delta_o} \leq \frac{\mu}{1/m - A}, \quad (13)$$

which is shown in Fig. 2b. In general, the ratio $\Delta_s/\Delta_o$ should depend on both interaction strength in each pairing channel and the orbital hybridization strength. This gives rise to the condition of nodal $A_{1g}$-type $s$-wave superconducting states. Therefore, it could not only explain the anisotropic gap functions observed in the FeSe thin film (fully gapped) but also the nodal super-conductivity in LaFePO and LiFeP. Around one linear Dirac node, the effective Hamiltonian up to linear-$k$ can be mapped out as

$$\mathcal{H}_D = k_1\tilde{\sigma}_0\tilde{\tau}_z + k_2\tilde{\sigma}_y\tilde{\tau}_y, \quad (14)$$

where $k_1, k_2$ are liner combinations of $k_x$ and $k_y$. All the other Dirac nodes are related to this one by reflection symmetries. Then, we only need to focus on $\mathcal{H}_D$, which is a Dirac Hamiltonian with topological charge (winding number) $\pm 2$, whose node is protected by the chiral symmetry (i.e., the product of time-reversal symmetry and particle-hole symmetry). The $2\mathbb{Z}$ winding number is due to the presence of inversion symmetry and time-reversal symmetry. To analytically show the topology of Dirac nodes, we apply perturbation analysis with respect to PT symmetry (i.e., the product of time-reversal symmetry and inversion symmetry) and Chiral symmetry. Note that the PT symmetry can be also $C_{2z}T$ symmetry for a 2D or quasi-2D SC. The projected symmetry representations are given by PT $= \tilde{\sigma}_y\tilde{\tau}_0$ and $\mathcal{C} = \tilde{\sigma}_y\tilde{\tau}_x$. As expected, the PT symmetry commutes with $\mathcal{H}_D$, while the Chiral symmetry anti-commutes with $\mathcal{H}_D$. Then, local perturbations preserving PT and Chiral are

$$\mathcal{H}'_D = m_1\tilde{\sigma}_0\tilde{\tau}_y + m_2\tilde{\sigma}_y\tilde{\tau}_z, \quad (15)$$

where $m_1$ and $m_2$ represent perturbation strengths or mass terms. The spectrum of $\mathcal{H}_D + \mathcal{H}'_D$ are given by

$$E = \pm\sqrt{k_1^2 + k_2^2 + m_1^2 + m_2^2 \pm 2|m_1k_2 + m_2k_1|}, \quad (16)$$

which indicates that the Dirac nodes are movable but not removable. For example, $k_1 = 510.7k_x + 76.5k_y$ and $k_2 = -14.7k_x - 40.9k_y$ around one Dirac node. Then, turning on the SOC $v_{so} = 15$ meV $\cdot$ Å, we numerically confirm the nodal SC phase with $\Delta_s = 3$ meV and $\Delta_o = 200$ meV $\cdot$ Å$^2$, shown in Fig. 2c, where the logarithm of superconducting gaps are plotted. The eight dark red points are the linear Dirac nodes. Based on the topology-protection argument, the interplay between intra- and inter-orbital pairings for nodal superconductivity is robust against local perturbations. Note that our results are different from a previous work[34], in which the $d$-wave pairing symmetry
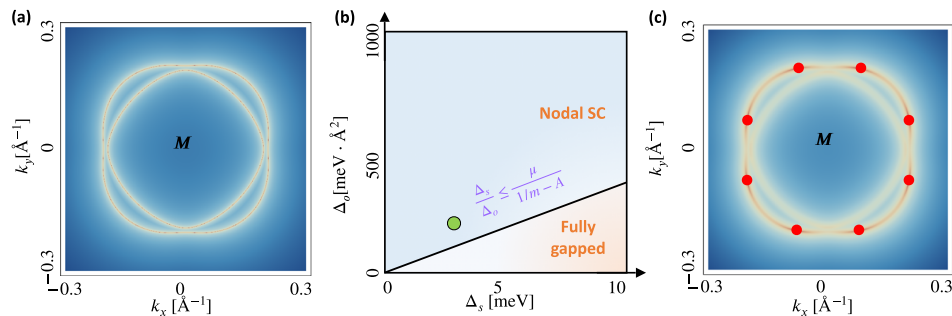


**Fig. 2 The application to iron-chalcogenide superconductors with/without linear Dirac nodes.** In (**a**), the two-electron pockets around the $M$ point. For zero spin-orbit coupling, $v_{so} = 0$, (**b**) shows the phase diagram as a function of the intra-orbital pairing $\Delta_s$ and the inter-orbital pairing $\Delta_o$. For the gap parameters represented by the green dot in (b), the nodal superconductor is exhibited in (**c**), where the eight dark red points represent the chiral symmetry-protected Dirac nodes.

induced nodal SC. In experiments, the nodal gap structure could be detected by measuring the temperature dependence of physical quantities like specific heat and penetration depth at low temperatures. A power law dependence usually indicates the existence of nodal structures (point nodes or line nodes), whereas exponential dependence implies the SC is fully gapped[3].

**Applications to superconductors with nematic order**. In addition to the crystal field splitting, the many-body electron-electron interactions may also lead to orbital hybridization, such as the nematic ordering in the normal states (See Supplementary Note 5 for details). The rotational symmetry reduction could either be from interaction-induced spontaneous symmetry breaking or from explicit symmetry breaking from, say, adding external strain. Then the natural question to ask is whether it is still possible to have an orbital-dependent pairing order characterized by some $\mathbf{d}_o$-vector. Interestingly, we find that the orbital-dependent pairing can coexist with the electronic nematic ordering as long as $\mathbf{d}_o$ is parallel to the $\mathbf{g}_{tot}$, which is an effective orbital-hybridization vector that also contains the nematic order. This establishes a deep connection between SCs with nematic order and spin-singlet orbital-triplet pairings. In the following, we study two typical examples.

- For case A [two-orbital system], we apply the theory to fit the anisotropic superconducting gap of the hole pocket in the bulk FeSe measured by the quasiparticle interference imaging[12].
- For case B [two-valley system], we use a toy model to demonstrate the possible existence of $s + d$-like nematic nodal superconductor in two-valley systems on a honeycomb lattice. We also show the transition between U-shaped and V-shaped quasi-particle density-of-state by tuning the chemical potential.

**Case A: two-orbital model for the bulk FeSe SC**. We discussed the possible anisotropic $A_{1g}$-type s-wave pairing states for the $C_4$-symmetric iron-chalcogenide SCs including fully gapped FeSe thin film and nodal SC in LiFeP and LaFePO. Here we investigate the $C_4$-breaking nematic SC in bulk FeSe. Let us revisit the iron-based SC with a well-established nematic ordering. We consider $\mathcal{H}_{int} = v_1 \hat{n}_1(\mathbf{r})\hat{n}_2(\mathbf{r})$, where $\hat{n}_i$ is electron density operator for the $i$-atomic orbital. If $\langle \hat{n}_1 \rangle \neq \langle \hat{n}_2 \rangle$, $C_n$ ($n > 2$) is spontaneously broken down to $C_2$ and we have the nematic order. The intra-orbital interaction does not alter the mean-field results for nematic orders (See Supplementary Note 5). The total inter-orbital hybridization contains two parts,

$$\mathbf{g}_{tot}(\mathbf{k}) = \mathbf{g}_o(\mathbf{k}) + \mathbf{g}_{nem}, \quad (17)$$

where $\mathbf{g}_o(\mathbf{k})$ is caused by the crystal field splitting and $\mathbf{g}_{nem} = (0, 0, \Phi)$ is induced due to the nematicity $\Phi = v_1 \langle \hat{n}_1 - \hat{n}_2 \rangle$, which is momentum-independent if translation symmetry is to be preserved. Hereafter, we focus on the hole pockets around the $\Gamma$ point to fit the experimental data of superconducting gap functions[12]. We will see that even this simplified weak-coupling model, where the coupling between the hole pockets at the $\Gamma$ point and the electron pockets at the $M$ point is ignored, can produce a descent fit the experimental data. A similar result is expected for the electron pockets near the $M$ point. Replacing $\mathbf{g}_o$ with $\mathbf{g}_{tot}$ in Eq. (5), we can still use Eq. (8) to investigate the interplay between superconductivity and nematic order, thus the orbital $\mathbf{d}_o$-vector satisfying $\mathbf{d}_o \| \mathbf{g}_{tot}$ leads to the nematic superconductivity. Thus, it generally shows the $A_{1g}$-type s-wave spin-singlet orbital-triplet pairings in nematic SCs.

This scenario can be adopted to study the quasi-two dimensional bulk FeSe, where superconductivity ($T_c \sim 8$ K) emerges inside a well-developed nematic phase (transition temperature $T_{nem} \sim 90$ K[36]), shown in Fig. 3a. For a minimal two-band model[37] for the bulk FeSe with $\{d_{xz}, d_{yz}\}$-orbitals, $\mathbf{g}_o = (2k_x k_y, 0, k_x^2 - k_y^2)$ and $\mathbf{g}_{nem} = (0, 0, \Phi)$[38,39]. Therefore, the nematic orbital $\mathbf{d}_o$-vector with $\mathbf{d}_o \| \mathbf{g}_{tot}$ breaks $C_4$ (see Supplementary Note 5 for more details). The projected pairing gap function on the large Fermi surface is given by

$$\Delta_{FS}(\mathbf{k}) = \Delta_s + \Delta_o \sqrt{\left(-\lambda_o(k_x^2 - k_y^2) + \Phi\right)^2 + (2\lambda_o k_x k_y)^2}. \quad (18)$$

If $\Phi = 0$, $\Delta_{FS}(\mathbf{k})$ is reduced to $\Delta_s + \Delta_o |\lambda_o|(k_x^2 + k_y^2)$ that is in the isotropic limit. The presence of $\Phi$ is the driving force for the anisotropy of $\Delta_{FS}(\mathbf{k})$. When the nematicity $\Phi$ is strong enough, the orbital $\mathbf{d}_o$-vector will be pinned along the $z$-axis, resulting in the so-called orbital-selective pairing states. We adopt the realistic parameters for the bulk FeSe SC from Ref. [39] to calculate the superconducting gap measured by the quasiparticle interference imaging[12]. In Fig. 3b, we show the angular dependence of the pairing gap around the hole pocket at the $\Gamma$-point of FeSe in the presence of nematic order. Our theory provides an equally decent fit to recent experimental data[12] as the intra-orbital $s + d$-pairing theory proposed by Kang et al.[39], even though our work uses a simplified model without considering the coupling to the other two electron pockets. Our theory shows more clearly the role of nematic order on the pairing symmetries. Therefore, the theory developed in this work may alternatively explain the experimental evidence of orbital-selective pairings of the FeSe SC in refs. [12,27], and reveal a deep connection between nematic SC and spin-singlet orbital-triplet pairings. It has to be mentioned that here we only focused on the hole pockets around the $\Gamma$ point and discussed the nematicity-induced gap anisotropy around the hole FS. There are other possible mechanisms for gap anisotropy in
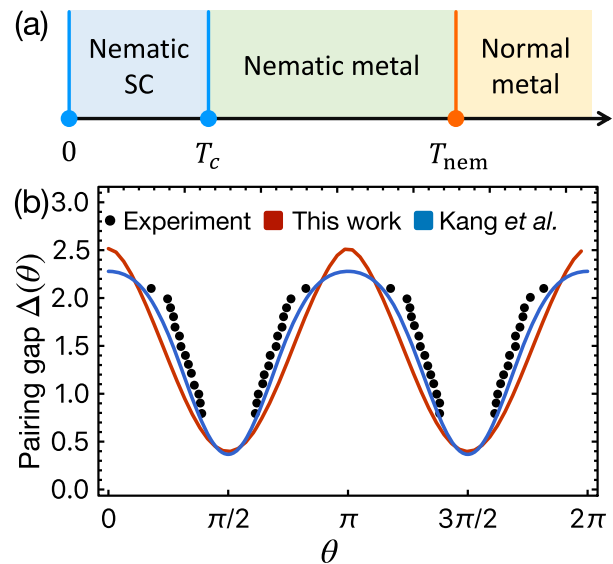


**Fig. 3 The application to bulk FeSe superconductors with nematicity.**
**a** Schematic phase diagram vs temperature $T$ for normal metal ($T > T_{nem}$), nematic metal ($T < T_{nem}$), and nematic superconductivity ($T < T_c$).
**b** Angular dependence of the superconducting pairing gap: comparison between experiment data (black dots) by Sprau et al. ref. [12], our theory (red line) and the theory proposed by Kang et al.[39] (blue line). Fitting parameters used for our model: $\Delta_s = 2.6$, $\Delta_o = -0.055$ in Eq. (18). All the other parameters used are the same[39], including the chemical potential, effective mass, orbital hybridization, and nematic order.

Fe-based SCs. For example, a previous work[40] discussed, among other things, the anisotropy/isotropy of the SC gap around the electron pockets at the $M$ point, where the degree of anisotropy depends on the $J_1$-$J_2$ magnetic frustration in the proposed five-orbital $t$-$J_1$-$J_2$ microscopic model.

**Case B: two-valley system superconductivity.** Similar to the two-orbital systems considered above, we discuss in this section superconductivity in two-valley systems, like single layer graphene SC[41] or transition metal dichalcogenide (TMD)[42], where the pairing can be between opposite valleys $K_\pm$. The spin-singlet pairing is merely characterized by the orbital $\mathbf{d}_o$-vector with $\Delta_s = 0$ in Eq. (2). For the single-particle Hamiltonian, the inter-valley hopping is naturally forbidden by translational symmetry, namely, $\lambda_o = 0$ in Eq. (5). Then, we consider the inter-valley scattering Hamiltonian, $\mathcal{H}_{int} = \sum_{\mathbf{k},\mathbf{k}',\sigma} V(\mathbf{k} - \mathbf{k}') c^\dagger_{+,\sigma}(\mathbf{k}) c_{+,\sigma}(\mathbf{k}') c^\dagger_{-,\sigma}(\mathbf{k}') c_{-,\sigma}(\mathbf{k})$. It generates the inter-valley coupling $\mathbf{g}_{int}$ by defining the order parameter $\Phi(\mathbf{k}) = \sum_{\mathbf{k}',\sigma} V(\mathbf{k} - \mathbf{k}') \langle c_{+,\sigma}(\mathbf{k}') c^\dagger_{-,\sigma}(\mathbf{k}') \rangle$ that spontaneously breaks the translational symmetry,

$$\mathbf{g}_{int}(\mathbf{k}) = (g_{int,1}(\mathbf{k}), g_{int,2}(\mathbf{k}), 0), \quad (19)$$

where $g_{int,1}(\mathbf{k}) = \text{Re}[\Phi(\mathbf{k})]$ and $g_{int,2}(\mathbf{k}) = -\text{Im}[\Phi(\mathbf{k})]$. In this case, TRS is $\mathcal{T} = i\tau_1\sigma_2\mathcal{K}$ and IS is $\mathcal{I} = \tau_1\sigma_0$. The $\mathbf{d}_o$-vector is manifested as $\mathbf{d}_o = (d_1(\mathbf{k}), id_2(\mathbf{k}), 0)$ with $d_1(\mathbf{k}) = d_1(-\mathbf{k})$ and $d_2(\mathbf{k}) = -d_2(-\mathbf{k})$. Both $d_1(\mathbf{k})$ and $d_2(\mathbf{k})$ are real to preserve TRS. As for the interaction-induced $\mathbf{g}_{int}$, $\mathcal{T}$ and $\mathcal{I}$ require $g_{int,1}(\mathbf{k}) = g_{int,1}(-\mathbf{k})$ and $g_{int,2}(\mathbf{k}) = 0$. By symmetry, there are two general possibilities. One is $g_{int,1}(\mathbf{k}) = 1$, so $C_3 \times \mathcal{I} = C_6$ is preserved, and it describes the charge-density-wave order[43,44]. The other one is $g_{int,1}(\mathbf{k}) \in \{k_x k_y, k_x^2 - k_y^2\}$ that spontaneously breaks $C_6$ down to $C_2$, forming a nematic order. This is experimentally possible for the strain-induced Kekul'e distortion (i.e., $\sqrt{3} \times \sqrt{3}$ type).

We next discuss superconductivity in the presence of inter-valley couplings, by replacing the $\mathbf{g}_o$-vector in Eq. (5) with the interaction-induced $\mathbf{g}_{int}$. As a result, Eq. (8) is still applicable. It is

similar to a recent work[45] where the charge order coexists with a sublattice-selective non-unitary pairing state.

The nematic inter-valley coupling is represented as $g_{int,1}(\mathbf{k}) = 1 + 2t_1 k_x k_y + t_2(k_x^2 - k_y^2)$, which requires that $\mathbf{d}_o(\mathbf{k}) = (1 + 2t_1 k_x k_y + t_2(k_x^2 - k_y^2), 0, 0)$ (see Supplementary Note 6). Here the normalization factor has been dropped without changing the essential physics. The system is fully gapped if the $s$-wave gap is dominant ($1 \gg \sqrt{t_1^2 + t_2^2}$), otherwise, it is a $d$-wave dominant nodal SC ($1 \ll \sqrt{t_1^2 + t_2^2}$).

As a concrete toy model, we look at superconductivity on a generic honeycomb lattice with two valleys $K_\pm$, with the Hamiltonian around the two valleys given by,

$$\mathcal{H}_0(\mathbf{k}) = \epsilon(\mathbf{k})\tau_0\sigma_0 + \alpha\left(k_x^3 - 3k_x k_y^2\right)\tau_3\sigma_0, \quad (20)$$

where the two-valley basis used here is given by $\psi^\dagger_{\mathbf{k}} = (c^\dagger_{K_+,\uparrow}(\mathbf{k}), c^\dagger_{K_+,\downarrow}(\mathbf{k}), c^\dagger_{K_-,\uparrow}(\mathbf{k}), c^\dagger_{K_-,\downarrow}(\mathbf{k}))$ and $\epsilon(\mathbf{k})$ takes the same form as in Eq. (5). The parameter $\alpha$ determines the $C_3$ anisotropy of the continuum model around each valley. This Hamiltonian was used as an effective model[46] to study twisted bilayer graphene.

Including the inter-valley scattering effects, the one-band model is given by

$$\mathcal{H}(\mathbf{k}) = \epsilon(\mathbf{k})\tau_0\sigma_0 + \alpha\left(k_x^3 - 3k_x k_y^2\right)\tau_3\sigma_0 + \lambda_{int}[\mathbf{g}_{int}(\mathbf{k})\cdot\boldsymbol{\tau}]\sigma_0, \quad (21)$$

where the $\lambda_{int}$ determines the strength of the inter-valley scattering. In Fig. 4, we present representative numerical results for Eq. (21). Panels (a–c) illustrate Fermi surfaces with varying parameters, while panels (d–f) depict the corresponding quasi-particle density of states (DOS).

In the absence of inter-valley scattering ($\lambda_{int} = 0$), the Fermi surfaces (FSs) around the two $K_\pm$ valleys are plotted in Fig. 4a. As expected, with a fully symmetric $s$-wave pairing characterized by $\mathbf{d}_o = (1, 0, 0)$, a fully gapped or U-shaped quasi-particle density-
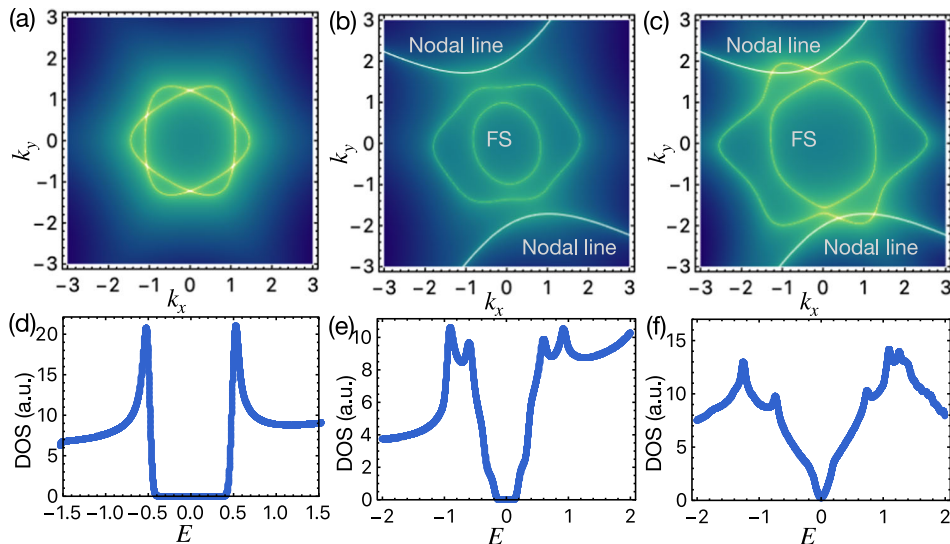


**Fig. 4 Fermi surfaces (FSs) at the $K_\pm$ valleys and the quasi-particle density of states (DOS).** Panels (**a–c**) show FSs with varying parameters, while panels (**d–f**) exhibit the corresponding quasi-particle DOS. The $C_6$ symmetric FS without inter-valley scattering is shown in (**a**) and its DOS with an isotropic $s$-wave pairing is given in (**d**). **b** Shows $C_6$-breaking FSs due to the inter-valley scattering, together with the nodal lines of nematic pairing. There are no nodes on the FSs and the corresponding DOS is shown in (**e**). **c** Is similar to (**b**) but with chemical potential $\mu$ adjusted so that the nodal lines intersect the FSs, hence a V-shaped DOS is obtained as in (**f**). Parameters used are the following, the $C_3$ anisotropy $\alpha = 0.2$, the coefficients for basis functions $t_1 = 0.15$, $t_2 = 0.25$, the orbital-dependent pairing gap $\Delta_o = 0.5$. For (**a**) and (**d**) $\mu = 1.5$ (chemical potential), the inter-valley coupling $g_{int} = 0$; for (**b**) and (**e**) $\mu = 1.5$, $g_{int} = 0.7$; for (**c**) and (**f**) $\mu = 2.7$, $g_{int} = 0.7$.

of-states (DOS) is obtained and shown in Fig. 4d. Then we include the aforementioned inter-valley scattering $\mathbf{g}_{int}$ that breaks $C_6$ down to $C_2$. As a result, our theory implies that the effective nematicity generated will favor a nematic pairing characterized by $\mathbf{d}_o \| \mathbf{g}_{int}$. Consider the generic form $\mathbf{d}_o = \mathbf{g}_{int} = (1 + 2t_1 k_x k_y + t_2(k_x^2 - k_y^2), 0, 0)$, the resulting $C_6$-breaking FS are shown in Fig. 4b, c, where the nodal lines of the pairing are also shown. By tuning the chemical potential $\mu$, the FSs and nodal lines can go from non-intersecting in Fig. 4b to intersecting in Fig. 4c, leading to the corresponding evolution from the gapped U-shaped DOS in Fig. 4e to the gapless V-shaped DOS in Fig. 4f. Our results may explain the experimental observations in magic-angle twist bilayer graphene that reports the nematic order[47], and V-shaped DOS[48] at the specific doping level.

## Discussions

We briefly discuss the difference between our theory and the previous studies[21] for nematic SCs. One example is a pairing state belonging to a 2D irreducible representation (Irrep), e.g., the $E$-pairing in Cu or Nb-doped $Bi_2Se_3$[49,50] and $UPt_3$[51,52]. A real order parameter vector $(\Delta_{E,1}, \Delta_{E,2})$ spontaneously breaks $C_3$, leading to nematic superconductivity. Alternatively, a nematic SC can be formed by mixing two different 1D-Irrep-pairing channels. In FeSe[53,54], the nematic order breaks the $C_4$ down to $C_2$, which mixes the $s$-wave and $d$-wave pairing channels. However, $T_c$ of the $(s + d)$ orbital-independent pairing state could be generally affected by increasing nematicity, because of the significant change in the density of states at the Fermi energy. In our theory, the $(s + d)$-like nematic $\mathbf{d}_o$-vector coexists with the nematic order, so $T_c$ is almost unaffected by increasing nematicity. Therefore, it may help to distinguish our results from previous proposals in experiments, where one may use the chemical or physical pressures to tune the nematicity and measure $T_c$ as a function of

pressure[55]. Nevertheless, more efforts are necessary to test the results established in this work for nematic SCs.

In addition to the above discussions for the time-reversal-invariant superconducting states, we also comment on the effects of the spontaneous TRS-breaking, where a complex orbital $\mathbf{d}_o$-vector generates the orbital orderings as $\mathbf{M}_o = -i\gamma_1/\alpha_M(\mathbf{d} \times \mathbf{d}^*)$, of which only the $y$-component breaks TRS (see details in Supplementary Note 7), as illustrated in Fig. 5a. Alternatively, the corresponding quasi-particle spectrum in Fig. 5b shows the two distinct gaps, similar to the range given by Eq. (6). More explicitly, we schematically plot the atomic orbital-polarized density of states (DOS) by defining $|\pm\rangle = |1\rangle + i|2\rangle$ for complex orbitals, where $D_+ \neq D_-$ at finite energy clearly indicates that the DOS is orbital-polarized, which is consistent with the Ginzburg-Landau theory, shown in Supplementary Note 2. Moreover, we also find that the orbital-spin conversion would lead to the spin-polarized DOS[56].

The above result for orbital-triplet pairings is similar to the superconducting gaps for non-unitary spin-triplet SCs[3]. By symmetry, the Gizburg-Landau free energy is the same. To show the similarity, for the single-band spin-triplet SCs[57], the spin-triplet pairing potential is generally given by $\hat{\Delta}(\mathbf{k}) = \Delta_0[\mathbf{d}_s(\mathbf{k}) \cdot \boldsymbol{\sigma}](i\sigma_2)$, where $\Delta_0$ is the pairing strength and $\boldsymbol{\sigma}$ are Pauli matrices in the spin subspace. Due to the Fermi statistics, the spin $\mathbf{d}_s(\mathbf{k})$-vector has to satisfy $\mathbf{d}_s(\mathbf{k}) = -\mathbf{d}_s(-\mathbf{k})$. The $\mathbf{d}_s$-vector formalism is firstly developed for $He^3$ superfluid[58]. And it also occurs in noncentrosymmetric SCs, the spin $\mathbf{d}_s(\mathbf{k})$-vector is usually pinned along a certain crystal axis since superconductivity is non-suppressed only for $\mathbf{d}_s(\mathbf{k}) \| \mathbf{g}_s(\mathbf{k})$, where $\mathbf{g}_s(\mathbf{k})$ represents the Rashba spin-orbit coupling (SOC)[4,6]. Besides, there is intrinsic spontaneous spin-polarization induced by the non-unitary pairing, $\mathbf{d}_s(\mathbf{k}) = k_z(1, -i\eta_0, 0)$ with real $\eta_0$. Fig. 5c shows the spin expectation value of the Cooper pairs $(\mathbf{M}_s \propto i\mathbf{d}_s^*(\mathbf{k}) \times \mathbf{d}_s(\mathbf{k}) = 2\eta_0 k_z^2 \vec{e}_z)$. It is an equal-spin pairing so that $\sigma_3$ is conserved, and
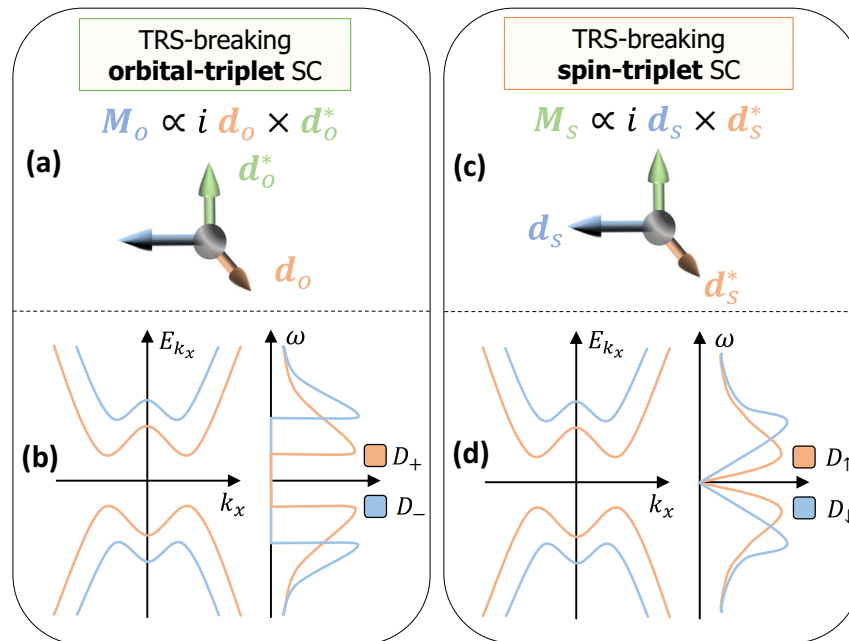


**Fig. 5 Schematic diagrams for the time-reversal symmetry (TRS) breaking effects. a, b** Are for orbital-triplet superconductors (SCs), while (**c**) and (**d**) are for spin-triplet SCs. As for orbital-triplet SCs characterized by a $\mathbf{d}_o$-vector, (**a**) shows a complex orbital $\mathbf{d}_o$-vector that spontaneously breaks TRS and results in the TRS-breaking orbital-polarization $\mathbf{M}_o \propto i\mathbf{d}_o \times \mathbf{d}_o^*$; and (**b**) shows the quasi-particle spectrum along $k_x$ and the orbital-polarized density of states (DOS) $D_\pm$ with $|\pm\rangle$ representing $|1\rangle \pm i|2\rangle$. As a comparison, in spin-triplet SCs, (**c**) shows the superconductivity-induced spontaneous spin-polarization $\mathbf{M}_s \propto i\mathbf{d}_s \times \mathbf{d}_s^*$; and (**d**) shows the two distinct gaps of the quasi-particle spectrum along $k_x$ and the spin-polarized DOS $D_\sigma$ with $\sigma = \{\uparrow, \downarrow\}$. The gapped spectrum is plotted for $k_z \neq 0$ and the node in DOS profile is due to the nodal line at $k_z = 0$.

non-zero $\mathbf{M}_s$ leads to two distinct superconducting gaps of the quasi-particle spectrum[59], shown in Fig. 5d. In addition, the density of states (DOS) is spin-polarized, namely, $D_\uparrow \neq D_\downarrow$ at finite energy $\omega$, as illustrated in Fig. 5d.

To summarize, we have derived a general weak-coupling criterion to investigate the spin-singlet orbital-triplet pairings in nematic SCs. For technical convenience, we adopt the orbital $\mathbf{d}_o$-vector to describe the spin-singlet orbital-dependent pairing states and the $\mathbf{g}_o$-vector for the orbital hybridizations. The main results of this work include, first, we demonstrate that an orbital $\mathbf{d}_o$-vector that is parallel with $\mathbf{g}_o$-vector for orbital hybridizations is possible to be realized in real superconducting materials. Second, the interplay between intra-orbital and orbital-dependent pairings that belong to the same symmetry representation can explain the observation of robust Dirac nodes in the quasi-2D iron-based SCs. Remarkably, we find that $\mathbf{d}_o$-vectors could even coexist with many-body interaction-induced nematic orders or charge-density-wave orders when $\mathbf{d}_o \propto \mathbf{g}_{tot} = \mathbf{g}_o + \mathbf{g}_{nem}$ (or $\mathbf{g}_{int}$). Moreover, our theory discovers the important role of nematic orders in SC pairing symmetry, which builds a possible bridge between repulsive interaction-induced nematic orders and nematic superconductivity and also reveals a deep connection between spin-singlet orbital-triplet pairings in nematic SCs. Our results may be helpful in understanding the nematic superconductivity in bulk FeSe. Our work will motivate more theoretical and experimental efforts to search for spin-singlet orbital-triplet SCs, even for topological superconductivity, which might contribute to further understanding the effects of spontaneous symmetry breaking on superconductivity.

## Methods
Here we present the derivation for the main result Eq. (8), which is first order in $\lambda_o$, by solving the linearized gap equation. The second-order results are presented in Supplementary Note 3. The general $\mathbf{k} \cdot \mathbf{p}$ normal Hamiltonian considered in the main text reads,

$$\mathcal{H}_0(\mathbf{k}) = \epsilon(\mathbf{k})\tau_0\sigma_0 + \lambda_o(\mathbf{g}_o(\mathbf{k}) \cdot \boldsymbol{\tau})\sigma_0, \tag{22}$$

where the electronic basis is made of $\{1, 2\}$-orbitals $\Psi_{\mathbf{k}}^\dagger = (c_{1,\uparrow}^\dagger(\mathbf{k}), c_{1,\downarrow}^\dagger(\mathbf{k}), c_{2,\uparrow}^\dagger(\mathbf{k}), c_{2,\downarrow}^\dagger(\mathbf{k}))$, $\epsilon(\mathbf{k}) = (k_x^2 + k_y^2)/2m - \mu$ is the band energy measured relative to the chemical potential $\mu$, $\lambda_o$ represents the orbital hybridization and $\mathbf{g}_o(\mathbf{k}) = (g_1(\mathbf{k}), g_2(\mathbf{k}), g_3(\mathbf{k}))$. The TRS $\mathcal{T} = i\sigma_2\tau_0\mathcal{K}$ requires $g_{1,3}(\mathbf{k}) = g_{1,3}(-\mathbf{k})$ and $g_2(\mathbf{k}) = -g_2(-\mathbf{k})$. It leads that

$$\mathbf{g}_o(\mathbf{k}) \cdot \boldsymbol{\tau} = [\mathbf{g}_o(-\mathbf{k}) \cdot \boldsymbol{\tau}]^*. \tag{23}$$

Besides, we set $\lambda_o > 0$ without loss of generality. The Matsubara Green's function for electrons is $G_e(\mathbf{k}, i\omega_n) = [i\omega_n - \mathcal{H}_0(\mathbf{k})]^{-1}$ and that for holes is $G_h(\mathbf{k}, i\omega_n) = -G_e^*(\mathbf{k}, i\omega_n)$. Here $\beta = 1/k_BT$ and $\omega_n = (2n+1)\pi/\beta$ with $n$ integer. Therefore,

$$G_e(\mathbf{k}, i\omega_n) = \frac{\mathcal{P}_-(\mathbf{k})}{i\omega_n - \epsilon(\mathbf{k}) + \lambda_o|\mathbf{g}_o(\mathbf{k})|} + \frac{\mathcal{P}_+(\mathbf{k})}{i\omega_n - \epsilon(\mathbf{k}) - \lambda_o|\mathbf{g}_o(\mathbf{k})|}$$
$$\triangleq G_e^-(\mathbf{k}, i\omega_n)\mathcal{P}_-(\mathbf{k}) + G_e^+(\mathbf{k}, i\omega_n)\mathcal{P}_+(\mathbf{k}), \tag{24}$$

$$G_h(-\mathbf{k}, i\omega_n) = \frac{\mathcal{P}_-(\mathbf{k})}{i\omega_n + \epsilon(\mathbf{k}) - \lambda_o|\mathbf{g}_o(\mathbf{k})|} + \frac{\mathcal{P}_+(\mathbf{k})}{i\omega_n + \epsilon(\mathbf{k}) + \lambda_o|\mathbf{g}_o(\mathbf{k})|}$$
$$\triangleq G_h^-(\mathbf{k}, i\omega_n)\mathcal{P}_-(\mathbf{k}) + G_h^+(\mathbf{k}, i\omega_n)\mathcal{P}_+(\mathbf{k}), \tag{25}$$

where $\mathcal{P}_\pm(\mathbf{k}) = \frac{1}{2}(1 \pm \hat{\mathbf{g}}_o(\mathbf{k}) \cdot \boldsymbol{\tau})$ with $\hat{\mathbf{g}}_o(\mathbf{k}) = \mathbf{g}_o(\mathbf{k})/|\mathbf{g}_o(\mathbf{k})|$. Here $G_e^\pm(\mathbf{k}, i\omega_n) = \frac{1}{i\omega_n - \epsilon(\mathbf{k}) \mp \lambda_o|\mathbf{g}_o(\mathbf{k})|}$ and $G_h^\pm(\mathbf{k}, i\omega_n) = \frac{1}{i\omega_n + \epsilon(\mathbf{k}) \pm \lambda_o|\mathbf{g}_o(\mathbf{k})|}$. We expand the attractive interactions as

$$V_{s_1'a', s_2'b'}^{s_1a, s_2b}(\mathbf{k}, \mathbf{k}') = -\sum_{\Gamma,l} v_0^\Gamma [\mathbf{d}_o^{\Gamma,l}(\mathbf{k}) \cdot \boldsymbol{\tau} i\sigma_2]_{s_1a, s_2b}$$
$$\times [\mathbf{d}_o^{\Gamma,l}(\mathbf{k}') \cdot \boldsymbol{\tau} i\sigma_2]_{s_1'a', s_2'b'}, \tag{26}$$

where $v_0^\Gamma > 0$ is the interaction strength of the irreducible representation channel $\Gamma$ of the crystalline group, and $l = 1, 2, ..., \text{Dim }\Gamma$. Each pairing channel $\Gamma$ gives rise to an SC critical temperature $T_c^\Gamma$, and the actual transition temperature of the system is given by the largest of these critical temperatures. In our work, we mainly focus on the case where $\text{Dim }\Gamma = 1$, which is sufficient for the applications discussed in the main text. The coupling between orbital-dependent pairings and orbital-independent pairings will be discussed in detail later. The transition temperature $T_c^\Gamma$ of orbital-dependent pairing channels is calculated by solving the linearized gap equation,

$$\Delta_{s_1, s_2}^{a,b}(\mathbf{k}) = -\frac{1}{\beta}\sum_{\omega_n} \sum_{s_1'a', s_2'b'} V_{s_1'a', s_2'b'}^{s_1a, s_2b}(\mathbf{k}, \mathbf{k}')$$
$$\times [G_e(\mathbf{k}', i\omega_n)\hat{\Delta}(\mathbf{k}')G_h(-\mathbf{k}', i\omega_n)]_{s_1'a', s_2'b'}, \tag{27}$$

which is reduced to $v_0^\Gamma \chi^\Gamma(T) - 1 = 0$ with the superconductivity susceptibility $\chi^\Gamma(T)$ in the channel $\Gamma$ defined as,

$$\chi^\Gamma(T) = -\frac{1}{\beta}\sum_{\mathbf{k},\omega_n} \text{Tr}\left[(\mathbf{d}_o^\Gamma(\mathbf{k}) \cdot \boldsymbol{\tau} i\sigma_2)^\dagger G_e(\mathbf{k}, i\omega_n)(\mathbf{d}_o^\Gamma(\mathbf{k}) \cdot \boldsymbol{\tau} i\sigma_2)G_h(-\mathbf{k}, i\omega_n)\right], \tag{28}$$

$$= -\frac{2}{\beta}\sum_{\mathbf{k},\omega_n} \sum_{\alpha,\beta} G_e^\alpha(\mathbf{k}, i\omega_n)G_h^\beta(\mathbf{k}, i\omega_n)$$
$$\times \text{Tr}\left[(\mathbf{d}_o^\Gamma(\mathbf{k}) \cdot \boldsymbol{\tau})^\dagger \mathcal{P}_\alpha(\mathbf{k})(\mathbf{d}_o^\Gamma(\mathbf{k}) \cdot \boldsymbol{\tau})\mathcal{P}_\beta(\mathbf{k})\right], \tag{29}$$

where $\alpha, \beta \in \{+, -\}$. For notional simplicity, the superscript $\Gamma$ will be dropped when there is no danger of confusion. Firstly, let us calculate the trace part. In the following calculation, we will use

$$\text{Tr}\left[(\mathbf{d}_o(\mathbf{k}) \cdot \boldsymbol{\tau})^\dagger \mathcal{P}_+(\mathbf{k})(\mathbf{d}_o(\mathbf{k}) \cdot \boldsymbol{\tau})\mathcal{P}_+(\mathbf{k})\right]$$
$$+ \text{Tr}\left[(\mathbf{d}_o(\mathbf{k}) \cdot \boldsymbol{\tau})^\dagger \mathcal{P}_-(\mathbf{k})(\mathbf{d}_o(\mathbf{k}) \cdot \boldsymbol{\tau})\mathcal{P}_-(\mathbf{k})\right]$$
$$= (\mathbf{d}_o^*(\mathbf{k}) \cdot \mathbf{d}_o(\mathbf{k})) + 2(\mathbf{d}_o^*(\mathbf{k}) \cdot \hat{\mathbf{g}}_o(\mathbf{k}))(\mathbf{d}_o(\mathbf{k})$$
$$\cdot \hat{\mathbf{g}}_o(\mathbf{k}))(\mathbf{d}_o^*(\mathbf{k}) \cdot \mathbf{d}_o(\mathbf{k}))(\hat{\mathbf{g}}_o(\mathbf{k}) \cdot \hat{\mathbf{g}}_o(\mathbf{k})). \tag{30}$$

And,

$$\text{Tr}\left[(\mathbf{d}_o(\mathbf{k}) \cdot \boldsymbol{\tau})^\dagger \mathcal{P}_+(\mathbf{k})(\mathbf{d}_o(\mathbf{k}) \cdot \boldsymbol{\tau})\mathcal{P}_-(\mathbf{k})\right]$$
$$+ \text{Tr}\left[(\mathbf{d}_o(\mathbf{k}) \cdot \boldsymbol{\tau})^\dagger \mathcal{P}_-(\mathbf{k})(\mathbf{d}_o(\mathbf{k}) \cdot \boldsymbol{\tau})\mathcal{P}_+(\mathbf{k})\right]$$
$$= (\mathbf{d}_o^*(\mathbf{k}) \cdot \mathbf{d}_o(\mathbf{k})) - 2(\mathbf{d}_o^*(\mathbf{k}) \cdot \hat{\mathbf{g}}_o(\mathbf{k}))(\mathbf{d}_o(\mathbf{k}) \cdot \hat{\mathbf{g}}_o(\mathbf{k}))$$
$$+ (\mathbf{d}_o^*(\mathbf{k}) \cdot \mathbf{d}_o(\mathbf{k}))(\hat{\mathbf{g}}_o(\mathbf{k}) \cdot \hat{\mathbf{g}}_o(\mathbf{k})). \tag{31}$$

Therefore, we arrive at

$$\text{Tr}\left[(\mathbf{d}_o(\mathbf{k}) \cdot \boldsymbol{\tau})^\dagger \mathcal{P}_\alpha(\mathbf{k})(\mathbf{d}_o(\mathbf{k}) \cdot \boldsymbol{\tau})\mathcal{P}_\beta(\mathbf{k})\right]$$
$$= \frac{1}{2}[(\mathbf{d}_o^*(\mathbf{k}) \cdot \mathbf{d}_o(\mathbf{k})) + i\alpha(\mathbf{d}_o(\mathbf{k}) \cdot (\mathbf{d}_o^*(\mathbf{k}) \times \hat{\mathbf{g}}_o(\mathbf{k})))$$
$$+ i\beta(\mathbf{d}_o^*(\mathbf{k}) \cdot (\mathbf{d}_o(\mathbf{k}) \times \hat{\mathbf{g}}_o(\mathbf{k})))$$
$$+ \alpha\beta(2(\mathbf{d}_o^*(\mathbf{k}) \cdot \hat{\mathbf{g}}_o(\mathbf{k}))(\mathbf{d}_o(\mathbf{k}) \cdot \hat{\mathbf{g}}_o(\mathbf{k}))$$
$$- (\mathbf{d}_o^*(\mathbf{k}) \cdot \mathbf{d}_o(\mathbf{k}))(\hat{\mathbf{g}}_o(\mathbf{k}) \cdot \hat{\mathbf{g}}_o(\mathbf{k})))]. \tag{32}$$

Then we have

$$\chi(T) = -\frac{1}{\beta}\sum_{\mathbf{k},\omega_n}\sum_{\alpha,\beta} G_e^\alpha(\mathbf{k},i\omega_n)G_h^\beta(\mathbf{k},i\omega_n)[(\mathbf{d}_o^*(\mathbf{k})\cdot\mathbf{d}_o(\mathbf{k}))$$
$$+ i\alpha(\mathbf{d}_o(\mathbf{k})\cdot(\mathbf{d}_o^*(\mathbf{k})\times\hat{\mathbf{g}}_o(\mathbf{k}))) + i\beta(\mathbf{d}_o^*(\mathbf{k})\cdot(\mathbf{d}_o(\mathbf{k})\times\hat{\mathbf{g}}_o(\mathbf{k})))$$
$$+ \alpha\beta(2(\mathbf{d}_o^*(\mathbf{k})\cdot\hat{\mathbf{g}}_o(\mathbf{k}))(\mathbf{d}_o(\mathbf{k})\cdot\hat{\mathbf{g}}_o(\mathbf{k}))$$
$$- (\mathbf{d}_o^*(\mathbf{k})\cdot\mathbf{d}_o(\mathbf{k}))(\hat{\mathbf{g}}_o(\mathbf{k})\cdot\hat{\mathbf{g}}_o(\mathbf{k})))]. \tag{33}$$

Next, we calculate the integration for $\sum_{\mathbf{k},\omega_n}$ by using,

$$\sum_{\mathbf{k},\omega_n} \to \frac{N_0}{4}\int_{-\omega_D}^{+\omega_D}d\epsilon\int_S\frac{d\Omega}{2\pi}\sum_{\omega_n}, \tag{34}$$

where $N_0$ is the density of states at Fermi surface and $\Omega$ is the solid angle of $\mathbf{k}$ on Fermi surfaces. Then,

$$-\frac{N_0}{\beta}\int_{-\omega_D}^{+\omega_D}d\epsilon\int_S\frac{d\Omega}{2\pi}\sum_{\omega_n} G_e^+(\mathbf{k},i\omega_n)G_h^+(\mathbf{k},i\omega_n)$$
$$= -\frac{N_0}{\beta}\int_{-\omega_D}^{+\omega_D}d\epsilon\int_S\frac{d\Omega}{2\pi}\sum_{\omega_n} G_e^-(\mathbf{k},i\omega_n)G_h^-(\mathbf{k},i\omega_n) \tag{35}$$
$$\equiv \chi_0(T),$$

On one hand,

$$\int_{-\omega_D}^{+\omega_D}d\epsilon\sum_{\omega_n} G_e^+(\mathbf{k},i\omega_n)G_h^+(\mathbf{k},i\omega_n)$$
$$= \int_{-\omega_D}^{+\omega_D}d\epsilon\sum_{\omega_n}\frac{1}{i\omega_n+\epsilon}\frac{1}{i\omega_n-\epsilon}$$
$$= \beta\int_{-\omega_D}^{+\omega_D}d\epsilon\frac{\tanh\frac{\beta\epsilon}{2}}{2\epsilon} \tag{36}$$
$$= \beta\int_0^{\beta\omega_D/2}dx\frac{\tanh x}{x} \approx \beta\ln\left(\frac{2e^\gamma\omega_D}{\pi k_B T}\right),$$

where the approximation is done at low temperature when $\beta\to\infty$.

On the other hand, we could find a series representation for $\chi_0$, which also applies to the case where $\lambda_o\neq 0$, so that $\chi_0\equiv\chi(\lambda_o=0)$ and $\chi(\lambda_o\neq 0)$ can be related by a simple relation. The way to do it is to perform the integration in $\epsilon$ first. More precisely,

$$\int_{-\omega_D}^{+\omega_D}d\epsilon\sum_{\omega_n} G_e^+(\mathbf{k},i\omega_n)G_h^+(\mathbf{k},i\omega_n)$$
$$= \int_{-\omega_D}^{+\omega_D}\sum_{\omega_n}\frac{1}{i\omega_n+\epsilon}\frac{1}{i\omega_n-\epsilon}$$
$$= 2\mathrm{Re}\sum_{n\geq 0}\int_{-\omega_D}^{\omega_D}d\epsilon\frac{1}{i\omega_n+\epsilon}\frac{1}{i\omega_n-\epsilon}$$
$$= 2\beta\mathrm{Re}\sum_{n\geq 0}\int_{-\beta\omega_D}^{\beta\omega_D}d\epsilon\frac{1}{i2\pi(n+1/2)+\epsilon}\frac{1}{i2\pi(n+1/2)-\epsilon} \tag{37}$$
$$\approx 2\beta\mathrm{Re}\sum_{n\geq 0}\int_{-\infty}^{\infty}d\epsilon\frac{1}{i2\pi(n+1/2)+\epsilon}\frac{1}{i2\pi(n+1/2)-\epsilon}$$
$$= \beta\mathrm{Re}\sum_{n\geq 0}\frac{1}{n+1/2},$$

where the low-temperature limit is again assumed and the integration is done using the residue theorem. In the same spirit, we have,

$$\int_{-\omega_D}^{+\omega_D}d\epsilon\sum_{\omega_n} G_e^+(\mathbf{k},i\omega_n)G_h^-(\mathbf{k},i\omega_n)$$
$$= \beta\mathrm{Re}\sum_{n\geq 0}\frac{1}{n+1/2+i\frac{\lambda_o|\mathbf{g}_o(\mathbf{k})|}{2\pi k_B T}}, \tag{38}$$

Now by introducing the digamma function defined on the complex plane,

$$\psi^{(0)}(z) = -\gamma + \sum_{n\geq 0}\left(\frac{1}{n+1}-\frac{1}{n+z}\right), \tag{39}$$

we have the following relation,

$$\int_{-\omega_D}^{+\omega_D}d\epsilon\sum_{\omega_n} G_e^+(\mathbf{k},i\omega_n)G_h^-(\mathbf{k},i\omega_n)$$
$$- \int_{-\omega_D}^{+\omega_D}d\epsilon\sum_{\omega_n} G_e^+(\mathbf{k},i\omega_n)G_h^+(\mathbf{k},i\omega_n) \tag{40}$$
$$= \beta\mathrm{Re}\left[\psi^{(0)}\left(\frac{1}{2}\right)-\psi^{(0)}\left(\frac{1}{2}+i\frac{\lambda_o|\mathbf{g}(\mathbf{k})|}{2\pi k_B T}\right)\right]$$
$$\equiv \beta\mathcal{C}_0(T),$$

where $\chi_0(T) = N_0\ln\left(\frac{2e^\gamma\omega_D}{\pi k_B T}\right)$, $\gamma = 0.57721\cdots$ is the Euler-Mascheroni constant and $\omega_D$ is the Debye frequency.

Therefore,

$$-\frac{N_0}{\beta}\int_{-\omega_D}^{+\omega_D}d\epsilon\int_S\frac{d\Omega}{2\pi}\sum_{\omega_n} G_e^-(\mathbf{k},i\omega_n)G_h^+(\mathbf{k},i\omega_n)$$
$$= -\frac{N_0}{\beta}\int_{-\omega_D}^{+\omega_D}d\epsilon\int_S\frac{d\Omega}{2\pi}\sum_{\omega_n} G_e^+(\mathbf{k},i\omega_n)G_h^-(\mathbf{k},i\omega_n) \tag{41}$$
$$= \chi_0(T) + N_0\int_S\frac{d\Omega}{2\pi}\mathcal{C}_0(T).$$

Now we can proceed to calculate $\chi(T)$ given in Eq. (33),

$$\chi(T) = \chi_0(T)\int_S\frac{d\Omega}{2\pi}|\mathbf{d}_o\cdot\hat{\mathbf{g}}_o|^2 \tag{42}$$
$$+\chi_0(T)\int_S\frac{d\Omega}{2\pi}\left(|\mathbf{d}_o|^2-|\mathbf{d}_o\cdot\hat{\mathbf{g}}_o|^2\right) \tag{43}$$
$$+N_0\int_S\frac{d\Omega}{2\pi}\mathcal{C}_0(T)\left(|\mathbf{d}_o|^2-|\mathbf{d}_o\cdot\hat{\mathbf{g}}_o|^2\right) \tag{44}$$
$$= \chi_0(T) + N_0\int_S\frac{d\Omega}{2\pi}\mathcal{C}_0(T)\left(|\mathbf{d}_o|^2-|\mathbf{d}_o\cdot\hat{\mathbf{g}}_o|^2\right). \tag{45}$$

In the calculation, we use normalized gap functions with $\int_S\frac{d\Omega}{2\pi}\mathbf{d}_o^*\cdot\mathbf{d}_o = 1$. It leads to,

$$\ln\left(\frac{T_c}{T_{c0}}\right) = \int_S\frac{d\Omega}{2\pi}\mathcal{C}_0(T_c)\left(|\mathbf{d}_o|^2-|\mathbf{d}_o\cdot\hat{\mathbf{g}}_o|^2\right), \tag{46}$$

where $T_{c0}$ is $T_c$ for $\lambda_o=0$ case by solving $\nu_0\chi_0(T_{c0})=1$. This is the Eq. (8) in the main text. In general, the right-hand side of Eq. (46) suppresses $T_c$. It clearly indicates that $T_c$ would not be suppressed by orbital hybridization once $\mathbf{d}_o\|\mathbf{g}_o$ for all $\mathbf{k}$. So we conclude that the orbital $\mathbf{d}_o$-vector is possible to be stabilized in materials.

### Data availability

### Code availability

## References

1. Dresselhaus, M. S., Dresselhaus, G. & Jorio, A. *Group theory: application to the physics of condensed matter* (Springer Science & Business Media, 2007).
2. Chaikin, P. M., Lubensky, T. C. & Witten, T. A. *Principles of condensed matter physics*, vol. 10 (Cambridge university press Cambridge, 1995).
3. Sigrist, M. & Ueda, K. Phenomenological theory of unconventional superconductivity. *Rev. Mod. Phys.* **63**, 239–311 (1991).
4. Frigeri, P. A., Agterberg, D. F., Koga, A. & Sigrist, M. Superconductivity without inversion symmetry: Mnsi versus cept$_3$Si. *Phys. Rev. Lett.* **92**, 097001 (2004).
5. Fischer, M. H. Gap symmetry and stability analysis in the multi-orbital fe-based superconductors. *N. J. Phys.* **15**, 073006 (2013).
6. Ramires, A., Agterberg, D. F. & Sigrist, M. Tailoring $T_c$ by symmetry principles: The concept of superconducting fitness. *Phys. Rev. B* **98**, 024501 (2018).
7. Andersen, L., Ramires, A., Wang, Z., Lorenz, T. & Ando, Y. Generalized anderson's theorem for superconductors derived from topological insulators. *Sci. Adv.* **6**, eaay6502 (2020).
8. Mackenzie, A. P. & Maeno, Y. The superconductivity of sr$_2$ruo$_4$ and the physics of spin-triplet pairing. *Rev. Mod. Phys.* **75**, 657–712 (2003).
9. Agterberg, D. F., Rice, T. M. & Sigrist, M. Orbital dependent superconductivity in sr$_2$ruo$_4$. *Phys. Rev. Lett.* **78**, 3374–3377 (1997).
10. Dai, X., Fang, Z., Zhou, Y. & Zhang, F.-C. Even parity, orbital singlet, and spin triplet pairing for superconducting lafeaso$_{1-x}$f$_x$. *Phys. Rev. Lett.* **101**, 057008 (2008).
11. Ong, T. T. & Coleman, P. Tetrahedral and orbital pairing: A fully gapped pairing scenario for the iron-based superconductors. *Phys. Rev. Lett.* **111**, 217003 (2013).
12. Sprau, P. O. et al. Discovery of orbital-selective cooper pairing in fese. *Science* **357**, 75–80 (2017).
13. Nica, E. M. & Si, Q. Multiorbital singlet pairing and d+ d superconductivity. *npj Quantum Mater.* **6**, 1–11 (2021).
14. Fu, L. & Berg, E. Odd-parity topological superconductors: Theory and application to cu$_x$bi$_2$se$_3$. *Phys. Rev. Lett.* **105**, 097001 (2010).
15. Brydon, P. M. R., Wang, L., Weinert, M. & Agterberg, D. F. Pairing of $j = 3/2$ fermions in half-heusler superconductors. *Phys. Rev. Lett.* **116**, 177001 (2016).
16. Yang, W., Li, Y. & Wu, C. Topological septet pairing with spin-$\frac{3}{2}$ fermions: High-partial-wave channel counterpart of the $^3\text{He} - b$ phase. *Phys. Rev. Lett.* **117**, 075301 (2016).
17. Savary, L., Ruhman, J., Venderbos, J. W. F., Fu, L. & Lee, P. A. Superconductivity in three-dimensional spin-orbit coupled semimetals. *Phys. Rev. B* **96**, 214514 (2017).
18. Yu, J. & Liu, C.-X. Singlet-quintet mixing in spin-orbit coupled superconductors with $j = \frac{3}{2}$ fermions. *Phys. Rev. B* **98**, 104514 (2018).
19. Scalapino, D. J. A common thread: The pairing interaction for unconventional superconductors. *Rev. Mod. Phys.* **84**, 1383–1417 (2012).
20. Fradkin, E., Kivelson, S. A., Lawler, M. J., Eisenstein, J. P. & Mackenzie, A. P. Nematic fermi fluids in condensed matter physics. *Annu. Rev. Condens. Matter Phys.* **1**, 153–178 (2010).
21. Fernandes, R. M., Orth, P. P. & Schmalian, J. Intertwined vestigial order in quantum materials: Nematicity and beyond. *Ann. Rev. Cond. Matter Phys.* **10**, 133–154 (2019).
22. Sigrist, M. Time-reversal symmetry breaking states in high-temperature superconductors. *Progr. Theor. Phys.* **99**, 899–929 (1998).
23. Lee, W.-C., Zhang, S.-C. & Wu, C. Pairing state with a time-reversal symmetry breaking in feas-based superconductors. *Phys. Rev. Lett.* **102**, 217002 (2009).
24. Hu, L.-H., Johnson, P. D. & Wu, C. Pairing symmetry and topological surface state in iron-chalcogenide superconductors. *Phys. Rev. Res.* **2**, 022021 (2020).
25. Lado, J. L. & Sigrist, M. Detecting nonunitary multiorbital superconductivity with dirac points at finite energies. *Phys. Rev. Res.* **1**, 033107 (2019).
26. Hu, L.-H., Wang, X. & Shang, T. Spontaneous magnetization in unitary superconductors with time reversal symmetry breaking. *Phys. Rev. B* **104**, 054520 (2021).
27. McQueen, T. M. et al. Tetragonal-to-orthorhombic structural phase transition at 90 k in the superconductor fe$_{1.01}$Se. *Phys. Rev. Lett.* **103**, 057002 (2009).
28. Ong, T., Coleman, P. & Schmalian, J. Concealed d-wave pairs in the s± condensate of iron-based superconductors. *Proc. Natl. Acad. Sci.* **113**, 5486–5491 (2016).
29. Agterberg, D. F., Shishidou, T., O'Halloran, J., Brydon, P. M. R. & Weinert, M. Resilient nodeless $d$-wave superconductivity in monolayer fese. *Phys. Rev. Lett.* **119**, 267001 (2017).
30. Smidman, M., Salamon, M. B., Yuan, H. Q. & Agterberg, D. F. Superconductivity and spin–orbit coupling in non-centrosymmetric materials: a review. *Reports on Progress in Physics* **80**, 036501 (2017).
31. Zhang, Y. et al. Superconducting gap anisotropy in monolayer fese thin film. *Phys. Rev. Lett.* **117**, 117001 (2016).
32. Fletcher, J. D. et al. Evidence for a nodal-line superconducting state in lafepo. *Phys. Rev. Lett.* **102**, 147001 (2009).
33. Hashimoto, K. et al. Nodal versus nodeless behaviors of the order parameters of lifep and lifeas superconductors from magnetic penetration-depth measurements. *Phys. Rev. Lett.* **108**, 047003 (2012).
34. Nakayama, T., Shishidou, T. & Agterberg, D. F. Nodal topology in $d$-wave superconducting monolayer fese. *Phys. Rev. B* **98**, 214503 (2018).
35. Eugenio, P. M. & Vafek, O. Classification of symmetry derived pairing at the $m$ point in fese. *Phys. Rev. B* **98**, 014503 (2018).
36. Böhmer, A. E. & Kreisel, A. Nematicity, magnetism and superconductivity in fese. *Journal of Physics: Condensed Matter* **30**, 023001 (2017).
37. Raghu, S., Qi, X.-L., Liu, C.-X., Scalapino, D. J. & Zhang, S.-C. Minimal two-band model of the superconducting iron oxypnictides. *Phys. Rev. B* **77**, 220503 (2008).
38. Chubukov, A. V., Khodas, M. & Fernandes, R. M. Magnetism, superconductivity, and spontaneous orbital order in iron-based superconductors: Which comes first and why? *Phys. Rev. X* **6**, 041045 (2016).
39. Kang, J., Fernandes, R. M. & Chubukov, A. Superconductivity in fese: The role of nematic order. *Phys. Rev. Lett.* **120**, 267001 (2018).
40. Yu, R., Zhu, J.-X. & Si, Q. Orbital-selective superconductivity, gap anisotropy, and spin resonance excitations in a multiorbital $t$-$J_1$-$J_2$ model for iron pnictides. *Phys. Rev. B* **89**, 024509 (2014).
41. Wang, W.-S. et al. Functional renormalization group and variational monte carlo studies of the electronic instabilities in graphene near $\frac{1}{4}$ doping. *Phys. Rev. B* **85**, 035414 (2012).
42. Hsu, Y.-T., Vaezi, A., Fischer, M. H. & Kim, E.-A. Topological superconductivity in monolayer transition metal dichalcogenides. *Nat. Commun.* **8**, 14985 (2017).
43. Gutiérrez, C. et al. Imaging chiral symmetry breaking from kekulé bond order in graphene. *Nat. Phys.* **12**, 950–958 (2016).
44. Bao, C. et al. Experimental evidence of chiral symmetry breaking in kekulé-ordered graphene. *Phys. Rev. Lett.* **126**, 206804 (2021).
45. Wolf, T. M. R., Holst, M. F., Sigrist, M. & Lado, J. L. Nonunitary multiorbital superconductivity from competing interactions in dirac materials. *Phys. Rev. Res.* **4**, L012036 (2022).
46. You, Y.-Z. & Vishwanath, A. Superconductivity from valley fluctuations and approximate so (4) symmetry in a weak coupling theory of twisted bilayer graphene. *npj Quantum Mater.* **4**, 1–12 (2019).
47. Cao, Y. et al. Nematicity and competing orders in superconducting magic-angle graphene. *Science* **372**, 264–271 (2021).
48. Kim, H. et al. Spectroscopic signatures of strong correlations and unconventional superconductivity in twisted trilayer graphene. *arXiv e-prints* arXiv:2109.12127 (2021). 2109.12127.
49. Fu, L. Odd-parity topological superconductor with nematic order: Application to cu$_x$bi$_2$se$_3$. *Phys. Rev. B* **90**, 100509 (2014).
50. Matano, K., Kriener, M., Segawa, K., Ando, Y. & Zheng, G.-q Spin-rotation symmetry breaking in the superconducting state of cu$_x$bi$_2$se$_3$. *Nat. Phys.* **12**, 852–854 (2016).
51. Sauls, J. The order parameter for the superconducting phases of upt$_3$. *Adv. Phys.* **43**, 113–141 (1994).
52. Strand, J. et al. The transition between real and complex superconducting order parameter phases in upt3. *Science* **328**, 1368–1369 (2010).
53. Fernandes, R. M. & Millis, A. J. Nematicity as a probe of superconducting pairing in iron-based superconductors. *Phys. Rev. Lett.* **111**, 127001 (2013).
54. Kang, J., Kemper, A. F. & Fernandes, R. M. Manipulation of gap nodes by uniaxial strain in iron-based superconductors. *Phys. Rev. Lett.* **113**, 217001 (2014).
55. Matsuura, K. et al. Maximizing tc by tuning nematicity and magnetism in fese$_{1-x}$s$_x$ superconductors. *Nat. Commun.* **8**, 1–6 (2017).
56. Zeng, M., Xu, D.-H., Wang, Z.-M. & Hu, L.-H. Spin-orbit coupled superconductivity with spin-singlet nonunitary pairing. *Phys. Rev. B* **107**, 094507 (2023).
57. Leggett, A. J. A theoretical description of the new phases of liquid $^3$He. *Rev. Mod. Phys.* **47**, 331–414 (1975).
58. Salomaa, M. M. & Volovik, G. E. Quantized vortices in superfluid $^3$He. *Rev. Mod. Phys.* **59**, 533–613 (1987).
59. Sigrist, M. Introduction to unconventional superconductivity. In *AIP Conference Proceedings*, vol. 789, 165–243 (American Institute of Physics, 2005). https://doi.org/10.1063/1.2080350.

## Author contributions

L.-H. H. and F.-C. Z. supervised the project. M. Z. performed all numerical calculations with the help of L.-H. H. M. Z., D.-H. X, Z.-M. W., L.-H. H. and F.-C. Z. all contributed to analyzing the data and writing the manuscript.

## Competing interests

The authors declare no competing interests.

## Additional information

**Supplementary information** The online version contains supplementary material available at https://doi.org/10.1038/s42005-023-01495-4.

**Correspondence** and requests for materials should be addressed to Lun-Hui Hu.

**Peer review information** *Communications Physics* thanks Yashar Komijani and the other, anonymous, reviewer(s) for their contribution to the peer review of this work. A peer review file is available.

**Reprints and permission information** is available at http://www.nature.com/reprints

# Supplementary materials for "Pseudospin-Triplet Pairing in Iron-Chalcogenide Superconductors"

Meng Zeng,[1] Dong-Hui Xu,[2,3] Zi-Ming Wang,[4] Lun-Hui Hu,[5,6,*] and Fu-Chun Zhang[7,8]

[1]*Department of Physics, University of California, San Diego, California 92093, USA*
[2]*Department of Physics and Chongqing Key Laboratory for Strongly Coupled Physics,*
*Chongqing University, Chongqing 400044, People's Republic of China*
[3]*Center of Quantum Materials and Devices, Chongqing University, Chongqing 400044, People's Republic of China*
[4]*Department of Physics, Hubei University, Wuhan 430062, China*
[5]*Department of Physics, The Pennsylvania State University, University Park, Pennsylvania 16802, USA*
[6]*Department of Physics and Astronomy, University of Tennessee, Knoxville, Tennessee 37996, USA*
[7]*Kavli Institute for Theoretical Sciences, University of Chinese Academy of Sciences, Beijing 100190, China*
[8]*CAS Center for Excellence in Topological Quantum Computation,*
*University of Chinese Academy of Sciences, Beijing 100190, China*

# Contents

# Supplementary Note 1   Two definitions for the orbital d$_o$-vector

In the main text, we take the general pairing potential of a two-orbital SC,

$$\hat{\Delta}_{tot}(\mathbf{k}) = (\Delta_s \Psi_s(\mathbf{k})\tau_0 + \Delta_o(\mathbf{d}_o(\mathbf{k}) \cdot \boldsymbol{\tau}))(i\sigma_2), \tag{1}$$

where $\Delta_s$ and $\Delta_o$ are pairing strengths in orbital-independent and orbital-dependent channels, respectively. Here $\boldsymbol{\tau}$ are Pauli matrices acting on the orbital subspace and $\tau_0$ is a 2-by-2 identity matrix. In the absence of band-splitting caused by spin-orbital couplings, the gap function on the Fermi surface is

$$\Delta(\mathbf{k}) = \sqrt{|\Delta_s|^2 \Psi_s^2(\mathbf{k}) + |\Delta_o|^2 |\mathbf{d}_o(\mathbf{k})|^2 \pm |\mathbf{q}_o|}, \tag{2}$$

where $\mathbf{q}_o = i|\Delta_o|^2(\mathbf{d}_o^*(\mathbf{k}) \times \mathbf{d}_o(\mathbf{k})) + \text{Re}[\Delta_s^* \Delta_o \mathbf{d}_o(\mathbf{k})]$. This expression is mathematically similar to the superconducting gap of non-unitary spin-triplet SCs.

———

\* hu.lunhui.zju@gmail.com

At this point, it is a good place to comment on the other possible way to define the orbital $\mathbf{d}_o$-vector. Different from the one used in the main text, this definition groups the pairing term into orbital-singlet and orbital-triplet parts. In the form of Eq. (A1), $\Psi_s(\mathbf{k})$ and $d_o^{1,3}(\mathbf{k})$ are even in $\mathbf{k}$, but $d_o^2(\mathbf{k})$ is odd in $\mathbf{k}$ due to Fermi statistics. By regrouping the terms based on the parity in $\mathbf{k}$, we have

$$\hat{\Delta}(\mathbf{k}) = [\Delta_o d_o^2(\mathbf{k})\tau_0 + (-i\Delta_o d_o^3(\mathbf{k}), \Delta_s \Psi_s(\mathbf{k}), i\Delta_o d_o^1(\mathbf{k})) \cdot \boldsymbol{\tau}](\tau_2 i\sigma_2), \tag{3}$$

which contains $\tilde{\mathbf{d}}_o \cdot \boldsymbol{\tau}$ with the new $\tilde{\mathbf{d}}_o$-vector redefined in terms of the original amplitudes and form factors. In this form, the first part is odd in $\mathbf{k}$, which is the orbital-singlet part, and the second part is even in $\mathbf{k}$ and gives orbital-triplet state. Supplementary Table I gives a detailed comparison between the two definitions of the orbital $\mathbf{d}_o$-vector. The spin $\mathbf{d}_s$-vector is also presented for completeness. It shows that the definition of orbital $\mathbf{d}_o$-vector used in the main text is more convenient to discuss the spontaneous TRS-braking pairing states.

| | orbital $\mathbf{d}_o$ | orbital $\tilde{\mathbf{d}}_o$ | spin $\mathbf{d}_s$ |
|---|---|---|---|
| Pairing potential | $[\Delta_s\Psi_s(\mathbf{k})\tau_0 + \Delta_o\mathbf{d}_o(\mathbf{k})\cdot\boldsymbol{\tau}]i\sigma_2$ | $[\tilde{\Delta}_s\tilde{\Psi}_s(\mathbf{k})\tau_0 + \tilde{\Delta}_o\tilde{\mathbf{d}}_o(\mathbf{k})\cdot\boldsymbol{\tau}]\tau_2 i\sigma_2$ | $[\Delta_t\mathbf{d}_s(\mathbf{k})\cdot\boldsymbol{\sigma}]i\sigma_2$ |
| Parity | $\Psi_s(\mathbf{k}), d_o^2(\mathbf{k})$ odd; $d_o^{1,3}(\mathbf{k})$ even | $\tilde{\Psi}_s(\mathbf{k})$ odd; $\tilde{\mathbf{d}}_o(\mathbf{k})$ even | $\mathbf{d}_s(\mathbf{k})$ odd |
| TRS | $\Psi_s^*(\mathbf{k}) = \Psi_s(\mathbf{k})$; $\mathbf{d}_o^*(\mathbf{k}) = \mathbf{d}_o(\mathbf{k})$; | $\tilde{\Psi}_s^*(\mathbf{k}) = \tilde{\Psi}_s(\mathbf{k})$; $\left(\tilde{d}_o^{1,3}(\mathbf{k})\right)^* = -\tilde{d}_o^{1,3}(\mathbf{k})$; $\left(\tilde{d}_o^2(\mathbf{k})\right)^* = \tilde{d}_o^2(\mathbf{k})$ | $\mathbf{d}_s^*(\mathbf{k}) = \mathbf{d}_s(\mathbf{k})$ |
| TRS breaking | complex $\mathbf{d}_o$ | $\tilde{d}_o^{1,3}(\mathbf{k})$ real or $\tilde{d}_o^2(\mathbf{k})$ complex | complex $\mathbf{d}_s$ |
| spontaneous AOP/SP | $\mathbf{M}_o \propto i\mathbf{d}_o^*(\mathbf{k}) \times \mathbf{d}_o(\mathbf{k})$ | $\mathbf{M}_o \propto i\tilde{\mathbf{d}}_o^*(\mathbf{k}) \times \tilde{\mathbf{d}}_o(\mathbf{k})$ | $\mathbf{M}_s \propto i\mathbf{d}_s^*(\mathbf{k}) \times \mathbf{d}_s(\mathbf{k})$ |

Supplementary Table I. Comparison between the two possible definitions of the orbital $\mathbf{d}_o$-vector in spin-singlet SCs, together with the spin $\mathbf{d}_s$-vector of spin-triplet SCs. The parity properties are obtained from Fermi statistics. The TRS row gives the transformation properties in order to preserve TRS. Both the atomic orbital polarization (AOP) and the spin polarization (SP) take the same form in terms of their respective $\mathbf{d}$-vectors.

# Supplementary Note 2 Classification of spin singlet pairing states with $C_n$ and TRS

In this section, we classify the possible spin-singlet pairing states constrained by $C_n$ about $z$-axis and TRS. We also discuss the spontaneous time-reversal symmetry-breaking pairings and the induced orbital polarized density-of-states.

## A. Classification of pairings

The pairing potential $\hat{\Delta}(\mathbf{k})$ transforms under the rotation $C_n$ as

$$C_n\hat{\Delta}_J(\mathbf{k})C_n^T = e^{i\frac{2\pi}{n}J}\hat{\Delta}_J(C_n^{-1}\mathbf{k}), \tag{4}$$

where $J$ labels the irreducible representations of the $C_n$ point group. For example, $J = 0$ is for $A$ representation and $J = 2$ is for $B$ representation. Firstly, the TRS requires the *coexistence* of $\hat{\Delta}_J$ and $\hat{\Delta}_{-J}$ with equal weight. If the rotation symmetry $C_n$ is further imposed, then $J$ and $-J$ have to be equivalent modulo $n$, i.e. $J \equiv -J \bmod n$. The results for the basis functions of $\Psi_s(\mathbf{k})$ and $\mathbf{d}_o(\mathbf{k})$ are summarized in Table (1) in the main text. Here, the $k_z$-dependent pairing symmetries are also presented for completeness. However, such pairings are neglected in the main text where we mainly focus on 2D systems.

When inversion symmetry is also present, it leads to the following constraints for different orbital basis,

1.) If the inversion symmetry is $\mathcal{I} = \tau_0\sigma_0$, two atomic orbitals have the same parity, it requires that $d_o^2 = 0$.

2.) If the inversion symmetry is $\mathcal{I} = \tau_3\sigma_0$, two atomic orbitals have opposite parities, it require that $d_o^1 = 0$.

3.) If the inversion symmetry is $\mathcal{I} = \tau_1\sigma_0$, two orbitals are the valley indexes, it require that $d_o^3 = 0$.

## B. Spontaneous TRS-breaking orbital-polarization

Next, we study spontaneous TRS-breaking and its consequences for a two-band SC with $\{d_{xz}, d_{yz}\}$-orbitals. $\mathcal{I} = \tau_0\sigma_0$ constrains the orbital $\mathbf{d}_o$-vector to be $(d_1\Psi_o^1(\mathbf{k}), 0, d_3\Psi_o^3(\mathbf{k}))$ for Eq. (**??**). Under $C_n$ ($\mathcal{T}$), the orbital $\mathbf{d}_o$ transforms as $\mathbf{d}_o \to e^{i2\pi J/n}\mathbf{d}_o$ ($\mathbf{d}_o \to \mathbf{d}_o^*$). Choosing $\sqrt{|d_1|^2 + |d_3|^2} = 1$, the set of superconducting order parameters are given by $\{\Delta_s, \Delta_o, \mathbf{d} \triangleq (d_1, 0, d_3)\}$. Furthermore, the orbital orderings can be characterized by $\mathbf{M}_o \propto \sum_{\mathbf{k},\sigma} \langle c_{\sigma a}^\dagger(\mathbf{k})\boldsymbol{\tau}_{ab}c_{\sigma b}(\mathbf{k})\rangle$. The total GL free energy preserving the $U(1) \times \mathcal{T} \times C_n \times \mathcal{I}$ symmetries is constructed as,

$$\mathcal{F}[\Delta_s, \Delta_o, \mathbf{d}, \mathbf{M}_o] = \mathcal{F}_1 + \mathcal{F}_2 + \mathcal{F}_3 + \mathcal{F}_4, \tag{5}$$

where $\mathcal{F}_1 = \frac{1}{2}\alpha_1(T)|\Delta_o|^2 + \frac{1}{4}\beta_1|\Delta_o|^4 + \frac{1}{2}\alpha_2(T)|\Delta_s|^2 + \frac{1}{4}\beta_2|\Delta_s|^4 + \frac{1}{2}\alpha_M|\mathbf{M}_o|^2$, determining the gap strengths by using $\alpha_{1,2}(T) = \alpha_0^{1,2}(T/T_c^{1,2} - 1)$ and $\alpha_0^{1,2}, \alpha_M, \beta_{1,2} > 0$. The second term is $\mathcal{F}_2 = \beta|d_1|^4 + \beta'|d_3|^4$ with $\beta, \beta' > 0$, which determines $\mathbf{d}$. In addition, there are two possibilities to achieve the spontaneously TRS-breaking states, which are described respectively by $\mathcal{F}_3$ and $\mathcal{F}_4$,

$$\mathcal{F}_3 = b_1\Delta_s^*\Delta_o + b_2(\Delta_s^*)^2(\Delta_o)^2 + \text{h.c.}, \tag{6}$$

$$\mathcal{F}_4 = \gamma_0(T)(\mathbf{d} \times \mathbf{d}^*)^2 + i\gamma_1\mathbf{M}_o \cdot (\mathbf{d} \times \mathbf{d}^*) + \text{h.c.}. \tag{7}$$

The $\mathcal{F}_3$ term in Eq. (6) helps to develop a relative phase difference between $\Delta_s$ and $\Delta_o$ of being $\pm\pi/2$ when $b_1 = 0$ and $b_2 > 0$ [1]. As for the $b_2 < 0$ case, the TRS-breaking is caused solely by the $\mathcal{F}_4$ term in Eq. (7). For example, $\gamma_0(T) = \gamma_0(T/T_c' - 1)$ and $T_c' < T_c$, where $T_c'$ is the critical temperature for the spontaneous TRS-breaking inside the superconducting states. When $T < T_c'$, the orbital $\mathbf{d}_o$-vector becomes complex, then it generates the orbital orderings as $\mathbf{M}_o = -i\gamma_1/\alpha_M(\mathbf{d} \times \mathbf{d}^*)$, of which only the $y$-component breaks TRS, as illustrated in the main text (see Fig. 1). More precisely, $M_o^y \propto \sum_{\mathbf{k},\sigma}\langle \hat{n}_{\sigma,+}(\mathbf{k}) - \hat{n}_{\sigma,-}(\mathbf{k})\rangle$. Here we define $|\pm\rangle = |1\rangle + i|2\rangle$ for complex orbitals, thus $M_o^y \neq 0$ indicates the TRS-breaking orbital-polarization (OP), similar to the time-reversal-odd polarization of the Cooper pairs discussed in Ref. [2, 3].

We next solve the Bogoliubov-de-Gennes Hamiltonian,

$$\mathcal{H}_{BdG}|E_n(\mathbf{k})\rangle = E_n(\mathbf{k})|E_n(\mathbf{k})\rangle, \tag{8}$$

$$|E_n(\mathbf{k})\rangle = (u_{d_{xz},\uparrow}^n, u_{d_{xz},\downarrow}^n, v_{d_{xz},\uparrow}^n, v_{d_{xz},\downarrow}^n, u_{d_{yz},\uparrow}^n, u_{d_{yz},\downarrow}^n, v_{d_{yz},\uparrow}^n, v_{d_{yz},\downarrow}^n)^T, \tag{9}$$

The quasi-particle spectrum is plotted in the main text (see Fig. 1), where two distinct gaps appear. Then, we calculate the atomic orbital-polarized density of states (DOS),

$$D_\kappa(E) = \frac{1}{2}\sum_{\sigma,n,\mathbf{k}}|u_{\kappa,\sigma}^n|^2\delta(E - E_n(\mathbf{k})), \tag{10}$$

where $u_{\kappa,\sigma}^n = u_{d_{xz},\sigma}^n - i\kappa u_{d_{yz},\sigma}^n$ with $\kappa = \pm$ for $d_{xz} \pm id_{yz}$ orbitals, and $\delta(x)$ is the delta function. In Supplementary Fig. 1, the numerical results help to confirm a two-gap feature due to the spontaneous breaking of TRS, compared with the quasi-particle spectrum. Moreover, $D_+ \neq D_-$ at finite energy clearly indicates that the DOS is orbital-polarized, which is consistent with the GL analysis. The orbital-spin conversion would lead to the spin-polarized DOS [4].

# Supplementary Note 3 The stability of orbital $\mathbf{d}_o$-vector under crystal fields

In the Method section of the main text, we derived our main result up to first-order in the coupling $\lambda_o$. Here, we first address the situation where multiple pairing channels with possibly different pairing strengths coexist. Then we show the second-order result in $\lambda_o$.

## A. First-order result applied to multiple coexisting pairing channels

We have the following first-order result,

$$\ln\left(\frac{T_c}{T_{c0}}\right) = \int_S \frac{d\Omega}{2\pi}\mathcal{C}_0(T_c)\left(|\mathbf{d}_o|^2 - |\mathbf{d}_o \cdot \hat{\mathbf{g}}_o|^2\right), \tag{11}$$
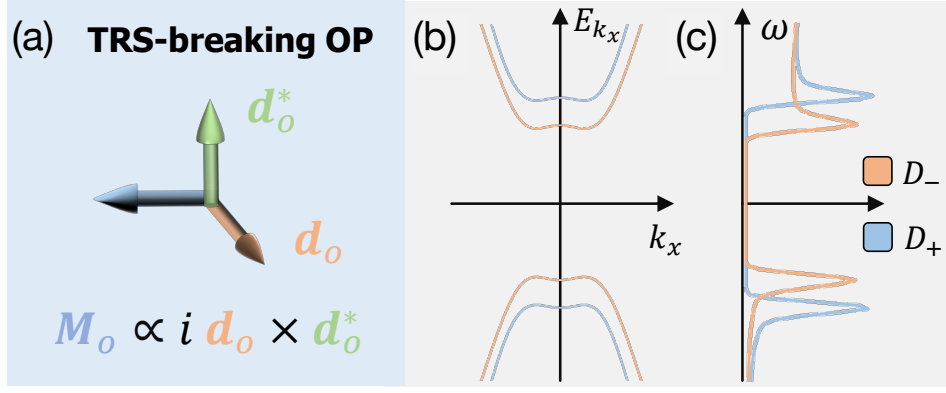
Supplementary Figure 1. The TRS-breaking effects for spin-singlet two-band SCs. (a) A complex orbital $\mathbf{d}_o$-vector spontaneously breaks TRS and may give rise to the TRS-breaking OP with $\mathbf{M}_o \propto i\mathbf{d}_o \times \mathbf{d}_o^*$, which is the same plot in Fig. (1b) in the main text. (b) The quasi-particle spectrum along $\mathbf{k} = (k_x, 0)$ is shown. (c) The orbital-polarized DOS $D_\pm$ with $\pm$ representing $d_{xz} \pm id_{yz}$ are exhibited. Parameters used are: $\lambda_o = 0.1$, $\Delta_o = 1$, $\Delta_s = 0.1$, $\mu = -0.5$, $t_0 = 1$, $\mathbf{d}_o = (\cos\frac{\pi}{20}, 0, i\sin\frac{\pi}{20})$.
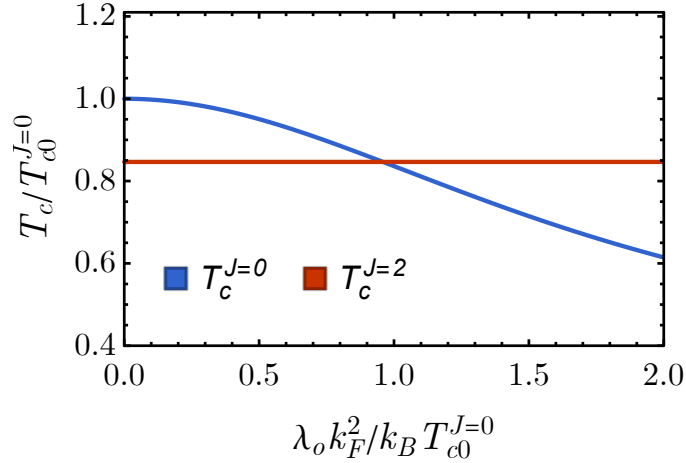


Supplementary Figure 2. Different behaviors of $T_c^{J=0}$ and $T_c^{J=2}$ under orbital hybridization. Here $\mathbf{d}_o^{J=0} = k_F^{-2}(k_x^2 - k_y^2, 0, 2k_x k_y)$, $\mathbf{d}_o^{J=2} = \frac{1}{\sqrt{2}}(1, 0, 1)$, and $\mathbf{g}_o = k_F^2(1, 0, 1)$.

which is derived with the assumption that there is only one pairing channel. Here, we elaborate on a subtlety mentioned in the main text that might arise due to coexisting multiple pairing channels belonging to different 1d irreducible representations. In the weak-coupling theory and without orbital hybridization, the critical temperature for a particular channel $\Gamma$ is simply obtained by solving the linearized gap equation $v^\Gamma \chi_0(T_{c0}) = 1$ and the solution is given by $T_{c0}^\Gamma = \frac{2e^\gamma \omega_D}{\pi k_B} e^{-\frac{1}{v^\Gamma N_0}}$. This means that the critical temperature in each channel is solely determined by the strength of the pairing interaction in that particular channel. The leading instability channel has the largest pairing interaction, which determines the $T_c$. However, when orbital hybridization is considered, the story could change. Depending on the relation between $\mathbf{d}_o^\Gamma$ and $\mathbf{g}_o$, some pairing channels will be suppressed more than the others. Therefore, the previous leading instability channel could become sub-leading in the presence of orbital hybridization. In Supplementary Figure 2 we take the $J = 0$ and $J = 2$ representations under $C_4$ as an example, with the assumption that $v^{J=0} > v^{J=2}$. We see that $T_c^{J=0}$ starts higher than $T_c^{J=2}$, but since $\mathbf{d}_o^{J=2}$ is parallel $\mathbf{g}_o$ and $\mathbf{d}_o^{J=0}$ is not, $T_c^{J=2}$ is not suppressed by $\lambda_o$ whereas $T_c^{J=0}$ is suppressed and eventually becomes lower than $T_c^{J=2}$.

## B. Second-order approximated results

In this subsection, we consider the coupling between orbital-independent pairing ($\Psi_s(\mathbf{k})$-part in Eq. (1)) and orbital-dependent pairing ($\mathbf{d}_o(\mathbf{k})$-part in Eq. (1)), and study the second-order approximated results for the above conclusion.

The attractive interaction is now decomposed as

$$V_{s_1'a',s_2'b'}^{s_1a,s_2b}(\mathbf{k},\mathbf{k}') = -v_0[\mathbf{d}_o(\mathbf{k})\cdot\boldsymbol{\tau}i\sigma_2]_{s_1a,s_2b}[\mathbf{d}_o(\mathbf{k}')\cdot\boldsymbol{\tau}i\sigma_2]_{s_1'a',s_2'b'} - v_1[\Psi_s(\mathbf{k})i\sigma_2]_{s_1,s_2}[\Psi_s(\mathbf{k}')i\sigma_2]_{s_1',s_2'}, \tag{12}$$

where $v_0$ is the interaction strength in the orbital-dependent channel and $v_1$ is the interaction strength in the orbital-independent channel. And they belong to the same representation of symmetry groups, leading to the coupled linearized gap equation,

$$\mathrm{Det}\begin{pmatrix} v_0\chi(T)-1 & v_0\chi_{os}(T) \\ v_1\chi_{so}(T) & v_1\chi_s(T)-1 \end{pmatrix} = 0, \tag{13}$$

where

$$\chi_{os}(T) \equiv -\frac{1}{\beta}\sum_{\mathbf{k},\omega_n} \mathrm{Tr}\left[(\mathbf{d}_o(\mathbf{k})\cdot\boldsymbol{\tau}i\sigma_2)^\dagger G_e(\mathbf{k},i\omega_n)(\Psi_s(\mathbf{k})i\sigma_2)G_h(-\mathbf{k},i\omega_n)\right],$$

$$\chi_{so}(T) \equiv -\frac{1}{\beta}\sum_{\mathbf{k},\omega_n} \mathrm{Tr}\left[(\Psi_s(\mathbf{k})i\sigma_2)^\dagger G_e(\mathbf{k},i\omega_n)(\mathbf{d}_o(\mathbf{k})\cdot\boldsymbol{\tau}i\sigma_2)G_h(-\mathbf{k},i\omega_n)\right]. \tag{14}$$

It leads to

$$(v_0\chi(T)-1)(v_1\chi_s(T)-1) - v_0v_1\chi_{so}(T)\chi_{os}(T) = 0, \tag{15}$$

Considering the $v_0 > v_1$ case firstly, then, the bare $T_c$ of orbital-dependent pairings are larger than that of orbital-independent pairings, we have

$$v_0\chi(T)-1 - \frac{v_0v_1\chi_{so}(T)\chi_{os}(T)}{v_1\chi_s(T)-1} = 0, \tag{16}$$

from which, we define the total superconductivity susceptibility as,

$$\chi'(T) = \chi(T) + \frac{\chi_{so}(T)\chi_{os}(T)}{1/v_1 - \chi_s(T)} \tag{17}$$

where $\chi(T)$ has been calculated in the above subsection (see Eq. (**??**)), and the second part is the second-order correction. After tracing out the spin degrees of freedom, we have $\chi_{os}(T) = \chi_{so}(T)$. Following the same procedure as in the first-order case, we have

$$\chi_{os}(T) = -\frac{2N_0}{\beta}\int_{-\omega_D}^{+\omega_D} d\epsilon \int_S \frac{d\Omega}{2\pi}\sum_{\omega_n}\sum_\alpha \alpha G_e^\alpha(\mathbf{k},i\omega_n)G_h^\alpha(\mathbf{k},i\omega_n)[(\mathbf{d}_o(\mathbf{k})\cdot\hat{\mathbf{g}}_o(\mathbf{k}))\Psi_s(\mathbf{k})]$$

$$= -\frac{2N_0}{\beta}\int_{-\omega_D}^{+\omega_D} d\epsilon \int_S \frac{d\Omega}{2\pi}\sum_{\omega_n}[G_e^+(\mathbf{k},i\omega_n)G_h^+(\mathbf{k},i\omega_n) - G_e^-(\mathbf{k},i\omega_n)G_h^-(\mathbf{k},i\omega_n)][(\mathbf{d}_o(\mathbf{k})\cdot\hat{\mathbf{g}}_o(\mathbf{k}))\Psi_s(\mathbf{k})], \tag{18}$$

which would vanish if $\lambda_o = 0$, i.e. no orbital hybridization, based on the definitions of $G_{e/h}^{+/-}$, which in turn, reproduces the first-order calculation above. At non-zero, but small $\lambda_o$ ($\lambda_o k_F^2 < \mu$), $\chi_{os}(T)$ will also be small but non-zero. For convenience of discussion, we define

$$\delta(T,\lambda_o) \equiv -\frac{N_0}{\beta}\int_{-\omega_D}^{+\omega_D} d\epsilon \sum_{\omega_n}[G_e^+(\mathbf{k},i\omega_n)G_h^+(\mathbf{k},i\omega_n) - G_e^-(\mathbf{k},i\omega_n)G_h^-(\mathbf{k},i\omega_n)], \tag{19}$$

where $\delta(T,\lambda_o)\sim\lambda_o k_F^2/\mu$ would vanish at leading order (see Eq. (**??**)). Then we have

$$\chi_{os}(T) = 2\delta(T,\lambda_o)\int_S \frac{d\Omega}{2\pi}[(\mathbf{d}_o(\mathbf{k})\cdot\hat{\mathbf{g}}_o(\mathbf{k}))\Psi_s(\mathbf{k})]. \tag{20}$$

With this, the total superconductivity susceptibility in Eq. (17) becomes

$$\chi'(T) = \chi(T) + \frac{\chi_{os}^2(T)}{2N_0\log(T/T_s)} \equiv \chi(T) + \delta\chi(T). \tag{21}$$

where $\delta\chi(T)$ is the second-order correction due to the coupling between orbital-independent pairings ($\Psi_s(\mathbf{k})$-part in Eq. (1)) and orbital-dependent pairing ($\mathbf{d}_o(\mathbf{k})$-part in Eq. (1)),

$$\delta\chi(T) = \frac{2\delta^2(T, \lambda_o)\left(\int_S \frac{d\Omega}{2\pi}[(\mathbf{d}_o(\mathbf{k}) \cdot \hat{\mathbf{g}}_o(\mathbf{k}))\Psi_s(\mathbf{k})]\right)^2}{N_0 \log(T/T_s)}. \tag{22}$$

Since we assumed $v_0 > v_1$, i.e. $T_{c0} > T_s$, then the actual transition temperature would be $T_c \sim T_{c0} > T_s$, giving $\log(T_c/T_s) > 0$. As a result, the correction to the susceptibility is positive: $\delta\chi(T) > 0$. Then following the same procedure as in the previous section, we have

$$\ln\left(\frac{T_c}{T_{c0}}\right) = \int_S \frac{d\Omega}{2\pi} \mathcal{C}_0(T_{c0})\left(|\mathbf{d}_o|^2 - |\mathbf{d}_o \cdot \hat{\mathbf{g}}_o|^2\right) + \frac{\delta\chi(T_{c0})}{N_0}, \tag{23}$$

where the first part is the first-order result (see Eq. (23) or Eq. (5) in the main text; order as $\mathcal{O}(\lambda_o k_F^2/\mu)$), and the second part is the second-order result (order as $\mathcal{O}((\lambda_o k_F^2/\mu)^2)$). Therefore, we conclude that,

- **The first part**: it determines the direction of orbital $\mathbf{d}_o$-vector to be $\mathbf{d}_o \parallel \hat{\mathbf{g}}_o$. Because of $\mathcal{C}_0(T_{c0}) \leq 0$, once $\mathbf{d}_o \parallel \hat{\mathbf{g}}_o$ at any momentum $\mathbf{k}$, the first part vanishes.

- **The second part**: it relates the form $\Psi_s(\mathbf{k})$ to the orbital $\mathbf{d}_o$-vector: $\mathbf{d}_o \propto \Psi_s(\mathbf{k})\hat{\mathbf{g}}_o$. Thus, the second part becomes maximum, leading to the maximal increase of $T_{c0}$.

Here we have used the fact,

$$\left(\int_S \frac{d\Omega}{2\pi}[\Psi_i(\mathbf{k})\Psi_j(\mathbf{k})]\right)^2 \leq 1, \text{ for any scalar } \Psi_i, \int_S \frac{d\Omega}{2\pi}[\Psi_i(\mathbf{k})\Psi_i(\mathbf{k})] = 1. \tag{24}$$

And $\left(\int_S \frac{d\Omega}{2\pi}[\Psi_i(\mathbf{k})\Psi_j(\mathbf{k})]\right)^2$ reaches 1 only when $i = j$.

Next, we briefly discuss the case where $v_0 < v_1$. The same result can be similarly argued. In this case, the dominant pairing channel is the orbital-independent pairing ($T_s > T_{c0}$), which can induce the orbital $\mathbf{d}_o$-vector via their couplings. Similar to Eq. (16), we define the total superconductivity susceptibility for orbital-independent pairings,

$$v_1\chi_s(T) - 1 - \frac{v_0 v_1 \chi_{so}(T)\chi_{os}(T)}{v_0\chi(T) - 1} = 0, \tag{25}$$

which leads to

$$\chi_s'(T) = \chi_s(T) + \frac{\chi_{so}(T)\chi_{os}(T)}{1/v_0 - \chi(T)} = N_0 \ln\left(\frac{2e^\gamma \omega_D}{\pi k_B T}\right) + \frac{\chi_{os}^2(T)}{N_0 \ln(\frac{T}{T_{c0}}) - \int_S \frac{d\Omega}{2\pi} \mathcal{C}_0(T_{c0})\left(|\mathbf{d}_o|^2 - |\mathbf{d}_o \cdot \hat{\mathbf{g}}_o|^2\right)}, \tag{26}$$

thus,

$$\ln\left(\frac{T_c}{T_s}\right) = 2\delta^2(T_c, \lambda_o) \times \frac{\left(\int_S \frac{d\Omega}{2\pi}[(\mathbf{d}_o(\mathbf{k}) \cdot \hat{\mathbf{g}}_o(\mathbf{k}))\Psi_s(\mathbf{k})]\right)^2}{N_0 \ln(\frac{T_c}{T_{c0}}) - \int_S \frac{d\Omega}{2\pi} \mathcal{C}_0(T_{c0})\left(|\mathbf{d}_o|^2 - |\mathbf{d}_o \cdot \hat{\mathbf{g}}_o|^2\right)} \geq 0, \tag{27}$$

here $T_c \sim T_s > T_{c0}$ so that $\ln(\frac{T_c}{T_{c0}}) > 0$. The correction is in order of $\mathcal{O}((\lambda_o k_F^2/\mu)^2)$. Therefore,

- **The denominate**: it determines the direction of orbital $\mathbf{d}_o$-vector to be $\mathbf{d}_o \parallel \hat{\mathbf{g}}_o$. Because of $\mathcal{C}_0(T_{c0}) \leq 0$, then, $-\int_S \frac{d\Omega}{2\pi} \mathcal{C}_0(T_{c0})\left(|\mathbf{d}_o|^2 - |\mathbf{d}_o \cdot \hat{\mathbf{g}}_o|^2\right) \geq 0$, once $\mathbf{d}_o \parallel \hat{\mathbf{g}}_o$ at any momentum $\mathbf{k}$, the denominate is positive and minimum.

- **The numerator**: it determines the local magnitude of orbital $\mathbf{d}_o$-vector to be $\mathbf{d}_o \propto \Psi_s(\mathbf{k})\hat{\mathbf{g}}_o$. Thus, the numerator becomes maximum, leading to the increasing of $T_{c0}$ maximally.

Therefore, according to both Eq. (23) and Eq. (27), we conclude that the orbital $\mathbf{d}_o$-vector that is parallel with orbital hybridization $\mathbf{g}_o$-vector could be generally stabilized in real materials. And we find that

$$\mathbf{d}_o = \pm\Psi_s(\mathbf{k})\hat{\mathbf{g}}_o, \tag{28}$$

which is shown in Eq. (6) in the main text. However, it has also a $Z_2$ phase $\pm$, which can be pinned by taking higher order corrections into account.

# Supplementary Note 4 Formation of the pairing near Fermi surface in band picture

Here, we provide another perspective on the pairing in orbital channel near the Fermi surface (FS) by looking at the total free energy of the system in band picture, where the pairing amplitude is treated perturbatively.

In the presence of orbital hybridization or nematic order, the Hamiltonian without pairing is given by

$$\mathcal{H}_0 = (\epsilon_{\mathbf{k}} - \mu)\tau_0\sigma_0 + \lambda(\mathbf{g}\cdot\boldsymbol{\tau})\sigma_0, \tag{29}$$

where $\lambda$ is taken to be positive. The degeneracy in the orbital channel will be lifted, whereas the spin channel still has the double-degeneracy. Effectively, the vector $\mathbf{g}$ acts as a "Zeeman field" in the orbital space, and the pseudo-spin will be parallel or anti-parallel to the field for the two splitting levels. And we notice that

$$[\mathbf{g}\cdot\boldsymbol{\tau}, \mathcal{H}_0] = 0. \tag{30}$$

More precisely, the two eigenstates of $\mathcal{H}_0$ can be denoted by $|E_\pm\rangle \equiv |\hat{\mathbf{g}}; \pm\rangle$, where $+/-$ means parallel/anti-parallel (eigenvalues of the symmetry operator $\hat{\mathbf{g}}\cdot\boldsymbol{\tau}$). Please note that $\hat{\mathbf{g}} = \mathbf{g}/|\mathbf{g}|$. And

$$\mathcal{H}_0|E_\pm\rangle = E_\pm|E_\pm\rangle, \quad \text{with } E_\pm = \epsilon_{\mathbf{k}} - \mu \pm \lambda|\mathbf{g}(\mathbf{k})|. \tag{31}$$

with $\lambda > 0$. Setting $E_\pm = 0$, it gives rise to two FSs (labeled as $FS_\pm$) with energy splitting as $2\lambda|\mathbf{g}(\mathbf{k})|$, which is approximately as $\sim \lambda k_F^2$ with respect to $\epsilon_{k_F} = \mu$.

Now we consider the spin-singlet pairing part in the original basis,

$$\mathcal{H}_\Delta = \sum_{\mathbf{k}}(c_{1,\uparrow}^\dagger(\mathbf{k}), c_{2,\uparrow}^\dagger(\mathbf{k}))\left[\Delta_s\Psi(\mathbf{k})\tau_0 + \Delta_o(\mathbf{d}_o(\mathbf{k})\cdot\boldsymbol{\tau})\right](c_{1,\downarrow}^\dagger(-\mathbf{k}), c_{2,\downarrow}^\dagger(-\mathbf{k}))^T + \text{H.c.}. \tag{32}$$

The BdG Hamiltonian is then given by

$$\mathcal{H}_{BdG} = ((\epsilon_{\mathbf{k}} - \mu)\tau_0\sigma_0 + \lambda(\mathbf{g}\cdot\boldsymbol{\tau})\sigma_0)\gamma_3 + [\Delta_s\Psi(\mathbf{k}) + \Delta_o(\mathbf{d}_o(\mathbf{k})\cdot\boldsymbol{\tau})](i\sigma_2)\gamma_2, \tag{33}$$

where $\gamma_i$ are the Pauli matrices in particle-hole channel.

Next, we consider weak-coupling limit (infinitesimal pairing strength, namely, $\Delta_o \to 0$) and we use the band picture to study the pairing Hamiltonian. For this purpose, we rewrite $\mathcal{H}_0$ as

$$\mathcal{H}_0 = \sum_{\mathbf{k},\tau,s} E_\tau(\mathbf{k})c_{\tau,s}^\dagger(\mathbf{k})c_{\tau,s}(\mathbf{k}). \tag{34}$$

where $\tau = \pm$ is the band index and $s$ is for spin. The unitary transformation matrix $U(\mathbf{k})$ in the orbital subspace leads to the diagonalization of $\mathcal{H}_0$,

$$U^\dagger(\mathbf{k})[(\epsilon_{\mathbf{k}} - \mu)\tau_0 + \lambda(\mathbf{g}\cdot\boldsymbol{\tau})]U(\mathbf{k}) = \text{Diag}[E_+(\mathbf{k}), E_-(\mathbf{k})], \tag{35}$$

where spin index has been dropped and the 2-by-2 $U(\mathbf{k})$ can be expressed by the eigenstates of $\mathcal{H}_0$,

$$U(\mathbf{k}) = \{|E_+(\mathbf{k})\rangle, |E_-(\mathbf{k})\rangle\}. \tag{36}$$

Thus, $U^\dagger(\mathbf{k})U(\mathbf{k}) = 1$. And the time-reversal symmetry requires that

$$U(\mathbf{k}) = (U(-\mathbf{k}))^*. \tag{37}$$

Acting on the basis, we have

$$(c_{1,s}^\dagger(\mathbf{k}), c_{2,s}^\dagger(\mathbf{k})) = (c_{+,s}^\dagger(\mathbf{k}), c_{-,s}^\dagger(\mathbf{k}))U^\dagger(\mathbf{k}) \tag{38}$$

where $s$ is for spin. We then project the spin-singlet pairing Hamiltonian in Eq. (32) into the band basis, thus, the spin-singlet pairing Hamiltonian becomes

$$\mathcal{H}_\Delta = \sum_{\mathbf{k}}(c_{+,\uparrow}^\dagger(\mathbf{k}), c_{-,\uparrow}^\dagger(\mathbf{k}))\left\{U^\dagger(\mathbf{k})[\Delta_s\Psi(\mathbf{k}) + \Delta_o(\mathbf{d}_o(\mathbf{k})\cdot\boldsymbol{\tau})]U(\mathbf{k})\right\}(c_{+,\downarrow}^\dagger(-\mathbf{k}), c_{-,\downarrow}^\dagger(-\mathbf{k}))^T. \tag{39}$$

Here $U(\mathbf{k}) = (U(-\mathbf{k}))^*$ has been used. Therefore, the spin-singlet pairing potential in the band basis becomes

$$\Delta_{\text{band}}(\mathbf{k}) = U^\dagger(\mathbf{k}) \left[\Delta_s \Psi(\mathbf{k})\tau_0 + \Delta_o(\mathbf{d}_o(\mathbf{k}) \cdot \boldsymbol{\tau})\right] U(\mathbf{k}). \tag{40}$$

Thus, the orbital-independent pairings only lead to the intra-band pairings, while the orbital-dependent pairings can give rise to both intra-band and inter-band pairings.

First of all, we focus on the pure orbital $\mathbf{d}_o$-vector (orbital-dependent pairings) by assuming $\Delta_s = 0$. To separate the intra-band pairings from the inter-band pairings, we decompose the orbital $\mathbf{d}_o$-vector as

$$\mathbf{d}_o(\mathbf{k}) = d_\parallel(\mathbf{k})\hat{\mathbf{g}}(\mathbf{k}) + \mathbf{d}_\perp(\mathbf{k}), \tag{41}$$

where $d_\parallel(\mathbf{k}) = \mathbf{d}_o(\mathbf{k}) \cdot \hat{\mathbf{g}}(\mathbf{k})$ and $\mathbf{d}_\perp(\mathbf{k}) \cdot \hat{\mathbf{g}}(\mathbf{k}) = 0$. Thus,

- **The parallel component**: the $d_\parallel(\mathbf{k})\hat{\mathbf{g}}(\mathbf{k})$-part commutes with $\mathbf{g} \cdot \boldsymbol{\tau}$, hence only generates intra-band pairing for the two FSs. Therefore, the projected intra-band pairing Hamiltonian reads,

$$\mathcal{H}_{\text{intra-band},\Delta} = \sum_{\mathbf{k},\tau} \left(\tau \Delta_o d_\parallel(\mathbf{k})\right) \left[c_{\tau,\uparrow}(\mathbf{k})c_{\tau,\downarrow}(-\mathbf{k}) - c_{\tau,\downarrow}(\mathbf{k})c_{\tau,\uparrow}(-\mathbf{k})\right] + \text{H.c.}. \tag{42}$$

  Here $\tau = \pm$ indicates that the intra-band pairing strengths on two FSs are opposite. And $d_\parallel(\mathbf{k}) = d_\parallel(-\mathbf{k})$, the intra-band pairing is a even-parity pairing.

- **The perpendicular component**: the $\mathbf{d}_\perp(\mathbf{k})$-part would mix the two states $|E_\pm\rangle$, then it only produces inter-band pairings. At a fixed $\mathbf{k}$, we now perform a rotation,

$$O(3) \text{ rotation: } R_o\hat{\mathbf{g}}_o R_o^\dagger = (0,0,g_z') \text{ and } R_o\mathbf{d}_\perp R_o^\dagger = (g_x', g_y', 0) \tag{43}$$

  at the same time, we perform a rotation in the orbital subspace

$$SU(2) \text{ rotation: } R_\tau \tau_{x,y,z} R_\tau^\dagger = \tau_{x,y,z}' \tag{44}$$

  Due to this rotation, the perpendicular components only couple $|E_+\rangle$ with $|E_-\rangle$. This proves that

$$\langle E_\tau|\mathbf{d}_\perp \cdot \boldsymbol{\tau}|E_\tau\rangle = 0. \tag{45}$$

  Here $|E_\tau\rangle$ are eigenstates of $\hat{\mathbf{g}}_o \cdot \boldsymbol{\tau}$. Thus, the projected inter-band pairing Hamiltonian reads,

$$\mathcal{H}_{\text{inter-band},\Delta} = \sum_{\mathbf{k},\tau} \Delta_{\tau,-\tau}(\mathbf{k}) \left[c_{\tau,\uparrow}(\mathbf{k})c_{-\tau,\downarrow}(-\mathbf{k}) - c_{\tau,\downarrow}(\mathbf{k})c_{-\tau,\uparrow}(-\mathbf{k})\right] + \text{H.c.}. \tag{46}$$

  where $\Delta_{\tau,-\tau}(\mathbf{k}) = \Delta_o\langle E_\tau(\mathbf{k})|\mathbf{d}_\perp(\mathbf{k}) \cdot \boldsymbol{\tau}|E_{-\tau}(\mathbf{k})\rangle$. In the limit $\lambda k_F^2 \gg \Delta_o$ (i.e., band splitting is much larger than the pairing gap), the inter-band pairing is not energetically favorable in the weak-coupling pairing theory (i.e., attractive interaction is infinitesimal small). It means the inter-band pairing will be severely suppressed if we increase the orbital hybridization $\lambda$, consistent with the calculation in the main text (see Fig. (2)).

From the above analysis, we conclude that the orbital $\mathbf{d}_o$-vector should be parallel with the orbital hybridization $\mathbf{g}$.

To determine the magnitude of the orbital $\mathbf{d}_o$-vector, we turn on the orbital-independent pairing $\Delta_s \neq 0$. We also assume both pairing channels are small. Assuming the two FSs have DOS $N_\pm$ near the FS (ignoring the momentum-dependence if the FS is almost isotropic), then the total condensation energy per volume and per spin of the two intra-band pairings is given by

$$\delta E = N_+ \sum_{\mathbf{k}\in\text{FS}_+} \left(\Delta_s \Psi_s(\mathbf{k}) + \Delta_o d_\parallel(\mathbf{k})\right)^2 + N_- \sum_{\mathbf{k}\in\text{FS}_-} \left(\Delta_s \Psi_s(\mathbf{k}) - \Delta_o d_\parallel(\mathbf{k})\right)^2, \tag{47}$$

with the approximation $\lambda k_F^2 \ll \mu$, $\delta E$ becomes

$$\delta E = (N_+ + N_-) \sum_{\mathbf{k}\in\text{FS}} [\Delta_s^2(\Psi_s(\mathbf{k}))^2 + \Delta_o^2(d_\parallel(\mathbf{k}))^2] + 2(N_+ - N_-)\Delta_s\Delta_o \sum_{\mathbf{k}\in\text{FS}} (\Psi_s(\mathbf{k})d_\parallel(\mathbf{k})), \tag{48}$$

where FS is for $\lambda \to 0$. And we see that in order to maximize the condensation energy, we require

$$d_\parallel(\mathbf{k}) \propto \Psi_s(\mathbf{k}), \text{ if } \text{sign}[(N_+ - N_-)\Delta_s\Delta_o] = 1, \tag{49}$$
$$d_\parallel(\mathbf{k}) \propto -\Psi_s(\mathbf{k}), \text{ if } \text{sign}[(N_+ - N_-)\Delta_s\Delta_o] = -1, \tag{50}$$

according to Eq. (24). The results from the weak-coupling limit are the same as the calculations from linearized gap equations.

# Supplementary Note 5 The coexistence of orbital $d_o$-vector and nematic order

In this section, we discuss the interaction effects on the stability of orbital $\mathbf{d}_o$-vector for a two-band superconductor. A general density-density interaction, including both inter-band and intra-band terms, is,

$$\mathcal{H}_{int} = v_1(\hat{n}_{1\uparrow} + \hat{n}_{1\downarrow})(\hat{n}_{2\uparrow} + \hat{n}_{2\downarrow}) + v_2(\hat{n}_{1\uparrow}\hat{n}_{1\downarrow} + \hat{n}_{2\uparrow}\hat{n}_{2\downarrow}), \tag{51}$$

where $\hat{n}$ is the electron density operator and $v_{1,2}$ are interaction strengths. With the following mean-field decomposition, we can define the nematic ordering that spontaneously breaks the rotational symmetry.

$$\mathcal{H}_{MF} = \hat{n}_{1\uparrow}\left(\frac{v_1}{2}\langle\hat{n}_2\rangle + v_2\langle\hat{n}_{1\downarrow}\rangle\right) + \hat{n}_{1\downarrow}\left(\frac{v_1}{2}\langle\hat{n}_2\rangle + v_2\langle\hat{n}_{1\uparrow}\rangle\right) + \hat{n}_{2\uparrow}\left(\frac{v_1}{2}\langle\hat{n}_1\rangle + v_2\langle\hat{n}_{2\downarrow}\rangle\right) + \hat{n}_{2\downarrow}\left(\frac{v_1}{2}\langle\hat{n}_1\rangle + v_2\langle\hat{n}_{2\uparrow}\rangle\right). \tag{52}$$

For the purpose of our discussion, we assume there is no spin ferromagnetism, i.e. $\langle\hat{n}_{\alpha\uparrow}\rangle = \langle\hat{n}_{\alpha\downarrow}\rangle = \frac{1}{2}\langle\hat{n}_\alpha\rangle$, then the mean field Hamiltonian simplifies to

$$\mathcal{H}_{MF} = \hat{n}_1\left(\frac{v_1}{2}\langle\hat{n}_2\rangle + \frac{v_2}{2}\langle\hat{n}_1\rangle\right) + \hat{n}_2\left(\frac{v_1}{2}\langle\hat{n}_1\rangle + \frac{v_2}{2}\langle\hat{n}_2\rangle\right) \equiv \hat{n}_1\Phi_1 + \hat{n}_2\Phi_2. \tag{53}$$

Then the nematic order parameter can be defined as

$$\Phi \equiv \Phi_1 - \Phi_2 = \frac{1}{2}(v_2 - v_1)(\langle\hat{n}_1\rangle - \langle\hat{n}_2\rangle). \tag{54}$$

Now the stage is set to define the total orbital hybridization as,

$$\mathbf{g}_{tot} = \mathbf{g}_o + t_{nem}\mathbf{g}_{nem} \tag{55}$$

where $\mathbf{g}_{nem} = (0, 0, \Phi)$ and $t_{nem} = \lambda_{nem}/\lambda_o$. Then, we apply Eq. (23) to study the stability of orbital $\mathbf{d}_o$-vector when nematic order develops above superconducting $T_{c0}$. The results are summarized in Supplementary Figure 3
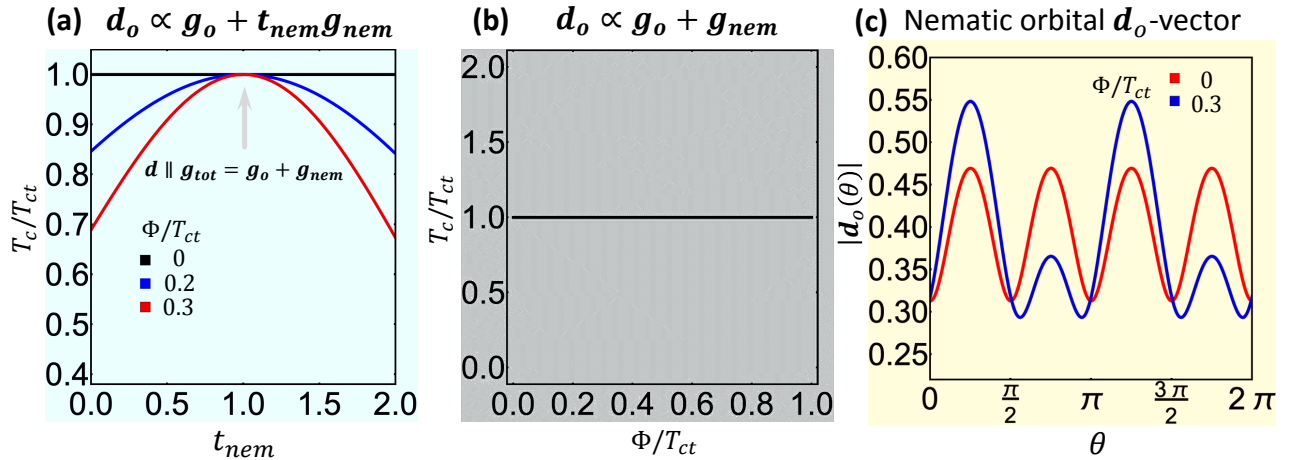


Supplementary Figure 3. The coexistence of orbital $\mathbf{d}_o$-vector and nematic order. In (a), each $t_{nem}$ corresponds to a particular form of the $\mathbf{d}$-vector, which determines $T_c$ based on Eq. (23). The three curves correspond to three different values for the nematic order $\Phi$. The $T_c$ is not suppressed by the nematic order as long as $\mathbf{d}_o \parallel \mathbf{g}_{tot}$, i.e. $t_{nem} = 1$. The $t_{nem} = 1$ case is further illustrated in (b), where it is shown that the magnitude of the nematic order does not change $T_c$ (up to the order of approximation made in Eq. (23)). (c) shows non-zero nematic order breaks the original $C_4$ (red line) down to $C_2$ (blue line). Here $\mathbf{g}_o = (k_x^2 - k_y^2, 0, 3k_x k_y)$.

# Supplementary Note 6 Application to single-layer graphene supercon-ductor

Based on the discussion in the main text, the nematic d-vector is characterized by $\mathbf{g}_{tot} = (g_{int,1}, 0, 0)$, with

$$g_{int,1} = 1 + 2t_1 k_x k_y + t_2(k_x^2 - k_y^2). \tag{56}$$

A closed Fermi surface (FS) can be parametrized by $k_F(\theta)$. By using Eq. (23), the nematic $\mathbf{d}_o$-vector represents a $(s+d)$-wave pairing states,

$$\begin{cases} \text{s-wave dominant: }, t_{1,2} \ll 1, \text{fully gapped superconductors} \\ \text{d-wave dominant: }, t_{1,2} \gg 1, \text{ndoal superconductors} \end{cases} \tag{57}$$

As a result, we have $|\mathbf{d}_o| \sim |\mathbf{g}_{tot}| = |1 + k_F(\theta)(t_1 \sin 2\theta + t_2 \cos 2\theta)|$. We see that the SC gap function can have nodes as long as $\sqrt{t_1^2 + t_2^2}$ is large enough. For graphene, the FS has $C_3$ symmetry, i.e. $k_F(\theta)$ has periodicity of $\frac{2}{3}\pi$, whereas $\sin 2\theta$ and $\cos 2\theta$ have periodicity of $\pi$, giving a periodicity of $2\pi$ to $|\mathbf{d}_o|$, which completely breaks the $C_3$ symmetry of the system. Supplementary Figure 4 shows the $C_3$-breaking nematic orders from inter-valley scattering, one with nodal gap function, the other with nodeless gap function.
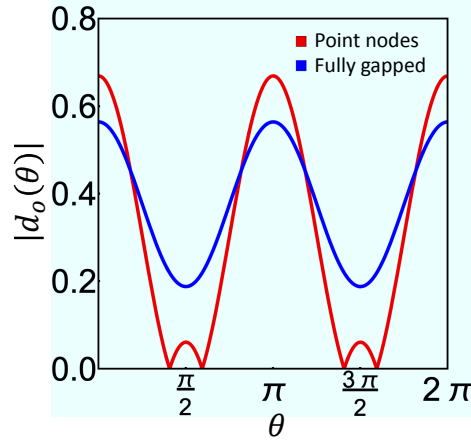


Supplementary Figure 4. The $C_3$-breaking nematic order from inter-valley scattering in graphene. $t_1 = 0, t_2 = 1.2$ for the nodal case (red) and $t_1 = 0, t_2 = 0.5$ for the fully gapped case (blue).

# Supplementary Note 7 Spin and orbital magnetizations: $\mathbf{M}_s$ and $\mathbf{M}_o$

Here we present the definitions of spin and orbital magnetizations in our mean-field analysis. The spin magnetization is defined as,

$$\mathbf{M}_s = \sum_{\mathbf{k}, s_1, s_2} \langle c_{s_1}^\dagger(\mathbf{k}) \boldsymbol{\sigma}_{s_1 s_2} c_{s_2}(\mathbf{k}) \rangle, \tag{58}$$

and the orbital magnetization is defined as,

$$\mathbf{M}_o = \sum_{\mathbf{k}, s, a, b} \langle c_{s,a}^\dagger(\mathbf{k}) \boldsymbol{\tau}_{ab} c_{s,b}(\mathbf{k}) \rangle. \tag{59}$$

More specifically, the orbital magnetization has the following components,

$$M_o^x = \sum_{\mathbf{k},s} \langle c_{s,d_{xz}}^\dagger c_{s,d_{yz}} + c_{s,d_{yz}}^\dagger c_{s,d_{xz}} \rangle, \tag{60}$$

$$M_o^y = -i \sum_{\mathbf{k},s} \langle c_{s,d_{xz}}^\dagger c_{s,d_{yz}} - c_{s,d_{yz}}^\dagger c_{s,d_{xz}} \rangle = \frac{1}{2} \sum_{\mathbf{k},s} \langle \hat{n}_{s,d_{xz}+id_{yz}} - \hat{n}_{s,d_{xz}-id_{yz}} \rangle, \tag{61}$$

$$M_o^z = \sum_{\mathbf{k},s} \langle c_{s,d_{xz}}^\dagger c_{s,d_{xz}} - c_{s,d_{yz}}^\dagger c_{s,d_{yz}} \rangle, \tag{62}$$

where $M_o^{x,z}$ breaks the $C_4$ rotation symmetry and $M_o^y$ breaks the TRS. In our work, we focus on spontaneous TRS breaking, with $C_4$ preserved. $M_o^y(\mathbf{k})$ gives the local density difference in mementum space for $d_{xz} \pm id_{yz}$ orbitals. A non-zero $M_o^y(\mathbf{k})$ implies TRS breaking at $\mathbf{k}$, because the two orbitals are TR partners. However, it has to be noted that, similar to the spin-triplet case, local TRS breaking does not necessarily imply the global TRS is broken. To obtain the total overall magnetization, we still need to sum over momentum around the FS. In the Ginzburg-Landau formalism, the $\text{Im}[\mathbf{d}_o \times \mathbf{d}_o^*]$, whose only non-zero component is the $y$-component based on symmetry constraints in our formalism, is coupled to the induced magnetization $M_o^y$ so that TRS is still retained at the Lagrangian level. Therefore, we have the following relevant terms

$$\alpha M_o^y \text{Im}[(\mathbf{d}_o \times \mathbf{d}_o^*)_y] + \beta \left(M_o^y\right)^2,$$

which upon functional derivative with respect to the induced magnetization would give

$$M_o^y \propto \text{Im}[(\mathbf{d}_o \times \mathbf{d}_o^*)_y] = -i \left(\mathbf{d}_o \times \mathbf{d}_o^*\right)_y.$$

## Supplementary References

[1] Y. Wang and L. Fu, Topological phase transitions in multicomponent superconductors, Phys. Rev. Lett. **119**, 187003 (2017).
[2] P. M. R. Brydon, D. F. Agterberg, H. Menke, and C. Timm, Bogoliubov fermi surfaces: General theory, magnetic order, and topology, Phys. Rev. B **98**, 224509 (2018).
[3] P. M. R. Brydon, D. S. L. Abergel, D. F. Agterberg, and V. M. Yakovenko, Loop currents and anomalous hall effect from time-reversal symmetry-breaking superconductivity on the honeycomb lattice, Phys. Rev. X **9**, 031025 (2019).
[4] M. Zeng, D.-H. Xu, Z.-M. Wang, and L.-H. Hu, Spin-orbit coupled superconductivity with spin-singlet nonunitary pairing, Phys. Rev. B **107**, 094507 (2023).

**Acknowledgements**

# Chapter 8

# Spin-orbit coupled superconductivity with spin-singlet nonunitary pairing

# Spin-orbit coupled superconductivity with spin-singlet nonunitary pairing

Meng Zeng [1] Dong-Hui Xu [2,3] Zi-Ming Wang [2,3] and Lun-Hui Hu [4,5,*]

[1]*Department of Physics, University of California, San Diego, California 92093, USA*
[2]*Department of Physics and Chongqing Key Laboratory for Strongly Coupled Physics, Chongqing University, Chongqing 400044, China*
[3]*Center of Quantum Materials and Devices, Chongqing University, Chongqing 400044, China*
[4]*Department of Physics, the Pennsylvania State University, University Park, Pennsylvania 16802, USA*
[5]*Department of Physics and Astronomy, University of Tennessee, Knoxville, Tennessee 37996, USA*

The gap functions for a single-band model for unconventional superconductivity are distinguished by their unitary or nonunitary forms. Here we generalize this classification to a two-band superconductor with two nearly degenerate orbitals. We focus on spin-singlet pairings and investigate the effects of the atomic spin-orbit coupling (SOC) on superconductivity, which is a driving force behind the discovery of a new spin-orbit coupled nonunitary superconductor. Multiorbital effects such as orbital hybridization and strain-induced anisotropy will also be considered. The spin-orbit coupled nonunitary superconductor has three main features. First, the atomic SOC locks the electron spins to be out-of-plane, leading to a new Type II Ising superconductor with a large in-plane upper critical field beyond the conventional Pauli limit. Second, it provides a promising platform to realize the topological chiral or helical Majorana edge state even without external magnetic fields or Zeeman fields. More surprisingly, a spin-polarized superconducting state could be generated by spin-singlet nonunitary pairings when time-reversal symmetry is spontaneously broken, which serves as a smoking gun to detect this exotic state by measuring the spin-resolved density of states. Our work indicates the essential roles of orbital-triplet pairings in both unconventional and topological superconductivity.

## I. INTRODUCTION

In condensed matter physics, research on unconventional superconductivity [1,2] remains a crucial topic and continues to uncover new questions and challenges in both theory and experiment, since the discovery of the heavy-fermion superconductors (SCs) [3] and the $d$-wave pairing states in high-temperature cuprate SCs [4–7]. In addition to the anisotropic gap functions (e.g., $p, d, f, g$ wave, etc.), the sublattice or orbital-dependent pairings [8–10] are shown to be an alternative avenue to realize unconventional SCs. They might be realized in multiorbital correlated electronic systems, whose candidate materials include iron-based SCs [11–22], Cu-doped $Bi_2Se_3$ [23,24], half-Heusler compounds [25–34], and possibly $Sr_2RuO_4$ [35–40], etc. In particular, considering the atomic orbital degrees of freedom, the classification of unconventional pairing states could be significantly enriched. Among them, SCs with spontaneous time-reversal symmetry (TRS) breaking is of special interest, in which two mutually exclusive quantum phenomena, spin magnetism and superconductivity, may coexist with each other peacefully [41–46].

On the other hand, the orbital multiplicity could also give rise to nonunitary pairings, which again include both time-reversal breaking (TRB) and time-reversal invariant (TRI) pairings. Very recently, prior studies have demonstrated the existence of spin-singlet nonunitary pairing states that break the inversion symmetry in Dirac materials [9]. One aim of this work is the generalization of unitary and nonunitary gap functions in a two-band SC while preserving inversion symmetry, which is possible exactly due to the multiorbital degrees of freedom [47]. We focus on a system with two nearly degenerate orbitals and find that the nonunitary pairing state is generally a mixed superconducting state with both orbital-independent pairings and orbital-dependent pairings. Recently, the interplay between orbital-independent pairings and spin-orbit coupling (SOC) has been shown to demonstrate the intriguing phenomenon of a large in-plane upper critical field compared with the Pauli paramagnetic field for a two-dimensional (2D) SC. For example, the Type I Ising superconductivity in monolayer $MoS_2$ [48,49] and $NbSe_2$ [50] and the Type II Ising superconductivity in monolayer stanene [51]. Therefore, the interplay of atomic SOC and the multiorbital pairing could potentially give rise to exciting physics. However, to the best of our knowledge, the influence of the atomic SOC on the orbital-dependent pairings remains unsolved. Furthermore, the multiorbital nature also gives rise to possible orbital hybridization effects and provides an experimentally controllable handle using lattice strains, both of which could lead to orbital anisotropy and could potentially change the pairing symmetry. In particular, lattice strain has been a useful experimental tool to study unconventional superconductors [52–54] and has even been proposed to induce the elusive charge-4e phase [55]. We will be doing an extensive investigation on all the aforementioned multiorbital effects.

*hu.lunhui.zju@gmail.com

Another topic of this work is concerned with the co-existence of TRB pairings and spin magnetism even in a spin-singlet SC. It is well known that spin polarization (SP) can be generated by nonunitary spin-triplet superconductivity, which is believed to be the case for LaNiC$_2$ [56] and LaNiGa$_2$ [57,58]. More recently, the coexistence of magnetism and spin-singlet superconductivity is experimentally suggested in multiorbital SCs, such as iron-based superconductors [59,60] and LaPt$_3$P [61]. Therefore, in addition to the spin-triplet theory, it will be interesting to examine how SP develops in multiorbital spin-singlet SCs as spontaneous TRS breaking in the absence of external magnetic fields or Zeeman fields.

In this work, we address the above two major issues by studying a two-band SC with two atomic orbitals (e.g., $d_{xz}$ and $d_{yz}$). We start with the construction of a $\mathbf{k} \cdot \mathbf{p}$ model Hamiltonian on a square lattice with applied lattice strain. The breaking of $C_{4v}$ down to $C_2$ point group generally leads to the degeneracy lifting of $d_{xz}$ and $d_{yz}$. Based on this model, we study the stability of superconductivity and the realization of 2D topological superconductors in both class D and DIII. First and foremost, the influence of atomic SOC is studied, which gives birth to a new spin-orbit coupled SC. This exotic state shows the following features: first, a large Pauli-limit violation is found for the orbital-independent pairing part, which belongs to the Type II Ising superconductivity. Furthermore, the orbital-dependent pairing part also shows a weak Pauli-limit violation even though it does not belong to the family of Ising SCs. Second, topological superconductivity can be realized with a physical set of parameters even in the absence of external magnetic fields or Zeeman fields. In addition, a spin-polarized superconducting state could be energetically favored with the spontaneous breaking of time-reversal symmetry. Our work implies a new mechanism for the establishment of spin magnetism in the spin-singlet SC. In the end, we also discuss how to detect this effect by spin-resolved scanning tunneling microscopy measurements.

The paper is organized as follows. In Sec. II, we discuss a two-orbital normal-state Hamiltonian on a 2D square lattice and also its variants caused by applied in-plane strain effects, then we show the spin-singlet unitary or nonunitary pairing states with or without TRS. The strain effect on pairing symmetries is also studied based on a weak-coupling theory. In Sec. III, the effects of atomic SOC on such pairing states are extensively studied, as well as the in-plane paramagnetic depairing effect. Besides, the topological superconductivity is studied in Sec. IV even in the absence of external magnetic fields or Zeeman fields, after which we consider the spontaneous TRB effects in Sec. V and show that spin-singlet SC-induced spin magnetism could emerge in the presence of orbital SOC. In the end, a brief discussion and conclusion are given in Sec. VI. We will also briefly comment on a very recent experiment [62], demonstrating that a fully gapped superconductor becomes a nodal phase by substituting S into single-layer FeSe/SrTiO$_3$.

## II. MODEL HAMILTONIAN

In this section, we first discuss the normal-state Hamiltonian that will be used throughout this work for an electronic system consisting of both spin and two locally degenerate

atomic orbitals (e.g., $d_{xz}$ and $d_{yz}$) on a 2D square lattice. We assume each unit cell contains only one atom, so there is no sublattice degree of freedom. The orbital degeneracy can be reduced by applying the in-plane lattice strain because the original $C_{4v}$ point group is reduced down to its subgroup $C_{2v}$ for strain $\sigma_{10}$, $\sigma_{01}$ or $\sigma_{11}$ (a more generic strain would reduce the symmetry directly to $C_2$). Here $\sigma_{n_1 n_2}$ represents the strain tensor whose form will be given later. We will apply the symmetry analysis to construct the strained Hamiltonian in the spirit of $\mathbf{k} \cdot \mathbf{p}$ theory. Then, we discuss the pairing Hamiltonian and the corresponding classification of spin-singlet pairing symmetries including nonunitary pairing states. The strain effect is also investigated on the superconducting pairing symmetries based on a weak-coupling scheme [10].

### A. Normal-state Hamiltonian

In this section, we construct the two-orbital normal-state Hamiltonian $\mathcal{H}_0(\mathbf{k})$ with lattice strain-induced symmetry-breaking terms. Before that, We first show $\mathcal{H}_0(\mathbf{k})$ in the absence of external lattice strains. For a square lattice as illustrated in Fig. 1(a), it owns the $C_{4v}$ point group that is generated by two symmetry operators: a fourfold rotation symmetry around the $\hat{z}$ axis $C_{4z} : (x, y) \rightarrow (y, -x)$ and a mirror reflection about the $\hat{y}$-$\hat{z}$ plane $M_x : (x, y) \rightarrow (-x, y)$. Other symmetries can be generated by multiplications, such as the mirror reflection about the $(\hat{x} + \hat{y}) - \hat{z}$ plane $M_{x+y} : (x, y) \rightarrow (y, x)$ is given by $C_{4z} \times M_x$. In the absence of Rashba spin-orbit coupling (SOC), the system also harbors inversion symmetry $\mathcal{I}$, enlarging the symmetry group to $D_{4h} = C_{4v} \otimes \{E, \mathcal{I}\}$. In the spirit of $\mathbf{k} \cdot \mathbf{p}$ expansion around the $\Gamma$ point or the $M$ point, we consider a two-orbital system described by the inversion-symmetric Hamiltonian in two dimensions,

$$\mathcal{H}_0(\mathbf{k}) = \epsilon(\mathbf{k})\tau_0\sigma_0 + \lambda_{\mathrm{soc}}\tau_2\sigma_3 + \lambda_o[\mathbf{g}_o(\mathbf{k}) \cdot \boldsymbol{\tau}]\sigma_0, \quad (1)$$

where the basis is made of $\{d_{xz}, d_{yz}\}$ orbitals $\psi_{\mathbf{k}}^{\dagger} = (c_{d_{xz},\uparrow}^{\dagger}(\mathbf{k}), c_{d_{xz},\downarrow}^{\dagger}(\mathbf{k}), c_{d_{yz},\uparrow}^{\dagger}(\mathbf{k}), c_{d_{yz},\downarrow}^{\dagger}(\mathbf{k}))$. Here $c^{\dagger}$ is the creation operator of electrons, $\boldsymbol{\tau}$ and $\boldsymbol{\sigma}$ are Pauli matrices acting on the orbital and spin subspace, respectively, and $\tau_0$, $\sigma_0$ are 2-by-2 identity matrices. Besides, $\epsilon(\mathbf{k}) = -(k_x^2 + k_y^2)/2m - \mu$ is the band energy measured relative to the chemical potential $\mu$, $m$ is the effective mass, $\lambda_{\mathrm{soc}}$ is the atomic SOC [63–65], and $\lambda_o$ characterizes the strength of orbital hybridization. This model could describe the two hole pockets of iron-based superconductors [17,66]. Moreover, the first two components of $\mathbf{g}_o(\mathbf{k})$ are for the interorbital hopping term, while the third term is for the anisotropic effective mass, explained below in detail.

The $C_{4v}$ (or $D_{4h}$) point group restricts $\mathbf{g}_o(\mathbf{k}) = (a_o k_x k_y, 0, k_x^2 - k_y^2)$, where $a_o = 2$ is a symmetric case that increases the $C_{4z}$ to a continued rotational symmetry about the $\hat{z}$ axis. To be precise, the $g_1$ term, $2\lambda_o k_x k_y \tau_1 \sigma_0$, is attributed to the interorbital hopping integral along the $\pm\hat{x} \pm \hat{y}$ directions,

$$\frac{\lambda_o}{2}(c_{d_{xz},\sigma}^{\dagger}(i_x, i_y) \, c_{d_{yz},\sigma}(i_x + 1, i_y + 1)$$

$$+ c_{d_{xz},\sigma}^{\dagger}(i_x, i_y) \, c_{d_{yz},\sigma}(i_x - 1, i_y - 1)$$

$$- c_{d_{xz},\sigma}^{\dagger}(i_x, i_y) \, c_{d_{yz},\sigma}(i_x + 1, i_y - 1)$$

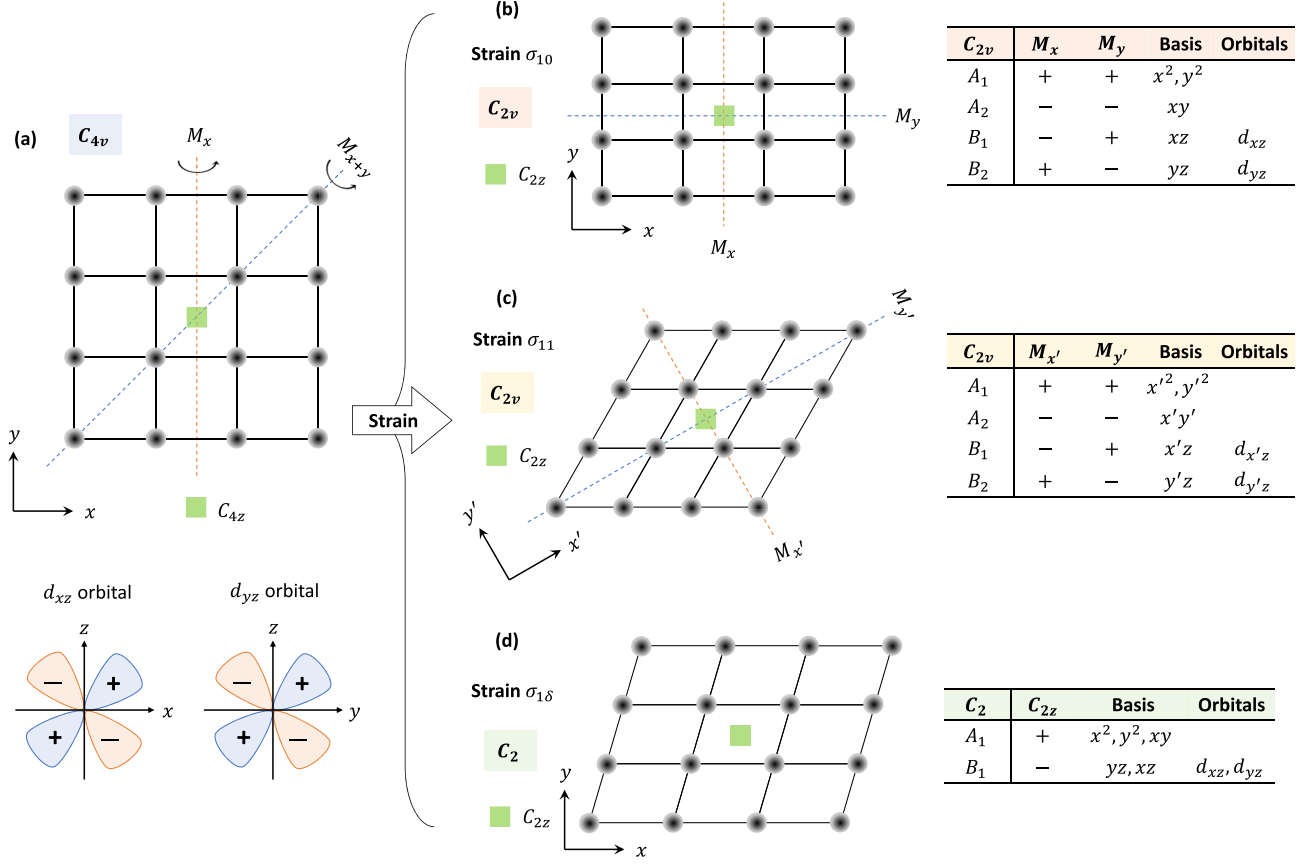$$- c_{d_{xz},\sigma}^{\dagger}(i_x, i_y) \, c_{d_{yz},\sigma}(i_x - 1, i_y + 1) + \mathrm{H.c.}), \quad (2)$$

FIG. 1. The strain effect on a two-dimensional square lattice. In the absence of lattice strain, (a) shows the square lattice owing the $C_{4v}$ point group that is generated by $C_{4z}$ and $M_x$. We consider the normal-state Hamiltonian with $d_{xz}, d_{yz}$ orbitals. Inversion symmetry ($\mathcal{I}$) is broken by growing crystal samples on an insulating substrate. The in-plane strain effects on the square lattice are illustrated in (b)–(d) for applied strain along different directions. (b) shows that the $\hat{x}$- or $\hat{y}$-axis strain breaks the square lattice into the rectangular lattice with two independent mirror reflection symmetries $M_x$ and $M_y$, obeying the subgroup $C_{2v}$ of $C_{4v}$. The $C_{2v}$ point group contains four one-dimensional irreducible representations (irrep.) $A_1, A_2, B_1, B_2$. (c) shows that the strain along the $\hat{x} + \hat{y}$ direction also reduces the $C_{4v}$ down to $C_{2v}$. (d) represents a general case, where the subgroup $C_2$ is preserved that only has $A_1$ and $B_1$ irreps.

where $(i_x, i_y)$ represents the lattice site. In addition, the $g_3$ term, $\lambda_o(k_x^2 - k_y^2)\tau_3\sigma_0$, causes the anisotropic effective masses. For example, the effective mass of the $d_{xz}$ orbital is $\frac{1}{1/m - 2\lambda_o}$ along the $\hat{x}$ axis while that is $\frac{1}{1/m + 2\lambda_o}$ along the $\hat{y}$ axis. This means that the hopping integrals are different along $\hat{x}$ and $\hat{y}$ directions,

$$\left(\frac{1}{2m} - \lambda_o\right)c^\dagger_{d_{xz},\sigma}(i_x, i_y)\, c_{d_{xz},\sigma}(i_x + 1, i_y)$$

$$+ \left(\frac{1}{2m} + \lambda_o\right)c^\dagger_{d_{xz},\sigma}(i_x, i_y)\, c_{d_{xz},\sigma}(i_x, i_y + 1)$$

$$+ \left(\frac{1}{2m} + \lambda_o\right)c^\dagger_{d_{yz},\sigma}(i_x, i_y)\, c_{d_{yz},\sigma}(i_x + 1, i_y)$$

$$+ \left(\frac{1}{2m} - \lambda_o\right)c^\dagger_{d_{yz},\sigma}(i_x, i_y)\, c_{d_{yz},\sigma}(i_x, i_y + 1) + \text{H.c..} \quad (3)$$

In this work, we focus on a negative effective mass case by choosing $1/m \pm 2\lambda_o > 0$. However, using a positive effective mass does not change our main conclusion. Moreover, our results can be generally applied to other systems with two orbitals $p_x, p_y$, once it satisfies the $C_{4v}$ point group.

The time-reversal symmetry operator is presented as $\mathcal{T} = i\tau_0\sigma_2\mathcal{K}$ with $\mathcal{K}$ being the complex conjugate. And the inversion symmetry is presented as $\mathcal{I} = \tau_0\sigma_0$. It is easy to show Eq. (1) is invariant under both $\mathcal{T}$ and $\mathcal{I}$. However, inversion can be broken by growing the sample on insulating substrates, the asymmetric Rashba SOC is described by

$$\mathcal{H}_R(\mathbf{k}) = \lambda_R\tau_0[\mathbf{g}_R(\mathbf{k}) \cdot \boldsymbol{\sigma}], \quad (4)$$

where $\lambda_R$ is the strength of the Rashba SOC with $\mathbf{g}_R(\mathbf{k}) = (-k_y, k_x, 0)$ as required by the $C_{4v}$ point group.

Next, we consider the lattice strain effect on the two-dimensional crystal with a square lattice, as summarized in Figs. 1(b)–1(d). The in-plane strain effect is characterized by the 2-by-2 strain tensor $\sigma$ whose elements are defined as $\sigma_{ij} = \frac{1}{2}(\partial_{x_i}u_j + \partial_{x_j}u_i)$, where $u_i$ is the displacement at $\mathbf{r}$ along the $\hat{e}_i$ direction. Even though it is an abuse of notation, it should be self-evident that the $\sigma$ here does not represent the Pauli matrices. The strain tensor $\sigma$ can be parametrized as the following:

$$\sigma_\phi = \begin{pmatrix} \cos^2\phi & \cos\phi\sin\phi \\ \cos\phi\sin\phi & \sin^2\phi \end{pmatrix}, \quad (5)$$

where $\phi$ is the polar angle with respect to the $\hat{x}$ axis. For the $\phi = 0$ ($\pi/2$) case, the compressive or tensile strain applied along the $\hat{x}$ axis ($\hat{y}$ axis) makes the square lattice as a rectangular lattice, as illustrated in Fig. 1(b). And the $\phi = \pi/4$ case is for the shear strain along the $(\hat{x} + \hat{y})$ direction in Fig. 1(c). All the above cases reduce the $C_{4v}$ point group into its subgroup $C_{2v}$ that is generated by two independent mirror reflections. Otherwise, it is generally reduced to $C_2$. The irreducible representations for $C_{2v}$ and $C_2$ are shown in Figs. 1(b)–1(d). Based on the standard symmetry analysis, to the leading order, the strained Hamiltonian is given by

$$\mathcal{H}_{str} = t_{str}[\sin(2\phi)\tau_1 + \cos(2\phi)\tau_3]\sigma_0, \quad (6)$$

where both $t_{str}$ and $\phi$ can be controlled in experiments [67]. And $\mathcal{H}_{str}$ can be absorbed into the $\mathbf{g}_o$ vector in Eq. (1), renormalizing the orbital hybridization as expected. Furthermore, one can check that $\mathcal{H}_{str}$ preserves both $\mathcal{T}$ and $\mathcal{I}$, but explicitly breaks the $C_{4z} = i\tau_2 e^{i\frac{\pi}{4}\sigma_3}$ because of $[\mathcal{H}_{str}, C_{4z}] \neq 0$. Interestingly, the orbital texture on the Fermi surface can be engineered by strain, and its effect on superconducting pairing symmetries is briefly discussed in Appendix C.

Therefore, a strained normal-state Hamiltonian is

$$\mathcal{H}_N(\mathbf{k}) = \mathcal{H}_0(\mathbf{k}) + \mathcal{H}_R(\mathbf{k}) + \mathcal{H}_{str}, \quad (7)$$

which will be used throughout this work. The Rashba SOC-induced spin-splitting bands are considered only when we discuss the topological superconducting phases in Secs. IV and V, even though the normal-state Hamiltonian $\mathcal{H}_N(\mathbf{k})$ is topologically trivial. For the superconducting states, we focus on the inversion symmetric pairings (i.e., spin-singlet $s$-wave pairing) and their response to applied strains or in-plane magnetic fields.

In the absence of Rashba SOC, the band structures of $\mathcal{H}_N(\mathbf{k})$ in Eq. (7) are given by

$$E_{\pm}(\mathbf{k}) = -\frac{1}{2m}(k_x^2 + k_y^2) \pm \sqrt{\lambda_{soc}^2 + \tilde{g}_1^2 + \tilde{g}_3^2}, \quad (8)$$

where we define the strained orbital hybridization $\tilde{\mathbf{g}}$ vector with $\tilde{g}_1 = a_o\lambda_o k_x k_y + t_{str}\sin(2\phi)$ and $\tilde{g}_3 = \lambda_o(k_x^2 - k_y^2) + t_{str}\cos(2\phi)$. Each band has twofold degeneracy, enforced by the presence of both $\mathcal{T}$ and $\mathcal{I}$. At the $\Gamma$ point ($k_x = k_y = 0$), $E_{\pm}^{\Gamma} = \pm\sqrt{\lambda_{soc}^2 + t_{str}^2}$. The two Fermi surfaces with and without strain are numerically calculated and shown in Fig. 2, where we choose $\mu < -\sqrt{\lambda_{soc}^2 + t_{str}^2}$. These are two hole pockets because of the negative effective mass of both orbitals. The Fermi surfaces in Fig. 2(a) are $C_4$ symmetric ($t_{str} = 0$), while those in Fig. 2(b) are only $C_2$ symmetric due to the symmetry breaking of lattice strains. Please note that there is only one Fermi surface when $|\mu| < \sqrt{\lambda_{soc}^2 + t_{str}^2}$, which is a necessary condition to realize topological superconductors as we will discuss in Sec. IV.

### B. Review of singlet-triplet mixed pairings

Before discussing the possible unconventional pairing symmetry for $\mathcal{H}_N$ in Eq. (7), we briefly review both unitary and nonunitary gap functions for a single-band SC in the absence of inversion symmetry. In this case, a singlet-triplet
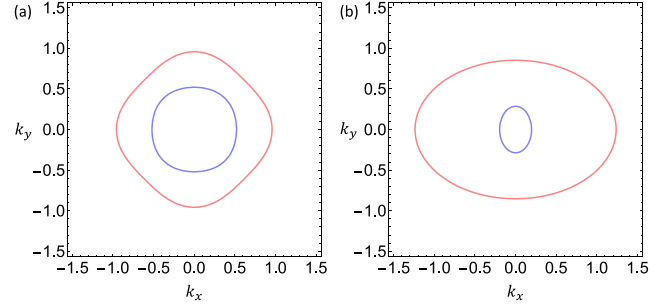


FIG. 2. The lattice strain effect on the Fermi surfaces of the normal-state Hamiltonian without Rashba SOC. (a) shows the two Fermi surfaces without lattice strain (i.e., $t_{str} = 0$), thus $C_{4z}$-symmetric energy contours are formed. (b) shows the breaking of $C_{4z}$ by lattice strain with $t_{str} = 0.4$ and $\phi = 0$, only $C_{2z}$-symmetric energy contours appear. Other parameters used here are $m = 0.5$, $a_0 = 1$, $\lambda_o = 0.4$, $\lambda_R = 0$, and $\mu = -0.5$.

mixed pairing potential is given by

$$\Delta(\mathbf{k}) = [\Delta_s\psi_s(\mathbf{k})\sigma_0 + \Delta_t(\mathbf{d}_s(\mathbf{k}) \cdot \boldsymbol{\sigma})](i\sigma_2), \quad (9)$$

where $\boldsymbol{\sigma}$ are Pauli matrices acting in the spin subspace. Here $\psi_s(\mathbf{k})$ represents even-parity spin-singlet pairings and the odd-parity $\mathbf{d}_s(\mathbf{k})$ is for the spin-triplet $d_s$ vector. Physically, the unitary SC has only one superconducting gap like in the conventional BCS theory, while a two-gap feature comes into being by the nonunitary pairing potential. More explicitly, the unitary or nonunitary is defined by whether the following is proportional to the identity matrix $\sigma_0$:

$$\Delta(\mathbf{k})\Delta^{\dagger}(\mathbf{k}) = |\Delta_s|^2\psi_s^2 + |\Delta_t|^2|\mathbf{d}_s|^2$$
$$+ 2\mathrm{Re}[\Delta_s\Delta_t^*\psi_s\mathbf{d}_s^*]$$
$$\cdot\boldsymbol{\sigma} + i|\Delta_t|^2(\mathbf{d}_s \times \mathbf{d}_s^*) \cdot \boldsymbol{\sigma}, \quad (10)$$

Therefore, Eq. (10) gives rise to a possible classification by assuming a nonvanishing $\Delta_s \in \mathbb{R}$ and a proper choice of a global phase. In principle, there are four possible phases, including the TRI nonunitary SCs ($\Delta_t \in \mathbb{R}$, $\mathbf{d}_s \in \mathbb{R}$), the TRB unitary SCs ($\Delta_t \sim i$, $\mathbf{d}_s \in \mathbb{R}$), and the TRB nonunitary SCs ($\Delta_t \in \mathbb{R}$, $\mathbf{d}_s \in \mathbb{C}$). On the other hand, the TRI unitary SCs are achieved only with $\Delta_s = 0$ or $\Delta_t = 0$ and real $\mathbf{d}_s$, meaning a purely spin-singlet SC or a purely spin-triplet SC. These states might be distinguished in experiments, for example, the TRB unitary pairing state might induce a spontaneous magnetization with the help of Rashba spin-orbit coupling [68], which can be detected by $\mu$SR [69].

As we know, the spin-singlet pairings do not coexist with the spin-triplet pairings in the presence of inversion symmetry (e.g., centrosymmetric SCs). Roughly speaking, it seems out of the question to realize nonunitary pairing states in purely spin-singlet SCs. However, this is a challenge but not an impossibility for an SC with multiorbitals, which is one of the aims of this work. In the following, we will discuss how to generalize the classification of TRI or TRB and unitary or nonunitary pairing states to a spin-singlet SC with two atomic orbitals in the presence of inversion symmetry. The four cases are summarized in Table I.

TABLE I. The four pairing states classified by time-reversal symmetry and unitary for a spin-singlet superconductor with both orbital-independent pairing $\Delta_s$ and orbital-dependent pairing $\Delta_o$ and $\mathbf{d}_o$.

| Pairings | TRS | Unitary | $\Delta_S$ | $\Delta_O$ | $\mathbf{d}_o$ |
|---|---|---|---|---|---|
| TRI unitary | Yes | Yes | Real Zero | Zero Real | Real |
| TRI nonunitary | Yes | No | Real | Real | Real |
| TRB unitary | No | Yes | Real | Purely imaginary | Real |
| TRB nonunitary | No | No | Real | Real | Complex |

### C. Pairing Hamiltonian of a two-orbital model

We now consider the pairing Hamiltonian for $\mathcal{H}_N$ in Eq. (7). By ignoring the fluctuations, the mean-field pairing Hamiltonian is generally given by,

$$\mathcal{H}_\Delta = \sum_{\mathbf{k}, s_1 a, s_2 b} \Delta_{s_1, s_2}^{a,b}(\mathbf{k}) c_{a s_1}^\dagger(\mathbf{k}) c_{b s_2}^\dagger(-\mathbf{k}) + \text{H.c.}, \quad (11)$$

where $s_1$, $s_2$ are index for spin and $a$, $b$ are for orbitals. As studied in Ref. [10], the orbital-triplet pairing is robust even against orbital hybridization and electron-electron interactions. Thus, we consider both orbital-independent and orbital-dependent pairings for generality. In analogy to spin-triplet SCs, we use an orbital $\mathbf{d}_o(\mathbf{k})$ vector for the spin-singlet orbital-dependent pairing potential [12], which takes the generic form

$$\Delta_{\text{tot}}(\mathbf{k}) = [\Delta_s \Psi_s(\mathbf{k}) \tau_0 + \Delta_o(\mathbf{d}_o(\mathbf{k}) \cdot \boldsymbol{\tau})](i\sigma_2), \quad (12)$$

where $\Delta_s$ and $\Delta_o$ are pairing strengths in orbital-independent and orbital-dependent channels, respectively. The Fermi statistics require that $\Psi_s(\mathbf{k}) = \Psi_s(-\mathbf{k})$, while the three components of $\mathbf{d}_o$ satisfy $d_o^{1,3}(\mathbf{k}) = d_o^{1,3}(-\mathbf{k})$ and $d_o^2(\mathbf{k}) = -d_o^2(-\mathbf{k})$. Namely, $d_o^2(\mathbf{k})$ represents odd-parity spin-singlet orbital-singlet pairings and the others are for even-parity spin-singlet orbital-triplet pairings. The pairing potential presented in this form is quite convenient, similar to the spin-triplet case [10,12,14,70]. The benefits of this form in Eq. (12) will be shown when we discuss the mixture of orbital-independent and orbital-dependent pairings. Combining Eq. (12) with Eq. (1), the Bogoliubov-de Gennes (BdG) Hamiltonian is

$$\mathcal{H}_{\text{BdG}}(\mathbf{k}) = \begin{pmatrix} \mathcal{H}_N(\mathbf{k}) & \Delta_{\text{tot}}(\mathbf{k}) \\ \Delta_{\text{tot}}^\dagger(\mathbf{k}) & -\mathcal{H}_N^*(-\mathbf{k}) \end{pmatrix}, \quad (13)$$

which is based on the Nambu basis $(\psi_{\mathbf{k}}^\dagger, \psi_{-\mathbf{k}}^T)$. Same with the spin case in Eq. (10), the nonunitarity of a spin-singlet pairing potential defined in Eq. (12) is determined by whether $\Delta_{\text{tot}}(\mathbf{k})\Delta_{\text{tot}}^\dagger(\mathbf{k})$ is proportional to an identity matrix. More explicitly we have

$$\Delta_{\text{tot}}(\mathbf{k})\Delta_{\text{tot}}^\dagger(\mathbf{k}) = |\Delta_s|^2 \psi_s^2 \tau_0 \sigma_0 + |\Delta_o|^2 |\mathbf{d}_o|^2 \tau_0 \sigma_0$$
$$+ 2\text{Re}|\Delta_s \Delta_o^* \psi_s \mathbf{d}_o^*| \cdot \boldsymbol{\tau}\sigma_0 + i|\Delta_o|^2 (\mathbf{d}_o \times \mathbf{d}_o^*) \cdot \boldsymbol{\tau}\sigma_0, \quad (14)$$

which could also exhibit four general possibilities: time-reversal-invariant (TRI) or time-reversal-breaking (TRB) and unitary or nonunitary SCs, with a simple replacement $\{\Delta_t, \mathbf{d}_s\} \to \{\Delta_o, \mathbf{d}_o\}$. In the absence of band splittings, i.e., $\lambda_{\text{soc}} = \lambda_o = \lambda_R = t_{\text{str}} = 0$ as an illustration, the superconduct-

ing excitation gaps on the Fermi surfaces of a TRI unitary SC are

$$E_{\kappa, \nu}(\mathbf{k}) = \kappa\sqrt{\epsilon^2(\mathbf{k}) + (\Delta_s \psi_s(\mathbf{k}) + \nu\Delta_o|\mathbf{d}_o|)^2}, \quad (15)$$

with $\kappa, \nu = \pm$. It is similar to the superconducting gaps for nonunitary spin-triplet SCs [1]. Moreover, the two-gap feature indicates the nonunitarity of the superconducting states, which implies the possibility of a nodal SC as long as $\Delta_s \psi_s(\mathbf{k}) \pm \Delta_o|\mathbf{d}_o| = 0$ is satisfied on the Fermi surfaces. And, the nodal quasiparticle states can be experimentally detected by measuring specific heat, London penetration depths, $\mu$SR, NMR, etc. As a result, this provides possible evidence to get a sight of TRI nonunitary phases in real materials (e.g., centrosymmetric SCs). Furthermore, the above conclusion is still valid when we turn on $\lambda_{\text{soc}}$, $\lambda_o$, and $t_{\text{str}}$.

### III. PAULI LIMIT VIOLATION: A LARGE IN-PLANE UPPER CRITICAL FIELD

In this section, we study the Pauli limit violation for the spin-singlet TRI nonunitary SC against an in-plane magnetic field (e.g., $H_{c2,\parallel} > H_P$). For a 2D crystalline SC or a thin film SC, the realization of superconducting states that are resilient to a strong external magnetic field has remained a significant pursuit, namely, the pairing mechanism can remarkably enlarge the in-plane upper critical field. Along this crucial research direction, one recent breakthrough has been the identification of Ising pairing formed with the help of Ising-type spin-orbit coupling (SOC), which breaks the SU(2) spin rotation and pins the electron spins to the out-of-plane direction. Depending on whether the inversion symmetry is broken or not by the Ising-type SOC, the Ising pairing is classified as Type I (broken) and Type II (preserved) Ising superconductivity, where the breaking of Cooper pairs is difficult under an in-plane magnetic field.

To demonstrate the underlying physics, in the following, we consider the interplay between atomic SOC $\lambda_{\text{soc}} \neq 0$ and spin-singlet TRI nonunitary pairing state. Thus, we consider the pairing potential

$$\Delta_{\text{tot}} = [\Delta_s \tau_0 + \Delta_o(d_o^1 \tau_1 + d_o^3 \tau_3)](i\sigma_2), \quad (16)$$

where $\Delta_s$, $\Delta_o$, $d_o^1$, and $d_o^3$ are all real constant. This can be realized once we have on-site attractive interactions in both orbital channels. Another reason for studying the atomic SOC is that it is not negligible in many real materials. It is interesting to note that the strength of SOC can be tuned in experiments, for example, by substituting S into single-layer FeSe/SrTiO$_3$ [62] or growing a superconductor/topological insulator heterostructure [71].

Without loss of generality, the direction of the magnetic field can be taken to be the $x$ direction, i.e., $\mathbf{H} = (H_x, 0, 0)$ with $H_x \geqslant 0$. Therefore, the normal Hamiltonian becomes

$$\mathcal{H}_N(\mathbf{k}) + h\tau_0\sigma_1, \quad (17)$$

where the first part is given by Eq. (7) and $h = \frac{1}{2}g\mu_B H_x$ is the Zeeman energy with $g = 2$ the electron's $g$ factor. To explicitly investigate the violation of the Pauli limit for the spin-orbit coupled SCs, we calculate the in-plane upper critical magnetic field normalized to the Pauli-limit paramagnetic field $H_{c2,\parallel}/H_P$ as a function of the normalized temperature $T_c/T_0$,

by solving the linearized gap equation. Here $H_P = 1.86T_0$ represents the Pauli limit with $T_0$ the critical temperature in the absence of an external magnetic field.

Following the standard BCS decoupling scheme [10], we first solve $T_c$ for the orbital-independent pairing channel by solving the linearized gap equation, $v_0 \chi_s(T) - 1 = 0$, where $v_0$ is effective attractive interaction and the superconductivity susceptibility $\chi_s(T)$ is defined by

$$\chi_s(T) = -\frac{1}{\beta} \sum_{\mathbf{k},\omega_n} \text{Tr}[G_e(\mathbf{k}, i\omega_n)G_h(-\mathbf{k}, i\omega_n)], \quad (18)$$

where the conventional s-wave pairing with $\psi_s(\mathbf{k}) = 1$ is considered for Eq. (16). Here $G_e(\mathbf{k}, i\omega_n) = [i\omega_n - \mathcal{H}_0(\mathbf{k})]^{-1}$ is the Matsubara Green's function for electrons and that for holes is defined as $G_h(\mathbf{k}, i\omega_n) = -\sigma_2 G_e^*(\mathbf{k}, i\omega_n)\sigma_2$. Here $\beta = 1/k_B T$ and $\omega_n = (2n+1)\pi/\beta$ with $n$ integer. Likewise, for the orbital-dependent pairing channels, the superconductivity susceptibility $\chi_o(T)$ is defined as

$$\chi_o(T) = -\frac{1}{\beta} \sum_{\mathbf{k},\omega_n} \text{Tr}[(\mathbf{d}_o(\mathbf{k}) \cdot \boldsymbol{\tau})^\dagger G_e(\mathbf{k}, i\omega_n)$$
$$\times (\mathbf{d}_o(\mathbf{k}) \cdot \boldsymbol{\tau})G_h(-\mathbf{k}, i\omega_n)], \quad (19)$$

where the orbital-dependent pairing ($A_g$ representation) with the vector form as $\mathbf{d}_o = (d_o^1, 0, d_o^3)$ for Eq. (16) is used for the $T_c$ calculations. However, the momentum-dependent $\mathbf{d}_o$ vector does not affect the formalism and main results, as we will discuss in Appendix C. The coupling between orbital-independent and orbital-dependent channels leads to a high-order correction ($\sim \lambda^2 k_F^2/\mu^2$, with $\lambda$ being the coupling strength of the effective $\tilde{\mathbf{g}}$ in the Hamiltonian representing orbital hybridization and strain), which can be ignored once $\lambda \ll \mu/k_F$.

## A. Type II Ising superconductivity

In this section, we first consider the orbital-independent pairing state (i.e., $\Delta_s \neq 0$ and $\Delta_o = 0$) and show it is a Type II Ising SC protected from the out-of-plane spin polarization by the atomic SOC $\lambda_{\text{soc}}\tau_2\sigma_3$. To demonstrate that, one generally needs to investigate the effects of atomic SOC on the SC $T_c$ as a function of the in-plane magnetic field $h$ based on Eq. (18), in the presence of both orbital hybridization $\lambda_o$ and strain $t_{\text{str}}$. As defined in Eq. (8), the effects of orbital hybridization and lattice strain on the system can be captured by an effective $\tilde{\mathbf{g}} \equiv [a_o \lambda_o k_x k_y + t_{\text{str}} \sin(2\phi), \lambda_o(k_x^2 - k_y^2) + t_{\text{str}} \cos(2\phi)]$. The case with $t_{\text{str}} = 0$ has been studied in Ref. [72], however, the strain effect on the Type II Ising SC has not been explored yet. To reveal the pure role of lattice strains, we consider $k_F$ to be close to the $\Gamma$ point so that the $k$-dependent hybridization part is dominated by the strain part for generic $\phi$. Therefore, we focus on $\tilde{\mathbf{g}} = t_{\text{str}}(\sin 2\phi, \cos 2\phi)$ in the following discussions.

After a straightforward calculation (see details in Appendix B), the superconductivity susceptibility $\chi_s(T)$ in Eq. (18) is calculated as

$$\chi_s(T) = \chi_0(T) + N_0 f_s(T, \lambda_{\text{soc}}, t_{\text{str}}, h), \quad (20)$$

with $N_0$ is the DOS near the Fermi surface and the pair-breaking term is given by

$$f_s(T, \lambda_{\text{soc}}, t_{\text{str}}, h)$$
$$= \frac{1}{2}[\mathcal{C}_0(T, \rho_-) + \mathcal{C}_0(T, \rho_+)]$$
$$+ [\mathcal{C}_0(T, \rho_-) - \mathcal{C}_0(T, \rho_+)]\left(\frac{\lambda_{\text{soc}}^2 + t_{\text{str}}^2 - h^2}{2E_+ E_-}\right), \quad (21)$$

where $E_\pm \equiv \sqrt{\lambda_{\text{soc}}^2 + (t_{\text{str}} \pm h)^2}$, $\rho_\pm = \frac{1}{2}(E_+ \pm E_-)$, and $\chi_0(T) = N_0 \ln(\frac{2e^\gamma \omega_D}{\pi k_B T})$ is the superconducting susceptibility when $\lambda_{\text{soc}}, t_{\text{str}}, h = 0$. Here $\gamma = 0.57721\cdots$ is the Euler-Mascheroni constant. Furthermore, the kernel function of the pair-breaking term $f_s$ is given by

$$\mathcal{C}_0(T, E) = \text{Re}\left[\psi^{(0)}\left(\frac{1}{2}\right) - \psi^{(0)}\left(\frac{1}{2} + i\frac{E}{2\pi k_B T}\right)\right], \quad (22)$$

with $\psi^{(0)}(z)$ being the digamma function. Note that $\mathcal{C}_0(T, E) \leqslant 0$ and it monotonically decreases as $E$ increases, indicating the reduction of $T_c$. Namely, $\mathcal{C}_0(T, E)$ gets smaller for a larger $E$.

We first discuss the simplest case with $\lambda_{\text{soc}} = t_{\text{str}} = 0$, where the pair-breaking function becomes $f_s(T, 0, 0, h) = \mathcal{C}_0(T, h)$, which just leads to the Pauli limit $H_{c2,\parallel} \approx H_P = 1.86T_c$, as shown in Fig. 3(a). Furthermore, we turn on $\lambda_{\text{soc}}$ while take the $t_{\text{str}} \to 0$ limit, the pair-breaking term in Eq. (21) is reduced to

$$f_s(T, \lambda_{\text{soc}}, 0, h) = \mathcal{C}_0\left(T, \sqrt{\lambda_{\text{soc}}^2 + h^2}\right)\frac{h^2}{\lambda_{\text{soc}}^2 + h^2}, \quad (23)$$

which reproduces the same results of Type II Ising superconductors in Ref. [72]. Under a relatively weak magnetic field ($h \ll \lambda_{\text{soc}}$), the factor $h^2/(\lambda_{\text{soc}}^2 + h^2) \ll 1$ leads to $f_s(T, \lambda_{\text{soc}}, 0, h) \to 0$, which in turn induces a large in-plane $H_{c2,\parallel}/H_P$.

Next, we investigate the effect of lattice strain $t_{\text{str}}$ on the in-plane upper critical field $H_{c2,\parallel}$. Interestingly, $t_{\text{str}}$ would generally instead reduce $H_{c2,\parallel}$. To see it explicitly, we expand the pair-breaking function $f_s$ in Eq. (21) up to the leading order of $t_{\text{str}}^2$,

$$f_s(T, \lambda_{\text{soc}}, t_{\text{str}}, h) \approx f_s(T, \lambda_{\text{soc}}, 0, h)$$
$$+ F(T, \lambda_{\text{soc}}, h)t_{\text{str}}^2 + O(t_{\text{str}}^4), \quad (24)$$

where $F(T, \lambda_{\text{soc}}, h)$ is given in Appendix B and we find it is always negative [i.e., $F(T, \lambda_{\text{soc}}, h) < 0$]. In addition to the first term $f_s(T, \lambda_{\text{soc}}, 0, h)$ discussed in Eq. (23), the second term $F(T, \lambda_{\text{soc}}, h)t_{\text{str}}^2$ also serves as a pair-breaking effect on $T_c$ at nonzero field. Therefore, the second $\lambda_o$ term further reduces $T_c$, leading to the reduction of the in-plane upper critical field.

We then numerically confirm the above discussions. We solve the linearized gap equation $v_0 \chi_s(T) - 1 = 0$ and arrive at $\log(T_c/T_0) = f_s(T_c, \lambda_{\text{soc}}, t_{\text{str}}, h)$, from which $T_c/T_0$ is numerically calculated in Fig. 3(a). Here $T_0$ is the critical temperature at zero external fields. The Pauli limit corresponds to $T_0(\lambda_{\text{soc}} = 0, t_{\text{str}} = 0, h = 0)$. The nonmonotonic behavior of the curves at small $T_c/T_0$ ($\lesssim 0.5$, i.e., dashed line) from solving the linearized gap equation calls for a comment. In the small temperature range, the transition by tuning the field strength becomes the first-order supercooling
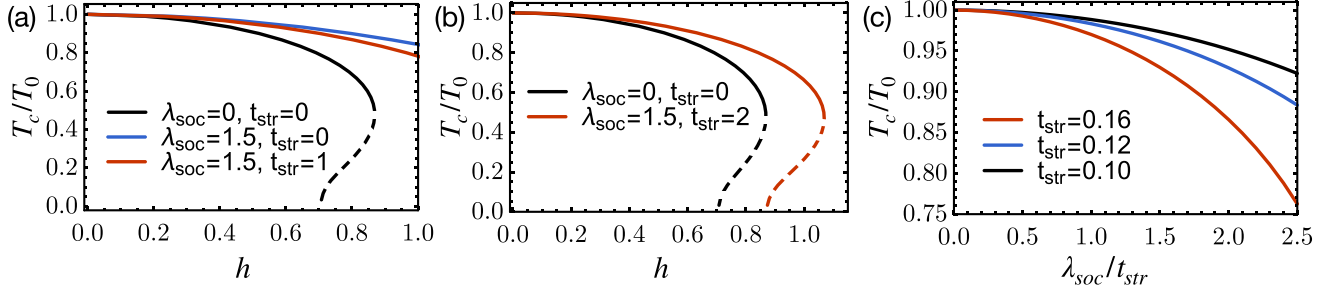
FIG. 3. The pair-breaking effects. (a) A significant Pauli limit violation is due to the atomic SOC for the orbital-independent pairing with $\Delta_s = 1$. However, the lattice strain might slightly suppress the $H_{c2}$ by comparing the blue and red curves. (b) A weak Pauli limit violation due to the atomic SOC for the orbital-dependent pairing with $\Delta_o = 1$. (c) The suppression of $T_c$ by atomic SOC for orbital-dependent pairing at zero external magnetic fields with $\Delta_o = 1$. For the three figures here, we have set the strain parameter $\phi = \frac{\pi}{8}$, i.e., $\tilde{\mathbf{g}} = (\frac{\sqrt{2}}{2}, 0, \frac{\sqrt{2}}{2})$.

transition [73]. Here we mainly focus on the solid line part, which is second order and gives the critical field $H_{c2}$. We see that in general there is a Pauli limit violation for nonzero $\lambda_{\text{soc}}$ and $t_{\text{str}}$. Furthermore, by comparing the two cases with $\lambda_{\text{soc}} = 1.5, t_{\text{str}} = 0$ and $\lambda_{\text{soc}} = 1.5, t_{\text{str}} = 1$, we confirm the above approximated analysis. We believe the strain effect on the Type II Ising SC will be tested in experiments soon.

### B. $H_{c2,\parallel}$ for orbital-dependent pairings

In this section, we further study the influence of the atomic SOC $\lambda_{\text{soc}}$ on the paramagnetic pair-breaking effect for orbital-dependent pairings (i.e., $\Delta_s = 0$ and $\Delta_o \neq 0$). We find a weak enhancement of the in-plane upper critical field $H_{c2,\parallel}$ compared with the Pauli limit. Following the criteria of the orbital $\mathbf{d}_o$ vector in Ref. [10] (also discussed in Appendix C), we take $\mathbf{d}_o$ to be parallel to the vector $\tilde{\mathbf{g}}$ by assuming $\lambda_{\text{soc}} \ll t_{\text{str}}$, which leads to the maximal condensation energy. This would be justified in the next section. After a straightforward calculation (see details in Appendix B), the superconductivity susceptibility $\chi_o(T)$ in Eq. (19) is calculated as,

$$\chi_o(T) = \chi_0(T) + N_0 f_o(T, \lambda_{\text{soc}}, t_{\text{str}}, h), \quad (25)$$

where the pair-breaking term is given by

$$f_o(T, \lambda_{\text{soc}}, t_{\text{str}}, h)$$
$$= \frac{1}{2}[\mathcal{C}_0(T, \rho_-) + \mathcal{C}_0(T, \rho_+)]$$
$$+ [\mathcal{C}_0(T, \rho_-) - \mathcal{C}_0(T, \rho_+)]\left(\frac{t_{\text{str}}^2 - \lambda_{\text{soc}}^2 - h^2}{2E_+E_-}\right), \quad (26)$$

which differs from $f_s(T, \lambda_{\text{soc}}, t_{\text{str}}, h)$ for orbital-independent pairings in Eq. (21). The only difference between them lies in the factor $(t_{\text{str}}^2 - \lambda_{\text{soc}}^2 - h^2)/2E_+E_-$, compared with that of $f_s(T, \lambda_{\text{soc}}, t_{\text{str}}, h)$ [i.e., $(t_{\text{str}}^2 + \lambda_{\text{soc}}^2 - h^2)/2E_+E_-$], which leads to a completely distinct superconducting state, demonstrated as follows.

To understand Eq. (26), we first discuss the simplest case with $\lambda_{\text{soc}} = t_{\text{str}} = 0$, where the pair-breaking function becomes $f(T, 0, 0, h) = \mathcal{C}_0(T, h)$, which just leads to the Pauli limit $H_{c2,\parallel} \approx H_P = 1.86T_c$, as shown in Fig. 3(b). Likewise, when $\lambda_{\text{soc}} = 0$ and $t_{\text{str}} \neq 0$, the pair-breaking function again simplifies to $\mathcal{C}_0(T, h)$. Therefore, the Pauli limit of the in-plane upper critical field is not affected by $t_{\text{str}}$ itself. Phys-

ically, this is because spin and orbital degrees of freedom are completely decoupled in this case, and it has also been shown that a similar orbital effect does not suppress $T_c$ when $\mathbf{d}_o \parallel \tilde{\mathbf{g}}$ [10], which is what we assumed here.

On the other hand, if we turn on merely the atomic SOC $\lambda_{\text{soc}} \neq 0$ while keeping $t_{\text{str}} = 0$, the pair-breaking function is given by

$$f_o(T, \lambda_{\text{soc}}, 0, h) = \mathcal{C}_0(T, \sqrt{\lambda_{\text{soc}}^2 + h^2}), \quad (27)$$

which leads to the reduction of the upper critical field, i.e., $H_{c2,\parallel} < H_P$, because of $f(T, \lambda_{\text{soc}}, 0, h) < f(T, 0, 0, h) < 0$. Remarkably, we find that the atomic SOC also plays a similar role of magnetic field to suppress the orbital-dependent pairing, as discussed in the next section. Thus, it does not belong to the family of Ising SCs, which makes the orbital-dependent pairing significantly different from the orbital-independent pairings. Moreover, their different dependence on the in-plane magnetic field might also be tested in experiments, which is beyond this work and left for future work. This also indicates the difference between orbital-triplet SC and spin-triplet SC in responses to Zeeman fields.

However, it is surprising to notice that there is a weak enhancement of the in-plane upper critical field $H_{c2,\parallel}$ for the case with both $t_{\text{str}} \neq 0$ and $\lambda_{\text{soc}} \neq 0$. Solving the gap equation $v_0\chi_o(T) - 1 = 0$, we obtain

$$\ln\left(\frac{T_c}{T_0}\right) = f_o(T, \lambda_{\text{soc}}, t_{\text{str}}, h). \quad (28)$$

Figure 3(b) shows how $T_c/T_0$ changes with the applied in-plane magnetic field, where the Pauli limit curve corresponds to $\lambda_{\text{soc}}, t_{\text{str}} = 0$. When both the atomic SOC and strain are included, the critical field $H_{c2}$ exceeds the Pauli limit by a small margin. Therefore, a spin-orbit coupled SC with spin-singlet nonunitary pairing symmetries does not belong to the reported family of Ising superconductivity.

### C. Atomic SOC-induced zero-field Pauli limit

As mentioned above, the atomic SOC breaks the spin degeneracy, which generally suppresses the even parity orbital-dependent pairings, in the case with $\Delta_s = 0$ and $\Delta_o \neq 0$. Thus, the robustness of such pairings in the presence of atomic SOC is the preliminary issue that we need to address.

And we find that the spin-singlet orbital-dependent pairing is also prevalent in solid-state systems when the energy scale of atomic SOC is smaller than that of the orbital hybridization or external strain. In this case, we focus on the zero magnetic field limit. Using the general results from the calculations in the previous section, we have

$$\ln\left(\frac{T_c}{T_0}\right) = f_o(T, \lambda_{\text{soc}}, t_{\text{str}}, h = 0)$$
$$= \mathcal{C}_0\left(T, \sqrt{t_{\text{str}}^2 + \lambda_{\text{soc}}^2}\right)\frac{\lambda_{\text{soc}}^2}{t_{\text{str}}^2 + \lambda_{\text{soc}}^2}, \quad (29)$$

where $\mathcal{C}_0(T, E)$ is defined in Eq. (22). In the case of $\lambda_{\text{soc}} = 0$, it can be seen that $T_c(t_{\text{str}}) = T_0(t_{\text{str}} = 0)$, i.e., the superconducting $T_c$ is not suppressed by stain or the orbital hybridization when the orbital $\mathbf{d}_o$ vector is parallel to $\tilde{\mathbf{g}}$ [10]. However, in the presence of nonzero atomic SOC $\lambda_{\text{soc}}$, the $T_c$ will be suppressed even when $\mathbf{d}_o \parallel \tilde{\mathbf{g}}$ is satisfied. Figure 3(c) shows the behavior of $T_c$ as a function of the $\lambda_{\text{soc}}/t_{\text{str}}$ for two different values of $t_{\text{str}}$. We see the suppression of $T_c$ as long as $\lambda_{\text{soc}} \neq 0$, and the suppression is more prominent when $t_{\text{str}}$ is larger.

To understand the suppression of orbital-dependent pairings by the atomic SOC, we take the $t_{\text{str}} = 0$ limit. Eq. (29) leads to

$$\ln\left(\frac{T_c}{T_0}\right) = \mathcal{C}_0(T, \lambda_{\text{soc}}), \quad (30)$$

which implies that $\lambda_{\text{soc}}$ plays the same role of magnetic field that suppresses the $T_c$ of the orbital-dependent pairing states. And $\lambda_{\text{soc}} \sim H_P$ roughly measures the zero-field Pauli-limit of the orbital-dependent pairing states. We dub this new effect as zero-field Pauli limit for orbital-dependent pairings induced by the atomic SOC, which can serve as the preliminary analysis of whether orbital-dependent pairings exist or not in real materials by simply calculating $\lambda_{\text{soc}}/T_c$.

Motivated by this observation, we notice that the normal Hamiltonian given in Eq. (7) satisfies $[\mathcal{H}_N(\mathbf{k}), \tau_2] = 0$ with both $\lambda_o \to 0$ and $t_{\text{str}} \to 0$. It stands for the U(1) rotation in the orbital subspace. As a result, we can project the normal Hamiltonian $\mathcal{H}_N(\mathbf{k})$ in Eq. (7) into block-diagonal form corresponding to the $\pm 1$ eigenvalues of $\tau_2$ by using the basis transformation

$$\mathcal{U} = \sigma_0 \otimes \frac{1}{\sqrt{2}}\begin{bmatrix} 1 & -i \\ 1 & i \end{bmatrix}. \quad (31)$$

The new basis is given by

$$\tilde{\Psi}^\dagger(\mathbf{k}) = (c_{+,\uparrow}^\dagger, c_{+,\downarrow}^\dagger, c_{-,\downarrow}^\dagger, c_{-,\uparrow}^\dagger), \quad (32)$$

where $c_{\pm,s}^\dagger \equiv \frac{1}{\sqrt{2}}(c_{d_{xz},s}^\dagger \mp i c_{d_{yz},s}^\dagger)$. On this basis, the normal Hamiltonian is given by

$$\mathcal{H}_0 = \mathcal{H}_0^+ \oplus \mathcal{H}_0^-, \quad (33)$$

where $\mathcal{H}_0^\pm$ are given by

$$\mathcal{H}_0^\pm = \epsilon(\mathbf{k}) \mp \lambda_{\text{soc}}\sigma_3. \quad (34)$$

Note that the time-reversal transforms $\mathcal{H}_0^\pm(\mathbf{k})$ to $\mathcal{H}_0^\mp(-\mathbf{k})$. Explicitly, the atomic SOC is indeed a magnetic field in each subspace, while it switches signs in the two subspaces to conserve TRS.

Next, we project the pairing Hamiltonian to the new basis, and we find that it also decouples as

$$\mathcal{H}_\Delta = \mathcal{H}_\Delta^+ \oplus \mathcal{H}_\Delta^-, \quad (35)$$

where $\mathcal{H}_\Delta^\pm$ are given by

$$\mathcal{H}_\Delta^\pm = 2\Delta_\pm[c_{\pm,\uparrow}^\dagger(\mathbf{k})c_{\pm,\downarrow}^\dagger(-\mathbf{k}) - (\uparrow \leftrightarrow \downarrow)] + \text{H.c.}, \quad (36)$$

where $\Delta_\pm \equiv \Delta_o(\mp id_o^1 + d_o^3)$ are the gap strengths in each subspace. In each subspace, it resembles an s-wave superconductor under an effective magnetic field of the atomic SOC along the out-of-plane direction. It naturally explains the zero-field Pauli-limit pair-breaking effect of atomic SOC on the orbital-dependent pairings with the $t_{\text{str}} \to 0$ limit. As a brief conclusion, our results demonstrate that the spin-singlet orbital-dependent pairings occur only in weak atomic SOC electronic systems.

## IV. 2D HELICAL SUPERCONDUCTIVITY

In the above sections, the spin-orbit coupled SCs concerning inversion symmetry have been comprehensively studied. In addition to that, it will be natural to ask if there exist more interesting superconducting states (e.g., topological phases) by including an inversion-symmetry breaking to the normal Hamiltonian in Eq. (7), namely, $\lambda_R \neq 0$. For this purpose, in this section, we focus on the Rashba SOC and explore its effect on the spin-orbit coupled SCs, especially the orbital-dependent pairings. Even though the 2D bulk SC or thin film SC preserves the inversion symmetry, a Rashba SOC appears near an interface between the superconducting layer and the insulating substrate. Remarkably, we find a TRI topological SC (helical TSC) phase generated by the interplay between the two types of SOC (atomic and Rashba) and spin-singlet orbital-dependent pairings. Since TRS is preserved, it belongs to Class DIII according to the tenfold classification. On the boundary of the interface, there exists a pair of helical Majorana edge states [74–83].

To explore the topological phases, we consider the normal-state Hamiltonian in Eq. (7), and the TRI spin-singlet nonunitary pairing symmetry in Eq. (16) for the BdG Hamiltonian (13), namely, a real orbital $\mathbf{d}_o$ vector is assumed for the orbital-dependent pairings.

In the $t_{\text{str}} \to 0$ and $\Delta_s \to 0$ limit, the bulk band gap closes only at the $\Gamma$ point for $\mu_c^\pm = \pm\sqrt{\lambda_{\text{soc}}^2 - 4|\Delta_o|^2}$ while no gap closing happens at other TRI momenta, leading to a topological phase transition. Thus, we conclude that the topological conditions are $\mu_c^- < \mu < \mu_c^+$ and an arbitrary orbital $\mathbf{d}_o$ vector. In Appendix D, we show the $\mathbb{Z}_2$ topological invariant can be analytically mapped to a BdG-version spin Chern number, similar to the spin Chern number in the 2D topological insulators. As mentioned in Sec. III C, the conservation of $\tau_2$, the U(1) symmetry in the orbital subspace, leads to the decomposition of the BdG Hamiltonian into two blocks for different eigenvalues of $\tau_2$. In each subspace, we can define the BdG Chern number as

$$\mathcal{C}_\pm = \frac{1}{2\pi}\sum_{\text{filled bands}}\int_{\text{BZ}} d\mathbf{k} \cdot \langle\phi_n^\pm(\mathbf{k})|i\nabla_{\mathbf{k}}|\phi_n^\pm(\mathbf{k})\rangle, \quad (37)$$
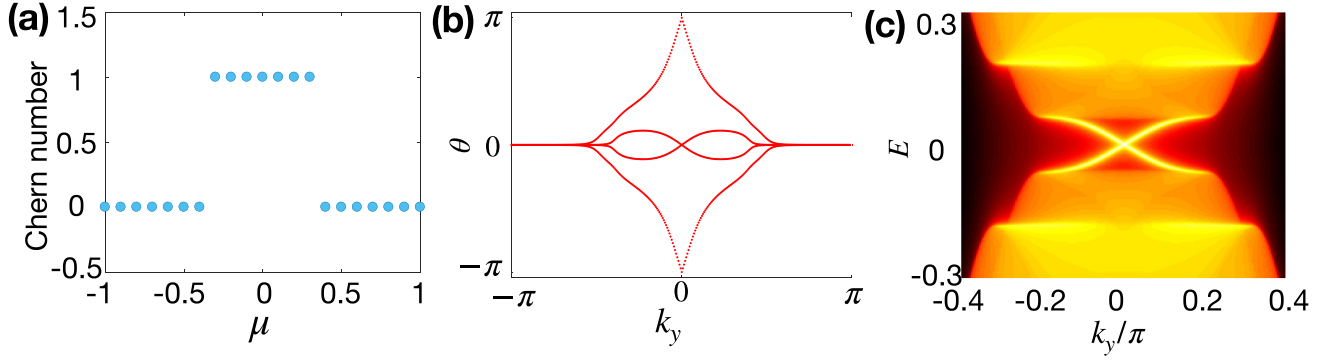
FIG. 4. Topological helical superconductivity for spin-singlet orbital-dependent pairing in the presence of Rashba SOC. (a) The $Z_2$ index is calculated by decoupling the BdG Hamiltonian into two chiral blocks when $\Delta_s = 0$ and $t_{str} = 0$. The other parameters used: $m = 0.5$, $\mu = 0.2$, $\lambda_{soc} = 0.4$, $\lambda_R = 1$, $\Delta_o = 0.1$, $\mathbf{d}_o = (1, 0, 1)$. (b) The Wilson loop calculation of the $Z_2$ invariant for $\Delta_s = 0.05$, $t_{str} = 0.1$, $\phi = \frac{\pi}{8}$, and $\mathbf{g}_o = (1, 0, 1)$. The other parameters remain the same as those in (a). The spectrum of edge states in (c) shows two counterpropagating Majorana edge states of the helical TSC.

with $|\phi_n^\pm\rangle$ being the energy eigenstate of $\mathcal{H}_{\text{BdG}}^\pm$ (see the details in Appendix D). Then the $Z_2$ topological invariant, in this case, is then explicitly given by,

$$\nu \equiv \frac{\mathcal{C}_+ - \mathcal{C}_-}{2}, \tag{38}$$

where $\mathcal{C}_\pm$ are the Chern numbers of the $\pm$ channels. $\nu = 1$ corresponds to the TSC phase, shown in Fig. 4(a). Based on the analysis for the topological condition, we learn that $\Delta_o$ should be smaller than $\lambda_{soc}$. However, as shown in Sec. III, the atomic SOC actually will reduce the $T_c$ of orbital-dependent pairings, which set a guideline to a physically realizable set of parameters, $T_0 \gg \lambda_{soc} \gg \Delta_o$, beyond the BCS theory ($\Delta_o \sim 1.76T_0$). For example, the monolayer FeSe superconductor films on different substrates achieve a very high critical temperature $T_0 \sim 70$ K [84].

As for a more general case with nonzero $\lambda_o$, $t_{str}$, and $\Delta_s$, the BdG Hamiltonian can no longer be decomposed into two decoupled blocks, hence the Chern number approach fails to characterize the $Z_2$ invariant. However, the more general Wilson-loop approach still works (see details in Appendix E). In general, the $Z_2$-type topological invariant of helical superconductivity could be characterized by the Wilson loop spectrum [85,86], shown in Fig. 4(b), which demonstrates the nontrivial $Z_2$ index. To verify the helical topological nature, we calculate the edge spectrum in a semi-infinite geometry with $k_y$ being a good quantum number. Figure 4(c) confirms clearly that there is a pair of 1D helical Majorana edge modes (MEMs) propagating on the boundary of the 2D system.

## V. TRB NONUNITARY SUPERCONDUCTOR

So far, the TRI nonunitary pairing states are investigated, which exhibit the Pauli-limit violation for in-plane upper critical field and topological phases. Furthermore, in this section, we study the TRB nonunitary pairing states characterized by a complex $\mathbf{d}_o$ vector when both $\Delta_s$ and $\Delta_o$ are real. As it is well known, the experiments by zero-field muon-spin relaxation ($\mu$SR) and the polar Kerr effect (PKE) can provide strong evidence for the observation of spontaneous magnetization or spin polarization in the superconducting states,

which indicates a TRB superconducting pairing symmetry. On the theory side, the nonunitary spin-triplet pairing potentials are always adopted to explain the experiments. However, for a spin-singlet SC, a theory with TRB pairing-induced spin-magnetization is in great demand. Addressing this crucial issue is one of the aims of this work, and we find that a spin-singlet TRB nonunitary SCs supports a TRB atomic orbital polarization, which in turn would give rise to spin polarization in the presence of atomic SOC.

### A. 2D chiral TSC

We first explore the possible 2D chiral topological phases by considering the simplest case with $\lambda_o = t_{str} = \Delta_s = 0$ to demonstrate the essential physics. For the TRB nonunitary pairing, a complex orbital $\mathbf{d}_o$ vector can be generally parameterized as $\mathbf{d}_o = (\cos\theta, 0, e^{i\phi}\sin\theta)$. And the relative phase $\phi = \pm\pi/2$ is energetically favored by minimizing the free energy.

At the $\Gamma$ point, the bulk gap closes at $\mu_{c,i}^\pm = \pm\sqrt{\lambda_{soc}^2 - 4|\Delta_i|^2}$, where $i = 1, 2$ and $\Delta_{1,2} = i\Delta_o(\sin\theta \pm \cos\theta)$. Due to TRB, $\mu_{c,1}^\pm \neq \mu_{c,2}^\pm$. Accordingly, we semiqualitatively map out the phase diagram in Fig. 5 by tuning $\theta$ and $\mu$, and label the different phase regions by the number of Majorana edge modes (MEMs), denoted as $\mathcal{Q}$. When $|\mu| > \max\{|\mu_{c,1}|, |\mu_{c,2}|\}$, the topologically trivial phase is achieved with $\mathcal{Q} = 0$. As for $\min\{|\mu_{c,1}|, |\mu_{c,2}|\} < |\mu| < \max\{|\mu_{c,1}|, |\mu_{c,2}|\}$, there is only one MEM on the boundary, corresponding to the $\mathcal{Q} = 1$ regions [87,88]. When $|\mu| < \min\{|\mu_{c,1}|, |\mu_{c,2}|\}$, there are $\mathcal{Q} = 2$ MEMs. The chiral TSC might be detected by anomalous thermal Hall conductivity $K_{xy} = \frac{\mathcal{Q}}{2}\frac{\pi T}{6}$ [89].

### B. Atomic orbital polarization and spin polarization

Next, we show how spin-singlet TRB nonunitary pairing can induce spin polarization, and discuss how to identify such pairings by using spin-polarized scanning tunneling microscopy measurements. We assume a TRB complex orbital $\mathbf{d}_o$ vector and find that it can generate the orbital orderings as

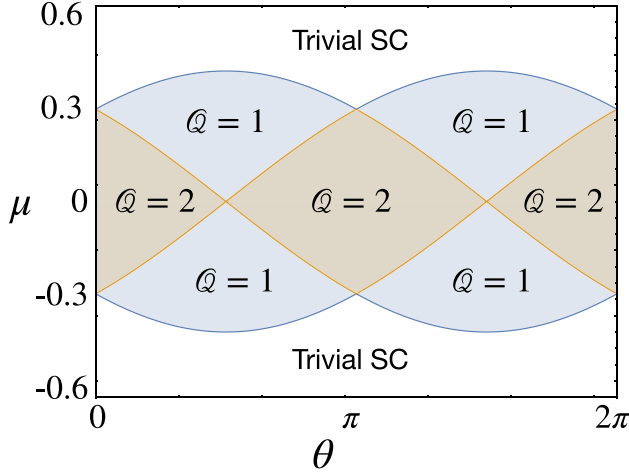$$\mathbf{M}_o = -i\gamma_1/\alpha_M(\mathbf{d}_o \times \mathbf{d}_o^*), \tag{39}$$

FIG. 5. Topological chiral superconductivity. We plot the phase diagram in terms of the number of MEMs ($\mathcal{Q}$) of the TSC. Parameters used: $\Delta_o = 0.14$, $\lambda_{soc} = 0.4$, $\phi = \pm\pi/2$, $\lambda_o = 0$, $t_{str} = 0$, and $\Delta_s = 0$.
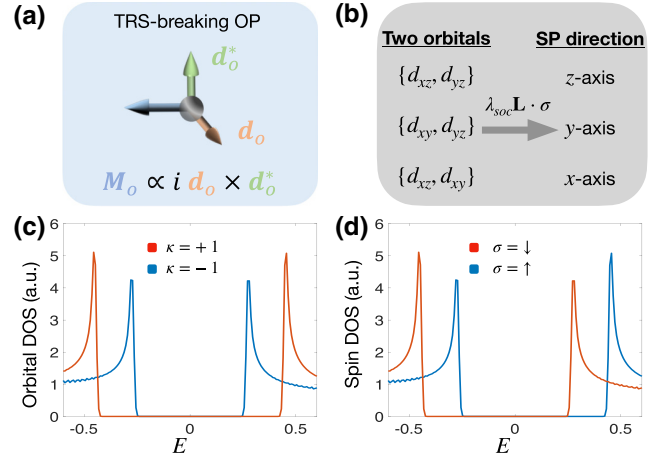


FIG. 6. (a) Schematic diagram showing the TRB orbital polarization (OP) induced by complex $\mathbf{d}_o$ vector. (b) Spin could be polarized in different directions based on the two active orbitals involved in the pairing. (c) Orbital DOS projected into the chiral $\kappa = \pm 1$ basis, showing a two-gap feature due to TRB. (d) The corresponding spin DOS, shifted relative to the Fermi level due to the nonzero effective Zeeman field from the OP. Parameters used: $m = 0.5$, $\mu = -2$, $\lambda_R = 0$, $\lambda_{soc} = 0.2$, $\Delta_o = 0.4$, $\lambda_o = 0$, $t_{str} = 0$, $\mathbf{d}_o = (1, 0, e^{i\pi/10})$.

of which the $y$ component breaks TRS shown in Fig. 6(a). More precisely, we find that $M_o^y \propto \sum_{\mathbf{k},\sigma} \langle \hat{n}_{d_{xz}+id_{yz},\sigma}(\mathbf{k}) - \hat{n}_{d_{xz}-id_{yz},\sigma}(\mathbf{k}) \rangle \neq 0$ indicates the atomic orbital-polarization (OP) (see Appendix F for details). Here, $\hat{n}$ is the density operator of electrons. Once $M_o^y$ develops a finite value, it leads to orbital-polarized DOS and two distinct superconducting gaps of the quasiparticle spectrum [Fig. 6(c), more details below]. Therefore, the orbital degree of freedom in spin-singlet SCs plays a similar role as the spin degree of freedom of spin-triplet SCs.

Once the atomic SOC is present, spin polarization (SP) could be induced indirectly. A possible Ginzburg-Landau term could be

$$\Delta\mathcal{F} = \alpha_s |\mathbf{M}_s|^2 + \gamma_{soc} M_s^z M_o^y, \tag{40}$$

with $\alpha_s > 0$ and $\gamma_{soc} \neq 0$. Here, $M_s^z \propto \sum_{\mathbf{k},\tau} \langle \hat{n}_{\tau,\uparrow} - \hat{n}_{\tau,\downarrow} \rangle$. Therefore, the complex orbital $\mathbf{d}_o$ vector can be identified by the spin-resolved density of states (DOS) for spin-singlet superconductors. Minimizing Eq. (40) directly leads to $M_s^z = \gamma_{soc} M_o^y / M_s^z$, which indicates the OP-induced spin magnetism. In addition, the direction of SP can be also aligned to $x$ or $y$ axes, discussed later.

To verify the above analysis, we numerically solve the BdG Hamiltonian (13), $\mathcal{H}_{BdG}|E_n(\mathbf{k})\rangle = E_n(\mathbf{k})|E_n(\mathbf{k})\rangle$, where the $n$th eigenstate is given by $|E_n(\mathbf{k})\rangle = (u_{d_{xz},\uparrow}^n, u_{d_{xz},\downarrow}^n, v_{d_{xz},\uparrow}^n, v_{d_{xz},\downarrow}^n, u_{d_{yz},\uparrow}^n, u_{d_{yz},\downarrow}^n, v_{d_{yz},\uparrow}^n, v_{d_{yz},\downarrow}^n)^T$. Thus, the atomic-orbital and spin-resolved DOS can be calculated as the following,

$$D_{orbit}^\kappa(E) = \sum_{\sigma,n,\mathbf{k}} |u_{\kappa,\sigma}^n|^2 \delta[E - E_n(\mathbf{k})],$$
$$D_{spin}^\sigma(E) = \sum_{\tau,n,\mathbf{k}} |u_{\tau,\sigma}^n|^2 \delta[E - E_n(\mathbf{k})], \tag{41}$$

where $u_{\kappa,\sigma}^n = \frac{1}{\sqrt{2}}(u_{d_{xz},\sigma}^n - i\kappa u_{d_{yz},\sigma}^n)$ and $\kappa = \pm 1$ for $d_{xz} \pm id_{yz}$ orbitals. In Fig. 6(c), $D_{orbit}^{+1} \neq D_{orbit}^{-1}$ indicates that the DOS is orbital polarized. Remarkably, we also have $D_{spin}^\uparrow \neq D_{spin}^\downarrow$.

due to coupling between electron spin and atomic orbitals, shown in Fig. 6(d). The difference in orbital DOS acts as an effective Zeeman field for the electron spins, hence shifting the spin DOS relative to the Fermi level in opposite directions for up spin and down spin. This interesting phenomenon is quite different from spin-triplet SCs. In TRB spin-triplet SCs the spin-up channel and spin-down channel will form different symmetric gaps in spin DOS, similar to the two orbital channels in Fig. 6(c) for our case. Therefore, the spin DOS profiles are distinct in the two cases. As a result, the spin-resolved DOS, which can be probed by spin-resolved STM [90] and muon-spin relaxation [91,92], can serve as a smoking gun evidence to identify TRB due to complex orbital $\mathbf{d}_o$ vector in multiorbital SCs.

## VI. DISCUSSIONS AND CONCLUSIONS

In the end, we briefly discuss the direction of spin polarization induced by atomic orbital polarization, summarized in Fig. 6(b). We consider the three-dimensional subspace of $t_{2g}$ orbitals spanned by $\{d_{yz}, d_{xz}, d_{xy}\}$, where the matrix form of the angular momentum operators $\mathbf{L}$ reads [63],

$$L_x = \begin{pmatrix} 0 & 0 & 0 \\ 0 & 0 & i \\ 0 & -i & 0 \end{pmatrix}, \quad L_y = \begin{pmatrix} 0 & 0 & -i \\ 0 & 0 & 0 \\ i & 0 & 0 \end{pmatrix},$$
$$L_z = \begin{pmatrix} 0 & i & 0 \\ -i & 0 & 0 \\ 0 & 0 & 0 \end{pmatrix}, \tag{42}$$

which satisfy the commutation relation $[L_m, L_n] = -i\epsilon_{mnl}L_l$. Therefore, the spin-orbit coupling for a system with the $t_{2g}$ orbitals is given by,

$$H_{soc} = \lambda_{soc}\mathbf{L} \cdot \boldsymbol{\sigma}. \tag{43}$$

Then, let us consider a two-orbital system, the above SOC Hamiltonian will be reduced to,

$$\text{For } \{d_{yz}, d_{xz}\}: \; H_{\text{soc}} = -\lambda_{\text{soc}} \tau_2 \sigma_3,$$
$$\text{For } \{d_{yz}, d_{xy}\}: \; H_{\text{soc}} = \lambda_{\text{soc}} \tau_2 \sigma_2,$$
$$\text{For } \{d_{xz}, d_{xy}\}: \; H_{\text{soc}} = -\lambda_{\text{soc}} \tau_2 \sigma_1. \quad (44)$$

Therefore, in the above three cases, the spin polarization is pointed to $z$, $y$, $x$ axis, respectively. Because the atomic orbital polarization is induced by the complex orbital $\mathbf{d}_o$ vector as $(0, M_o^y, 0) \propto i\mathbf{d}_o^* \times \mathbf{d}_o$.

To summarize, we establish a phenomenological theory for spin-singlet two-band SCs and discuss the distinct features of both TRI nonunitary pairings and TRB nonunitary pairings by studying the effects of atomic spin-orbit coupling (SOC), lattice strain effect, and Rashba SOC. Practically, we demonstrate that the stability of orbital-dependent pairing states could give birth to the nonunitary pairing states in a purely spin-singlet SC. Remarkably, the interplay between atomic SOC and orbital-dependent pairings is also investigated and we find a new spin-orbit coupled SC with spin-singlet nonunitary pairing. For this exotic state, there are mainly three features. First, the atomic SOC could enlarge the in-plane upper critical field compared to the Pauli limit. A new effect dubbed as zero-field Pauli limit for orbital-dependent pairings is discovered. Second, topological chiral or helical superconductivity could be realized even in the absence of external magnetic fields or Zeeman fields. Furthermore, a spontaneous TRB SC could even generate a spin-polarized superconducting state that can be detected by measuring the spin-resolved density of states. We hope our theory leads to a deeper understanding of spin-singlet nonunitary SCs.

Our theory might have potential applications to the intriguing Sr$_2$SuO$_4$ [93,94], LaNiGa$_2$ [58], iron-based SCs [59,60], and ultracold atomic systems with large spin alkali and alkaline-earth fermions [95–99].

## APPENDIX A: TOY MODEL FOR TWO-BAND SUPERCONDUCTING PHASE DIAGRAMS

In this Appendix, we explore a possible superconducting phase diagram including the nonunitary pairing states in the GL framework. Here we assume a two-band SC with

$$\Delta_{\text{tot}} = \left[\Delta_s \tau_0 + \Delta_o (d_o^1 \tau_1 + d_o^3 \tau_3)\right](i\sigma_2). \quad (A1)$$

In terms of the superconducting order parameters $\{\Delta_s, \Delta_o, \mathbf{d}_o = (d_o^1, 0, d_o^3)\}$ and the order parameter for the orbital orderings $\mathbf{M}_o \propto \sum_{\mathbf{k},\sigma} \langle c_{a\sigma}^\dagger(\mathbf{k}) \boldsymbol{\tau}_{ab} c_{b\sigma}(\mathbf{k}) \rangle$, the total GL free energy can be constructed to address the homogeneous superconducting phase without external magnetic fields,

$$\mathcal{F}[\Delta_s, \Delta_o, \mathbf{d}_o, \mathbf{M}_o] = \mathcal{F}_0 + \mathcal{F}_b + \mathcal{F}_o, \quad (A2)$$

where

$$\mathcal{F}_0 = \tfrac{1}{2}\alpha(T)|\Delta_o|^2 + \tfrac{1}{2}\alpha'(T)|\Delta_s|^2 + \tfrac{1}{2}\alpha_M|\mathbf{M}_o|^2$$
$$+ \tfrac{1}{4}\beta|\Delta_o|^4 + \tfrac{1}{4}\beta'|\Delta_s|^4 + \beta''|\Delta_s|^2|\Delta_o|^2$$
$$+ \beta_o|d_o^1|^4 + \beta_o'|d_o^3|^4, \quad (A3)$$

where $|\mathbf{d}_o| = 1$ is adopted, $\alpha(T) = \alpha_0(T/T_{c1} - 1)$, $\alpha'(T) = \alpha_0'(T/T_{c2} - 1)$ and the coefficients $\alpha_0$, $\alpha_0'$, $\alpha_M$, $\beta$, $\beta'$, $\beta''$, $\beta_o$, $\beta_o'$ are all positive. $T_{c1}$, $T_{c2}$ are critical temperatures in orbital-dependent and orbital-independent channels respectively, which are in general different from each other. And $\alpha_M > 0$ means that there is no spontaneous atomic orbital polarization. In the superconducting state with both nonzero $\Delta_s$ and $\Delta_o$ developed already, additionally, there are two possible ways to pursue the spontaneous TRB, denoted as $\mathcal{F}_b$ and $\mathcal{F}_o$. First, we consider the $\mathcal{F}_b$ term

$$\mathcal{F}_b = b_1 \Delta_s^* \Delta_o + b_2 (\Delta_s^* \Delta_o)^2 + \text{h.c.}, \quad (A4)$$

where the sign of $b_2$ determines the breaking of TRS. Here we focus on the generic case where $\Delta_s$ and $\Delta_o$ belong to different symmetry representations so that there is no linear order coupling between them, i.e. $b_1 = 0$. Given $b_1 = 0$ and $b_2 > 0$, we have a $\theta_o = \pm\pi/2$ relative phase difference between $\Delta_s$ and $\Delta_o e^{i\theta_o}$ [100], which gives to the achievement of the TRB unitary pairing state ($\Delta_s \in \mathbb{R}$, $\Delta_o \sim i$, $\mathbf{d}_o \in \mathbb{R}$).

More generally, a TRB nonunitary SC arises from the nonzero bilinear $b_1$ term, which is symmetry allowed only when $\Delta_s$ and $\Delta_o$ belong to the same symmetry representation of the crystalline symmetry group. Namely, the case with $b_1 \neq 0$ and $b_2 > 0$ can pin the phase difference $\theta_o$ to an arbitrary nonzero value, i.e., $\theta_o \in (0, \pi)$. Then, this case can also give rise to TRB nonunitary pairing with ($\Delta_s \in \mathbb{R}$, $\Delta_t \in \mathbb{C}$, $\mathbf{d}_o \in \mathbb{R}$) or ($\Delta_s \in \mathbb{R}$, $\Delta_t \in \mathbb{C}$, $\mathbf{d}_o \in \mathbb{C}$). On the other hand, the $b_2 < 0$ situation makes TRI nonunitary pairing states ($\Delta_s \in \mathbb{R}$, $\Delta_o \in \mathbb{R}$, $\mathbf{d}_o \in \mathbb{R}$).

However, even in the case with $b_2 < 0$, we still have an alternative approach to reach TRB pairing states, driven by the $\mathcal{F}_o$ term

$$\mathcal{F}_o = \gamma_0 |\mathbf{d}_o \times \mathbf{d}_o^*|^2 + i\gamma_1 \mathbf{M}_o \cdot (\mathbf{d}_o \times \mathbf{d}_o^*) + \text{H.c.}, \quad (A5)$$



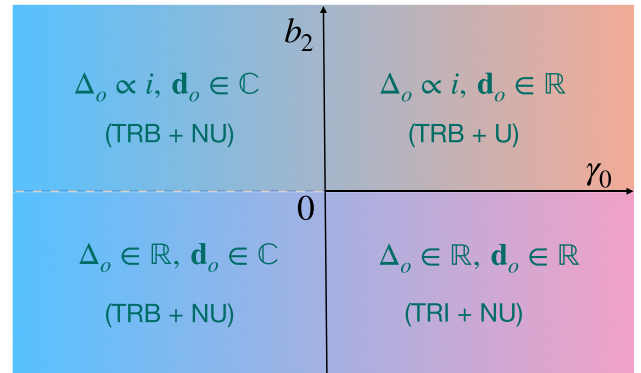FIG. 7. Schematic superconducting phase diagrams on the $b_2 - \gamma_0$ plane when $b_1 = 0$ and $\Delta_s$ is real and nonzero. Here, TRB and TRI are short for TR-breaking and TR-invariant, respectively; U and NU represent unitary and nonunitary, respectively.

where the sign of $\gamma_0$ identifies the TRB due to a complex $\mathbf{d}_o$. In particular $\gamma_0 < 0$ results in a TRB nonunitary state ($\Delta_s \in \mathbb{R}$, $\Delta_o \in \mathbb{R}$, $\mathbf{d}_o \in \mathbb{C}$).

We summarize many of the possible interesting superconducting phases in Fig. 7, which schematically shows a superconducting phase diagram as a function of $b_2$ and $\gamma_0$ by setting $b_1 = 0$, i.e., the generic case where $\Delta_o$, $\Delta_s$ belong to different representations. Notice that this phase diagram characterized by $b_2$ and $\gamma_0$ does not contain the TRI unitary pairing phase.

## APPENDIX B: DERIVATION OF $T_C$ FROM LINEARIZED GAP EQUATION

Starting from the generic Hamiltonian, containing atomic SOC, generic $\tilde{\mathbf{g}} = (\tilde{g}_1, 0, \tilde{g}_2)$ with $|\tilde{\mathbf{g}}| = 1$ and in-plane magnetic field,

$$H_0(\mathbf{k}) = \epsilon(\mathbf{k}) + \lambda_{\text{soc}}\sigma_3\tau_2 + \lambda(\tilde{g}_1\tau_1 + \tilde{g}_3\tau_3) + h\sigma_1. \tag{B1}$$

The Matsubara Green's function for electrons is

$$\begin{aligned}
G_e(\mathbf{k}, i\omega_n) &= [i\omega_n - \mathcal{H}_0(\mathbf{k})]^{-1} \\
&= \frac{P_{---}}{i\omega_n - \epsilon_\mathbf{k} + E_-} + \frac{P_{+-+}}{i\omega_n - \epsilon_\mathbf{k} + E_+} + \frac{P_{-+-}}{i\omega_n - \epsilon_\mathbf{k} - E_-} + \frac{P_{+++}}{i\omega_n - \epsilon_\mathbf{k} - E_+},
\end{aligned} \tag{B2}$$

where the projection operator

$$P_{\alpha\beta\gamma} = \frac{1}{4}[1 + \alpha(\tilde{g}_1\sigma_1\tau_1 + \tilde{g}_3\sigma_1\tau_3)] \cdot [1 + \frac{\beta}{E_\gamma}(\lambda_{\text{soc}}\sigma_3\tau_2 + \lambda_o(\tilde{g}_1\tau_1 + \tilde{g}_3\tau_3) + h\sigma_1)], \tag{B3}$$

with $\alpha, \beta, \gamma \in \{+, -\}$ and $E_\gamma = \sqrt{\lambda_{\text{soc}}^2 + (\lambda + \gamma h)^2}$. The Green's function for hole is $G_h(\mathbf{k}, i\omega_n) = -G_e^*(\mathbf{k}, i\omega_n)$. Here $\omega_n = (2n + 1)\pi k_B T$.

The linearized gap equation is given by

$$\Delta_{s_1,s_2}^{a,b}(\mathbf{k}) = -\frac{1}{\beta}\sum_{\omega_n}\sum_{s_1'a',s_2'b'} V_{s_1'a',s_2'b'}^{s_1a,s_2b}(\mathbf{k}, \mathbf{k}') \times [G_e(\mathbf{k}', i\omega_n)\Delta(\mathbf{k}')G_h(-\mathbf{k}', i\omega_n)]_{s_1'a',s_2'b'}, \tag{B4}$$

where the generic attractive interaction can be expanded as

$$V_{s_1'a',s_2'b'}^{s_1a,s_2b}(\mathbf{k}, \mathbf{k}') = -v_0\sum_{\Gamma,m}\left[\mathbf{d}_o^{\Gamma,m}(\mathbf{k}) \cdot \boldsymbol{\tau}i\sigma_2\right]_{s_1a,s_2b}\left[\mathbf{d}_o^{\Gamma,m}(\mathbf{k}') \cdot \boldsymbol{\tau}i\sigma_2\right]_{s_1'a',s_2'b'}, \tag{B5}$$

where $v_0 > 0$ and $\Gamma$ labels the irreducible representation with $m$ dimension of crystalline groups. The linearized gap equation is reduced to $v_0\chi(T) - 1 = 0$ where $\chi(T)$ is the superconductivity susceptibility. We have

(i) For orbital-independent pairing:

$$\chi(T)_s = -\frac{1}{\beta}\sum_{\mathbf{k},\omega_n}\text{Tr}[(\psi_s(\mathbf{k})i\sigma_2)^\dagger G_e(\mathbf{k}, i\omega_n)(\psi_s(\mathbf{k})i\sigma_2)G_h(-\mathbf{k}, i\omega_n)]. \tag{B6}$$

(ii) For orbital-dependent pairing:

$$\chi(T)_o = -\frac{1}{\beta}\sum_{\mathbf{k},\omega_n}\text{Tr}[(\mathbf{d}_o(\mathbf{k}) \cdot \boldsymbol{\tau}i\sigma_2)^\dagger G_e(\mathbf{k}, i\omega_n)(\mathbf{d}_o(\mathbf{k}) \cdot \boldsymbol{\tau}i\sigma_2)G_h(-\mathbf{k}, i\omega_n)]. \tag{B7}$$

Then we take the standard replacement,

$$\sum_{\mathbf{k},\omega_n} \rightarrow \frac{N_0}{4}\int_{-\omega_D}^{+\omega_D} d\epsilon \iint_S d\Omega \sum_{\omega_n}, \tag{B8}$$

where $N_0$ is the density of states at Fermi surface, $\Omega$ is the solid angle of $\mathbf{k}$ on Fermi surfaces and $\omega_D$ the Debye frequency. We will also be making use of,

$$-\frac{N_0}{\beta}\int_{-\omega_D}^{+\omega_D}\sum_{\omega_n}d\epsilon\, G_e^+(\mathbf{k}, i\omega_n)G_h^+(\mathbf{k}, i\omega_n) = -\frac{N_0}{\beta}\int_{-\omega_D}^{+\omega_D}\sum_{\omega_n}G_e^-(\mathbf{k}, i\omega_n)G_h^-(\mathbf{k}, i\omega_n) = \chi_0(T), \tag{B9}$$

$$-\frac{N_0}{\beta}\int_{-\omega_D}^{+\omega_D}\sum_{\omega_n}d\epsilon\, G_e^-(\mathbf{k}, i\omega_n)G_h^+(\mathbf{k}, i\omega_n) = -\frac{N_0}{\beta}\int_{-\omega_D}^{+\omega_D}\sum_{\omega_n}G_e^+(\mathbf{k}, i\omega_n)G_h^-(\mathbf{k}, i\omega_n) = \chi_0(T) + N_0\mathcal{C}_0(T), \tag{B10}$$

where $\chi_0(T) = N_0\ln(\frac{2e^\gamma\omega_D}{\pi k_B T})$, $\gamma = 0.57721\cdots$ the Euler-Mascheroni constant and $\mathcal{C}_0(T) = \text{Re}[\psi^{(0)}(\frac{1}{2}) - \psi^{(0)}(\frac{1}{2} + i\frac{E(\mathbf{k})}{2\pi k_B T})]$ with $\psi^{(0)}(z)$ being the digamma function.

For orbital-independent pairing considered in the main text $\Delta_s \tau_0 i\sigma_2$, we have

$$\chi_s(T) = \chi_0(T) + \frac{N_0}{2}\left[\mathcal{C}_0\left(T, \frac{E_+ - E_-}{2}\right) + \mathcal{C}_0\left(T, \frac{E_+ + E_-}{2}\right)\right]$$

$$+ \frac{N_0}{2}\left[\mathcal{C}_0\left(T, \frac{E_+ - E_-}{2}\right) - \mathcal{C}_0\left(T, \frac{E_+ + E_-}{2}\right)\right] \times \frac{\lambda^2 + \lambda_{\mathrm{soc}}^2 - h^2}{E_+ E_-}$$

$$\equiv \chi_0(T) + N_0 f_s(T, \lambda_{\mathrm{soc}}, \lambda, h). \tag{B11}$$

In order to look at the effect of $\lambda$ on the Pauli limit, we could Taylor expand $f_s(T, \lambda_{\mathrm{soc}}, \lambda, h)$ for small $\lambda$:

$$f_s(T, \lambda_{\mathrm{soc}}, \lambda, h) = f_s(T, \lambda_{\mathrm{soc}}, 0, h) + F(T, \lambda_{\mathrm{soc}}, h)\lambda^2 + \mathcal{O}(\lambda^4), \tag{B12}$$

with

$$F(T, \lambda_{\mathrm{soc}}, h) = \psi^{(2)}\left(\tfrac{1}{2}\right)\frac{\lambda_{\mathrm{soc}}^2 h^2}{4\pi k_B^2 T^2 \left(\lambda_{\mathrm{soc}}^2 + h^2\right)^2}$$

$$- \mathrm{Re}\left\{\psi^{(0)}\left(\tfrac{1}{2}\right) - \psi^{(0)}\left(\tfrac{1}{2} + i\frac{\sqrt{\lambda_{\mathrm{soc}}^2 + h^2}}{2\pi k_B T}\right)\right\}\frac{4\lambda_{\mathrm{soc}}^2 h^2}{\left(\lambda_{\mathrm{soc}}^2 + h^2\right)^3}$$

$$+ \mathrm{Im}\left\{\psi^{(1)}\left(\tfrac{1}{2} + i\frac{\sqrt{\lambda_{\mathrm{soc}}^2 + h^2}}{2\pi k_B T}\right)\right\}\frac{\lambda_{\mathrm{soc}}^2 h^2}{2\pi k_B T \left(\lambda_{\mathrm{soc}}^2 + h^2\right)^{5/2}}. \tag{B13}$$

This is used in the main text.

For orbital-dependent pairing $\Delta_o(d_1\tau_1 + d_3\tau_3)i\sigma_2$ with $\mathbf{d}_o = \tilde{\mathbf{g}}$, we have

$$\chi_o(T) = \chi_0(T) + \frac{N_0}{2}\left[\mathcal{C}_0\left(T, \frac{E_+ - E_-}{2}\right) + \mathcal{C}_0\left(T, \frac{E_+ + E_-}{2}\right)\right]$$

$$+ \frac{N_0}{2}\left[\mathcal{C}_0\left(T, \frac{E_+ - E_-}{2}\right) - \mathcal{C}_0\left(T, \frac{E_+ + E_-}{2}\right)\right] \times \frac{\lambda^2 - \lambda_{\mathrm{soc}}^2 - h^2}{E_+ E_-}$$

$$\equiv \chi_0(T) + N_0 f_o(T, \lambda_{\mathrm{soc}}, \lambda, h). \tag{B14}$$

## APPENDIX C: STRAIN EFFECT ON $T_C$ AND PAIRING SYMMETRY

The strain effect characterized by Eq. (6) in the main text can be absorbed into the orbital hybridization vector $\mathbf{g}_o$ and gives rise to an effective $\tilde{\mathbf{g}} \equiv \mathbf{g}_o + t_{\mathrm{str}}/\lambda_o(\sin 2\phi, 0, \cos 2\phi)$. Then in the absence of SOC terms, the corrected critical temperature $T_c$ due to the strain and hybridization effects is perturbatively given by

$$\ln\left(\frac{T_c}{T_0}\right) = \iint_S d\Omega \, \mathcal{C}_0(T_0)(|\mathbf{d}_o|^2 - |\mathbf{d}_o \cdot \hat{\tilde{\mathbf{g}}}|^2), \tag{C1}$$

where $T_0$ is the critical temperature without strain or hybridization and the integration is over the solid angle of $\mathbf{k}$ over the Fermi surface. Similar to previous discussions, the strain generally suppresses the critical temperature when $\tilde{\mathbf{g}}$ is not exactly parallel to $\mathbf{d}_o$, as shown in Fig. 8(a). For nonzero strain, the $T_c$ is not suppressed when $\mathbf{d}_o \| \tilde{\mathbf{g}}$. Figure 8(b) shows the symmetry-breaking pattern of the $|\mathbf{d}_o|$, which is proportional to the SC gap (the proportionality constant has been normalized to 1 in the figure), around the Fermi surface. The strain would reduce the symmetry from $C_4$ to $C_2$, as expected.

## APPENDIX D: TSC WITH $\Delta_s = 0$, $\lambda_o = 0$

To demonstrate the topology, we also show a simple case with $\Delta_s = 0$ and $\lambda_o = 0$, where the $Z_2$ can be characterized analytically.

In this section, we focus on the simplified case without orbital-independent pairing or orbital hybridization. In Fig. 4(c), we calculate the edge spectrum with $k_x$ being a good quantum number in a semi-infinite geometry, and it shows the corresponding bulk band structure together with two
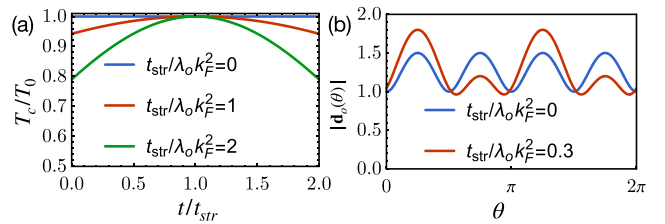


FIG. 8. (a) shows the suppression of $T_c$ for different strain strengths. Here $\mathbf{d}_o = \mathbf{g}_o + \frac{t}{\lambda_o}\mathbf{g}_{\mathrm{str}}$ whereas $\tilde{\mathbf{g}} = \mathbf{g}_o + \frac{t_{\mathrm{str}}}{\lambda_o}\mathbf{g}_{\mathrm{str}}$. (b) shows the symmetry breaking of the SC gap from $C_4$ to $C_2$ due to the existence of the external strain. We have chosen $\mathbf{g}_o = (3k_x k_y, 0, k_x^2 - k_y^2)$ and the strain parameter $\phi = 0$ in $\mathbf{g}_{\mathrm{str}}$.

counterpropagating MEMs. The bulk topology of the 2D helical TSC phase is characterized by the $Z_2$ topological invariant $\nu$, which can be extracted by calculating the Wilson-loop spectrum. And $\nu = 1$ mod 2 characterizes the helical TSC. In Fig. 4(b), we plot the evolution of $\theta$ as a function of $k_y$, and the winding pattern indicates the topological $Z_2$ invariant $\nu = 1$.

On the other hand, with $\Delta_s = 0$, which is the case if we only consider on-site attractive interactions between electrons [101,102], the BdG Hamiltonian (13) can be decomposed into two orbital subspaces that are related through time-reversal transformation. Each of these blocks has a well-defined Chern number because each block alone breaks TRS. The two Chern numbers can then be used to define the $Z_2$ invariant of the whole BdG system. The detailed procedures are the following.

For the normal Hamiltonian given in Eq. (1), we have $[\mathcal{H}_0, \tau_2] = 0$. As a result, we can project the normal Hamiltonian $\mathcal{H}_0$ in Eq. (1) into block-diagonal form corresponding to the $\pm 1$ eigenvalues of $\tau_2$ by using the basis transformation $\mathcal{U} = \sigma_0 \otimes \frac{1}{\sqrt{2}} \begin{bmatrix} 1 & -i \\ 1 & i \end{bmatrix}$. The new basis is given by

$$\tilde{\Psi}^\dagger(\mathbf{k}) = (c_{+,\uparrow}^\dagger, c_{+,\downarrow}^\dagger, c_{-,\downarrow}^\dagger, c_{-,\uparrow}^\dagger), \tag{D1}$$

where $c_{\pm,s}^\dagger \equiv \frac{1}{\sqrt{2}}(c_{d_{xz},s}^\dagger \mp i c_{d_{yz},s}^\dagger)$. On this basis, the normal Hamiltonian is given by

$$\mathcal{H}_0 = \mathcal{H}_0^+ \oplus \mathcal{H}_0^-, \tag{D2}$$

where $\mathcal{H}_0^\pm$ are given by

$$\mathcal{H}_0^\pm = \epsilon(\mathbf{k}) + \lambda_R(k_x \sigma_2 - k_y \sigma_1) \mp \lambda_{\text{soc}} \sigma_3. \tag{D3}$$

Note that the time-reversal transforms $\mathcal{H}_0^\pm(\mathbf{k})$ to $\mathcal{H}_0^\mp(-\mathbf{k})$. In the new basis the pairing Hamiltonian also decouples as $\mathcal{H}_\Delta = \mathcal{H}_\Delta^+ \oplus \mathcal{H}_\Delta^-$ with $\mathcal{H}_\Delta^\pm$ given by

$$\mathcal{H}_\Delta^\pm = 2\Delta_\pm [c_{\pm,\uparrow}^\dagger(\mathbf{k}) c_{\pm,\downarrow}^\dagger(-\mathbf{k}) - (\uparrow \leftrightarrow \downarrow)] + \text{H.c.}, \tag{D4}$$

where $\Delta_\pm \equiv \Delta_o(\mp i d_o^1 + d_o^3)$ are the gap strengths in each subspace. Therefore, the Bogoliubov-de Gennes (BDG) Hamiltonian takes the following block-diagonal form,

$$\mathcal{H}_{\text{BdG}} = \mathcal{H}_{\text{BdG}}^+ \oplus \mathcal{H}_{\text{BdG}}^-, \tag{D5}$$

where

$$\mathcal{H}_{\text{BdG}}^\pm(\mathbf{k}) = (\epsilon(\mathbf{k}) \mp \lambda_{\text{soc}} \sigma_3) \gamma_3 + \lambda_R(k_x \sigma_2 \gamma_3 - k_y \sigma_1 \gamma_0)$$
$$\pm 2 d_1 \sigma_2 \gamma_1 - 2 d_3 \sigma_2 \gamma_2, \tag{D6}$$

with $\gamma_\mu$ being the Pauli matrices in the particle-hole space. The Nambu basis is $\Psi_\pm^\dagger(\mathbf{k}) = (c_{\pm,\uparrow}^\dagger(\mathbf{k}), c_{\pm,\downarrow}^\dagger(\mathbf{k}), c_{\pm,\uparrow}(-\mathbf{k}), c_{\pm,\downarrow}(-\mathbf{k}))$. Each subspace has its own particle-hole symmetry.

By symmetry, the 2D BdG Hamiltonian in Eq. (D5) belongs to Class DIII of the A–Z classification [103,104] for topological insulators and superconductors because both TRS and particle-hole symmetry are preserved. However, it is not the case for our model. The BdG Hamiltonian here could exhibit topological states with $Z_2$-type topological invariant, which can be defined as the following. In each subspace, we define the BdG Chern number as

$$\mathcal{C}_\pm = \frac{1}{2\pi} \sum_{\text{filled bands}} \int_{\text{BZ}} d\mathbf{k} \cdot \langle \phi_n^\pm(\mathbf{k}) | i \nabla_\mathbf{k} | \phi_n^\pm(\mathbf{k}) \rangle, \tag{D7}$$

with $|\phi_n^\pm\rangle$ being the energy eigenstate of $\mathcal{H}_{\text{BdG}}^\pm$. Then the $Z_2$ invariant, in this case, is then explicitly given by,

$$\nu \equiv \frac{\mathcal{C}_+ - \mathcal{C}_-}{2}, \tag{D8}$$

where $\mathcal{C}_\pm$ are the Chern numbers of the $\pm$ channels. This has been discussed in the main text.

## APPENDIX E: WILSON-LOOP CALCULATION FOR $\mathcal{Z}_2$ TSC

In the thermodynamics limit, the Wilson-loop operator along a closed path $p$ is expressed as

$$\mathcal{W}_p = \mathcal{P} \exp\left[ i \oint_p \mathcal{A}(\mathbf{k}) \, d\mathbf{k} \right], \tag{E1}$$

where $\mathcal{P}$ means path ordering and $\mathcal{A}(\mathbf{k})$ is the non-Abelian Berry connection

$$\mathcal{A}^{nm}(\mathbf{k}) = i\langle \phi^n(\mathbf{k}) | \nabla_\mathbf{k} | \phi^m(\mathbf{k}) \rangle, \tag{E2}$$

with $|\phi^{m,n}(\mathbf{k})\rangle$ the occupied eigenstates. The Wilson line element is defined as

$$G^{nm}(\mathbf{k}) = \langle \phi^n(\mathbf{k} + \Delta\mathbf{k}) | \phi^m(\mathbf{k}) \rangle, \tag{E3}$$

where the $\mathbf{k} = (k_x, k_y)$, and $\Delta\mathbf{k} = (0, 2\pi/N_y)$ is the steps. In the discrete case, the Wilson-loop operator on a path along $k_y$ from the initial point $\mathbf{k}$ to the final point $\mathbf{k} + (0, 2\pi)$ can be written as $\mathcal{W}_{y,\mathbf{k}} = G(\mathbf{k} + (N_y - 1)\Delta\mathbf{k})G(\mathbf{k} + (N_y - 2)\Delta\mathbf{k})...G(\mathbf{k} + \Delta\mathbf{k})G(\mathbf{k})$, which satisfies the eigenvalue equation

$$\mathcal{W}_{y,\mathbf{k}} |\nu_{y,\mathbf{k}}^j\rangle = e^{i2\pi \nu_y^j(k_x)} |\nu_{y,\mathbf{k}}^j\rangle. \tag{E4}$$

The phase of eigenvalue $\theta = 2\pi \nu_y^j(k_x)$ is the Wannier function center.

## APPENDIX F: SPIN AND ORBITAL MAGNETIZATIONS: $\mathbf{M}_s$ AND $\mathbf{M}_o$

In this section, we show the definition of spin and orbital magnetization at the mean-field level. The spin magnetization in orbital-inactive systems takes the form

$$\mathbf{M}_s \propto \sum_{\mathbf{k}, s_1, s_2} \langle c_{s_1}^\dagger(\mathbf{k}) \boldsymbol{\sigma}_{s_1 s_2} c_{s_2}(\mathbf{k}) \rangle, \tag{F1}$$

which tells us the magnetic moments generated by spin polarization. Similarly, the orbital magnetization in orbital-active system is given by

$$\mathbf{M}_o \propto \sum_{\mathbf{k}, s, a, b} \langle c_{s,a}^\dagger(\mathbf{k}) \boldsymbol{\tau}_{ab} c_{s,b}(\mathbf{k}) \rangle. \tag{F2}$$

The different components of the orbital magnetization vector represent different orders in the SC ground state. More specifically, we have

$$M_o^x = \sum_{\mathbf{k}, s} \langle c_{s,d_{xz}}^\dagger c_{s,d_{yz}} + c_{s,d_{yz}}^\dagger c_{s,d_{xz}} \rangle, \tag{F3}$$

$$M_o^y = -i \sum_{\mathbf{k}, s} \langle c_{s,d_{xz}}^\dagger c_{s,d_{yz}} - c_{s,d_{yz}}^\dagger c_{s,d_{xz}} \rangle \tag{F4}$$

$$= \frac{1}{2} \sum_{\mathbf{k},s} \left\langle \hat{n}_{s,d_{xz}+id_{yz}} - \hat{n}_{s,d_{xz}-id_{yz}} \right\rangle, \tag{F5}$$

$$M_o^z = \sum_{\mathbf{k},s} \left\langle c_{s,d_{xz}}^\dagger c_{s,d_{xz}} - c_{s,d_{yz}}^\dagger c_{s,d_{yz}} \right\rangle. \tag{F6}$$

We see that $M_o^{x,z}$ breaks the $C_4$ rotation symmetry and $M_o^y$ breaks TRS. In our work, we only consider the possibility of spontaneous TRS breaking, thus the $M_o^{x,z}$ will not couple to

the superconducting order parameters, which are required to be invariant under $C_n$. Because $M_o^y$ breaks TRS so that it could be coupled to the superconducting order parameters, which spontaneously breaks TRS. This is one of the main results of our work,

$$\left(0, M_o^y, 0\right) \propto i\mathbf{d}_o^* \times \mathbf{d}_o, \tag{F7}$$

where the complex orbital $\mathbf{d}_o$ vector breaks TRS.

[1] M. Sigrist and K. Ueda, Rev. Mod. Phys. **63**, 239 (1991).

[2] V. P. Mineev, K. Samokhin, and L. Landau, *Introduction to Unconventional Superconductivity* (CRC Press, Boca Raton, 1999).

[3] F. Steglich, J. Aarts, C. D. Bredl, W. Lieke, D. Meschede, W. Franz, and H. Schäfer, Phys. Rev. Lett. **43**, 1892 (1979).

[4] J. G. Bednorz and K. A. Müller, Z. Phys. B **64**, 189 (1986).

[5] F. C. Zhang and T. M. Rice, Phys. Rev. B **37**, 3759 (1988).

[6] P. W. Anderson, P. Lee, M. Randeria, T. Rice, N. Trivedi, and F. Zhang, J. Phys.: Condens. Matter **16**, R755 (2004).

[7] D. J. Scalapino, Rev. Mod. Phys. **84**, 1383 (2012).

[8] P. M. R. Brydon, D. S. L. Abergel, D. F. Agterberg, and V. M. Yakovenko, Phys. Rev. X **9**, 031025 (2019).

[9] T. M. R. Wolf, M. F. Holst, M. Sigrist, and J. L. Lado, Phys. Rev. Res. **4**, L012036 (2022).

[10] M. Zeng, D.-H. Xu, Z.-M. Wang, L.-H. Hu, and F.-C. Zhang, arXiv:2109.06039 [cond-mat.supr-con].

[11] X. Dai, Z. Fang, Y. Zhou, and F.-C. Zhang, Phys. Rev. Lett. **101**, 057008 (2008).

[12] T. T. Ong and P. Coleman, Phys. Rev. Lett. **111**, 217003 (2013).

[13] Z. P. Yin, K. Haule, and G. Kotliar, Nature Phys. **10**, 845 (2014).

[14] T. Ong, P. Coleman, and J. Schmalian, Proc. Natl. Acad. Sci. **113**, 5486 (2016).

[15] R. Nourafkan, G. Kotliar, and A.-M. S. Tremblay, Phys. Rev. Lett. **117**, 137001 (2016).

[16] A. V. Chubukov, O. Vafek, and R. M. Fernandes, Phys. Rev. B **94**, 174518 (2016).

[17] M. Yi, Y. Zhang, Z.-X. Shen, and D. Lu, npj Quantum Mater. **2**, 57 (2017).

[18] E. M. Nica, R. Yu, and Q. Si, npj Quantum Mater. **2**, 24 (2017).

[19] P. O. Sprau, A. Kostin, A. Kreisel, A. E. Böhmer, V. Taufour, P. C. Canfield, S. Mukherjee, P. J. Hirschfeld, B. M. Andersen, and J. S. Davis, Science **357**, 75 (2017).

[20] H. Hu, R. Yu, E. M. Nica, J.-X. Zhu, and Q. Si, Phys. Rev. B **98**, 220503(R) (2018).

[21] W. Chen and W. Huang, Phys. Rev. Res. **3**, L042018 (2021).

[22] E. M. Nica and Q. Si, npj Quantum Mater. **6**, 3 (2021).

[23] L. A. Wray, S.-Y. Xu, Y. Xia, Y. San Hor, D. Qian, A. V. Fedorov, H. Lin, A. Bansil, R. J. Cava, and M. Z. Hasan, Nature Phys. **6**, 855 (2010).

[24] L. Fu and E. Berg, Phys. Rev. Lett. **105**, 097001 (2010).

[25] P. M. R. Brydon, L. Wang, M. Weinert, and D. F. Agterberg, Phys. Rev. Lett. **116**, 177001 (2016).

[26] W. Yang, Y. Li, and C. Wu, Phys. Rev. Lett. **117**, 075301 (2016).

[27] D. F. Agterberg, P. M. R. Brydon, and C. Timm, Phys. Rev. Lett. **118**, 127001 (2017).

[28] L. Savary, J. Ruhman, J. W. F. Venderbos, L. Fu, and P. A. Lee, Phys. Rev. B **96**, 214514 (2017).

[29] W. Yang, T. Xiang, and C. Wu, Phys. Rev. B **96**, 144514 (2017).

[30] C. Timm, A. P. Schnyder, D. F. Agterberg, and P. M. R. Brydon, Phys. Rev. B **96**, 094526 (2017).

[31] J. Yu and C.-X. Liu, Phys. Rev. B **98**, 104514 (2018).

[32] I. Boettcher and I. F. Herbut, Phys. Rev. Lett. **120**, 057002 (2018).

[33] B. Roy, Sayed Ali Akbar Ghorashi, M. S. Foster, and A. H. Nevidomskyy, Phys. Rev. B **99**, 054505 (2019).

[34] H. Kim, K. Wang, Y. Nakajima, R. Hu, S. Ziemak, P. Syers, L. Wang, H. Hodovanets, J. D. Denlinger, P. M. Brydon *et al.*, Sci. Adv. **4**, eaao4513 (2018).

[35] D. F. Agterberg, T. M. Rice, and M. Sigrist, Phys. Rev. Lett. **78**, 3374 (1997).

[36] T. Takimoto, Phys. Rev. B **62**, R14641(R) (2000).

[37] W. Huang, Y. Zhou, and H. Yao, Phys. Rev. B **100**, 134506 (2019).

[38] Z.-M. Wang, M. Zeng, C. Lu, L.-H. Hu, and D.-H. Xu (unpublished).

[39] J. Clepkens, A. W. Lindquist, X. Liu, and H.-Y. Kee, Phys. Rev. B **104**, 104512 (2021).

[40] A. Ramires and M. Sigrist, Phys. Rev. B **100**, 104501 (2019).

[41] W. Yang, C. Xu, and C. Wu, Phys. Rev. Res. **2**, 042047(R) (2020).

[42] N. F. Q. Yuan, W.-Y. He, and K. T. Law, Phys. Rev. B **95**, 201109(R) (2017).

[43] L. Chirolli, F. de Juan, and F. Guinea, Phys. Rev. B **95**, 201110(R) (2017).

[44] A. Robins and P. Brydon, J. Phys.: Condens. Matter **30**, 405602 (2018).

[45] J. L. Lado and M. Sigrist, Phys. Rev. Res. **1**, 033107 (2019).

[46] L.-H. Hu, P. D. Johnson, and C. Wu, Phys. Rev. Res. **2**, 022021(R) (2020).

[47] A. Ramires, J. Phys.: Condens. Matter **34**, 304001 (2022).

[48] Y. Saito, Y. Nakamura, M. S. Bahramy, Y. Kohama, J. Ye, Y. Kasahara, Y. Nakagawa, M. Onga, M. Tokunaga, T. Nojima *et al.*, Nature Phys. **12**, 144 (2016).

[49] J. Lu, O. Zheliuk, I. Leermakers, N. F. Yuan, U. Zeitler, K. T. Law, and J. Ye, Science **350**, 1353 (2015).

[50] X. Xi, Z. Wang, W. Zhao, J.-H. Park, K. T. Law, H. Berger, L. Forró, J. Shan, and K. F. Mak, Nature Phys. **12**, 139 (2016).

[51] J. Falson, Y. Xu, M. Liao, Y. Zang, K. Zhu, C. Wang, Z. Zhang, H. Liu, W. Duan, K. He *et al.*, Science **367**, 1454 (2020).

[52] J. P. Ruf, H. Paik, N. J. Schreiber, H. P. Nair, L. Miao, J. K. Kawasaki, J. N. Nelson, B. D. Faeth, Y. Lee, B. H. Goodge *et al.*, Nature Commun. **12**, 59 (2021).

[53] S. Beck, A. Hampel, M. Zingl, C. Timm, and A. Ramires, Phys. Rev. Res. **4**, 023060 (2022).

[54] K. Ahadi, L. Galletti, Y. Li, S. Salmani-Rezaie, W. Wu, and S. Stemmer, Sci. Adv. **5**, eaaw0120 (2019).

[55] R. M. Fernandes and L. Fu, Phys. Rev. Lett. **127**, 047001 (2021).

[56] A. D. Hillier, J. Quintanilla, and R. Cywinski, Phys. Rev. Lett. **102**, 117007 (2009).

[57] A. D. Hillier, J. Quintanilla, B. Mazidian, J. F. Annett, and R. Cywinski, Phys. Rev. Lett. **109**, 097001 (2012).

[58] Z. F. Weng, J. L. Zhang, M. Smidman, T. Shang, J. Quintanilla, J. F. Annett, M. Nicklas, G. M. Pang, L. Jiao, W. B. Jiang, Y. Chen, F. Steglich, and H. Q. Yuan, Phys. Rev. Lett. **117**, 027001 (2016).

[59] V. Grinenko, R. Sarkar, K. Kihou, C. Lee, I. Morozov, S. Aswartham, B. Büchner, P. Chekhonin, W. Skrotzki, K. Nenkov *et al.*, Nature Phys. **16**, 789 (2020).

[60] N. Zaki, G. Gu, A. Tsvelik, C. Wu, and P. D. Johnson, Proc. Natl. Acad. Sci. **118**, e2007241118 (2021).

[61] P. K. Biswas, S. K. Ghosh, J. Z. Zhao, D. A. Mayoh, N. D. Zhigadlo, X. Xu, C. Baines, A. D. Hillier, G. Balakrishnan, and M. R. Lees, Nature Commun. **12**, 2504 (2021).

[62] Q. Zou, B. D. Oli, H. Zhang, T. Shishidou, D. Agterberg, M. Weinert, and L. Li, arXiv:2212.13603.

[63] W.-C. Lee, D. P. Arovas, and C. Wu, Phys. Rev. B **81**, 184403 (2010).

[64] J. Clepkens, A. W. Lindquist, and H.-Y. Kee, Phys. Rev. Res. **3**, 013001 (2021).

[65] J. Böker, P. A. Volkov, P. J. Hirschfeld, and I. Eremin, New J. Phys. **21**, 083021 (2019).

[66] S. Raghu, X.-L. Qi, C.-X. Liu, D. J. Scalapino, and S.-C. Zhang, Phys. Rev. B **77**, 220503(R) (2008).

[67] C. Guo, L. Hu, C. Putzke, J. Diaz, X. Huang, K. Manna, F.-R. Fan, C. Shekhar, Y. Sun, C. Felser *et al.*, Nature Phys. **18**, 813 (2022).

[68] L.-H. Hu, X. Wang, and T. Shang, Phys. Rev. B **104**, 054520 (2021).

[69] T. Shang, J. Zhao, L.-H. Hu, J. Ma, D. J. Gawryluk, X. Zhu, H. Zhang, Z. Zhen, B. Yu, Y. Xu *et al.*, Sci. Adv. **8**, eabq6589 (2022).

[70] P. A. Frigeri, D. F. Agterberg, A. Koga, and M. Sigrist, Phys. Rev. Lett. **92**, 097001 (2004).

[71] H. Yi, L.-H. Hu, Y. Wang, R. Xiao, J. Cai, D. R. Hickey, C. Dong, Y.-F. Zhao, L.-J. Zhou, R. Zhang *et al.*, Nature Mater. **21**, 1366 (2022).

[72] C. Wang, B. Lian, X. Guo, J. Mao, Z. Zhang, D. Zhang, B.-L. Gu, Y. Xu, and W. Duan, Phys. Rev. Lett. **123**, 126402 (2019).

[73] K. Maki and T. Tsuneto, Prog. Theor. Phys. **31**, 945 (1964).

[74] X.-L. Qi, T. L. Hughes, S. Raghu, and S.-C. Zhang, Phys. Rev. Lett. **102**, 187001 (2009).

[75] C.-X. Liu and B. Trauzettel, Phys. Rev. B **83**, 220510(R) (2011).

[76] S. Nakosai, Y. Tanaka, and N. Nagaosa, Phys. Rev. Lett. **108**, 147003 (2012).

[77] S. Deng, L. Viola, and G. Ortiz, Phys. Rev. Lett. **108**, 036803 (2012).

[78] F. Zhang, C. L. Kane, and E. J. Mele, Phys. Rev. Lett. **111**, 056402 (2013).

[79] J. Wang, Y. Xu, and S.-C. Zhang, Phys. Rev. B **90**, 054503 (2014).

[80] A. Haim and Y. Oreg, Phys. Rep. **825**, 1 (2019).

[81] O. E. Casas, L. Arrachea, W. J. Herrera, and A. L. Yeyati, Phys. Rev. B **99**, 161301(R) (2019).

[82] Y. Volpez, D. Loss, and J. Klinovaja, Phys. Rev. Res. **2**, 023415 (2020).

[83] R.-X. Zhang and S. Das Sarma, Phys. Rev. Lett. **126**, 137001 (2021).

[84] J.-F. Ge, Z.-L. Liu, C. Liu, C.-L. Gao, D. Qian, Q.-K. Xue, Y. Liu, and J.-F. Jia, Nature Mater. **14**, 285 (2014).

[85] R. Yu, X. L. Qi, A. Bernevig, Z. Fang, and X. Dai, Phys. Rev. B **84**, 075119 (2011).

[86] W. A. Benalcazar, B. A. Bernevig, and T. L. Hughes, Phys. Rev. B **96**, 245115 (2017).

[87] X.-L. Qi, T. L. Hughes, and S.-C. Zhang, Phys. Rev. B **82**, 184516 (2010).

[88] J. D. Sau, R. M. Lutchyn, S. Tewari, and S. Das Sarma, Phys. Rev. Lett. **104**, 040502 (2010).

[89] T. Meng and L. Balents, Phys. Rev. B **86**, 054504 (2012).

[90] R. Wiesendanger, Rev. Mod. Phys. **81**, 1495 (2009).

[91] G. Csire, J. Annett, J. Quintanilla, and B. Újfalussy, arXiv:2005.05702 [cond-mat.supr-con].

[92] T. Shang, M. Smidman, S. K. Ghosh, C. Baines, L. J. Chang, D. J. Gawryluk, J. A. T. Barker, R. P. Singh, D. M. Paul, G. Balakrishnan, E. Pomjakushina, M. Shi, M. Medarde, A. D. Hillier, H. Q. Yuan, J. Quintanilla, J. Mesot, and T. Shiroka, Phys. Rev. Lett. **121**, 257002 (2018).

[93] G. M. Luke, Y. Fudamoto, K. Kojima, M. Larkin, J. Merrin, B. Nachumi, Y. Uemura, Y. Maeno, Z. Mao, Y. Mori *et al.*, Nature (London) **394**, 558 (1998).

[94] J. Xia, Y. Maeno, P. T. Beyersdorf, M. M. Fejer, and A. Kapitulnik, Phys. Rev. Lett. **97**, 167002 (2006).

[95] T.-L. Ho and S. Yip, Phys. Rev. Lett. **82**, 247 (1999).

[96] C. Wu, J.-p. Hu, and S.-c. Zhang, Phys. Rev. Lett. **91**, 186402 (2003).

[97] B. J. DeSalvo, M. Yan, P. G. Mickelson, Y. N. Martinez de Escobar, and T. C. Killian, Phys. Rev. Lett. **105**, 030402 (2010).

[98] S. Taie, Y. Takasu, S. Sugawa, R. Yamazaki, T. Tsujimoto, R. Murakami, and Y. Takahashi, Phys. Rev. Lett. **105**, 190401 (2010).

[99] A. V. Gorshkov, M. Hermele, V. Gurarie, C. Xu, P. S. Julienne, J. Ye, P. Zoller, E. Demler, M. D. Lukin, and A. Rey, Nature Phys. **6**, 289 (2010).

[100] Y. Wang and L. Fu, Phys. Rev. Lett. **119**, 187003 (2017).

[101] C.-X. Liu, Phys. Rev. Lett. **118**, 087001 (2017).

[102] L.-H. Hu, C.-X. Liu, and F.-C. Zhang, Commun. Phys. **2**, 25 (2019).

[103] S. Ryu, A. P. Schnyder, A. Furusaki, and A. W. Ludwig, New J. Phys. **12**, 065010 (2010).

[104] C.-K. Chiu, J. C. Y. Teo, A. P. Schnyder, and S. Ryu, Rev. Mod. Phys. **88**, 035005 (2016).

**Acknowledgements**

# Chapter 9

# Theory of $d + id$ second-order topological superconductors

# Theory of $d+id$ Second-Order Topological Superconductors

Zi-Ming Wang,[1, *] Meng Zeng,[2, *] Chen Lu,[3, *] Da-Shuai Ma,[1] Rui-Xing Zhang,[4, 5] Lun-Hui Hu,[4, 6, 7, †] and Dong-Hui Xu[1, ‡]

[1]*Department of Physics and Chongqing Key Laboratory for Strongly Coupled Physics, Chongqing University, Chongqing 400044, China*
[2]*Department of Physics, University of California, San Diego, California 92093, USA*
[3]*New Cornerstone Science Laboratory, Department of Physics,*
*School of Science, Westlake University, Hangzhou 310024, Zhejiang, China*
[4]*Department of Physics and Astronomy, University of Tennessee, Knoxville, Tennessee 37996, USA*
[5]*Department of Materials Science and Engineering, University of Tennessee, Knoxville, Tennessee 37996, USA*
[6]*Center for Correlated Matter and School of Physics, Zhejiang University, Hangzhou 310058, China*
[7]*Department of Applied Physics, Aalto University School of Science, FI-00076 Aalto, Finland*
(Dated: May 24, 2024)

We explore the manifestation of second-order topology in a two-orbital superconductor with spin-orbital couplings, characterized by the emergence of anomalous gapless boundary modes. This state arises from the spontaneous breaking of time-reversal symmetry, driven by a $d+id$-wave orbital-dependent pairing, which can be energetically favored. Notably, the orbital-active $d$-wave pairing leads to anomalous zero-energy Majorana corner modes, contrasting with conventional chiral $d$-wave pairing that typically produces one-dimensional Majorana edge modes. Our theory offers a natural explanation for the absence of edge supercurrent in a $d+id$ superconductor. Additionally, we establish a correspondence between bulk second-order topology and dislocation lines, where a Kramers Majorana doublet emerges, albeit with a small gap. These findings demonstrate a connection between second-order topology and orbital-dependent pairings, offering new insights into the behavior of multi-band superconductors.

*Introduction.*— Topological superconductors (TSCs) are exotic quantum condensed matter phases with topologically nontrivial Cooper pair wavefunction structures. As one of the most remarkable consequences of TSCs, spatially localized Majorana zero modes (MZMs) can be trapped within the vortex cores of a two-dimensional (2D) $p$-wave TSC [1–3] or be formed at the ends of a one-dimensional $p$-wave superconductor [4]. MZMs exhibit non-Abelian quantum statistics, naturally encoding topological qubits that pave the way for fault-tolerant quantum computation [5, 6]. Although naturally occurring topological superconductors are rare and elusive, the past few decades have seen a tremendous effort to discover artificial topological superconductivity in various quantum materials [7–10], following theories [11–13]. So far, evidence of MZMs has been experimentally reported in several systems, ranging from one-dimensional superconducting hybrids [14–16] to vortex cores on a proximitized topological insulator surface [17] or an iron-based superconductor surface [18].

The recent advances of topological band theory have unveiled an entirely new category of "higher-order" TSCs with an unprecedented bulk-boundary relation [19–66]. For example, in two dimensions (2D), a second-order TSC generally binds 0D MZMs around the geometric corners of a finite-size system. In pursuit of corner MZMs, a crucial conceptual question is looking for new simple, feasible recipes applicable to real-world superconductors. Given the important role of orbital degrees of freedom in unconventional superconducting systems, a comprehension of whether multi-orbital pairing can enable higher-order TSC is certainly necessary but still largely incomplete [67–70].

This study demonstrates that orbital-active $d+id$-wave pairing can stabilize a second-order class-D topological superconducting phase protected by $C_4$ rotation symmetry. The topological nature of this superconducting phase is confirmed by numerically revealing Majorana corner modes and conducting a topological quantum chemistry analysis. It naturally explains the absence of edge supercurrent in a time-reversal-symmetry broken $d+id$ superconductor. Furthermore, apart from appearing at sample corners, we find that lattice dislocations can also trap Majorana zero modes due to the inherent weak topology of the system. Our findings establish a promising platform for the design and construction of Majorana qubits within multi-band superconductors.

*Model of $d+id$ TSCs and symmetry analysis.*— We consider a normal state two-orbital $\{d_{xz}, d_{yz}\}$ tight-binding model on the square lattice with SOC,

$$H_{\mathrm{n}} = \sum_{\boldsymbol{k}} \Psi^{\dagger}(\boldsymbol{k}) \{ \epsilon(\boldsymbol{k}) \sigma_0 s_0 + \widetilde{\epsilon}(\boldsymbol{k}) \sigma_z s_0 + \epsilon''(\boldsymbol{k}) \sigma_x s_0$$
$$+ \lambda_{\mathrm{I}} \sigma_y s_z + \lambda_{\mathrm{R}} \sin k_x \sigma_0 s_y - \lambda_{\mathrm{R}} \sin k_y \sigma_0 s_x \} \Psi(\boldsymbol{k}), \quad (1)$$

where $\Psi^{\dagger}(\boldsymbol{k}) = (c_{d_{xz},\uparrow}^{\dagger}, c_{d_{xz},\downarrow}^{\dagger}, c_{d_{yz},\uparrow}^{\dagger}, c_{d_{yz},\downarrow}^{\dagger})$, $\epsilon(\boldsymbol{k}) = -2t\cos k_x - 2t\cos k_y + 4t - \mu$, $\widetilde{\epsilon}(\boldsymbol{k}) = -2\widetilde{t}\cos k_x + 2\widetilde{t}\cos k_y$, and $\epsilon''(\boldsymbol{k}) = 4t''\sin k_x \sin k_y$. $\sigma_{x,y,z}$ and $s_{x,y,z}$ are Pauli matrices for the orbital and spin degrees of freedom, respectively. $t$ describes the intra-orbital nearest-neighbor hopping, $\widetilde{t}$ depicts the hopping anisotropy along the different direction of $d_{xz}$, $d_{yz}$ orbitals and $t''$ is the inter-orbital next-nearest-neighbor hopping. The $\lambda_{\mathrm{I}}$ and $\lambda_{\mathrm{R}}$ are the strengths of intrinsic and Rashba SOCs, respectively. This normal Hamiltonian breaks inversion symmetry but preserves TRS: $\mathcal{T} H_{\mathrm{n}}(\boldsymbol{k}) \mathcal{T}^{-1} = H_{\mathrm{n}}(-\boldsymbol{k})$, where $\mathcal{T} = i\sigma_0 s_y \mathcal{K}$ with $\mathcal{K}$ the complex conjugation operator. In addition, the normal Hamiltonian has the four-fold rotation symmetry $r_{4z} = i\sigma_y e^{-i\pi s_z/4}$.

In the Nambu basis $\{\Psi^{\dagger}(\boldsymbol{k}), \Psi^{T}(-\boldsymbol{k})\}$, the Bogoliubov-de-Gennes (BdG) Hamiltonian reads

$$H = \begin{bmatrix} H_{\mathrm{n}}(\boldsymbol{k}) & \Delta(\boldsymbol{k}) \\ \Delta^{\dagger}(\boldsymbol{k}) & -H_{\mathrm{n}}^{T}(-\boldsymbol{k}) \end{bmatrix}. \quad (2)$$

Here, the pairing potential $\Delta(\boldsymbol{k})$ consists of both orbital-independent and orbital-dependent pairings,

$$\Delta(\boldsymbol{k}) = [\Delta_i \Phi(\boldsymbol{k})\sigma_0 + \Delta_o(\boldsymbol{d}_o(\boldsymbol{k})\cdot\boldsymbol{\sigma})]is_y. \quad (3)$$

Here $\Delta_i$ and $\Delta_o$ are pairing amplitudes in orbital-independent and orbital-dependent channels, respectively. In this work, we are particularly interested in the $d$-wave pairings, and consider $\Phi(\boldsymbol{k}) = -2\cos k_x + 2\cos k_y$. Without breaking the crystalline symmetry, a uniform orbital-dependent pairing $\boldsymbol{d}_o(\boldsymbol{k}) = (0,0,1)$ is also allowed. For example, they belong to the same irreducible representation ($B_1$) of the $C_{4v}$ point group [71–73]. In the Supplementary Materials (SM), we self-consistently calculate the above gap function by using random phase approximation in the absence of SOCs and further find a spontaneous TRS breaking $d+id$ pairing by minimizing the free energy. Different from the traditional $d_{xy} + id_{x^2-y^2}$ (or $B_1 + iB_2$), this $d+id$ pairing (or $B_1 + iB_1$) preserves mirror symmetry, which enforces the vanishing of the BdG Chern number for Eq. (2). While the first-order topology has thus been ruled out, we will show below that 2nd-order TSC can emerge naturally based on symmetry analysis [74–80].

Because of the $d$-wave pairing $r_{4z}\Delta(\mathbf{k})r_{4z}^T = -\Delta(C_4^{-1}\mathbf{k})$, the BdG Hamiltonian preserves $C_{4z} = r_{4z} \oplus -r_{4z}^*$, together with other symmetries $C_{2x} = i\tau_z\sigma_0 s_z$ and $M_x = i\tau_z\sigma_z s_x$, we are capable of diagnosing the topology of the superconducting spectrum once it is fully gapped. In Fig. 1, we present the band structures of superconductors with fully gapped trivial and higher-order topological superconductor phases. To diagnose spatial symmetry-protected topological states, we employ the topological quantum chemistry theory [81, 82] to obtain elementary band representations (EBRs) [83–85] that is constituted by irreducible representations (irreps) of little groups at the maximal momenta in the first Brillouin Zone, as tabulated in Table. I and inserted in Fig. 1. Referring to Table. I, we observe that the topological trivial system, as shown in Fig. 1(a), is equivalent to a configuration involving $s$ and $p_z$ orbitals at the Wyckoff position of $1a$. In sharp contrast, the higher-order topological phase in Fig. 1(b), is equivalent to that of two $p_z$ orbitals at the $1a$ and $1b$ Wyckoff positions. Notice that the $1b$ site is at the center of the square lattice and cannot be occupied by any orbitals in real space. Thus, the potential spatial symmetry-protected topological states fall within the scope of a superconducting analog of an obstructed atomic insulator (OAI) [81, 82, 86, 87], whose BdG Wannier orbitals are displaced from the lattice sites. The OAI can be effectively diagnosed by the real space invariant (RSI) [86] defined at the $1b$ site. As defined in the SM, we find the non-trivial second-order topology corresponds to $(\delta_1, \delta_2) = (-1, 1)$, whereas the trivial phase is represented as $(\delta_1, \delta_2) = (0, 0)$.

*Superconducting phase diagram.*— In Fig. 2(a), we present the $\mu$-$\Delta_o$ superconducting phase diagram, which contains nodal superconductor, second-order TSC, and trivial phases. The gap closing and reopening of bulk dispersion at off-high-symmetry points ($\mathbf{k} \notin \{\Gamma, X, Y, M\}$) distinguishes a nodal superconductor from a fully gapped one. For the fully gapped
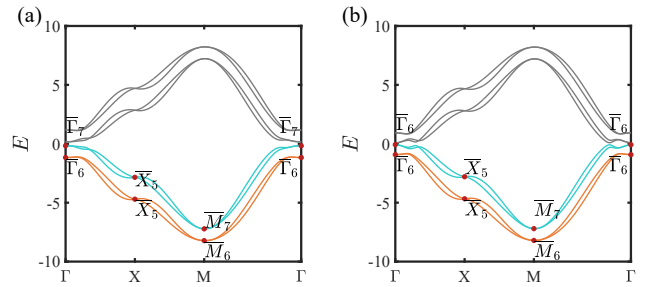


FIG. 1. Bulk band structure and irreducible representations at high-symmetry points of the TRS breaking $d + id$ superconductor. (a) Topologically trivial superconducting phase for $\Delta_o = 0.6$. (b) $C_4$ protected second-order TSC for $\Delta_o = 0.3$. Using EBRs analysis of double space group $P4mm$, we can obtain $C_4$ index $J_z$ at $\Gamma$-point and M-point which is also $z$-direction angular momentum, where $J_z = \pm\frac{3}{2}$ of $\Gamma_6$ or $M_6$ and $J_z = \pm\frac{1}{2}$ of $\Gamma_7$ or $M_7$. Common parameters: $t = 1, \tilde{t} = 0.2, t'' = 0.1, \mu = 0.3, \lambda_I = 0.5, \lambda_R = 0.3, \Delta_i = 0.1$.

TABLE I. The EBRs of space group $P4mm$ with SOC. The first row labels the Wyckoff positions. The second row is the irreducible representation of the double space group. The third row represents the orbits that induce the irreducible representation. The fourth row is the irreducible representations at high-symmetry points.

| WPs | $1a$ (000) | | $1b$ ($\frac{1}{2}\frac{1}{2}0$) | |
|---|---|---|---|---|
| EBRs | $\overline{E}_1 \uparrow G(2)$ | $\overline{E}_2 \uparrow G(2)$ | $\overline{E}_1 \uparrow G(2)$ | $\overline{E}_2 \uparrow G(2)$ |
| Orbitals | $s$ | $p_z$ | $s$ | $p_z$ |
| $\overline{\Gamma}$ (000) | $\overline{\Gamma}_7(2)$ | $\overline{\Gamma}_6(2)$ | $\overline{\Gamma}_7(2)$ | $\overline{\Gamma}_6(2)$ |
| $\overline{X}$ ($\frac{1}{2}00$) | $\overline{X}_5(2)$ | $\overline{X}_5(2)$ | $\overline{X}_5(2)$ | $\overline{X}_5(2)$ |
| $\overline{M}$ ($\frac{1}{2}\frac{1}{2}0$) | $\overline{M}_7(2)$ | $\overline{M}_6(2)$ | $\overline{M}_6(2)$ | $\overline{M}_7(2)$ |

phase, we employ the RSI method discussed above to determine its bulk topology. First, the gap function changes sign with respect to the reflection line along the [11] or [1$\bar{1}$] directions, suggesting a mirror symmetry-protected nodal superconductor [88], which is highlighted in blue in Fig. 2 (a). For example, it must be a nodal $d$-wave superconductor in the limit $\Delta_o = 0$. More details can be found in the SM. Furthermore, the fully gapped superconductor can be either topologically trivial or nontrivial as we discussed above. When $\Delta_o$ is large enough, it is a fully gapped but trivial phase [the white region in Fig. 2 (a)]. While the red region represents the second-order TSC phase. On the other hand, the TRS-breaking nodal superconductor is also topological, whose bulk nodes are protected by the mirror symmetry. Namely, the topological nodes are stable along the mirror-invariant lines (i.e., movable but irremovable by local perturbations). To show that, we perform a slab calculation with open boundary condition along the [1$\bar{1}$] direction and find the Majorana flat band states connecting two bulk nodes, as shown in $E_{k'_x}$ of Fig. 2 (b). At fixed $k'_x$, the 1D Hamiltonian $H(k'_y)$ exhibits particle-hole symmetry (mirror⊗PHS), leading to the $\mathbb{Z}_2$ topological invariant.
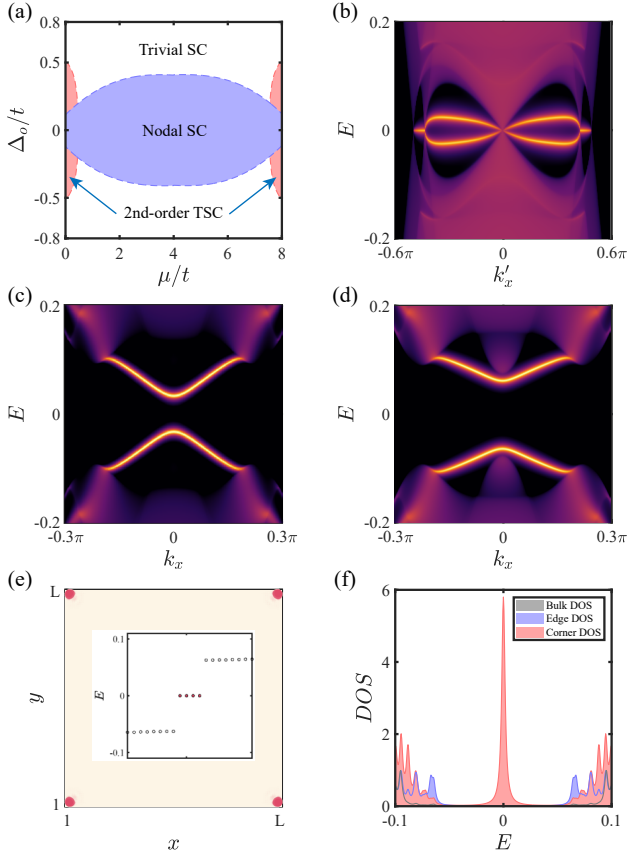
FIG. 2. (a) Superconducting phase diagram on the plane of $\Delta_\mathrm{o}$ and $\mu$. The white region represents the trivial phase, the blue region is the nodal superconducting phase and the red region is the second-order TSC phase. (b) The spectral function of the nodal superconductor for open boundary condition along [1$\bar{1}$] when $\Delta_\mathrm{o} = 0.01$. There are two pairs of bulk nodes, and each pair of nodal points is connected by Majorana flat-band edge states. All the nodes are gapped out when $\Delta_\mathrm{o} \neq 0$, as shown in (c-d). The energy gap increases as $\Delta_\mathrm{i}$ is increased. (c) The spectral function for open boundary condition along [01] when $\Delta_\mathrm{i} = 0.05$, and (d) is $\Delta_\mathrm{i} = 0.1$. (e) The wave function profile of the four corner modes, where the inset shows the finite system spectrum near zero energy and four MZMs (red dots). The sample size is $120 \times 120$. (f) The density of states near zero energy with the density distributions of bulk, edge, and corner. Common parameters unless otherwise specified: $t = 1$, $\tilde{t} = 0.2$, $t'' = 0.1$, $\mu = 0.3$, $\lambda_I = 0.5$, $\lambda_R = 0.5$, $\Delta_\mathrm{o} = 0.3$, $\Delta_\mathrm{i} = 0.1$.

We next explore the second-order TSC phase as $\mu$ approaches the band bottom or top. First, we employ Green's function method to compute the spectral function along the [10] or [01] direction. The results, depicted in Figs. 2 (c) and (d), exhibit fully gapped features. The gap opening for the in-gap edge states increases as $\Delta_\mathrm{i}$ is raised, with the gap of edge states approximately 0.06 in (c) and approximately 0.12 in (d). Then, we perform a full tight-binding simulation on a square lattice to visualize the Majorana corner states, as depicted in Fig. 2 (e). Inset exhibits the energy spectra, revealing four zero-energy states. We additionally analyze the local density of states (DOS) shown in Fig. 2 (f) to identify the MZMs.

As anticipated, both bulk and edge DOS exhibit a "U" shape, while a sharp zero-bias peak is observed in the DOS measured at the corners.

Starting from a nodal superconductor [see Figs. 3 (a) and (b)], the transition to a second-order TSC or trivial superconductor can be elucidated by the elimination of the nodes. Specifically, the removal of a single pair of nodes results in a phase transition from a nodal superconductor to a second-order TSC, as illustrated in Figs. 3 (c). The gap-closing at the $\Gamma$ point in Fig. 3 (d) further leads to a trivial superconductor. However, the simultaneous annihilation of two pairs of nodes corresponds to the transition directly from a nodal superconductor to a trivial superconductor, as illustrated in (f-j).

*Helical TSC and second-order TSC.*—In the spirit of "boundary of boundary", we aim to derive an edge theory to illustrate the occurrence of corner states akin to Jackiw-Rebbi modes [89]. We start with an interesting observation that when $\Delta_\mathrm{i} = 0$, the system is a first-order helical TSC [70]. The topological condition is $-\sqrt{\lambda_\mathrm{I}^2 - \Delta_\mathrm{o}^2} < \mu < \sqrt{\lambda_\mathrm{I}^2 - \Delta_\mathrm{o}^2}$. We solve Eq. (2) in the long-wavelength limit and focus on the edge along the $y$-axis as an illustrative example. Hence, $k_x$ can be replaced by $-i\partial_x$ while $k_y$ remains a good quantum number in the BdG Hamiltonian, $H(-i\partial_x, k_y) = H_0 + H'$, where $H_0 = -i\lambda_R\partial_x\tau_z\sigma_0 s_y - \mu\tau_z\sigma_0 s_0 + \lambda_\mathrm{I}\tau_0\sigma_y s_z - \Delta_\mathrm{o}\tau_y\sigma_z s_y$ needs to be solved analytically to obtain MZMs, and $H' = -\partial_x^2(t\tau_z\sigma_0 s_0 + \Delta_\mathrm{i}\tau_x\sigma_0 s_y) - \lambda_R k_y\tau_0\sigma_0 s_x$ is treated as a perturbation in the zero modes basis.

To solve for the zero modes, we create a domain wall along the $y$-axis between a topologically trivial superconductor ($x < 0$) and a topologically non-trivial superconductor ($x > 0$). For simplicity, we set the chemical potential $\mu = 0$, resulting in a non-trivial (trivial) superconductor region with $\Delta_\mathrm{o} < \lambda_\mathrm{I}$ ($\Delta_\mathrm{o} > \lambda_\mathrm{I}$). Taking the ansatz $\psi(x) = \mathcal{N}e^{-\kappa x}\chi$ for the zero modes, where $\kappa_R \equiv \kappa(x > 0) > 0$ and $\kappa_L \equiv \kappa(x < 0) < 0$ since the bulk on both sides of the domain wall is gapped, and $\chi$ is the spinor part. After solving $H_0\psi = 0$, we find only $\kappa = (\Delta_\mathrm{o} + \lambda_\mathrm{I})/\lambda_R$ satisfies the sign condition given the topological condition on both sides of the domain wall. The corresponding spinor parts are $\chi_1 = (-i, 0, 0, -1, -i, 0, 0, 1)^\mathrm{T}/2$ and $\chi_2 = (0, 1, -i, 0, 0, 1, i, 0)^\mathrm{T}/2$. Therefore, we obtain $\psi_{1,2}(x) = \mathcal{N}e^{-\kappa(x)x}\chi_{1,2}$ with the normalization constant $\mathcal{N} = \sqrt{2\kappa_R\kappa_L/(\kappa_L - \kappa_R)}$. Then, projecting $H'$ onto this Majorana basis $\{\psi_1, \psi_2\}$, we find

$$H_\mathrm{edge}(k_y) = \mathcal{N}^2\lambda_R k_y\tau_y - m_\mathrm{meff}\tau_x, \qquad (4)$$

where the effective mass is $m_\mathrm{eff} = -|\mathcal{N}|^2\Delta_\mathrm{i}\delta\Delta_\mathrm{o}/(2\lambda_R)$. Below, we use Pauli matrices $\tau_{x,y,z}$ for this Majorana basis. Please notice that the $d$-wave pairing naturally induces a sign-changing feature for $\delta\Delta_\mathrm{o} \equiv \Delta_\mathrm{o}(x < 0) - \Delta_\mathrm{o}(x > 0)$ between two neighboring edges ($\Delta_\mathrm{o} \to -\Delta_\mathrm{o}$ under $C_{4z}$). Due to the sign change of the mass term at each corner, localized zero modes emerge at the four corners of the system, establishing the $d+id$ second-order topological superconductor.

*Topological defects in TSCs.*— Detecting Majorana corner modes experimentally may pose challenges, as the loss of
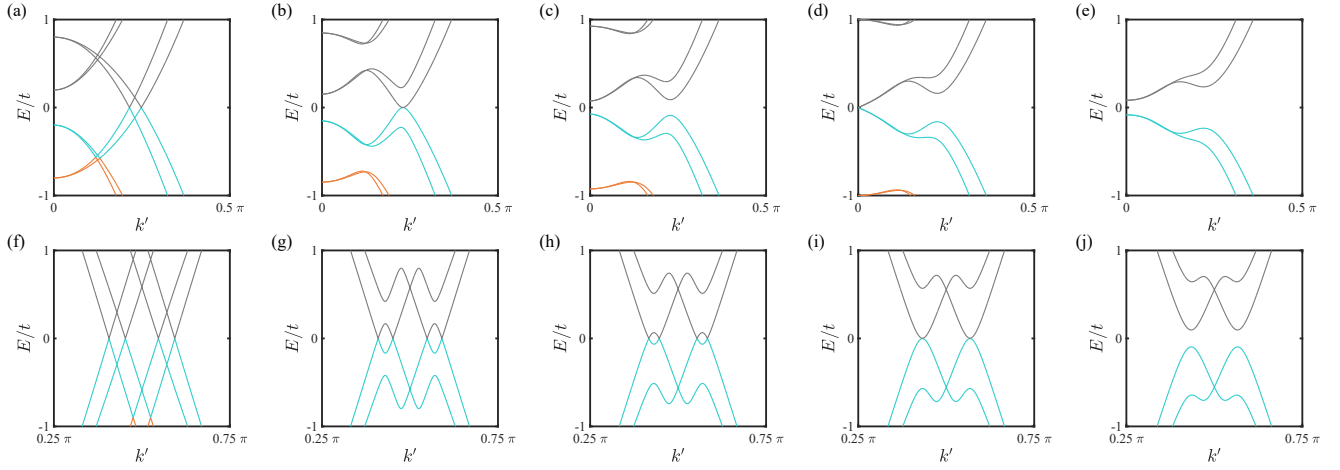
137

FIG. 3. Bulk energy spectrum evolution under increasing $\Delta_o$ from $\Delta_o = 0$ to 0.5 of $\Gamma$-M line, where $k' = k_x = k_y$. (a-e) Display the bulk energy spectrum evolution when $\mu = 0.3$. The nodal superconductor can transition to second-order SC when $\Delta_o \approx 0.17$ in (b), and the critical point between second-order and trivial SC phase when $\Delta_o \approx 0.4$ in (d). (f-j) Exhibit the bulk energy spectrum evolution when $\mu = 4$. The nodal superconductor can transition to a trivial superconductor when $\Delta_o \approx 0.38$ in (i). Common parameters: $t = 1$, $\tilde{t} = 0.2$, $t'' = 0.1$, $\lambda_I = 0.5$, $\lambda_R = 0.5$, $\Delta_i = 0.1$.
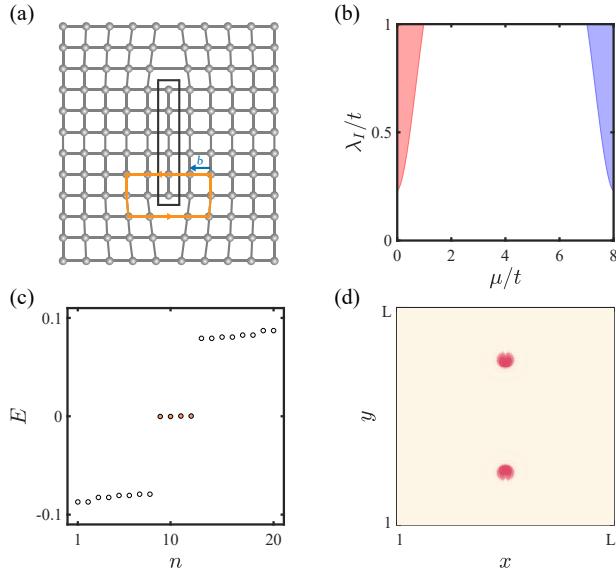


FIG. 4. Topological defect on a sample of square shape. (a) The single side edge dislocation of Volterra cut-and-glue. The black orthogon displays a dislocation line. The orange and blue arrow lines show the Burgers circuit and the Burgers vector $\boldsymbol{b} = (-1, 0)$. (b) Phase diagram of the trivial phase and $\mathcal{Z}_2$ non-trivial phase. Different weak topological indices mark the red and blue color regions as $(0, 0)$ or $(1, 1)$ for the first-order TSC. (c) The energy spectrum of the TRS-protected first-order topological superconductor with $\Delta_i = 0$. The orange dots are the fourfold dislocation MZMs. (d) The wave function profile of the four dislocation modes. Common parameters: $t = 1$, $\tilde{t} = 0.2$, $t'' = 0.1$, $\mu = 7.7$, $\lambda_I = 0.5$, $\lambda_R = 0.5$, $\Delta_o = 0.3$.

phase coherence near the sample boundary can obscure their observation. However, a bulk-defect correspondence could potentially address this issue, particularly if the bulk TSC ex-

hibits a non-zero weak index [90–94]. In Fig. 4 (a), we illustrate an edge dislocation on a 2D square lattice, characterized by a Burger vector $\boldsymbol{b} = (-1, 0)$. This configuration induces an effective $\pi$-flux, capable of trapping MZMs when

$$\boldsymbol{b} \cdot \boldsymbol{M_\nu} = 1 \, \textbf{mod} \, 2. \tag{5}$$

Here, $\boldsymbol{M_\nu}$ is defined as $\boldsymbol{M_\nu} = \nu_1 \boldsymbol{G_1} + \nu_2 \boldsymbol{G_2}$, where $\boldsymbol{G_i}$ represents the reciprocal lattice vectors, and the vector $(\nu_1, \nu_2)$ denotes the weak topological indices. These indices can be computed based on the positions of Wannier centers in our 2D system. In the case where $\Delta_o = 0$, the model in Eq. (2) preserves TRS and thus belongs to class DIII of the A-Z classification, which can be characterized by the $\mathcal{Z}_2$ topological invariant [95, 96]. The phase diagram in Fig. 4 (b) shows $\mathcal{Z}_2 = 1$ for both blue and red regions, while only the helical TSC phase in the blue region ($\mu \sim 8$) carries a weak index $(1, 1)$. Our system exhibits $C_{4z}$, leading to band inversions occurring simultaneously at $(\pi, 0)$ and $(0, \pi)$ points. Consequently, the nematicity driven by orbital fluctuations breaks $C_{4z}$, a phenomenon detectable through the bulk-defect correspondence.

We then study the bulk-defect correspondence to reveal the presence of dislocation MZMs. Performing a full tight-binding model calculation with an edge dislocation, we present the energy spectrum in Fig. 4 (c) and the wave function in Fig. 4 (d). A periodic boundary condition for both $x$ and $y$ directions has been assumed, thereby excluding the presence of Majorana corner states. Thus, Fig. 4 (d) only exhibits confined Majorana Kramers pairs at each dislocation core due to the presence of TRS. As outlined in the SM, we utilize the cut-and-glue procedure to derive the effective 1D Hamiltonian for MKPs. Firstly, the edge dislocation bisects the square lattice into two segments, as depicted in Fig. 4 (a). The low-energy edge Hamiltonian for the left segment is expressed by Eq. (4), employing the Majorana basis $\{\psi_1, \psi_2\}$. The mirror

$M_x$ symmetry leads to that for the right segment. In terms of $\{\psi_1, \psi_2, M_x\psi_2, M_x\psi_1\}$, the dislocation Hamiltonian is

$$H_{\text{dis}}(k_y) = \lambda_R k_y \varrho_z \tau_y + m_{\text{eff}} \varrho_0 \tau_x, \qquad (6)$$

where Pauli matrices $\varrho_{x,y,z}$ refer to the left and right segments. The matrix representation of $M_x$, TRS and particle-hole symmetry become $i\varrho_y\tau_x$, $i\varrho_z\tau_y\mathcal{K}$, and $\varrho_z\tau_z\mathcal{K}$, respectively. The $m_{\text{eff}}$ term breaks TRS because of the TRS-breaking $d$-wave pairing $\Delta_i$. Next, we consider the effect of the "gluing" step on $H_{\text{dis}}$, which induces the hybridization between the left and right edges due to the Rashba SOC, and thus find $m'_{\text{eff}}(y)\varrho_x\tau_y$. Once Eq. (5) is satisfied, the mass $m'_{\text{eff}}(y)$ changes sign around the dislocation core [97–103].
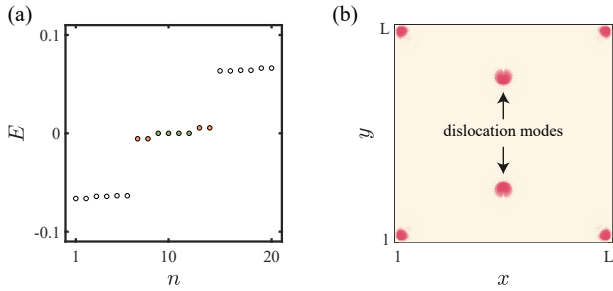
FIG. 5. (a) Energy spectrum of the square sample for TRS-breaking second-order TSC. The green dots are the fourfold degenerate zero-energy Majorana corner modes. The two pairs of orange dots are dislocation modes with a finite gap. (b) The wave function profile of the four Majorana corner modes and four dislocation modes. Common parameters: $t = 1$, $\tilde{t} = 0.2$, $t'' = 0.1$, $\mu = 7.7$, $\lambda_I = 0.5$, $\lambda_R = 0.5$, $\Delta_i = 0.1$ and $\Delta_o = 0.3$.

When $m_{\text{eff}} = 0$ for a helical $d$-wave SC, $H_{\text{dis}} = \lambda_R k_y \varrho_z \tau_y + m'_{\text{eff}}(y)\varrho_x\tau_y$ elucidates the emergence of dislocation KMPs. After further introducing $m_{\text{eff}}$ ($d+id$-wave), its anti-commutation with the $m'_{\text{eff}}$ term results in a small gap for the dislocation KMP, as TRS is broken by $\Delta_i \neq 0$ [see gap in Fig. 5 (a)]. This is inherited from the anti-commutation relations between bulk terms in Eq. (2), where the Rashba term ($\lambda_R$) anti-commutes with the $d$-wave pairing ($\Delta_i$). Despite the finite gap of KMPs, this observation indicates the bulk-defect correspondence for the second-order $d+id$ superconductor.

*Conclusions.*— We propose a theory for a $C_{4z}$ symmetry-protected second-order topological superconducting phase characterized by a $d+id$-wave pairing. It can manifest as either a topological and fully gapped superconductor (an obstructed atomic insulator with $C_{4z}$) or a nodal superconductor (protected by mirror symmetry). For the OAI case, we also explore the bulk-defect correspondence using a non-zero weak index. This orbital-dependent pairing is unique to multi-band superconductors. Some candidate materials demonstrating $d$-wave pairing and spontaneous breaking of time-reversal symmetry include: $Sr_2RuO_4$ [104], $LaPt_3$ [105], and $SrPtAs$ [106].

* These authors contributed equally to this work.
† hu.lunhui.zju@gmail.com
‡ donghuixu@cqu.edu.cn

[1] N. Read and D. Green, Paired states of fermions in two dimensions with breaking of parity and time-reversal symmetries and the fractional quantum Hall effect, Phys. Rev. B **61**, 10267 (2000).

[2] G. Volovik, Fermion zero modes on vortices in chiral superconductors, JETP. Lett. **70**, 609 (1999).

[3] D. A. Ivanov, Non-Abelian statistics of half-quantum vortices in $p$-wave superconductors, Phys. Rev. Lett. **86**, 268 (2001).

[4] A. Y. Kitaev, Unpaired Majorana fermions in quantum wires, Phys.-Usp. **44**, 131 (2001).

[5] A. Y. Kitaev, Fault-tolerant quantum computation by anyons, Ann. Phys. (Amsterdam) **303**, 2 (2003).

[6] C. Nayak, S. H. Simon, A. Stern, M. Freedman, and S. Das Sarma, Non-Abelian anyons and topological quantum computation, Rev. Mod. Phys. **80**, 1083 (2008).

[7] C. Beenakker, Search for Majorana fermions in superconductors, Annu. Rev. Condens. Matter Phys. (2011).

[8] J. Alicea, New directions in the pursuit of Majorana fermions in solid state systems, Rep. Prog. Phys. **75**, 076501 (2012).

[9] S. R. Elliott and M. Franz, Colloquium: Majorana fermions in nuclear, particle, and solid-state physics, Rev. Mod. Phys. **87**, 137 (2015).

[10] M. Sato and Y. Ando, Topological superconductors: a review, Rep. Prog. Phys. **80**, 076501 (2017).

[11] L. Fu and C. L. Kane, Superconducting proximity effect and Majorana fermions at the surface of a topological insulator, Phys. Rev. Lett. **100**, 096407 (2008).

[12] M. Sato, Y. Takahashi, and S. Fujimoto, Non-Abelian topological order in $s$-wave superfluids of ultracold fermionic atoms, Phys. Rev. Lett. **103**, 020401 (2009).

[13] J. D. Sau, R. M. Lutchyn, S. Tewari, and S. Das Sarma, Generic new platform for topological quantum computation using semiconductor heterostructures, Phys. Rev. Lett. **104**, 040502 (2010).

[14] R. M. Lutchyn, E. P. Bakkers, L. P. Kouwenhoven, P. Krogstrup, C. M. Marcus, and Y. Oreg, Majorana zero modes in superconductor–semiconductor heterostructures, Nat. Rev. Mater. **3**, 52 (2018).

[15] K. Flensberg, F. von Oppen, and A. Stern, Engineered platforms for topological superconductivity and Majorana zero modes, Nat. Rev. Mater. **6**, 944 (2021).

[16] S. Nadj-Perge, I. K. Drozdov, J. Li, H. Chen, S. Jeon, J. Seo, A. H. MacDonald, B. A. Bernevig, and A. Yazdani, Observation of Majorana fermions in ferromagnetic atomic chains on a superconductor, Science **346**, 6027 (2014).

[17] H.-H. Sun, K.-W. Zhang, L.-H. Hu, C. Li, G.-Y. Wang, H.-

Y. Ma, Z.-A. Xu, C.-L. Gao, D.-D. Guan, Y.-Y. Li, C. Liu, D. Qian, Y. Zhou, L. Fu, S.-C. Li, F.-C. Zhang, and J.-F. Jia, Majorana zero mode detected with spin selective Andreev reflection in the vortex of a topological superconductor, Phys. Rev. Lett. **116**, 257003 (2016).

[18] D. Wang, L. Kong, P. Fan, H. Chen, S. Zhu, W. Liu, L. Cao, Y. Sun, S. Du, J. Schneeloch, *et al.*, Evidence for Majorana bound states in an iron-based superconductor, Science **362**, 333 (2018).

[19] J. Langbehn, Y. Peng, L. Trifunovic, F. von Oppen, and P. W. Brouwer, Reflection-symmetric second-order topological insulators and superconductors, Phys. Rev. Lett. **119**, 246401 (2017).

[20] Z. Yan, F. Song, and Z. Wang, Majorana corner modes in a high-temperature platform, Phys. Rev. Lett. **121**, 096803 (2018).

[21] Q. Wang, C.-C. Liu, Y.-M. Lu, and F. Zhang, High-temperature majorana corner states, Phys. Rev. Lett. **121**, 186801 (2018).

[22] X. Zhu, Tunable Majorana corner states in a two-dimensional second-order topological superconductor induced by magnetic fields, Phys. Rev. B **97**, 205134 (2018).

[23] E. Khalaf, Higher-order topological insulators and superconductors protected by inversion symmetry, Phys. Rev. B **97**, 205136 (2018).

[24] M. Geier, L. Trifunovic, M. Hoskam, and P. W. Brouwer, Second-order topological insulators and superconductors with an order-two crystalline symmetry, Phys. Rev. B **97**, 205135 (2018).

[25] Y. Wang, M. Lin, and T. L. Hughes, Weak-pairing higher order topological superconductors, Phys. Rev. B **98**, 165144 (2018).

[26] T. Liu, J. J. He, and F. Nori, Majorana corner states in a two-dimensional magnetic topological insulator on a high-temperature superconductor, Phys. Rev. B **98**, 245413 (2018).

[27] C.-H. Hsu, P. Stano, J. Klinovaja, and D. Loss, Majorana Kramers pairs in higher-order topological insulators, Phys. Rev. Lett. **121**, 196801 (2018).

[28] H. Shapourian, Y. Wang, and S. Ryu, Topological crystalline superconductivity and second-order topological superconductivity in nodal-loop materials, Phys. Rev. B **97**, 094508 (2018).

[29] Y. Volpez, D. Loss, and J. Klinovaja, Second-order topological superconductivity in $\pi$-junction Rashba layers, Phys. Rev. Lett. **122**, 126402 (2019).

[30] X.-H. Pan, K.-J. Yang, L. Chen, G. Xu, C.-X. Liu, and X. Liu, Lattice-symmetry-assisted second-order topological superconductors and Majorana patterns, Phys. Rev. Lett. **123**, 156801 (2019).

[31] S. Franca, D. V. Efremov, and I. C. Fulga, Phase-tunable second-order topological superconductor, Phys. Rev. B **100**, 075415 (2019).

[32] Z. Yan, Higher-order topological odd-parity superconductors, Phys. Rev. Lett. **123**, 177001 (2019).

[33] C. Zeng, T. D. Stanescu, C. Zhang, V. W. Scarola, and S. Tewari, Majorana corner modes with solitons in an attractive Hubbard-Hofstadter model of cold atom optical lattices, Phys. Rev. Lett. **123**, 060402 (2019).

[34] X. Zhu, Second-order topological superconductors with mixed pairing, Phys. Rev. Lett. **122**, 236401 (2019).

[35] N. Bultinck, B. A. Bernevig, and M. P. Zaletel, Three-dimensional superconductors with hybrid higher-order topology, Phys. Rev. B **99**, 125149 (2019).

[36] R.-X. Zhang, W. S. Cole, and S. Das Sarma, Helical hinge Majorana modes in iron-based superconductors, Phys. Rev. Lett. **122**, 187001 (2019).

[37] R.-X. Zhang, W. S. Cole, X. Wu, and S. Das Sarma, Higher-order topology and nodal topological superconductivity in Fe(Se,Te) heterostructures, Phys. Rev. Lett. **123**, 167001 (2019).

[38] Z. Wu, Z. Yan, and W. Huang, Higher-order topological superconductivity: Possible realization in fermi gases and $Sr_2RuO_4$, Phys. Rev. B **99**, 020508 (2019).

[39] S. A. A. Ghorashi, X. Hu, T. L. Hughes, and E. Rossi, Second-order Dirac superconductors and magnetic field induced Majorana hinge modes, Phys. Rev. B **100**, 020509 (2019).

[40] Z. Yan, Majorana corner and hinge modes in second-order topological insulator/superconductor heterostructures, Phys. Rev. B **100**, 205406 (2019).

[41] Y. Peng and Y. Xu, Proximity-induced Majorana hinge modes in antiferromagnetic topological insulators, Phys. Rev. B **99**, 195431 (2019).

[42] Y. You, D. Litinski, and F. von Oppen, Higher-order topological superconductors as generators of quantum codes, Phys. Rev. B **100**, 054513 (2019).

[43] Y.-T. Hsu, W. S. Cole, R.-X. Zhang, and J. D. Sau, Inversion-protected higher-order topological superconductivity in monolayer $WTe_2$, Phys. Rev. Lett. **125**, 097001 (2020).

[44] X. Wu, W. A. Benalcazar, Y. Li, R. Thomale, C.-X. Liu, and J. Hu, Boundary-obstructed topological high-$T_c$ superconductivity in iron pnictides, Phys. Rev. X **10**, 041014 (2020).

[45] M. Kheirkhah, Z. Yan, Y. Nagai, and F. Marsiglio, First- and second-order topological superconductivity and temperature-driven topological phase transitions in the extended Hubbard model with spin-orbit coupling, Phys. Rev. Lett. **125**, 017001 (2020).

[46] M. Kheirkhah, Y. Nagai, C. Chen, and F. Marsiglio, Majorana corner flat bands in two-dimensional second-order topological superconductors, Phys. Rev. B **101**, 104502 (2020).

[47] Y.-J. Wu, J. Hou, Y.-M. Li, X.-W. Luo, X. Shi, and C. Zhang, In-plane Zeeman-field-induced Majorana corner and hinge modes in an $s$-wave superconductor heterostructure, Phys. Rev. Lett. **124**, 227001 (2020).

[48] J. Ahn and B.-J. Yang, Higher-order topological superconductivity of spin-polarized fermions, Phys. Rev. Research **2**, 012060 (2020).

[49] S.-B. Zhang, W. B. Rui, A. Calzona, S.-J. Choi, A. P. Schnyder, and B. Trauzettel, Topological and holonomic quantum computation based on second-order topological superconductors, Phys. Rev. Research **2**, 043025 (2020).

[50] S.-B. Zhang and B. Trauzettel, Detection of second-order topological superconductors by Josephson junctions, Phys. Rev. Research **2**, 012018 (2020).

[51] B. Roy, Higher-order topological superconductors in $\mathcal{P}$-, $\mathcal{T}$-odd quadrupolar Dirac materials, Phys. Rev. B **101**, 220506 (2020).

[52] S. A. A. Ghorashi, T. L. Hughes, and E. Rossi, Vortex and surface phase transitions in superconducting higher-order topological insulators, Phys. Rev. Lett. **125**, 037001 (2020).

[53] T. E. Pahomi, M. Sigrist, and A. A. Soluyanov, Braiding majorana corner modes in a second-order topological superconductor, Phys. Rev. Research **2**, 032068 (2020).

[54] A. Tiwari, A. Jahin, and Y. Wang, Chiral Dirac superconductors: Second-order and boundary-obstructed topology, Phys. Rev. Research **2**, 043300 (2020).

[55] F. Schindler, B. Bradlyn, M. H. Fischer, and T. Neupert, Pairing obstructions in topological superconductors, Phys. Rev. Lett. **124**, 247001 (2020).

[56] B. Roy and V. Juričić, Mixed-parity octupolar pairing and corner Majorana modes in three dimensions, Phys. Rev. B **104**, L180503 (2021).

[57] D. Varjas, A. Lau, K. Pöyhönen, A. R. Akhmerov, D. I. Pikulin, and I. C. Fulga, Topological phases without crystalline counterparts, Phys. Rev. Lett. **123**, 196401 (2019).

[58] R. Chen, C.-Z. Chen, J.-H. Gao, B. Zhou, and D.-H. Xu, Higher-order topological insulators in quasicrystals, Phys. Rev. Lett. **124**, 036803 (2020).

[59] C.-A. Li, S.-B. Zhang, J. Li, and B. Trauzettel, Higher-order Fabry-Pérot interferometer from topological hinge states, Phys. Rev. Lett. **127**, 026803 (2021).

[60] B. Fu, Z.-A. Hu, C.-A. Li, J. Li, and S.-Q. Shen, Chiral Majorana hinge modes in superconducting Dirac materials, Phys. Rev. B **103**, L180504 (2021).

[61] S. Ikegaya, W. B. Rui, D. Manske, and A. P. Schnyder, Tunable Majorana corner modes in noncentrosymmetric superconductors: Tunneling spectroscopy and edge imperfections, Phys. Rev. Research **3**, 023007 (2021).

[62] S. Qin, C. Fang, F.-C. Zhang, and J. Hu, Topological superconductivity in an extended $s$-wave superconductor and its implication to iron-based superconductors, Phys. Rev. X **12**, 011030 (2022).

[63] H. D. Scammell, J. Ingham, M. Geier, and T. Li, Intrinsic first- and higher-order topological superconductivity in a doped topological insulator, Phys. Rev. B **105**, 195149 (2022).

[64] Z. Wu and Y. Wang, Nodal higher-order topological superconductivity from a c 4-symmetric dirac semimetal, Physical Review B **106**, 214510 (2022).

[65] M. Amundsen and V. Juričić, Controlling majorana modes by p-wave pairing in two-dimensional p+ i d topological superconductors, Physical Review Research **4**, 013088 (2022).

[66] X.-J. Luo, X.-H. Pan, and X. Liu, Higher-order topological superconductors based on weak topological insulators, Phys. Rev. B **104**, 104510 (2021).

[67] T. T. Ong and P. Coleman, Tetrahedral and orbital pairing: A fully gapped pairing scenario for the iron-based superconductors, Phys. Rev. Lett. **111**, 217003 (2013).

[68] T. Ong, P. Coleman, and J. Schmalian, Concealed d-wave pairs in the s±condensate of iron-based superconductors, Proc. Natl. Acad. Sci. U.S.A. **113**, 5486 (2016).

[69] E. M. Nica, R. Yu, and Q. Si, Orbital-selective pairing and superconductivity in iron selenides, npj Quantum Materials **2**, 24 (2017).

[70] M. Zeng, D.-H. Xu, Z.-M. Wang, and L.-H. Hu, Spin-orbit coupled superconductivity with spin-singlet nonunitary pairing, Phys. Rev. B **107**, 094507 (2023).

[71] T. Nakayama, T. Shishidou, and D. F. Agterberg, Nodal topology in $d$-wave superconducting monolayer fese, Phys. Rev. B **98**, 214503 (2018).

[72] E. M. Nica and Q. Si, Multiorbital singlet pairing and d+ d superconductivity, npj Quantum Materials **6**, 3 (2021).

[73] M. Smidman, O. Stockert, E. M. Nica, Y. Liu, H. Yuan, Q. Si, and F. Steglich, Colloquium: Unconventional fully gapped superconductivity in the heavy-fermion metal cecu2si2, Rev. Mod. Phys. **95**, 031002 (2023).

[74] R.-J. Slager, A. Mesaros, V. Juričić, and J. Zaanen, The space group classification of topological band-insulators, Nature Physics **9**, 98 (2013).

[75] J. Kruthoff, J. De Boer, J. Van Wezel, C. L. Kane, and R.-J. Slager, Topological classification of crystalline insulators through band structure combinatorics, Physical Review X **7**, 041069 (2017).

[76] B. Bradlyn, L. Elcoro, J. Cano, M. G. Vergniory, Z. Wang, C. Felser, M. I. Aroyo, and B. A. Bernevig, Topological quantum chemistry, Nature **547**, 298 (2017).

[77] L. Elcoro, B. Bradlyn, Z. Wang, M. G. Vergniory, J. Cano, C. Felser, B. A. Bernevig, D. Orobengoa, G. de la Flor, and M. I. Aroyo, Double crystallographic groups and their representations on the Bilbao Crystallographic Server, Journal of Applied Crystallography **50**, 1457 (2017).

[78] M. G. Vergniory, L. Elcoro, Z. Wang, J. Cano, C. Felser, M. I. Aroyo, B. A. Bernevig, and B. Bradlyn, Graph theory data for topological quantum chemistry, Phys. Rev. E **96**, 023310 (2017).

[79] J. Cano, B. Bradlyn, Z. Wang, L. Elcoro, M. G. Vergniory, C. Felser, M. I. Aroyo, and B. A. Bernevig, Building blocks of topological quantum chemistry: Elementary band representations, Phys. Rev. B **97**, 035139 (2018).

[80] H. C. Po, A. Vishwanath, and H. Watanabe, Symmetry-based indicators of band topology in the 230 space groups, Nature Communications **8**, 50 (2017).

[81] B. Bradlyn, L. Elcoro, J. Cano, M. G. Vergniory, Z. Wang, C. Felser, M. I. Aroyo, and B. A. Bernevig, Topological quantum chemistry, Nature **547**, 298 (2017).

[82] L. Elcoro, B. J. Wieder, Z. Song, Y. Xu, B. Bradlyn, and B. A. Bernevig, Magnetic topological quantum chemistry, Nature Communications **12**, 10.1038/s41467-021-26241-8 (2021).

[83] J. Zak, Symmetry specification of bands in solids, Phys. Rev. Lett. **45**, 1025 (1980).

[84] J. Zak, Band representations and symmetry types of bands in solids, Phys. Rev. B **23**, 2824 (1981).

[85] J. Zak, Band representations of space groups, Phys. Rev. B **26**, 3010 (1982).

[86] Z.-D. Song, L. Elcoro, and B. A. Bernevig, Twisted bulk-boundary correspondence of fragile topology, Science **367**, 794 (2020), https://www.science.org/doi/pdf/10.1126/science.aaz7650.

[87] Y. Xu, L. Elcoro, Z.-D. Song, M. G. Vergniory, C. Felser, S. S. P. Parkin, N. Regnault, J. L. Mañes, and B. A. Bernevig, Filling-enforced obstructed atomic insulators (2021), arXiv:2106.10276 [cond-mat.mtrl-sci].

[88] C.-K. Chiu and A. P. Schnyder, Classification of reflection-symmetry-protected topological semimetals and nodal superconductors, Phys. Rev. B **90**, 205136 (2014).

[89] R. Jackiw and C. Rebbi, Solitons with fermion number ½, Phys. Rev. D **13**, 3398 (1976).

[90] D. Asahi and N. Nagaosa, Topological indices, defects, and majorana fermions in chiral superconductors, Phys. Rev. B **86**, 100504 (2012).

[91] J. C. Y. Teo and T. L. Hughes, Existence of majorana-fermion bound states on disclinations and the classification of topological crystalline superconductors in two dimensions, Phys. Rev. Lett. **111**, 047006 (2013).

[92] T. L. Hughes, H. Yao, and X.-L. Qi, Majorana zero modes in dislocations of sr2ruo4, Phys. Rev. B **90**, 235123 (2014).

[93] W. A. Benalcazar, J. C. Y. Teo, and T. L. Hughes, Classification of two-dimensional topological crystalline superconductors and majorana bound states at disclinations, Phys. Rev. B **89**, 224503 (2014).

[94] D. Asahi and N. Nagaosa, Topological indices, defects, and majorana fermions in chiral superconductors, Phys. Rev. B **86**, 100504 (2012).

[95] A. Altland and M. R. Zirnbauer, Nonstandard symmetry classes in mesoscopic normal-superconducting hybrid structures, Phys. Rev. B **55**, 1142 (1997).

[96] C.-K. Chiu, J. C. Y. Teo, A. P. Schnyder, and S. Ryu, Classification of topological quantum matter with symmetries, Rev. Mod. Phys. **88**, 035005 (2016).

[97] L.-H. Hu and R.-X. Zhang, Dislocation majorana bound states in iron-based superconductors, Nature Communications **15**,

2337 (2024).

[98] R.-X. Zhang, Bulk-vortex correspondence of higher-order topological superconductors (2022), arXiv:2208.01652 [cond-mat.str-el].

[99] J. C. Teo and T. L. Hughes, Topological defects in symmetry-protected topological phases, Annual Review of Condensed Matter Physics **8**, 211 (2017).

[100] D. Asahi and N. Nagaosa, Topological indices, defects, and majorana fermions in chiral superconductors, Phys. Rev. B **86**, 100504 (2012).

[101] W. A. Benalcazar, J. C. Y. Teo, and T. L. Hughes, Classification of two-dimensional topological crystalline superconductors and majorana bound states at disclinations, Phys. Rev. B **89**, 224503 (2014).

[102] S. B. Chung, C. Chan, and H. Yao, Dislocation majorana zero modes in perovskite oxide 2deg, Scientific Reports **6**, 25184

(2016).

[103] Y. Ran, Y. Zhang, and A. Vishwanath, One-dimensional topologically protected modes in topological insulators with lattice dislocations, Nature Physics **5**, 298 (2009).

[104] A. Steppke, L. Zhao, M. E. Barber, T. Scaffidi, F. Jerzembeck, H. Rosner, A. S. Gibbs, Y. Maeno, S. H. Simon, A. P. Mackenzie, *et al.*, Strong peak in t c of sr2ruo4 under uniaxial pressure, Science **355**, eaaf9398 (2017).

[105] P. K. Biswas, S. K. Ghosh, J. Zhao, D. A. Mayoh, N. Zhigadlo, X. Xu, C. Baines, A. Hillier, G. Balakrishnan, and M. R. Lees, Chiral singlet superconductivity in the weakly correlated metal lapt3p, Nat. Commun. **12**, 2504 (2021).

[106] M. H. Fischer, T. Neupert, C. Platt, A. P. Schnyder, W. Hanke, J. Goryo, R. Thomale, and M. Sigrist, Chiral $d$-wave superconductivity in srptas, Phys. Rev. B **89**, 020509 (2014).

# Supplemental Material to: "Theory of $d + id$ Second-Order Topological Superconductors: Possible Application to Sr$_2$RuO$_4$"

Zi-Ming Wang,[1, *] Meng Zeng,[2, *] Chen Lu,[3, *] Da-Shuai Ma,[1] Rui-Xing Zhang,[4,5] Lun-Hui Hu,[4, †] and Dong-Hui Xu[1,6, ‡]

[1] *Department of Physics and Chongqing Key Laboratory for Strongly Coupled Physics, Chongqing University, Chongqing 400044, China*
[2] *Department of Physics, University of California, San Diego, California 92093, USA*
[3] *School of Physics and Technology, Wuhan University, Wuhan 430072, China*
[4] *Department of Physics and Astronomy, University of Tennessee, Knoxville, Tennessee 37996, USA*
[5] *Department of Materials Science and Engineering, University of Tennessee, Knoxville, Tennessee 37996, USA*
[6] *Center of Quantum Materials and Devices, Chongqing University, Chongqing 400044, China*

## SYMMETRY ANALYSIS

For our model, we use the normal state Hamiltonian Eq. (1) of the two-orbital square lattice in the main text to describe a metallic material with space group $P4mm$, which breaks inversion symmetry and twofold rotation symmetry along the $x$ or $y$ directions by incorporating orbital-dependent hopping terms: the lattice nematic term $\widetilde{\epsilon}(\boldsymbol{k})$ and the orbital-hybridization next-nearest-neighbor hopping term $\epsilon''(\boldsymbol{k})$. Furthermore, we add spin-orbit coupling terms, including the intrinsic term $\lambda_I$ and the Rashba term $\lambda_{\mathrm{R}} \sin k_x s_y - \lambda_{\mathrm{R}} \sin k_y s_x$. The symmetries of the normal state include time-reversal symmetry $\mathcal{T} = i\sigma_0 s_y \mathcal{K}$, fourfold rotation $r_{4z} = i\sigma_y e^{-i\pi s_z/4}$, and mirror symmetries $m_x = i\sigma_z s_x$. Notice that under $r_{4z}$, the normal state Hamiltonian satisfies $r_{4z} H_\mathrm{n}(k_x, k_y) r_{4z}^{-1} = H_\mathrm{n}(-k_y, k_x)$.

The $d$-wave $B_{1g} + iB_{1g}$ superconducting pairing is allowed in magnetic materials. There could be a phase difference $\phi$ between the two gap functions, and we choose the $d+id$ pairing to be $\Delta(\boldsymbol{k}) = [\Delta_\mathrm{i} \Phi(\boldsymbol{k}) \sigma_0 + \Delta_\mathrm{o}(\boldsymbol{d}_\mathrm{o}(\boldsymbol{k}) \cdot \boldsymbol{\sigma})] is_y$, where $\Phi(\boldsymbol{k}) = i(-2\cos k_x + 2\cos k_y)$, and the uniform orbital-dependent pairing is chosen as $\boldsymbol{d}_\mathrm{o}(\boldsymbol{k}) \cdot \boldsymbol{\sigma} = \sigma_z$. This means two $d$-wave pairings have the phase difference equal to $\pi/2$, which breaks time-reversal symmetry (TRS). The full BdG Hamiltonian is given by

$$
\begin{aligned}
H = & (4t - 2t\cos k_x - 2t\cos k_y - \mu)\tau_z\sigma_0 s_0 + (-2\widetilde{t}\cos k_x + 2\widetilde{t}\cos k_y)\tau_z\sigma_z s_0 + 4t''\sin k_x \sin k_y \tau_z\sigma_x s_0 \\
& + \lambda_{\mathrm{R}} \sin k_x \tau_z\sigma_0 s_y - \lambda_{\mathrm{R}} \sin k_y \tau_0\sigma_0 s_x + \lambda_{\mathrm{I}}\tau_0\sigma_y s_z + (2\Delta_\mathrm{i}\cos k_x - 2\Delta_\mathrm{i}\cos k_y)\tau_x\sigma_0 s_y - \Delta_\mathrm{o}\tau_y\sigma_z s_y.
\end{aligned} \tag{S1}
$$

In Nambu basis, the symmetries of BdG Hamiltonian are particle-hole symmetry $\Xi = \tau_x\sigma_0 s_0 \mathcal{K}$, fourfold rotation $C_{4z} = r_{4z} \oplus -r_{4z}^*$, and mirror symmetry $M_x = i\tau_z\sigma_z s_x$. The $d$-wave pairing break TRS $\Theta = \tau_0\sigma_0 s_y \mathcal{K}$.

We look at the elementary band representations (EBRs) under the $C_{4z}$ rotation symmetry of our model. The eigenvalue $c_{4z}^n(K_i)$ of the $C_{4z}$ symmetry for the occupied states is given by $c_{4z}^n(K_i)|u_{K_i}^n\rangle = C_{4z}|u_{K_i}^n\rangle$ at the high-symmetry point $K_i$, where $n = 1, 2, 3, 4$ represents the label of occupied bands. The eigenvalue $c_{2z}(K_i)$ is also given by $c_{2z}^n(K_i)|u_{K_i}^n\rangle = C_{4z}^2|u_{K_i}^n\rangle$. According to Table S1, the higher-order topological phase and the trivial phase can be distinguished by the different EBRs at the high-symmetry points ($\Gamma$, $M$ and $X$). The irreps have shown the Wannier center localized at Wyckoff position $a$ of the trivial phase and shifted to Wyckoff position $b$ of the second-order TSC phase.

TABLE S1. The EBRs of space group $P4mm$ with SOC and without TRS. The first row and second row are the label for the Wyckoff positions and irreps for $P4mm$. The third row to fifth row show the little group representations at $\Gamma$ and $M$-point which are defined by rotational symmetry $C_{4z}$, and the representations at $X$-point are defined by $C_{2z}$.

| WPs | $1a$ (000) | | $1b$ ($\frac{1}{2}\frac{1}{2}0$) | |
|---|---|---|---|---|
| EBRs | $\overline{E}_1 \uparrow G(2)$ | $\overline{E}_2 \uparrow G(2)$ | $\overline{E}_1 \uparrow G(2)$ | $\overline{E}_2 \uparrow G(2)$ |
| Orbitals | $s$ | $p_z$ | $s$ | $p_z$ |
| $\overline{\Gamma}$ (000) | $\overline{\Gamma}_7(2)$ | $\overline{\Gamma}_6(2)$ | $\overline{\Gamma}_7(2)$ | $\overline{\Gamma}_6(2)$ |
| $\overline{X}$ ($\frac{1}{2}00$) | $\overline{X}_5(2)$ | $\overline{X}_5(2)$ | $\overline{X}_5(2)$ | $\overline{X}_5(2)$ |
| $\overline{M}$ ($\frac{1}{2}\frac{1}{2}0$) | $\overline{M}_7(2)$ | $\overline{M}_6(2)$ | $\overline{M}_6(2)$ | $\overline{M}_7(2)$ |

## NODAL SUPERCONDUTOR PHASE

In the main text, we illustrate the higher-order phase transition from the $d$-wave nodal superconductor by varying $\Delta_\mathrm{o}$ and $\mu$, while keeping $\Delta_\mathrm{i}$ constant. In the nodal d-wave superconductor, four pairs of Weyl nodes emerge along two mirror high-symmetry
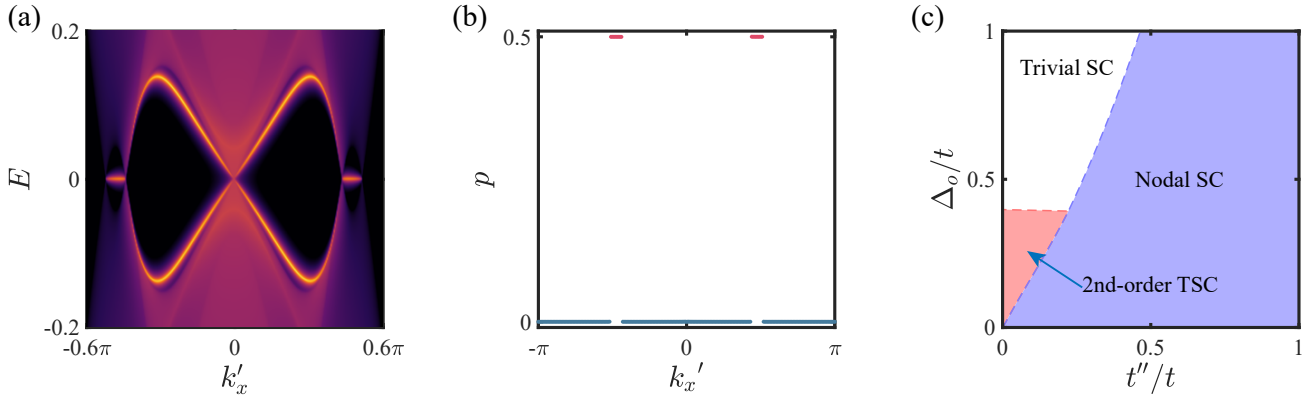
FIG. S1. Nodal superconductor phase in the $d+id$ superconductor system. (a) Spectrum of the open boundary along $[1\bar{1}]$ direction of the $d+id$ nodal superconductor while $t'' = 0.2$ and $\Delta_o = 0.3$. (b) The $k'_x$-dependent polarization $p$ of the nodal phase. The red and blue dots represent different values of polarization $p$. (c) Phase diagram of the nodal SC and the HOTSC with varying $\Delta_o$ and $t''$. The blue and red regions indicate the nodal SC phase and the HOTSC phase respectively. The white region denotes the trivial SC phase. Common parameters: $t = 1$, $\tilde{t} = 0.2$, $\mu = 0.3$, $\lambda_I = 0.5$, $\lambda_R = 0.5$, $\Delta_i = 0.1$.

lines from the $\Gamma$-point to the $M$-point. The nodal phase hosts Fermi arc edge states with open boundaries along the $x$ or $y$ axis and there are four Weyl nodes and two flat band Fermi arcs link each pair of Weyl nodes with open boundaries along the $[1\bar{1}]$ direction, as shown in Fig. S1(a). In the 2D system, we can use bulk polarization to characterize the flat band edge states as the momentum-dependent Chern number in the 3D Weyl nodal phase using the Wilson loop method. There are two quantized plateaus of $p$ correspond to two segments of flat band edge states in Fig. S1(b).

Notice, the contribution to bulk polarization from two unpaired Fermi arcs will be zero when the nodal phase indicator is calculated in the one-dimensional effective Hamiltonian $H_{k_x}(k_y)$ by treating $k_y$ as a parameter. Now, we rotate $\pi/4$ of $(k_x, k_y)$ under the rectangular coordinate system to $(k'_x, k'_y)$ and reduce the effective Hamiltonian $H_{k_x}(k_y)$ to $H_{k'_x}(k'_y)$, where

$$k'_x = \frac{1}{\sqrt{2}}(k_x + k_y), \qquad k'_y = \frac{1}{\sqrt{2}}(-k_x + k_y). \tag{S2}$$

Therefore, the bulk polarization along the different directions $i, j$ can be written as

$$p(k_j) = -\frac{1}{2\pi} \int_0^{2\pi} \mathbf{Tr}[\mathcal{A}_{\mathbf{k}}] dk_i, \tag{S3}$$

where the $\mathcal{A}_{\mathbf{k}}^{\alpha\beta} = -i \langle u_{\mathbf{k}}^{\alpha}| \partial_{\mathbf{k}} |u_{\mathbf{k}}^{\beta}\rangle$ is the non-Abelian Berry connection, and $\alpha$, $\beta$ label the occupied energy bands. Fig. S1(b) display the bulk polarization along the $k'_x$ that is quantized as $1/2$ between a pair of Weyl nodes and vanished at other $k'_x$. The $k'_x$-dependent polarization $p$ can characterize the nodal superconductor phase, and the plateau of quantized polarization corresponds to the flat band edge states in Fig. S1(a).

Next, we discuss the effect of this $d+id$ wave superconductor due to next-nearest neighbor hopping $t''$. Consider the simplified nodal phase while $\Delta_o \neq 0$, the system becomes a $d$-wave Dirac superconductor with $\lambda_R = 0$. We choose a pair of Dirac nodes along the $k_x = k_y = k_0$ line, the low-energy continuum nodal phase Hamiltonian $H(k_x, k_y)$ around the $\Gamma$-point as

$$H_{\text{Nodal}}(\mathbf{k}) = (2tk_0^2 - \mu)\tau_z\sigma_0 s_0 + (4t''k_0^2)\tau_z\sigma_x s_0 + \lambda_I\tau_0\sigma_y s_z - \Delta_o\tau_y\sigma_z s_y. \tag{S4}$$

There are two four-fold degenerate nodes at $k_0 = \pm\sqrt{t\mu + \sqrt{4t''^2\mu^2 - (t^2 - 4t''^2)(\Delta_o^2 - \lambda_I^2)}}/\sqrt{2(t^2 - 4t''^2)}$ along the mirror line, if $t'' < \frac{t\sqrt{\Delta_o^2 - \lambda_I^2}}{2\sqrt{\Delta_o^2 - \lambda_I^2 + \mu^2}}$ and $\Delta_o^2 > \lambda_I^2$.

If we further introduce the Rashba SOC $\lambda_R$, then there could be a HOTSC phase appearing in the phase diagram shown in Figure S1(c).

**EDGE THEROY**

In this section, we discuss the edge theory of the other edges for the $d+id$-wave pairing. The edges along the $y$ direction on the left side, along the $x$ direction on the bottom, the right side along the $x$-axis, and the top side along the $y$ axis of the sample are

called the I, II, III, and IV edges. To understand the effect of each edge by the $d + id$-wave pairing, we consider the simplified case of the low-energy Hamiltonian as

$$H\left(\boldsymbol{k}\right) = (tk_x^2 + tk_y^2 - \mu)\tau_z\sigma_0 s_0 + \lambda_\mathrm{R} k_x \tau_z \sigma_0 s_y - \lambda_\mathrm{R} k_y \tau_0 \sigma_0 s_x + \lambda_\mathrm{I} \tau_0 \sigma_y s_z + (\Delta_\mathrm{i} k_x^2 - \Delta_\mathrm{i} k_y^2)\tau_x \sigma_0 s_y - \Delta_\mathrm{o} \tau_y \sigma_z s_y. \quad \text{(S5)}$$

For simplicity, we can set the chemical potential $\mu = 0$. The effective Hamiltonian of edge I is given in Eq. (4) of the main text. For the edge II, the Hamiltonian is decomposed as $H(k_x, -i\partial_y) = H_0 + H'$, where

$$
\begin{aligned}
H_0 &= -\mu\tau_z\sigma_0 s_0 + i\lambda_\mathrm{R}\partial_y\tau_0\sigma_0 s_x + \lambda_\mathrm{I}\tau_0\sigma_y s_z - \Delta_\mathrm{o}\tau_y\sigma_z s_y. \\
H' &= -t\partial_y^2\tau_z\sigma_0 s_0 + \lambda_\mathrm{R} k_x \tau_z \sigma_0 s_y + \Delta_\mathrm{i}\partial_y^2\tau_x\sigma_0 s_y.
\end{aligned}
\quad \text{(S6)}
$$

To create the domain wall at $y = 0$, we can use the ansatz $\psi(y) = \mathcal{N}e^{-\eta(y)y}\xi$ for the zero modes, where $\eta_U \equiv \eta(y > 0) > 0$ and $\eta_D \equiv \eta(y < 0) < 0$ since the bulk on both sides of the domain wall is gapped, and $\xi$ is the spinor part. The zero modes can be found by solving the eigenvalue equation $H_0\phi(y) = 0$ which $\eta = \frac{-\Delta_\mathrm{o}+\lambda_\mathrm{I}}{\lambda_\mathrm{R}}$ for the non-trivial phase. Following two corresponding zero modes, we have the solution

$$\psi_{1,2}(y) = \mathcal{N}e^{-\eta(y)y}\varkappa_{1,2}, \quad \text{(S7)}$$

with the normalization constant given by $\mathcal{N} = \sqrt{\frac{2\eta_U\eta_D}{\eta_D-\eta_U}}$. The two orthonormal solutions for the spinor part are as

$$
\begin{aligned}
\varkappa_1 &= \frac{1}{2}(1, 0, 0, 1, i, 0, 0, i)^\mathrm{T} \\
\varkappa_2 &= \frac{1}{2}(0, -1, 1, 0, 0, i, -i, 0)^\mathrm{T}.
\end{aligned}
\quad \text{(S8)}
$$

In this basis, the matrix elements of the perturbation $H'$ are

$$H_{\mathrm{II},\alpha\beta}(k_x) = \int_0^{+\infty} dy\,\psi_{1,2}^*(y)H'\psi_{1,2}(y). \quad \text{(S9)}$$

The effective Hamiltonian is

$$H_\mathrm{II}(k_x) = -|\mathcal{N}|^2\lambda_\mathrm{R} k_x \zeta_y - m_\mathrm{eff}\zeta_x, \quad \text{(S10)}$$

where $m_\mathrm{eff} = -|\mathcal{N}|^2\frac{\Delta_\mathrm{i}\delta\Delta_\mathrm{o}}{2\lambda_\mathrm{R}}$ is the effective mass, $\zeta_i$ are Pauli matrices in this basis.

Similarly, for the edge III, the Hamiltonian is decomposed as $H(-i\partial_x, k_y) = H_0 + H'$, where

$$
\begin{aligned}
H_0 &= -\mu\tau_z\sigma_0 s_0 - i\lambda_\mathrm{R}\partial_x\tau_z\sigma_0 s_y + \lambda_\mathrm{I}\tau_0\sigma_y s_z - \Delta_\mathrm{o}\tau_y\sigma_z s_y. \\
H' &= -t\partial_x^2\tau_z\sigma_0 s_0 - \lambda_\mathrm{R} k_y \tau_0 \sigma_0 s_x - \Delta_\mathrm{i}\partial_x^2\tau_x\sigma_0 s_y.
\end{aligned}
\quad \text{(S11)}
$$

In the bulk, we can use the ansatz $\psi(x) = \mathcal{N}e^{\gamma(x)x}\widetilde{\chi}$ for the zero modes, where $\gamma_\mathrm{R} \equiv \gamma(x > 0) < 0$ and $\gamma_\mathrm{L} \equiv \gamma(x < 0) > 0$ since the bulk on both sides of the domain wall is gapped, and $\widetilde{\chi}$ is the spinor part. We also have the solution

$$\psi_{1,2}(x) = \mathcal{N}e^{\gamma(x)x}\widetilde{\chi}_{1,2}, \quad \text{(S12)}$$

with the normalization constant given by $\mathcal{N} = \sqrt{\frac{2\gamma_\mathrm{R}\gamma_\mathrm{L}}{\gamma_\mathrm{L}-\gamma_\mathrm{R}}}$. The two orthonormal solutions for the spinor part are as

$$
\begin{aligned}
\widetilde{\chi}_1 &= \frac{1}{2}(i, 0, 0, -1, -i, 0, 0, -1)^\mathrm{T} \\
\widetilde{\chi}_2 &= \frac{1}{2}(0, 1, i, 0, 0, -1, i, 0)^\mathrm{T}.
\end{aligned}
\quad \text{(S13)}
$$

Then the effective Hamiltonian is

$$H_\mathrm{III}(k_y) = -|\mathcal{N}|^2\lambda_\mathrm{R} k_y \zeta_y + m_\mathrm{eff}\zeta_x. \quad \text{(S14)}$$

Similarly, for the edge IV, the effective Hamiltonian is

$$H_\mathrm{IV}(k_x) = |\mathcal{N}|^2\lambda_\mathrm{R} k_x \zeta_y - m_\mathrm{eff}\zeta_x. \quad \text{(S15)}$$

For the $d + id$-wave pairing, the effective Hamiltonian of the four edges are

$$
\begin{aligned}
H_{\mathrm{I}}(k_y) &= |\mathcal{N}|^2 \lambda_{\mathrm{R}} k_y \zeta_y + m_{\mathrm{eff}} \zeta_x, \\
H_{\mathrm{II}}(k_x) &= -|\mathcal{N}|^2 \lambda_{\mathrm{R}} k_x \zeta_y - m_{\mathrm{eff}} \zeta_x, \\
H_{\mathrm{III}}(k_y) &= -|\mathcal{N}|^2 \lambda_{\mathrm{R}} k_y \zeta_y + m_{\mathrm{eff}} \zeta_x, \\
H_{\mathrm{IV}}(k_x) &= |\mathcal{N}|^2 \lambda_{\mathrm{R}} k_x \zeta_y - m_{\mathrm{eff}} \zeta_x.
\end{aligned}
\tag{S16}
$$

where $m_{\mathrm{eff}} = -|\mathcal{N}|^2 \frac{\Delta_{\mathrm{i}} \delta \Delta_{\mathrm{o}}}{2\lambda_{\mathrm{R}}}$. The mass terms have opposite signs on arbitrary two neighboring edges, giving rise to zeros modes a the corners. This explains the appearance of four Majorana corner modes.

## MIRROR SYMMETRY OF TOPOLOGICAL DEFECT

The edge or screw dislocation can induce topological defect modes in 3D weak TIs or weak TSC materials. In our work, we distinguish the strong and weak topological phase in the 2D case by Wannier center in momentum space, and show the existence of dislocation Majorana zero modes claimed in the main text. For the dislocation area, which is effectively an 1D chain which, the 1D Jackiw-Rebbi domain wall is helpful to understand the localized Majorana zero mode. Before the Volterra glue, the Volterra cut create two boundaries that are bridged by a line of atoms ending at two dislocation cores.

If the edge dislocation is along the $y$ direction, the two boundaries respect mirror symmetry $M_x$. The effective Hamiltonian on each side follows from previous discussion on edge theory. Considering both sides of the dislocation, the basis is $\widetilde{X} = (\chi_1, \chi_2, \widetilde{\chi}_1, \widetilde{\chi}_2) = (\chi_1, \chi_2, M_x \chi_2, M_x \chi_1)$. At the line defect, the perturbation part $H_V'$ is

$$
H_V' = -t \partial_x^2 \tau_z \sigma_0 s_0 - \lambda_{\mathrm{R}} k_y \tau_0 \sigma_0 s_x - \Delta_{\mathrm{i}} \partial_x^2 \tau_x \sigma_0 s_y,
\tag{S17}
$$

and the effective Hamiltonian is

$$
H_V(k_y) = |\mathcal{N}|^2 \lambda_{\mathrm{R}} k_y \rho_z \zeta_y + m_{\mathrm{eff}} \rho_0 \zeta_x,
\tag{S18}
$$

where $\rho_i$ are Pauli matrices in mirror symmetry subspace. The mass term opens a bulk gap. In the area of two boundaries bridging by a line of atoms, the perturbation part $H_B'$ is

$$
H_B' = -t \partial_x^2 \tau_z \sigma_0 s_0 + \lambda_{\mathrm{R}} \tau_z \sigma_0 s_y - \lambda_{\mathrm{R}} k_y \tau_0 \sigma_0 s_x - \Delta_{\mathrm{i}} \partial_x^2 \tau_x \sigma_0 s_y.
\tag{S19}
$$

Here, $\lambda_{\mathrm{R}} \tau_z \sigma_0 s_y$ term provides the hopping between two boundaries. The effective Hamiltonian is

$$
H_{B,m}(k_y) = |\mathcal{N}|^2 \lambda_{\mathrm{R}} k_y \rho_z \zeta_y + m_{\mathrm{eff}} \rho_0 \zeta_x + m_{\mathrm{eff}}' \rho_y \zeta_y,
\tag{S20}
$$

where $m_{\mathrm{eff}}' = |\mathcal{N}|^2 \lambda_{\mathrm{R}}$. The two mass terms will compete with each other. We can project the effective Hamiltonian into a block-diagonal form corresponding to different directions of the Volterra cut-and-glue line linking two dislocation modes by using the basis transformation

$$
U = \frac{1}{\sqrt{2}}
\begin{pmatrix}
-1 & 0 & 1 & 0 \\
0 & -1 & 0 & 1 \\
0 & 1 & 0 & 1 \\
1 & 0 & 1 & 0
\end{pmatrix}.
\tag{S21}
$$

On this basis, the effective Hamiltonian is given by

$$
H_{B,m}(k_y) = H_{B,m}^+(k_y) \oplus H_{B,m}^-(k_y),
\tag{S22}
$$

where $H_{B,m}^{\pm}(k_y)$ are given by

$$
H_{B,m}^{\pm}(k_y) = \lambda_{\mathrm{R}} k_y \varrho_y + m_{\mathrm{eff}} \varrho_x \pm m_{\mathrm{eff}}' \varrho_z.
\tag{S23}
$$

Here, we have $m_{\mathrm{eff}} = 0$ and $m_{\mathrm{eff}}' \neq 0$ if $d_{x^2-y^2}$-paring $\Delta_{\mathrm{i}} = 0$. The effective mass $m_{\mathrm{eff}}'$ will flips sign on the different directions of the Volterra cut-and-glue line and create a domain wall with localized Majorana zero modes at two dislocation cores. If $m_{\mathrm{eff}} \neq 0$, the sum of a mass term will gap out the Majorana dislocation modes. The $d_{x^2-y^2}$-paring bring an energy gap between two pairs of dislocation modes shown in Fig. 4 of our main text.
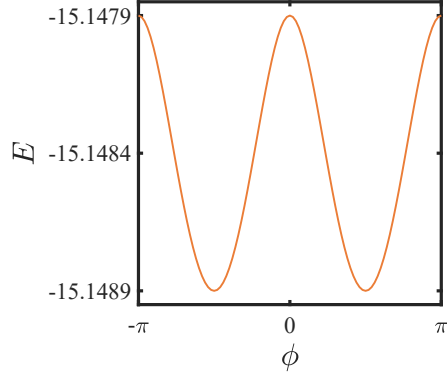
FIG. S2. The Free-energy with SOC and $d + id$-wave pairing that the phase difference $\phi$ between $s$-wave and $d$-wave pairing.

## FREE ENERGY

For the spontaneous TRS breaking with SOC, we take the $d + id$-wave pairing as $\Delta(\boldsymbol{k}) = [e^{i\phi}\Delta_i(-2\cos k_x + 2\cos k_y)\sigma_0 + \boldsymbol{d} \cdot \boldsymbol{\sigma}]is_y$. The free-energy is

$$F(\phi) = \sum_{n,k_x,k_y} E(\boldsymbol{k}), \tag{S24}$$

where $n = 1, 2, 3, 4$ is the label of occupied bands and the $\phi$ is the phase difference between the two gap functions. The free-energy calculation shows the minimum energy at $\phi = \pm\pi/2$ in Fig. S2.

## MORE INFORMATION ON RPA APPROACH

Next, we discuss the possible application of the theory to $Sr_2RuO_4$. Due to the inherent multi-orbital nature of $Sr_2RuO_4$ [1–4], we use a $(d_{xz}, d_{yz})$ two-orbital model [5] to illustrate the essential physics. The normal state Hamiltonian reads

$$H_{\mathrm{n}} = \epsilon(\boldsymbol{k})\sigma_0 + \widetilde{\epsilon}(\boldsymbol{k})\sigma_3 + \epsilon''(\boldsymbol{k})\sigma_1, \tag{S25}$$

where, $\epsilon_{\boldsymbol{k}} = -(t + \widetilde{t})(_x +_y) - \mu$; $\widetilde{\epsilon}_{\boldsymbol{k}} = -(t - \widetilde{t})(_x -_y)$; $\epsilon''_{\boldsymbol{k}} = -4t''_{xy}$. Here $t$ labels the nearest-neighbor hopping integral of the $d_{xz(yz)}$ orbital along the $x(y)$ direction, $\widetilde{t}$ is that of the $d_{xz(yz)}$ orbital along the $y(x)$ direction, and $t''$ denotes the hybridization of the two orbitals between next-nearest-neighboring sites. The band parameters used in our calculation are $(t, \widetilde{t}, t'', \mu) = (1, 0.1, 0.05, 1)$ [5]. Fig. S3(a) shows the Fermi surface in the Brillouin zone (BZ).
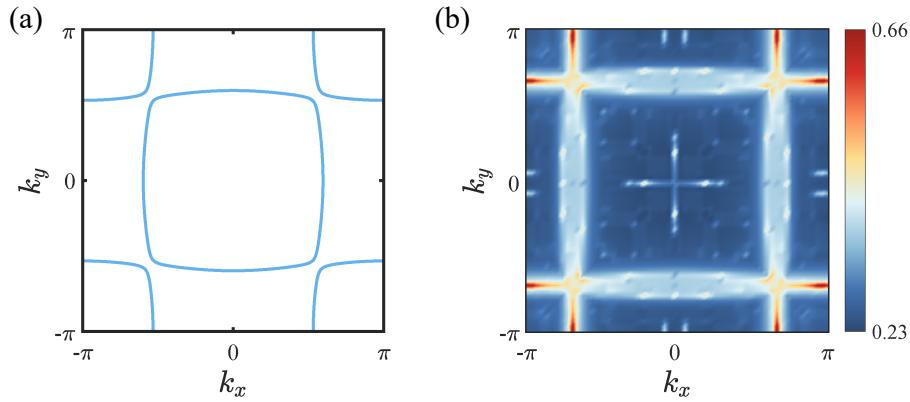


FIG. S3. (a) Fermi surface in the Brillouin Zone. and (b) Distribution of $\chi^{(0)}(i\omega = 0)$ in the Brillouin Zone.

147

We adopt the following extended Hubbard model Hamiltonian in our RPA calculations:

$$H = H_n + H_{int}$$

$$H_{int} = U \sum_{i\mu} n_{i\mu\uparrow} n_{i\mu\downarrow} + V \sum_{i\mu<\nu} n_{i\mu} n_{i\nu}$$

$$+ J_H \sum_{i,\mu<\nu} \left[ \sum_{\sigma\sigma'} c_{i\mu\sigma}^\dagger c_{i\nu\sigma'}^\dagger c_{i\mu\sigma'} c_{i\nu\sigma} + \left( c_{i\mu\uparrow}^\dagger c_{i\mu\downarrow}^\dagger c_{i\nu\downarrow} c_{i\nu\uparrow} + h.c. \right) \right]. \tag{S26}$$

Here, $H_n$ is the normal Hamiltonian. The $U$, $V$, and $J_H$ terms denote the intra-orbital, inter-orbital coulomb repulsion and the Hund's rule coupling as well as the pair hopping. The spacial rotation symmetry requires $U = V + 2J_H$. The interaction parameters used in our calculation are $(U, J_H, V) = (1.2t, 0.2U, 0.6U)$.

According to the standard multi-orbital RPA approach [6–15], the following bare susceptibility is defined for the non-interacting case, namely,

$$\chi_{st}^{(0)pq}(\boldsymbol{k}, \tau) \equiv \frac{1}{N} \sum_{\boldsymbol{k}_1 \boldsymbol{k}_2} \left\langle T_\tau c_p^\dagger(\boldsymbol{k}_1, \tau) c_q(\boldsymbol{k}_1 + \boldsymbol{k}, \tau) \right.$$

$$\left. \times c_s^\dagger(\boldsymbol{k}_2 + \boldsymbol{k}, 0) c_t(\boldsymbol{k}_2, 0) \right\rangle_0, \tag{S27}$$

Here $\langle \cdots \rangle_0$ denotes the thermal average for the noninteracting system, $T_\tau$ denotes the time-ordered product, and $p, q, s, t = 1, 2$ are the orbital indices. Fourier transformed to the imaginary frequency space, the bare susceptibility can be expressed by the following explicit formulism:

$$\chi_{st}^{(0)pq}(\boldsymbol{k}, i\omega_n) = \frac{1}{N} \sum_{\boldsymbol{k}'\alpha\beta} \xi_t^\alpha(\boldsymbol{k}') \xi_p^{\alpha*}(\boldsymbol{k}') \xi_q^\beta(\boldsymbol{k}' + \boldsymbol{k})$$

$$\times \xi_s^{\beta*}(\boldsymbol{k}' + \boldsymbol{k}) \frac{\eta_F(\varepsilon_{\boldsymbol{k}'+\boldsymbol{k}}^\beta - \mu_c) - \eta_F(\varepsilon_{\boldsymbol{k}'}^\alpha - \mu_c)}{i\omega_n + \varepsilon_{\boldsymbol{k}'}^\alpha - \varepsilon_{\boldsymbol{k}'+\boldsymbol{k}}^\beta}, \tag{S28}$$

where $\alpha, \beta = 1, 2$ are band indices, $\varepsilon_{\boldsymbol{k}}^\alpha$ and $\xi_l^\alpha(\boldsymbol{k})$ are the $\alpha$-th eigenvalue and eigenvector of the $H_n(\boldsymbol{k})$ matrix, respectively, and $\eta_F$ is the Fermi-Dirac distribution function. The distribution of the largest eigenvalue of $\chi^{(0)}(\boldsymbol{q}, i\omega = 0)$ is shown in Fig. S3(b).

When interactions are turned on, we define the following renormalized spin and charge susceptibilities,

$$\chi_{st}^{(c)pq}(\boldsymbol{k}, \tau) \equiv \frac{1}{2N} \sum_{\boldsymbol{k}_1, \boldsymbol{k}_2, \sigma_1, \sigma_2} \left\langle T_\tau c_{p,\sigma_1}^\dagger(\boldsymbol{k}_1, \tau) c_{q,\sigma_1}(\boldsymbol{k}_1 + \boldsymbol{k}, \tau) \right.$$

$$\left. c_{s,\sigma_2}^\dagger(\boldsymbol{k}_2 + \boldsymbol{k}, 0) c_{t,\sigma_2}(\boldsymbol{k}_2, 0) \right\rangle,$$

$$\chi_{st}^{(s)pq}(\boldsymbol{k}, \tau) \equiv \frac{1}{2N} \sum_{\boldsymbol{k}_1, \boldsymbol{k}_2, \sigma_1, \sigma_2} \left\langle T_\tau c_{p,\sigma_1}^\dagger(\boldsymbol{k}_1, \tau) c_{q,\sigma_1}(\boldsymbol{k}_1 + \boldsymbol{k}, \tau) \right.$$

$$\left. c_{s,\sigma_2}^\dagger(\boldsymbol{k}_2 + \boldsymbol{k}, 0) c_{t,\sigma_2}(\boldsymbol{k}_2, 0) \right\rangle \sigma_1 \sigma_2. \tag{S29}$$

In the RPA level, the renormalized spin/charge susceptibilities for the system are,

$$\chi^{(s)}(\boldsymbol{q}, i\nu) = \left[ I - \chi^{(0)}(\boldsymbol{q}, i\nu) U^{(s)} \right]^{-1} \chi^{(0)}(\boldsymbol{q}, i\nu),$$

$$\chi^{(c)}(\boldsymbol{q}, i\nu) = \left[ I + \chi^{(0)}(\boldsymbol{q}, i\nu) U^{(c)} \right]^{-1} \chi^{(0)}(\boldsymbol{q}, i\nu), \tag{S30}$$

where $\chi^{(s,c)}(\boldsymbol{q}, i\nu_n)$, $\chi^{(0)}(\boldsymbol{q}, i\nu_n)$ and $U^{(s,c)}$ are $4 \times 4$ matrices. Labelling orbital $\{d_{xz}, d_{yz}\}$ as $\{1, 2\}$, the nonzero elements of the matrix $U_{l_3 l_4}^{(s,c)l_1 l_2}$ are listed as follows:

$$U_{11}^{(s)11} = U_{22}^{(s)22} = U$$

$$U_{22}^{(s)11} = U_{11}^{(s)22} = J_H$$

$$U_{12}^{(s)12} = U_{21}^{(s)21} = J_H$$
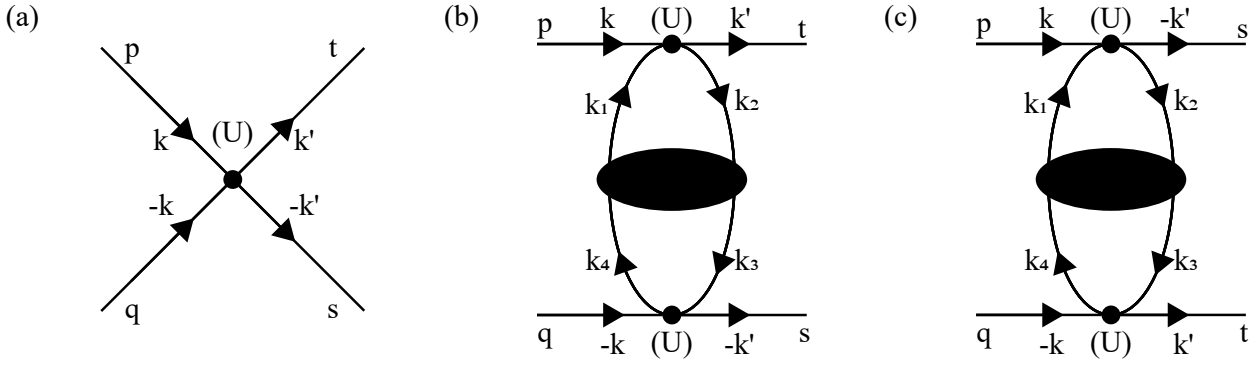
$$U_{21}^{(s)12} = U_{12}^{(s)21} = V \tag{S31}$$

FIG. S4. The three processes which contribute the renormalized effective vertex considered in the RPA, with (a) the bare interation vertex and (b) (c) the two second order perturbation processes during which spin or charge fluctuations are exchanged between a cooper pair.

$$
\begin{aligned}
U_{11}^{(c)11} &= U_{22}^{(c)22} = U \\
U_{22}^{(c)11} &= U_{11}^{(c)22} = 2V - J_H \\
U_{12}^{(c)12} &= U_{21}^{(c)21} = J_H \\
U_{21}^{(c)12} &= U_{12}^{(c)21} = 2J_H - V
\end{aligned}
\tag{S32}
$$

Note that there is a critical interaction strength $U_c$ which depends on the ratio $V/U$ and dopping. When $U > U_c$, the denominator matrix $I - \chi^{(0)}(\boldsymbol{q}, i\nu) U^{(s)}$ in Eq. (S30) will have zero eigenvalues for some $\boldsymbol{q}$ and the renormalized spin susceptibility diverges there, which invalidates the RPA treatment. This divergence of spin susceptibility for $U > U_c$ implies magnetic order. When $U < U_c$, the short-ranged spin or charge fluctuations would mediate Cooper pairing in the system.

Let's consider a Cooper pair with momentum/orbital $(\boldsymbol{k}'t, -\boldsymbol{k}'s)$, which could be scattered to $(\boldsymbol{k}p, -\boldsymbol{k}q)$ by exchanging charge or spin fluctuations. At the RPA level, The effective interaction induced by this process is as follow,

$$
V_{\text{eff}}^{\text{RPA}} = \frac{1}{N} \sum_{pqst, \boldsymbol{k}\boldsymbol{k}'} \Gamma_{st}^{pq}(\boldsymbol{k}, \boldsymbol{k}') c_p^\dagger(\boldsymbol{k}) c_q^\dagger(-\boldsymbol{k}) c_s(-\boldsymbol{k}') c_t(\boldsymbol{k}'),
\tag{S33}
$$

We consider the three processes in Fig. S4 which contribute to the effective vertex $\Gamma_{st}^{pq}(\boldsymbol{k}, \boldsymbol{k}')$, where (a) represents the bare interaction vertex, (b) and (c) represent the two second order perturbation processes during which spin or charge fluctuations are exchanged between a cooper pair. In the singlet channel, the effective vertex $\Gamma_{st}^{pq}(\boldsymbol{k}, \boldsymbol{k}')$ is given as follow,

$$
\begin{aligned}
\Gamma_{st}^{pq(s)}(\boldsymbol{k}, \boldsymbol{k}') = {}& \left( \frac{U^{(c)} + 3U^{(s)}}{4} \right)_{qs}^{pt} + \\
& \frac{1}{4} \left[ 3U^{(s)} \chi^{(s)}(\boldsymbol{k} - \boldsymbol{k}') U^{(s)} - U^{(c)} \chi^{(c)}(\boldsymbol{k} - \boldsymbol{k}') U^{(c)} \right]_{qs}^{pt} + \\
& \frac{1}{4} \left[ 3U^{(s)} \chi^{(s)}(\boldsymbol{k} + \boldsymbol{k}') U^{(s)} - U^{(c)} \chi^{(c)}(\boldsymbol{k} + \boldsymbol{k}') U^{(c)} \right]_{qt}^{ps},
\end{aligned}
\tag{S34}
$$

while in the triplet channel, it is

$$
\begin{aligned}
\Gamma_{st}^{pq(t)}(\boldsymbol{k}, \boldsymbol{k}') = {}& \left( \frac{U^{(c)} - U^{(s)}}{4} \right)_{qs}^{pt} - \\
& \frac{1}{4} \left[ U^{(s)} \chi^{(s)}(\boldsymbol{k} - \boldsymbol{k}') U^{(s)} + U^{(c)} \chi^{(c)}(\boldsymbol{k} - \boldsymbol{k}') U^{(c)} \right]_{qs}^{pt} + \\
& \frac{1}{4} \left[ U^{(s)} \chi^{(s)}(\boldsymbol{k} + \boldsymbol{k}') U^{(s)} + U^{(c)} \chi^{(c)}(\boldsymbol{k} + \boldsymbol{k}') U^{(c)} \right]_{qt}^{ps},
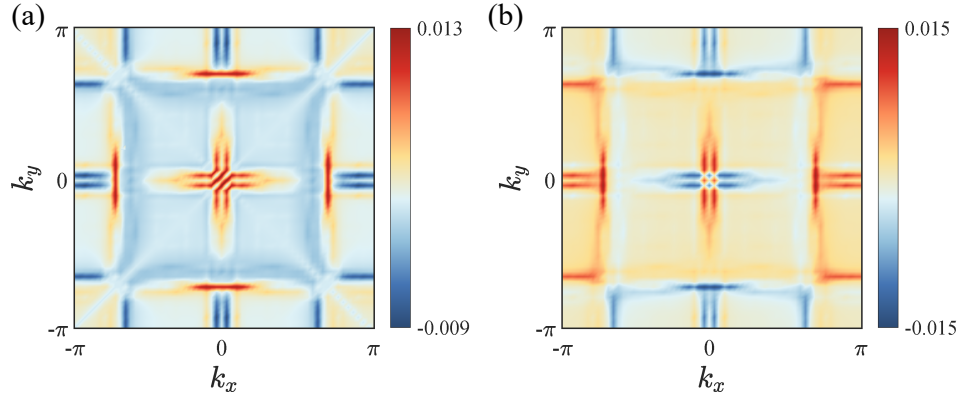\end{aligned}
\tag{S35}
$$

149

FIG. S5. The distribution of the relative gap function. (a) Gap function of $\Delta_{11}(\boldsymbol{k}) - \Delta_{22}(\boldsymbol{k})$. (b) Gap function of $\Delta_{11}(\boldsymbol{k}) + \Delta_{22}(\boldsymbol{k})$.

The effective Hamiltonian in the RPA level is shown as follow,

$$H_{\text{eff}} = \sum_{\boldsymbol{k}\alpha\sigma} c^{\dagger}_{\boldsymbol{k}\alpha\sigma} c_{\boldsymbol{k}\alpha\sigma} \varepsilon^{\alpha}_{\boldsymbol{k}} + \frac{1}{N} \sum_{\boldsymbol{k}\boldsymbol{q}} V^{\alpha\beta}(\boldsymbol{k},\boldsymbol{q}) c^{\dagger}_{\boldsymbol{k}\alpha\uparrow} c^{\dagger}_{-\boldsymbol{k}\alpha\downarrow} c_{-\boldsymbol{q}\beta\downarrow} c_{\boldsymbol{q}\beta\uparrow},\tag{S36}$$

where,

$$V^{\alpha\beta}(\boldsymbol{k},\boldsymbol{q}) = \sum_{pqst,\boldsymbol{k}\boldsymbol{q}} \Gamma^{pq}_{st}(\boldsymbol{k},\boldsymbol{q}) \xi^{\alpha,*}_p(\boldsymbol{k}) \xi^{\alpha,*}_q(-\boldsymbol{k}) \xi^{\beta}_s(-\boldsymbol{q}) \xi^{\beta}_t(\boldsymbol{q}).\tag{S37}$$

The effective Mean-Field Hamiltonian is given as follow,

$$H_{\text{MF}} = \sum_{\boldsymbol{k}\alpha\sigma} c^{\dagger}_{\boldsymbol{k}\alpha\sigma} c_{\boldsymbol{k}\alpha\sigma} \varepsilon^{\alpha}_{\boldsymbol{k}} + \left[ \frac{1}{N} \sum_{\boldsymbol{k}\boldsymbol{q}\alpha\beta} V^{\alpha\beta}(\boldsymbol{k},\boldsymbol{q}) c^{\dagger}_{\boldsymbol{k}\alpha\uparrow} c^{\dagger}_{-\boldsymbol{k}\alpha\downarrow} \langle c_{-\boldsymbol{q}\beta\downarrow} c_{\boldsymbol{q}\beta\uparrow} \rangle + \text{h.c.} \right],\tag{S38}$$

a self-consistent pairing gap equation can be derived,

$$\Delta_{\alpha}(\boldsymbol{k}) \equiv \frac{1}{N} \sum_{\boldsymbol{q}\gamma\delta} V^{\alpha\beta}(\boldsymbol{k},\boldsymbol{q}) \langle c_{-\boldsymbol{q}\beta\downarrow} c_{\boldsymbol{q}\beta\uparrow} \rangle.\tag{S39}$$

Which gives the linearised gap equation (LGE) when linearised near $T_c$:

$$\Delta_{\alpha}(\boldsymbol{k}) = -\sum_{\beta\boldsymbol{q}} V^{\alpha\beta}(\boldsymbol{k},\boldsymbol{q}) \times \frac{\tanh(\frac{\beta_c}{2} \left| \varepsilon^{\beta}_{\boldsymbol{q}} - \mu_c \right|)}{\left| \varepsilon^{\beta}_{\boldsymbol{q}} - \mu_c \right|} \times \Delta_{\beta}(\boldsymbol{q})\tag{S40}$$

After projecting the gap function to orbital-basis, our calculations show that the leading pairing symmetry is singlet inter-orbital $B1g$ in $\tau_z$ form, with the near-zero $\Delta_{12}(\boldsymbol{k})$. The pairing gap function $\Delta_{11}(\boldsymbol{k}) - \Delta_{22}(\boldsymbol{k})$ and $\Delta_{11}(\boldsymbol{k}) + \Delta_{22}(\boldsymbol{k})$ are shown in Fig. S5(a) and (b) respectively.

## REAL SPACE TOPOLOGICAL INVARIANT

In Fig.2(e) of the main text, we observe the presence of Majorana zero modes localized at each corner. To understand the corner Majorana zero modes, we can define the local invariant at Wyckoff position as the real space invariant (RSI) based on the $P4mm$ group. In the theory of obstructed atomic insulators (OAIs), topological trivial insulators can transition into a higher-order topological phase when the Wannier charge center moves to an unoccpied position from the occpied position of lattice unit-cell. The OAI hosts quantized fractional corner charge at each corner in 2D case.

Referring to Table S1, there are two Wcykoff positions: $a = (0,0)$ and $b = (\frac{1}{2}, \frac{1}{2})$, and the RSIs as $(\delta_a, \delta_b)$ that are defined at two Wyckoff positions according to the EBRs theory. The non-zero RSI index indicate the localization of the Wannier charge

center the Wyckoff position $n$, which represented by $\delta_n$. In our lattice configuration, the position $a$ is occupied by atoms, and the position $b$ is unoccupied. Consequently, the $d+id$ superconductor can transition into a second-order topological phase when $\delta_b$ is non-zero. Based on the space group $G$, referencing to the tools given in BANDREP (www.cryst.ehu.es/cryst/bandrep), the two RSIs defined at $b$ as

$$\delta_1 = -m(\overline{E}_2@b) + m(\overline{E}_1@b), \tag{S41}$$

$$\delta_2 = m(\overline{E}_2@b) \mod 2. \tag{S42}$$

For the second-order topological phase shown in Fig. 2(b) of the main text, the band representation of the occupied bands reads

$$B_{\text{SOTI}} = \overline{E}_2@a \oplus \overline{E}_2@b, \tag{S43}$$

while that of the higher-order trivial phase is

$$B_{\text{Trival}} = \overline{E}_1@a \oplus \overline{E}_2@a. \tag{S44}$$

Thus, we have the RSI at Wcykoff position $b$, i.e., $(\delta_1, \delta_2) = (0, 0)$ and $(-1, 1)$ for the higher-order trivial phase and non-trivial phase, respectively. Therefore, the second-order TSC corresponds to a superconductor-OAI phase.

\* These authors contributed equally to this work.
† hu.lunhui.zju@gmail.com
‡ donghuixu@cqu.edu.cn

[1] N. Read and D. Green, Paired states of fermions in two dimensions with breaking of parity and time-reversal symmetries and the fractional quantum hall effect, Physical Review B **61**, 10267 (2000).
[2] E. Taylor and C. Kallin, Intrinsic hall effect in a multiband chiral superconductor in the absence of an external magnetic field, Physical Review Letters **108**, 157001 (2012).
[3] K. Wysokiński, J. F. Annett, and B. Györffy, Intrinsic optical dichroism in the chiral superconducting state of sr 2 ruo 4, Physical Review Letters **108**, 077004 (2012).
[4] Z. Wang, J. Berlinsky, G. Zwicknagl, and C. Kallin, Intrinsic ac anomalous hall effect of nonsymmorphic chiral superconductors with an application to upt 3, Physical Review B **96**, 174511 (2017).
[5] W. Huang and Z. Wang, Possibility of mixed helical p-wave pairings in sr 2 ruo 4, Physical Review Research **3**, L042002 (2021).
[6] T. Takimoto, T. Hotta, and K. Ueda, Strong-coupling theory of superconductivity in a degenerate Hubbard model, Phys. Rev. B **69**, 104504 (2004).
[7] K. Yada and H. Kontani, Origin of weak pseudogap behaviors in $Na_{0.35}CoO_2$: Absence of small hole pockets, Journal of the Physical Society of Japan **74**, 2161 (2005).
[8] K. Kubo, Pairing symmetry in a two-orbital Hubbard model on a square lattice, Phys. Rev. B **75**, 224509 (2007).
[9] K. Kuroki, S. Onari, R. Arita, H. Usui, Y. Tanaka, H. Kontani, and H. Aoki, Unconventional pairing originating from the disconnected Fermi surfaces of superconducting $LaFeAsO_{1-x}F_x$, Phys. Rev. Lett. **101**, 087004 (2008).
[10] S. Graser, T. A. Maier, P. J. Hirschfeld, and D. J. Scalapino, Near-degeneracy of several pairing channels in multiorbital models for the Fe pnictides, New J. Phys. **11**, 025016 (2009).
[11] T. A. Maier, S. Graser, P. J. Hirschfeld, and D. J. Scalapino, $d$-wave pairing from spin fluctuations in the $K_xFe_{2-y}Se_2$ superconductors, Phys. Rev. B **83**, 100515 (2011).
[12] F. Liu, C.-C. Liu, K. Wu, F. Yang, and Y. Yao, $d + id'$ chiral superconductivity in bilayer Silicene, Phys. Rev. Lett. **111**, 066804 (2013).
[13] X. Wu, J. Yuan, Y. Liang, H. Fan, and J. Hu, $g$-wave pairing in $BiS_2$ superconductors, EPL (Europhysics Letters) **108**, 27006 (2014).
[14] T. Ma, F. Yang, H. Yao, and H.-Q. Lin, Possible triplet $p+ip$ superconductivity in graphene at low filling, Phys. Rev. B **90**, 245114 (2014).
[15] L.-D. Zhang, F. Yang, and Y. Yao, Possible electric-field-induced superconducting states in doped Silicene, Sci. Rep. **5**, 8203 (2015).

**Acknowledgements**